Crystal Engineering and Bifunctionality in Spin-Crossover Materials

Laurence Jonas Kershaw Cook

Submitted in accordance with the requirements for the degree of Doctor of Philosophy.

The University of Leeds

School of Chemistry

June 2014

The candidate confirms that the work submitted is his own except where work which has formed part of jointly authored publications has been included. The contribution of the candidate and the other authors to this work has been explicitly indicated. The candidate confirms that appropriate credit has been given where reference has been made to the work of others.

Acknowledgements

I should like to begin by thanking Professor Malcolm Halcrow without whom I would never have been gifted with such a wonderful opportunity to further both myself and, in some small way, the very frontiers of science. His countless suggestions from the vast breadth and depth of his knowledge has proved simply invaluable to the completion of this work.

I must also let it be known that I am greatly appreciative of the following technical staff for their positive contributions: Mr. Simon Barrett for acquisition of low temperature NMR spectra, Dr. Helena Shepherd for the training and assistance she provided during some of the more involved X-ray diffraction experiments and Mrs Tanya Marinko-Covell and Mr. Ian Blakeley for running the mass spectrometric and microanalytical measurements respectively.

I express my gratitude to the other occupants of the office/laboratory, namely members of the Halcrow and McGowan groups past and present for tolerating me and my awkward ways for the past three plus years, and for the useful chemical discussions we would have upon occasion. Raf I thank you for arriving when you did, for your “Ponglish” and your assistance and advice during the writing process. A thank you is also due to Flora Thorp-Greenwood for the sample which she prepared and supplied of 4-methyl-2,6-di(pyrazol-1’-yl)pyridine whose coordination chemistry is the subject of discussion in Chapter 5.

I am, of course, extremely grateful to my family for the continued support and encouraging me to always achieve my best. Thank you to Rachel Richardson for proving that Vardis aren’t the only great thing from Wakefield. Lastly, and definitely not least, I express thanks to my friends, in particular Joanne Payne, James Harris and Chris Warburton for keeping me in line, both with respect to my Ph. D and beyond. We may be restless and wild but together we can stand the night.

One paper has been published at the time of writing, which contains results from Chapters 2 and 3 of the thesis. The reference is: “Iron(II) and cobalt(II) complexes of tris-azinyl analogues of 2,2’:6’,2’’-terpyridine”, L.J. Kershaw Cook, F. Tuna and M.A. Halcrow*, Dalton Transactions 2013, 42, 2254–2265. Although I contributed to the preparation of the manuscript the final version was completed by my supervisor Prof Halcrow, who is also the corresponding author on the paper. The description of these results in Chapters 2 and 3 is not directly reproduced from the paper, and has been written in my own words.

Abstract

This thesis focuses on crystal engineering metal salts of 2,2':6',2''-terpyridine and 2,6-di(pyrazol-1'-yl)pyridine to tune and better understand the cooperative spin crossover in the solid state and incorporation of a second functionality towards bifunctional spin crossover materials.

Chapter 1 can be considered an introduction to the phenomenon of spin crossover in first row transition metal complexes and outlines its discovery, recent developments and progression towards real-world application.

Chaper 2 is a discussion of the methodology of synthetic efforts undertaken in the acquisition of the wealth of *tris*-chelating organic compounds whose coordination chemistry is the subject of later chapters.

Chapter 3 details the spectroscopic, electrochemical and magnetic properties of cobalt(II) and iron(II) complexes of *tris*-azinyl analogues of 2,2':6',2''-terpyridine in efforts towards tuning their electronic spin-equilibria.

Chapter 4 presents a series of novel ruthenium(II) based materials exhibiting enhanced room temperature emission and their incorporation into an inert spin crossover host material. Retention of parent functionalities is screened for over an operable temperature regime.

Chapter 5 concerns iron(II) complex salts of 2,6-di(pyrazol-1'-yl)pyridine derivatives, whose ligand backbones are modified in an attempt to tune the solid state spin crossover behaviour both electronically and sterically.

Chapter 6 is an account of all synthetic procedures carried out during this work, their standard characterisation and details the instrumentation performed on all materials which are the subject of discussion in this thesis.

Contents

Figures

Tables

List of Abbreviations

mA	milliampere
Å	Ångstrom; 10^{-10} m
bipy	2,2'-bipyridine
1-bpp	2,6-di(pyrazol-1'-yl)pyridine
3-bpp	2,6-di(pyrazol-3'-yl)pyridine
C	Celcius
ca.	*Circa*; approximately
cm	centimetre
D	dimension
d	doublet
dd	doublet of doublets
dt	doublet of triplets
δ	chemical shift in parts per million
Δ_o	ligand-field splitting energy (octahedral geometry)
Δ_T	ligand-field splitting energy (tetrahedral geometry)
DCM	dichloromethane
diglyme	2-methoxy ethyl ether
Dist	Distal
DMF	*N*,*N*-dimethylformamide
DMSO	dimethylsulfoxide
e.g.	*Exempli gratia*; for example
EI	Electron Impact
EPR	Electron Paramagnetic Resonance
eq.	equivalent
ES	Electrospray
et al.	*et alii*; and others
Et	ethyl

Eq.	equivalent
Fc	ferrocene
G	gauss, 10^{-4} tesla
g	grams
glyme	1,2-dimethoxy ethane
HMBC	Heteronuclear multiple bond correlation
HMQC	Heteronuclear multiple quantum correlation
HS	High Spin
hr	hours
Hz	hertz, cm^{-1}
Im	Imidazole
IR	infra-red
J	spin-spin coupling constant, Hz
K	Kelvin
LS	Low Spin
m	multiplet
M	Molarity; mol cm^{-3}
MHz	Mega Hertz; 10^6 Hz
m.p.	melting point
Me	methyl
min.	minutes
mg	milligram
ml	millilitres
mm	millimetres
mmol	millomole
MLCT	Metal to Ligand Charge Transfer
mol	moles
nm	nanometre

NMR	Nuclear Magnetic Resonance
NRD	Non-radiative decay
Ph	Phenyl
pH	potential of hydrogen
ppm	parts per million
^{i}Pr	Isopropyl
Prox	Proximal
Py	Pyridine
Pym	Pyrimidine
Pyz	Pyrazole
Pz	Pyrazine
q	quartet
s	Singlet
SAM	Self-assembled Monolayer
SCO	Spin Crossover
sp	septuplet
Sq.	Squared
SQUID	Superconducting Quantum Interference Device
t	triplet
TBAT	tertiary butyl ammonium tetrafluroborate
TBAH	tertiary butyl ammonium hexafluorophosphate
td	triplet of doublets
TFE	trifluoroethanol
tt	triplet of triplets
$T_{1/2}$	Spin-transition temperature midpoint
terpy	2,6-di(2'-pyridyl)pyridine
terpyOH	4-hydroxy-2,6-di(2'-pyridyl)pyridine
THF	tetrahydrofuran

TMS	tetramethylsilane
TPB	tetraphenylborate
UV	Ultra Violet
Vs	*versus*; against
V	volt
VE	Vibrational excitement

Ligand Abbreviations

Bipypz	2,6-di(2’-pyridyl)pyrazine
Bipzpy	2,6-di(2’-pyrazinyl)pyridine
Terpz	2,6-di(2’-pyrazinyl)pyrazine
4-bipympy	2,6-di(4’-pyrimidyl)pyridine
4-bipympz	2,6-di(4’-pyrimidyl)pyrazine
2-bipympy	2,6-di(2’-pyrimidyl)pyridine
2-bipympz	2,6-di(2’-pyrimidyl)pyrazine
bipzpyOH	2,6-di(2’-pyrazinyl)-4-hydroxy pyridine
bipzpyOMe	2,6-di(2’-pyrazinyl)-4-methoxy pyridine
2-bipympyOH	2,6-di(2’-pyrimidyl)-4-hydroxy pyridine
2-bipympyOMe	2,6-di(2’-pyrimidyl)-methoxy pyridine
bitrzpy	2,6-di(1’,2’,4’-triazin-3’-yl)pyridine
MeImpy	2,6-di(1’-methylimidazolium-3’-yl)pyridine dibromide
PrImpy	2,6-di(1’-isopropylimidazolium-3’-yl)pyridine dibromide
Ctpy	2,2’:6’,4’’-terpyridine
Pybzim	2,6-di(*N*-{4’’-pyridyl}benzimidazol-2’-yl)pyridine
Phbzim	2,6-di(*N*-phenylbenzimidazol-2’-yl)pyridine
1-bpp	2,6-di(pyrazol-1’-yl)pyridine
1-bppMe	4-methyl-2,6-di(pyrazol-1’-yl)pyridine

1-tpp	2,4,6-tri(pyrazol-1’-yl)pyridine
1-bppCOOH	2,6-di(pyrazol-1’-yl)pyridine-4-carboxylic acid
1-bppNH_2	4-amino-2,6-di(pyrazol-1’-yl)pyridine
1-bppNO_2	4-nitro-2,6-di(pyrazol-1’-yl)pyridine
1-bppOH	4-hydroxy-2,6-di(pyrazol-1’-yl)pyridine
1-bppOMe	4-methoxy-2,6-di(pyrazol-1’-yl)pyridine
1-bppSH	4-mercapto-2,6-di(pyrazol-1’-yl)pyridine
1-bppSMe	4-thiomethyl-2,6-di(pyrazol-1’-yl)pyridine
1-bppDS	Bis(2,6-di{pyrazol-1’-yl}pyridine-4-yl)disulfide
1-bppF	4-fluoro-2,6-di(pyrazol-1’-yl)pyridine
1-bppCl	4-chloro-2,6-di(pyrazol-1’-yl)pyridine
1-bppBr	4-bromo-2,6-di(pyrazol-1’-yl)pyridine
1-bppI	4-iodo-2,6-di(pyrazol-1’-yl)pyridine
qpbpy	2,2,6,6-tetrakis(pyrazol-1’-yl)-4,4-bipyridine

Complex Salt List

The full structures of all of the organic compounds and complex salts are given in Chapter 6.

$[M(bipypz)_2][BF_4]_2$	M= Fe (**1a**), Co (**1b**)	$[M(bipzpy)_2][BF_4]_2$	M= Fe (**2a**), Co (**2b**)
$[M(terpz)_2][BF_4]_2$	M= Fe (**3a**), Co (**3b**)	$[M(4\text{-}bipympy)_2][BF_4]_2$	M= Fe (**4a**), Co (**4b**)
$[M(4\text{-}bipympz)_2][BF_4]_2$	M= Fe (**5a**), Co (**5b**)	$[M(bitrzpy)_2][BF_4]_2$	M= Fe (**6a**), Co (**6b**)
$[M(bipzpyOH)_2][BF_4]_2$	M= Fe (**7a**), Co (**7b**)	$[M(2\text{-}bipympyOH)_2][BF_4]_2$	M= Fe (**8a**), Co (**8b**)
$[M(terpy)_2][BF_4]_2$	M= Fe (**9a**), Co (**9b**)	$[M(terpyOH)_2][BF_4]_2$	M= Fe (**10a**), Co (**10b**)
$[Ru(bipypz)_2][X]_2$	X = BF_4^- (**11a**), PF_6^- (**11b**)	$[Ru(bipzpy)_2][X]_2$	X = BF_4^- (**12a**)
$[Ru(terpz)_2][X]_2$	X = BF_4^- (**13a**), PF_6^- (**13b**)	$[Ru(4\text{-}bipympy)_2][X]_2$	X = BF_4^- (**14a**), PF_6^- (**14b**)
$[Ru(bitrzpy)_2][X]_2$	X = BF_4^- (**15a**), PF_6^- (**15b**)	$[Ru(bipzpyOH)_2][X]_2$	X = BF_4^- (**16a**), PF_6^- (**16b**)
$[Ru(2\text{-}bipympyOH)_2][X]_2$	X = BF_4^- (**17a**), PF_6^- (**17b**)	$[Ru(terpy)_2][X]_2$	X = BF_4^- (**18a**)
$[Ru(terpyOH)_2][X]_2$	X = BF_4^- (**19a**), PF_6^- (**19b**)	$[Ru(MeImpy)_2][X]_2$	X = BF_4^- (**20a**)
$[Ru(PrImpy)_2][X]_2$	X = BF_4^- (**21a**)	$[Ru(Cterpy)(terpy)][X]_2$	X = BF_4^- (**22a**)
$[Ru(1\text{-}bpp)_2][X]_2$	X = BF_4^- (**23a**)	$[Ru(1\text{-}bpp)(terpy)][X]_2$	X = BF_4^- (**24a**)
$[Fe(1\text{-}bpp)_2][X]_2$	X = BF_4^- (**25a**)	$[Fe(qpbpy)_2][X]_2$	X = BF_4^- (**26a**)
$[Fe(1\text{-}bppMe)_2][X]_2$	X = BF_4^- (**27a**), ClO_4^- (**27b**), PF_6^- (**27c**), $CF_3SO_3^-$ (**27d**)	$[Fe(1\text{-}tpp)_2][X]_2$	X = BF_4^- (**28a**), ClO_4^- (**28b**), PF_6^- (**28c**)
$[Fe(1\text{-}bppCOOH)_2][X]_2$	X = BF_4^- (**29a**)	$[Fe(1\text{-}bppNH_2][X]_2$	X = BF_4^- (**30a**)
$[Fe(1\text{-}bppNO_2][X]_2$	X = BF_4^- (**31a**),	$[Fe(1\text{-}bppOH)_2][X]_2$	X = BF_4^- (**32a**),

			ClO_4^- (**32b**), PF_6^- (**32c**)
$[Fe(1\text{-}bppOMe)_2][X]_2$	X = BF_4^- (**33a**), PF_6^- (**33c**)	$[Fe(1\text{-}bppSH)_2][X]_2$	X = BF_4^- (**34a**), ClO_4^- (**34b**), $CF_3SO_3^-$ (**34d**)
$[Fe(1\text{-}bppSMe)_2][X]_2$	X = BF_4^- (**35a**)	$[Fe(1\text{-}bppS2)_2][X]_2$	X = BF_4^- (**36a**), ClO_4^- (**36b**),
$[Fe(1\text{-}bppF)_2][X]_2$	X = BF_4^- (**37a**)	$[Fe(1\text{-}bppCl)_2][X]_2$	X = BF_4^- (**38a**)
$[Fe(1\text{-}bppBr)_2][X]_2$	X = BF_4^- (**39a**)	$[Fe(1\text{-}bppI)_2][X]_2$	X = BF_4^- (**40a**)
$[Ru(1\text{-}bppS2)_2][X]_2$	X = PF_6^- (**41c**)	$[Zn(1\text{-}bppS2)_2][X]_2$	X = BF_4^- (**42a**)

Ligand numbering scheme

Below is a series of diagrams to illustrate the numbering schemes employed in the discussion and characterisation of the *tris*-heterocyclic organic compounds. The numbering system in the homoleptic *bis*-chelate complexes is the same as that used for the free organics. At the foot of the diagram the numbering of the two heteroleptic complexes **22a** and **24a** is shown.

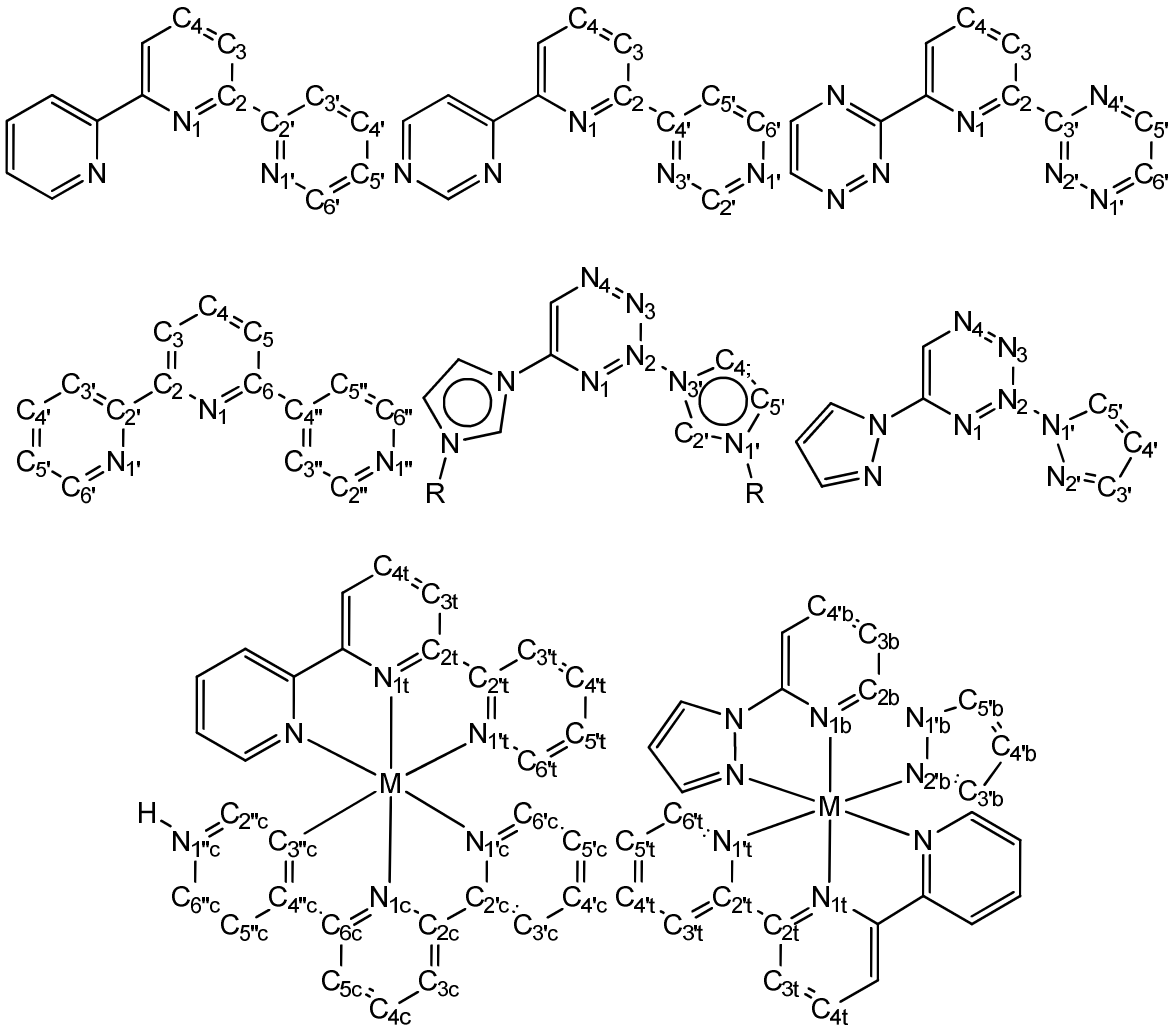

Chapter 1

Introduction

1 Introduction

1.1 The spin-crossover phenomenon

1.1.1 Background and discovery

A curious property of d^4-d^7 transition metal ion complexes is their ability to adopt either a high or low-spin electronic configuration depending upon the energy difference between the valence d-orbitals, the classification of which depends upon the coordination geometry.[1, 2] It can be seen that the electronic configurations possessed by a metal ion may have varying numbers of unpaired electrons, and on the surface it is obvious that this would cause the two to differ both magnetically and energetically (Figure 1).

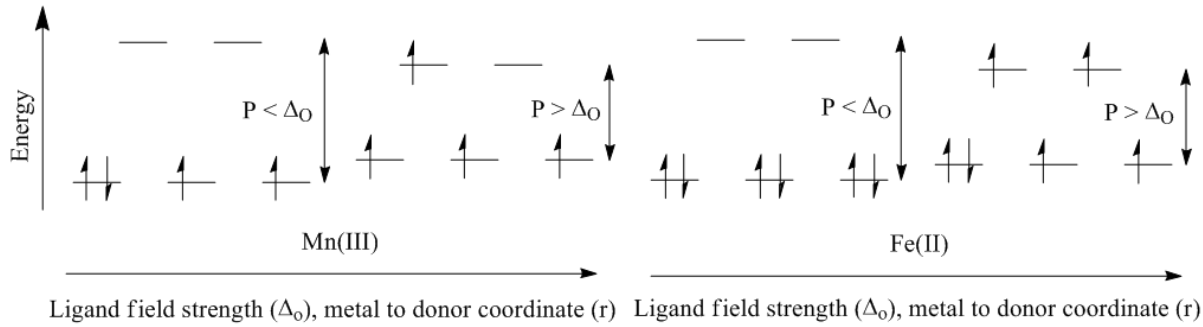

Figure 1 – Qualitative pictorial representation of the electronic configuration for low and high spin d_4 manganese(III) (left) and d_6 iron(II) (right); P is the mean spin-pairing energy for the individual metal ions.

Whether a high or low-spin configuration is adopted is an intrinsic property of the metal centre, its formal charge, the coordinated ligands and, if applicable, the nature of any counter-ions present.[2, 3] Halide and pseudo-halide donor ligands produce a very small splitting between the non-degenerate set of d-orbitals orbitals, routinely resulting in high-spin complexes. Carbonyl and phosphine ligand systems do the exact opposite, in which the destabilised orbital set is of such high energy that the penalty paid for the repulsion between a pair of electrons is less than that if one electron was to be promoted to the higher level and thus the low spin configuration dominates. Ligands which fall between these two extremes, particularly when coordinated to first row transition metals which possess inherently smaller ligand fields than their heavier homologues can result in complexes in which there is only a very small energy difference between the two different spin states. In such complexes it is possible to use an external stimulus, such as a change in pressure, temperature or irradiation with light of a specific wavelength to induce a change in the configuration of the valence d-electrons.[4-7]

The discovery of the first spin-crossover complex was made by Cambi *et al*. In 1931, however it was thought that the iron(III) *tris*(*N*,*N*-dialkyldithiocarbamato) complexes in question actually existed in two different isomeric co-crystallised forms in the solid, which

seemingly explained the anomalous magnetic moments lying halfway between the values expected for the high and low spin forms.[8] The compounds exhibiting magnetic moments between the expected fully high and low spin values were shown not to behave as dictated by the Curie-Weiss law, and thus a fluxional process which showed a temperature dependence was thought to be responsible however its nature was unclear. It was only 30 years later, with the strange magnetic behaviour attracting further study, that the spin-crossover process was proposed to be responsible for the existence of the different "magnetic isomers".[9] This newly discovered phenomenon was not limited to iron(III) centres, and a number of complexes containing cobalt(II) and nickel(II) metal ions could also have their "magnetic isomerism" ascribed to this spin-crossover process.[10]

A lot of the work concerning the understanding of the spin-crossover phenomenon has focused on six-coordinate octahedral and pseudo-octahedral metal ions.[11, 12] One reason for this is that the electronic situation is simplified in an octahedral field with respect to the more complicated splitting of trigonal pyramidal or square planar systems.[13] The orbital splitting in an octahedral field splits the five d-orbitals into just two discreet levels, labelled as the stabilised t_{2g} and destabilised e_g levels.[14] Square planar systems, for example, have their d-set split into four levels even before one takes into account any additional lowering of symmetry as a result of inequivalent ligands. The principle reason, however, is a result of the size of the splitting in an octahedral field as compared to other geometries using an equivalent donor set which is of similar magnitude to kT over convenient temperature ranges meaning that the energetic differences between the two configurations is small and a thermal equilibrium between the two can be established. With an ideal octahedral geometry, firstly there are six metal-to-ligand interactions as opposed to five in trigonal pyramidal and four in both tetrahedral and square planar complexes. Secondly, the ligand donor orbitals point directly into both of the non-bonding d_z^2 and d_x^2-d_y^2 as a consequence of the bonding combination t_{1u} arising from favourable overlap between the σ-donor orbitals and the metal ion p_x, p_y and p_z levels. This promotes the orbitals lying along the axes, the d_z^2 and d_y^2-d_x^2 levels, to higher energy causing a concomitant stabilisation of the d_{xy}, d_{xz} and d_{yz} levels to offset this destabilisation. The consequence is that the energy difference between the two sets of orbitals is relatively large and the filling of the lower energy t_{2g} levels occurs preferentially as they now possess slight bonding character.

In transition metal ions of comparable size, the enthalpic penalty paid by the metal ion in pairing two electrons together in the same orbital varies only slightly and can hitherto be regarded as constant per pair of anti-parallel electrons in the same orbital.[15] Thus, it is the ligand field which is more important in determining the relative stabilities of the high and low spin states. In tetrahedral systems, the field imposed is often so small that even with strong

field ligands the pairing energy is often larger than the d-orbital splitting, and thus the high spin configuration is invariably adopted. Octahedral fields, being much larger, can be more readily tuned so that they are of comparable magnitude to the combined pairing energy difference between the two states, P. Thus, both electronic configurations possess similar energies and one can effectively tune the difference between the two states, and hence which is the electronic ground state, over a temperature or pressure range.[16]

1.1.2 Thermal spin crossover: Overview and factors at play in mediating cooperative switching and thermal hysteresis

If one is to look at a switchable metal centre as an isolated entity, its transition is purely a function of a thermodynamic balance between the two spin-states through the equation $\Delta G = \Delta H - T\Delta S$. As the temperature is increased, the entropic term becomes more significant than the enthalpic term and the additional disorder wins out over the smaller, less diffuse low spin system. Because of the stronger bonds, interactions between metal ion and donor atoms vary hugely, with up to a 10% difference observed in iron(II) examples. The smaller molecular volume associated with the low spin state exerts a “negative pressure” with respect to the high spin state, partly offsetting an externally applied higher pressure and stabilising the low spin state.

In reality, completely isolated magnetic centres are somewhat of a rarity in the solid state. A number of commonly observed temperature vs. spin-state population curves are displayed below (Figure 2). In order to observe a Boltzmann-like distribution of spin states, reflecting solely the thermal population of vibrationally excited states, one must make the systems magnetically dilute. This gradual type of transition is typically observed when solvated, or when a magnetically inert compound is doped into the spin-switchable host lattice in order to dilute the system with a non-switchable material, for example doping copper(II) or zinc(II) into the sites ordinarily occupied by a spin-switchable metal ion.[17-19] In this case the individual molecules are essentially non-interacting and the spin-state populations can be considered to vary as a function of temperature or pressure according to the relative energy difference between the two electronic configurations.

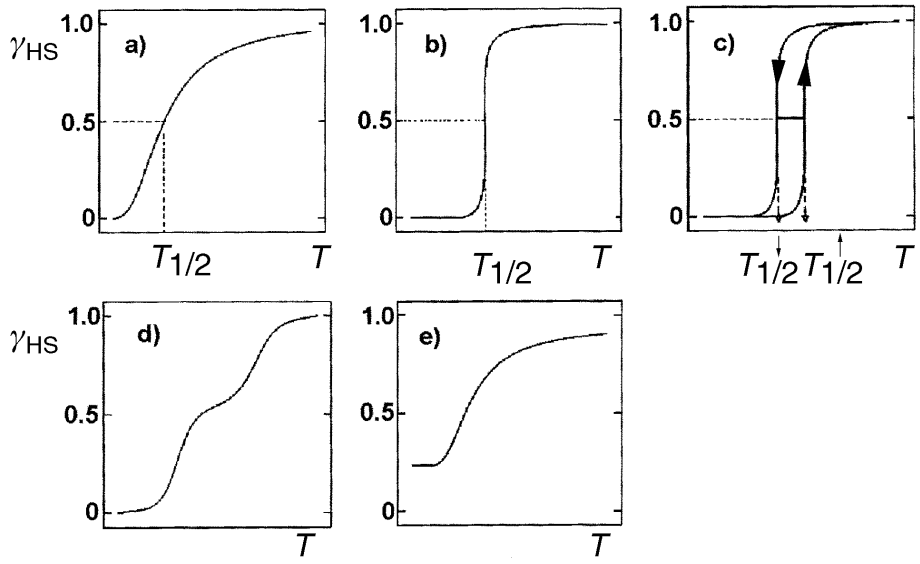

Figure 2 – Series of thermal spin transition curves plotted as the mole fraction of high spin centres vs. temperature; a) gradual, b) abrupt, c) abrupt with hysteresis, d) multistep, e) incomplete.[20]

In magnetically non-dilute systems, a sharper curve is observed in which the metal ions switch from one configuration to the other over a very small temperature range, the centre of which, when there is a 1:1 ratio of centres in either spin state, is known as the transition temperature $T_{1/2}$. These compounds exhibit strong inter-metal interactions. The cause of cooperative switching between nearby centres is often a combination of electronic changes mitigated by a change of spin state but is also of a mechano-elastic nature which results from intrinsic differences in lattice pressure exerted by metal complexes of different electronic configurations and, thus, volume.[21] When one centre switches, the effect of this change is transmitted to the neighbouring metal ions, and the transition propagates through the lattice rapidly until essentially all of the material has undergone a change in spin state. In extremely cooperative systems, the communication between centres is so significant that the transition takes place at a different temperature when cooling than it does when the material is warmed up. This is known as a hysteretic transition, as the molecule possesses bistability within the hysteresis loop; that is the spin state of the bulk material depends entirely upon its thermal history.[22, 23]

More complicated behaviour is seen in compounds which possess multiple unique metal coordination environments, be the materials hetero- or homometallic.[24] In the former case, the susceptibility curve clearly documents two complete transitions accounting for 50% of the centres switching per transition (Figure 2). This may arise from two different metallic centres possessing intrinsically different switching temperatures, for example a homometallic SCO material containing two distinct iron(II) environments.[25] This sort of multi-step transition is also often seen in examples which are only able to effectively transmit their switching

behaviour in one or two directions along the lattice.[26] The residual unswitched centres neighbouring in the third direction will be expected now to exhibit either a stabilisation of either the low or high spin state, depending upon small changes in the lattice pressure felt by the centres, and thus may switch completely or otherwise at a different temperature. This brings us to the last example of curve in which a residual amount of material remains "trapped" in either the low or high spin state. This often happens in the situation described above in which a material possesses two unique metal coordinate sites, however the subtle changes in the lattice pressure when part of the material switches inhibit the residual centres ability to switch.[27, 28] Incomplete transitions are also observed in material which may not be phase pure and may be contaminated with an impurity that is unable to switch the spin state of its metal centres.[29] This could be accidental, in that solvent is lost upon annealing and part of the material undergoes a phase change, or deliberate if a magnetically inert dopant is added to better magnetically insulate the switching centres.[17]

The nature of the spin transition is dependent, first and foremost, on the transition metal ion of interest, but also the relative levels of its split d-orbitals with respect to the donor set employed and the steric considerations of the donor ligand backbone upon the metal.[30, 31] However, as mentioned, the road towards functionally viable spin-switchable materials (Section 1.1.5) relies on the tuning of the ligand field in tandem with crystal engineering the electronically ideal complex materials in order to maximise cooperative interactions between switching sites. To promote cooperativity across the lattice, compounds possessing bimetallic three-dimensional networks, one-dimensional co-ordination polymers, co-crystallised bifunctional materials and structures containing discrete supramolecular units have been shown to exhibit spin-crossover to a lesser or greater degree.[6, 17, 32-36] One of the caveats of covalently bridged switching centres is that there is a rigidity threshold, across which the network possess insufficient flexibility to propagate the transition.[37] Consideration must be made, as always, as to the specific metal ions involved, and most spin crossover materials rely on the switching of the first row metals iron, cobalt and manganese, more specifically the respective ions possessing a formal 2+ and 3+ charge.[27, 38-42] No examples exist of switchable discreet mononuclear second row transition elements, the metal ions instead remaining low spin indefinitely because of the larger, more diffuse valence orbitals associated with second row ions which have far larger energy separations. There are however a few multiply bonded second row metal cluster compounds which undergo gradual spin transitions attributed to smaller differences in the inter-metal orbitals.[43-45]

Though cobalt(II) and iron(III) spin crossover compounds are also routinely studied within the field, by far the most common metal ion involved in spin crossover research is iron(II).[46] Iron(II), specifically octahedral iron(II), is special in that upon going from high to low

spin, its spin changes from a completely diamagnetic singlet ($t_{2g}^6e_g^0$) to a strongly paramagnetic quintuplet ($t_{2g}^4eg^2$). Because of this, large perturbations in the electronic structure of the complex molecules are caused by a change of spin state. Upon population of the e_g levels in the high spin state, the ligand-to-metal bonding interactions are weakened which increases the distance between the metal ion and the ligating atom as well as often causing large angular distortions. This has huge implications on inter-metal communication and lattice pressure changes caused by the switching of a complex molecule, particularly with regards to cooperative switching in the solid state. Not only that, but iron(II) is of particular interest because its ligand field strength with an N_6 donor set commonly resides in the region of 132 – 251 kJ mol^{-1}, meaning it often possesses the ability to switch thermally over temperature regimes of interest.[47, 48] Cobalt(III), which is also a d_6 ion with a tendency to adopt octahedral geometries, exhibits larger field strengths than its iron(II) analogues due primarily to its higher charge, and thus, with the exception of a few examples of ligating molecules stable to the highly oxidising ability of cobalt(III), adopts the low spin configuration.[41] From this point henceforth, only octahedral iron(II) systems shall be discussed with regards to spin-switching.

1.1.3 Low temperature spin state trapping: The LIESST effect

It was mentioned previously that in addition to altering the distribution of spin states in a material by the variation of external pressure or temperature, it is also possible to excite low spin centres into their high spin states by irradiation with an appropriate wavelength of light signature to the discreet metal centre of interest. In fact, it has been shown that with transitions possessing large hysteresis loops it is possible to shuttle between the two spin states using alternating pulses of light of wavelengths specific to the LS → HS and HS → LS transitions.[20, 49, 50] Iron(II) is ideal here, firstly as its ligand field strengths in complexes which permit possible transitions are of energies corresponding to visible and near-IR radiation.[51] Secondly, the large differences in Fe-D distance (where D is the ligating donor atom), in the range of 0.1 – 0.2 Å, mean that the wavelengths for shuttling between the two states are well separated in energy. In practical terms means this reduces the likelihood of inducing an accidental reverse transition with respect to each wavelength applied.[49, 52]

The next logical step is to ask what would happen if a complex is irradiated outside of the hysteresis loop in order to bring about a LS → HS transition. Take for example the fully dehydrated polymorph of [($Fe(C_4H_4N_2)(PtCN_4)$)], which is a three dimensional network with its iron(II) linked by bridging pyrazinyl moieties.[53] The compound switches completely and abruptly with 24 K hysteresis, the $T_{1/2}$ values being 283 and 307 K in cooling and warming modes respectively, and it has been reported that the material can be robustly shuttled between the spin states using laser irradiation.[32, 50] If the material were to be excited into the

high spin state below this temperature, without the use of very fast spectroscopic techniques it would be impossible to detect any of the high spin centres. This is because at such a temperature, the material relaxes very quickly into the thermodynamically lower in energy low spin state at a rate of magnitude 10^7 s^{-1}.[54, 55]

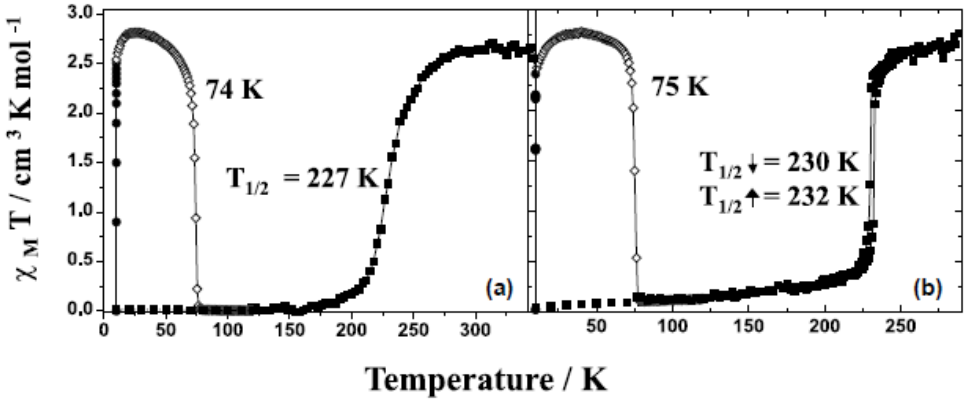

Figure 3 – Temperature susceptibility vs. temperature plots for $[Fe(3\text{-}bpp)_2][NCS]_2.2H_2O$ (a) and $[Fe(3\text{-}bpp)_2][NCSe]_2$ (b). Data recorded in cooling mode before irradiation (squares), with irradiation at 10 K (black circles) and one hour after irradiation in warming mode (white circles).[56]

Though thermal relaxation of excited high spin centres dominates near the transition temperature, if it is lowered sufficiently the possibility arises to "trap" the complex centres in their metastable high spin states through appropriate irradiation.[48, 52, 57, 58] The phenomenon is known as light-induced excited spin state trapping, LIESST. It can be seen at work in the susceptibility curves for the thiocyanato and selenocyanato salts of the *bis*-(2,6-di(pyrazol-3'-yl)pyridine) iron(II) dication, which switch gradually and abruptly respectively, centred at almost identical temperatures (Figure 3).[56] One can see, in both cases, that after irradiation with 647.7 – 676.4 nm light to excite the centres into the high spin state, below 50 K the population remains constant, in that the material is unable to relax back into the low spin state which is thermodynamically lower in energy. Below 50 K, there is insufficient thermal energy required to populate the vibrationally excited levels close to the crossing point of the overlapping energy wells.[59] Indeed, as thermal relaxation is effectively quenched, the only method of relaxation is via quantum tunnelling which is extremely slow, inhibited by the very different atomic coordinates between the two spin states, and the metal centres can be considered to be trapped indefinitely in the high spin configuration.[54, 59] This temperature below which the metal ions are trapped in their metastable high spin states is denoted as the material's T_{LIESST}, the temperature at which 50% of the switching centres remain high spin trapped.[56] As a result of the variation of the thermal high-to-low spin relaxation rate with temperature, the T_{LIESST} is sensitive to the speed of warming, and thus the T_{LIESST} values must be reported alongside the heating rates in order to gain information on the kinetics of the relaxation process(es).[60, 61]

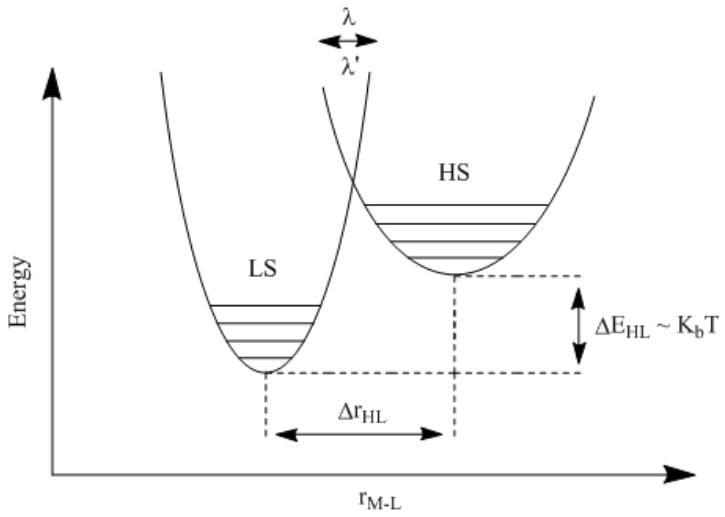

Figure 4 – Potential well diagram for the high spin and low spin states of an octahedral metal ion spin crossover system; K_b is Boltzmann's constant and λ and λ' the wavelengths specific to the metal complex necessary to optically switch between spin states.

T_{LIESST} values above 50 K are rare, however there is a drive to raise the temperature for a metastable trapped high spin centre so as to allow, potentially, fully light induced switching at or around room temperature. Létard *et al*, using data acquired documenting the thermal spin transitions of a number of iron(II) complexes with N_6 donor sets, but with varied denticity, proposed a number of relationships between the transition temperature and the energy separation between the metastable high spin state and the high spin to low spin crossing point.[51, 62, 63] The crossing point between the two electronic configurations naturally determines the rate at which the metastable state should relax back into the low spin configuration at a given temperature, and as a consequence determines the temperature after which quantum tunnelling is no longer the dominant pathway for HS → LS relaxation, quantified as T_{LIESST}. If one is to consider mononuclear centres, as is the primary focus of this work, a correlation of T_{LIESST} both with the reproducible $T_{1/2}$ values and ligand denticity can be made. Following on from the work of Hauser *et al*, an inverse energy gap law was proposed which states that, as the $T_{1/2}$ of a material moves toward lower temperature, which correlates with the degree of structural rearrangement in undergoing a transition, the metastable high spin state has to traverse a higher activation barrier in order to relax, and thus T_{LIESST} is observed at higher values (Figure 4).[52, 57, 63] The equation defining this relationship, $T_{LIESST} = T_0 - 0.3T_{1/2}$ is dependent upon a third parameter, T_0, which is where the denticity of the ligating system factors in.[51]

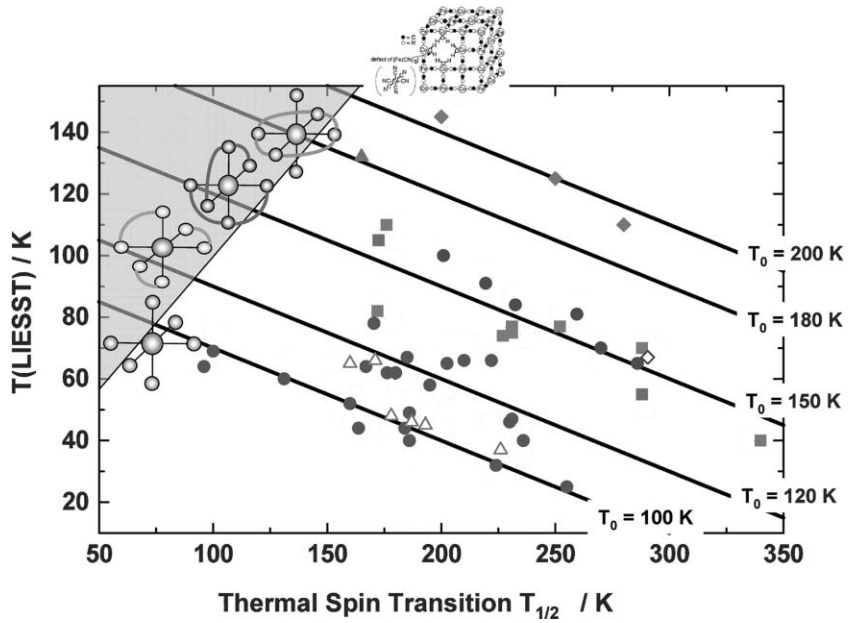

Figure 5 – Adapted plots of the $T_{1/2}$ values vs. T_{LIESST} for a series of compounds of varying denticity whose magnetic behaviour is well understood.[60] Using the equation $T_{LIESST} = T_0 - 0.3T_{1/2}$, the points corresponding to compounds of specific ligand denticity can be seen to match closely with the substituted T_0 values. Data points on the plot correspond to FeL_6^m (circles), FeL_3^b (white triangles), FeL_2^t (squares), $FeL^{q\text{-}p}$ (grey triangles) and FeL_∞ (diamonds). The greyed out area of the plot can be disregarded as T_{LIESST} must be smaller in magnitude than $T_{1/2}$.[63]

Plots of T_{LIESST} vs. $T_{1/2}$ illustrate that T_0 for FeL_6^m, FeL_3^b and FeL_2^t can be substituted as 100 K, 120 K and 150 K for the monodentate, bidentate and tridentate systems respectively (Figure 5). This is a clear indication that structural rigidity plays a large part in determining T_{LIESST}, and a complex containing an iron(II) centre chelated by a pentadentate macrocyclic system, of the form FeL^pX_2, where X are monodentate cyanide ligands, were shown to fit with an increased T_0 of 180 K. The T_{LIESST} for this compound was extrapolated as 130 K which is currently the record for a pure spin crossover material. A number of Prussian blue analogues exhibited even higher T_{LIESST} values, the highest being 180 K, and though they belong to a family known as charge-transfer induced spin crossover materials, the T_{LIESST} vs. $T_{1/2}$ values allowed deduction of the T_0 parameter at 200 K. The three-dimensional network of iron and cobalt centres bridged by cyanato moieties imparts large constraints on the individual centres, necessitating the highest crossing point of all the material types discussed.[64, 65] The challenge now is focussed on further increasing the T_0 parameter, in order to characterise materials with long-lived metastable lifetimes which retain their light induced information over relevant temperature regimes for industrial and commercial application (Section 1.1.5).

1.1.4 Monitoring the spin state

Spin crossover, whether it be a result of irradiation or a change in pressure and temperature, involves not only metric changes in the coordinates of the atoms constituting the system, but is also a process of a diathermal nature. The path is thus paved for

investigation through a wealth of spectroscopic and gravimetric techniques, both as material solids and solutions. Indeed, one can often gain a visual handle upon the spin state of the centres involved, at least qualitatively, because of the large differences in magnitude of the energy of MLCT absorbances associated with a change in electronic spin state (Figure 6).[66, 67] Since the spin transition itself is concomitant with a change in spin ($\Delta S > 0$), in an applied magnetic field it is possible to observe the magnetism, and thus magnetic susceptibility, of a bulk solid providing information on the spin population provided the composition of the material is known.

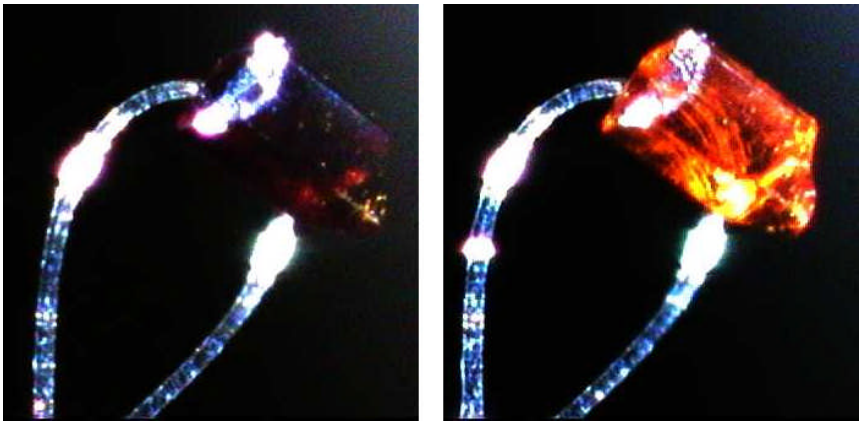

Figure 6 – Images of a single crystal of $[Fe(1\text{-}bppSMe)_2][BF_4]_2$, 35a, at 240 K (left) and 290 K (right) illustrating the thermochroism upon a spin transition of $^2I_3$ of the iron(II) complex centres.

Two of the most important and widely used techniques for materials characterisation in the field of spin crossover are X-ray crystallography and determination of the spin state through magnetic susceptibility measurements.[68] The former method requires the acquisition of single crystals, which can be troublesome, as spin crossover materials appear to crystallise, in general, less well than their inert diamagnetic analogues. Obtaining single crystals of a material can be particularly difficult if the material is polymeric or possesses a coordination network type structure, as these tend to exhibit extremely low solubilities. In conjunction with this is the problem of polymorphism and the existence of multiple solvates and hydrates which can occur when growing crystals from different solvents.[36, 69-71] This complicates the understanding of spin crossover behaviour as different polymorphs solvates of materials invariably have very different magnetic behaviour.[69, 71] Of particular note is the behaviour of *bis*-(2,6-di(5'-methylpyrazol-3'-yl)pyridine) iron(II) tetrafluoroborate, which has been observed to exist in as least five polymorphs, one a dihydrate and two of which show interesting magnetic behaviour.[72, 73]

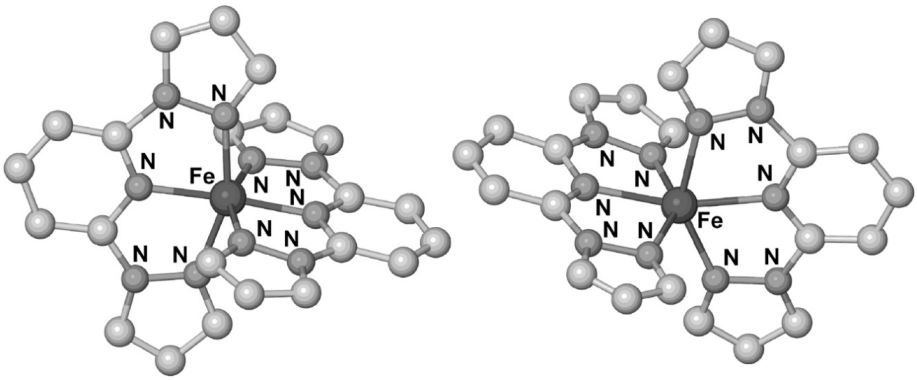

Figure 7 –The two unique complex dications in $[Fe(1\text{-}bpp)_2][Co(C_2B_9H_{11})_2]_2.MeNO_2$ occupying the lattice in a 1:1 ratio at 150 K with all H atoms omitted for clarity; the dication on the left switches gradually between 200 and 400 K, whilst the second dication remains indefinitely high spin.[74]

With that in mind, X-ray crystallography is incredibly powerful in not only quantifying the spin state of metal ions within a material but also based on structural information to better understand its behaviour. The spin state of a centre can be deduced purely on the basis of bond lengths, as a transition from LS → HS involves the transferral of electron(s) into higher lying orbitals, the e_g set, which are effectively antibonding in character with respect to the ligand σ-donors, causing a net repulsive effect resulting in a significant bond elongation.[75, 76] This can be reinforced if, say, a lowering of symmetry of the molecule is expected upon a spin transition. For example, in Fe(II) systems, the LS → HS transition is concomitant with the introduction of a symmetry lowering Jahn-Teller distortion removing the energetic degeneracy between the $d_{xy,}$ d_{xz} and d_{yz} orbitals. The donors with a larger displacement from the z direction are repelled to a lesser degree, sometimes resulting in large angular distortions for the ligating atoms located along the z direction which are commonplace in meridional *bis*-tridentate SCO complexes (Figure 7).[66, 77] In cobalt(II), a transition from LS → HS, both spin states exhibit Jahn-Teller distortions, specifically tetragonal contractions, however the effect is less pronounced in the high spin state, evidenced by the reduced difference in bond lengths between the iron centre and its axial and equatorial donors.[12, 40, 78]

The distortions experienced by a metal are not just a result of inner-sphere electronics, but also how the material packs in the lattice. Huge distortions can also arise purely from the nature of the ligand backbone itself as well as closely associating neighbours or solvates, forcing large displacements from ideal geometries.[38] The magnitude of the angular deviations can not only be used to reliably ascertain the electronic configuration of the metal ions of interest, but also the likelihood that the necessary structural changes can be accommodated both by the lattice and the metal ion itself as to allow a change in spin state. Because such geometric and angular distortions are so inherently important, a number of commonly used parameters are used to quantify the degrees of distortion from idealised

geometries. Three of particular general relevance in spin crossover research are the polyhedron volume about the metal centre, and the trigonal and rhombic distortion parameters Θ and Σ. These parameters are properly introduced and explained, along with others specific to tridentate *mer*-chelating ligands about an octahedral metal, in Section 1.2.

Magnetic susceptibility measurements provide particularly useful information on switching temperatures because of the change in spin associated with a rearrangement of electron configuration. It is possible to perform variable pressure studies at a constant field in order to determine a pressure induced crossover, however there is more prevalence in the literature to perform temperature based studies because, firstly, thermal spin transitions are better understood and secondly because thermally varied measurements are easier to perform with standardised commercially purchased equipment. To clarify the correlation of switching in the single crystal with that of either a bulk powder of ground crystalline sample, a powder pattern is obtained on the material to ensure the positions of the peaks in the pattern match with those simulated from the experimental single crystal data. This is also informative concerning the identity of phase-contamination, or the loss of crystallinity of a material through exposure to air and subsequent desolvation or hydration of the lattice, resulting in broadening and loss of resolution in the powder data.[72]

Further spectroscopic techniques can help support evidence of spin crossover, and indeed even assist in quantifying the process for a given material or hybrid material thermodynamically. Differential scanning calorimetry (DSC) is often used in conjunction with crystallographic and magnetic measurements to determine the enthalpy of a change in spin state, and from the data the ΔS of the process can also be deduced. This can also be used to reinforce evidence of further changes in the solid state, such as a crystallographic phase change or the change in the order of a particular substituent, counter-ion or solvate molecule, if for instance, ΔS deviates markedly from the usual range of 50 – 80 J K^{-1} mol^{-1}.[79, 80] The data can be used to assess the degree of cooperativity between interacting switching centres by varying the temperature ramp rate and quantifying the entropic and enthalpic dependence. A number of mathematical models exist, invoking the implementation of deduced “interaction parameters” and “excess heat capacities”, and have been shown to effectively ascertain the degree of inter-metal cooperativity spanning a transition.[81-83] Theoretical transition curves obtained by implementing these parameters consistently show a close fit with the experimental data, and in particular the Slichter and Drickamer model provides significant insight into predicting the size of any hysteresis loop.[81]

One further technique of note for identifying the degree of spin state of solids is Mössbauer spectroscopy, a spectroscopic implementation of the phenomenon discovered by

Rudolf Mössbauer, involving the recoilless nuclear resonance of absorbed gamma rays.[84] Mössbauer spectroscopy is particularly useful in probing changes in electron density about ^{57}Fe, and hence the spin state in iron(II) containing spin crossover materials, because of its exceptionally narrow linewidth compared to the Mössbauer gamma-ray source allowing the acquisition of incredibly high resolution spectra. The distinctly different isomer shifts between the two spin states, in conjunction with the significantly larger quadrupole splitting of the signals originating from high spin ions of approximately an order of magnitude allow facile assignment of the signals to iron(II) centres of specific electronic configuration (Figure 8).[85] Mössbauer spectroscopy has found widespread use regarding spin switchable materials, and studies can be conducted over variably temperature/pressure regimes to assess their influence on the spin state of individual centres, rather than just of the bulk material itself which is of interest in systems incorporated into bulk media or attached to nanoparticles.[6, 66, 86-90] It is this specificity that allows the detection of unique switching centres, for example in materials which undergo multistep transitions or exhibit comparably complicated behaviour.[91-93]

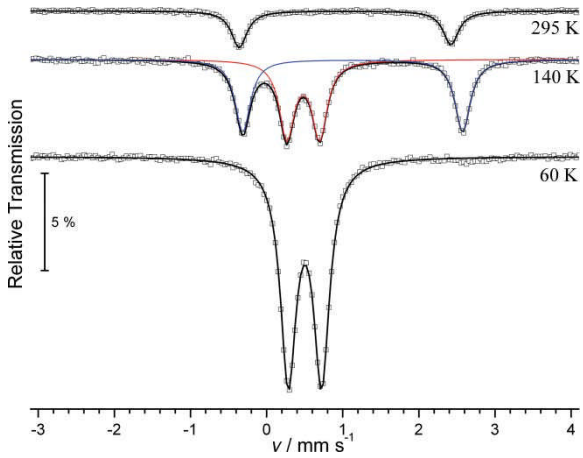

Figure 8 – ^{57}Fe Mössbauer spectra of the two step spin transition complex [Fe(2,6-di-(2'-pyridyl)-1,3,4-thiadiazole)$_2$(NCS)$_2$] at temperatures of 295, 140 and 60 K showing the fully high spin material (top), the intermediate phase containing 50% high spin centres (centre) and the fully low spin material at low temperature (bottom).[94]

Though spin state distributions in the solution phase are dictated by a thermal Boltzmann-like distribution, these systems are of little viability when pondering their implementation into devices and industrial applications. With that duly noted, study of the solution phase can however yield information about the individual spin states on molecules which can be considered to be magnetically diluted, and thus the intrinsic spin crossover of metal ions in isolated mononuclear complexes to oligomeric systems can be deconvoluted from the effect of crystal packing in the solid (Figure 9). The primary spectroscopic techniques which find the widest general application in assessing solution phase switching are discussed below.

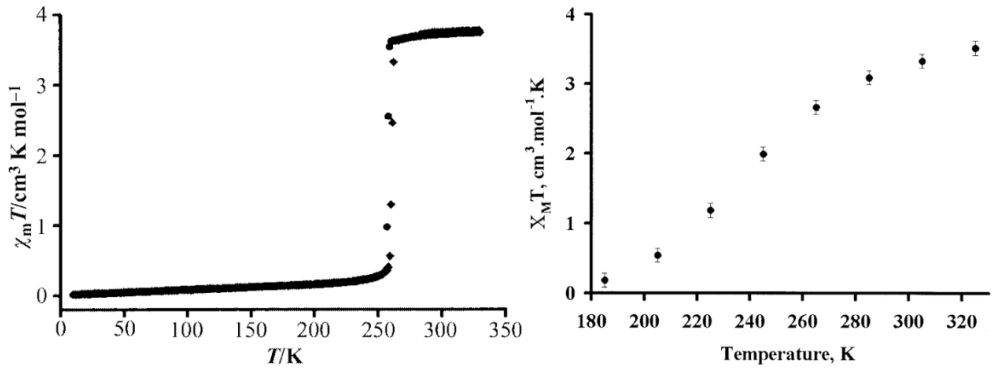

Figure 9 – Variable temperature magnetic behaviour for $[Fe(1\text{-}bpp)_2][BF_4]_2$, 23a, as a polycrystalline sample (left) and as a solution in acetone-d_6 (right).[67, 95]

Conveniently, the magnetic susceptibility of a solvated material, of known purity and hence concentration, can be calculated using a technique originally reported by Evans for the solvated susceptibility of paramagnetic ions, known simply as Evans' method.[96] Evans' method relies on the quantification of paramagnetically shifted reference signals, often that of the solvent, $SiMe_4$ or an added inert reference compound, whose chemical shifts vary from their known reference values according to the bulk susceptibility of the medium. Naturally, a more paramagnetic medium would cause larger shifts of the reference signal from its ideal diamagnetic value and from this the susceptibility of a known concentration of material can be calculated, and by extinction the spin state population.[13, 96, 97] Though errors of 5 – 10% are expected due to the nature of the experiment, in systems which undergo large changes in susceptibility upon a change in electronic configuration, such as iron(II) (S = 0 → S = 2) and iron(III) (S = ½ → S = 5/2), these errors are marginalised and useful information regarding the electronic structure of the metal ions involved in the spin transition can be acquired. The equation through which the gram susceptibility of the material, χ_g, can be calculated is $\chi_g = (3\Delta f/2\pi fm) + \chi_0 + \chi_0(d_0 - d_s)/m$, where Δf is the frequency difference between the reference signal and its position in the presence of the solute; f is the frequency of the spectrometer employed; m is the mass of the solute per cm^3 of the solution; χ_0 is the susceptibility of the solvent medium calculated from Faraday's constants; d_0 is the density of the solvent; d_s is the density of the entire solution. In most instances the last term can be negated because the density difference between the solvent and solution is negligible. χ_g is commonly converted to $\chi_m T$ so that the susceptibilities of complexes with differing molecular weights can be accurately plotted against one another. Thermodynamic information on the entropic and enthalpic differences between the two spin states can be affirmed by deducing the spin-only values of the magnetic moments of the pure high and low spin states in Bohr-Magnetons, and the solution-based $T_{1/2}$ in accord with the Boltzmann distribution.[98]

Electronic absorption spectroscopy is also often used in quantifying spin state distributions, but one can also infer information on d-orbital splitting and ligand field strength in differing spin states from the position of absorption bands in the spectra.[99, 100] Changes in the intensities and positions of both MLCT and d-d bands can provide information on structural and electronic differences between the two d-orbital configurations, and explain the thermochroism of the materials, however care must be taken not to neglect the solvent effect upon these absorption energies. Because the ligand field can be up to double the strength in low spin configurations as it is in the corresponding high spin configurations, the position of the d-d absorption bands are well separated and rarely do excitations overlap. If one knows the spin population at a given temperature in solution, for example the temperature at which 100% of the centres can be considered high spin, then molar absorptivities can be calculated for the high spin and low spin complexes, and through thermal variation the spin state populations can be plotted against temperature. If the $T_{1/2}$ value falls below that of the solvent freezing point, then this can be extrapolated through fitting of the data to a simple Boltzmann relationship. If one is aware of the symmetry of the metal ions involved, and thus the number of allowed and expected transitions, then, particularly for the high spin complexes whose d-d absorptions are of such low energy that they rarely overlap with charge transfer bands, the bands can be tentatively assigned to transitions within the d-orbital set.[101] In instances where it is suspected that bands overlap, or that a prominent shoulder is present, Gaussian deconvolution can be applied with the appropriate parameters in order to obtain symmetrical band shapes for each predicted transition.[102] From this various d-orbital splitting values can be extracted, and thus the ligand field strength, however care must be taken due to further lowering of symmetry because of increased spin-orbit coupling in the “loose” solvated complex molecules which are experiencing rapid thermal tumbling.[103]

1.1.5 Application and real world goals

Spin crossover systems present a situation in which there exist potentially two domains of bistability, that within the hysteresis loop over a pressure or temperature range, and that observed in the context of low temperature trapping of a metal centre through light irradiation. This bistability, in effect permitting the rapid switching between two electronic configurations depending upon the specific stimulus, makes them ideal candidates as nanoscale and above switchable materials, whose information can be read through a number of means, for example visibly or by changes in conductivity, reflectivity and magnetism. Below, the discussion is focussed on the tuning of spin crossover materials towards use in two primary commercial applications which their properties govern their suitability for, in molecular data storage and optical display devices and sensors. The

necessary requirements for such materials are presented, alongside caveats and potential obstacles to implementation, and finally examples of primitive devices and functional systems documented in the literature thus far.

The limitations of today's information storage result from the requirement to ever-miniaturise computing equipment and portable data storage devices to store more information in smaller, more confined spaces whilst also retaining the device's robustness, as well as sufficiently fast read and write speeds. Data storage is dominated by magnetic encoding in hard drives, optical read/write capacity in CD/DVD technology, and a combination of the two, known as magneto-optical storage, in modern day solid state storage. Though magneto-optical storage is at the forefront of commercially available bit/cm^2 capacity in addition to read/write speeds, the constant drive to downsize components in hardware means that we are approaching the physical limit for the size of the bits themselves. Bits that are too small are predicted to require higher energy lasers to write, as well as retaining their state less reliably resulting in a loss of information, and efforts to combat these problems would prove too costly to implement in devices. Spin-crossover remains but one of the phenomena which finds itself researched intensively in an attempt to further improve our ability to read and write vast amounts of data through molecular-based memory. Since the potential for information storage arises through existence of hysteresis, only highly ordered crystalline materials exhibiting high cooperativity can be employed. Decreases in size of crystallites and clusters, characterised by reflectivity or electron microscope techniques, evidently have an effect upon the hysteretic behaviour.[104-106] Clusters of iron(II) materials containing 1,2,4-triazolyl bridges have been shown to remain highly hysteretic down to 5 μm in diameter, which though too large for molecular data storage, promises that by promoting highly cooperative communication between switching centres we can further reduce the size of clusters, down to that which is required for molecular storage, whilst retaining the sharp, abrupt hysteretic transition. The challenge now remains, firstly, to further understand the nature of cooperative transitions in the solid state, in order to produce materials which are not susceptible to fatigue over repeated cycles, relying on further increasing the hysteresis width, which, of course, must span working temperatures. Secondly, uniformly-sized clusters of these materials less than 10 nm in diameter must be grown and characterised, with retention of robust hysteretic behaviour. Current limits are in the region of 100 nm, which can be obtained effectively involving water droplet dispersed microemulsions, but with nanoscience advancing rapidly this limit is set to be broken within the very near future.

The thermochroism often observed upon a change of spin state opens up the prospect of the use of spin crossover materials in imaging, display devices and optical

temperature sensors. There is a particular need to fabricate display technology with ever smaller displays, yet retaining the high resolution, display rate and the low power consumption necessary for the market. Current display devices are fabricated of either light emitting diodes (LEDs) or plasma-based displays (PDPs), yet the push towards microdisplays, designed to be observed through magnifier on or close to the eye highlight the limitations of these display technologies. The high manufacturing cost behind PDPs limits their dominance in the industrial and commercial markets, and both LEDs and PDPs require overly complex methods of writing and addressing, meaning that their efficacy in devices has a natural threshold. Suitable spin crossover materials incorporated into such a device could be addressed thermally, optically or purely electronically. With such a simple system in employ, conversion efficiency would be high, which could offset the potentially expensive manufacturing process. The architecture would probably involve adhesion to an inert, insulating substrate, capable of transmitting thermal information to switching material or being fully penetrable by an incoming radiation source so as to not hinder the absorption by the metal complexes themselves.

Unfortunately, thus far, no material has met all the criteria required for such device fabrication. A number of compounds with highly cooperative transition curves do not show strong enough thermochroism due to the obstruction of d-d bands with those of broader, more strongly absorption charge transfer bands arising from transition to and between the necessary aromatic and conjugated ligands and linkers. Typically, most highly thermochromic materials were shown to switch far too gradually, with the requirement that the conversion from fully HS → LS and vice versa occur over, ideally, very subtle changes in temperature of the order 1-2 K. Progress has been made in overcoming these encumbrances after extensive research on octahedral iron(II) complexes chelated by bidentate triazolyl moieties, yet spin transition temperatures were still too high to be used in operative day-to-day devices.[107-109] Attempts to subvert this included diluting the switching iron centres with magnetically inert ions, for example zinc(II) and copper(I), or the co-crystallisation of two different but very closely related complex salts, for example of two or three identical complexes with differing cations, to exert additional control over the $T_{1/2}$. Only limited successes were met pursuing this strategy, in the former case the degree of thermochroism was reduced alongside more gradual transitions as a result of the inert ions effectively blocking the transition propagation, while in the latter case though $T_{1/2}$ values were lower, some of the doped materials proved to have lower crystallinities, reflected in the less abrupt transitions observed.[110] Clearly there is much work to be done regarding these materials before viability is achieved.

More recent endeavours have also focussed on bifunctional materials, with regards to display devices and temperature sensors this necessarily means that the second functionality must either be that of an increased thermochromic effect, or the ability of the hybrid material to luminesce. The principle is that, with an ideal bifunctional material, the spin crossover process occurring abruptly and robustly over a narrow temperature range mediates perturbs the second functional entity in the solid state to such a degree that either much starker thermochromism manifests itself, or the luminescence is either switched on and off completely or simply switched to a different wavelength – effectively thermochromic emission. Generally, these sort of materials are suitable to thermal and optical addressing, however an example does exist of an electroluminescent device based on a thin film of chlorophyll a doped with $[Fe(1\text{-}bpp)_2][BF_4]_2$.[111] Remarkably, the electrochemically generated emission is switched off at low temperatures, and indeed plotting these relative emission maxima revealed an abrupt transition with $T_{1/2}$ of ca. 270 K, consistent with pure $[Fe(1\text{-}bpp_2)][BF_4]_2$ at ca. 260 K. This suggests highly crystalline $[Fe(1\text{-}bpp)_2][BF_4]_2$ in the film, and this was confirmed in the photoluminescence spectra which showed that emission was quenched not through energy transfer, but through the low spin iron complex's lower charge mobility essentially preventing quantitatively the electrochemically generated excited chlorophyll. Nano-materials containing a triazolyl iron(II) complex doped with rhodamine-110 have shown that emission is switched off by an electron transfer process between the two sites due to good band overlap between the emitting rhodamine-110 and the LS iron centre, however this is negligible in the HS state and emission is unhindered, yet the transition is too gradual to be of any commercial viability despite it being centred just above ambient.[112]

Recent reports present an example of a material containing discreet mononuclear iron(II) cations doped with emissive ruthenium(II) centres, and the magnetism and emission studied as a function of the relative ratios of the two functional complexes.[35] This is based on the co-crystallisation of a phase pure material, promoted by supramolecular packing effects due to the size and shape compatibility of the two functional complexes. It is advantageous in that the relative ratios of the metal complexes in the hybrid material can be varied trivially, in addition to their relative locations. Unfortunately the spin crossover process and the emission could not be observed over the same temperature regime, and this study merely illustrated a proof of principle, yet it is clear it presents yet another path towards emissive spin crossover materials.[35] An extension upon this work is presented chapter four, which focuses on doping ruthenium complexes into the SCO host, $[Fe(1\text{-}bpp)_2][BF_4]_2$, with longer luminescence lifetimes that persist over the SCO regime. The solid solutions must still exhibit complete thermal transitions over a narrow range, which limits the dopant concentrations which can be employed, dependent upon the cooperativity of the pure SCO

host, yet emit strongly enough as to require low power consumption. Regrettably it is unclear as to whether the changes in the co-crystallised lattice upon a change of spin state will significantly affect the emission of the dopant, and this warrants further study than that which is currently documented (Section 1.3).[35, 113]

Spin crossover materials may in the future also find use as MRI imaging contrast agents and in non-linear optics, a result of differences in conductivities, magnetic susceptibility, ordering and hyperpolarizability, in metal complexes possessing appropriate symmetry between the electronic configurations of their respective spin states. No examples exist currently which report non-linear optical changes induced by a spin transition, which likely reflects the current lack of interest in probing spin switchable materials for such properties, yet theoretical studies in conjunction with the large hyperpolarizabilities observed in a number of highly paramagnetic compounds containing either HS iron(II) or manganese(II) suggest that the response would differ hugely.[114-116] This is clearly a research area still very much in its infancy. Thermochroism and changes in magnetism mean that the spin crossover phenomena could additionally find application in molecular sensors, as successors to the current technology used in small-scale temperature sensing in industrial and biological applications. Two examples could be the temperature sensing in ultra small electronic components, and as MRI contrast agents which would allow the temperature of living tissue to be monitored during the treatment of cancer. Aside from an understanding of toxicities towards healthy cells and the organism as a whole, it is obvious that spin crossover imparts properties which would be very desirable for such specific application, including materials which are abrupt thermochromic switches over such biologically relevant regimes, ca. 30-40 K. What is required henceforth is an interest in further developing these materials for biological use, perhaps to decrease their toxicity towards living organisms, to optimise their stability in aqueous media across appropriate pH ranges, and to perhaps encapsulate clusters of these materials or bind them to an inert host to further inhibit their degradation and adverse effects they may pose.

1.2 Mononuclear iron(II) complexes of tridentate N-donor chelators

1.2.1 Mononuclear spin crossover centres: comparison with polymeric materials

To date, iron(II) remains by far the most widely studied transition ion with regards to spin crossover research, and this comes as no great surprise. Octahedral iron(II), upon undergoing a rearrangement in electronic configuration from the $^{1}A_{1g}$ to the $^{5}T_{2g}$ state, experiences the largest structural and electronic changes due to a transition involving a change in spin from completely diamagnetic S = 0 to highly paramagnetic S = 2. This is concomitant, often, with significant thermochroism, large changes in conductivity, and

magnetic moments are reported to increase from ~0 to values up to ~6, which manifests itself as a huge increase in the magnetic susceptibility of the materials.[17, 117-119] The electronic rearrangement, resulting in drastic decreases of the ligand field, forces elongations of the Fe-N bond lengths of around 10%, alongside significant angular distortions from the ideal octahedron.[76] It is these structural distortions, often in tandem with a change in electron distribution over the entire metal complex units, which instils cooperative spin state switching. The changes in lattice pressure and electron distribution associated with a spin transition have a profound effect upon nearby iron(II) centres, resulting in a propagation of the switching information through the crystal lattice, so that the spin crossover is no longer dominated purely by the electronic structure of isolated iron(II) centres, but also by the degree of inter-metal communication. Highly cooperative systems exhibiting switching over very narrow temperature ranges, ca 2 K, and those exhibiting hysteresis and thus history-dependent bistability, are of particular interest (Section 1.1.5), and therefore the focus has shifted towards engineering materials which exhibit highly cooperative spin switching behaviour.

Two approaches have been taken towards encouraging cooperative switching by increasing inter-metal communication, one which involves covalently linked clusters, chains and networks, and the second concentrating specifically on the intermolecular communication between discreet units, mediated by supramolecular lattice-based non-covalent interactions.[83, 95, 120-124] By their nature, covalently linked metal centres, bridged for example by an organic linker, are held more tightly than inter-complex interactions involving hydrogen bonds or transient van der waals forces. One would perhaps then think that polymeric chains and networks hold the key to instilling highly cooperative spin transitions, yet this is not always the case. A number of fine examples highlight the potential of covalently bridged complex centres possessing rigid linkers which, by exerting sharp changes in lattice pressures felt by neighbouring metal ions, cause a concomitant change in their spin state with the switching information propagating across the crystal lattice.[23, 125, 126] The two dimensional network compound $[Fe(4,4'\text{-bi-}1,2,4\text{-triazole})_2(NCS)_2]_n.nH_2O$ exhibits an abrupt transition at ca. 140 K with a 20 K hysteresis loop, however it is likely that the hydrogen-bonded water molecules are also responsible for the shape and position of the crossover.[127] The three dimensional coordination polymer $[Fe(pyrazine)][M(CN)_4]$, where M = Ni, Pd or Pt, has been investigated exhaustively, possessing spin transitions with thermal hysteresis of up to 20 K dependent upon the water content.[32, 53] Furthermore, it was shown that varying the size of the ancillary bridging square planar complex by changing its central atom did not impart significant changes in cooperativity but altered the position of the $T_{1/2}$ values.[32] This is important, as the elasticity of the lattice is shown to remain fairly constant,

yet the size of the ancillary complex ion exerts intrinsic lattice pressures on the switchable iron(II) centres which can be seen in the position of the $T_{1/2}$ values across the series of analogous materials.

Yet, discreet mononuclear complexes appear within the spin crossover literature just as regularly, with spin transition curves which are indicative of behaviour which is often just as interesting, if not more so on occasion, than their non-discreet counterparts.[4, 68, 94] The complex [Fe(*E*,*E*)-((diethyl-2,2'-[1,2-phenylenebis(iminomethylidyne)]*bis*(3-oxobutanato)))(imidazole)$_2$] possesses 70 K hysteresis, notably centred just below room temperature, a result of close hydrogen-bond contacts between the axial imidazole N-H and a carbonyl group appended to the equatorial ligating arm of a neighbouring complex molecule.[128] Iron(II) centres chelated by tridentate planar N_3 donors such as derivatives of 2,6-di(pyrazol-1'-yl)pyridine, 2,6-di(pyrazol-3'-yl)pyridine and 2,6-di(benzimidazol-2'-yl)pyridine also routinely show abrupt hysteretic transitions.[70, 72, 73, 76, 129] In the dicationic systems mentioned above, there exists a lot of potential to tune, through effective crystal engineering, the packing by way of altering the size, shape and relative coordinating ability of the counterions within the lattice, in addition to the usual variation of appended substituents.[67] Analogously, studies on series of 1D chain materials containing different counterions found that small changes in the counterion volume showed marked changes in spin crossover behaviour, which could be rationalised by interchain distances and interruption of π-π overlap between aromatic rings as deduced from crystallographic data. Often such additional factors are just as crucial to the solid-state magnetic behaviour as, for instance, the rigidity of a rigid linker between neighbouring centres, and in discreet systems, which are often easier materials to obtain single crystals of, spin transitions are regularly triggered by changes in ion/solvent disorder at crucial temperatures, which can have drastic effects upon the lattice pressure of the bulk crystalline solid and the donor strength of individual ligating atoms.

1.2.2 2,2':6',2''-Terpyridine and related planar tridentate ligands

2,2':6',2''-Terpyridine, which will henceforth be referred to as terpy, belongs to a class of organic compounds which coordinate meridionally to a metal ion because of its planar tri-heterocyclic backbone containing three N-donor atoms, and is most often observed chelating metal ions adopting square planar or octahedral geometries.[130-132] Defined as moderate-to-strong field splitters, they exhibit diverse coordination chemistry and can bind metals in multiple coordination modes via rotation about the inter-ring bonds, and are commonly employed as part of metal complexes and materials involved in catalysis, functionalised photovoltaic cells, antibacterial agents and supramolecular networks and assemblies.[133-138] However, relevant to this work is terpy's strong σ-donating ability, in conjunction with its

relatively large, low-energy π*-orbitals which make it a moderately strong π-acceptor.[139, 140] These two properties of terpy and related tricyclic *tris*-imine donors tailor them as candidates in spin crossover research, where their exerted ligand fields may be of such magnitude that small external stimuli may bring about a change in spin state in suitable metal ions.

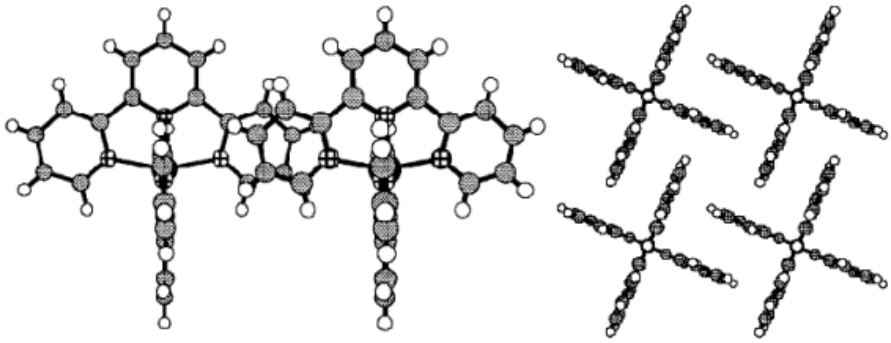

Figure 10 – Schematic representation of $[Co(terpy)_2]^{2+}$ dications in $[Co(terpy)_2]I_2$ adopting a form of the terpyridine embrace; shown perpendicular to the principle axes of the complex dications, revealing the off-centre π-stacking of the distal rings of neighbouring molecules (left) and an array of four interlocking complex molecules shown parallel to their principle axes (right).

Another notable feature is the existence of the crystal packing motif the "terpyridine embrace", first observed in hydrates of $[Co(terpy)_2][ClO_4]_2$.[141] The terpyridine embrace is a supramolecular motif adopted by numerous complexes and complex salts which feature a mononuclear octahedral metal ion *bis*-chelated by terpy, and is of particular relevance to engineering interesting and commercially appealing spin crossover materials. Its formation is a result of favourable off-centre π-π interactions between the distal rings of neighbouring units, and edge-to-face C-H interactions between the central pyridine of one complex with that of a neighbour, with the molecules associated into distinct layers (Figure 10).[142-145] This motif is highly sensitive to the shape of the molecule, and thus a metal ion in two different spin states, complete with octahedral distortions and therefore a change in shape and size, strongly affect the packing. Consequently, these interactions involved in the terpyridine embrace are of vital importance in transmitting spin switching information across the crystal lattice, hence propagating the transition and therefore systems can be tuned so as to possess abrupt, hysteretic transitions under the appropriate stimuli.[95, 146, 147]

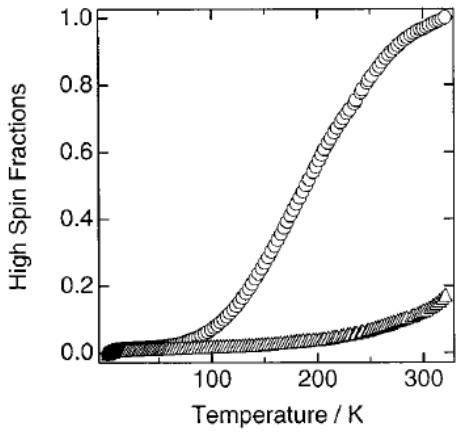

Figure 11 – High spin fraction vs. temperature plot of the magnetic susceptibility of the bulk solids $[Co(terpy)_2]Cl_2.5H_2O$ (triangles) and $[Co(terpy)_2][ClO_4]_2.0.5H_2O$ (circles).[148]

Iron(II) and cobalt(II) are two such metal ions which strongly favour octahedral or pseudo-octahedral geometries, being d^6 and d^7 transition ions respectively, and their *bis*-terpyridyl salts commonly adopt forms of the terpyridine embrace.[141, 142, 145] Cobalt(II) *bis*-terpyridyl derivatives also routinely possess a spin equilibrium in the region 0-350 K, and numerous salts and solvates of the parent dication $[Co(terpy)_2]^{2+}$ have been studied, as well as complex salts with extensively derivatised ligand backbones.[40] Numerous cobalt(II) salts containing the parent terpy ligand, of the form $[Co(terpy)_2]X_2$, where X = PF_6, BF_4, ClO_4, F, Cl, Br, I, and larger more complex anions such as the dianion $[Co(CN)_4]^{2-}$ have been structurally, optically and magnetically characterised.[100, 149-151] The salts, often isolable as different hydrates, display various spin crossover behaviour which routinely feature gradual, incomplete spin transitions which are highly dependent upon water content (Figure 11). The relatively small electronic and geometric rearrangement associated with promotion of one electron from the t_{2g} level in the Jahn-Teller compressed low spin state to the high spin state means that spin orbit coupling between the two states is large, and an optical study concluded that the lability and possible dechelation/rechelation rearrangement occurring during a spin transition makes the spin equilibrium process in cobalt(II) *bis*-terpy salts very rapid.[152] Hence the susceptibility curves are generally all indicative of gradual transitions in which no phase change transpires.[153]

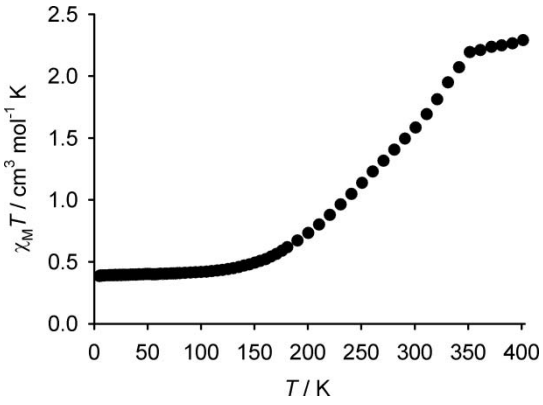

Figure 12 – Magnetic susceptibility curve for bulk polycrystalline $[Co(terpy)_2][BF_4]_2$.[149]

Exceptions to these observations do exist, however, with the complexes $[Co(terpy)_2][BF_4]_2$ and $[Co(terpyOH)_2][CF_3SO_3]_2.H_2O$ both retaining the ability to pack in the terpyridine embrace yet showcasing unusual magnetic behaviour.[149, 154] Though $[Co(terpy)_2][BF_4]_2$ displays the usual, gradual spin crossover behaviour as the material switches from LS → HS over the 150 – 350 K range, it is set apart due to the existence of a reproducible discontinuity at ca. 350 K (Figure 12). Unit cell parameters obtained through variable temperature X-ray data reinforce the presence of the gradual spin transition alongside regular thermal expansion, and there exists no evidence for a crystallographic phase change. Instead, the discontinuity has been ascribed to subtle changes in steric contacts between neighbouring dications, rather than a distinct phase change or order-disorder transition as is usually responsible for such features in the susceptibility curves of SCO materials. It was concluded that, though powder and single crystal data reinforced one another, the materials cannot be unambiguously correlated due to the 50 K difference in observations suggesting the discontinuity. This being said, the differences may simply in part arise because of differing degrees of crystallinity between the single crystal and the bulk powder upon which the magnetic measurements were performed.[149]

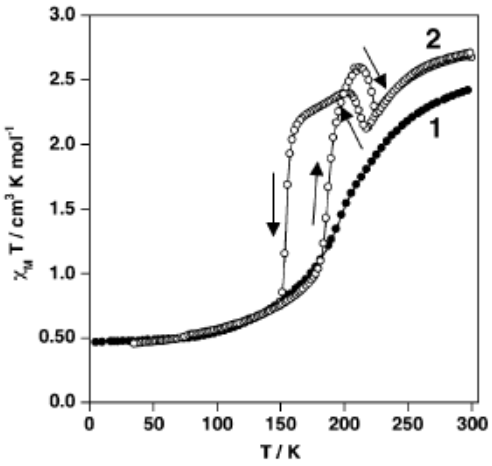

Figure 13 – Magnetic susceptibility curves recorded in cooling and warming modes for the gradually switching polymorph 1 (black circles) and hysteretic polymorph 2 (white circles) of$[Co(terpyOH)_2][CF_3SO_3]_2.H_2O$.[154]

The behaviour of $[Co(terpyOH)_2][CF_3SO_3]_2.H_2O$ is complicated to an even greater degree, as it possesses two distinct polymorphs of the same composition with very different magnetic behaviour, dependent upon the rate of crystallisation.[154] The first polymorph, crystallised very slowly over the course of a week, possesses an uninteresting temperature dependence, switching gradually and incompletely over a 150 K interval not unlike the majority of SCO cobalt(II) complexes. The second polymorph, which is precipitated over a shorter time scale, differs structurally and actually exhibits dual hysteresis, one of which is a reverse spin crossover process. To our knowledge, it is the only reported example of a cobalt(II) *bis*-terpy complex exhibiting such behaviour in the absence of long alkyl chains appended to the backbone, which are usually necessary to bring about the large order-disorder phase change necessary for hysteretic thermal spin crossover in cobalt(II).[155-158] Structurally, the two compounds differ (Figure 14) in that in polymorph 1, pairs of dications form discreet units, strongly hydrogen bonded via their hydroxy moieties to a pair of lattice water molecules which are in turn held in place by two symmetry related bridging trifluoromethansulfonate anions. In polymorph 2, the hydrogen bonding has directionality. One of the hydroxy groups of the dication and trifluoromethansulfonate ion are bridged by a water molecule, whilst the other interacts directly with an oxygen atom belonging to a second trifluoromethansulfonate anion. The “normal” hysteresis (Figure 13) probably arises from a subtle disorder change upon heating to 150 K, with the hydrogen bonding directionality transmitting the information across the lattice resulting in a metastable high spin state. The sharp decrease in magnetism between 210 and 220 K suggests that less than 20% of the metastable cobalt(II) centres relax back into the low spin configuration, before the susceptibility rises further beyond 220 K analogously to polymorph 1. Though the reverse spin crossover process is clearly a cooperative process due to the hysteresis observed, upon cooling the metastable intermediate phase is perceived to contain a smaller proportion of high spin centres due to pre-saturation of the high-spin state for the temperature regime resulting in lower observed cooperativity. This behaviour, however, is very unpredictable and, notably, uncommon in cobalt(II). Additionally, the multiple-phases are not fully populated, with the intermediate phase population being very scan-rate dependent, which is a significant drawback if one is to firstly promote robust, reproducible cooperative cycles and secondly to harvest as much switching information per given quantity of material.

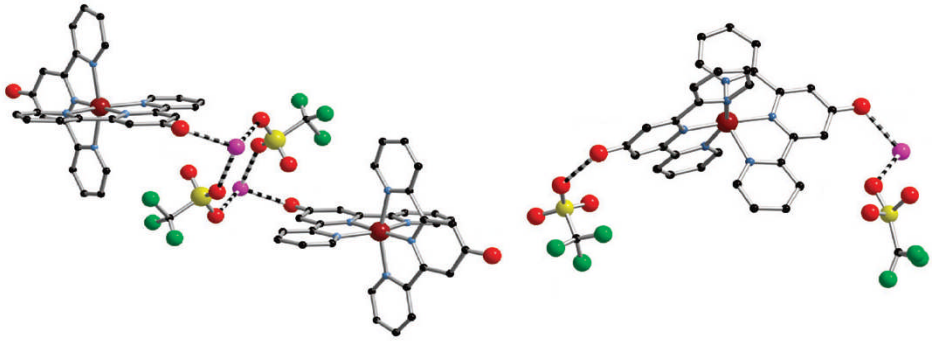

Figure 14 – Crystal packing diagrams for polymorph 1 (left) and polymorph 2 (right) of $[Co(terpy)_2][CF_3SO_3]_2.H_2O$ at 293 K to illustrate hydrogen bonding interactions made by the appended hydroxy substituents. Atom code: black (carbon), blue (nitrogen), green (fluorine), orange-red (dication/anion oxygen), pink (water oxygen), yellow (sulfur) and crimson (cobalt) with H atoms omitted for clarity.[154]

Despite much larger structural changes associated with the LS → HS transition in iron(II) complexes of meridionally chelating tridentate ligands, iron(II) salts of the parent terpy ligand all remain low spin indefinitely. The structural distortions and changes upon a change in ground state to high spin include, but are not limited to, a ca. 10% bond length increase and the onset of a significant Jahn-Teller contraction, both of which cause stark changes in molecular volume and shape, which is ideal for transmitting switching information across closely interacting discreet dications in a terpyridine embrace motif (Figure 15). Yet, the ligand fields associated with iron(II) salts containing non-coordinating anions of the form $[Fe(terpy)_2]X_2$, where X = BF_4, ClO_4, PF_6 possess ligand fields too large to permit thermal access to the HS state.[159-161] The deep purple colour of its salts both in the solid state and as solutions are indicative of a low spin ground state, and the existence of a charge transfer band in the region 520 – 580 nm in the absorption spectrum plus sharp, well-resolved coupled signals in the proton NMR spectrum further substantiate that a thermal spin transition is inaccessible before the onset of decomposition.[160, 162]

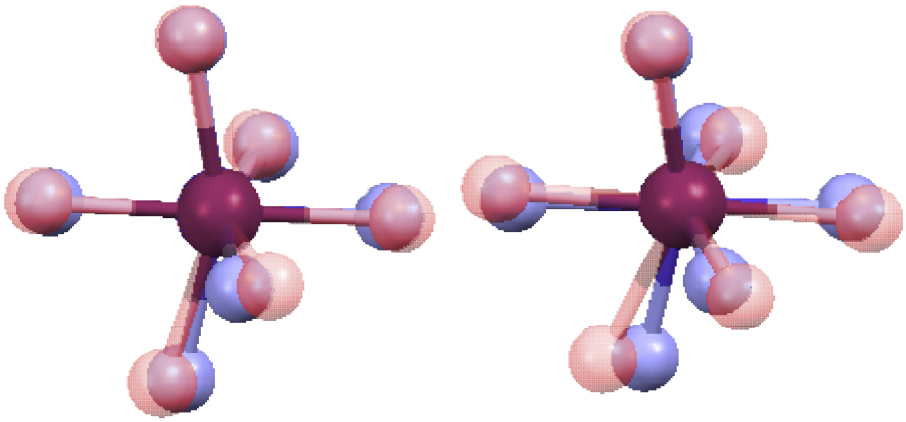

Figure 15 – High spin (red) and low spin (blue) overlays of the ML_6 octahedral coordination spheres in $[Co(terpy)_2][BF_4]_2$ (left) and $[Fe(3'\text{-methylpyrazol-1'-yl})pyridine)_2][BF_4]_2$ (right).[63, 149]

The ligand field strength dependence upon metal to donor distance means that, in accordance with $10dq_{HS}/10dq_{LS} \sim r_{LS}^6/r_{HS}^6$, it is expected that appropriately substituting the terpyridine backbone in a manner so as to sterically crowd the iron(II) centre, the field could be decreased in magnitude and effectively tuned so as to allow a thermally accessible promotion of the centre to the high spin configuration. This is precisely the case in a number of terpy complexes of iron(II) substituted at the distal rings, whose appended substituents point almost directly into the iron's $d_x^2\text{-}_y^2$ lobes. Constable *et al* prepared a series of ligands, both symmetrically and unsymmetrically substituted, with methyl and phenyl groups at the distal pyridine 6-position.[163] The iron(II) complexes prepared exhibit electronic ground states which are primarily decided by the symmetry of the terpy chelating the iron(II) core. The distally disubstituted derivative containing complexes all possess high spin centres in the solid as orange perchlorate and hexafluorophosphate salts, and experience paramagnetically contact shifted signals in the ^{1}H NMR spectrum telling that the solution LS → HS equilibrium lies far to the right under ambient conditions. Crystallographically, the salts appear to possess highly distorted Fe-N_6 octahedra, with two of the distal rings experiencing very long Fe-N lengths over 2.4 Å imposed by the substituents, meaning the complexes can be considered pseudo-4 coordinate and unable to accommodate a contraction of the coordination sphere necessary to adopt a low spin configuration.

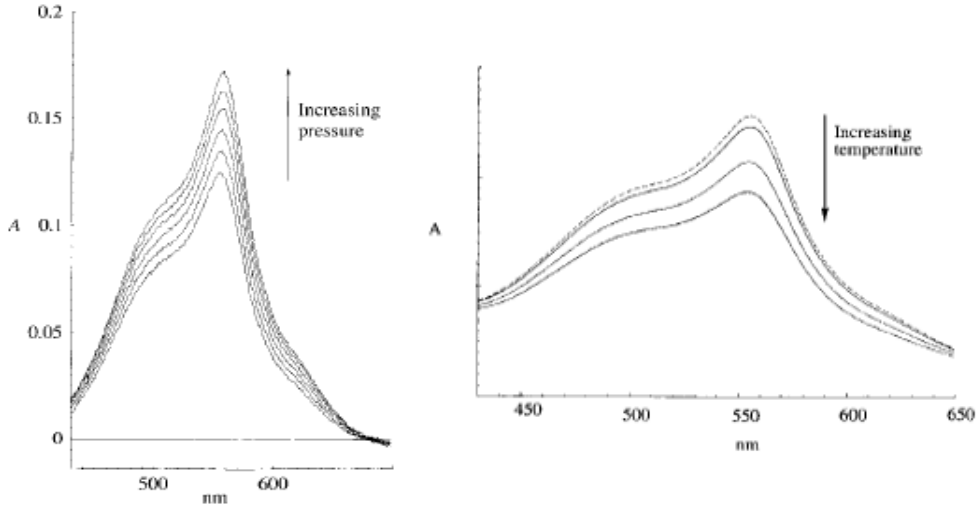

Figure 16 – Pressure and temperature dependence of the spin equilibrium of $[Fe(2\text{-}(4',6'\text{-diphenylpyridin-}2'\text{-yl})\text{-}6\text{-}(pyridin\text{-}2''\text{-yl})pyridine)_2][PF_6]_2$ in acetonitrile solution as a function of the MLCT band of the low spin form centred at 554 nm.[163]

The unsymmetrical substituted complex salts appear to comprise a mixture of spin states in acetone solution, exhibiting signals in the ^{1}H NMR which are contact shifted to a lesser extent than their disubstituted counterparts, suggestive of a rapid spin exchange

process occurring for solutions of [Fe(2-(4',6'-diphenylpyridine-2'-yl)-6-(pyridin-2''-yl)pyridine)$_2$]$^{2+}$. This is clarified by the increase in intensity of the low spin MLCT absorption band at 554 nm as the pressure is increased as the equilibrium favours the formation of the smaller low spin complexes (Figure 16). The dependence in the solid state, however, is clearly one of steric reasoning, as the solid perchlorate and hexafluorophosphate salts are fully low and high spin respectively, substantiated by magnetic measurements which indicate no thermal dependence over the 4 – 290 K range. Oddly, no further salts and polymorphs were isolated, as electronically the ligand field is obviously within the range required to undergo a spin transition, with the spin population in the solid a delicate balance of the octahedral distortion against the size of the counterion employed.

The spin equilibria of complex salts chelated by the sterically encumbered 2,6-di(2'-quinolyl)pyridine derivative of terpy were also investigated, yet these structural modifications to the distal aromatic rings resulted in complexes in which the high spin state was deemed significantly more stable.[164] The complex, of the form [Fe(2,6-di(2'-quinolyl)pyridine)$_2$][ClO_4]$_2$ was isolated as a red solid, and displayed magnetic moments between 5 and 6 B.M over a 100 – 400 K temperature range, with a steep decline in the moment below 100 K consistent with the large zero field splitting of high spin iron(II).[165] Absorption measurements in nitromethane solution concluded the high spin ground state of the complex, with a ligand field of the dominant high spin species of ca. 10,000 cm^{-1}, too small to accommodate spin pairing of the valence d electrons. The effect of the steric repulsion is highly significant here, as the imposed length of the M-N contacts as estimated from ligand field parameters prevent contraction of the coordination sphere and omit the possibility of the low spin configuration being adopted.[164]

Another method of reducing the imposed ligand field by terpy and thus promote a thermally allowed spin transition may be to reduce its basicity, orbital overlap and thus its resulting effect upon the t_{2g} stabilisation of the respective chelated metal ion. This presents a potentially facile route towards spin crossover iron(II) complexes of terpy, without the need for large substituents which are shown to necessitate extreme distortions about the iron's octahedron, resulting in high spin trapped complexes with large, non-spherical volumes unable to adopt the crystallographically favourable terpyridine embrace packing motif.[165, 166] A number of *bis*-terpyridine iron(II) complexes appended with relatively small electron withdrawing groups have come under investigation for the purposes of electrochemical and spin equilibrium analysis. The complexes worthy of discussion are not functionalised at the distal pyridine 6-positions, so as to rule out any dictation of spin state equilibrium by steric factors. The series of complexes functionalised on the central pyridine, of the form [Fe(4-X-terpy)$_2$][PF_6]$_2$, where X = Cl, $SOCH_3$, SO_2CH_3 and NO_2, were all isolated as either dark blue

or purple solids, indicating a highly electron deficient low spin core. Solution-based variable temperature susceptibility readings on the chloro, sulfoxide and sulfone complexes showed no paramagnetic contribution to the bulk susceptibility, and though the nitro functionalised derivative was not subject to such a study, its sharp proton NMR spectrum, with signals appearing between 7 and 9 ppm, is also consistent with an entirely low spin iron(II) population. The same can be said for two other highly electron deficient *bis*-terpy complexes, $[Fe(2,6\text{-di}(5'\text{-nitro-pyridin-2'-yl})\text{pyridine})_2][PF_6]_2$ and $[Fe(4\text{-chloro-2,6-di}(4'\text{-chloro-pyridin-2'-yl})\text{pyridine})_2][ClO_4]_2$.[167, 168] Additionally, consistent with the absence of a thermal spin equilibrium under ambient conditions, the iron(III/II) redox couples are in linear agreement with the calculated Hammett constants, σ, for the free ligands which are used as a measure of a substituent's electron withdrawing/releasing capacity attached to an aromatic system.[169, 170]

The focus of this work with regard to preparing new *bis*-terpy derivative iron(II) and cobalt(II) complexes is one in which the electronic structure is tuned primarily by the nitrogen content of the constituent heterocycles comprising the *tris*-azinyl ligand backbone. The reasoning behind the proposal is two-fold. Firstly, iron(II) coordinated by pyrazine, pyrimidine and 1,2,4-triazine exist, however there has been no study into the effects of the unsubstituted parent *tris*-heterocyclic analogues of terpy, which can result in spin-equilibrium iron(II) centres if the large ligand field of terpy is diminished appropriately.[163] The σ-donating ability of the respective heterocycles, reflected in their pK_a values (Figure 17), is reduced for the electron deficient donors which should have a stabilising effect upon the d-orbital set, however induce smaller ligand fields than terpy through a reduced M-N energy overlap. What is unclear is the importance of the increased propensity to accept back-donating π-density of the electron poor *tris*-azines. In the 2,6-di(5'-nitropyridin-2'-yl)pyridine iron(II) complex, for example, the lowest energy MLCT band is shifted to significantly lower energy than in the parent terpyridine complex.[167, 171] This is actually telling of increased π-back donation from the iron(II) t_{2g} set into vacant π* levels on the aromatic system. The reduced σ-donation and increased π-withdrawal by the ligand probably act semi-synergistically, with an overall effect of leaving the ligand field much unchanged. The parent electron deficient *tris*-azines of interest to us, however, lack groups able to remove electron density from the heterocyclic system via π-induction, and therefore it is predicted that the π* levels about the chelating ligand will be of higher energy. The speculation is thus that the novel complexes will experience a reduced σ-interaction due to lower intrinsic basicities of the constituent heterocyclic donors involved, but also a diminished π-backdonation contribution to the M-N interaction, resulting in ligand fields of smaller magnitude.

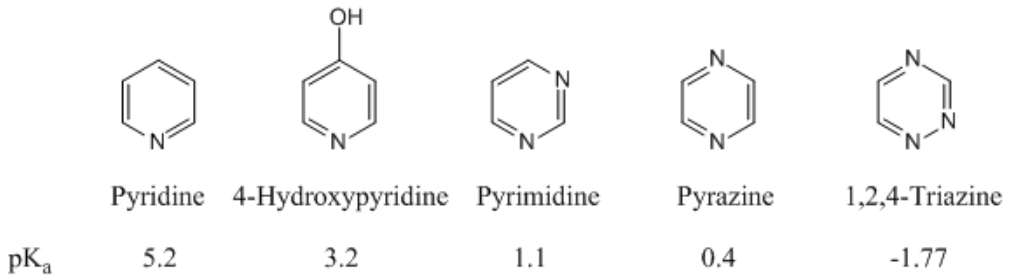

Figure 17 – Experimental pK$_a$ values for the free base heterocycles comprising the diazinyl terpy analogues in aqueous solution.[172, 173]

The second reason for the study of the parent *tris*-azinyl heterocyclic iron(II) and cobalt(II) complexes is in a concerted effort to maintain the same roughly spherical shape of the *bis*-chelated complex dications. Altering the electronics of the metal centre by modification of the nitrogen content of the ligand system disposes of the need to append relatively large, repulsive substituents to the ligand backbone, which would inconveniently cause the shape of the molecules to deviate from the preferred pseudo-sphere, and inhibit formation of the close packed layers comprising the terpyridine embrace. The exception, it must be noted, is the use of 4-hydroxypyridine, which shall be employed only in place of the central pyridine ring comprising the terpy system. The OH group is the smallest substituent which can be incorporated into the system at this position to encourage strong intermolecular hydrogen bonding. It is proposed that this substituent could, theoretically, promote 1D cooperativity within layers of complex molecules making up the terpyridine embrace through hydrogen bonding with lattice water, inter-layer tetrafluoroborate counterions or some combination of the two.

1.2.3 2,6-Di(pyrazol-1'-yl)pyridine derivatives: a problem of crystal engineering

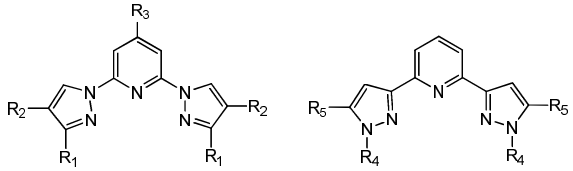

Figure 18 – Basic framework for the two meridionally *tris*-chelating structural isomers of the type 2,6-di(pyrazolyl)pyridine, 2,6-di(pyrazol-1'-yl)pyridine (left) and 2,6-di(pyrazol-3'-yl)pyridine (right). Synthetic routes employed in the preparation of their substituted derivatives make substitution elsewhere about the backbone other than where indicated by a variable R group very difficult.

A vast amount of work involving mononuclear complexes of terpy analogues within the field of spin-crossover have very much focused upon the coordination of 2,6-di(pyrazolyl)pyridine derivatives to an iron(II) core.[76, 174-176] Pyrazoles are less basic than their pyridyl counterparts, manifested primarily in their weaker σ-interactions observed in their coordination chemistry to metal ions.[31] Moreover, their complexes exhibit diminished π-backdonation by virtue of the smaller, more constrained ring size, culminating in reduced d-

π* overlap, both spatially and energetically. Accordingly, there are a vast number of reports of iron(II) complexes containing pyrazole donors which are spin crossover active, in particular complexes of the structural isomers 2,6-di(pyrazol-1'-yl)pyridine (1-bpp) and 2,6-di(pyrazol-3'-yl)pyridine (3-bpp) (Figure 18). They have received much attention which is due to a combination of reasons, chiefly their meridional coordination mode, relative ease of backbone modification and the adoption of their terpyridine embrace in the crystal of a number of their mononuclear octahedral transition metal ion complexes. The latter of which is responsible for really driving interest in their SCO behaviour, as the closely packed complex units comprising the terpyridine embrace motif is key to transmitting the spin switching information of the individual metal complexes across the lattice, necessary for magnetically and optically interesting spin crossover materials.[174, 177]

The discussion will now focus solely on iron(II) salts of 2,6-di(pyrazol-1'-yl)pyridine derivatives, by virtue of the fact that it is the more heavily studied structural isomer, and that the preparative techniques employed exhibit higher tolerance to the range of functional groups which can be introduced at the specified positions on the backbone (Figure 18). Much work has been done using the parent ligand 1-bpp, the most interesting salt of which is the tetrafluoroborate. Its SCO has been extensively studied, with the solvent-free crystalline phase undergoing an abrupt first-order thermal spin transition centred at 261 K with a 4 K hysteresis width.[95] In addition, below 80 K the material remains high spin trapped after irradiation at 632.8 nm due to thermal quenching of the HS → LS relaxation process.[178] Crystal structures of both the solvent-free high- and low-spin forms have been well studied, and like many of its derivatives it adopts the terpyridine embrace, with cooperativity governed by the electrostatic interactions, which are subject to large changes upon lattice pressure fluctuations. A second solvated phase of the material can be obtained by performing the crystallisation process from $MeNO_2$ at 240 K instead of at ambient temperature, yielding the material $[Fe(1\text{-}bpp)_2][BF_4]_2 2.9MeNO_2.0.25H_2O$. The solvated polymorph is obtained as dark brown crystals, and crystallographically was shown to contain two unique iron centres completely low spin below 240 K. Above 260 K, the crystals were shown to decompose into a bright yellow powder, consistent with complete or partial loss of lattice solvent/water, in tandem with a change in space group. Unfortunately no crystallographic study could be performed on this new high spin material, yet the powder pattern suggested that this desolvated material was not isostructural with crystalline $[Fe(1\text{-}bpp)_2][BF_4]_2$.

With one exception, all other reported salts of the form $[Fe(1\text{-}bpp)_2]X_2$, where X = PF_6, ClO_4, SbF_6, I_3 and a mixed iodide/triiodide salt crystallise as solvent free materials which remain trapped in the high spin configuration down to 5 K. The salt [Fe(1-

bpp)$_2$][Co($C_2B_9H_{11}$]$_2$ is the other spin crossover active material, shown crystallographically to possess two unique cations, one of which changes spin gradually over the range of 220-340 K with the other, experiencing severe angular distortions about the iron(II) centre, remaining fully high spin indefinitely (Figure 7). Though the isolated dication $[Fe(1\text{-bpp})_2]^{2+}$ is electronically suited to thermal spin crossover, possessing a $T_{1/2}$ of ~250 K in acetone solution, the range of behaviour observed in different salts and solvates illustrates the dependence of the desirable properties upon intermolecular interactions. The materials remaining high spin trapped all exhibit severe angular distortions, and from analysis of the iron(II) coordination sphere in *bis*-chelated 1-bpp complex dications one can improve the understanding of a given material's spin crossover behaviour or lack thereof.

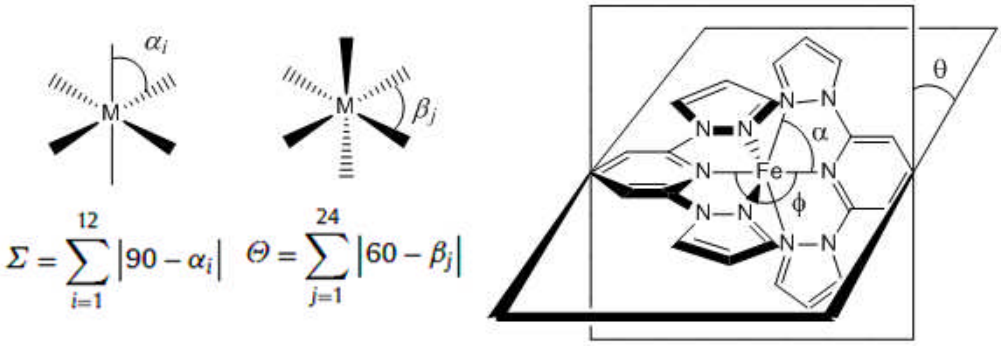

Figure 19 – Distortion parameters commonly employed to quantify the degree of distortion about octahedral centres; rhombic distortion parameter, Σ. (left); trigonal distortion parameter, Θ, (centre); a schematic representation of the intraligand *cis*-bite angle, α, and the angular Jahn-Teller distortions Φ and θ (right).

In addition to the elongation of the Fe-N bonds upon change in spin state from low to high and thus an increase in molecular volume of the dication, a number of other changes transpire about the coordination sphere which can be quantified and parameterised. These, like the variation in Fe-N distance, are diagnostic of the electronic configuration in a given iron(II) centre. Furthermore, as these parameters quantify angular distortions about the local coordination sphere, and the extent of deviation from ideal octahedron, one can infer information about the form of a spin transition curve from these changes in the coordination geometry upon a change of spin state, and even predict the likelihood that a material will prove magnetically interesting. Firstly, a result of the expansion of the Fe-N distances results in an obvious increase in volume of the Fe-N polyhedron volume. This is calculated by summing together the eight individual Fe-N_3 tetrahedron volumes, and is typically 9 – 10 Å^3 for low spin centres, and is in the region of 12 – 13 Å^3 for fully high spin centres. The two octahedral distortion parameters Σ and Θ are used to quantify octahedral distortions across the breadth of coordination chemistry, however are of particular utility in SCO research because of the differences in the values possessed by centres of differing electronic configuration. Σ quantifies the rhombic distortion, which is an angular measure of the

distortion about the octahedral donor set, obtained by the summation of the differences between the twelve *cis* N-Fe-N from the ideal value 90 (Figure 19). The trigonal distortion parameter Θ is a summation of the deviation of the 24 unique torsion angles between *cis* N-donors on opposite triangular faces, measured along their common pseudo-threefold axis. Θ is particularly informative, generally appearing below 300 in fully low spin iron(II) centres possessing dipyrazolylpyridine architectures, whereas the values can be in excess of 500 for highly distorted high spin ions.

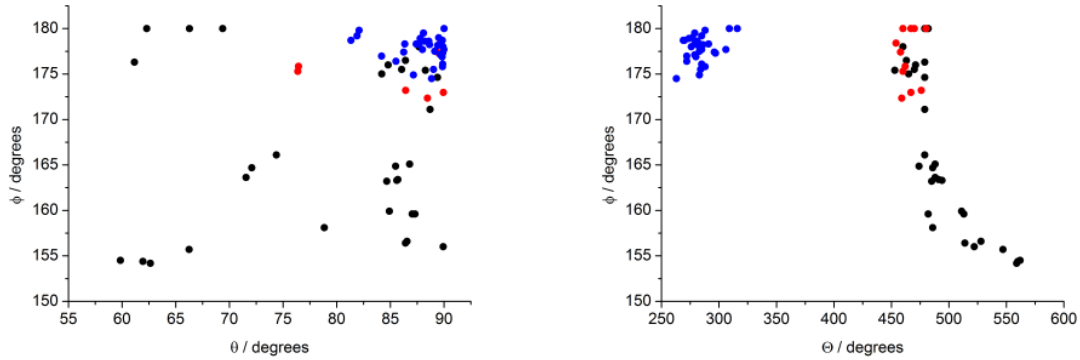

Figure 20 – Plots of θ vs. Φ (left) and Θ vs. Φ (right) illustrating the geometric distortions for about the central iron(II) atom for a number of high spin trapped (black), high spin $[Fe(1\text{-}bpp)_2]^{2+}$ type complexes which do thermal spin crossover (red) and unambiguously low spin centres (blue) at the temperature of measurement.[38, 46, 63, 66, 67, 69, 70, 74, 123, 175, 178-192]

The latter three parameters of note are highly specific to octahedral metal ions chelated meridionally by tridentate ligands. The ligand bite angle α is an average of the four N_{py}-iron-N_{pyz} bite angles, and upon promotion of an iron(II) centre to the high spin state decreases in magnitude as the Fe-N_{py} lengths undergo larger increases as the centre is forced to adopt a Jahn-Teller elongated pseudo-octahedron. The final two parameters commonly used, Φ and θ, can be used to assess the likelihood that crystal lattice will be able to accommodate a switch from HS → LS. Φ is a direct measure of the N_{py}-Fe-N_{py} *trans* angle, usually seen very close to the ideal value of 180 in low spin centres, and appearing at lower values in high spin centres concomitant with the structural changes associated with a change in spin state (Figure 20). $[Fe(1\text{-}bpp)_2][PF_6]_2$ for example possesses an extremely distorted FeN_6 octahedron with a trans angle of 154° and, unsurprisingly, cannot accommodate a transition to the LS state (Figure 21). Finally, θ is best described as a twist in the plane of one or both ligands resulting in a reduction of the dihedral angle of the least squares planes between the two *tris*-imine ligands.

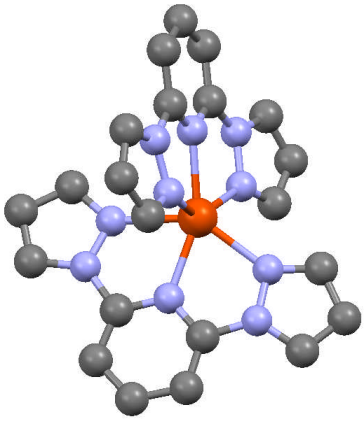

Figure 21 – X-ray structure of the highly distorted dication in high spin trapped $[Fe(1\text{-}bpp)_2][PF_6]_2$ at 120 K with H atoms removed for clarity.[67] Atom colour code: carbon (grey), iron (orange) and nitrogen (periwinkle).

It is clear to see that the 2,6-di(pyrazol-1'-yl)pyridine backbone represents an ideal ligand system to work with in developing new magnetically and optically interesting spin crossover complexes of iron(II), yet to be successful one must be carefully tune the materials both electronically and sterically. Specifically, the problem becomes one of crystal engineering – the electronics of isolated centres can be tuned according to their known influence on related aromatic systems, however intercomplex communication is to be encouraged through modification of the system to retain the closely associated terpyridine embrace, and to mediate interlayer interactions. The effect of substituting at the pyrazole 3-position is already well understood, with substituents such as the mesityl or phenyl groups sitting perpendicular to the dipyrazolylpyridine backbone, forming fully low and high spin complexes based on their relative Fe-N σ-interaction strengthening and weakening respectively. Groups which are unable to rotate into a conformation so as to relieve steric strain about the iron(II) centre either result in a completely high spin trapped complex, as in $[Fe(2,6\text{-di}(3'\text{-isopropylpyrazol-1'-yl})pyridine)_2][BF_4]_2$ which cannot accommodate the unfavourable steric contacts resulting from Fe-N bond contraction, or simply singly chelate the iron(II) core.[175, 193] The behaviour of the salts of 2,6-di(3'-hydroxymethylpyrazol-1'-yl)pyridine and 2,6-di(3'-methylpyrazol-1'-yl)pyridine are interesting, with the tetrafluoroborate salts exhibiting a number of crystallographic phases, however only the methyl functionalised dipyrazolylpyridine backbone is small enough to accommodate crystal packing of the dications in the terpyridine embrace.[63, 74] Similarly, the coordination chemistry of numerous 4-substituted pyrazole derivatives of 1-bpp with iron(II) has been investigated due to relative ease of functionalisation at this position, and large appendages as expected inhibit cooperative switching through adoption of the terpyridine embrace. Interestingly, atoms as large as bromine have been incorporated at the pyrazole 4-position with retention of this crystallographic motif in addition to a thermally induced cooperative spin transition,

however the 2,6-di(4'-iodopyrazol-1'-yl)pyridine salts all remain low spin indefinitely and crystallise in space groups incompatible with the terpyridine embrace.[70]

On the contrary, direct functionalisation of the central pyridine ring in the 1-bpp aromatic *tris*-heterocyclic system and incorporation into salts of iron(II) has not been explored in any great deal. Due to the synthetic methodology employed, examples of 1-bpp derivatised at the 4-position generally include a methylene spacer which not only adds additional steric bulk to the backbone, further hindering the adoption of the desired terpyridine embrace motifs in the crystal, but reduces the electronic effect of the substituent upon the coordinated iron(II) centre by virtue of the increased spatial separation. Directly appending small, electron withdrawing and donating substituents at the 4-position of the pyridine will have a larger effect upon the σ-basicity and π-acidity of the respective nitrogen donor atoms, and thus of the magnitude of the d-orbital splitting localised on the iron(II) centre. As a potential added bonus, it is hoped that small substituents, particularly those with strong hydrogen bonding ability such as that of a mercaptan or hydroxy moiety will increase inter-layer communication between layers of complexes in the terpyridine embrace. It is predicted this will further increase communication in this highly cooperative system, and the incorporation of lattice water or solvent will stabilise the low spin state as has been observed in related examples due to a combined effect of lowering of the ligand's basicity and increase intrinsic lattice pressure.[72, 194] It is theorised that in effect, one can engineer highly cooperative systems crystallising in the terpyridine embrace, with increased intercomplex communication spanning the transition due to the small substituents pointing in between the lattice layers.

1.3 Multifunctional Materials

1.3.1 Overview

Though significant work is concerned with the development and optimisation of singly functional bistable spin crossover materials, another prime interest in spin crossover research is that of incorporating a second functionality into the switching materials.[124] Multifunctional materials which, on the nanoscale retain their hysteretic, abruptly switching behaviour are of interest due to the fact that the second functionality, be it for example an emissive or semiconducting material, could have their second functionality switched or tuned, depending upon the electronic configuration of the spin crossover moieties.[195] This in essence means the signal by which the spin state of the material is read is enhanced by the presence of the second function, and thus would be suited to optical data storage and sensing.

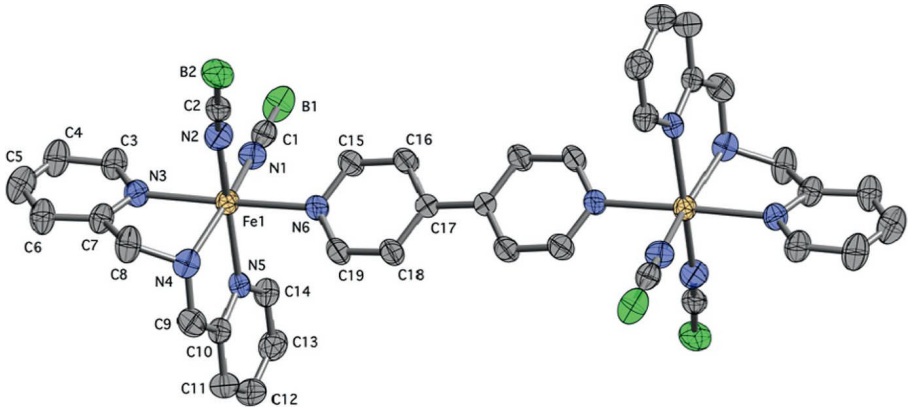

Figure 22 – X-ray structure of fully high spin [(Fe(dipicolin-2-ylamine)($NCBH_3$)$_2$)$_2$-4,4'bipyridine at 290 K; Ellipsoids are plotted at the 30% level with H atoms omitted for clarity.[91]

There exist a few potential methods for incorporating dual functionality into a spin crossover material, but these are often dependent upon what the additional functionality of interest is and how the second functional material or complex is to interact with the spin crossover centres. A lot of work has been performed on symmetrical dinunclear iron(II) complexes which exhibit thermal and pressure induced magnetic bifunctionality, through short range ferromagnetic and antiferromagnetic coupling which stabilises the intermediate spin state.[71, 195, 196] The complexes, which are most commonly bridged by cyanide, or by a bidentate imine linker, possess three spin states within the discreet dinuclear units, [HS-HS], [HS-LS] and [LS-LS] (Figure 22). The antiferromagnetic exchange between the singly occupied iron(II) centres actually stabilises the intermediate phase, with respect to the pure HS and LS phases, hence a plateau is observed in their susceptibility curves where the centres are roughly 50:50 HS to LS (Figure 23).[92] The findings concluded that antiferromagnetic exchange was largest in dinuclear iron(II) complexes whose magnetic orbitals have diagonal symmetry along the same plane, and that engineering these tristable magnetic materials was a matter of optimising intramolecular iron(II) communication whilst retaining the cooperative switching mediated through intermolecular interactions.[86, 197] This phenomenon however is not unique to discreet binuclear complexes, and it is possible to engineer materials exhibiting either ferromagnetic or antiferromagnetic exchange in the crystal whose magnetic behaviour is even more complicated, with examples in the literature featuring iron(II)/(III) clusters and 1D and 2D chain materials.[26, 121, 198-201]

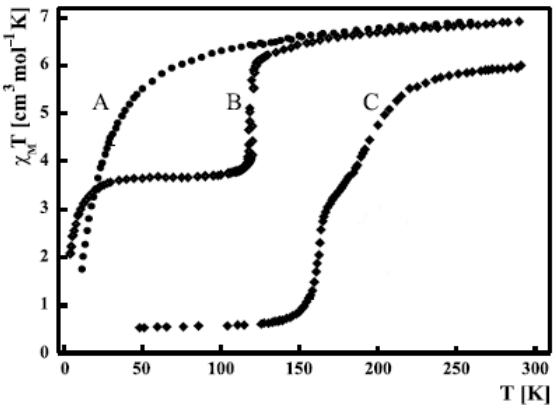

Figure 23 – Thermal susceptibility plot for solid samples of the three antiferromagnetically coupled dinculear spin crossover complexes [(Fe(bipym)(NCS)$_2$)$_2$bipym] (A), [(Fe(bipym)(NCSe)$_2$)$_2$bipym] (B) and [(Fe(bt)(NCS)$_2$)$_2$bipym] (C); bipym: 2,2'-bipyrimidine; bt: 2,2'-bithiazoline.[92]

One can also instigate a change in spin state through a phase change mediated by an order-disorder transition, and liquid crystal based SCO materials have proven strong focal points for study of these phenomena in tandem.[108, 155] Thermotropic liquid crystals form intermediate phases exhibiting both crystalline three-dimensionality but also significant anisotropy, as is associated with liquid phases.[202, 203] Their multi-phase capacity, mediated by entropic order-disorder changes, has been shown substantial enough to promote cooperative changes in the spin state to the complex centres the long alkyl changes are attached or doped into as counterions.[122] Their fluid nature is also highly amenable for processing into films, a clear benefit toward their incorporation in ultra thin display devices.[122, 202, 204] Up to a point, the cooperativity of the phase change was shown to be highly dependent upon alkyl chain length and alignment at the lower temperature, more ordered phase.[33, 108] There still remains much to be done in improving liquid crystal SCO iron(II) based materials, as is illustrated by an unusual example involving cobalt(II). Though cobalt(II) *bis*-terpy complexes usually undergo gradual, incomplete spin transitions spanning some 200 – 300 K, [Co(4-hexadecyloxy-terpy)$_2$][BF$_4$]$_2$ exhibits an unusual reverse spin transition with ca. 50 K hysteresis, which is a result of ordering of the chains upon cooling, with the ordering phase change occurring almost midway between the two transition temperatures.[100, 155, 158]

Multifunctional spin crossover materials exhibiting increased electrical or optical responses to the switching process as a result of their added functionality are hugely sought after. Polymeric materials of a directional nature, or spin crossover centres crystallised with electrically conducting counterions, combining spin crossover with conductivity, have been investigated and in the former case conductivity has been shown to drop, albeit relatively weakly, as the spin state of the iron centres adopt a high spin ground state.[205, 206] More focus has been placed on the incorporation of a luminescent material into a spin crossover host,

however, as the need for directionality in the crystal is made redundant. One approach which has seen some success is the grafting of polymeric spin crossover materials onto a highly emissive nanoparticle. Polymeric iron(II) chains bridged by substituted 1,2,4-triazoles showed a remarkable retention of cooperativity in their thermal spin transitions grafted onto nanoparticles containing rhodamine-110 and 3-(dansylamido)propyltrimethoxysilane.[112, 207] Yet, the emission intensity in the presence of the pure low spin complex centres, whose absorption band overlaps strongly with that of the fluorophore, is only reduced by a factor of two. Clearly, these systems are models for luminescent spin crossover materials, yet there is much work to be done, not only on improving the emission contrast between the two states but also with regards to incorporation of a spin crossover material whose spin transition spans room temperature. Other efforts have focussed on attaching fluorophores directly to an iron(II) complex, allowing full characterisation of the resulting phase pure materials. The systems under current literature investigation are based on iron(II) salts containing a 1-bpp core, with planar fluorescent pyrene moieties directly bound to the backbone or linked by alkyl spacers.[208] So far, they have shown to be promising, with the planar pyrene appendages offering the potential to promote addition cooperativity in the switching process, but the only changes in emission so far were down to non-magnetic quenching by the high spin state, and no change in emission band positions was observed. Another potential method in pursuit of this goal is to exploit solid state packing and crystallographic motifs of complexes and materials exhibiting different functionality, and preparing phase pure solid solutions in an attempt to retain or modulate their respective isolated functionalities. This specific aim is central to chapter four and is an expansion on previous work carried out within the group (Section 1.3.2).[35]

1.3.2 Doping of a spin crossover host lattice

The approach this work will take towards the assimilation of a second functionality into a spin crossover material is one which involves the co-crystallisation of two structurally similar complex salts of similar molecular volume, to form homogenous solid solutions of the two materials. Subject to previous discussion, the terpyridine embrace frequently adopted by undistorted meridionally chelated complexes of *tris*-imine ligands, such as terpy, can be used to promote homogenous co-crystallisation of two different metal complex salts, which as pure materials crystallise in either the same, or very similarly related, forms of this crystal packing motif.[35] The terpyridine embrace motif is not exclusive to *bis*-terpyridine complexes, but has also been observed in polymorphs of a number of transition metal complexes coordinated by related ligands, such as substituted terpyridine derivatives, 2,6-di(pyrazol-1'-yl)pyridine and 2,6-di(pyrazol-3'-yl)pyridine to name but a few. In addition, complex salts of this form which preferentially adopt the terpyridine embrace also possess interesting and

potentially useful solid state functionalities making them ideal as dopants into a switchable lattice, such as strong emission in the visible spectrum and antiferromagnetic/ferromagnetic coupling.[209-213]

Complex salt	T / K	Space group	Dicationic volume / Å^3
$[Fe(1\text{-}bpp)_2][BF_4]_2$ (LS)	150	$P2_1$	587
$[Fe(1\text{-}bpp)_2][BF_4]_2$ (HS)	300	$P2_1$	621
$[Ru(terpy)_2][BF_4]_2$	150	Cc	677
$[Co(terpy)_2][BF_4]_2$ (LS)	100	Cc	655
$[Co(terpy)_2][BF_4]_2$ (HS)	375	Cc	693
$[Ni(1\text{-}bpp)_2][BF_4]_2$	150	$P2_1$	590

Table 1 – Selected crystallographic data for $[Fe(1\text{-}bpp)_2][BF_4]_2$ and structurally compatible complex salts which have been successfully doped into the spin crossover host lattice.[30, 95, 149]

A previous study found that $[Fe(1\text{-}bpp)_2][BF_4]_2$ and $[Ru(terpy)_2][BF_4]_2$, which crystallise in closely related forms of the terpyridine embrace in $P2_1$ and Cc respectively, were structurally compatible. A series of solid solutions of the general formula $[Fe(1\text{-}bpp)_2]_x[Ru(terpy)_2]_{1-x}[BF_4]_2$ were prepared where x was found to be 1, 0.95, 0.75, 0.57, 0.47 and 0.28 by CHN microanalysis.[35] By analysis of the powder patterns, the solid solutions were deemed to be phase pure except when x approached 0.5, with the X = 0. 75, 0.57 and 0.47 solid solutions primarily comprising of co-crystallised material in the $P2_1$ phase, with a very minor Cc contaminant phase. Susceptibility curves of the hybrid materials were promising, and though even at X = 0.95 the narrow hysteresis is lost, the curve is still abrupt with the $T_{1/2}$ value remaining as in pure $[Fe(1\text{-}bpp)_2][BF_4]_2$. The molecular volumes occupied by the dications of high and low spin $[Fe(1\text{-}bpp)_2][BF_4]_2$ and $[Ru(1\text{-}bpp)_2][BF_4]_2$ are 621, 587 and 677 Å^3 respectively, and intuitively this exertion of the privative "negative lattice pressure" by the larger ruthenium dications would be predicted to stabilise the high spin state, thus lowering $T_{1/2}$ (Table 1). As the iron complexes are doped the transition becomes more gradual, telling of the statistical replacement of nearest neighbour centres by the inert ruthenium(II) dications, and reflecting the reduction in ΔS and ΔH of the spin crossover process in the doped materials. A slight decrease in $T_{1/2}$ is noticeable down to X = 0.75, but this then increases slightly again as the iron complex concentration of the solid solution is further reduced, the origin of which still requires further investigation. Subject to irradiation at 676 nm at 10 K, the iron centres in the solid solutions can be converted fully to their thermally trapped metastable high spin states, with $\chi_m T$ values consistent with the $[Fe(1\text{-}bpp)_2]^{2+}$ concentration. As X is decreased, the T_{LIESST} value tends to a slightly lower temperature, which is not yet fully understood but may be a result of reduced ΔS between the two states in the diluted systems, and the increased vibrational flexibility imparted by negative lattice pressures which arise by exertion of negative lattice pressures by the larger ruthenium complex centres.[113]

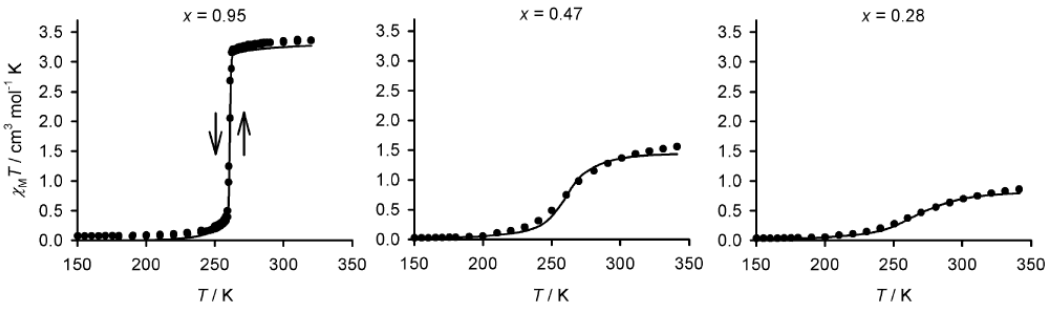

Figure 24 – Variable temperature susceptibility plots for three selected solid solutions of general formula $[Fe(1\text{-}bpp)_2]_x[Ru(terpy)_2]_{1-x}[BF_4]_2$.[35]

The dopant $[Ru(terpy)_2][BF_4]_2$ emits strongly below 80 K, but at temperatures higher than this is subject to a thermally activated non-radiative decay process which all but entirely quenches the emission (Section 1.3.3).[214] Consequently, the effect of switching upon the emissive ruthenium(II) centres in the doped solid solutions cannot be studied, as bifunctionality is not observed over the same temperature regime. Yet the findings serve as a proof of principle, in that two complexes of similar shape yet which deviate in size by more than 10% can be successfully co-crystallised together in various compositions with a high degree of retention of the abruptly switching nature of $[Fe(1\text{-}bpp)_2]^{2+}$ across the lattice (Figure 24). Unfortunately emission of the ruthenium(II) cores drops off sharply as x is increased, with essentially no detected emission at x > 0.47. This is probably not a lattice pressure based reduction of the emission intensity on the ruthenium(II) cores themselves, but instead a result of the overlap between the $^1A_{1g} \rightarrow {}^1T_{1g}$ absorption manifold of the low spin iron(II) centres and the emitted light of wavelength 622 – 663 nm (Figure 25).[67, 175] Clearly a new compatible dopant must be pursued based on an octahedral *tris*-imine donor set, which is strongly emissive at room temperature and, ideally, possesses emission energies which overlap to a lesser extent with the absorption bands of the low spin iron(II) complex cores (Section 1.3.3).

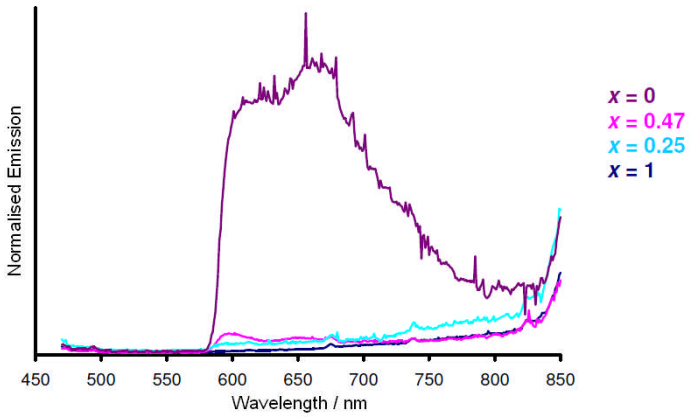

Figure 25 – Emission spectra of bulk solid solutions $[Fe(1\text{-}bpp)_2]_x[Ru(terpy)_2]_{1-x}[BF_4]_2$ at 77 K.[35]

1.3.3 Emissive ruthenium(II) salts

The system, consisting of $[Fe(1\text{-}bpp)_2]_x[Ru(terpy)_2]_{1-x}[BF_4]_2$ solid solutions, has laid the foundation for the incorporation of luminescent functionality into a spin crossover host by doping of the spin crossover centres, based on either $[Fe(1\text{-}bpp)_2][BF_4]_2$ or [Fe(3-methylpyrazol-1'-yl)pyridine$)_2][BF_4]_2$ with a structurally compatible octahedral ruthenium(II) complex dication.[35, 113] The thermal quenching of the ruthenium's luminescence at temperatures above 80 K culminates in a model system whereby the two functionalities can be observed, however not over the same temperature regime, and thus they must be discussed separately. The thermal promotion of the non-radiative decay process in the $[Ru(terpy)_2]^{2+}$ dication both in fluid solution and as a solid is attributable to geometric distortions invoked by the increased rigidity and smaller bite angles between neighbouring N-donor atoms than in related polypyridyl complexes of ruthenium(II). The culmination is a reduced ligand field than in the related dication $[Ru(2,2'\text{-bipyridine})_3]^{2+}$ meaning the non-emissive metal-centred triplet level, from which fast non-radiative decay occurs, is within reach of the upper vibrational levels of the excited state above 80 K.

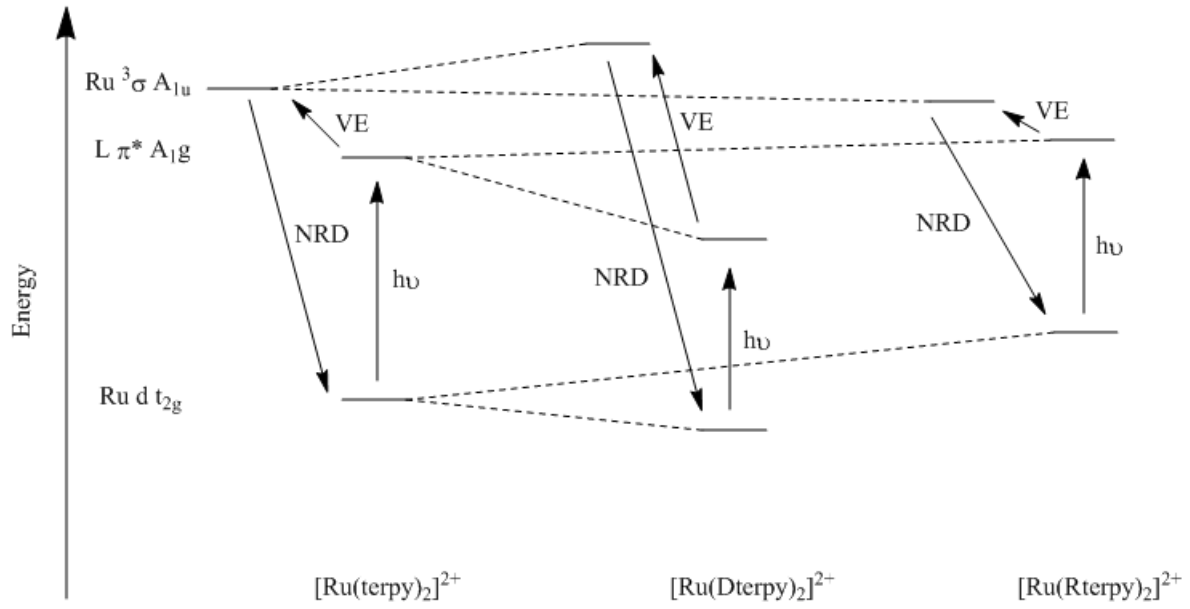

Figure 26 – Simplified pictorial representation of the energy levels involved in the absorption and subsequent non-radiative decay process of homoleptic ruthenium(II) *bis*-terpy complexes; Dterpy: electron deficient terpyridine; Rterpy: electron rich terpyridine.

In order to increase the favourability of the radiative process during decay of the excited state(s), it becomes imperative to tune the energy of the ruthenium(II) core and its respective chelating *tris*-imine ligands. A series of ruthenium(II) complex salts of terpys with a variety of electron withdrawing and donating groups, namely NO_2, SO_2Me, NH_2 and NMe_2, attached to the central pyridine 4-position showed a decrease in the lowest lying MLCT absorption regardless of the stabilisation or destabilisation of the ruthenium t_{2g} levels with

respect to the parent *bis*-terpyridine complex.[215, 216] Emission spectra below 80 K echoed this finding, with the emission maxima red-shifted regardless of the substituted terpyridine employed. Yet, the electron rich ruthenium centres were found to have particularly low luminescence lifetimes, with emission effectively quenched above 80K but the electron poor counterparts showed the converse. The finding, diagrammatically represented in Figure 26, can be rationalised by considering the effect the substituent has not only on the metal itself, but also of the recipient π* levels about the aromatic ligand. In the case of the electron rich complexes, the ruthenium(III) state is stabilised relative to ruthenium(II) in the ground state because of the highly basic ligands' propensity to interact more strongly with the oxidised centre. Non-radiative decay dominates at high temperature as a result of this additional stabilisation of the ruthenium(III) based energy levels. The electron poor complexes also possess lower MLCT excitation energies, an effect of the larger ligand fields exerted by the π-acidic ligands. Non-radiative decay no longer dominates in these complexes a result of the reduced vibrational overlap between the excited π* orbitals and the triplet-metal centred level.

The intention is to further increase the luminescence of *bis*-terpyridyl ruthenium(II) complexes by tuning the electronics of the valence orbitals with a view to inhibiting non-radiative decay from the lower lying ^{3}MC state. Whereas one method to go about introducing such favourable electronics would be by stabilisation of the ruthenium(II) state by stabilisation of the terpy backbone with additional strongly electron withdrawing groups, such as NO_2 or SO_2Me moieties. Frustratingly, this approach cannot be taken as the size increase on appending these substituents to the complex would hinder the ability of the dications to pack efficiently in the terpyridine embrace, and through this and size discrepancies make it structurally incompatible for incorporation into a spin crossover host lattice consisting of the much more compact iron(II) complexes. Electrochemical data on a number of carboxylated terpyridyl and related bipyridyl complexes revealed that the reduction in energy of the ruthenium(II) based HOMO upon replacing a pyridyl CH group with a non-coordinating nitrogen atom affording a diazinyl ring was essentially equivalent to that when an SO_2Me substituent was added. Therefore, in using unsubstituted diazines, and extending the studies to triazinyl containing 2,2:6',2''-terpyridine analogues, the benefits are two-fold. Firstly, the preparation of the parent diazinyl and triazinyl *tris*-heterocycles will likely prove less synthetically challenging than trying to substitute multiple electron withdrawing groups about the 2,2':6',2'-terpyridine backbone. More importantly, the use of *tris*-heterocycles without large, sterically demanding substituents should result in near-spherical ruthenium(II) dications of comparable size to the parent complex which still retain structural compatibility with $[Fe(1\text{-bpp})_2][BF_4]_2$ and [Fe(2,6-di(3'-methylpyrazol-1'-yl)pyridine$_2$][BF_4]$_2$.[147]

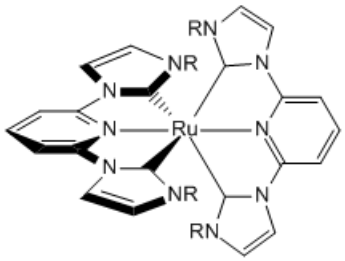

Figure 27 – General structure of the dicationic dopants of interest, of formula [Ru(2,6-di(1'-alkylimidazolium-3'-yl)pyridine)$_2$][BF_4]$_2$, where R = Me, Et, ^{i}Pr.

A second type of octahedral meridionally chelated ruthenium(II) ions are also of significance as dopants due to their structural similarity to $[Fe(1\text{-}bpp)_2]^{2+}$ dications (Figure 27). Recent papers have shown that complexes of the type [Ru(2,6-di(1'-R-imidazolium-3'-yl)pyridine)$_2$]X_2, where R is an alkyl or aromatic substituent and X is a non-coordinating, inert counterion such as hexafluorophosphate or tetraphenylborate are highly emissive in the visible spectrum (Figure 28). The cyclometallated imidazolium donors are extremely strong σ-donors due to their high energy and interact very strongly with the ruthenium(II) core, with the *bis*-CNC donor sets imparting a larger ligand field than the *bis*-N_3 donor sets of the terpyridyl analogues by virtue of the shorter distances between the distal donors and the ruthenium centre.[217] This actually yields a system where room temperature emission is permitted as the large ligand field promotes the ^{3}MC state to a level inaccessible at room temperature.[218] Non-radiative decay in these alkylimidazolium complexes occurs primarily through the energy gap law between the excited and ground states which, considering the lowest energy MLCT transition occurs between 400 and 430 nm, is negligible.[219, 220] The nature of the substituents at the 1*N*-position of the imidazolium ring have been shown to show very little effect upon the energies and quantum yield of emission, however their careful selection is necessary in the proposed dopants, as the increased steric bulk will result in a cationic volume which is incompatible with the already significantly smaller $[Fe(1\text{-}bpp)_2]^{2+}$ cations.[35, 95, 217] If preparation of solid solutions containing these cations is met with success, however, a decrease in $T_{1/2}$ might be expected because of the privative 'negative lattice pressure' exerted by the much larger volume of the ruthenium ions with respect to $[Fe(1\text{-}bpp)_2]^{2+}$, which would stabilize the larger and more distorted high-spin state.

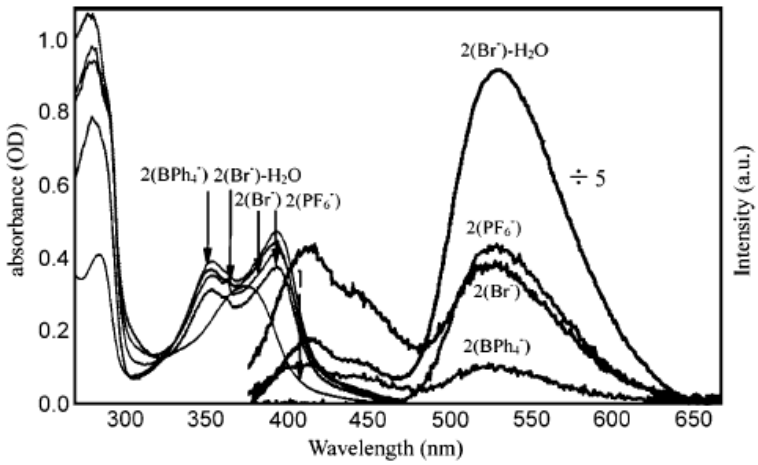

Figure 28 – Absorption and emission spectra, with excitation at 354 nm, of salts of [Ru(2,6-di(1'-methylimidazolium-3'-yl)pyridine)$_2$]X_2, where X = BPh_4, PF_6 and Br in solutions of MeCN unless otherwise noted.[217]

1.4 Progression of work

The original aims of this project were focused on engineering complex salts of electron deficient *tris*-azinyl analogues of terpy whose size and shape were relatively unchanged relative to the parent iron(II), cobalt(II) and ruthenium(II) dications. With respect to the iron(II) and cobalt(II) materials this was expected to yield a reduction in ligand field strength resulting in thermally accessible SCO. Put simply, this was found not to be the case and, to determine the origin of the findings, a spectroscopic investigation was carried out which is the documented and discussed in Chapter 3. The new ruthenium-based materials were predicted to exhibit greater room temperature emission lifetimes relative to the parent complex. The series were developed to be employed as luminescent dopants for incorporation into the SCO host lattice *bis*-2,6-di(pyrazol-1'-yl)pyridine iron(II) tetrafluoroborate, **25a**, to impart bifunctionality over an operable temperature regime. Chapter 4 concerns primarily the synthetic aspects of obtaining these complex materials which could not be acquired pure in sufficient quantities to be used in doping. A spectroscopic study is also included to explain any increase in emission or lack thereof.

A new set of ruthenium(II) salts were then pursued which would prove less synthetically challenging to isolate appreciable quantities of and which would exhibit greater emission than the relatively weakly emitting *tris*-azinyl complexes. Three new complex materials were prepared and studied as dopants adapted from the literature which is presented in the latter part of Chapter 4. Regrettably, only one of the three salts could be successfully doped into the SCO host lattice which was shown magnetically and through the comparison of the powder patterns of the solid solutions with those of the pure materials. The two complex salts which were not structurally compatible with the host lattice **25a** were

shown crystallographically to possess dicationic volumes too large to crystallise alongside the significantly smaller iron(II) dications in **25a**.

With only small successes in the formation of bifunctional doped SCO materials, a decision was made to pursue synthetic routes towards novel 1-bpp derivatives functionalised at the central pyridine 4-position of which existed only a small number of examples. It was theorised that in the study of complex salts possessing only small atoms/groups at the 4-position, the influence on the chelated iron(II) core would be primarily electronic in nature and that as a result to close-packed terpyridine embrace motifs – which consistently display abrupt hysteretic behaviour – would still be adopted in the crystal lattice. A systematic investigation was undertaken in Chapter 5 to test the limitations of terpyridine embrace formation with a number of the iron(II) complex salts possessing highly cooperative spin transitions between 150 and 340 K. Where possible, the abruptly switching materials were studied crystallographically over the switching regime and the adoption of the close-packed terpyridine embrace motif was found to be responsible for the cooperative switching behaviour in the majority of cases – it was also found that even in the presence of large iodide and thiomethyl substituents a terpyridine embrace-type motif is still favourably adopted in the solid state. To deconvolute lattice effects in the solid from the electronic influence on the iron(II) cores, the solvated SCO behaviour was also probed by means of Evans' method NMR experiments and a trend between π-donation/π-withdrawing ability and that of the isotropic $T_{1/2}$ values was observed.

1.5 References

1. H. Goodwin, *Coord. Chem. Rev.*, 1976, **18**, 293-325.
2. P. Comba, *Coord. Chem. Rev.*, 1993, **123**, 1-48.
3. L. Vanquickenborne and A. Ceulemans, *Coord. Chem. Rev.*, 1983, **48**, 157-202.
4. J. Letard, P. Guionneau, L. Rabardel, J. Howard, A. Goeta, D. Chasseau and O. Kahn, *Inorg. Chem.*, 1998, **37**, 4432-4441.
5. J. Letard, C. Carbonera, J. Real, S. Kawata and S. Kaizaki, *Chem. Eur. J.*, 2009, **15**, 4146-4155.
6. F. Yang, B. Li, T. Hanajima, Y. Einaga, R. Huang, L. Zheng and J. Tao, *Dalton Trans.*, 2010, **39**, 2288-2292.
7. G. Agusti, A.Gaspar, M. Munoz and J. Real, *Inorg. Chem.*, 2007, **46**, 9646-9654.
8. L. Cambi and L. Szego, *Ber.*, 1931, **64**, 2591-2598.
9. A. White, R. Roper, E. Kokot, H. Waterman and R. Martin, *Aust. J. Chem.*, 1964, **17**, 294-303.
10. G. Melson and D. Busch, *J. Am. Chem. Soc.*, 1964, **86**, 4830-4833.
11. M. Cowan and S. Brooker, *Coord. Chem. Rev.*, 2012, **256**, 2944-2971.
12. I. Krivokapic, M. Zerara, M. Daku, A. Vargas, C. Enachescu, C. Ambrus, P. Tregenna-Piggott, N. Amstutz, E. Krausz and A. Hauser, *Coord. Chem. Rev.*, 2007, **251**, 364-378.
13. N. Juranic, *Coord. Chem. Rev.*, 1989, **96**, 253-290.

14. R. Handel, H. Willms, G. Jameson, K. Berry, B. Moubaraki, K. Murray and S. Brooker, *Eur. J. Inorg. Chem.*, 2010, 3317-3327.
15. L. Vanquickenborne and L. Haspeslagh, *Inorg. Chem.*, 1982, **21**, 2448-2454.
16. H. Spiering, T. Kohlhaas, H. Romstedt, A. Hauser, C. Bruns-Yilmaz, J. Kusz and P. Gutlich, *Coord. Chem. Rev.*, 1999, **190-192**, 629-647.
17. P. Chakraborty, C. Enachescu and A. Hauser, *Eur. J. Inorg. Chem.*, 2013, 770-780.
18. C. Balde, C. Desplanches, M. Grunert, Y. Wei, P. Gutlich and J. Letard, *Eur. J. Inorg. Chem.*, 2008, 5382-5389.
19. R. Docherty, F. Tuna, C. Kilner, E. McInnes and M. Halcrow, *Chem. Commun.*, 2012, **48**, 4055-4057.
20. P. Gutlich, Y. Garcia and H. Goodwin, *Chem. Soc. Rev*, 2000, **29**, 419-427.
21. P. Amo-Ochoa, O. Castillo and F. Zamora, *Dalton Trans*, 2013, **42**, 13453-13460.
22. L. Stoleriu, P. Chakraborty, A. Hauser, A. Stancu and C. Enachescu, *Phys. Rev. B: Condens. Matter Mater. Phys.*, 2011, **84**, 134102-134108.
23. J. Krober, E. Codjovi, O. Kahn, F. Groliere and C. Jay, *J. Am. Chem. Soc.*, 19931, **115**, 9810-9811.
24. M. Griffin, S. Shakespeare, H. Shepherd, C. Harding, J. Letard, C. Desplanches, A. Goeta, J. Howard, A. Powell, V. Mereacre, Y. Garcia, A. Naik, H. Muller-Bunz and G. Morgan, *Angew. Chem. Int. Ed.*, 2011, **50**, 896-900.
25. R. Wei, Q. Huo, J. Tao, R. Huang and L. Zheng, *Angew. Chem. Int. Ed.*, 2011, **50**, 8940-8943.
26. M. Kepenekian, J. Sanchez Costa, B. Le Guennic, P. Maldivi, S. Bonnet, J. Reedijk, P. Gamez and V. Robert, *Inorg. Chem.*, 2010, **49**, 11057-11061.
27. P. Martinho, B. Gildea, M. Harris, T. Lemma, A. Naik, H. Muller-Bunz, T. Keyes, Y. Garcia and G. Morgan, *Angew. Chem. Int. Ed.*, 2012, **51**, 12597-12601.
28. X. Xing, X. Mei and L. Li, *J. Mol. Struct.*, 2011, **992**, 89-95.
29. S. Hayami, G. Juhasz, Y. Maeda, T. Yokoyama and O. Sato, *Inorg. Chem. Commun.*, 2005, **44**, 7289-7291.
30. J. Holland, C. Kilner, M. Thornton-Pett and M. Halcrow, *Polyhedron*, 2001, **20**, 2829-2840.
31. T. Ayers, R. Turk, C. Lane, J. Goins, D. Jameson and S. Slattery, *Inorg. Chim. Acta.*, 2004, **357**, 202-206.
32. V. Niel, J. Martinez-Agudo, M. Munoz, A. Gaspar and J. Real, *Inorg. Chem.*, 2001, **40**, 3838-3839.
33. M. Seredyuk, A. Gaspar, V. Ksenofontov, Y. Galyametdinov, M. Verdaguer, F. Villain and P. Gutlich, *Inorg. Chem.*, 2010, **49**, 10022-10031.
34. F. El Hajj, G. Sebki, F. Patinec, M. Marchivie, S. Triki, H. Handel, S. Yefsah, R. Tripier, C. Gomez-Garcia and E. Coronado, *Inorg. Chem.*, 2009, **48**, 10416-10423.
35. C. Tovee, C. Kilner, J. Thomas and M. Halcrow, *CrystEngComm*, 2009, **11**, 2069-2077.
36. K. Sugiyarto, D. Craig and H. Goodwin, *Aust. J. Chem.*, 1996, **49**, 497-503.
37. S. Neville, B. Leita, G. Halder, C. Kepert, B. Moubaraki, J. Letard and K. Murray, *Chem. Eur. J.*, 2008, **14**, 10123-10133.
38. J. Elhaik, V. Money, S. Barrett, C. Kilner, I. Evans and M. Halcrow, *Dalton Trans.*, 2003, 2053-2060.
39. S. Hayami, K. Hiki, T. Kawahara, Y. Maeda, D. Urakami, K. Inoue, M. Ohama, S. Kawata and O. Sato, *Chem. Eur. J.*, 2009, **15**, 3497-3508.

40. Y. K. S. Hayami, T. Shimizu, H. Kamihata, Y. Hoon Lee, *Coord. Chem. Rev.*, 2011, **255**, 1981-1990.
41. W. Klaui, W. Eberspach and P. Gutlich, *Inorg. Chem.*, 1987, **26**, 3977-3982.
42. S. Scheuermayer, F. Tuna, M. Bodensteiner, M. Scheer and R. Layfield, *Chem. Commun.*, 2012, **48**, 8087-8089.
43. P. Angaridis, F. Albert Cotton, C. Murillo, D. Villagran and X. Wang, *J. Am. Chem. Soc.*, 2005, **127**, 5008-5009.
44. J. Finley, H. Nohl, E. Vogel, H. Imoto, R. Camley, V. Zevin, O. Anderson and A. Simon, *Phys. Rev. Lett.*, 1981, **46**, 1472-1475.
45. H. Imoto and A. Simon, *Inorg. Chem.*, 1982, **21**, 308-319.
46. R. Pritchard, C. Kilner and M. Halcrow, *Chem. Commun.*, 2007, 577-579.
47. E. Konig, G. Ritter and S. Kulshreshtha, *Chem. Rev.*, 1985, **85**, 219-234.
48. P. Gutlich, A. Hauser and H. Spiering, *Angew. Chem. Int. Ed. Engl.*, 1994, **33**, 2024-2054.
49. A. Hauser, A. Vef and P. Adler, *Chem. Phys. Lett*, 1986, **124**, 543-548.
50. S. Bonhommeau, G. Molnar, A. Galet, A. Zwick, J. Real, J. McGarvey and A. Bousseksou, *Angew. Chem. Int. Ed.*, 2005, **44**, 4069-4073.
51. J. Letard, L. Capes, G. Chastanet, N. Moliner, S. Letard, J. Real and O. Kahn, *Chem. Phys. Lett*, 1999, **313**, 115-120.
52. A. Hauser, *Coord. Chem. Rev.*, 1991, **111**, 275-290.
53. T. Tayagaki, A. Galet, G. Molnar, M. Camen Munoz, A. Zwick, K. Tanaka, J. Real and A. Bousseksou, *J. Phys. Chem. B*, 2005, **109**, 14859-14867.
54. T. Buchen, P. Gutlich, K. Sugiyarto and H. Goodwin, *Chem. Eur. J.*, 1996, **2**, 1134-1138.
55. J. McCusker, A. Rheingold and D. Hendrickson, *Inorg. Chem.*, 1996, **35**, 2100-2112.
56. S. Marcen, L. Lecren, L. Capes, H. Goodwin and J. Letard, *Chem. Phys. Lett.*, 2002, **358**, 87-95.
57. A. Hauser, A. Vef and P. Adler, *J. Chem. Phys.*, 1991, **95**, 8710-8717.
58. M. Halcrow, *Chem. Soc. Rev*, 2008, **37**, 278-289.
59. T. Buchen, P. Gutlich and H. Goodwin, *Inorg. Chem.*, 1994, **33**, 4573-4576.
60. J. Letard, *J. Mater. Chem.*, 2006, **16**, 2550-2559.
61. J. Sanchez Costa, C. Balde, C. Carbonera, D. Denux, A. Wattiaux, C. Desplanches, J. Ader, P. Gutlich and J. Letard, *Inorg. Chem.*, 2007, **46**, 4114-4119.
62. N. Moliner, M. Munoz, S. Letard, J. Letard, X. Solans, R. Burriel, M. Castro, O. Kahn and J. Real, *Inorg. Chim. Acta.*, 1999, **291**, 279-288.
63. V. Money, C. Carbonera, J. Elhaik, M. Halcrow, J. Howard and J. Letard, *Chem. Eur. J.*, 2007, **13**, 5503-5514.
64. A. Bleuzen, C. Lomenech, V. Escax, F. Villain, F. Varret, C. Cartier dit Moulin and M. Verdaguer, *J. Am. Chem. Soc.*, 2000, **122**, 6648-6652.
65. N. Shimamoto, S. Ohkoshi, O. Sato and K. Hashimoto, *Inorg. Chem.*, 2022, **41**, 678-684.
66. J. Elhaik, D. Evans, C. Kilner and M. Halcrow, *Dalton Trans.*, 2005, 1693-1700.
67. J. Holland, J. McAllister, C. Kilner, M. Thornton-Pett, A. Bridgeman and M. Halcrow, *Dalton Trans.*, 2002, 548-554.
68. M. Halcrow, *Chem. Soc. Rev*, 2011, **40**, 4119-4142.
69. F. H. M. Haryono, K. Petukhov, K. Gieb, P. Muller, A. Grohmann, *Eur. J. Inorg. Chem.*, 2009, 2136-2143.

70. R. Pritchard, H. Lazar, S. Barrett, C. Kilner, S. Asthana, C. Carbonera, J. Letard and M. Halcrow, *Dalton Trans.*, 2009, 6656-6666.
71. G. Matouzenko, E. Jeanneau, A. Verat and A. Bousseksou, *Dalton Trans.*, 2011, **40**, 9608-9618.
72. T. Roberts, F. Tuna, T. Malkin, C. Kilner and M. Halcrow, *Chem. Sci.*, 2012, **3**, 349-354.
73. T. Roberts, M. Little, F. Tuna, C. Kilner and M. Halcrow, *Chem. Commun.*, 2013, **49**, 6280-6282.
74. J. Elhaik, C. Kilner and M. Halcrow, *Dalton Trans.*, 2006, 823-830.
75. K. Kepp, *Coord. Chem. Rev.*, 2013, **257**, 196-209.
76. M. Halcrow, *Coord. Chem. Rev.*, 2009, **253**, 2493-2514.
77. M. Halcrow, *Chem. Soc. Rev*, 2013, **42**, 1784-1795.
78. P. Guionneau, M. Marchivie, G. Bravic, J. Letard and D. Chasseau, *J. Mater. Chem.*, 2002, **12**, 2546-2551.
79. J. England, G. Britovsek, N. Rabadia and A. White, *Inorg. Chem.*, 2007, **46**, 3752-3767.
80. Z. Ni, A. McDaniel and M. Shores, *Chem. Sci.*, 2010, **1**, 615-621.
81. C. Slichter and H. Drickamer, *J. Chem. Phys.*, 1972, **56**, 2142-2160.
82. M. Sorai and S. Seki, *J. Phys. Chem. Solids*, 1974, **35**, 555-557-.
83. D. Chiruta, J. Linares, Y. Garcia, P. Richard Dahoo and M. Dimian, *Eur. J. Inorg. Chem.*, 2013, 3601-3608.
84. R. Mössbauer, *Science*, 1962, **137**, 731-738.
85. I. Dezsi, B. Molnar, T. Tarnoczi and K. Tompa, *J. Inorg. Nucl. Chem.*, 1967, **29**, 2486-2490.
86. J. Real, I. Castro, A. Bousseksou, M. Verdaguer, R. Burriel, M. Castro, J. Linares and F. Varret, *Inorg. Chem.*, 1997, **36**, 455-464.
87. K. Nakano, N. Suemura, S. Kawata, A. Fuyuhiro, T. Yagi, S. Nasu, S. Morimoto and S. Kaizaki, *Dalton Trans*, 2004, 982-988.
88. Y. Zhang and E. Oldfield, *J. Phys. Chem. A*, 2003, **107**, 4147-4150.
89. P. Adler, H. Spiering and P. Gutlich, *Inorg. Chem.*, 1987, **26**, 3840-3845.
90. K. Sugiyarto, K. Weitzner, D. Craig and H. Goodwin, *Aust. J. Chem.*, 1997, **50**, 869-873.
91. Y. de Gaetano, A. Y. V. E. Jeanneau, L. Rechignat, A. Bousseksou and G. Matouzenko, *Eur. J. Inorg. Chem.*, 2012, 1015-1023.
92. V. Ksenofontov, H. Spiering, S. Reiman, Y. Garcia, A. Gaspar, N. Moliner, J. Real and P. Gutlich, *Chem. Phys. Lett*, 2001, **348**, 381-386.
93. J. Scepaniak, D. Harris, C. Vogel, J. Sutter, K. Meyer and J. Smith, *J. Am. Chem. Soc.*, 2011, **133**, 3824-3827.
94. J. Klingele, D. Kaase, M. Klingele, J. Lach and S. Demeshko, *Dalton Trans*, 2010, **39**, 1689-1691.
95. J. Holland, J. McAllister, Z. Lu, C. Kilner, M. Thornton-Pett and M. Halcrow, *Chem. Commun.*, 2001, 577-578.
96. D. Evans, *J. Chem. Soc.*, 1959, 2003-2005.
97. B. Weber and A. Walker, *Inorg. Chem.*, 2007, **46**, 6794-6803.
98. D. Evans and T. James, *J. Chem Soc.*, 1979, 723-726.
99. A. Ewald, R. Martin, E. Sinn and A. White, *Inorg. Chem.*, 1969, **8**, 1837-1846.
100. J. Judge and W. Baker, *Inorg. Chim. Acta.*, 1967, 68-72.

101. E. Buhks, G. Navon, M. Bixon and J. Jortner, *J. Am. Chem. Soc.*, 1980, **102**, 2918-2923.
102. H. Li Chum, J. Vanin and M. Holanda, *Inorg. Chem.*, 1982, **21**, 1146-1152.
103. D. Hathcock, K. Stone, J. Madden and S. Slattery, *Inorg. Chim. Acta.*, 1998, **282**, 131-135.
104. C. Mayer, G. Cucchiaro, J. Jullien, F. Dumur, J. Marrot, E. Dumas and F. Secheresse, *Eur. J. Inorg. Chem.*, 2008, 3614-3623.
105. A. Bousseksou, G. Molnar, L. Salmon and W. Nicolazzi, *Chem. Soc. Rev*, 2011, **40**, 3313-3335.
106. T. Forestier, S. Mornet, N. Daro, T. Nishihara, S. Mouri, K. Tanaka, O. Fouche, E. Freysz and J. Letard, *Chem. Commun.*, 2008, **4327-4329**.
107. L. Lavrenova and O. Shakirova, *Eur. J. Inorg. Chem.*, 2013, 670-682.
108. T. Fujigaya, D. Jiang and T. Aida, *J. Am. Chem. Soc.*, 2003, **125**, 14690-14691.
109. N. Ould Moussa, D. OStrovskii, V. Martinez Garcia, G. Molnar, K. Tanaka, A. Gaspar, J. Real and A. Bousseksou, *Chem. Phys. Lett*, 2009, **477**, 156-159.
110. O. Kahn and C. J. Martinez, *Science*, 1998, **279**, 44-48.
111. M. Matsuda, H. Isozaki and H. Tajima, *Chem. Lett.*, 2008, **37**, 374-375.
112. L. Salmon, G. Molnar, D. Zitouni, C. Quintero, C. Bergaud, J. Micheau and A. Bousseksou, *J. Mater. Chem.*, 2010, **20**, 5499-5503.
113. G. Chastanet, C. Tovee, G. Hyett, M. Halcrow and J. Letard, *Dalton Trans.*, 2012, **41**, 4896-4902.
114. J. Letard, S. Montant, P. Guionneau, P. Martin, A. Le Calvez, E. Freysz, D. Chasseau, R. Lapouyade and O. Kahn, *Chem. Commun.*, 1997, 745-746.
115. L. Wen, L. Zhou, B. Zhang, X. Meng, H. Qu and D. Li, *J. Mater. Chem.*, 2012, **22**, 22603-22609.
116. Y. Li, Z. Zhang, F. Fang, W. Song, K. Li, Y. Miao, C. Gu and L. Pan, *J. Mol. Struct.*, 2007, **837**, 269-273.
117. A. Grosjean, P. Negrier, P. Bordet, C. Etrillard, D. Mondieig, S. Pechev, E. Lebraud, J. Letard and P. Guionneau, *Eur. J. Inorg. Chem.*, 2013, 796-802.
118. C. Faulmann, K. Jacob, S. Dorbes, S. Lampert, I. Malfant, M. Doublet, L. Valade and J. Real, *Inorg. Chem.*, 2007, **46**, 8548-8559.
119. E. Kent Barefield, D. Busch and S. Nelson, *Q. Rev. Chem. Soc.*, 1968, **22**, 457-498.
120. C. Balde, C. Desplanches, P. Gutlich, E. Freysz and J. Letard, *Inorg. Chim. Acta.*, 2008, **361**, 3529-3533.
121. D. Wu, O. Sato, Y. Einaga and C. Duan, *Angew. Chem.*, 2009, **48**, 1475-1478.
122. N. White, H. Feltham, C. Gandolfi, M. Albrecht and S. Brooker, *Dalton Trans.*, 2010, **39**, 3751-3758.
123. F. S. C. Rajadurai, S. Brink, O. Fuhr, M. Ghafari, R. Kruk, M. Ruben, *Inorg. Chem.*, 2006, **45**, 10019-10021.
124. I. Gass, S. Batten, C. Forsyth, B. Moubaraki, C. Schneider and K. Murray, *Coord. Chem. Rev.*, 2011, **255**, 2058-2067.
125. Y. Bai, J. Tao, R. Huang, L. Zheng, S. Zheng, K. Oshida and Y. Einaga, *Chem. Commun.*, 2008, 1753-1755.
126. A. Desaix, O. Roubeau, J. Jeftic, J. Haasnoot, K. Boukheddaden, E. Codjovi, J. Linares, M. Nogues and F. Varret, *Eur. Phys. J. B*, 1998, **6**, 183-193.
127. A. Ozarowski, Y. Shunzhong, B. McGarvey, A. Mislankar and J. Drake, *Inorg. Chem.*, 1991, **30**, 3167-3174.
128. B. Weber, W. Bauer and J. Obel, *Angew. Chem. Int. Ed.*, 2008, **47**, 10098-10101.

129. M. Boca, R. Jameson and W. Linert, *Coord. Chem. Rev.*, 2011, **255**, 290-317.
130. E. Constable, *Chem. Soc. Rev*, 2007, **36**, 246-253.
131. E. Baranoff, J. Collin, L. Flamigni and J. Sauvage, *Chem. Soc. Rev*, 2004, **33**, 147-155.
132. I. Eryazici, C. Moorefield and G. Newkome, *Chem. Rev.*, 2008, **108**, 1834-1895.
133. D. Gnanamgari and R. Crabtree, *Organometallics*, 2009, **28**, 922-924.
134. C. Klein, Md. Nazeeruddin, P. Liska, D. Di Censo, N. Hirata, E. Palomares, J. Durrant and M. Gratzel, *Inorg. Chem.*, 2005, **44**, 178-180.
135. M. Gratzel, *Inorg. Chem.*, 2005, **44**, 6841-6851.
136. G. Lowe, A. Sophie Droz, T. Vilaivan, G. Weaver, L. Tweedale, J. Pratt, P. Rock, V. Yardley and S. Croft, *J. Med. Chem.*, 1999, **42**, 999-1006.
137. D. Beauchamp and S. Loeb, *Supramol. Chem.*, 2007, **17**, 617-622.
138. H. Hofmeier and U. Schubert, *Chem. Soc. Rev*, 2004, **33**, 373-399.
139. A. Hofmann, D. Jaganyi, O. Munro, G. Liehr and R. v. Eldik, *Inorg. Chem.*, 2003, **42**, 1688-1700.
140. M. Beley, J. Collin, J. Sauvage, H. Sugihara, F. Heisel and A. Miehe, *Dalton Trans.*, 1991, 3157-3159.
141. B. Figgis, E. Kurcharkski and A. White, *Aust. J. Chem.*, 1983, **36**, 1537-1561.
142. M. Scudder, H. Goodwin and I. Dance, *New J. Chem.*, 1999, **23**, 695-705.
143. J. Mcmurtrie and I. Dance, *CrystEngComm*, 2005, **7**, 216-229.
144. J. McMurtrie and I. Dance, *CrystEngComm*, 2005, **7**, 230-236.
145. J. McMurtrie and I. Dance, *CrystEngComm*, 2010, **12**, 2700-2710.
146. J. S. C. G. Craig, O. Roubeau, S. Teat, G. Aromi, *Chem. Eur. J.*, 2012, **18**, 11703-11715.
147. M. Halcrow, *Chem. Commun.*, 2010, **46**, 4761-4763.
148. H. Oshio, H. Spiering, V. Ksenofontov, F. Renz and P. Gutlich, *Inorg. Chem.*, 2001, **40**, 1143-1150.
149. C. Kilner and M. Halcrow, *Dalton Trans.*, 2010, **39**, 9008-9012.
150. S. Kremer, W. Henke and D. Reinen, *Inorg. Chem.*, 1982, **21**, 3013-3022.
151. T. Ayers, S. Scott, J. Goins, N. Caylor, D. Hathcock, S. Slattery and D. Jameson, *Inorg. Chim. Acta.*, 2000, **307**, 7-12.
152. C. Enachescu, I. Krivokapic, M. Zerara, J. Real, M. Amstutz and A. Hauser, *Inorg. Chim. Acta.*, 2007, **360**, 3945-3950.
153. E. Dose, M. Hoselton, N. Sutin, M. Tweedle and L. Wilson, *J. Am. Chem. Soc.*, 1978, **100**, 1141-1147.
154. G. Agusti, C. Bartual, V. Martinez, F. Munoz-Lara, A. Gaspar, M. Carmen Munoz and J. Real, *New J. Chem.*, 2009, **33**, 1262-1267.
155. S. Hayami, Y. Shigeyoshi, M. Akita, K. Inoue, K. Kato, K. Osaka, M. Takata, R. Kawajiri, T. Mitani and Y. Maeda, *Angew. Chem. Int. Ed.*, 2005, **44**, 4899-4903.
156. S. Hayami, K. Murata, D. Urakami, Y. Kojima, M. Akita and K. Inoue, *Chem. Commun.*, 2008, 6510-6512.
157. S. Hayami, Y. Kojima, D. Urakami, K. Ohta and K. Inoue, *Polyhedron*, 2009, **28**, 2053-2057.
158. S. Hayami, D. urakami, Y. Kojima, H. Yoshizaki, Y. Yamamoto, K. Kato, A. Fuyuhiro, S. Kawata and K. Inoue, *Inorg. Chem.*, 2010, **49**, 1428-1432.
159. F. Lovecchio, S. Pace and D. Macero, *Inorg. Chim. Acta.*, 1969, **3**, 94-96.
160. P. Braterman, J. Song and R. Peacock, *Inorg. Chem.*, 1992, **31**, 555-559.
161. Y. Tanabe and S. Sugano, *J. Phys. Soc. Jpn.*, 1954, **9**, 753-766.

162. J. Rao, M. Hughes and D. Macero, *Inorg. Chim. Acta.*, 1976, **16**, 231-236.
163. E. Constable, G. Baum, E. Bill, R. Dyson, R. van Eldik, D. Fenske, S. Kaderli, D. Morris, A. Neubrand, M. Neuburger, D. Smith, K. Wieghardt, M. Zehnder and A. Zuberbuhler, *Chem. Eur. J.*, 1999, **5**, 498-508.
164. R. Bonomo, S. Musumeci, E. Rizzarelli and S. Sammartano, *Inorg. Chim. Acta.*, 1974, **11**, 217-222.
165. C. Harris, H. Patil and E. Sinn, *Inorg. Chem.*, 1969, **8**, 101-104.
166. T. Roberts, M. Little, L. Kershaw Cook, S. Barrett, F. Tuna and M. Halcrow, *Polyhedron*, 2013, **64**, 4-12.
167. E. Constable, J. Davies, D. Phillips and P. Raithby, *Polyhedron*, 1998, **17**, 3989-3997.
168. P. Liu, E. Lai-Ming Wong, A. Wing-Hoi Yuen and C. Che, *Org. Lett.*, 2008, **10**, 3275-3278.
169. D. McDaniel and H. Brown, *J. Org. Chem.*, 1958, **23**, 420-427.
170. J. Chambers, B. Eaves, D. Parker, R. Claxton, P. Ray and S. Slattery, *Inorg. Chim. Acta.*, 2006, **359**, 2400-2406.
171. M. Maestri, N. Armaroli, V. Balzani, E. Constable and A. C. Thompson, *Inorg. Chem.*, 1995, **34**, 2759-2767.
172. T. Brinck, J. Murray and P. Politzer, *J. Org. Chem.*, 1991, **56**, 2934-2936.
173. R. Casasnovas, J. Frau, J. Ortega-Castro, A. Salva, J. Donoso and F. Munoz, *J. Mol. Struct. (THEOCHEM)*, 2009, **912**, 5-12.
174. K. Sugiyarto and H. Goodwin, *Aust. J. Chem.*, 1988, **41**, 1645-1663.
175. J. Holland, S. Barrett, C. Kilner and M. Halcrow, *Inorg. Chem. Commun.*, 2002, **5**, 328-332.
176. R. Mohammed, G. Chastanet, F. Tuna, T. Malkin, S. Barrett, C. Kilner, J. Letard and M. Halcrow, *Eur. J. Inorg. Chem.*, 2013, 819-831.
177. K. Sugiyarto and H. Goodwin, *Aust. J. Chem.*, 1987, **40**, 775-783.
178. V. Money, J. Elhaik, M. Halcrow and J. Howard, *Dalton Trans.*, 2004, 1516-1518.
179. M. Halcrow, *Coord. Chem. Rev.*, 2005, **249**, 2880-3009.
180. C. Kilner and M. Halcrow, *Polyhedron*, 2006, **25**, 235-240.
181. J. E. V. Money, M. Halcrow and J. Howard, *Dalton Trans.*, 2004, 65-69.
182. M. Nihei, L. Han, H. Tahira and H. Oshio, *Inorg. Chim. Acta.*, 2008, **361**, 3926-3930.
183. J. Elhaik, C. Kilner and M. Halcrow, *CrystEngComm*, 2005, **7**, 151-157.
184. R. Pritchard, C. Kilner, S. Barrett and M. Halcrow, *Inorg. Chim. Acta.*, 2009, **362**, 4365-4371.
185. R. Pritchard, C. Kilner and M. Halcrow, *Tetrahedron Lett.*, 2009, **50**, 2484-2486.
186. C. Carbonera, C. Kilner, J. Letard and M. Halcrow, *Dalton Trans*, 2007, 1284-1292.
187. C. Carbonera, J. Costa, V. Money, J. Elhaik, J. Howard, M. Halcrow and J. Letard, *Dalton Trans.*, 2006, 3058-3066.
188. L. Han, M. Nihei and H. Oshio, *Polyhedron*, 2005, **24**, 2409-2412.
189. R. Chandrasekar, F. Schramm, O. Fuhr and M. Ruben, *Eur. J. Inorg. Chem.*, 2008, 2649-2653.
190. N. Madhu, I. Salitros, F. Schramm, S. Klyatskaya, O. Fuhr and M. Ruben, *C. R. Chim.*, 2008, **11**, 1166-1174.
191. M. Nihei, T. Maeshima, Y. Kose and H. Oshio, *Polyhedron*, 2007, **26**, 1993-1996.
192. F. Pelascini, M. Wesolek, F. Peruch, A. De Cian, N. Kyritsakas, P. Lutz and J. Kress, *Polyhedron*, 2003, **24**, 3193-3199.
193. C. Kilner and M. Halcrow, *Acta Crystallogr. Sect. C*, 2006, **62**, M437-M439.

194. S. Barrett, C. Kilner and M. Halcrow, *Dalton Trans.*, 2011, **40**, 12021-12024.
195. A. Gaspar, V. Ksenofontov, M. Seredyuk and P. Gutlich, *Coord. Chem. Rev.*, 2005, **249**, 2661-2676.
196. J. Real, J. Zarembowitch, O. Kahn and X. Solans, *Inorg. Chem.*, 1987, **26**, 2939-2943.
197. O. Kahn, *Angew. Chem. Int. Ed. Engl.*, 1985, **24**, 834-850.
198. S. Bedoui, G. Molnar, S. Bonnet, C. Quintero, H. Shepherd, W. Nicolazzi, L. Salmon and A. Bousseksou, *Chem. Phys. Lett*, 2010, **499**, 94-99.
199. M. Clemente-Leon, E. Coronado, M. Lopez-Jorda, G. Minguez Espallargas, A. Soriano-Portillo and J. Waerenborgh, *Chem. Eur. J.*, 2010, **16**, 2207-2219.
200. M. Clemente-Leon, E. Coronado, M. Lopez-Jorda and J. Waerenborgh, *Inorg. Chem.*, 2011, **50**, 9122-9130.
201. M. Clemente-Leon, E. Coronado and M. Lopez-Jorda, *Eur. J. Inorg. Chem.*, 2012.
202. A. Giroud-Godquin and P. Maitlis, *Angew. Chem. Int. Ed. Engl.*, 1991, **30**, 375-402.
203. Y. Galyametdinov, V. Ksenofontov, A. Prosvirin, I. Ovchinnikov, G. Ivanova, P. Gutlich and W. Haase, *Angew. Chem. Int. Ed.*, 2001, **40**, 4269-4271.
204. I. Mathew and W. Sun, *Dalton Trans*, 2010, **39**, 5885-5898.
205. S. Dorbes, L. Valade, J. Real and C. Faulmann, *Chem. Commun.*, 2005, 69-71.
206. B. Djukic and M. Lemaire, *Inorg. Chem.*, 2009, **48**, 10489-10491.
207. S. Titos-Padilla, J. Manuel Herrera, X. Chen, J. Jose Delgado and E. Colacio, *Angew. Chem. Int. Ed.*, 2011, **50**, 3290-3293.
208. R. Gonzalez-Prieto, B. Fleury, F. Schramm, G. Zoppellaro, R. Chandrasekar, O. Fuhr, S. Lebedkin, M. Kappes and M. Ruben, *Dalton Trans*, 2011, **40**, 7564-7570.
209. J. Collin, I. Dixon, J. Sauvage, G. Williams, F. Barigelletti and L. Flamigni, *J. Am. Chem. Soc.*, 1999, **121**, 5009-5016.
210. R. Berger and D. McMillin, *Inorg. Chem.*, 1988, **27**, 4245-4249.
211. R. Allmann, W. Henke and D. Reinen, *Inorg. Chem.*, 1978, **17**, 378-382.
212. J. Folgado, W. Henke, R. Allmann, H. Stratemeier, D. Beltran-Porter, T. Rojo and D. Reinen, *Inorg. Chem.*, 1990, **29**, 2035-2042.
213. E. Constable, S. Decurtins, C. Housecroft, T. Keene, C. Palivan, J. Price and J. Zampese, *Dalton Trans*, 2010, **39**, 2337-2343.
214. A. Juris, V. Balzani, F. Barigelletti, S. Campagna, P. Belser and A. v. Zelewsky, *Coord. Chem. Rev.*, 1988, **84**, 85-277.
215. R. Fallahpour, M. Neuburger and M. Zehnder, *New J. Chem.*, 1998, **22**, 53-61.
216. E. Constable, A. Thompson, N. Armaroli, V. Balzani and M. Maestri, *Polyhedron*, 1992, **11**, 2707-2709.
217. S. Son, K. Park, Y. Lee, B. Kim, C. Choi, M. Lah, Y. Jang, D. Jang and Y. Chung, *Inorg. Chem.*, 2004, **43**, 6896-6898.
218. H. Park, K. Kim, S. Choi, H. Kim, W. Lee, Y. Kang and Y. Chung, *Inorg. Chem.*, 2010, **49**, 7340-7352.
219. H. Park and Y. Chung, *Dalton Trans.*, 2012, **41**, 5678-5686.
220. H. Park, S. Yoo, I. Shin, Y. Chung and J. Kim, *Electroanalysis*, 2013, **25**, 1111-1115.

Chapter 2

Synthesis and analysis of organic ligands and precursors

2 Synthesis and analysis of organic ligands and precursors

2.1 Introduction

This chapter documents the efforts undertaken towards the preparation of novel planar *tris*-chelating organic compounds and any relevant synthetic intermediates. An array of ligating compounds has been isolated, which differ either in their heterocyclic content or by the substituents appended onto the aromatic backbone. The synthetic techniques and methodology employed in pursuit of these compounds are numerous and varied, and are discussed in detail here to better understand the problems encountered and the appearance of any unexpected side-products.

2,2':6'2''-Terpyridines, terpys, are the archetypal *tris*-imines, with the unsubstituted parent compound first reported in 1932, synthesised by oxidative dehydrogenation of pyridine which is neither a safe or economically efficient route.[1] Synthetic methodology has advanced in leaps and bounds in the last 80 years, and commonly the preparation of appropriately substituted terpyridines relies on either the Krohnke or Potts methods which are relatively mild and have high functional group tolerance.[2-5] Lesser utilised pathways involve cross-coupling of the substituted heterocycles via Ullman or Stille type reactions, or by the attack of two equivalents of a deprotonated acetyl pyridine upon an aldehyde and subsequent oxidation and closing of the central ring to form the terpyridine motif.[6-13] This versatility in their synthesis has meant that to this day hundreds of examples of compounds containing the terpy backbone have been reported, and indeed a quick literature search reveals that in only the past six months over three hundred articles concerning terpyridines have been published.[14-19]

In contrast, there is relatively little literature on analogues of terpy containing 6-membered diazinyl and triazinyl rings in place of either the distal or central rings. A few papers concern the preparation and coordination chemistry of some substituted diazinyl and triazinyl terpyridines, but only five papers to date have focussed on the unsubstituted parent *tris*-heterocyclic systems.[8, 9, 20-25] This is primarily due to the reactivity of six membered diazines which differ profoundly to pyridine, substituted or otherwise, and as a consequence the absence of commercially available reagents and precursors which make their syntheses inherently more challenging.[26-29]

Though the most frequently reported, *tris*-imines are not limited to only six membered heterocyclic rings. Five membered heterocycles are also hugely important for a variety of applications, with tricyclic systems containing various pyrazoles, imidazoles and 1,3,5-triazoles in place of the distal pyridine being some of the most prevalent. Additionally, one can introduce much larger bicyclic systems in place of the terminal pyridines such as

indazoles and benzimidazoles, which are the fused bicyclic analogues of pyrazoles and imidazoles respectively. The indazolyl and pyrazolyl analogues are prepared analogously to one another, the simplest and most widely used of which is by deprotonation of the 1*H*-derivative at high temperature which forces substitution in place of a halide at the 2 and 6 positions in 2,6-dihalo azines.[30-32] Another method relies on hydrazine to displace the halides from the central pyridine, followed by cyclisation of the 2,6-dihydrazinopyridine with an appropriate dicarbonyl compound to form the terminal rings.[33, 34] The lack of papers reporting the application of this route arises from the difficulty in preparing, purifying and handling 2,6-dihydrazinopyridine.[34] However, the scope of the pathway is yet to be fully realised as potentially it allows for the preparation of unsymmetrical 2,6-di(pyrazol-1'-yl)pyridines which is troublesome using the direct substitution of pyrazoles.[35] Imidazoles and benzimidazoles on the other hand require a 1,2-diamine or 1,2-phenylene diamine derivative respectively to cyclise with 2,6-dicarboxylated azines at the carbonyl.[36, 37] It is also possible for further modification due to the imidazolyl and benzimidazolyl pyridines possessing retained NH functionality.[38]

2,6-Di(pyrazol-1'-yl)pyridines represent a particularly important family of *tris*-imines, due to their general ease of preparation, stability, use in magnetic materials and as hemilabile analogues of terpy in catalysis.[32, 39-41] Preparation of the 3- and 4-pyrazole substituted derivatives is mostly trivial because of the commercial availability of a large number of substituted pyrazoles.[31, 42, 43] It is also simple to halogenate at the pyrazole 4 position in 1-bpp derivatives as a result of the nucleophilic character at this position.[44, 45] This in turn makes further functionalisation via substitution or coupling at this position feasible. A number of examples exist of 2,6-di(pyrazol-1'-yl)pyridine derivatised at the 4 position on the pyridine ring, but almost all reported possess an alkyl spacer because of the difficulty in incorporating reactive groups at this position during the course of preparation.[46, 47] The goal of this work was to selectively prepare and modify compounds bearing a directly bound substituent at this position whilst leaving the remaining backbone completely untouched.

2.2 Diazinyl and triazinyl heterocycle containing analogues of terpy

2.2.1 *Tris*-imines involving pyrazinyl donors

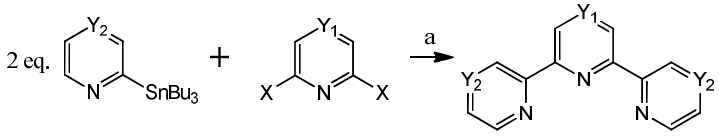

Figure 29 - One-pot preparation of unsubstituted pyrazine containing *tris*-imines via a palladium catalysed Stille cross-coupling pathway; a) 0.05 – 0.1 eq. $Pd(PPh_3)_4$, toluene; X = Cl, Br; Y_1 = CH, N; Y_2 = CH, N.

The pyrazine containing analogues of terpy were all synthesised initially according to a previously published literature preparation.[9] As shown in Figure 29, their formation involves the coupling together of the appropriate aryl chloride or bromide with the corresponding tributylstannyl azine via a palladium catalysed Stille cross-coupling of the heterocycles. The mechanism, which shall not be discussed in depth, involves oxidative addition of the aryl halide to the palladium centre, *cis-trans* isomerisation of the initial four-coordinate palladium (II) centre, transmetallation resulting in loss of trialkylstannyl halide and finally reductive elimination yielding the desired coupled heterocyclic system. High temperatures are required due to the large activation barrier (> 80 kJ mol^{-1}) associated with the initial oxidative addition step.[48, 49]

It was found that yields varied typically from 40 – 60%, comparable with previous reports on aryl-aryl coupling via the Stille reaction. Often, during extraction, ammonium hydroxide was required to solubilise the tin-containing byproducts into the aqueous layer. This results in what appears to be an almost triphasic system, complicating the separation of the aqueous and organic phases. A consequence of this is that because of the low solubility of the three pyrazine containing compounds large quantities of DCM are required in all cases to maximise the efficiency of the separation and prevent significant loss of material. Indeed an initial preparation of terpz resulted in isolation of just 1% yield of the material. This material exhibits extremely low solubilities in all common solvents except 2,2,2-trifluroethanol. It was seen that during the drying/filtration of the resulting organic phase post-separation, addition of 2,2,2-trifluoroethanol to the suspension solubilised the compound and increased yields up to 48%. Column chromatography was initially used to separate the resulting organic solids, but this was generally very arduous and inefficient due to the length of the silica gel column that the sparingly soluble compounds necessitated in order to achieve the required separation. Instead it was found that if one uses a small excess of the tributylstannyl azine which contains the terminal heterocycles, it was possible to triturate the crude organic solid in pentane and filter which completely removes any alkylstannyl containing byproducts and yields the *tris*-imines as analytically pure colourless solids.

Proton NMR spectroscopy could in general be trivially interpreted for bipypz and bipzpy on the basis of multiplicity and chemical shift alone. Bipypz possesses a sharp singlet at 9.68 ppm which arises from the uncoupled protons on the central symmeterical pyrazine ring. The increased complexity of the signals at 7.40 and 7.90 with respect to those at 8.55 and 8.76 ppm reflect the fact that these resonances are coupled to two chemically unique vicinal protons, and hence can be assigned to 5’ and 4’ respectively. The broadening of the doublets which are seen for the 3’ and 6’ resonances are a result of the smaller coupling between protons separated by a larger number of bonds about the distal rings. The splitting

is partially obscured by the relatively large line widths on a 500 MHz spectrometer relative to the magnitude of the $^{4}J/^{5}J$ coupling. In the case of bipzpy, the doublet and triplet at 8.49 and 8.04 ppm couple with J = 7.7 Hz, and can be unambiguously assigned to the protons at the 3 and 4 positions on the central pyridine ring respectively. The multiplet centred at 8.66 ppm, accounting for four protons is the result of coincident overlapping multiplets arising from the 3' and 4' positions. The sharp doublet at ~10 ppm arises from the highly deshielded proton on the pyrazinyl 6' position, and its splitting is telling of $^{4}J/^{5}J$ through-bond coupling. The carbon spectra were assigned simply through a 2D HMQC NMR experiment which exploits the coupling between directly bonded carbon and proton nuclei. The 3'/4'/6' signals in the ^{13}C NMR spectrum of bipzpy could not be reliably assigned to a specific environment, due to their almost identical resonance frequencies. Additionally, the proton spectrum of terpz was almost fully unassignable because of the compound's insoluble nature – CD_2Cl_2 was the only solvent which any signals in the aromatic region could be observed. However, on the basis of resonant frequency alone it can be deduced that the coincident singlet at 8.70 ppm arises from the 4' and 5' protons, and those at 9.66 ppm and 9.76 the 3 and 3' positions due to the deshielded protons located at these positions. It was impossible to observe anything other than solvent signals in the ^{13}C NMR spectra.

One final note is that it was attempted to make 2-bipympy and 2-bipympz by first preparing 2-tributylstannylpyrimidine and then reacting separately with 2,6-dibromopyridine and 2,6-dichloropyrazine. In neither instance was it possible to isolate, or even conclusively observe spectroscopically the desired compounds. It is highly probable, due to the reliability of Stille cross-coupling reactions under these conditions, that the materials were lost during the work up and separation as a consequence of their probable insoluble nature.

2.2.2 The 4-pyrimidyl derivatives

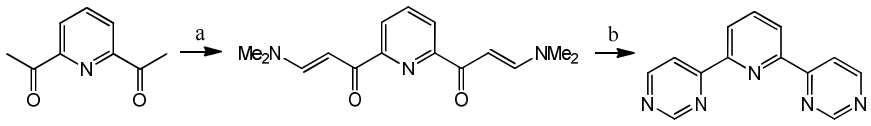

Figure 30 – Schematic representation of the synthesis of 2,6-di(4'-pyrimidyl)pyridine and its intermediate; a) *N*,*N*-dimethyl formamide dimethyl acetal; b) formamidine acetate, EtONa, EtOH.

To form the 4-pyrimidyl *tris*-heterocycles it was chosen to start with the corresponding 2,6-diacetyl compounds and first form the symmetrical 2,6-di[(*N*,*N*,-dimethylamino)-1'-oxoprop-2'-en-1'-yl]azines before ring-closing with formamidine acetate under basic conditions to form the distal 4-pyrimidyl rings (Figure 30). 2,6-Diacetylpyridine is commercially available, however the pyrazinyl derivative had first to be prepared. Because of the unsuitability of electron poor heterocycles toward electrophilic substitution, a method was adapted from the literature which proceeds via radical carbonylation of monoacetyl

pyrazine.[50] This reaction is performed in light-free conditions due to the presence of catalytic silver and acyl radicals. The strongly electron withdrawing nature of the acetyl group in acetyl pyrazine deactivates the 3 positions towards radical nucleophilic substitution, such that at the operating temperature only the formation 2,6-diacetylpyrazine is promoted. Spectroscopic analysis was in agreement with a symmetrically disubstituted acetylated pyrazine consistent with the literature.[50, 51]

The 2,6-disubstituted cycles are readily converted to the unsaturated intermediates using dimethyl formamide dimethyl acetal as both solvent and reagent. At 120°C, the methoxide anion deprotonates the acetyl α-carbon which goes on to attack dimethyl acetal dimethyl formamide and displace further methoxide. Loss of a second proton from the α-carbon forms a double bond between the α and β carbons resulting in the 1,2-unsaturated ketonic system. The pyridyl and pyrazinyl intermediates were isolated through recrystallistion in THF-MeCN as orange-yellow and brick-red microcrystalline solids in 60% and 58% yields respectively. The *trans* alkenes are isolated exclusively in both cases, and the molecules both possess two chemically independent methyl group signals in the ^{1}H NMR spectra arising due to the very slow rotation about the C-N bond. ^{13}C NMR spectra show, in addition to the aromatic and methyl signals, two peaks whose positions are virtually unchanged upon replacing the central heterocycle. Heteronuclear ^{1}H-^{13}C correlation spectra allowed assignment of the higher and lower field resonances to the α and β-carbon atoms respectively, consistent with the α position lying in the centre of the conjugated π-cloud. The broadening of the proton and carbon signals at the α and β positions, is indicative of an unsaturated carbonyl group, the delocalisation perhaps increased by the presence of the electron donating ability of the tertiary amine directly bound to the β-carbon.

Lastly, to form the 4-pyrimidyl ring containing systems, deprotonated formamidine acetate attacks the β-carbon of the unsaturated enaminone and after proton transfer the second, more basic formamidine nitrogen forms the basis of the 6-membered ring by coordinating to the carbonyl carbon. The oxygen atom then uses one of its lone pairs to bind to a proton, and after further proton transfer a molecule of water is lost with the 2,6-di(4'-pyrimidyl)azines retaining electroneutrality.[52] The pyridyl and pyrazinyl compounds were isolated chromatographically in 39% and 11% yields respectively. The reason for the severe material loss in the case of the 4-bipympz is not known, but it is not likely to be a complication arising from the material's solubility as it exhibited high solubility in common polar solvents such as DCM and $CHCl_3$. The ^{1}H NMR spectrum of the crude $CHCl_3$ soluble residue also appeared to contain 4-bipympz as the major species, so it is proposed that the most likely reason is that the reaction proceeds more slowly than in the pyridyl derivative's case, and that the majority of pyrazinyl containing material consisted of polyamines which

were filtered off during the initial stage of isolation. The ^{1}H NMR spectra of both compounds were very similar, each showing two doublets and a doublet of doublets characteristic of the 4-pyrimidyl system. The only differences lie in the expected 2:1 ratio of doublet to triplet signals observed in 4-bipympy from the central pyridyl resonances as opposed to the sharp singlet at very low field arising from the pyrazinyl 3 positions in the spectrum of 4-bipympz.

2.2.3 Terpyridines appended with a hydroxy functionality

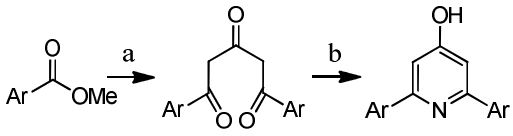

Figure 31 – Reaction scheme outlining the preparation of diazinyl hydroxypridines; a) acetone, NaH, glyme; b) ammonium acetate, ethanol; Ar = pyrazinyl (bipzpyOH), 2'-pyrimidyl (2-bipympyOH).

The diazinyl 4-hydroxy terpyridines were the only compounds in the terpy derivative series to possess an appended substituent about the backbone. It was deemed that to first pre-form the corresponding *tris*-heterocycles and then to try and hydroxylate would prove unsuccessful. No control over the selectivity of hydroxylation, coupled with the extreme conditions required to perform the transformation would be likely to confound matters and make isolation and separation very difficult.[53] Instead, a method commonly used to prepare 4-substituted terpyridines was adapted.[10, 54] This involves the attack of what is essentially a dienolate on the carbonyl carbon of two equivalents either an ester or aldehyde which results in a 1,3,5-triketonic bridged moiety. Next, the 1,5 carbonyl carbons are tethered together using NH_4OAc with loss of water to form the central pyridine ring (Figure 31).

The formation of the intermediate triketonic species first required the isolation of the corresponding heterocyclic esters, methyl pyrazine carboxylate and methyl-2-pyrimidine carboxylate which would act as the electrophile. These were formed from the commercially available pyrazine carboxylic acid and 2-cyanopyrimidine respectively, by refluxing in excess methanolic solution in the presence of H_2SO_4 to catalyse the reaction. Both were isolated as off-white crystalline solids whose properties matched with those documented in the literature.[55-57] Reaction of two equivalents of the respective esters with one equivalent of acetone yielded the two triketone-bridged moieties 1,5-di(pyrazinyl)pentane-1,3,5-trione and 1,5-di(2'-pyrimidyl)pentane-1,3,5-trione. The two triones were isolated in 22% and 44% yields as yellow and bright orange solids respectively. The yields obtained here are considerably less than are reported for the pyridyl derivative, with perhaps a lower solubility in aqueous base being one possible reason for the loss.[10] The basic solutions are filtered, and the triketones precipitated by careful neutralisation. This was successful for the pyrazinyl triketone, but in the pyrimidyl derivative's case no dissolution of any material was noted upon neutralisation. Indeed it happened that the orange solid initially filtered off from the basic

solution was pure 1,5-di(2'-pyrimidyl)pentane-1,3,5-trione. All efforts to precipitate any further trione in both cases from the aqueous solutions, either via modification of pH or removal of water under vacuum at elevated temperatures resulted in a darkening of the solutions. Mass spectrometric analysis indicated that the triketones, in particular the 2-pyrimidyl derivative, was extremely sensitive to hydrolysis with azinyl carboxylic acid being the major species after elevation of temperatures above 40-50°C in water.

Structural characterisation of the triones was made difficult both by their limited solubility in most solvents when uncharged as well as their ability to, once in solution, exist in a number of different tautomeric keto-enol forms. The proton NMR spectrum of 1,5-pyrazinyl)pentane-1,3,5-trione is complicated. The purely triketonic compound in the absence of enolisation should exhibit four signals, two sets of doublets and a doublet of doublets accounting for the pyrazinyl resonances, and a singlet for the protons neighbouring the carbonyl groups. Instead, we see a number of multiplets at 8.5 – 9.5 ppm which account for the pyrazinyl protons of the various tautomers. Three singlets also occur in the 6.5 – 7.5 ppm region. The signals here are caused by protons directly bound on the central pentane bridge. The ratio of the downfield to upfield aggregation of multiplets is approximately 2:3. Additional evidence of uncertain speciation comes from two very broadened signals located at 14 – 16 ppm, which only arise due to two chemically distinct OH resonances which are exchanging slowly enough to be resolved as two separate signals. The intensity of the signals relative to one another also vary depending both upon how long the sample has been left standing and its concentration. The ketones both retain water quite strongly, so it is possible that water content increases over time. In previous solution-based studies on triketonic moieties, very polar solvents have been shown to favour the enolised forms to a greater degree because of stronger interactions with the polarised OH groups, which is possibly what is being observed here as the water content increases effectively heightening solvent polarity.[58, 59] It was impossible to observe any signals corresponding to 1,5-di(2'-pyrimidyl)pentane-1,3,5-trione because of its almost complete insolubility in its neutral form.

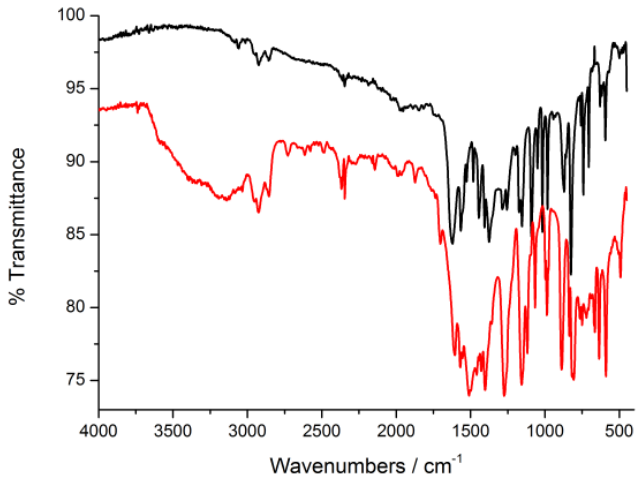

Figure 32 – Fourier Transform Infra-red spectra of 1,5-di(pyrazinyl)pentane-1,3,5-trione (black) and 1,5-di(2'-pyrimidyl)pentane-1,3,5-trione (red) in the solid state.

After multiple recrystallisations, the triketones persisted in remaining analytically impure despite profuse desiccation, with CHN values deviating from the calculated figures by 1-2%. It is thought that retention of water mediated by strong intra-lattice hydrogen bonding is responsible for these discrepancies. No single crystals formed during the repeated recrystallisations, which prevented definite structural identity for either compound. The infra-red spectra are a useful handle on the solid-state structures of these triketones, and aside from the fingerprint region below 900 cm^{-1} the spectra contain mostly the same dominating features (Figure 32). Firstly, the presence of three bands at 2800 – 3000 cm^{-1} is indicative of some retention of a keto tautomer as that region signifies lower energy aliphatic C-H stretches. Between 1550 and 1650 cm^{-1} is where the strongly absorbing β-diketone normally appears, however the existence of a multitude of aryl C-C and C-N bond stretches of similar energy overlap with this region making interpretation more difficult. Two more striking features are notable however, the first of which being the sharp, relatively weak absorptions in both spectra centred at 2350 cm^{-1}. This peak, which is more pronounced in the pyrimidyl derivative than in the pyrazyl indicates that one of the nitrogen atoms within the cyclic system is protonated, further complicating the keto-enol equilibria situation. Finally, the very broad absorption above 3200 cm^{-1} is only observed in the spectrum of the pyrimidyl triketone. The lack of well defined maxima in this broad region makes any reliable assignments very difficult, however it can certainly be concluded that there a number of different hydrogen bonding environments present, which are likely to arise from bonding to lattice water as well as hydrogen atoms shared intramolecularly. It appears however that in the solid state, enolic tautomers are preferred to a lesser degree in the pyrazinyl derivative.

With the exact structural nature of the triketones unknown yet the formation of the 1,3,5-trioxo bridge in both cases highly probable, it was decided to attempt to synthesise the central pyridine ring required by using NH_4OAc by attacking the 1,5-carbonyls sequentially. Reaction in EtOH under aerated refluxing conditions yielded, after cooling, precipitates which were collected and washed with cold EtOH. ^{1}H NMR spectroscopy in DMSO-d_6 on the collected powders showed environments characteristic of the symmetrical 4-hydroxy pyridines including the protic signal, however in 2-bipympyOH's case two further recrystallisations were necessary to remove an organic contaminant.

Though nevertheless indicative of their formation, the ^{1}H NMR spectra display some marked contrasts. All signals in the spectrum of bipzpyOH were sharp enough to observe the splitting of signals where coupling occurs. In contrast, all resonances in 2-bipympyOH's spectrum were broadened severely. This is due to the symmetrical nature of the pyrimidine ring – ordinarily in free terpyridines, to avoid unfavourable interaction the distal rings flip and spend the vast majority of their time with the 1*N* trans to the one on the central pyridine. In 2,6-di(pyrazinyl)pyridines such as bipzpyOH this is also the situation, and the spectrum acquired is one in which the ring spends the majority of its time with the two nitrogen atoms pointing away from each other. 2-BipympyOH is a special case – no matter which way the ring sits when planar to the rest of the aromatic system, the nitrogens' occupied p-orbitals still point towards one another. To minimise this interaction, the rings are probably flipping at a much faster rate and spending more time out of plane with the central ring. This means that the chemical environment seen by the spectrometer in solution extends over a larger range, hence the broadening of the signals. This actually happens so quickly that even in DMSO where the ring flipping is slower than in less strongly coordinating solvents that the protons on the 4' and 6' positions of the pyrimidine ring are chemically identical.

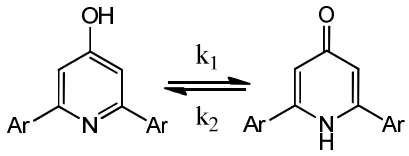

Figure 33 – Isomerisation between the hydroxypyridine and pyridone tautomers in bipzpyOH and 2-bipympyOH. k_1 and k_2 denote the equilibrium constants for the forward and back reaction for the formation of the keto tautomer; Ar = pyrazinyl, 2'-pyrimidyl.

Furthermore, the bipzpyOH and 2-bipympyOH experience tautomerisation between the hydroxypyridine and the pyridone isomers (Figure 33). Though the keto form in related 4-hydroxypyridines tends to be energetically favourable, both have been shown to exist in the same crystal, with the enolic form stabilised by hydrogen bonding between neighbouring molecules.[60] In solution, solvents with lower dielectric solvents favour the enolic form. Unfortunately we were limited to working with DMSO for solubility reasons, in which the keto

tautomer would be expected to dominate.[61] For a direct comparison, the hydroxy functionalities in bipzpyOH and 2-bipympyOH were methylated. Electronically, the *O*-methylated compound is very similar to the hydroxy tautomer, due to the methylation effectively locking the molecule in that conformation with the three rings adopting the planar energetically favourable *trans-trans* configuration. The hydroxy compounds were thus methylated in order to use their ^{1}H NMR spectra to confidently deduce the tautomeric nature of bipzpyOH and 2-bipympyOH as DMSO solutions.

Compound	3	3'	4'	5'	6'
Terpy[a,62]	8.45	8.62	7.85	7.33	8.69
TerpyOH[b]	7.88	8.58	7.97	7.46	8.69
TerpyOMe[a,63]	8.04	8.64	7.87	7.34	8.71
Bipzpy[a]	8.49	9.85	-	8.66	8.66
BipzpyOH[b]	7.85	9.80	-	8.76	8.76
BipzpyOMe[a]	8.02	9.83	-	8.64	8.64
2-Bipympy[a,25]	8.59	-	8.96	7.33	8.96
2-BipympyOH[b]	7.37	-	9.06	7.69	9.06
2-BipympyOMe[a]	8.18	-	8.96	7.34	8.96

Table 2 – Selected proton magnetic resonance signals for the unsubstituted, 4-hydroxy and 4-methoxy derivatives of 2,2':6',2''-terpyridine, 2,6-di(pyrazinyl)pyridine and 2,6-di(2'-pyrimidyl)pyridine. Spectra recorded on a Bruker Avance 500 FT 500 MHz spectrometer as a) $CDCl_3$ and b)DMSO-d_6 solutions.

It is the central pyridine 3 and 5 and the distal 3' proton resonance energies which are particularly useful as a handle in understanding the solvated structures of these hydroxypyridines. The central pyridine protons are, by virtue of their location, strongly affected by the position of the tautomeric proton. In the keto-form, to retain aromaticity a partial negative charge builds up about the oxygen, causing an increase in the resonance energy of these protons manifesting itself in their lower chemical shifts that they exhibit in comparison to the respective hydroxy tautomers.[10, 60] The 3' protons are also very sensitive, as ordinarily, when the *trans-trans* rotamer is adopted, they point directly towards the central pyridine nitrogen's filled sp^2 orbital. To stabilise the keto-tautomer, the *cis-cis* rotamer is dominant because the nitrogen atoms of the distal rings form intramolecular hydrogen bonds with the central N-H hydrogen. The effect is that the protons experience closer interactions with the central 3 and 5 hydrogens (Figure 34).

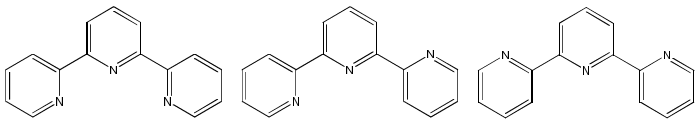

Figure 34 – The three rotamers of terpy, from left to right the *cis-cis*, *cis-trans* and *trans-trans* rotamer.

Analysis of the tabulated values (Table 2) informs us that, as a DMSO solution, terpyOH is actually present unexpectedly as its hydroxy tautomer, contrary to what is seen in chloroform.[60] The central pyridine signals are seen at low energy, as is observed in the

methylated compound. Additionally, the distal 3' resonance signals for terpy, terpyOH and terpyOMe all fall within 0.06 ppm of each other, allowing us to conclude that the *trans-trans* rotamer is adopted by terpyOH in DMSO due the absence of the proton at the central nitrogen. The same is seen for bipzpyOH, with the clear adoption of the *trans-trans* rotamer reinforced by the low-field 3 resonance signals meaning the hydroxy form is ubiquitous. The exception is 2-bipympyOH, for which only the keto form is observed. Though evidence based on the 3' handle cannot be used here because of the absence of a CH group at this position, the 3 signals provide all the information necessary in deducing its solvated structure. The shift seen is 0.8 ppm upfield of the *O*-methylated derivative, meaning the proton is bound to the central pyridine's nitrogen. The reasoning behind this is because the symmetry about the 2-pyrimidyl rings means that, no matter how the rings flip, when a planar conformation is adopted there is always an interaction between a pyrimidyl and pyridyl nitrogen. This means that a stabilisation of the hydroxy tautomer by the removal of this unfavourable interaction as in terpyOH and bipzpyOH is not possible in 2-bipympyOH's case. The result is that the keto tautomer now becomes the more stable, with the N-H proton held rigidly through distal N-H intramolecular contacts.

2.2.4 2,6-Di(1',2',4'-triazin-3'-yl)pyridine

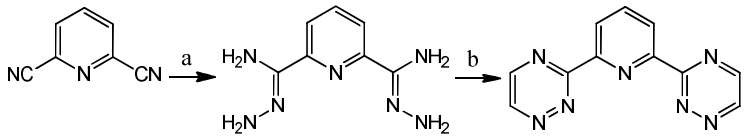

Figure 35 – Reaction scheme showing the formation of 2,6-di(1,2,4-triazin-3-y)pyridine and the intermediate dicarbamidrazone; a) $N_2H_4.H_2O$, EtOH; b) glyoxal trimer dihydrate, MeOH.

The unsubstituted *bis*-triazinyl terpy analogue was also of interest, and a synthetic route taken from the literature was followed (Figure 35).[23] N_2H_4 attacks the nitrile carbons of 2,6-dicyanopyridine, with charge build up on the non-hydrazinyl nitrogen atom which invokes a rapid double proton transfer resulting in the *bis*-dicarbamidrazone substituted cycle. Disubstitution was evident from the ^{1}H NMR spectrum, which showed two distinct aromatic signals indicative of a symmetrical pyridine, and a ratio of 8:3 between the aromatic and amino proton signal integrals.

The formation of the 1,2,4-triazinyl rings from the dicarbamidrazone proceeds via attack of the terminal nitrogen atoms upon the simplest 1,2-dialdehyde, glyoxal.[23] Monomeric glyoxal only exists as a solid at low temperatures due to its tendency to acquire additional oxygen atoms through latent water and oligomerise.[64] Producing monomeric glyoxal for the purpose of this transformation from its oligomers has previously been shown to be both unnecessary and wasteful as the carbamidrazones undergo condensations in high yield using the commercially available solid glyoxal trimer dihydrate in appropriate protic media.

High temperatures and drying agents such as P_2O_5 are required to “crack” oligomeric glyoxal so it is probable that when the reaction is heated to reflux, using an excess of “glyoxal”, the monomer present in small quantities is rapidly attacked and used up, resulting in the production of further monomer from the trimer until the reaction has run to completion.[64]

Issues were encountered regarding the purity of bitrzpy whose unfortunate low solubility in all solvents but DMSO even at elevated temperatures made purification by recrystallisation, Soxhlet extraction or chromatographic methods impossible. ^{1}H and ^{13}C NMR spectra of the first preparation of the isolated yellow-brown solid were as reported previously for bitrzpy the pair of coupled doublets at low field indicative of triazinyl ring formation. Daughter peaks, some with integrals of up to 40% of the bitrzpy signals plagued the spectrum. Two unknown resonances which stood out were singlets noted at 8.05 and 10.84 ppm, which could correspond to signals originating from protons ortho to a carbamidrazone group and an NH or an aldehyde respectively. This in mind, the detected impurities are either partially reacted carbamidrazone or oligomeric in nature due to two different carbamidrazone nitrogens having attacked the carbonyl groups of two individual glyoxal molecules. Previous literature preparations of triazine rings via a carbamidrazone intermediate using excess 1,2-dialdehydes to bridge the terminal nitrogens have also reported unidentifiable byproducts.[23, 64] Numerous attempts to remove the contaminants, including a Soxhlet extraction, yielded only marginal gains in purity. Eventually it was possible, simply by reducing the amount of glyoxal with respect to dicarbamidrazone, to isolate a bright yellow solid consisting of a much purer sample of bitrzpy as observed both spectroscopically and by microanalysis.

2.3 Cyclometallating *tris*-heterocyclic systems

2.3.1 *Bis*-alkylimidazolium-3’-yl pyridine salts

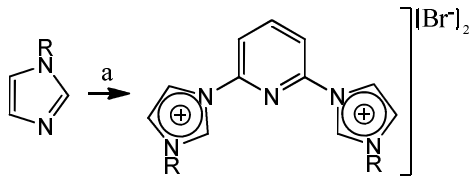

Figure 36 – One-pot preparation for the *bis*-alkylimidazolium-3-yl pyridine dibromide salts from the relevant alkyl imidazole; a) 2,6-dibromopyridine melt; R = methyl, isopropyl

Two *bis*-pyridyl imidazolium salts were prepared, 2,6-di(1’-methylimidazolium-3’-yl)pyridine dibromide and 2,6-di(1’-isopropylimidazolium-3’-yl)pyridine dibromide by melting an excess of 2,6-dibromopyridine at high temperatures in the presence of the appropriate N-substituted imidazole which has been shown to be a facile, reliable route towards alkylimidazolium substituted pyridines (Figure 36).[65, 66] In the case of the isopropyl derivative

N-isopropyl imidazole was first obtained by the reaction of the *in situ* prepared sodium imidazolide salt with isopropyliodide and purified by reduced pressure distillation. Both salts are reasonably soluble in polar protic salts, however the added alkyl bulk in the isopropyl compound renders it insoluble in H_2O.

Proton NMR spectroscopy allows us to observe marked differences in the solution behaviour of the two salts. The delocalised positive charge about the 5-membered imidazole rings causes a distinct downfield shift of all its ^{1}H NMR resonances. A consequence of this is that position 2' becomes quite acidic and in D_2O exchange is complete within minutes, evidenced by the lack of a signal corresponding to the proton at 2' and the presence of the coupled 4' and 5' resonances as sharp doublets. In the less acidic CD_3OD exchange is notably occurring at a much slower rate, and after a two hour period it is still possible to observe signals originating from the 2' position above 10 ppm. Interestingly, the additional steric bulk imposed by isopropyl groups in PrImpy acts as a "trap" for the acidic protons, resulting in much slower exchange with the deuterated methanolic solvent. After two hours, only around 2% of the protonated imidazolium rings remain in the methyl imidazolium salt, whereas over half are present in the isopropyl substituted compound. Tellingly, the 4' and 5' signals have also begun to broaden into unsymmetrical multiplets, as the idealised doublet of doublets collapses into a doublet in absence of coupling to the 2' proton.

2.3.2 2,2':6,4''-Terpyridine

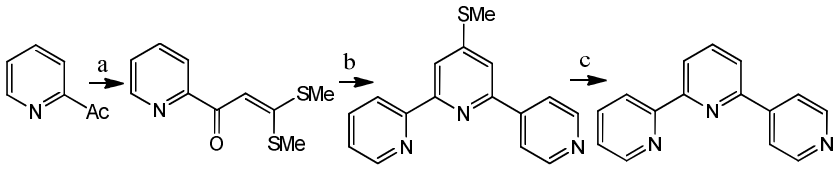

Figure 37 – Synthetic pathway taken toward 2,2':6,4'':terpyridine; a) ^{t}BuOK, CS_2, MeI, THF; b) (i) ^{t}BuOK, 4-acetylpyridine, THF; (ii) NH_4OAc, AcOH; c) $NiCl_2.6H_2O$, $NaBH_4$, NaOH, EtOH.

2,2':6,4''-Terpyridine, Ctpy, was synthesised via a modification of the Potts terpyridine synthesis according to a previous preparation of this compound.[67, 68] This involves a simple attack of the 2-pyridyl enolate upon the electrophilic carbon atom of CS_2, followed by methylation at both sulphur atoms (Figure 37). Mass spectrometry showed a peak at 226.0 corresponding to $[M + H]^+$, and the NMR spectra were in agreement with previously published assignments.[68]

Formation of the 2,2':6,4''-terpyridine core required displacement of a thiomethyl anion by an incoming 4-pyridyl enolate species, followed by ring closure mediated by NH_3 bridging the carbonyl carbon atoms and loss of water through acid workup. Two doublet of doublets, one triplet of doublets and a doublet of triplets in the ^{1}H NMR spectrum arise from the 2-substituted pyridyl moiety, and two second-order doublets signature of para-substituted

pyridines are seen each corresponding to two protons from the 4''-pyridyl ring. The central pyridyl resonances appear as two doublets because of the unsymmetrical 2,6-substitution.

Removal of the thiomethyl appendage is achieved through hydrodesulfurisation using *in situ* prepared nickel boride.[69, 70] Nickel boride precipitates out of ethanolic solution as a black solid upon addition of a basic solution of $NaBH_4$ to $NiCl_2.6H_2O$. Large quantities of dihydrogen gas are produced, some of which are adsorbed onto the nickel boride surface forming a transient active "nickel hydride" which subsequently reduced the C-S bond forming the hydrodesulfurised 2,2':6,4'':terpyridine.[71-73] Isolation of the compound required hot filtration through celite to remove nickel boride and extraction from an aqueous solution using DCM to remove unreacted $NaBH_4$ and water soluble salts. The resulting residue was extracted once more using boiling hexane yielding the pure cream-coloured solid. In the NMR, the terminal ring signal positions remain largely unchanged with identical multiplicity to those in the thiomethyl precursor. The central pyridyl 3 and 5 resonances had moved downfield and split further into doublet of doublets, reflecting the replacement of the electron donating thiomethyl group with a proton. The appearance of a sharp pseudo-triplet at 7.96 ppm, split nearly identically by 3 and 5 protons, confirms the existence of proton at the 4-position on the central ring. To clarify the origin of all of the signals in the ^{13}C NMR spectrum of Ctpy, both short and long range heteronuclear correlation spectra were analysed.

2.4 4-pyridine substituted 2,6-di(pyrazol-1'-yl)pyridine derivatives

2.4.1 4-Hydroxy-2,6-di(pyrazol-1'-yl)pyridine: protection and oversubstitution

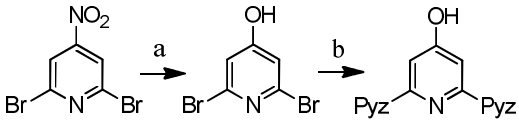

Figure 38 – Scheme detailing the proposed route towards 4-hydroxy-2,6-di(pyrazol-1'-yl)pyridine; a) ^{t}BuNOH, THF; b) 1*H*-pyrazole, KH, diglyme.

4-Hydroxy-2,6-di(pyrazol-1'-yl)pyridine was chosen as a synthetic target as it was a novel, 4-substituted 1-bpp derivative with the potential to offer hydrogen bonding functionality without significantly affecting the size of the molecule. Additionally, it is a potential synthetic intermediate towards the sulphur analogue, 4-mercapto-2,6-di(pyrazol-1'-yl)pyridine. Because of the synthetic strategy generally used in forming the 1-bpp backbone (Figure 38), it was theorised difficulties would arise in substituting amines, in this case deprotonated pyrazoles, at the 2 and 6 positions due to competitive deprotonation at the 4-position and deactivation towards substitution as a consequence of delocalised negative charge. However, previously, examples of substitution reactions on halopyridines containing directly bound protic groups have been shown to proceed smoothly, with no requirement for modification of conditions or observed side-reactions.[44, 74-77]

Four equivalents of sodium pyrazolide formed *in situ* with 4-hydroxy-2,6-dibromopyridine in diglyme were heated to 110°C for five days. The work up consisted of removal of the residual diglyme followed by addition of water and neutralisation precipitating a colourless solid which was confirmed spectroscopically as unreacted 4-hydroxy-2,6-dibromopyridine. Even so, in the ^{1}H NMR spectrum a number of daughter peaks were discernible just above the baseline, two of which were situated above 8 ppm, which likely arise from protons about a pyrazolylpyridine. To combat the deactivation of the hydroxyhalopyridine towards nuclephilic substitution in the presence of strong base, the conditions and reagents were modified. A subsequent attempt employed four and nine equivalents of base and 1*H*-pyrazole respectively in order to slightly reduce the ratio of pyridinolate to pyrazolide anions present. The hydride base was changed from NaH to KH to better "activate" the pyrazolide anions towards attacking the halopyridine, and the temperature was taken to 180°C to further promote the substitution.[78, 79] Some decomposition was noted during the course of the reaction, with the suspension becoming brown in colour and during workup a dark, base-insoluble solid was removed by filtration. The crude precipitate obtained after neutralisation was shown by electrospray mass spectrometry to contain both the mono- and disubstituted pyrazolylpyridines, which by inspection of peak integrals in the ^{1}H NMR spectra could be estimated to be present in an approximate 1:1 ratio. Elution through silica gel chromatography yielded the mono- and disubstituted compounds in 24% and 11% yields respectively. The large yield losses during the pyrazolide substitution step made this pathway impractical for multigram synthesis of 1-bppOH because of the expensive cost this would require.

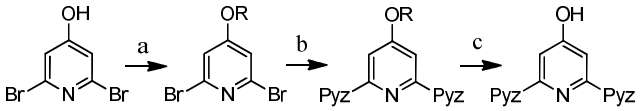

Figure 39 – Proposed pathway towards 4-hydroxy-2,6-di(pyrazol-1'-yl)pyridine involving protection of the hydroxyl group using a dihydropyranyl moiety; a) 3,4-dihydropyran, pyridinium *para*-toluene sulfonate, DCM; b) 1*H*-pyrazole, NaH, diglyme; c) pyridinium *para*-toluene sulfonate, EtOH.

To combat the loss of yield of the hydroxypyridine core due to decomposition at high temperatures, it was theorised that protection of the hydroxyl group would allow gram-scale preparation of 1-bppOH under milder conditions (Figure 39). Previously in the group, 4-hydroxymethyl-2,6-di(pyrazol-1'-yl)pyridine was prepared efficiently from 4-hydroxymethyl-2,6-dibromopyridine through protection of the alcohol functionality with a pyranyl group.[46] This was shown to proceed cleanly, with the protection and deprotection steps each only responsible for a yield loss of 20%. Analogously, from 4-hydroxy-2,6-dibromopyridine the corresponding protected pyridine was isolated in moderately high yield as a colourless microcrystalline solid (Figure 40).

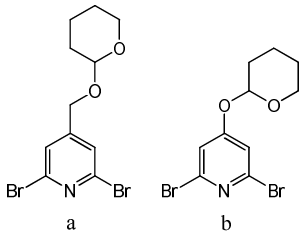

Figure 40 – Schematic representation of the protected dibromopyridine cores; a) 2,6-dibromo-4-(tetrahydropyran-2'-yloxymethyl)pyridine; b) 2,6-dibromo-4-(tetrahydropyran-2'-yloxy)pyridine.

With the hydroxyl functionality now "inert" towards deprotonation, the substitution reaction was performed at a much milder temperature and without the need for wasteful excesses of 1*H*-pyrazole. Following the usual workup for aprotic dipyrazolylpyridines, a colourless precipitate was isolated. Spectroscopically, the aliphatic pyranyl resonances were completely absent, and the crude solid contained what appeared to be two unique pyrazolyl environments in 2:1 ratio. A recrystallisation yielded sand-coloured crystals, which possessed this same ratio of major-to-minor pyrazolyl signals. A single pyridinyl resonance at 8.25 ppm indicated the equivalence of the 3 pyridinyl protons, and thus that both bromine atoms had been substituted for pyrazolyl rings. ^{13}C NMR spectroscopy supported this symmetry, and it was thus proposed that the pyranyl group had been displaced by pyrazolide forming 2,4,6-tri(pyrazol-1'-yl)pyridine, 1-tpp. This was further confirmed with the compound exhibiting a molecular ion at 300.1 in the electrospray mass spectrum, evidential of 1-tpp plus a sodium ion. Protecting the hydroxyl functionality with a methyl group also yielded solely the trisubstituted 1-tpp during the pyrazolide substitution.

Ordinarily, protecting groups such as the tetrahydropyran-2-yloxy moiety employed are not abstracted under nucleophilic substitution type reactions upon alkyl substrates as attack at this position is simply not possible. In our attempts to protect the hydroxyl functionality, we were dealing with a phenolic derivative. The aromatic nature of the protected alcohol means that an incoming nucleophile can attack at the 4-position of the ring, temporarily removing the aromaticity through the formation of a tetrahedral intermediate about the carbon atom. Reformation of the planar aromatic system is hugely favourable energetically, and electron density is pushed towards the 4-carbon requiring the reformation of its trigonal geometry. The high temperatures employed in addition to the 4-carbon's relative δ^+ promote nucleophilic attack and thus formation of a tetrahedral intermediate at this position. Unfortunately, in both attempts to selectively substitute the protected pyridines, the preferred leaving group is the alkoxy substituent which is intrinsically less basic than pyrazolide and, additionally, not present in solution in excess unlike pyrazolide.

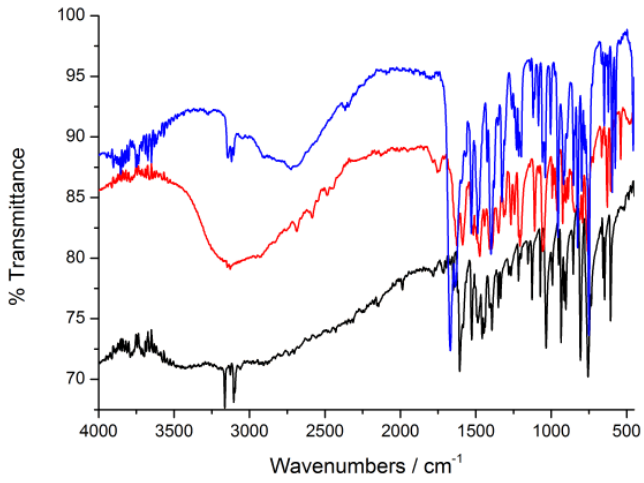

Figure 41 - Fourier Transform Infra-red spectra of 1-bpp (black), 1-bppOH (red) and 2-hydroxy-4,6-di(pyrazol-1'-yl)pyridine (blue) in the solid state.

The phenolic character of the central pyridine ring in 1-bppOH means that, like tpyOH, bipzpyOH and 2-bipympyOH, adoption of one of two tautomeric forms is possible in both the solid state and in solution (Figure 33). No material suitable for single crystal analysis was obtained, so the compound was subjected to solid state IR analysis in order to shed light upon its speciation. The instantly noticeable aspect of the IR spectrum of 1-bppOH is the broad, almost featureless band between 2500 and 3300 cm^{-1}, which is signature of a strongly hydrogen bonded hydroxy group (Figure 41). The lack of any strong, sharp absorptions between 1650 and 1800 cm^{-1} indicates that only hydroxy tautomer exists in the solid. The weak absorption at ~1750 cm^{-1} arises from the carbonyl stretch of a residual acetone contaminant on the plates which was used as a cleaning fluid and is also observed in the IR spectra of other compounds. The aromatic region between 1400 – 1650 cm^{-1}, consisting primarily of numerous C-C and C-N stretches within the rings, is complicated however all but identical to that of the other 1-bpp derivatives.

Deuterated solvent	3	3'	4'	5'
DMSO-d_6	7.21	7.82	6.58	8.86
Acetone-d_6	7.38	7.74	6.53	8.78
CD_2Cl_2	7.35	7.73	6.49	8.57
$CDCl_3$	7.36	7.74	6.48	8.53

Table 3 – Proton resonances about the aromatic backbone in 1-bppOH to elucidate solvent dependence Spectra recorded on a Bruker Avance 500 FT 500 MHz spectrometer.

1-bppOH exhibits low solubility in most common organic solvents meaning solution-based characterisation was carried out mostly as DMSO solutions of the compound. It was, however, possible to solubilise enough of the material in acetone, DCM and chloroform to observe its proton NMR spectra and use this to probe its speciation in these solvents. In all

four solvents, there exist five resonances indicating the presence of a single tautomer. Additionally, the pyrazolyl resonances are all sharp enough to observe the coupling which precludes any rapid exchange between the two tautomeric forms. The position of the signals does not vary significantly between solvents (Table 3), of importance is that the 3 proton signals, which in the terpyridyl derivative move 0.95 ppm upfield on going from the hydroxy to the keto form, change by no more than 0.15 ppm.[60]

The ^{1}H NMR spectra of the unsubstituted and *O*-methylated 2,6-di(pyrazol-1-yl)pyridines were recorded in DMSO so as to allow a direct comparison with 1-bppOH. 1-bppOMe represents a molecule locked into the same conformation as the hydroxy tautomer of 1-bppOH due to its inability to adopt the keto form. The chemical shifts of protons about the aromatic backbone in these two compounds are almost identical which is telling that the form adopted by 1-bppOH in all solvents is the hydroxy tautomer (Table 4). To avoid unfavourable overlap between the nitrogen sp^2 lone-pairs, the *trans-trans* isomer is ordinarily adopted. In the keto tautomer, the rings would be expected to possess a flipped *cis-cis* orientation to allow for the formation of intramolecular hydrogen bonds between the nitrogen atoms on the terminal rings and the central N-H. The 5' resonances in 1-bpp, 1-bppOMe and 1-bppOH vary by less than 0.1 ppm, indicating that the trans-trans orientation is adopted by 1-bppOH in solution and thus only the hydroxy tautomer is observed.

1-bppX, X =	3	3'	4'	5'
OH	7.21	7.82	6.58	8.86
OMe	7.33	7.85	6.62	8.92
H	7.81	7.86	6.63	8.95

Table 4 – Selected proton resonance signals for 1-bppOH, 1-bppOMe and 1-bpp. Spectra recorded in DMSO-d_6 on a Bruker Avance 500 FT 500 MHz spectrometer.

Quite why 1-bppOH adopts only the hydroxy tautomer, even in solvents possessing very high dielectric constants, could possibly be explained qualitatively by considering the differences between the tpy and 1-bpp backbones. The most crucial factor in stabilisation of the hydroxy form in 1-bppOH are the relative basicities of the central pyridine nitrogen and the carbonyl oxygen in the keto form. Due to proximity reasons, the effect of substituents at the *ortho* positions upon the basicity of the pyridinyl nitrogen need only be considered. Though the 3 proton resonances about the central ring tend to exhibit resonances 0.6 – 0.8 ppm downfield in tpy derivatives relative to the analogous 1-bpp compounds, this cannot be ascribed reliably to an inductive effect as it is also heavily influenced by the inter-ring bond distances. It is clear that the electron deficient pyrazolyl ring exerts a strong inductive effect by electron withdrawal, subsequently reducing the basicity on the central pyridinyl nitrogen atom by such an amount that in both the solid state and even strongly polar media the keto-form is not observed. Lastly, the inter-ring angles (Figure 42) α and β are larger about the 1-

bpp backbone than in derivatives of tpy. In particular, α is important as it is informative on the direction in which the pyrazole nitrogen lone pairs point relative to the central pyridine nitrogen atom. 1-bpp derivatives, possessing larger values of α compared to tpy, would be expected to hydrogen-bond less strongly in the *trans-trans* conformation of the keto-tautomer, which causes a further destabilisation of the keto relative to the hydroxy form.

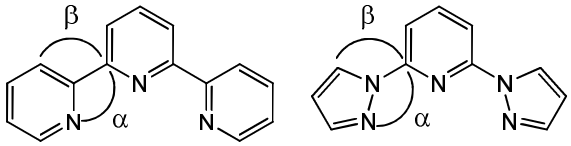

Figure 42 – The 2,2':6',2''-terpyridines (left) and 2,6-di(pyrazol-1'-yl)pyridine (right) backbones in the *cis-cis* conformations illustrating the two inter-ring angles α and β.

Oddly, one attempted preparation of 2,6-dibromo-4-hydroxypyridine (Figure 38) yielded the back to back di(2,6-dibromopyridin-4-yl)ether (Figure 43). It was thought that the ^{t}BuNOH employed had partially decomposed over time to the carbonate, resulting in the displacement of the nitro group from ca. 50% of the 2,6-dibromo-4-nitropyridine. The deprotonated hydroxypyridine then went on to attack the remaining nitropyridine, bridging the two at the pyridine 4 positions via an ether linkage. The compound is base insoluble, possesses ^{1}H/^{13}C NMR spectra typical of a single, symmetrical pyridinyl ring very similar to that of 2,6-dibromo-4-hydroxypyridine however lacks the broad signal originating from the phenolic proton. The compound unfortunately fragments under electrospray conditions and has not been identified through mass spectrometry.

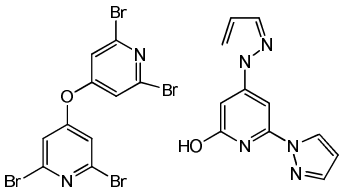

Figure 43 – Structures of the two unexpected compounds formed during the synthesis of 1-bppOH; di(2,6-dibromopyridin-4-yl)ether (left) and 2-hydroxy-4,6-di(pyrazol-1'-yl)pyridine (right).

Substitution of the halide atoms for pyrazolyl rings yielded even further surprises, with no evidence for the formation of the predicted back to back di(2,6-di(pyrazol-1'-yl)pyridin-4-yl)ether. Instead, two structural isomers were isolated, 1-bppOH and 2-hydroxy-4,6-di(pyrazol-1'-yl)pyridine (Figure 43). This was unexpected based on the fact that, at the temperatures employed with an excess of pyrazolide anion it was predicted that either a) tetrasubstitution would occur, replacing the bromo substituents only or b) attack by pyrazolide would occur at the 2 and 6 positions, but also at the 4 position of one of the two pyridines in the dipyridyl ether, resulting in the formation of equimolar amounts of 1-bppOH and 1-tpp. The formation of 2-hydroxy-4,6-di(pyrazol-1'-yl)pyridine must have taken place via

an initial abstraction of a bromide upon the back-to-back ether, followed by the attack of a pyrazolide anion at the 4-position of the same pyridine, resulting in the formation of both 1-bppOH and its structural analogue once the mixture is acidified. It cannot presently be explained as to why this series of events transpires, particular when it is considered how dry solvents were used in conjunction with inert atmosphere conditions.

In the solid state, the situation looks to be a little more complicated for 2-hydroxy-4,6-di(pyrazol-1'-yl)pyridine than in 1-bppOH. This compound displays an extremely sharp absorption at 1668 cm^{-1}, its intensity dwarfing that of the other stretches in the C=C/C=N region in the compound, which is absent in the spectra of 1-bpp, 1-bppOH and, additionally, 1-tpp which also contains a pyrazolyl substituent at the 4 position (Figure 41). The energy is suggestive of an aromatic ketone, however the complete lack of absorption above 3200 cm^{-1} rules out the existence of the keto form as clearly no N-H stretching is detected. There is clearly a strongly hydrogen bonded O-H region centred around 2724 cm^{-1}, but it appears at lower energy and is narrower than in 1-bppOH probably reflecting an increases in rigidity of the system mediated by intramolecular hydrogen bonding to the central pyridine nitrogen.

2.4.2 The path to 4-mercapto-2,6-di(pyrazol-1'-yl)pyridine

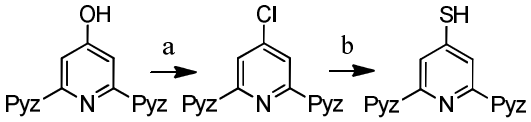

Figure 44 – Synthetic pathway towards 4-mercapto-2,6-di(pyrazol-1'-yl)pyridine through the 4-chloro substituted intermediate; a) PCl_5, $POCl_3$; c) NaSH, DMF.

Originally, the intention was to isolate large quantities of 1-bppOH as a precursor towards the sulphur analogue 1-bppSH which has a far higher affinity for gold surfaces/particles. Subsequently preparing the 4-chloro intermediate 1-bppCl using a chlorinating agent in a method typical for the conversion of phenolic systems into aromatic chlorides, it was predicted the chloride could then be efficiently substituted for a mercaptan at high temperatures using NaSH (Figure 44). The fact that only a small fraction of the amount of 1-bppOH that was required was isolated, however, meant that alternate pathways towards 1-bppSH must be researched. Interestingly, the chlorination step was performed on a small scale on 1-bppOH in order to isolate 1-bppCl – a novel compound in its own right whose coordination chemistry has not been investigated – yet the reaction did not proceed as expected which is discussed in greater detail in 2.4.3. The rest of this section will now focus on the preparation and isolation of 1-bppSH from 4-amino-2,6-dichloropyridine (Figure 45).

Adopting a finding previously made within the group, 1-bppNH$_2$ was synthesised from commercially available 4-amino-2,6-dichloropyridine under the standard conditions employed in the formation of the 2,6-di(pyrazol-1'-yl)pyridine backbone. Despite the reactivity of protic amines towards superbases, the only reaction to have occurred was that of the formation of a bond between a pyrazole nitrogen and the 2 and 6 positions on the pyridine as 1-bppNH$_2$ was isolated purely in almost quantitative yield. It is not completely understood as to why the 4-amino group does not react at all, indeed once deprotonated the additional negative charge about the delocalised system would actually deactivate the compound towards nucleophilic substitution yet the pyrazolide substitution proceeds cleanly at a rate which appears to be comparable to non-protic pyridines. It is postulated that, unlike 2,6-dibromo-4-hydroxypyridine which possesses a similar pKa to 1*H*-pyrazole, the amino precursor employed in preparing 1-bppNH$_2$ is much less acidic.[80-82] There are thus several orders of magnitude less of the deprotonated pyridine in solution than there is pyrazolide anion, meaning the reaction proceeds smoothly with the NH$_2$ group considered to be inert as long as the 1:1 ratio of base to 1*H*-pyrazole is effectively achieved. The compound is a pale beige in colour in accord with literature reports, and though it exhibits low solubility in most solvents its ^{1}H NMR spectrum in DMSO-d_6 displays five sharp signals with the amino protons appearing as a single resonances as a consequence of the C_2 symmetry.[44, 77]

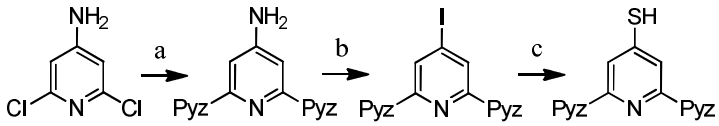

Figure 45 – Successful synthetic route to 4-mercapto-2,6-di(pyrazol-1-yl)pyridine via 4-iodo-2,6-di(pyrazol-1'-yl)pyridine; a) 1*H*-pyrazole, NaH, diglyme; b) I_2, KI, isopentyl nitrite, DCM; c) NaSH, DMF.

The conversion to 1-bppI required the transformation of NH$_2$ into a stable leaving group in order for nucleophilic substitution of iodide to take place. This was achieved using isoamyl nitrite to convert the compound into a diazonium salt, which then is attacked by an appropriate nucleophile, in this instance iodide using a method modified from the literature.[83, 84] The exact mechanism of substitution of the diazonium salt depends on the nucleophile itself, but in the case of iodination it is thought to proceed via a radical aromatic intermediate, with diatomic iodine acting as both a radical trap and catalyst for the conversion to the aryl halide.[83, 85, 86]

1-bppI's spectroscopic properties matched with those previously documented, however two additional components were isolated during the purification process by silica gel chromatography. The first of these two components is of little interest, as it was confirmed to be unsubstituted 1-bpp which formed in a yield of less than 1% as a result of radical abstraction of a hydrogen atom from the DCM/isoamyl nitrite solvent by the aryl

radical intermediate species. The second byproduct was confirmed as the 4-nitro derivative, 1-bppNO$_2$, exhibiting a molecular ion at 279.1 corresponding to $C_{11}H_8N_6O_2$ + Na^+. In the ^{1}H NMR spectrum, the chemical shifts about the backbone all appear at low frequencies due to the removal of electron density from the π-system by the nitro group. Single cuboidal crystals, bright yellow in colour, were obtained by slow vapour-diffusion of n-pentane into $CHCl_3$ solutions of the compound and an X-ray structure was acquired.

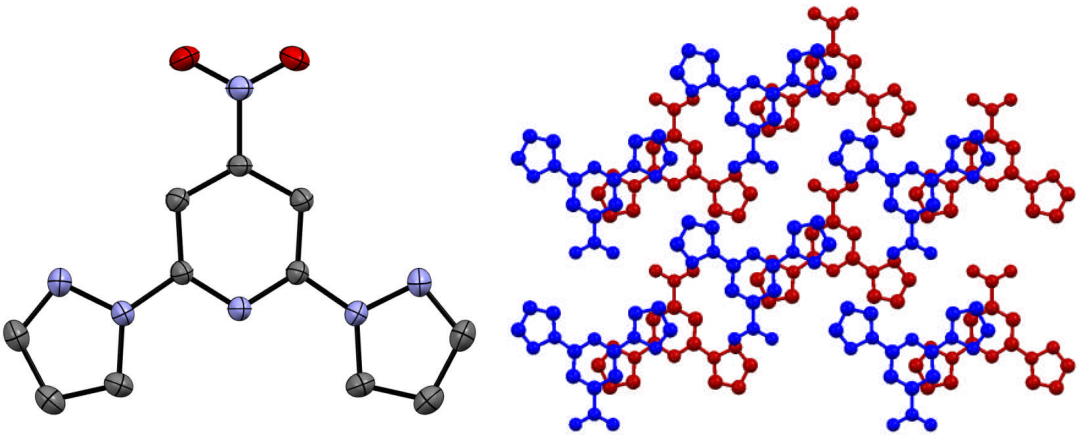

Figure 46 – Left: view of a molecule of 1-bppNO$_2$ down the crystallographic c-axis.). H atoms have been omitted for clarity and all thermal ellipsoids are plotted at the 50% probability level, tom colour code: carbon (grey), nitrogen (periwinkle) and oxygen (red). Right: Crystal packing diagram of 1-bppNO$_2$ illustrating the array of alternating layers along the a-axis as represented by blue and red molecules.

The structure obtained of 1-bppNO$_2$ crystallises as a solvent-free material, in the centrosymmetric monoclinic space group C2/c. The molecules pack in alternating layers, with the nitro groups pointing in opposing directions parallel to the b-axis. The terminal rings exist in the *trans-trans* conformation as in all but one reported 2,6-di(pyrazol-1'-yl)pyridine derivative to prevent unfavourable overlap between the pyrazolyl-pyridyl nitrogen lone pairs.[45, 46, 87-93] There is no π-π interaction between molecules in the alternating layers, with the closest stacking interaction being between a pyrazolyl and pyridyl ring off-centre by over 2 Å, and the inter-ring distance 3.998 Å (Figure 46).

In order to obtain 1-bppSH, the iodo-substituted precursor was subsequently reacted with NaSH in refluxing DMF to provide enough thermal energy to substitute iodide for HS^-. The reaction proceeds quantitatively, with the thiol precipitating out of aqueous solution as a fluffy off-white solid after careful neutralisation with HCl. Due to the relatively high strength of the disulfide bond, thiols possess low oxidation potentials and have been observed to oxidise readily both in solid form and in solution. This potential ability to oxidise, coupled with the tautomeric potential of 1-bppSH meant that structural characterisation was problematic. To assist with the identification of tautomeric species in both the solid state and in solution, 1-bppSMe was synthesised, along with the disulfide 1-bppDS which allowed direct

comparison of the as-prepared thiol with the oxidised compound. Full conversion to the disulfide proceeded through the reduction of molecular iodine in a basic aqueous solution, with the compound precipitating out of the mixture over the course of a day and subsequently collected. 1-bppSMe was formed using a standard alkylating procedure, involving a mildly basic polar solution containing the methylating agent MeI. Isolation of pure 1-bppSMe proved to be no straightforward task, with the crude solid extracted containing a ca. 30% impurity which was shown by mass spectrometric and ^{1}H NMR analyses to be a second disulfide of the form (methyl-2,6-di(pyrazol-1'-yl)pyridine-4-yl)disulfide which, regrettably, could not be isolated. The thioether and sulfone both exhibited coincident Rf values on both silica and alumina in all solvent combinations tested, and even repeated recrystallisation proved inadequate in removing the sulfone contaminant. Eventually, sublimation under high vacuum at 130°C yielded the pure thioether as a colourless powder.

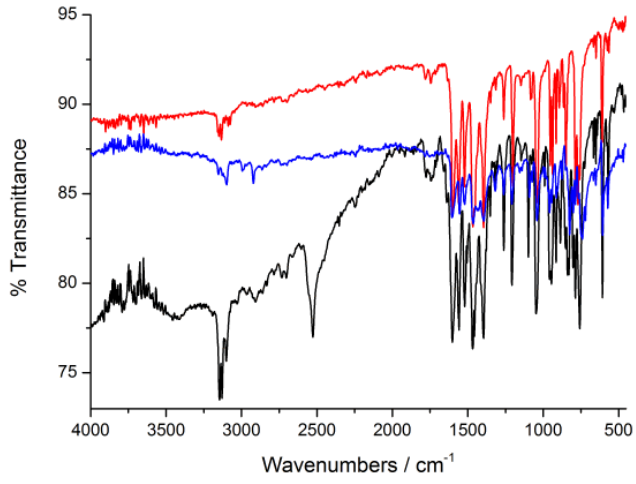

Figure 47 - Fourier Transform Infra-red spectra of 1-bppSH (black), 1-bppDS (red) and 1-bppSMe (blue) in the solid state.

In solid form, it was uncomplicated enough to unambiguously assign the structure of the molecules in the lattice as adopting solely the mercapto-configuration by analysis of its IR spectrum (Figure 47). The strong and sharp absorption at 2526 cm^{-1} is indicative of a single SH environment, the lack of significant broadening reflecting the relatively unpolarised S-H bond which is only capable of forming weak hydrogen bonds. Neither 1-bppDS nor 1-bppSMe absorb in this region telling of the full conversion of 1-bppSH to the respective derivatives. The region between 3075 – 3160 cm^{-1} is reasonably similar across the triad, which all possess an identical aromatic C-H backbone, and 1-bppSMe also absorbs weakly at 2920 cm^{-1}, a consequence of the alkyl C-H stretching vibrations about the thiomethyl group. The complete dominance of the mercapto tautomer is reinforced by the absence of any sharp absorption at 3200 – 3300 cm^{-1} which lies in the energy region of aromatic N-H

stretches. Finally, the position of the bands between 600 – 1600 cm^{-1} which encompasses both the fingerprint and aromatic region does not vary by more than one or two wavenumbers between compounds, though the intensities do fluctuate slightly. This is telling that there are no additional peaks between 1000 – 1200 cm^{-1} which arise from thiocarbonyl stretches and rules out the existence of said tautomer in the solid state (Figure 48).

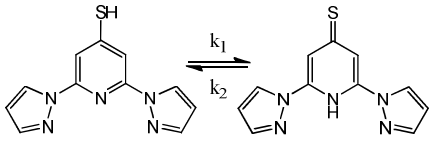

Figure 48 - Isomerisation between the mercaptopyridine and thiocarbonyl tautomers in 1-bppSH. k_1 and k_2 denote the equilibrium constants for the forward and back reaction for the formation of the thiocarbonyl tautomer.

Analogously to 1-bppOH, an NMR study was performed upon 1-bppSH in conjunction with 1-bppDS and 1-bppSMe in order to quantify and analyse the changes in the spectra upon alkylation and dimerisation, and what this tells us of the molecular structure of solvated 1-bppSH. 1-bbpSH converts fully over the course of three days to the disulfide, as can be seen from the proton chemical shifts, which sharpen in the final six hours of study to represent fully those of the as-prepared disulfide (Table 5). The first row can be considered to be “pure” 1-bppSH, as this spectrum was run within 0.5 h of dissolution in DMSO.

By comparison with 4-mercapto-2,6-di(2’-pyridyl)pyridine, whose central pyridine resonances moved downfield by 0.16 ppm upon methylation of the sulphur, the contrary is seen when methylating 1-bppSH with the 3 + 5 proton signals moving upfield by 0.21 ppm which is telling that the deshielded protons are accepting more electron density in the methylated version, consistent with the stronger π-donating ability of the methylated sulphur[4, 94]. In thiocarbonyl species, the additional electron density supplied by the sulphur is actually lessened once the atom is methylated and a permanent C=S bond can no longer be maintained, thus the upfield shift upon methylation points towards the adoption of the mercapto-tautomer. This is reinforced by the only minor changed in the 5’ proton’s chemical environment across the triad, meaning that unlike in the terpyridyl cousin the *trans-trans* rotamer is favoured in absence of an intramolecularly bound N-H proton which would favour a *cis-cis* configuration to stabilise the thiocarbonyl species. To further clarify, a study of the change in shift of the SH/NH proton over a temperature range would have indicated whether or not the proton was intramolecularly bound, however it was broadened to such an extent that it could not be observed even at very high concentrations. Even if it could be observed, it would have been likely that heating would speed up the dimerisation process leading to the loss of any SH/NH signal. A final piece of evidence cements the sole existence of the mercapto-tautomer in DMSO solutions. The carbon directly bound to sulphur is highly

dependent upon the nature of the bond, and experiences a very low field resonance when a π-bond links the two atoms[95, 96]. The lowest field resonance 1-bppSH possesses is situated at 152.1 ppm, consistent with the existence of a C-S single bond and thus the exclusivity of the mercapto-tautomer's existence. Despite the fact the energetic preference for the keto form has been shown to be much greater in sulphur derivatives than in their corresponding oxygen analogues, the mercapto-tautomer still dominates in 1-bppSH[97]. It can be concluded that the pyrazolyl rings at the 2 and 6 position exert a profound influence upon the lowering of the basicity of the pyridyl nitrogen atom, hence the evasiveness of the keto tautomers of both 1-bppOH and 1-bppSH both in the solid state and when solvated in highly polar solvents in which keto-tautomers are usually favoured.

Compound (t / h)	3	3'	4'	5'
1-bppSH (0)	7.82	7.84	6.60	8.87
1-bppSH (18)	7.91	7.84	6.61	8.88
1-bppSH (24)	7.93	7.84	6.60	8.89
1-bppSH (42)	8.00	7.84	6.62	8.93
1-bppSH (48)	8.00	7.85	6.62	8.93
1-bppSH (66)	8.01	7.85	6.62	8.93
1-bppSH (72)	8.01	7.85	6.62	8.93
1-bppDS (N/A)	8.01	7.85	6.63	8.93
1-bppSMe (N/A)	7.61	7.86	6.63	8.91

Table 5 – Proton magnetic resonance signals for 1-bppSH, 1-bppDS and 1-bppSMe taken over set of time intervals. Spectra recorded in DMSO-d_6 on a Bruker Avance 500 FT 500 MHz spectrometer.

To obtain structural information and perhaps divulge as to why the mercapto-tautomer dominates in the solid state, endeavours were made to grow single crystals of the material. Prismatic, transparent blocks were obtained via both vapour diffusion of various solvents into DMSO, and by allowing concentrated solutions of the material to stand for upwards of 3 days. In all instances, the crystals were found to consist entirely of solvent-free 1-bppDS, further reflecting its lability towards dimerisation in polar solvents.

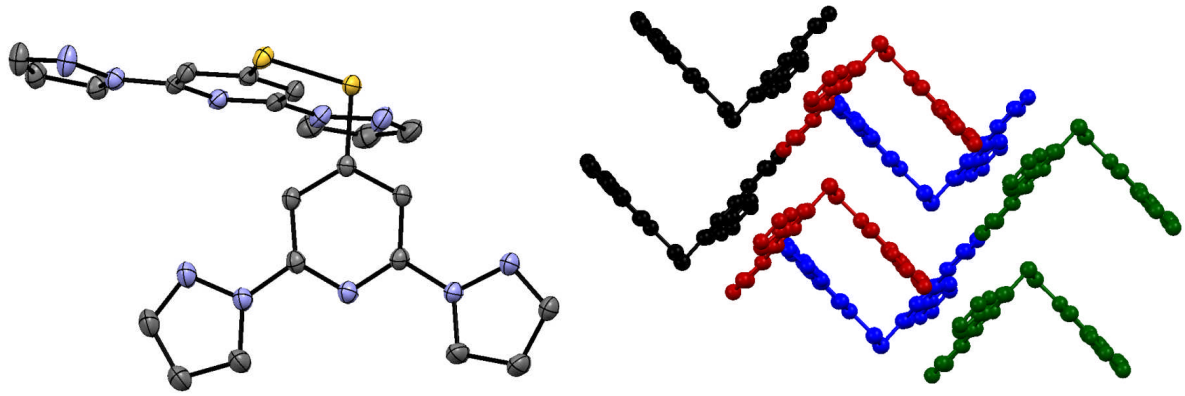

Figure 49 – Left: View of a molecule of 1-bppDS perpendicular to the plane of one of the pyridine rings. H atoms have been omitted for clarity and all thermal ellipsoids are plotted at the 50% probability level, atom colour code: carbon (grey), nitrogen (periwinkle) and sulfur (yellow). Right: Packing diagram for 1-bppDS, with the arbitrarily assigned layers shown in different colours. The view shown is along a plane parallel to one of the 2,6-di(pyrazol-1'-yl)pyridine backbones.

It was found that 1-bppDS crystallises in the centrosymmetric triclinic space group P-1 with no close contacts between neighbouring molecules. The carbon-to-sulfur bond lengths, at 1.804 and 1.805 Å are typical of an aromatic singly bonded C-S interaction, if slightly longer than average.[98, 99] The C-S-S bond angles are less than typical, at 104.97 and 104.74°, suggesting a slightly compressed tetrahedron about the sulfur centres. The tortion angle between the S-S bond is 82.4, almost 10° smaller than in the *bis*-terpyridyl analogue, which may arise as a consequence of the longer S-S bonds.[94] The molecule adopts the usual *trans-trans* conformation between neighbouring rings (Figure 49), with the system maintaining almost complete planarity, C-N-C-N torsion angles between the rings comprising the two 1-bpp backbones are 1.4, 2.9 and 2.1 and 3.6 respectively.

2.4.3 Endeavours to selectively halogenate at the 4 position

Halogenation selectively at the 4-position of the pyridine ring about the 1-bpp backbone has only previously been achieved using iodine (Section 2.4.2).[44, 77] These reactions, as discussed, require a primary amino precursor and via the formation of a diazonium salt allow nucleophilic substitution at the 4-position by iodide. The derivatisation of the 1-bpp backbone at the 4-position on the central ring is of interest as the electronegativity varies greatly across the period 2 to 5 halides, whilst only iodide possesses a volume larger than that of a methyl group thus lowering the probability that intermolecular stacking interactions will be disrupted by the halides in the crystal. [100]

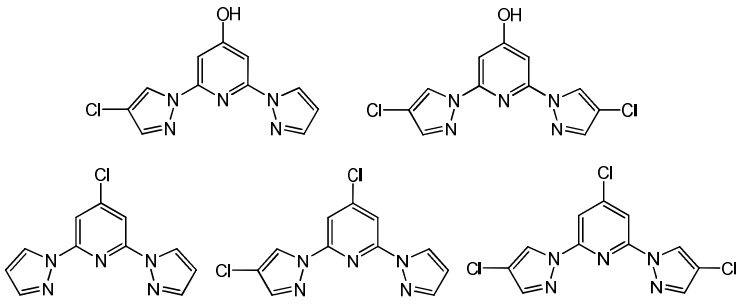

Figure 50 – Structures of the components observed mass spectrometrically in the crude solid obtained from the reaction of $POCl_3$ and PCl_5 with 1-bppOH.

Initially it was proposed that 1-bppOH could be chlorinated simply by reaction with PCl_5 in the presence of $POCl_3$ which proceeds in high yield for the terpyridyl derivative.[10, 101] Reaction between 1-bppOH and PCl_5 under anaerobic conditions in fact yielded an array of mono- and multiply chlorinated compounds. Basicification of the heavily acidic reaction media and extraction with $CHCl_3$ yielded a crude solid consisting, as evidenced by the mass

spectrum and ^{1}H NMR spectrum, of the mono-, di- and tri-substituted 2,6-di(pyrazol-1'-yl)pyridine derivatives (Figure 50, bottom row). The aqueous phase was then neutralised using HCl and extracted once again allowing the collection of all the derivatives containing a hydroxyl functionality (Figure 50 – top row). The hydroxy derivatives, including a significant quantity of unreacted 1-bppOH, could unfortunately not be separated from one another because of a tendency to streak dramatically on all chromatographic material, and their low solubilities precluded efficient recrystallisation. Additionally, the compounds could only be observed in the electrospray mass spectrum as, again, their insoluble nature meant a well resolved ^{1}H NMR spectrum of the components could not be obtained.

The non-protic mono-, di- and tri-chlorinated compounds exhibited Rf values large enough to be individually isolated chromatographically; elution through silica gel with DCM gave the largest apparent separation. The Rf values of the three components decreases in the order tri- > di- > mono-chlorinated compound. Regrettably, only small quantities (< 5 mg) of each of the three derivatives were isolated, with the majority of the 1-bpp backbone-containing material present as hydroxy derivatives which as mentioned were inseparable on such a scale. This precluded any further analyses of the novel compounds other than ^{1}H/^{13}C NMR spectroscopy. Four, seven and three signals could be seen in the proton NMR spectra of the mono-, di- and tri-chlorinated compounds respectively which is in agreement with the number of proton environments present in each of the molecules. The correlation between chemical environments and observed signals also matched in the carbon spectra with six, eleven and six signals for the mono-, di- and tri-chlorinated compounds. Due to the reduced symmetry in 2-(4'-chloropyrazol-1'-yl)-6-(pyrazol-1'-yl)pyridine, the 3 protons were split into two distinct doublets at 7.84 ppm and 7.92 ppm corresponding to 3 and 5 positions respectively. The identity of these signals was clarified by employing a long-range heteronuclear correlation experiment, which allowed identification of which carbon signals originating about the central ring was coupled with either the chlorinated or non-chlorinated pyrazolyl 5-proton. From simple analysis of an heteronuclear ^{1}J coupling experiment it was deduced which of the two ^{1}H doublets correspond to the protons at either the 3 or 5 positions on the central ring – with the 3-proton being responsible for the higher field signal at 7.84 ppm and the 5-proton the doublet at 7.92 ppm.

This method of chlorination relies upon nucleophilic substitution via coordination of the hydroxy oxygen to the phosphorus centre of PCl_5, followed by attack of "effective Cl^-" at the 4-position and loss of $POCl_3$. Replacement of a hydrogen atom for chlorine at the 4'-position on the pyrazole rings requires an electrophilic mechanism. The chemical shifts of both the carbon and proton at 4' are telling of a highly shielded chemical environment, and previously this has been reflected in its ability to undergo electrophilic substitution at this

location.[44] In both PCl_5 and $POCl_3$, the chlorine atoms are heavily polarised by the electronegativity difference between phosphorus and chlorine. The source of the electrophilic chlorine must thus be Cl_2. Cl_2 and PCl_3 are in equilibrium with PCl_5, the favourability of the bimolecular side increasing with elevating temperatures.[102] Interestingly, the relative product distribution actually points to a faster electrophilic substitution process occurring at the pyrazole rings, than of nucleophilic replacement of the hydroxy functionality.

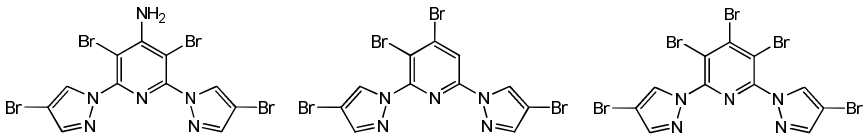

Figure 51 - Structures of the compounds isolated from the reaction of 1-bppNH$_2$ with Br$_2$/KBr via diazotisation with isopentyl nitrite.

Due to the difficulty in preparing large quantities of 1-bppOH relative to 1-bppNH$_2$, a route towards the 4-halo-2,6-di(pyrazol-1'-yl)pyridines was investigated via diazotization of the amino-functionality and substitution with the appropriate halide. Analogously to the synthesis of 1-bppI, 1-bppNH$_2$ was reacted under anaerobic conditions with isopentyl nitrite in DCM in the presence of Br_2 and KBr. Unlike when performing the iodide substitution however, a mixture of compounds was isolated containing over-brominated species, whereby the electron rich positions about the *tris*-heterocycle, the pyridine 3 and pyrazole 4 positions, have undergone electrophilic substitution. As in the initial attempt to prepare 1-bppCl using PCl_5/$POCl_3$, the dihalide present in solution is large and polarisable and hence able to react in a manner opposite to which is desired and substitute via an electrophilic mechanism at the pyrazole 4 positions. The substitution at the pyridine 3 and 5 position is telling of the 4-amino substituent's activating effect upon the *ortho*-positions towards electrophilic substitution (Figure 52). The appearance of 4-amino-3,5-dibromo-2,6-di(4'-bromopyrazol-1-yl)pyridine (Figure 51 - left) suggests that the electrophilic substitution proceeds much more quickly upon 1-bppNH$_2$ than does the diazotisation process, even when reacted in large excesses of isopentyl nitrite. The byproducts, from left to right (Figure 51) were isolated through column chromatography in yields of 14, 34, and 10% yields respectively and characterised fully by ^{1}H/^{13}C NMR spectroscopy and mass spectrometry.

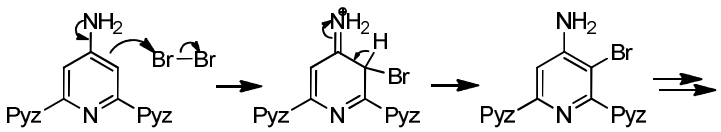

Figure 52 – Simplified mechanism showing electrophilic bromination of the central pyridine 3 and 5 positions made possible by the mesomeric effect of the 4-amino substituent.

It was found that the 4-halo-2,6-di(pyrazol-1'-yl)pyridines could be successfully prepared by the exclusion of X_2 (X = Br, Cl, F) during the reaction. Instead, $NaNO_2$ was employed as the diazotisation agent which meant aqueous solutions of the appropriate acid could be used to catalyse the formation of the diazonium salt, thus negating the need for the corresponding dihalogen. The conditions in which the bromide and chloride derivative were formed were identical, first reacting $NaNO_2$ with 1-bppNH$_2$ in acetonitrilic solution to form the diazonium salt in the presence of aqueous HX/KX (X = Br, Cl) which formed orange-brown solutions. The contents were stirred at ambient temperature during which it was noted that in the case of the bromide derivative, N_2 gas was evolved. Both reaction mixtures were heated to 80°C for 1 h, and it was observed that N_2 was not evolved in chloride's case until a temperature of almost 80°C attained. Post work-up, both 1-bppBr and 1-bppCl were isolated in 32 and 48% yields respectively. 2-(4'-bromopyrazol-1'-yl)-6-(pyrazol-1'-yl)pyridine was also isolated in 5% yield during the bromination of 1-bppNH$_2$, which probably arose as a result of a residual amount of Br_2 present in the solution at high temperatures because of bromide's low oxidation potential compared to that of chlorine. 1-bppF was acquired using a modified procedure which employed HBF_4 as both the acid catalyst and fluorinating agent due to HF's highly corrosive and extremely toxic nature. The diazonium salt formed as a bright yellow flocculate, and upon heating to 80°C no evolution of N_2 was observed until a small amount of MeCN was added which appeared to be necessary to solubilise the salt. The mixture was heated for only 0.5 h, after which the contents were worked up as in previous halogenations via this procedure. The large amount of water present during the fluorination meant that the crude mixture contained a mixture of desired 1-bppF contaminated with 1-bppOH due the water having acted competitively as a nucleophile. The compounds were separated chromatographically, isolated in 20 and 23% yields respectively.

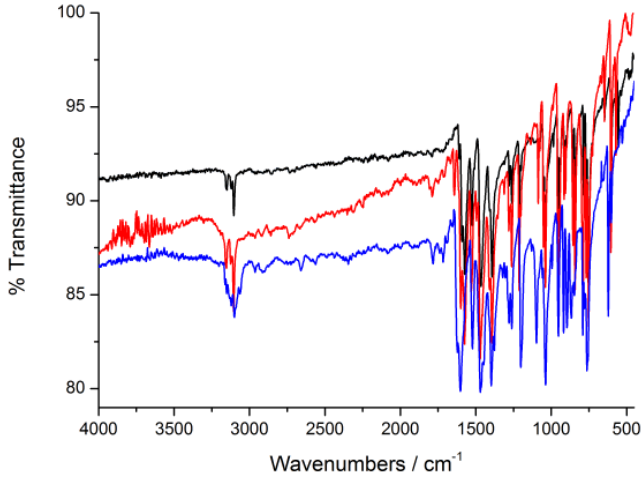

Figure 53 - Fourier Transform Infra-red spectra of the 4-halo-2,6-di(pyrazol-1'-yl)pyridine derivatives 1-bppBr (black), and 1-bppCl (red) and 1-bppF (blue) in the solid state.

All of the novel halides are white crystalline solids and exhibit similar high solubility in most common moderately polar organic solvents. The melting points increase as the group of homologues is ascended, with the largest increase between the fluoro- and chloro-derivatives which reflects the substantially weaker van der waals forces in the lattice attributed to the extremely small, electronically compact fluorine atom which is difficult to polarise. The IR spectra across the series of solid compounds are almost identical (Figure 53), the sequence of peaks in the aromatic C-H stretching region between 3035 – 3070 cm^{-1} possessing very similar relative intensities with the positions of each individual minima varying by less than 5 cm^{-1} across the series. The fingerprint region below 1650 cm^{-1} is very complicated and the arrangement of absorbances follows the same sequence amongst the compounds – this casts a degree of uncertainty about the validity of assigning a specific absorbance to the C-F bond stretch.

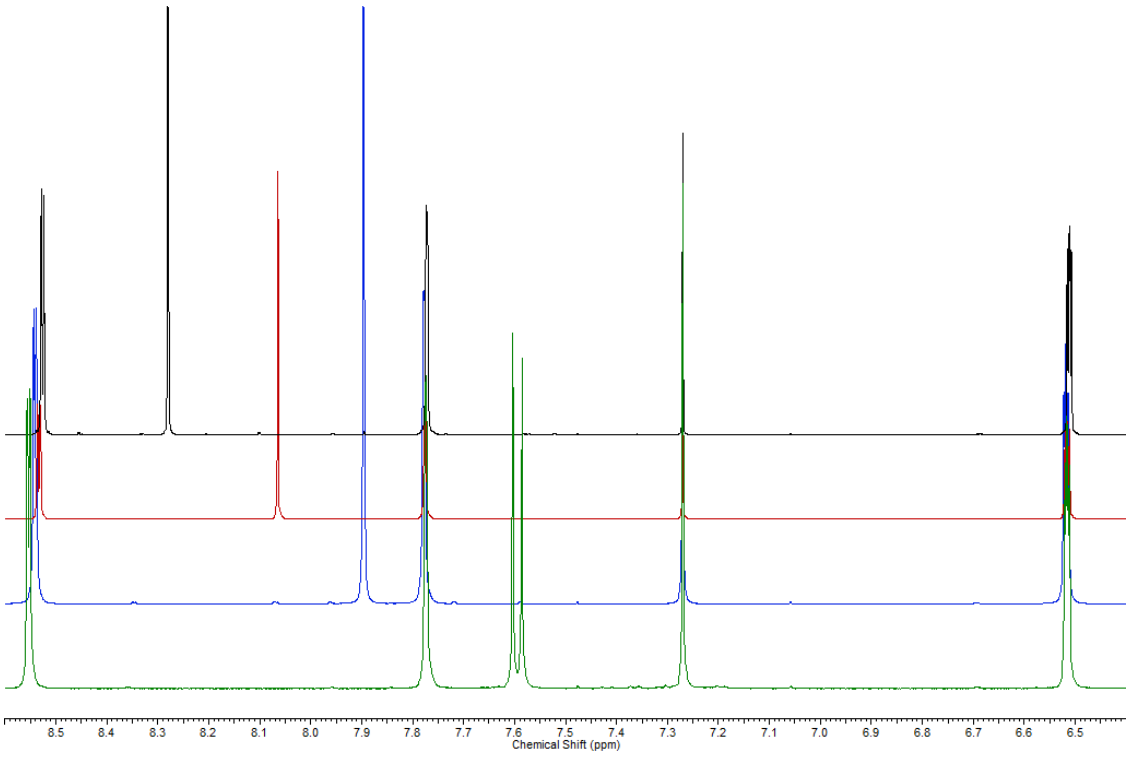

Figure 54 - ^{1}H NMR spectra of the 4-halo-2,6-di(pyrazol-1'-yl)pyridines: 1-bppI (black), 1-bppBr (red), 1-bppCl (blue) and 1-bppF (green). Spectra recorded in $CDCl_3$, with the singlet at 7.27 arising from residual $CHCl_3$, performed on a Bruker Avance 500 FT 500 MHz spectrometer.

Spectroscopic measurements performed in solution were typical for the series of aryl halides. ^{1}H NMR spectra, as with all of the 4-functionalised 1-bpp derivatives in this work, show that the pyrazole rings are located sufficiently far enough away from the substituent that its proton signals vary only very slightly in their position (Figure 54). The equivalent 3 proton signals move upfield in the order I < Br < Cl < F, a consequence of the protons

experiencing greater shielding by the halide substituent as the halide is held more closely to the ring.[98] ^{13}C NMR shifts about the central ring are very informative as to which halide is tethered to the 4-position (Table 6). The carbon at the 4-position is particularly sensitive to the differing electronic effects exerted by the halides, with the shifts moving from 108.5 to 171.8 as the group is ascended from 1-bppI to 1-bppF. The more highly polarised bonds in the derivatives bound to the very electronegative halides are responsible for the 4-carbon's resonance to shift to much lower fields as the electronegativity of the bound halide is ramped. The 3 position carbon atoms, on the other hand, experience the opposite in terms of shielding effects. This is best explained by considering the size of the halides; the fluorine atom being comparable in size to that of the sp^2 carbon with which it is bonded. The consequence is that contribution to the delocalised π-system is greatest in the case of 1-bppF, which experience's greatest overlap between the 4-carbon's π-lobes and the fluorine's partially sp^3 hybridised orbital perpendicular to the plane of the ring. This greater conjugation which arises by donation of π-density into the ring by fluorine results in a larger partial negative charge on the 3 position carbon atoms through resonance, hence higher field signals are observed originating from these carbons as the halide series is ascended.

1-bppX, X =	2	3	4	3'	4'	5'
I	149.5	118.3	108.5	142.6	108.1	126.9
Br	150.4	112.7	136.7	142.9	108.4	127.3
Cl	150.7	109.7	148.4	142.9	108.4	127.3
F	152.1	97.7	171.8	142.8	108.4	127.3

Table 6 – ^{13}C NMR signals for the 4-halo-2,6-di(pyrazol-1'-yl)pyridines. Spectra recorded in $CDCl_3$ on a Bruker Avance 500 FT 500 MHz spectrometer.

A final point to note concerning 1-bppF is the coupling observed in the ^{1}H/^{13}C/^{18}F NMR spectra, confirming the presence and location of the fluoride substituent. The 3 + 5 protons in the ^{1}H NMR spectrum are observed as a 1:1 doublet, with a coupling interaction of 9.4 Hz to the *ortho*-substituted fluorine. Coupling to the fluorine atom is also observed in the ^{13}C spectrum with, as expected, the magnitude of the coupling increasing as the through-bond distance between the resonating carbons and the fluorine atom is reduced. The fluorine atom's resonance itself manifests itself as a 1:2:1 triplet at -95.6 ppm, split by 9.2 Hz attributable to the interaction with the 3 + 5 protons. The signal is at the far low-field end of aryl-fluoride resonance frequencies, probably because of the dual electron withdrawing effect of both the pyridine nitrogen and the 2,6-dipyrazolyl appendages which lessens the degree of polarisation about the C-F bond.[63] Coupling to ^{13}C is not observed as part of the main triplet due to the very low abundance of ^{13}C nuclei making up the carbon skeleton. However, weak satellites, the pattern of which cannot be clearly deduced, are present just above the baseline arising from the coupling of ^{18}F to a small proportion of ^{13}C nuclei.

2.5 Conclusions

An array of *tris*-heterocyclic organic compounds have been prepared to be used as chelating ligands in spin-crossover iron(II) and cobalt(II) and emissive ruthenium(II) complex salts. In addition to novel compounds, which were synthesised by applying known transformations to the organic backbones, a number of the compounds of discussion were isolated as byproducts or, for those previously published, via modified procedures which improved either the time efficiency or yield of the reactions.

Though the preparation of the three unsubstituted pyrazinyl containing *tris*-heterocycles was initially adapted from the literature and followed the course of a typical Stille palladium catalysed cross-coupling reaction, the reported use of chromatography in isolation of the compounds could be avoided by ensuring that a small excess of the tributylstannyl cycle is present during the cross-coupling.[7, 9] Excess of the stannyl reagent ensures that after extraction, the only components in the crude residue are that of the *tris*-heterocycle and its tributylstannyl precursor, which is readily removed by extraction with a hydrocarbon solvent such as pentane, allowing facile isolation of the desired compounds in comparable yield to the literature preparations.

Three novel *tris*-heterocyclic systems appended with a hydroxy functionality were also prepared which, being 4-hydroxypyridines, all possess equilibria between two tautomeric forms. It was shown that this equilibrium unexpectedly lies far to the side of the hydroxy tautomer in the case of bipzpyOH and 1-bppOH, contrary to what is observed in 4-hydroxyterpy (terpyOH), however only the keto tautomer is present in solutions of 2-bipympyOH.[10] It was postulated that the terminal heterocycles, pyrazinyl and pyrazolyl in the case of 2-bipzpyOH and 1-bppOH respectively, both of which are electron deficient in comparison to a 2-pyridyl cycle, lower the basicity of the central pyridine's nitrogen effectively culminating in a stabilisation of the hydroxy tautomer in both instances. This was not observed in 2-bipympyOH though, despite the basicity of the central nitrogen atom of similar magnitude to that of bipzpyOH, and was concluded to be a consequence of the *tris*-heterocycle's inability to remove the *cis*-*cis* interaction between nitrogen lone pairs on adjacent cycles, which favours the formation of the keto tautomer in which the proton is intramolecularly held between the lone pairs of three nitrogen atoms. All three hydroxypyridines/pyridones as well as 1-bppOH's sulfur analogue 1-bppSH were readily converted to their respective methyl ethers/thioethers, however though the ethers were obtainable pure through simple recrystallisation or chromatography, the thioether could not be isolated in this manner. Sulfur's possession of several easily accessible oxidation states yielded (methyl-2,6-di(pyrazol-1'-yl)pyridin-4-yl)disulfide as a byproduct which, due to exhibition of almost identical solubilities and chromatographic retention factors as 1-bppSMe

had to be removed through reduced pressure, high temperature sublimation which came at a cost to the yield. This formation of an unsymmetrical disulfide, which probably proceeds through a trisulfide intermediate, could potentially be exploited in future to yield access to a variety of unsymmetrical disulfides containing the 1-bpp *tris*-chelating core.[103, 104]

The final finding of significance pertains to the efficiency of halogenation at the 1-bpp core's 4-position, involving conversion of 1-bppNH$_2$ to a diazonium salt and substitution with a halide which was found to vary depending upon the nature of the halide source. In organic media in the presence of I_2, 1-bppI forms cleanly but for the lighter homologues, the presence of the dihalide actively promotes electrophilic substitution at the more electron rich positions about 1-bpp. The lighter halide derivatives, 1-bppBr, 1-bppCl and 1-bppF could only be prepared efficiently by performing the diazotisation and substitution instead in aqueous media omitting the dihalide source which precludes the existence of any halonium ions. Noteworthy is that 1-bppOH is a byproduct in these reactions due to the action of H_2O as a nucleophile on the diazonium salt, and its prevalence was found to increase as the halide series is ascended, in particular drastically reducing the yield of 1-bppF formed during its preparation which likely reflects fluoride's decrease nucleophilicity. Because of 1-bpp's electron rich sites, careful consideration of reaction conditions and halide source is required to reduce loss of yield through formation of undesirable byproducts.

2.6 References

1. G. Morgan and F. Burstall, *J. Chem Soc.*, 1932, 20-30.
2. F. Krohnke, *Synthesis*, 1976, 1-24.
3. K. Potts, *Bull. Soc. Chim. Belg.*, 1990, **99**, 741-768.
4. K. Potts, M. Cipullo, P. Ralli and G. Theodoridis, *J. Org. Chem.*, 1982, **47**, 3027-3038.
5. K. Potts, M. Cipullo, P. Ralli and G. Theodoridis, *J. Am. Chem. Soc.*, 1981, **103**, 3586-3588.
6. F. Burstall, *J. Chem Soc.*, 1938, 1662-1672.
7. M. Heller and U. Schubert, *J. Org. Chem.*, 2002, **67**, 8269-8272.
8. L. Kershaw Cook, F. Tuna and M. Halcrow, *Dalton Trans.*, 2013, **42**, 2254-2265.
9. M. Darabantu, L. Boully, A. Turck and N. Ple, *Tetrahedron*, 2004, **61**, 2897-2905.
10. E. Constable and M. Ward, *Dalton Trans.*, 1990, 1405-1409.
11. J. Collin, S Guillerez, J. Sauvage, F. Barigelletti, L. De Cola, L. Flamigni and F. Balzani, *Inorg. Chem.*, 1991, **30**, 4230-4238.
12. E. Constable, A. Thompson, N. Armaroli, V. Balzani and M. Maestri, *Polyhedron*, 1992, **11**, 2707-2709.
13. M. Maestri, N. Armaroli, V. Balzani, E. Constable and A. C. Thompson, *Inorg. Chem.*, 1995, **34**, 2759-2767.
14. H. Hofmeier, P. Andres, R. Hoogenboom, E. Herdtweck and U. Schubert, *Aust. J. Chem.*, 2004, **57**, 419-426.
15. E. Medlycott and G. Hanan, *Chem. Soc. Rev*, 2005, **34**, 133-142.

16. A. Wild, A. Winter, F. Schlutter and U. Schubert, *Chem. Soc. Rev*, 2011, **40**, 1459-1511.
17. H. Hofmeier and U. Schubert, *Chem. Soc. Rev*, 2004, **33**, 373-399.
18. C. Bazzicalupi, A. Bencini, A. Bianchi, A. Danesi, E. Faggi, C. Giorgi, S. Santarelli and B. Valtancoli, *Coord. Chem. Rev.*, 2008, **252**, 1052-1068.
19. E. Constable, *Chem. Soc. Rev*, 2007, **36**, 246-253.
20. R. Leigghio, P. Potvin and A. Lever, *Inorg. Chem.*, 2001, **40**, 5485-5486.
21. F. Al-mutlaq, P. Potvin, A. Philippopoulos and P. Falaras, *Eur. J. Inorg. Chem.*, 2007, 2121-2128.
22. J. Dai, B. Li, Y. Chen, G. Huang, B. Cai, Y. Yu and J. wu, *Inorg. Chem. Commun.*, 2010, **13**, 625-629.
23. C. Boucher, M. Drew, P. Giddings, L. Harwood, M. Hudson, P. Iveson and C. Madic, *Inorg. Chem. Commun.*, 2002, **5**, 596-599.
24. E. Bejan, A. Ait Haddou, J. Daran and G. Balavoine, *Synthesis*, 1996, 1012-1018.
25. J. Groen, P. van Leeuwen and K. Vrieze, *Dalton Trans.*, 1998, 113-117.
26. R. Takeuchi, K. Suzuki and N. Sato, *Synthesis*, 1990, 923-924.
27. N. Sato and N. Narita, *J. Heterocycl. Chem.*, 1999, **36**, 783-786.
28. N. Sato and N. Narita, *Synthesis*, 2001, 1551-1555.
29. H. Yamanaka, S. Nishimura, S. Kaneda and T. Sakamoto, *Synthesis*, 1984, 681-683.
30. R. Pritchard, C. Kilner and M. Halcrow, *Tetrahedron Lett.*, 2009, **50**, 2484-2486.
31. D. Jameson, J. Blaho, K. Kruger and K. Goldsby, *Inorg. Chem.*, 1989, **28**, 4312-4314.
32. D. Jameson and K. Goldsby, *J. Org. Chem.*, 1990, **55**, 4992-4994.
33. N. Duncan and C. Garnder, *Tetrahedron Lett.*, 2011, **52**, 5214-5216.
34. K. Brien, C. Garner and K. Pinney, *Tetrahedron*, 2006, **62**, 3663-3666.
35. N. Duncan, C. Garner, T. Nguyen, F. Hung and K. Klausmeyer, *Tetrahedron Lett.*, 2008, **49**, 4766-4769.
36. M. Boca, R. Jameson and W. Linert, *Coord. Chem. Rev.*, 2011, **255**, 290-317.
37. Y. Z. W. Yang, S. Yoshikawa, J. Shao, S. Masaoka, K. Sakai, J. Yao, M. Haga, *Inorg. Chem.*, 2011, **51**, 890-899.
38. I. Mathew and W. Sun, *Dalton Trans*, 2010, **39**, 5885-5898.
39. J. Olguin and S. Brooker, *Coord. Chem. Rev.*, 2011, **255**, 203-240.
40. A. Karam, E. Catari, F. Lopez-Linares, G. Agrifoglio, C. Albano, A. Diaz-Barrios, T. Lehmann, S. Pekerar, L. Albornoz, R. Atencio, T. Gonzalez, H. Ortega and P. Joskowics, *Appl. Catal., A* 2005, **280**, 165-173.
41. D. Gong, X. Jia, B. Wang, X. Zhang and L. Jiang, *J. Organomet. Chem.*, 2012, **702**, 10-18.
42. J. Holland, S. Barrett, C. Kilner and M. Halcrow, *Inorg. Chem. Commun.*, 2002, **5**, 328-332.
43. J. Elhaik, V. Money, S. Barrett, C. Kilner, I. Evans and M. Halcrow, *Dalton Trans.*, 2003, 2053-2060.
44. S. Basak, P. Hui and R. Chandrasekar, *Synthesis*, 2009, 4042-4048.
45. R. Pritchard, H. Lazar, S. Barrett, C. Kilner, S. Asthana, C. Carbonera, J. Letard and M. Halcrow, *Dalton Trans.*, 2009, 6656-6666.
46. J. Elhaik, C. Pask, C. Kilner and M. Halcrow, *Tetrahedron*, 2007, **63**, 291-298.
47. C. Tovee, C. Kilner, S. Barrett, J. Thomas and M. Halcrow, *Eur. J. Inorg. Chem.*, 2010, 1007-1012.
48. L. Xue and Z. Lin, *Chem. Soc. Rev*, 2010, **39**, 1692-1705.

49. D. Milstein and J. Stille, *J. Am. Chem. Soc.*, 1979, **101**, 4992-4998.
50. F. Fontana, F. Minisci, M. Barbosa and E. Vismara, *J. Org. Chem.*, 1991, **56**, 2866-2869.
51. L. Beaufort, F. Benvenuti and A. Noels, *J. Mol. Catal. A: Chem.*, 2006, **260**, 210-214.
52. E. Constable, A. Thompson and D. Tocher, *New J. Chem.*, 1992, **16**, 855-867.
53. K. Thomas and D. Jerchel, *Angew. Chem.*, 1958, **70**, 719-737.
54. A. Bunzli, H. Bolink, E. Constable, C. Housecroft, M. Neuburger, E. Orti, A. Pertegas and J. Zampese, *Eur. J. Inorg. Chem.*, 2012, 3780-3788.
55. S. Hall and P. Spoerri, *J. Am. Chem. Soc.*, 1940, **62**, 664-665.
56. R. Cox and A. Bothner-By, *J. Phys. Chem.*, 1968, **72**, 1646-1649.
57. E. Lewandowska and D. Chatfield, *Eur. J. Inorg. Chem.*, 2005, 3297-3303.
58. D. Chizhov, K. Pashkevich and G. Roschenthaler, *J. Flourine Chem.*, 2003, **123**, 267-272.
59. S. Forsen and M. Nilsson, *Acta Chemica Scandinavica*, 1959, **13**, 1383-1394.
60. E. Murguly, T. Norsten and N. Branda, *J. Chem. Soc., Perkin Trans. 2*, 1999, 2789-2794.
61. A. Gordon and A. Katritzky, *Tetrahedron Lett.*, 1968, 2767-2770.
62. D. Jameson and L. Guise, *Tetrahedron Lett.*, 1991, **32**, 1999-2002.
63. G. Lowe, A. Sophie Droz, T. Vilaivan, G. Weaver, L. Tweedale, J. Pratt, P. Rock, V. Yardley and S. Croft, *J. Med. Chem.*, 1999, **42**, 999-1006.
64. Y. Wang, A. Arif and J. Gladysz, *Organometallics*, 1994, **13**, 2164-2169.
65. H. Park and Y. Chung, *Dalton Trans.*, 2012, **41**, 5678-5686.
66. H. Park, K. Kim, S. Choi, H. Kim, W. Lee, Y. Kang and Y. Chung, *Inorg. Chem.*, 2010, **49**, 7340-7352.
67. K. Potts, D. Usifer, A. Guadalupe and H. Abruna, *J. Am. Chem. Soc.*, 1987, **109**, 3961-3967.
68. E. Constable, A. Thompson, J. Cherryman and T. Liddiment, *Inorg. Chim. Acta.*, 1995, **235**, 165-171.
69. E. Wenkert, J. Hanna Jr, M. Leftin, E. Michelotti, K. Potts and D. Usifer, *J. Org. Chem.*, 1985, **50**, 1125-1126.
70. E. Wenkert and T. Ferreira, *J. Chem. Soc., Chem. Commun.*, 1982, 840-841.
71. T. Back, K. Yang and H. R. Krouse, *J. Org. Chem.*, 1992, **57**, 1986-1990.
72. W. Truce and F. Perry, *J. Org. Chem.*, 1965, **30**, 1316-1317.
73. T. Back, D. Baron and K. Yang, *J. Org. Chem.*, 1993, **58**, 2407-2413.
74. T. Vermonden, D. Branowska, A. Marcelis and E. Sudholter, *Tetrahedron*, 2003, **59**, 5039-5045.
75. C. Klein, E. Baranoff, M. Gratzel and M. K. Nazeeruddin, *Tetrahedron Lett.*, 2011, **52**, 584-587.
76. S. Ganesan, B. Muthuraaman, V. Mathew, M. Kumara Vadivel, M. Maruthamuthu, M. Ashokkumar and S. A. Suthanthiraraj, *Electrochim. Acta*, 2011, **56**, 8811-8817.
77. F. S. C. Rajadurai, S. Brink, O. Fuhr, M. Ghafari, R. Kruk, M. Ruben, *Inorg. Chem.*, 2006, **45**, 10019-10021.
78. J. Smid, *Ions and Ion Pairs in Organic Reactions*, Wiley-Interscience, New York, 1972.
79. S. Hwang, J. Kim, S. Deuk Lee, H. Lee, H. Sik Kim and H. Kim, *J. Ind. Eng. Chem.*, 2007, **13**, 537-544.
80. R. Taft, F. Anvia, M. Taagepera, J. Catalan and J. Elguero, *J. Am. Chem. Soc.*, 1986, **108**, 3237-3239.

81. S. Angyal and C. Angyal, *J. Chem Soc.*, 1952, 1461-1466.
82. X. Zhou, C. Welch and J. Chattopadhyaya, *Acta Chemica Scandinavica B*, 1986, **40**, 806-816.
83. L. Friedman and J. Chlebowski, *J. Org. Chem.*, 1968, **33**, 1636-1638.
84. J. Sauer, D. Heldmann and G. Pabst, *Eur. J. Inorg. Chem.*, 1999, 313-321.
85. W. Smith and O. C. Ho, *J. Org. Chem.*, 1990, **55**, 2543-2545.
86. C. Galli, *Chem. Rev.*, 1988, **88**, 765-792.
87. C. Bessel, R. See, D. Jameson, M. Rowen Churhill and K. Takeuchi, *J. Chem. Soc. Dalton Trans.*, 1992, 3223-3228.
88. Y. Hasegawa, R. Sakamoto, K. Takahashi and H. Nishihara, *Inorg. Chem.*, 2013, **52**, 1658-1665.
89. F. Schramm, R. Chandrasekar, T. Zevaco, M. Rudolph, H. Gorls, W. Poppitz and M. Ruben, *Eur. J. Inorg. Chem.*, 2009, 53-61.
90. C. Rajadurai, O. Fuhr, R. Kruk, M. Ghafari, H. Hahn and M. Ruben, *Chem. Commun.*, 2007, 2636-2638.
91. P. Cornago, C. Escolastico, M. Santa Maria, M. Claramunt, C. Fernandez-Castano, C. Foces-Foces, J. Fayet and J. Elguero, *Tetrahedron*, 1996, **52**, 11075-11094.
92. G. Zoppellaro, A. Geies, V. Enkelmann and M. Baumgarten, *Eur. J. Org. Chem.*, 2004, 2367-2374.
93. L. Han, M. Nihei and H. Oshio, *Polyhedron*, 2005, **24**, 2409-2412.
94. E. Constable, B. Hermann, C. Housecroft, M. Neuburger, S. Schaffner and L. Scherer, *New J. Chem.*, 2005, **29**, 1475-1481.
95. L. Stefaniak, *Org. Magn. Resonance*, 1979, **12**, 379-382.
96. T. Ollerenshaw, S. Bristow, B. Anand and C. D. Garner, *J. Chem. Soc. Dalton Trans.*, 1986, 2013-2015.
97. M. Karelson, A. Katritzky, M. Szafran and M. Zerner, *J. Org. Chem.*, 1989, **54**, 6030-6034.
98. F. Allen, O. Kennard, D. Watson, L. Brammer, G. Orpen and R. Taylor, *J. Chem. Soc., Perkin Trans. 2*, 1987, S1-S19.
99. M. Little, M. Halcrow and M. Hardie, *Chem. Commun.*, 2013, **49**, 1512-1514.
100. R. Shannon, *Acta. Cryst. A*, 1976, **32**, 751-767.
101. B. Whittle, S. Batten, J. Jeffery, L. Rees and M. Ward, *J. Chem. Soc. Dalton Trans.*, 1996, 4249-4255.
102. L. Bezgubenko, S. Pipko and A. Sinitsa, *ZH. OBSHCH. KHIM.*, 2009, **79**, 740-746.
103. S. Smallcombe and M. Caserio, *J. Am. Chem. Soc.*, 1971, **93**, 5826-5833.
104. E. Tsuchida, K. Yamamoto, H. Nishide, S. Yoshida and M. Jikei, *Macromolecules*, 1990, **23**, 2101-2106.

Chapter 3

Iron(II) and cobalt(II) complexes of diazinyl 2,2’:6’,2’’-terpyridine analogues

3 Iron(II) and cobalt(II) complexes of diazinyl 2,2':6',2''-terpyridine analogues

3.1 Introduction

2,2':6',2''-Terpyridine, terpy, is a stable, planar tridentate ligand capable of chelating a metal ion with three vacant coordination sites in a *mer* arrangement. Due to its strong basicity and relatively low lying π* antibonding orbitals it is an intermediate field strength ligand, and its coordination chemistry is diverse across the transition metal series.[1-5] Iron(II) and cobalt(II), d^6 and d^7 metal ions respectively, have shown promise as interesting magnetic, particularly spin-crossover materials, when chelated by terpyridines due to the ligand field imposed often being of comparable magnitude to the spin-pairing energy difference between the two spin states.[6, 7] Though *bis*-chelated iron(II) salts of terpy itself do not undergo thermal spin transitions, instead remaining trapped in the low spin state at all temperatures below decomposition, it is possible to promote a spin transition to the high spin state by substituting the terpy backbone appropriately.[8, 9] Indeed, it has been seen that the high spin state can be stabilised via the introduction of suitable groups which, either via steric and electron-electron repulsion, cause large angular distortions about the metal ion or electronically reduce the basicity of the heterocyclic system which likewise causes a reduction in Δ_o.[10, 11] Cobalt(II) *bis*-terpyridines are already a well established class of spin crossover compounds, with the parent complex salts often undergoing transitions, complete or otherwise, below room temperature because of the reduced spin-pairing energy difference in cobalt(II).[12-16] Due to the ability of *bis*-terpyridine complexes to pack in the "terpyridine embrace" motif, intermolecular interactions can often be relatively strong, and close π-π contacts have shown that the materials are routinely very sensitive to changes in lattice pressure which promotes communication between neighbours and thus are routinely responsible for the increased cooperativity the spin transitions have been shown to regularly possess.[17-23]

The approach adopted in this chapter was to prepare a series of iron(II) and cobalt(II) complexes chelated by diazinyl and triazinyl terpy analogues. The replacement of CH fragments with non-coordinating nitrogen atoms alters the nature of the *tris*-heterocyclic systems by reducing the basicities of the individual donors, which can, it was theorised, be used to "tune" the ligand field strength in their respective complexes.[24-26] The avoidance in using electron withdrawing substituents, which are often large and sterically hindering is necessary to facilitate crystal packing in the terpyridine embrace. Crystallography was an important tool in this work, distinguishing trivially between materials of different spin states and can often help explain the nature, or lack thereof, of observed cooperativity in a spin

transition. The electronic structures of the complexes was also investigated, with a variety of techniques employed including absorption and EPR spectroscopy and voltammetric techniques which help provide an insight into the electronic structure and ligand field strength of the individual complex dications.

3.2 Aims and objectives

It was proposed that the electronics of *bis*-chelated first row octahedral complex salts could be varied not by attaching inductive substituents, but by varying the heterocyclic content of the chelating ligand systems. This would be advantageous in maintaining a consistent size and shape of the dication units and promote the formation of the close-packed terpyridine embrace motif in the solid state. By the systematic replacement of pyridyl donors with those of less basic six-membered heterocycles, the intention was to assess this affect on Δ_o with respect to the parent iron(II)/cobalt(II) *bis*-terpyridyl dications. This can be deduced from a combination of spectroscopic and electrochemical experiments in the solution phase in the hope that the expected reduction in Δ_o yielded a stabilisation of the HS configuration and thus a decrease in $T_{1/2}$. The electronic structures in addition to the solid state packing were to be investigated as part of our continued interest in engineering materials which are most likely to exhibit thermally induced spin-crossover which proceeds cooperatively as a result of intermolecular interactions in the condensed phase.

3.3 Discussion

3.3.1 Solution Lability and Paramagnetic NMR spectra

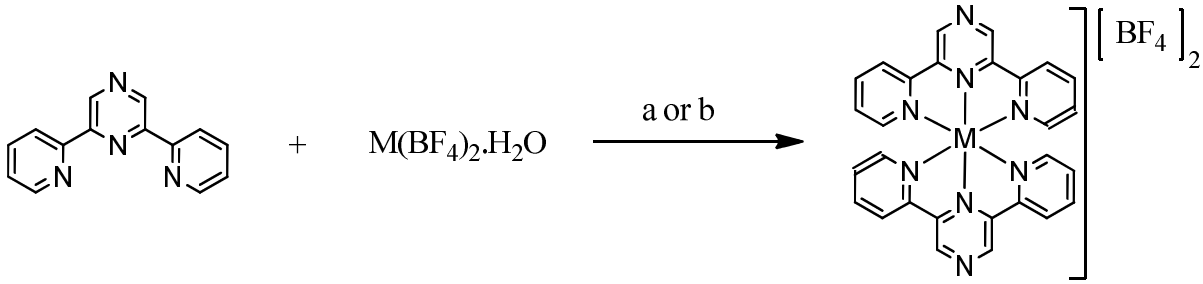

Figure 55 – Schematic representation of the one-pot synthesis of the disubstituted *tris*-azinyl iron(II)/cobalt(II) ditetrafluoroborate salts where M = Fe, Co; a) Stirring the two components together in either $MeNO_2$ or MeOH before carefully vacuuming the solution to dryness; b) Dissolution in $MeNO_2$ or MeOH before careful addition of Et_2O and collection of the resulting precipitate by vacuum filtration.

The iron(II) and cobalt(II) salt series were prepared analogously to one another, utilising methods that didn't necessitate heating above 50°C to circumvent any potential thermal decomposition (Figure 55). The seven novel iron(II) salts **1a**-**4a**, **6a**-**8a** showed no presence of any high-spin species in both the solid state and in solution. This allows us to conclude that the reduced basicities of the donor atoms of the *tris*-heterocycles was not sufficient to lower Δ_o enough to allow a thermally accessible transition to the high-spin state.

With the exception of **6a**, all complexes fully inert in solution with no evidence of any ligand exchange processes occurring seen by NMR or voltammetry. **6a** is anomalous in that even though it was obtained microanalytically pure in powder form, there is clearly some sort of fluxional process occurring in solution, as evidenced by additional peaks surrounding the most dominant species' resonances accounting for ca. 25% of the integrals. A reason for this could be a result of the possibility for multiple binding modes of the triazinyl rings. A previous study of 5',6'-disubstituted analogues of bitrzpy concluded that for octahedral iron(II), 0.76 eV of stability is gained when the metal is coordinated by N2' rather than N4' due to the reduced steric clash of the adjacent nitrogen N1' in comparison to the CH fragment at C5'.[27] The enthalpic penalty would be much smaller if just one of the triazinyl rings were to bind through N4' however, in the region of 0.3-0.4 eV. If in solution, where the molecule is held less rigidly in its geometry, the high-spin state was thermally accessible to a very small number of molecules due to the decreased ligand field strength of this complex, it is entirely possible that a number of different fluxional isomers could exist accounting for the additional minor resonances of very similar chemical shift. Though such processes are deemed less likely with the more strongly bound 2-bipympyOH ligands in **8a**, broadening of the resonances in the ^{1}H NMR spectra are observed indicating either rapid relaxation or an exchange process – however it must be noted that even if the distal rings were switching donor atoms the resultant complexes would be identical due to the symmetry of the pyrimidine rings.

All five novel cobalt salts prepared exhibited paramagnetic shifts no higher than 120 ppm which is indicative of low-spin prominence in solutions of MeCN and $MeNO_2$.[15] The cobalt complexes could be characterised using this method (though other techniques were necessary to confirm purity) and as such the effects of deshielding upon paramagnetically shifted protons could be investigated within the series. The consequences are not always trivial and a combination of electronic effects and fluxional processes must be considered. Following on from previous work by constable *et al* on the parent terpyridine complex, it was possible to discern between the 3' and 5' resonances on the distal rings in this series of related complexes.[28, 29] There is a general trend amongst the series of Co(II) complexes that as the *tris*-imine ligands are made more electron deficient, the paramagnetic contact shifts felt by the respective protons tend to smaller values. Indeed, the proton ortho to the coordinating nitrogen points almost directly into the partially filled $d_{x^2-y^2}$ and in all but one complex (**5b**) it appears as the most highly contact shifted resonance. The paramagnetically shifted ^{1}H NMR spectra illustrates this well (Figure 56) as pyridine rings are replaced by the less basic pyrazines, the effect of the cobalt centre's unpaired electron upon the proton resonances lessens. The 4' protons have been excluded as they all resonate in the

diamagnetic region, are not significantly altered by the heterocyclic nature and thus trivial to assign. Note the reduced solubility of the salts as CH fragments of the heterocycles are replaced by non-coordinating nitrogen atoms.

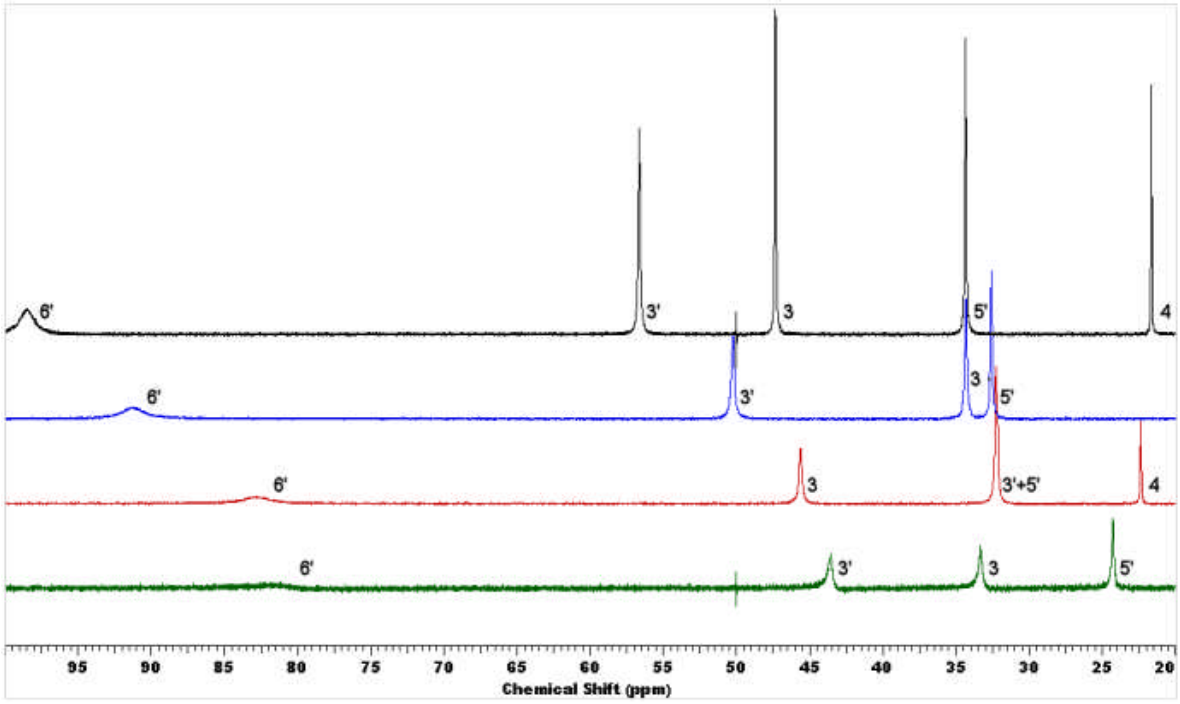

Figure 56 - Paramagnetic ^{1}H NMR spectra run in CD_3NO_2 of 9b (black), 1b (blue), 2b (red), and 3b (green) run at 300 MHz on a Bruker DPX300 FT

The reason behind the contact shifted signals in the ^{1}H NMR spectra is the unpaired electron "character" on the resonating nucleus itself, which arises due to spin-polarisation from the unpaired electron in $d_{x^2-y^2}$ onto the proton causing anomalously large chemical shifts – known as the contact shift. The most important factor which determines the positions of the contact shifted resonances is that of the averaged spin state population of the individual solubilised species. In fluid solution, the cobalt(II) centres are rapidly interconverting between the two spin states, with only a single signal set of ligand environments observed for each species on the NMR timescale. The positions of the signals are thus dominated by the spin state distribution present at ambient temperature, the increase in resonance frequency correlating with a greater amount of centres in the HS $t_{2g}^5e_g^2$ configuration. The reduced contact shifts observed in the highly electron deficient complexes are telling of a stabilisation of the LS state, that is in effect an increase in $T_{1/2}$ suggestive of greater Δ_o in these complexes, supporting the theory of increased π-backbonding contribution to the Co-N interactions as the heterocyclic nitrogen content is increased (Section 3.3.3).

A minor contributor may also be the lability of octahedral Co(II) complexes towards substitution. Due to the partial population of the e_g level, individual donors are potentially

able to decoordinate and recoordinate rendering the Co(II) complexes kinetically unstable. This is not considered significant in complexes **1b**-**4b**, **7b**-**10b** as the voltammetry is consistent with related Co(II) complexes which suggest that the only species in solution are the *bis*-chelated complexes and thus the contact shifts are instead determined by the position of $T_{1/2}$ in the thermal spin-equilibrium.

It is complex **6b** however whose speciation in solution is uncertain, as like its iron(II) analogue **6a** the metal centre is chelated by a particularly weak *tris*-imine ligand. **6b** exhibits a distinctly odd NMR spectrum, with four barely resolvable and highly broadened peaks appearing between 8 and 20 ppm. Calculations on related substituted 2,6-di(1',2',4'-triazin-3'-yl)pyridine chelated Co(II) complexes, which should sterically be more inclined to adopt a high spin state compared to the unsubstituted analogues, show that the low spin state is 2 eV lower in energy and thus high spin **6b** is essentially thermally out of reach at RT. To convolute matters further, unresolvable daughter peaks surround these four "primary" resonances which, because this complex was obtained as a crystalline solid and shown to be microanalytically pure, suggest a fluxional process is occurring in MeCN/$MeNO_2$ solutions in which the ligand spends the majority of the time uncoordinated to the cobalt(II) centre. It is suggested that because of this rapid fluxional dechelation and rechelation process the resonances observed, which are essentially impossible to assign to a specific proton environment, appear at a much higher field than would otherwise be expected.

An attempt was also made to prepare **5b**, as only a small amount of 4-bipympz was isolated. It must be noted that unlike every other complex in this series in which it is possible to observe the reaction occurring instantly by visual inspection, no darkening of the solution toward an orange hue occurred until heating to 70°C in $MeNO_2$. All attempts to analyse the orange-brown solid eventually obtained proved fruitless. Paramagnetic proton NMR spectroscopy yielded no conclusive speciation in solution – a number of different resonances were seen in the aromatic diamagnetic region, however one broadened resonance was observed at 11 ppm which is evidence of at least one weakly contact shifted environment, whose nature is uncertain. In addition, no couple was observed during the voltammetric oxidation sweep of this material. The complex was predicted to oxidise in the 0.50-0.55 V region from inspection of the other Co(III/II) potentials listed in 3.3.2, which would make it the most electron deficient species in the series. Perhaps, due to the extremely low basicity of 4-bipympz, it was simply not possible to form a stable *bis*-chelated moiety and the Co(II) centres present in intermediates or oligomeric species were oxidised to Co(III) which would explain the absence of the III/II redox couple.

3.3.2 Electrochemical measurements

Cyclic voltammograms run on the successfully isolated complex salts show a great deal of variation in their redox processes. In particular the easy to assign M(III/II) couples, are well resolved and show an appreciable degree of chemical and electrochemical reversibility. Table 7 documents the metal (III/II) wave alongside any detectable reductions occurring during the reverse sweep. Alongside this is the sum of the basicities of the heterocycles comprising the ligands, ΣpK_a, and the voltage difference between the metal (III/II) and first reduction potentials, $E_{ox} - 1^{st} E_{red}$, in order to better interpret the data as discussed below.

Complex Salt	ΣpK_a	M(III/II) / V	Reduction potentials / V	$E_{ox} - 1^{st} E_{red}$ / V
1a	21.6	+0.95	-1.30[a], -1.43[a], -2.13, -2.23	2.25
2a	12	+1.07[a]	-1.25, -1.42, -1.90, -2.16	2.32
3a	2.4	+1.37[a]	-0.98, -1.07, -1.73, -1.96[a]	2.35
4a	14.8	+0.98	-1.25, -1.42, -1.86, -2.07	2.23
6a	3.32	+1.20[a]	-1.10[c]	2.30
7a	8	+0.90[a]	-1.09[c]	1.99
8a	10.8	+0.75[a]	-1.37[c], -1.59[c]	2.12
9a	31.2	+0.71	-1.66, -1.81, -1.99	2.37
10a	27.2	+0.54	-1.76[c], -1.99[a], -2.25	2.30
1b	21.6	+0.12	-0.81, -1.65, -1.95[a], -2.17[a]	0.93
2b	12	+0.22	-0.81[a], -1.63[a], -1.90[a], -2.19[a]	1.03
3b	2.4	+0.49	-0.49, -1.32, -1.71, -1.93[a]	0.98
4b	14.8	+0.25[a]	-0.86, -1.59, -1.91, -2.12[a]	1.11
6b	3.32	+0.18[a]	-0.76[c]	0.94
7b	8	+0.12[a]	-1.11[c], -1.92[c], -2.06[a]	1.23
8b	10.8	+0.17[b]	-1.24[c], -1.76[a], -2.11[a]	1.41
9b	31.2	-0.13	-1.17, -2.04	1.04
10b	27.2	-0.22	-1.41[c], -1.95[a]	1.19

Table 7 – Cyclic Voltammetric data for the Fe/Co complex salts. Measurements performed in 0.1 M TBAT MeCN at a scan rate of 100 mV s^{-}. Couples are fully electrochemically reversible, correspond to a one electron process and are quoted as their $E_{1/2}$ values unless otherwise stated against an Fc(III/II) internal reference. [a]Quasi-reversible process. [b]Chemically irreversible process, E_a quoted. [c]Chemically irreversible process, E_c quoted. ΣpK_a corresponds to the sum of the basicities of the respective heterocycles comprising the ligands.[25, 30]

All of the complexes display a characteristic M(III/II) wave which is significantly more anodic than the terpy parent complexes **9a** and **9b**, in agreement with the literature data.[8, 31, 32] The replacement of two proximal pyridines with pyrazine donors results in a shift of the M(III/II) wave of 0.24-0.30 mV towards the anode which reflects the increased stabilisation of the t_{2g} and e_g levels in the iron(II) and cobalt(II) species respectively. The stabilisation is a little less pronounced at the distal site which reflects the reduced overlap between the nitrogen p-orbital and the lobes of the metal d-orbitals.[33] Despite the first oxidation potential

corresponding to the removal of an electron from orbitals which differ in energy, t_{2g} in iron(II) and the e_g level in cobalt(II) which has slight antibonding character, the shifts in oxidation potential are broadly similar between the two series of complexes. There are, however, two notable exceptions which showcase the subtle differences between heterocycle replacement on the t_{2g} and e_g energy levels.

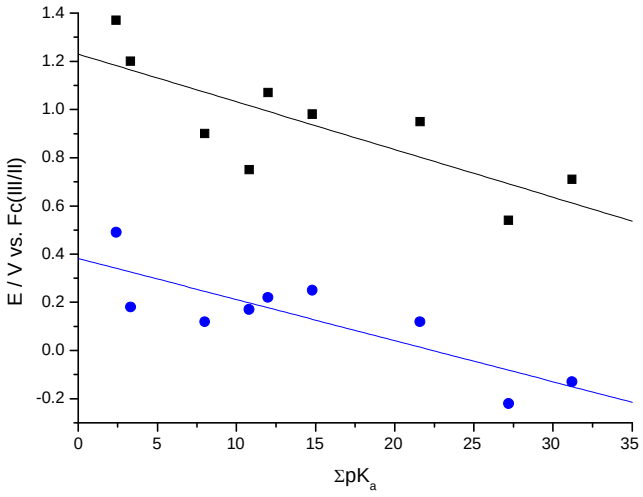

Figure 57 - Plot of the sum of the ligand basicities, ΣpK_a, against the M(III/II) formal oxidation potentials vs. the Fc(III/II) couple. Black squares represent the Fe(II) series, and blue circles Co(II). For the irreversible processes the E_{pa} values have been used.

Firstly, distal pyrazine donors appear to have a far greater stabilisation effect upon the HOMO, the t_{2g} levels in iron(II), than either 2- or 4-pyrimidyl rings. For cobalt(II), the converse is true in which a slightly higher degree of stabilisation is achieved employing pyrimidyl rings over the pyrazinyl analogues. Figure 57 illustrates this contrasting data, with the iron(II) potentials in slightly closer agreement with the trend, decreasing as the basicity is reduced. In cobalt's case, for the 4 points with increasing ΣpK_a from 8 to 14.8, complexes **7b**, **8b**, **12b** and **14b** respectively, the oxidation potentials increase progressively which is counter intuitive. Why this is the case is not immediately obvious, but π-backbonding may well play a part in rationalising these unexpected findings. A greater degree of charge localisation may be present on the aromatic rings in the pyrazine rich moieties, that is to say they are better suited to accepting residual electron density from the metal centre via d to π overlap. This would effectively increase the degree of bonding in the complexes containing pyrazine rich ligands and accentuate the ligand field strength. The consequence is that the t_{2g} levels are stabilised further in pyrazine rich complexes than the e_g levels as a result of the larger ligand field imposed, which would explain the more anodic potentials observed in the iron(II) series than for the corresponding cobalt(II) complexes where the electron is actually being removed from the slightly destabilised e_g level. The solid state magnetic data of the

cobalt(II) salts, Section 3.3.2, reinforces this, as those complexes chelated by pyrazine rich ligands, **2b**, **3b** and **7b**, contrast with the others in the series in that they have a much larger percentage of low spin centres in the bulk solid which is concomitant with a greater ligand field.

Secondly is the oddly cathodic oxidation potential of **6b**. Despite coordinated by four hugely electron deficient triazinyl ring, the $E_{1/2}$ value lies at a smaller voltage than for the more basic heterocycle containing complexes **2b** and **4b**. This is not understood currently, with the potential occurring ca. 100 mV more cathodic than was predicted from inspection of the iron series. Due to previous reports on aforementioned 5,6-disubstituted-1,2,4-triazinyl cobalt(II) complexes, based on electronics **6b** adopting the low spin state would be far preferable, so the high spin species will not be considered.[27] Complicated exchange processes possibly occurring rapidly still shroud the exact speciation of **6b** in solution, as discussed in Section 3.3.1. The scan rates were run up to 5000 mV s^1, but even at such sweep speeds the position of the $E_{1/2}$ did not appear to change and no additional peaks were observed. The separation of E_a and E_c grew in magnitude which is further evidence of quasi-reversibility due to slow electron transfer.

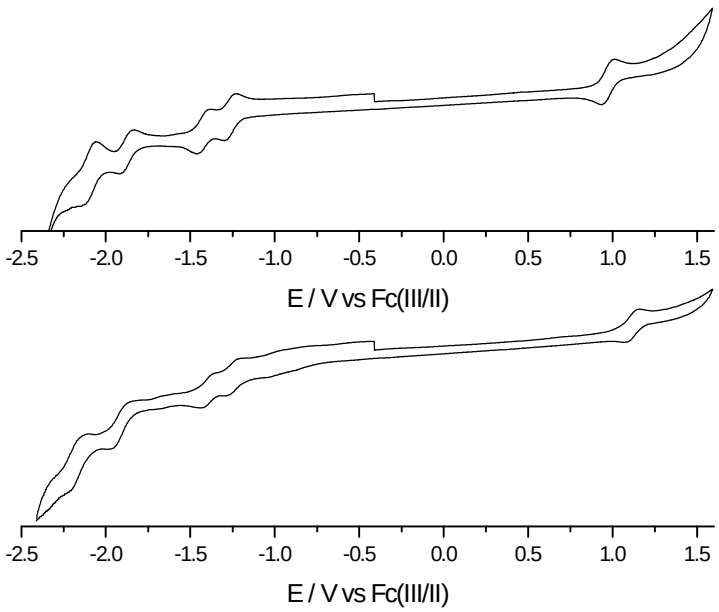

Figure 58 – Cyclic voltammograms of the iron(II) complexes 4a (top) and 2a (bottom). The voltammograms were measured in 0.1 M TBAT MeCN, at 100 mV s^{-1}. The spikes in current above 1.3 V and below -2.3 V arise due to oxidation and reduction respectively of the solvent.

The voltammetric reduction of the two series is a little more varied, with all of the complexes displaying one to four reductive processes. The exact number of resolved

reductions and their reversibility is highly dependent upon the heterocyclic content, but in general the number of processes correlates well between complexes in the two series chelated by the same ligand which is evidence that many of these processes are ligand based (Figure 58). In the parent cobalt(II) *bis*-terpyridine complex, the first reduction has assigned to a Co(II/I) reduction process, in keeping with the smaller ligand fields present within the cobalt(II) series in relation to iron(II) due to the weaker metal to ligand bonds.[31, 34] This is also the case for the majority of the novel cobalt(II) complexes (Figure 59), with the first reduction appearing at potentials ca. 300-500 mV more negative than in the respective iron(II) compound. The exceptions are the complexes **7b**, **8b** and **10b**, whose potentials deviate strongly from the correlation with ΣpK_a compared to the others in the cobalt(II) series. For complexes **7b** and **8b** it can be said that it is highly probably that these are ligand based reductions due to the potentials appearing very closely to the corresponding iron(II) first reductions, but for **10b** it is less easy to be so certain of its nature. The strongly electron donating hydroxy pyridine rings present in these complexes would destabilise the Co(I) state and increase the ligand field strength making a ligand based reduction more likely, however the hydroxypyridine π* levels are also significantly promoted to higher energy due to its electron richness. In complexes **7b** and **8b**, distal rings with strong electron withdrawing propensity stabilise these π* levels, whilst the hydroxy pyridine donor appears to be interacting strongly enough with the cobalt centre to raise the e_g orbitals to a higher energy hence we see a first reduction centred on one of the chelating ligands. It is still possible that the first reduction wave of **10b** could be attributable to the ligand, but its appearance at a potential 350 mV less negative than for **10a** indicates that it is probably more likely that this corresponds to insertion of an electron into the destabilised e_g level.

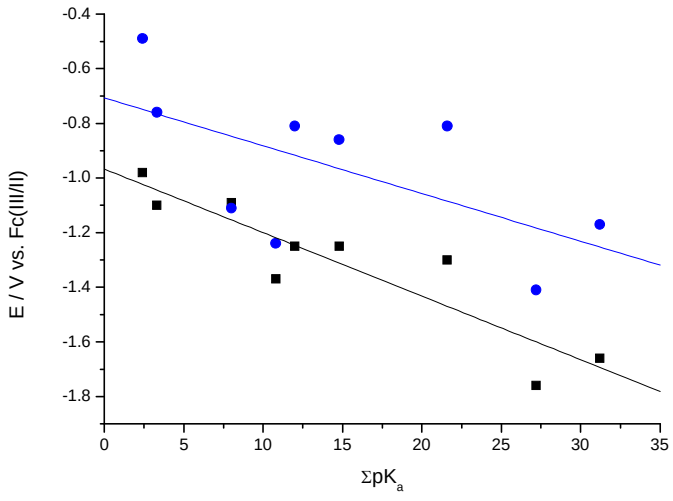

Figure 59 - Plot of the sum of the ligand basicities, ΣpKa, against the first ligand reduction potentials vs. the Fc(III/II) couple. Black squares represent the Fe(II) series, and blue circles Co(II). For the irreversible processes the E_{pc} values have been used.

In addition to electrochemistry performed on the dicationic complexes, the three iron(II) species containing OH moieties, **7a**, **8a** and **10a**, were individually mono- and fully deprotonated and the oxidative and reductive behaviour of the *in situ* prepared species probed. Evidence for the formation of these partially and fully deprotonated complexes comes chiefly from the oxidation waves since the electron rich ligands instil the species with a greater degree of stability towards oxidation than reduction. Towards the cathode, no easily identifiable reduction processes are observed as a result of the higher lability of deprotonated hydroxypyridine ligands and their inability to accept additional metal-centred electron density which heavily destabilises the cobalt(I) state. For this reason, the reductive voltammograms of the complexes in various stages of protonation will not be discussed and compared in any great detail.

Complex Salt	$[Fe(LOH)_2]^{2+}$	$[Fe(LOH)(LO^-)]^+$	$[Fe(LO^-)_2]^0$
7a	+0.90[a]	-[c]	-[c]
8a	+0.75[a]	+0.48[b]	+0.08[b]
10a	+0.54	+0.38[a]	-0.12

Table 8 – Voltammetric data indicating the Fe(III/II) potentials for the Fe(II) *bis*-chelated homoleptic 4-hydroxypyridine complexes intact, monodeprotonated and fully deprotonated using the appropriate equivalent of methanolic NH_4OH. Measurements performed in 0.1 M TBAT MeCN at a scan rate of 100 mV s^-. Couples are fully electrochemically reversible, correspond to a one electron process and are quoted as their $E_{1/2}$ values unless otherwise stated against an Fc(III/II) internal reference. [a]Quasi-reversible process. [b]Chemically irreversible process, E_a quoted. [c]No couple observed due to precipitation of the complex upon addition of base.

The relatively strong acidity of the phenolic protons permits ready deprotonation of the hydroxypyridine salts by addition of stoichiometric quantities of a strong non-coordinating base. These *in situ* prepared complexes, with formulae $[Fe(LOH)(LO^-)]^+$ and $[Fe(LO^-)_2]^0$ for the mono- and fully deprotonated complexes exhibit oxidation waves which are significantly different to that of the parent dicationic complexes (Table 8). It was impossible to detect any of **7a**'s conjugate bases by electrochemical methods as addition of the NH_4OH initiated almost total precipitation of the complex from solution which was met with no observable oxidation processes even after prolonged aggravation. The Fe(III/II) couple for the mono and fully deprotonated forms of **10a** appear at 0.16 and 0.66 V more cathodic potentials than in the parent dication respectively. The cathodic potential shifts during deprotonation of **8a** are similar to those in **10a**, with the potentials shifting by 0.27 and 0.67 V respectively. These values are in agreement with the strongly destabilising nature of the electron rich deprotonated hydroxypyridine donors.[35, 36] Interestingly, for both complexes, the addition of one and two equivalents of base yields the appearance of one new oxidation wave in each instance (Figure 60). This is suggestive, since stoichimetric quantities of base were employed, that there isn't an observable equilibrium between the different protonation states

in solution. The explanation for this could possibly lie in the distance between the protic sites, but more likely is a consequence of a large perturbation of nuclear coordinates about the iron centres upon oxidation of the deprotonated complex from +2 to +3.

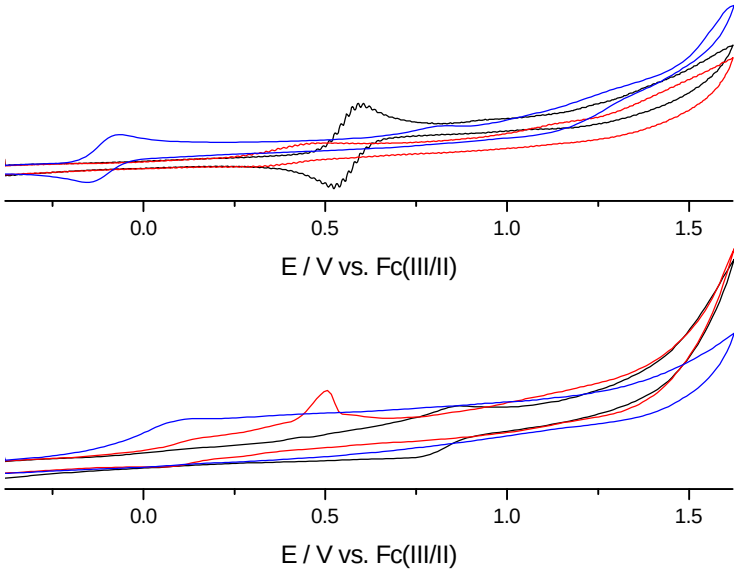

Figure 60 – Cyclic voltammograms showing the oxidation sweep of the hydroxypyridine containing iron(II) salts 10a (top) and 8a (bottom). Black, red and blue lines represent the scan after adding zero, one and two equivalents of methanolic NH_4OH respectively. The voltammograms were measured in 0.1 M TBAT MeCN, at 100 mV s^{-1}. The spike in current above 1.3 V arises due to oxidation of the solvent.

3.3.3 Absorption Spectroscopy

To further understand the effect of the nature of the donor heterocycles on the structure and bonding of the two analogous series of complexes, their spectroscopic properties were probed using UV/visible/NIR light. The salts coordinated by bitrzpy, **6a** and **6b**, were omitted from screening as other spectroscopic techniques cast doubt on their speciation in solution (see sections 3.3.1 and 3.3.2).

Complex Salt	λ / nm (ε / dm^3 mol^{-1} cm^{-1})
1a	249 (23130) *sh*, 278 (28783), 328 (31304), 345 (18870) *sh*, 552 (7939)
2a	230 (36404), 246 (24737) *sh*, 285 (34912), 330 (18246), 350 (9298) *sh*, 552 (3052)
3a	221 (36460), 227 (35575) *sh*, 243 (30885), 282 (47080), 339 (33982), 360 (23540), 462 (1805), 545 (7938)
4a	220 (34825), 263 (21930) *sh*, 272 (26140), 278 (24474) *sh*, 315 (32895), 319 (29123) *sh*, 574 (57105)
7a	218 (21651), 238 (24862), 245 (23578) *sh*, 283 (28349), 323 (10183) *sh*, 586 (2661)
8a	252 (54587), 292 (14220) *sh*, 305 (10826), 397 (4844), 545 (6128),
9a	220 (47478) *sh*, 273 (41565), 280 (37478), 319 (51130), 504 (5965) *sh*, 552 (11130)
10a	243 (54545), 272 (52000), 281 (38364) *sh*, 315 (45000), 362 (5091), 515 (8600) *sh*, 553 (11636)
1b	280 (24210), 337 (21173), 348 (20566) *sh*, 440 (971) *sh*, 509 (1104), 573 (169) *sh*
2b	288 (52724), 332 (31810), 437 (1336) *sh*, 511 (1137), 548 (614) *sh*
3b	225 (33451), 285 (41416), 346 (19558), 474 (653) *sh*, 510 (794), 558 (159) *sh*
4b	263 (36228) *sh*, 280 (33947) *sh*, 315 (44561), 459 (438) *sh*, 521 (350), 566 (66) *sh*
7b	232 (55872), 285 (35872), 312 (27982) *sh*, 386 (7514), 499 (2165)
8b	232 (40642), 251 (52661), 379 (4724), 480 (846)
9b	225 (49123) *sh*, 273 (30175), 280 (31140), 317 (33772), 447 (1150), 506 (1042), 551 (472) *sh*
10b	232 (40642), 251 (52661), 379 (4724), 480 (846)

Table 9 – UV/vis/NIR spectroscopic data for the two series of complexes in MeCN at 298 K. *Sh* denotes a shoulder. Note that no spectra were recorded for 6a and 6b due to the questionable solution phase identity of the iron and cobalt salts respectively.

All of the complexes screened exhibit an envelope at lower energy, λ_{max} varying from 545-574 and 480-521 nm for the iron and cobalt series respectively which consist of two or more overlapping MLCT transitions. The spectra display variation, particularly in the higher energy ligand-to-ligand transfer bands (Table 9), but are in general agreement with previously published data on related salts of **9a** and **9b**.[12, 13, 37-39]

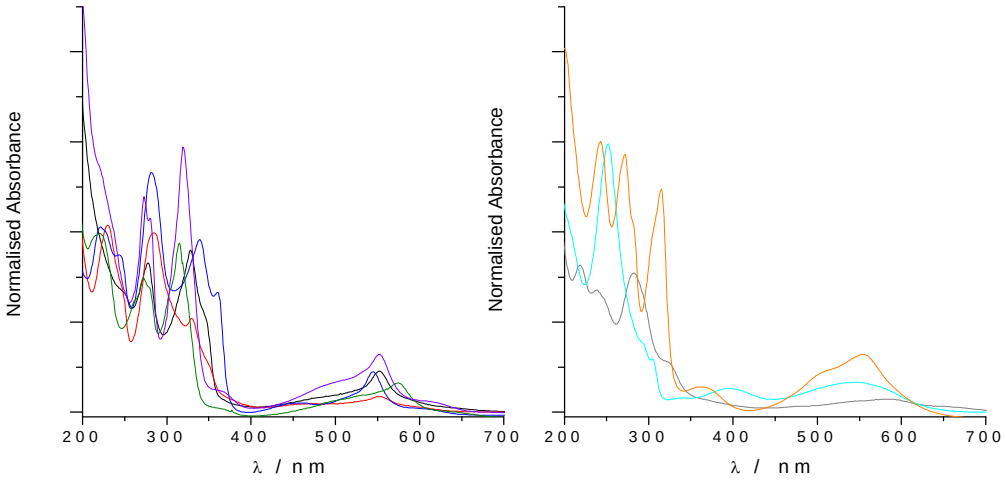

Figure 61 - Absorption spectra for the iron(II) complexes run as 1.10 x 10^{-5} mol dm^{-3} MeCN solutions at 298 K. Left: Unsubstituted azine complexes 1a (black), 2a (red), 3a (blue), 4a (green) and 9a (purple). Right: Hydroxypyridine complexes 7a (grey), 8a (cyan) and 10a (orange).

In each of the spectra for the iron(II) series, the high energy region (< 400 nm) is dominated by one to three strongly absorbing bands complete with a multitude of less intense daughter peaks and shoulder bands. The majority of these will be intra-ligand in nature due to their large extinction values, however higher energy π* ← t_{2g} absorptions also contribute towards these bands particularly at the lower energy end of the spectrum between 300 and 400 nm.[39, 40] Valuably, it is possible to assign these higher energy MLCT transitions in the hydroxypyridine complexes **7a**, **8a** and **10a** (Figure 61) as a consequence of the blue-shift of the more prevalent intra-ligand bands that previously had them obscured. The hydroxypyridine salts' π-π* bands hypsochromic shifts are a probable consequence of reduced orbital contribution by the central ring to the excited states due to destabilisation by the hydroxy substituent by reducing "conjugation" and essentially communication across the proximal pyridine's π-cloud. The exact number and energy of the LLCT bands across the iron series appears to be complicated in nature and would be nigh on impossible to explain without computational studies on orbital contributions to the various excited states, however all complexes containing exclusively pyridine, pyrazine or mixed pyrazine/pyridine ligands exhibit three reasonably regularly spaced very intense (ε > 20,000) bands. As one moves in order of electron richness from most to least in the order **9a**>**1a**>**2a**>**3a**, the energy of this triplet of bands follows a general trend moving to lower energy, in accord with the stabilisation of the various π* excited states present on the ligand backbone (discussed below). It is probable that as the electron withdrawing nitrogen content about the ligand increases, the π-cloud in the excited state is delocalised further around the backbone increasing inter-ring communication and lowering the energy of these states. Another thing to notice is that in this same order the bands begin to broaden, indeed two of the bands in

the spectrum of **3a** actually possess a daughter peak red-shifted ca. 25-30 nm. Again, an attempt to explain this with such limited spectral information is deemed unjustified without detailed computational studies, but could reflect the stabilisation of an excited state of one transition with respect to another of similar energy due to increased interaction of the solvent with additional non-coordinating nitrogen atoms.

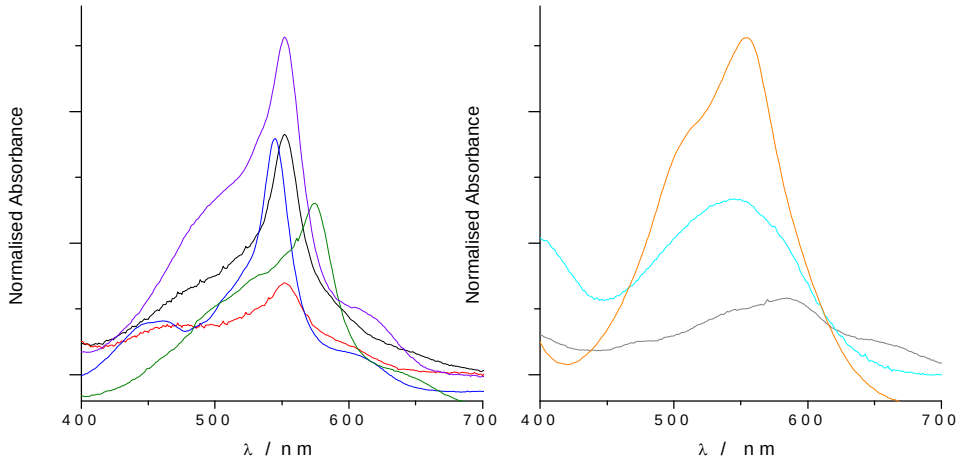

Figure 62 – Absorption spectra displaying the lowest energy MLCT envelope for the iron(II) complexes run as 1.10 x 10^{-5} mol dm^{-3} MeCN solutions at 298 K. Left: unsubstituted azine complexes 1a (black), 2a (red), 3a (blue), 4a (green) and 9a (purple). Right: Hydroxypyridine complexes 7a (grey), 8a (cyan) and 10b (orange).

Ignoring the higher energy MLCT bands previously discussed, the absorption corresponding to the lowest energy π* ←t_{2g} transition in the complexes varies to a lesser extent within the series, characterised by a very similar band shape in all of the complexes comprising of a λ_{max} and a higher energy shoulder (Figure 62). Exact identification of the literal λ_{max} of the lowest energy MLCT is made complex by the fact that these absorptions clearly contain a manifold of two to three transitions of very similar energy. In particular, within the non-hydroxy substituted pyridine complexes, the band shape is almost identical which suggests the heterocyclic content has little effect upon the separation of the t_{2g} and two close in energy π* levels.

The three hydroxypyridine complexes do, however, possess a slightly broadened absorption which probably reflects increased hydrogen bonding between the OH moiety and rapidly interchanging MeCN molecules. Oddly, converse to what might be expected, the band maxima hardly shifts at all within the series. The pyrazine/pyridine complexes **1a**, **2a**, **3a** and **9a** all display, within error, indistinguishable values of λ_{max} despite the extinction coefficients varying by up to a factor of three. Previously, it has been seen that addition of electron withdrawing substituents to the *tris*-heterocyclic system chelating metal ions such as iron(II) would lower the energy of the HOMO-LUMO gap.[41-45] This is brought about by an

increased removal of electron density of the aromatic system through the substituent, which lowers the π* antibonding levels relative to the metal centred orbitals, effectively decreasing the energy gap between them. In this study, the ligand-centred levels which form the lowest energy excited state appeared to be stabilised to a lesser extent relative to the t_{2g} levels, which are evidently much lower in energy due to their more anodic oxidation potentials (section 3.3.2). Indeed, the two appear to be stabilised by an essentially coincident amount, which could reflect an additional nitrogen atom's smaller π-lobes which overlap less effectively with the rest of the aromatic system, increasing the energy π-system relative to a substituent of the same electron withdrawing ability (eg. methylsulfonyl) which actively removes electron density from the ring.[41]

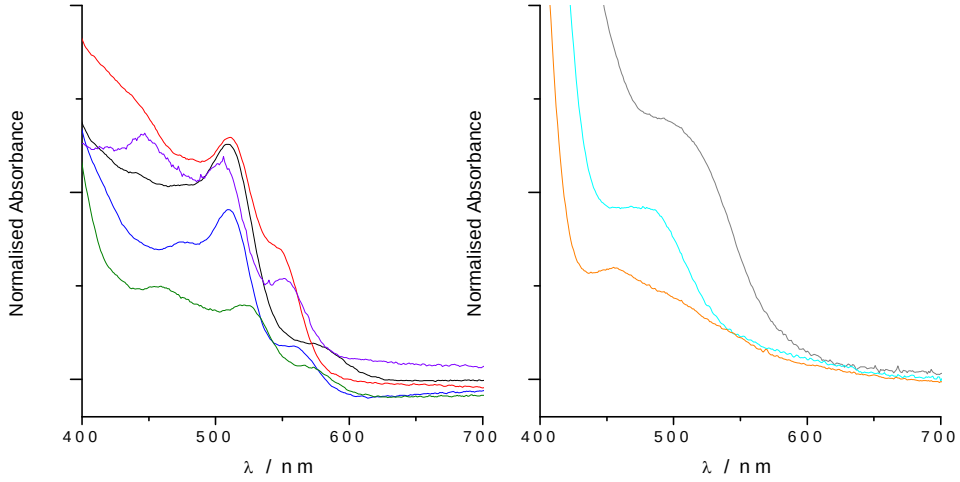

Figure 63 - Absorption spectra displaying the lowest energy MLCT envelope for the cobalt(II) complexes run as 5.50 x 10-5 mol dm-3 MeCN solutions at 298 K. Left: Unsubstituted azine complexes 1b (black), 2b (red), 3b (blue), 4b (green) and 9b (purple). Right: Hydroxypyridine complexes 7b (grey), 8b (cyan) and 10b (orange).

In the case of the cobalt(II) spectra, the complexes absorb weakly in the region 400-600 nm, under which fall the lowest energy MLCT transmissions.[7, 37, 46] The hydroxypyridine complexes, again due to the ability to strongly hydrogen bond, show a much less sharp band with only one clear maximum, in which it is impossible to observe any secondary peaks or shoulders (Figure 63 – right graph). What can be seen is that, more so than in the hydroxypyridine iron(II) complexes, there is a clear trend that the λ_{max} tends to lower energy in the order **10b**>**8b**>**7b**. This is in agreement with the reduction potential trends vs. ΣpK_s (Figure 59) at least as far as **7b** and **8b** are concerned, suggesting that the less basic pyrazinyl containing ligands are easier to reduce, and from inspection of the t_{2g} levels (Table 7) of the iron(II) complexes this energy separation should be decreased in this same order. It is very probable that this would hold true for **10b**, but due to the high energy of the π* orbitals of terpyOH this potential is shrouded by the less negative Co(II/I) wave. This

observed correlation in peak maxima must be treated with caution, however, as it is clear from the paramagnetic NMR spectra of the solubilised complexes that they LS configuration dominates to a greater degree in the more electron deficient species. The absorption envelopes are hence a result of excitation of both the HS and LS complexes, whose relative proportion varies from complex to complex.

The parent complex *bis*-terpy, **9b**, possesses a triplet of maxima between 400 and 600 nm, under which reside the lowest energy MLCT absorptions. The central maximum is in all cases the most intense of the well defined peaks, and doesn't shift by more than 12 nm from **1b**-**4b** (Figure 63– left graph). The daughter peaks however, on going from **9b** to the more electron withdrawing chelators, become less well defined and tend to become hidden under the more intense charge transfer bands at higher energy. The central peak, with ε values between 350-1137, can be more or less entirely said to originate from the lowest energy MLCT transition which is partially allowed. It is also credible to assign the higher energy maxima with extinction coefficients of similar magnitude to be of primarily MLCT character, but it is unlikely to correspond to the precise maximum in each spectrum as there is evidently overlap with LLCT and high energy d-d transitions.[12, 37] The lowest in energy of the triplet is unambiguously d-d in origin, with very low extinction coefficients indicative of a laporte forbidden transition enabled to a small degree brought about through spin-orbit coupling and the additional loss of symmetry due to the tetragonal distortion of the molecules. Cobalt(II) *bis*-terpy also possesses d-d transitions of lower energy, but the equivalent set of transitions was not observed in any of the cobalt complexes in this study due to the relatively low concentrations employed. The novel complexes would be expected to exhibit similar d-d transitions, indicative of Δ_{oct} values between 1.9 and 2 eV as seen in related cobalt(II) complexes with similar strength ligands.[7] Cobalt(II) *bis*-chelated *tris*-imine complexes of this type display a larger number and higher energy metal centred transitions than in the iron(II) situation due to the further splitting of the t_{2g} and e_g levels imposed by the tetragonal contraction, and the subsequent lowering of symmetry increases their probability of occurring. Reverting back to discussion of the lowest energy MLCT band, again the pyrazine/pyridine species have an almost coincident maxima, yet like in iron(II) it is the 4-bipympy chelated complex **4b** which exhibits the lowest energy maximum. It is proposed that the 4-pyrimidyl donors, due to their ability to reduce the symmetry about the metal ion like bipzpy yet act as stronger σ donors, interact a little more strongly with the a_{1g} and t_{1u} set, increasing symmetry imposed splitting between the d_{xy} and d_{xz}/d_{yz} orbitals. This would explain why the M(III/II) oxidation potential of the 4-bipympy complex is larger than that of bipzpy in their respective cobalt complexes, yet in the iron complexes the converse is seen.

3.3.4 Susceptibility and Electron Paramagnetic Resonance Measurements

With the exception of **6b** where exchange appears to complicate solution characterisation, all cobalt(II) complexes in this study have a low spin ground state in MeCN and $MeNO_2$ solutions at room temperature. The behaviour is more difficult to predict in the solid state, where multiple phase materials, mixtures of solvates and hydrates can confound matters somewhat. Powder diffraction asserted that generally the cobalt salts appear to be monophasic, however the ratio of crystalline to amorphous material depends on the individual complex salt and would be expected to influence the cooperativity of any observed transitions.

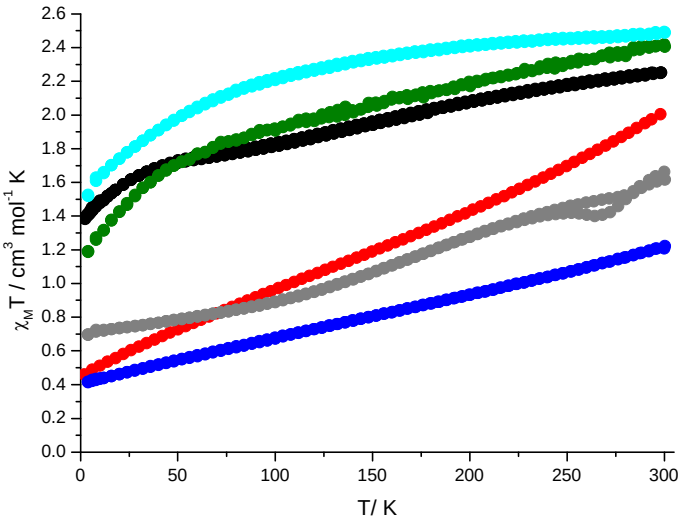

Figure 64 – Variable temperature magnetic susceptibility data for six novel cobalt(II) complexes from 0-300 K in both warming and cooling modes. 1b (black), 2b (red), 3b (blue), 4b (green), 7b (grey) and 8b (cyan).

All but one of the novel cobalt(II) salts do not appreciably switch over the temperature range that the susceptibilities were probed (Figure 64). The pyrazine rich complexes **3b** and **7b** remain majorly low spin, those with a higher number of pyrimidine or pyridine rings about the ligand backbone appearing to possess a high spin ground state in the solid. The exception to this is **2b**, whose susceptibility curve is steeper, appearing to undergo a more prominent transition, closer to the uncooperative yet complete transitions reported for a number of cobalt(II) salts chelated by the parent terpy ligand. This data is not purely a result of the ligand fields of the individual complexes, and instead is likely a result of the crystal packing. However, crystallographically it was only possible to analyse **2b** and **4b**. **4b** appears to remain trapped in the high state inferred through its single crystal data (Section 3.3.5), and its susceptibility mirrors this with the only significant drop in magnetism being the drop off below 50 K due to the large zero field splitting of high spin octahedral cobalt(II) ions.

2b contains closely packed dication layers with intra layer π-π and agnostic C-H...π interactions between neighbouring molecules, not unlike the gradually switching salts of terpy. This is evidence that said interactions in these mononuclear are necessary for the transition to propagate throughout the lattice and go to completion.

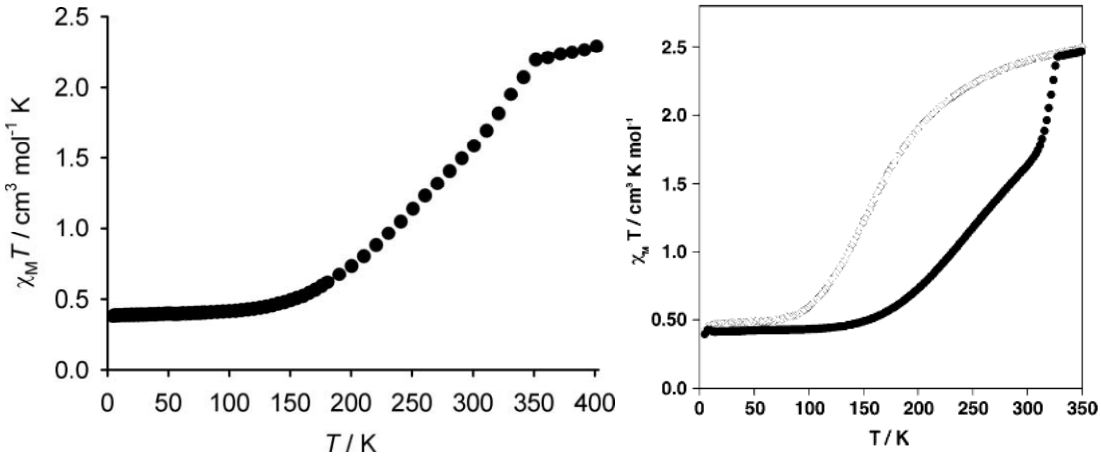

Figure 65 - Variable temperature magnetic susceptibility plots adapted from previous studies on 9b and 10b for comparison.[16, 47] Left: 9b. Right: 10b, The black and grey data points represent two different polymorphs which can be differentiated between crystallographically however both material phases have the identical chemical composition 10b.H_2O.[47]

None of the susceptibility curves demonstrate a crystallographic phase change or discontinuity, evidence that there is unlikely to be any significant change in anion/solvent disorder over the temperature range. The origin of **9b**'s discontinuity (Figure 65) hasn't been fully explained, however it likely reflects subtle changes in cation-cation interactions as the cobalt centres become almost fully high spin, which causes a decrease in cooperativity. In **10b**.H_2O, upon warming to 320 K the material experiences a phase change. The anions redistribute irreversibly with each water molecule interacting with two fluorine atoms of two discreet anions, causing a stabilisation of the high spin state between 80-320 K relative to that of the initial polymorph.

Complex Salt	120±5 K	180 K	290 K
1b	$g_{\|\|} = 2.24$[b]	$g_{iso} = 2.10$	-[a]
	$g_{\perp} = 2.08$		
2b	$g_{iso} = 2.10$	$g_{iso} = 2.10$	$g_{iso} = 2.10$[c]
3b	$g_{iso} = 2.11$	$g_{iso} = 2.11$[b]	$g_{iso} = 2.11$
4b	$g_{\|\|} = 2.18$, $A_{\|\|} = 77$	$g_{\|\|} = 2.18$, $A_{\|\|} = 70$	$g_{\|\|} = 2.18$, $A_{\|\|} = 65$
	$g_{\perp} = 2.12$	$g_{\perp} = 2.12$	$g_{\perp} = 2.12$
6b	$g_{iso} = 2.12$[b]	$g_{iso} = 2.12$[b]	$g_{iso} = 2.12$[b]
7b	$g_{iso} = 2.11$	$g_{iso} = 2.11$	$g_{iso} = 2.11$[c]
8b	$g_{\|\|} = 2.23$, $A_{\|\|} = 115$	$g_{iso} = 2.14$[b]	-[a]
	$g_{\perp} = 2.12$		
9b	$g_{\|\|} = 2.20$	$g_{iso} = 2.12$	-[a]
	$g_{\perp} = 2.11$		
10b	$g_{iso} = 2.12$	$g_{iso} = 2.12$	$g_{iso} = 2.12$[c]

Table 10 - X-band powder EPR data for the cobalt(II) complex series. A and g values have been deduced from simulations of the experimental spectra with A quoted as coupling to ^{59}Co ($I = {}^{7}/_{2}$). [a]EPR silent. [b]Some hyperfine coupling was observed but was impossible to reliably resolve due to extreme broadening. [c]weak.

The X-band EPR spectra for the complexes in the series are characteristic of *bis*-terpy cobalt(II) salts containing measurable quantities of low spin cobalt(II) centres within the bulk solid at low temperature. Where discernable, the low temperature spectra showcase axial systems with $g_{||} = 2.18$-2.24 and $g_{\perp} = 2.08$-2.12, or isotropic $g_{iso} = 2.10$-2.14 consistent with related low spin *tris*-imine chelated centres (Figure 66). At high temperature, often the spectra are too broad to reliably assign g values or indeed the complexes were deemed to be EPR silent at these temperatures (Table 10). The line broadening is often a combined effect of increased dipole-dipole relaxation of any remaining low spin centres by neighbouring high spin ($S = {}^{3}/_{2}$) centres and the promotion of remaining low spin centres to the high spin state which is EPR silent over this temperature regime. Two notable exceptions to this expected broadening are noted, with **3b** and **4b** retaining their narrow linewidths and in the case of **4b** even appearing to sharpen slightly at elevated temperatures. This is not entirely unexpected in **3b**, which remains principally low spin at all temperatures its susceptibility was recorded. The sharpening of **4b**'s spectra at high temperatures is a little surprising (Figure 67), but it may reflect either an isolated low spin phase within the bulk high spin material difficult to detect in the powder spectra, or the lack of close packing between dications in the solid (Section 3.3.5) resulting in essentially magnetically isolated ions subject to only minor broadening via dipole-dipole interactions.

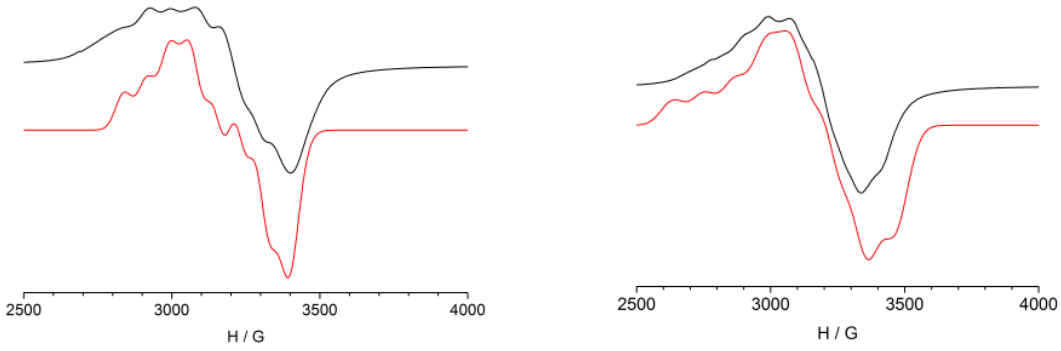

Figure 66 – Experimental (black) and simulated (red) X-band EPR spectra of 4b (left) and 8b (right) at 120 K. Simulation parameters: 4b, $g_{||}$ = 2.18, $g_{\perp}$ = 2.12, $A_{||}$ = 77 G; 8b, $g_{||}$ = 2.23, $g_{\perp}$ = 2.12, A = 115 G.

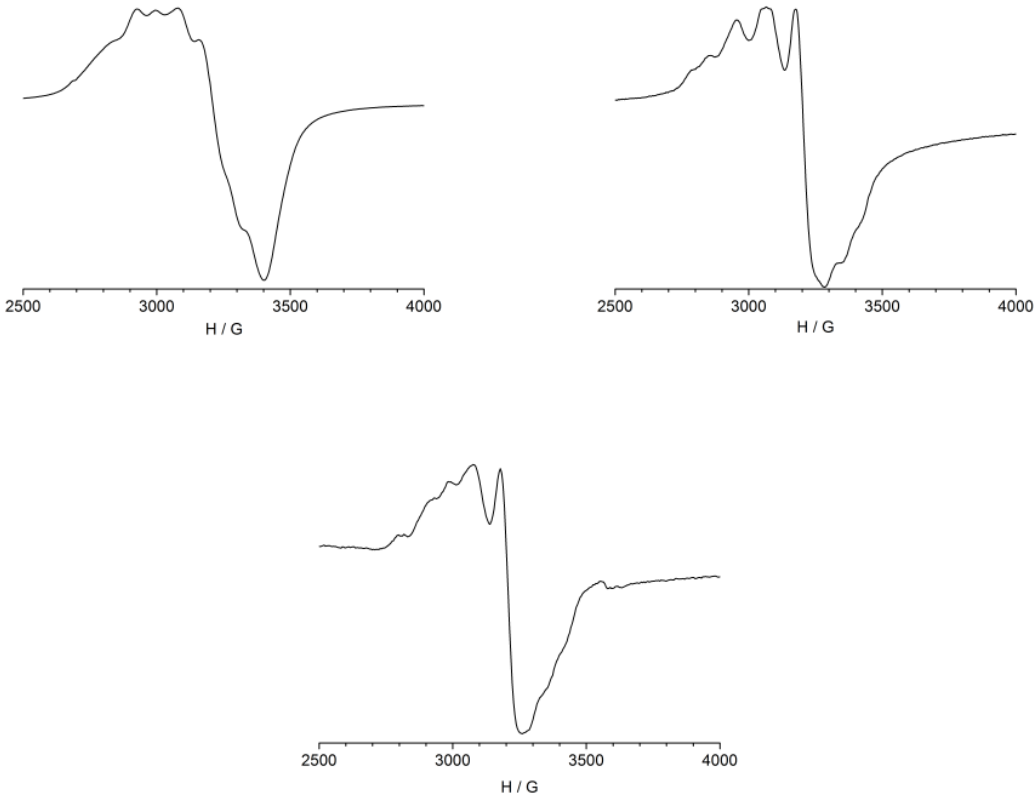

Figure 67 – Variable temperature X-band EPR spectra of a powder sample 4b. The spectra were run at 121 (top left), 180 (top right) and 290 K (bottom).

3.3.5 Crystallographic and Powder Diffraction Studies

Single crystals suitable for X-ray diffraction were acquired for the complex salts **1a**, **2b**, **3a**, **4a**, **4b** and **6b**, via diffusion of $^{i}Pr_2O$ into filtered $MeNO_2$ solutions of the respective salts. Data and crystallographic parameters are listed and discussed below for all structures except for that of **3a** which remains as of yet unsolved. Exhaustive attempts using numerous methods and solvent combinations were made to crystallise the 4-hydroxy complexes **7a**-**8a** and **7b**-**8b** but no suitable crystalline material was observed or isolated. This could reflect

the OH group's ability to inhibit potential π-π stacking between neighbouring dication units due to its strong affinity to bond with and thus retain water and other polar solvents. As a result only very poorly crystalline or purely amorphous material (Figure 71) was isolated for these salts.

Both of the iron salts **1a** and **4a** crystallise as solvates, shown to contain one and three $MeNO_2$ molecules per discreet dication unit respectively. In keeping with spectroscopic data, it comes as no surprise that both complex salts are entirely low spin as deduced from the range of Fe-N bond lengths and *trans*-*cis*-N-Fe-N bond angles and the clear undistorted octahedra (Figure 68). The cobalt complexes **2b** and **6b** which crystallise as solvent free and disolvate materials respectively are fully low spin at 150 K, yet **4b**, also free of solvent, is distinct in that it contains one fully high spin cobalt(II) centre showing a highly distorted coordination geometry (Figure 69). To clarify this further, three structural distortion parameters have also been calculated for each complex which can be used to correlate deviation from an ideal octahedron with ratio of HS-LS species in a mixed spin-state material. The parameters can also help explain, both on the grounds of electronics and sterics, whether the structural modifications required upon a change of spin state would be too great to accommodate in materials containing severely distorted metal centres. The rhombic and trigonal distortion parameters (Table 11) are in strong agreement with literature values for closely related *bis*-chelated planar *tris*-imine complexes of iron and cobalt(II).[23] The parameters Σ and Θ are much greater in high spin **4b**, reflecting the increased repulsion between the half occupied e_g level with that of the σ-donors. The distortions display more variation between the two series of low spin complexes than within as a consequence of the reduced bite angle of the ligands due to the Jahn-Teller imposed elongation of the equatorial bonds in low spin cobalt(II). Significant deviation of θ from 90° is rarely observed except in strongly distorted structures whereby the planarity of the ligand is compromised by bulky substituents or clashing between neighbouring molecules which prevents adoption of the low spin state.

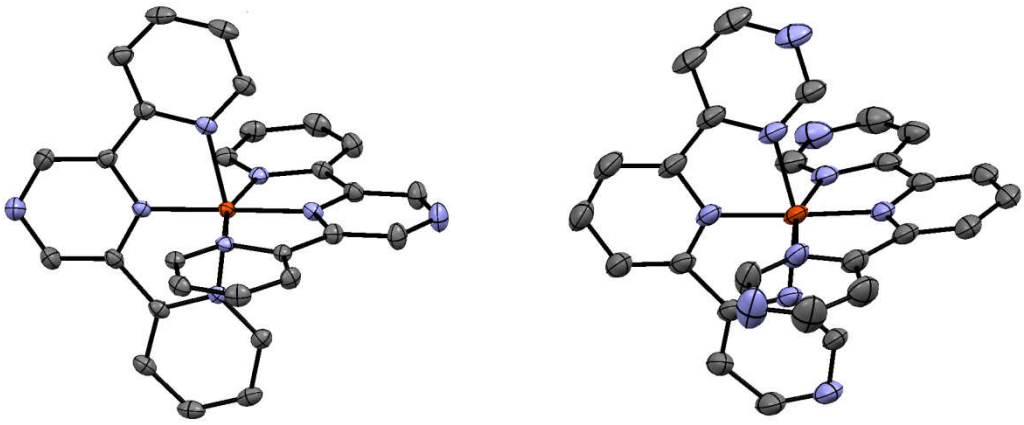

Figure 68 – Views of the dication units in the iron(II) salts 1a.$MeNO_2$ (left) and 4a.3$MeNO_2$ (right). H atoms have been omitted for clarity and all thermal ellipsoids are plotted at the 50% probability level. Atom colour code: carbon (grey), iron (orange) and nitrogen (periwinkle).

Oddly, none of these complexes, despite their very similar size and shape, are isostrucutural with any of the parent terpyridine complexes of the form $[M(terpy)_2][BF_4]_2$ (M = Co, Cu, Ru, Zn) which all adopt a version of the "terpyridine embrace" motif with the space group Cc.[16, 48, 49] That said, **1a** and **2b** adopt related yet different forms of the terpyridine embrace. **2b** is isostructural with $[Cu(terpy)_2][PF_6]_2$, possessing alternating dication layers at 45° to each other with the counterions occupying the deep grooves between layers.[17] **1a** packs in a form of the terpyridine embrace hitherto not documented before in $P2_1/c$, with four individual cation layers. Interlayer cations are related by 2-fold screw axes situated between layers one and two and layers three and four, as well as inversion centres between layers two and three. Off-centre face-to-face stacking interactions between the distal rings of neighbouring molecules of 2.727 Å in **1a** and 3.756 Å in **2b** are present accounting for the driving force for the adoption of these motifs. Many of the parent terpyridine embrace adopting complexes pack as either solvent free materials or hydrates, which may show why these complexes which preferentially tend to crystallise as nitromethane solvates more often than not abstain from packing in conventional terpyridine embrace motifs as is seen for **1a**, **4a**, **4b** and **6b**.

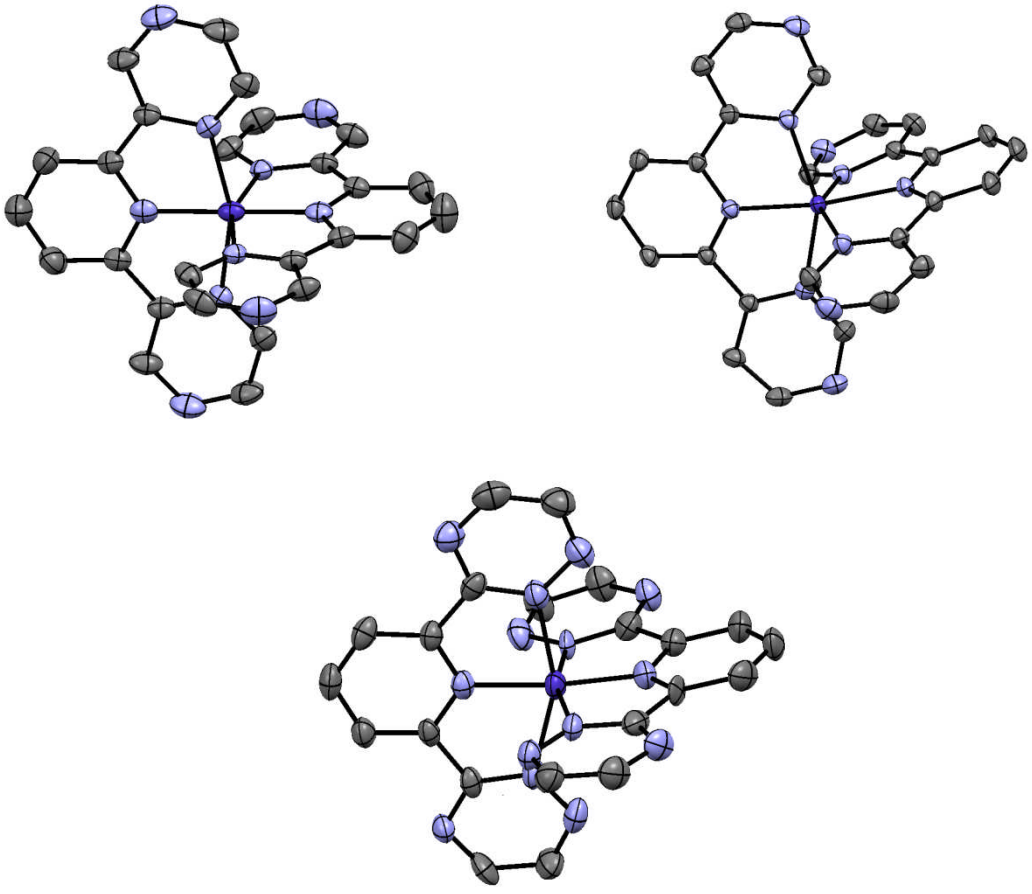

Figure 69 – Views of the dication units in the cobalt(II) salts 2b (top left), 4b (top right) and 6b.2MeNO$_2$ (bottom). H atoms have been omitted for clarity and all thermal ellipsoids are plotted at the 50% probability level. Atom colour code: carbon (grey), cobalt (indigo) and nitrogen (periwinkle).

Powder diffraction data of **4b** has shown that almost all of the material in the powder sample was highly crystalline. The simulated pattern matches up all but identically with that of the experimental data, showing there is little doubt that the complex crystallises as a single phase material. Susceptibility measurements (Section 3.3.4) suggesting that the material remains fully high spin at all temperatures measured are in agreement with metric data obtained through crystallographic structure determination. Reasons as to why this complex remains trapped in the high spin state must be deduced from geometric implications resulting in its solid state packing. Its lattice is quite tightly packed, with intermolecular fluorine-carbon/nitrogen distances of 3-3.2 Å which may be the source of the structural distortions required to accommodate these highly disordered anions.

No. / polymorph	**1a**.MeNO$_2$	**2b**	**4a**.3MeNO$_2$	**4b**	**6b**.2MeNO$_2$
T / K	150	150	150	150	150
Volume of M polyhedron / Å^3	9.7046(3)	10.988(14)	10.121(9)	12.062(5)	10.3373(6)
Rhombic / °	81.77(41)	88.10(30)	80.20(39)	130.08(18)	88.82(94)
Trigonal / °	272	296	265	403	295
Trans Angle /°	179.33300(4)	180.00	177.91(10)	171.26(5)	172.8912(9)
Least sq. planes difference / °	89.917(3)	90.000(8)	89.35(3)	83.209(18)	85.7862(9)
Av. bite angle / °	80.56(24)	79.88(16)	80.74(23)	76.25(10)	80.03(60)
Av. M-N$_{prox}$ / Å	1.884(4)	1.932(6)	1.918(4)	2.0616(18)	1.891(9)
Av. M-N$_{dist}$ / Å	1.993(6)	2.098(6)	2.017(6)	2.1716(29)	2.063(14)

Table 11 - Geometric distortion parameters for the iron(II) and cobalt(II) azinyl *bis*-2,2':6'2''-terpyridyl derivative tetrafluoroborate salts

The powder diffraction patterns for the rest of the cobalt(II) series show more variation (Figure 70), but were run in an attempt to ascertain whether or not multiple phases were present in the bulk powder samples to shed light on disagreements between EPR spectra and variable temperature suscepbility data (Section 3.3.4). Experimental and simulated spectra for **2b** also show good agreement, clarifying that the bulk powder was a fully low spin phase pure material in the solid state at 150 K. Though, due to lack of crystallographic analysis, no simulated data could produced for **1b** and **3b**, the small number of peaks at low θ values suggest that these materials are probably single phase in nature, with the spectra being slightly broadened and possessing a high level of noise ratio due to the presence of amorphous material.

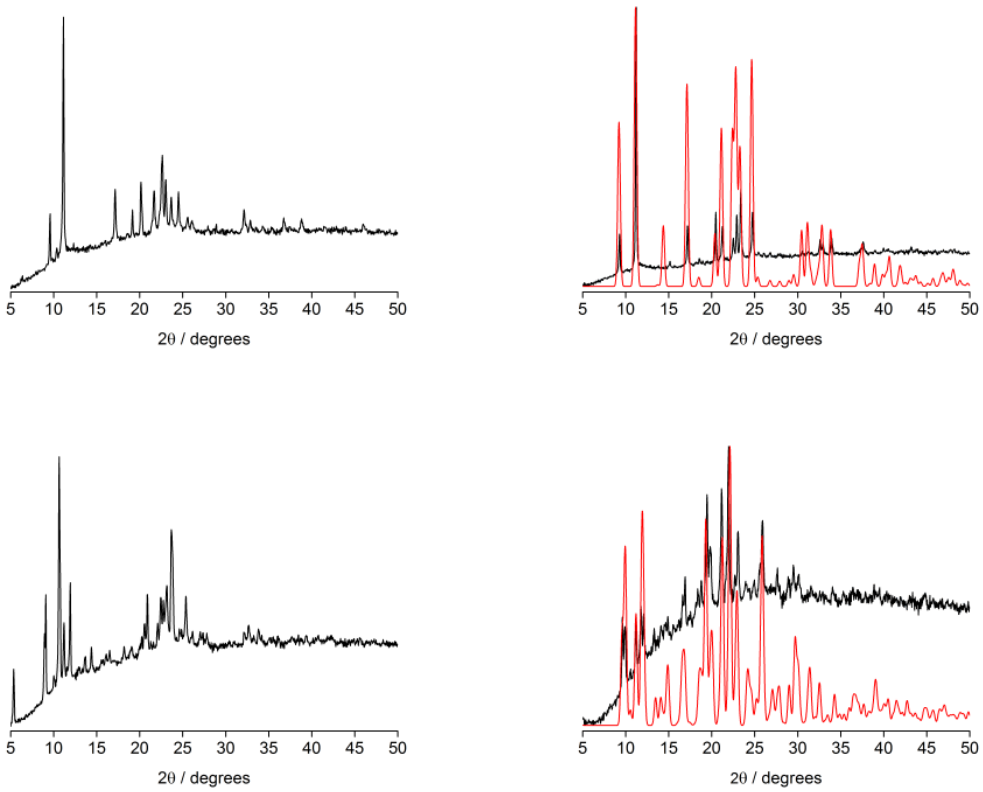

Figure 70 – Experimental (black) and simulated (red) powder patterns of selected cobalt(II) complexes, from 1b (top left), 2b (top right), 3b (bottom left) and 4b (bottom right).

Data for the hydroxylated complexes **7b** and **8b** is less informative, due to their highly amorphous nature evidenced by the extreme broadening of the spectra at almost the full θ range scanned. This likely reflects their difficulty to form single crystals, and their retention of water molecules as revealed in some of the microanalytical data. It has been reported that in related hydroxylated terpyridines, the highly acidic phenolic proton can be spontaneously deprotonated upon coordination to a metal centre, which would further reduce their likelihood to form single phase crystalline materials.[35 47]

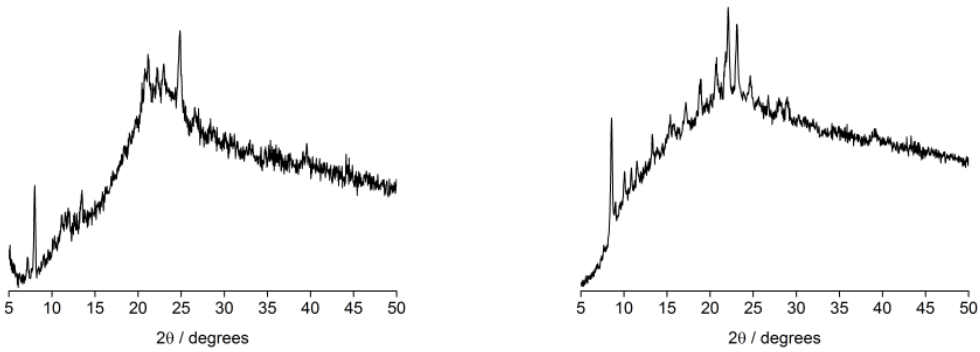

Figure 71 - Experimental powder patterns of the cobalt(II) complexes 7b (top) and 8b (bottom).

3.4 Conclusions

For the first time the six-membered parent heterocycles about the iron(II) and cobalt(II) *bis*-chelated architectures have been modified in an electronic and structural investigation upon their homoleptic complex centres. The energies of the metal-centred hybrid orbitals were shown to be highly sensitive to substitution of the pyridine heterocyclic donors with that of electron deficient diazinyl and triazinyl analogues. The reduction in σ-basicity of the donor cycles induces pronounced stabilisation of the valence metal-based levels towards electrochemical oxidation of 0.07-0.13 and 0.08-0.12 V for every pyridine that is replaced with a diazinyl or triazinyl donor respectively. Unsurprisingly, the steric restrictions imposed by the relatively small bite angles preferred by the *tris*-chelates showed that the electronic effect was greater upon varying the proximal donors than those at the distal positions by virtue of the greater metal-to-nitrogen σ interactions.

Converse to predictions, the more electron poor *tris*-heterocyclic chelators impose larger ligand fields on the iron(II)/cobalt(II) centres than in their parent *bis*-terpyridyl complex ions. Every iron(II) based material was fully diamagnetic in both the solid and solution phases, and the LS cobalt(II) configuration is stabilised by the heterocycles electronically in the order 1,2,4-triazin-3-yl>4-pyrimidyl>2-pyrimidyl>pyrazinyl as deduced from the contact shifted ^{1}H NMR signals. This is explained upon consideration of the UV/visible spectral transitions whose band positions suggest π-back-donation makes a significant contribution towards the metal-to-ligand bonding interactions and thus is primarily responsible for the increase in ligand field strength observed in the electron poor complexes.

The electron deficient complexes do not crystallise as readily as the parent iron(II)/cobalt(II) salts, but as is exhibited by the parent cobalt(II) *bis*-terpyridyl salt **9b** one of the five structural solutions, **2b**, adopts a solvent free terpyridine embrace type lattice.[16, 49] Incorporation of non-coordinating nitrogen atoms about the ligand backbone does not, it appears, prevent formation of the highly sought after terpyridine embrace packing motif however the complexes have an increased tendency to crystallise with non hydrogen bonded solvate molecules which inhibits the formation of discreet layers of interlocked molecules signature to the terpyridine embrace.

3.5 References

1. S. Romain, C. Baffert, C. Duboc, J. Lepretre, A. Deronzier and M. Collomb, *Inorg. Chem.*, 2009, **48**, 3125-3131.
2. E. Constable, *Chem. Soc. Rev*, 2007, **36**, 246-253.
3. E. Medlycott and G. Hanan, *Chem. Soc. Rev*, 2005, **34**, 133-142.
4. G. Albano, V. Balzani, E. Constable, M. Maestri and D. Smith, *Inorg. Chim. Acta.*, 1998, **277**, 225-231.

5. E. Constable, B. Hermann, C. Housecroft, M. Neuburger, S. Schaffner and L. Scherer, *New J. Chem.*, 2005, **29**, 1475-1481.
6. Y. K. S. Hayami, T. Shimizu, H. Kamihata, Y. Hoon Lee, *Coord. Chem. Rev.*, 2011, **255**, 1981-1990.
7. I. Krivokapic, M. Zerara, M. Daku, A. Vargas, C. Enachescu, C. Ambrus, P. Tregenna-Piggott, N. Amstutz, E. Krausz and A. Hauser, *Coord. Chem. Rev.*, 2007, **251**, 364-378.
8. J. Rao, M. Hughes and D. Macero, *Inorg. Chim. Acta.*, 1976, **16**, 231-236.
9. A. Baker and H. Goodwin, *Aust. J. Chem.*, 1985, **38**, 207-214.
10. E. Constable, G. Baum, E. Bill, R. Dyson, R. van Eldik, D. Fenske, S. Kaderli, D. Morris, A. Neubrand, M. Neuburger, D. Smith, K. Wieghardt, M. Zehnder and A. Zuberbuhler, *Chem. Eur. J.*, 1999, **5**, 498-508.
11. S. Brauchli, E. Constable, K. Harris, D. Haussinger, C. Housecroft, P. Rosel and J. Zampese, *Dalton Trans.*, 2010, **39**, 10739-10748.
12. J. Judge and W. Baker, *Inorg. Chim. Acta.*, 1967, 68-72.
13. S. Kremer, W. Henke and D. Reinen, *Inorg. Chem.*, 1982, **21**, 3013-3022.
14. E. Constable, J. Davies, D. Phillips and P. Raithby, *Polyhedron*, 1998, **17**, 3989-3997.
15. E. Constable, C. Housecroft, T. Kulke, C. Lazzarini, E. Schofield and Y. Zimmermann, *Dalton Trans.*, 2001, 2864-2871.
16. C. Kilner and M. Halcrow, *Dalton Trans.*, 2010, **39**, 9008-9012.
17. M. Scudder, H. Goodwin and I. Dance, *New J. Chem.*, 1999, **23**, 695-705.
18. J. Mcmurtrie and I. Dance, *CrystEngComm*, 2005, **7**, 216-229.
19. J. McMurtrie and I. Dance, *CrystEngComm*, 2005, **7**, 230-236.
20. J. McMurtrie and I. Dance, *CrystEngComm*, 2010, **12**, 2700-2710.
21. J. Holland, J. McAllister, Z. Lu, C. Kilner, M. Thornton-Pett and M. Halcrow, *Chem. Commun.*, 2001, 577-578.
22. R. Pritchard, C. Kilner and M. Halcrow, *Chem. Commun.*, 2007, 577-579.
23. M. Halcrow, *Coord. Chem. Rev.*, 2009, **253**, 2493-2514.
24. J. E. V. Money, M. Halcrow and J. Howard, *Dalton Trans.*, 2004, 65-69.
25. T. Brinck, J. Murray and P. Politzer, *J. Org. Chem.*, 1991, **56**, 2934-2936.
26. A. Stublla and P. Potvin, *Eur. J. Inorg. Chem.*, 2010, 3040-3050.
27. M. Drew, M. Foreman, A. Geist, M. Hudson, F. Marken, V. Norman and M. Weigl, *Polyhedron*, 2006, **25**, 888-900.
28. H. Chow, E. Constable, C. Housecroft, K. Kulicke and Y. Tao, *Dalton Trans.*, 2004, 236-237.
29. E. Constable, C. Housecroft, V. Jullien, M. Neuburger and S. Schaffner, *Inorg. Chem. Commun.*, 2006, **9**, 504-506.
30. R. Casasnovas, J. Frau, J. Ortega-Castro, A. Salva, J. Donoso and F. Munoz, *J. Mol. Struct. (THEOCHEM)*, 2009, **912**, 5-12.
31. C. Arana, S. Yan, M. Keshavarz-K, K. Potts and H. Abruna, *Inorg. Chem.*, 1992, **31**, 3680-3682.
32. T. Ayers, S. Scott, J. Goins, N. Caylor, D. Hathcock, S. Slattery and D. Jameson, *Inorg. Chim. Acta.*, 2000, **307**, 7-12.
33. V. Souza, H. Rechenberg, J. Bonacin and H. Toma, *Spectrochim. Acta, Part A*, 2008, **71**, 1296-1301.
34. G. Storrier, S. Colbran and D. B. Hibbert, *Inorg. Chim. Acta.*, 1995, **239**, 1-4.
35. E. Constable, A. Thompson and D. Tocher, *New J. Chem.*, 1992, **16**, 855-867.

36. S. Klein, W. Dougherty, W. Kassel, T. Dudley and J. Paul, *Inorg. Chem.*, 2011, **50**, 2754-2763.
37. C. Enachescu, I. Krivokapic, M. Zerara, J. Real, M. Amstutz and A. Hauser, *Inorg. Chim. Acta.*, 2007, **360**, 3945-3950.
38. P. Braterman, J. Song and R. Peacock, *Inorg. Chem.*, 1992, **31**, 555-559.
39. J. Dai, B. Li, Y. Chen, G. Huang, B. Cai, Y. Yu and J. wu, *Inorg. Chem. Commun.*, 2010, **13**, 625-629.
40. A. Roy, M. Biswas, T. Weyhermuller and P. Ghosh, *Inorg. Chim. Acta.*, 2010, **363**, 2874-2880.
41. M. Maestri, N. Armaroli, V. Balzani, E. Constable and A. C. Thompson, *Inorg. Chem.*, 1995, **34**, 2759-2767.
42. E. Constable, A. Thompson, N. Armaroli, V. Balzani and M. Maestri, *Polyhedron*, 1992, **11**, 2707-2709.
43. S. Furukawa, Y. Hitomi, T. Shishido, K. Teramura and T. Tanaka, *J. Phys. Chem. A*, 2011, **115**, 13589-13595.
44. R. Fallahpour, M. Neuburger and M. Zehnder, *New J. Chem.*, 1998, **22**, 53-61.
45. R. Fallahpour, *Eur. J. Inorg. Chem.*, 1998, 1205-1207.
46. L. Kershaw Cook, F. Tuna and M. Halcrow, *Dalton Trans.*, 2013, **42**, 2254-2265.
47. A. Galet, A. Gaspar, M. Munoz and J. Real, *Inorg. Chem.*, 2006, **45**, 4413-4422.
48. C. Tovee, C. Kilner, J. Thomas and M. Halcrow, *CrystEngComm*, 2009, **11**, 2069-2077.
49. R. Docherty, F. Tuna, C. Kilner, E. McInnes and M. Halcrow, *Chem. Commun.*, 2012, **48**, 4055-4057.

Chapter 4

Novel emissive ruthenium(II) salts: spectroscopic analysis and incorporation into a spin-switchable host lattice

4 Novel emissive ruthenium(II) salts: spectroscopic analysis and incorporation into a spin switchable host lattice

4.1 Introduction

The primarily focus of this chapter is concerned with the engineering of novel mononuclear ruthenium(II) salts, with the octahedral core coordinated by two planar, meridionally chelating ligands analogously to the parent ruthenium(II) *bis*-terpyridine dication, however with increased room temperature emission.[1, 2] The complexes are to be screened electrochemically and spectroscopically to gain insight into their electronic structures and from this the complexes, initially in fluid solution, will be excited with appropriate wavelengths of light and their emission intensities and band positions elucidated. Promising candidates featuring notable increases in room temperature emission will thus be doped as their ditetrafluoroborate salts into a $[Fe(1\text{-bpp})_2][BF_4]_2$, **25a**, host lattice with the goal of achieving a homogenous, bifunctional abruptly switching SCO material whose core functionalities are observed over the same temperature regime.

The work is a continuation of findings made previously within the group, showing that a number of octahedral transition metal dications *bis*-chelated either by 1-bpp or terpy can be successfully co-crystallised together as their ditetrafluoroborate salts even if the pure materials are not crystallographically isostructural.[3-6] Of particular relevance is the case of the doping of $[Ru(terpy)_2][BF_4]_2$, **18a**, into the abruptly switching material $[Fe(1\text{-bpp})_2][BF_4]_2$, **25a** which retains homogenous phase purity over almost the entire iron-ruthenium complex ratio except when very close to equimolar quantities are employed.[5, 6] Both functionalities of the individual complex centres are retained in the doped materials, with a very abrupt transition being maintained up until an iron-ruthenium ratio of 9:1, below which the spin transition broadens yet with only very minor change in the exact position of the transition, $T_{1/2}$. The ruthenium(II) centre is, detrimentally, not emissive at ambient temperature, and thus its emission could only be studied at 77 K which is almost 200 K below the transition temperature, hence the two functionalities could not be studied over the same temperature range and the effect of the spin transition upon the emission of the ruthenium cores still unknown. At 77 K, however, the fluorescence intensity from the ruthenium centres was much lower than expected in the solid solutions, but this is ascribed to overlap between the emission band of **18a** and absorption from LS centres of the iron complexes within the lattice.

To overcome the emission quenching in ruthenium *bis*-terpyridyl systems above 80 K, which is caused by a thermally accessible non-radiative metal-centred triplet state within reach of the vibrationally hot levels of the ^{3}MLCT excited state, a multitude of attempts to

modify the terpy backbone to increase separation between the states or reduce spin-orbit coupling have been reported.[7, 8] Significant progress has been made in increasing this energy gap and hence emission lifetimes. This has been achieved by attaching suitably electron withdrawing moieties or extending the aromatic π-system and by optimising the bite angle through inter-ring spacer groups. Unfortunately the size and shape of the complex units in the vast majority of examples renders them incompatible for use in replacing the $[Fe(1\text{-}bpp)_2]^{2+}$ sites in **25a**.[9-19] Instead, our efforts principally are focused on evaluating the emission of a series of new ruthenium(II) *bis*-terpyridyl derivatives, whereby the pyridine heterocycles are to be replaced with less basic diazinyl and triazinyl rings in the hope to optimise the electronics of the ruthenium(II) core to not only diminish the non-radiative decay processes at higher temperatures but also to lower the emission energy band.[20, 21] The secondary set of materials to be screened for use as emissive dopants all contain at least one cyclometallated Ru-C bond, and are based on systems adapted from the literature containing either dialkylimidazolium pyridine chelators or 2,2':6,4''-terpyridine which are known to be emissive in the visible region.[22, 23] The two sets of ruthenium *bis*-terpyridyl analogues have been chosen for investigation as their constituent meridionally chelating ligands retain planarity, and don't contribute significant additional steric hindrance with respect to 2,2':6',2''-terpyridine and, thus, stand the maximum theorised chance of successful incorporation into the host lattice of **25a**.

4.2 Aims and objectives

The aim of this chapter was to develop a series of novel *bis*-chelated ruthenium(II) complex salts with increased room temperature emission relative to the parent *bis*-terpyridyl salts. The candidates were chosen based upon electronic predictions in tandem with consideration of the size/shape characteristics of the individual dicationic units so as to cause minimal increase in volume of the dications and likelihood of interference of appended groups/substituents with the ability to adopt the terpyridine embrace. Through the use of absorption spectroscopy, the energies of the low lying MLCT absorptions can be quantified and used to selectively irradiate the solvated materials in order to screen for emission over the UV/visible/near IR range. Single crystals will be studied crystallographically where viable in order to extract accurate dicationic volumes. Candidates which are both emissive in the visible spectrum and possess a comparable dicationic volume to ruthenium(II) *bis*-terpy were to be co-crystallised alongside a spin-crossover host. Phase purity of the doped materials can be assessed through powder diffraction and the effect of the doping upon the materials of variable stoichiometry investigated, with the chief aim being acquisition of a robust material whose emission can effectively be "tuned" over a temperature range, depending upon the spin state of the iron(II) centres.

4.3 Synthesis and isolation of the ruthenium(II) complex salts

4.3.1 The diazinyl and triazinyl terpyridine complex salts

Serious problems were encountered not only in the formation of this series of electron deficient ruthenium(II) *bis*-terpyridyl analogues but also in their isolation as the pure tetrafluoroborate salts. Formation of the ruthenium(II) centre requires the employment of highly polar, non-volatile solvents to facilitate reduction of the ruthenium from Ru(III) to Ru(II) at high temperatures (Figure 72).[24] A number of the reactions were observed to turn orange/red, indicative of a *bis*-chelated ruthenium(II) species, however the time and temperatures required varies erratically. In addition, the non-coordinating nitrogen atoms about the diazinyl and triazinyl rings make isolation from the highly polar solvents troublesome, meaning some of the complexes had to be isolated as the less soluble hexafluorophosphate salts for the purposes of spectroscopic study. A number of methods were employed in attempting to isolate the various complexes, involving one-pot syntheses to the use of pre-formed and pre-reduced intermediates so as to reduce reaction times, optimise the reactions and prevent thermal decomposition in conjunction with improving their ease of isolation which are discussed in more depth below.

The parent *bis*-terpyridine ruthenium complex was isolated as its ditetrafluoroborate salt, **18a**, according to its reported literature preparation by heating terpy and $RuCl_3.3H_2O$ together at 110°C in ethylene glycol and performing a salt exchange on the resulting dichloride salt to give the pure material. **19a** was acquired pure through the utilisation of a number of synthetic schemes, however reacting two equivalents of terpyOH with the pre-reduced intermediate $RuCl_2(DMSO)_4$ before performing the salt exchange to produce the ditetrafluoroborate salt resulted in the highest recorded yields. The method employed in the formation of **18a** is a one-pot reaction which relies on the high boiling point of the solvent, ethylene glycol in combination with its tendency to act as a weak reductant of the in-situ formed *bis*-chelated ruthenium(III) complex and is widely used in the preparation of homoleptic imine-chelated ruthenium complex cores.[14, 25, 26] As such it was adapted as the focal method for preparation of the novel homoleptic ruthenium(II) salts. **11a** forms readily over the course of 4 h at 110°C, analogously to the parent *bis*-terpyridine complex, with the ditetrafluoroborate salt isolated as a dark red-brown powder. The material was pure by NMR spectroscopy, and the darker coloured impurities, possibly polynuclear in nature, could be gradually removed through repeated recrystallisation of the crude substance.

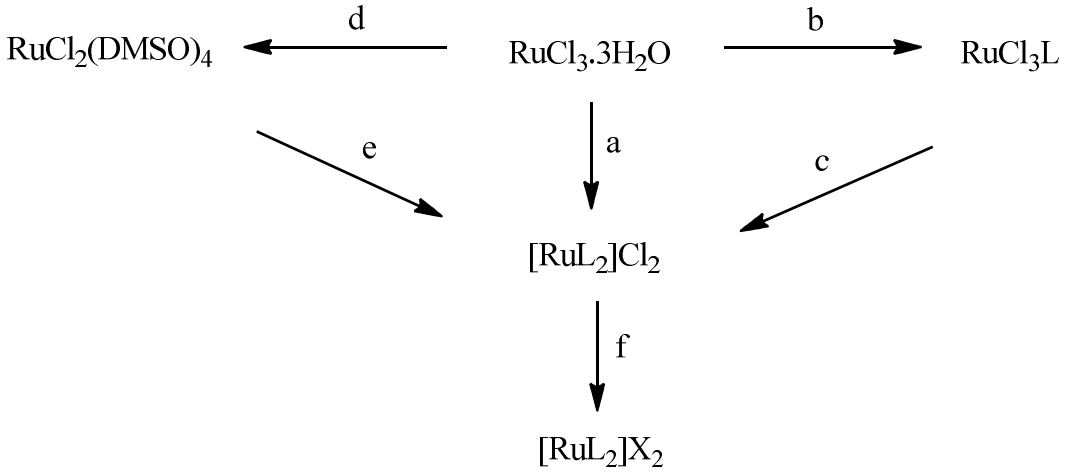

Figure 72 – Scheme displaying synthetic routes used in attempts to obtain the *bis*-diazinyl ruthenium(II) salts, where L = azinyl *tris*-chelating ligand and X = tetrafluoroborate or hexafluorophosphate; a) Δ, 2L, ethylene glycol; b) Δ, L, EtOH; c) Δ, L, *N*-ethylmorpholine, MeOH; d) Δ, DMSO; e) Δ, MeOH-H_2O, 2L; f) addition of aqueous/methanolic $NaBF_4$ or NH_4PF_6 and collection of the salt precipitated.

The homoleptic complexes containing 4-bipympy and 2-bipympyOH were prepared according to this general preparative method, however were instead isolated as their dihexafluorophosphate salts **14b** and **17b** respectively. All attempts to isolate the tetrafluoroborates, **14a** and **17a** yielded no precipitation during the salt exchanges, owing to their increased hydrogen bonding capacity provoked by the non-coordinating nitrogen atoms of their diazinyl heterocycles and, in the case of the 2-bipympyOH containing complex, the appended hydroxy functionality. The ease of reduction of the transient ruthenium(III) complex cores was also observed to vary hugely, depending upon the heterocyclic content. As the reactions proceed the solutions become deep green in hue indicating the formation of the *bis*-chelated ruthenium(III) complexes, however the ease of reduction to the orange-red ruthenium(II) complexes is unpredictable.[27-29] In contrast to **11a** and **19a** which reduce almost quantitatively in a matter of hours, the reduction has to be encouraged through the employment of much harsher temperatures and longer reaction times, often several days, in order to form and thus isolate an appreciable yield of **14b** and **17b**. Indeed **14b** must be heated to 150°C for 5 days before the solution takes on significant red character. The finding is surprising, as intuitively it was expected that the electron deficient complex cores, particularly those with less basic heterocycles coordinating along the xy plane of the ruthenium core would in reduce far more readily, in accord with the electrochemical data (Section 4.4.1) and the fact that the added electron populates the d_{xy} level. Evidently, the process possesses an intrinsic thermal activation energy barrier, the nature of which cannot be speculated upon, which appears to be greater in the electron deficient salts, however is likely a function of the degree of solvation by the highly coordinating polar ethylene glycol solvent/reductant employed.

15a was the last of the homoleptic azinyl terpyridine derivative complex salts to be successfully isolated, however formation of the desired ruthenium(II) core proved troublesome. Utilising the one-pot method from commercially available ruthenium trichloride hydrate the pure homoleptic salt could not be isolated. The reduction process, noted during the preparation of **14b** and **17b**, is extremely sluggish and the reaction does not progress beyond a dark orange-brown suspension in appearance. Increasing temperature promotes either decomposition or dechelation and subsequent formation of black-brown insoluble matter which is completely uncharacterisable and probably comprised of a multitude of oligomeric/polymeric ruthenium containing species. Endeavours to precipitate the complex, both as its hexafluorophosphate and tetrafluoroborate salts were largely unsuccessful, with only very small quantities of a very dark coloured powder ever materialising out of solution. Promising, however, was that both mass spectrometric and ^{1}H NMR spectroscopic analysis confirmed the presence of the homoleptic dication within the crude material. The minute quantities of material at our disposal precluded purification of the material obtained through this preparation, while small scale-crystallisations only yielded dark residues and films of no higher purity than the original crude solid sample.

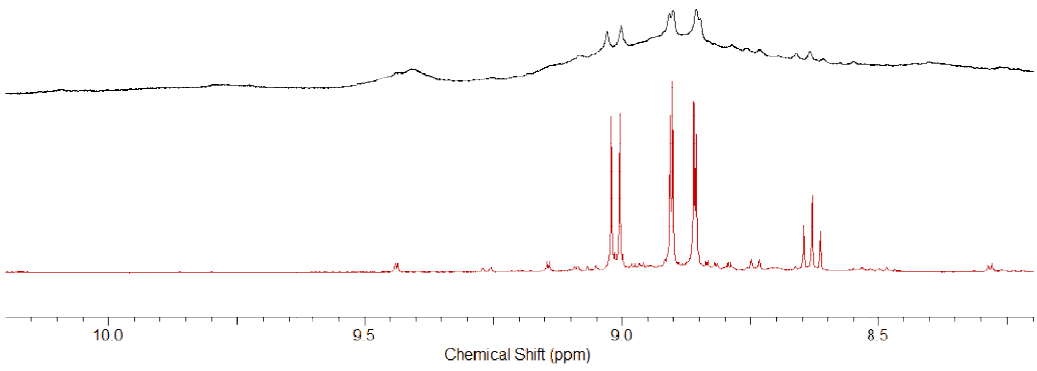

Figure 73 – ^{1}H NMR spectra run in CD_3CN of crude, inseparable 15a prepared using $RuCl_2(DMSO)_4$ (black) and of NMR pure 15a using ruthenium trichloride (red) as the ruthenium source. Spectra were recorded at 300 MHz on a Bruker DPX300 FT NMR spectrometer.

To counter the difficultly in reducing the homoleptic ruthenium(III) species, an approach was taken involving the use of the pre-formed ruthenium(II) precursor $RuCl_2(DMSO)_4$, which is also commonly used as a starting material for ruthenium(II) polypyridyls, both containing tridentate N-donor ligands and those chelated by more complicated systems.[15, 21, 30-33] The ligand bitrzpy was heated to 80°C for between four and 72 hours along with the ruthenium source using a mixed EtOH-H_2O solvent system. In the first instance, a stoichiometric amount of $AgBF_4$ relative to the ruthenium source was added to perform the salt exchange during the course of the reaction, and the resulting AgCl filtered

off once the solution had cooled. Removal of the volatiles and analysis of the residue revealed the complex dication to be the major species in solution, however the aromatic region showed a busy, heavily broadened region between 8 and 10 ppm, indicative of a number of ligand environments (Figure 73). Purification through crystallisation again failed, and attempts to chromatograph the material resulted in its loss as it stuck indefinitely to both silica gel and alumina, even when flushed with highly concentrated aqueous KNO_3 solutions. The second time the reaction was performed, $AgBF_4$ was excluded and the salt exchange performed upon the resulting dark red reaction mixture after an insoluble black residue had been removed by filtration. No precipitation occurred, as per expectation based on its predicted higher solubility in H_2O, and the volatiles were removed. The material was isolated pure, as shown by ^1H NMR spectroscopy (Figure 73), by extracting with $MeNO_2$ and precipitation with Et_2O. The dark red solid does not crystallise readily and cannot easily be further purified either by any other conventional means, therefore although shown to be clean by NMR spectroscopy the material was never isolated microanalytically pure.

Extreme difficulty was experienced both in the formation and isolation of the remaining complexes of interest, those chelated by the ligands bipzpy, terpz and bipzpyOH. In absence of sufficient quantities of the pure complex salts. These were not subject to electrochemical or further spectroscopic analysis beyond ^1H NMR. All homoleptic ruthenium(II) complexes of these ligands were observed by NMR and mass spectrometric analysis, however issues with solubility and the presence of numerous, what are presumed to be multinuclear impurities meant that the complexes were only ever obtained as intractable, near-black residues.

Particular trouble was had not just in the isolation, but in the formation of the $[Ru(bipzpyOH)_2]^{2+}$ dication during ventures to obtain it as its tetrafluoroborate salt **16a**. Initial synthetic efforts employed the use of heating to modest temperatures in ethylene glycol with ruthenium trichloride, and resulted mostly deep green solutions and insoluble black residues and pastes which were very cumbersome to dry sufficiently, and spectroscopically consisted of no identifiable species, which were probably majorly ruthenium(III) based. No observable precipitation occurred upon addition of tetrafluoroborate salts. Complete removal of all traces of ethylene glycol was achieved through the use of heating to extremely high temperatures at very low pressure, and multiple extractions with water allowed elimination of the ruthenium(III) species from the residue. The H_2O of the combined extracts was removed, and extraction with $MeNO_2$ removed the excess inorganic salts. Removal of the $MeNO_2$ yielded a pink-red solid in minute quantity, and evidence of complex dication formation was visible in the mass spectrum.

A second approach involved the use of $RuCl_2(DMSO)_4$, but only brown/green suspensions were ever obtained, and the complex appeared not to have formed from analyses of the solutions and residues during extraction attempts. Heating to higher temperatures gave only completely insoluble black solids, the makeup of which could not be concluded. Another method of interest involved the stepwise formation of the complex, relying on the preformed monochelated ruthenium(III) trichloride intermediate to react with a further equivalent of tridentate ligand, under relatively mild conditions involving the use of an appropriate non-coordinating additive as a reducing agent.[34-37] The method, which has a number of reported variants, has seen use with great success in the preparation of heteroleptic ruthenium(II) complexes chelated by tridentate ligands, most commonly derivatives of terpy.[10, 18, 35, 38-43] The monochelated ruthenium(III) intermediates possess extremely low solubilities, and though air stable are labile and troublesome to characterise.[18, 44] The crude, solid burgundy-brown precursor $Ru(bipzpyOH)Cl_3$ was used as collected from the original reaction vessel, as is often reported for monochelated precursors of this form, and reacted with a second equivalent of bipzpyOH in refluxing EtOH with a few drops of *N*-ethylmorpholine used as the reductant. The homoleptic complex appeared not to form, again with only black, intractable and uncharacterisable solids collected. It is noted that utilising this method, an attempt was made to isolate the ditetrafluoroborate salt of the heteroleptic dication $[Ru(terpyOH)(bipzpyOH)]^{2+}$, going via the intermediate $Ru(terpyOH)Cl_3$, but even in the presence of an excess of bipzpyOH during the second coordination only homoleptic $[Ru(terpyOH)_2]^{2+}$ was isolated as its ditetrafluoborate salt **19a**. The lability of the monochelated precursors is evident here, as is the drastically reduced basicity of bipzpyOH towards octahedral ruthenium(III) which does not coordinate at the lower reaction temperatures conditioned by this synthetic route.

Returning to the method of preparation of which most success has been achieved in the work on this series of complexes, it was shown that as in the other pyrazinyl and pyrimidyl coordinated ruthenium(II) complexes discussed above, the second chelation and reduction of the ruthenium core has a high barrier of activation and requires prolonged reaction times. Heating ruthenium trichloride with two equivalents of bipzpyOH to 150°C resulted in colourisation of the solution to a dark green much more rapidly than when held at 110°C. With extended time of heating, the formation of purely ruthenium(II) containing materials was judged to be complete after 8 days, as judged by the deep ruby red hue of the reaction solution. The complex, which failed to precipitate as its tetrafluoroborate salt even with addition of HBF_4 to ensure the phenolic group is fully protonated was obtained by drying at high temperature, and extracting multiple times with $MeNO_2$. Observable in the ^1H NMR, its signals corresponded to a single bipzpyOH environment about a fully diamagnetic

ruthenium(II) core (Table 12). The dark red solid was subject to no further analyses as the aromatic region is broadened and littered with signals corresponding to multiple ruthenium(II) containing impurities which we were unable to remove.

Complex Salt	3 / ppm	4 / ppm	3' / ppm	4' / ppm	5' / ppm	6' / ppm
12b	8.90	8.55	9.61	-	8.35	7.41
13b	10.03	-	9.76	-	8.42	7.48
16a[a]	8.55	-	9.53	-	8.33	7.62

Table 12 – Proton magnetic resonance signals for 12b, 13b and 16a which were observable in crude, inseparable samples of the complex materials; spectra were performed in CD_3CN unless otherwise stated. Spectra recorded on a Bruker Avance 500 FT 500 MHz spectrometer; [a]spectrum recorded in $MeNO_2$-d_3.

Interestingly, the other two complex dications which were unobtainable pure, $[Ru(bipzpy)_2]^{2+}$ and $[Ru(terpz)_2]^{2+}$ were also chelated by ligand backbones typified by distally coordinated pyrazinyl rings. These too necessitated high temperatures and long reaction times to promote reduction of all the ruthenium(III) centres to ruthenium(II), with **12b** requiring 4 days at 160°C and **13b** requiring 3 days at the slightly lower temperature of 130°C. Both reactions were performed analogously in ethylene glycol using ruthenium trichloride, and post reaction were heated under vacuum complete dryness to negate solubilisation by residual ethylene glycol during the salt exchange. Collected as dark purple red crude solids, ^{1}H NMR (Table 12) and mass spectrometric analyses permitted the identification of the complex dications in solution, however a multitude of other ruthenium(II) containing coordination compounds, likely oligomeric in nature, which were all but unidentifiable contaminated the material, rendering the collected solids unsuitable for further analyses.

4.3.2 Cyclometallated complexes containing 2,2':6,4''-terpyridine and dialkylimidazolium pyridine chelators

The complex salts of **20a**, **21a** and **22a** all contain at least one cyclometallated Ru-C bond about the octahedral coordination sphere, and are formed via very similar derivatives of the same reaction scheme involving cyclometallation of the ruthenium(III) core and reduction of the complex to the 2+ oxidation state by ethylene glycol, also functioning as the solvent at very high temperature.[22, 23, 45-48]

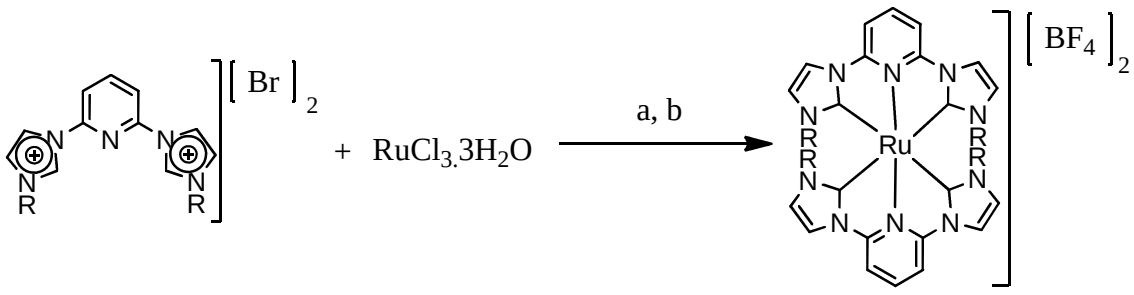

Figure 74 - Schematic representation of the one-pot synthesis of the disubstituted homoleptic cyclometallated ruthenium(II) ditetrafluoroborate salts; a) Stirring the two components together at 190°C in ethylene glycol; b) addition of H_2O and saturation with $NaBF_4$ before collection through vacuum filtration. R = methyl, isopropyl.

20a and **21a** were synthesised identically (Figure 74), using an exact replica of a synthetic procedure previously reported on the hexafluorophosphate analogue of **20a** which involves aerobically heating two equivalents of the pincer dialkylimidazolium pyridine ligand with ruthenium trichloride, utilising ethylene glycol not only as both the high boiling point solvent but also as a mild reductant.[22] Post-heating, any insoluble material was removed through simple filtration and $NaBF_4$ added to precipitate the desired ditetrafluoroborate salts, which transpired gradually during stirring over a period of 0.5 and 12 h for **20a** and **21a** respectively. The yellow powders as collected were dried thoroughly *in vacuo*, and $^{1}H/^{13}C$ NMR analyses were telling of high purity, with **20a**'s spectra congruous with that previously reported.[22] The ^{1}H chemical shifts about the alkylimidazolium pyridine backbone in **21a** were comparable to those in **20a**, showing a set of sharp, well-resolved signals telling of a single ligand environment, corresponding to averaged D_{2d} symmetry in fluid solution.

Using a similar method, adapted from the literature to prepare the hexafluorophosphate analogue of **22a**, the monochelated ruthenium(III) preformed precursor $Ru(terpy)Cl_3$ was heated to reflux above 200°C for 30 minutes with one equivalent of ctpy in ethylene glycol.[23] The filtered, viscous and intensely red coloured solution was treated with aqueous $NaBF_4$, and a burgundy solid collected. Spectroscopically this was shown to consist primarily of the homoleptic *bis*-terpy salt **18a** and considered no further. The filtrate was vacuumed to dryness with great difficulty to remove all trace of ethylene glycol, and the dark solid remaining chromatographed. Two observable bands were collected, a major red band which was characterised as **18a** after salt exchange, and a very small quantity of the cyclometallated heteroleptic complex **22a** as a bright pink/purple band.

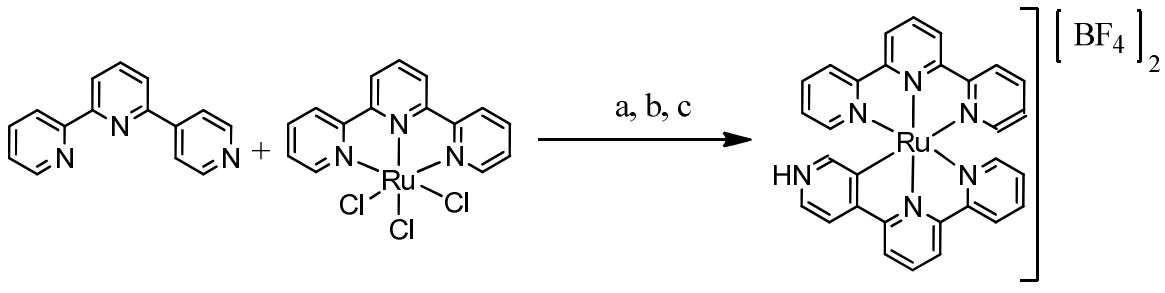

Figure 75 - Schematic representation of the synthesis of the heteroleptic cyclometallated ruthenium(II) ditetrafluoroborate salt 22a; a) Stirring the two components together at reflux in ethylene glycol; b) addition of $NaBF_4$ saturated H_2 before collection through vacuum filtration; c) recrystallisation from $MeNO_2/Et_2O$.

A second and far more successful preparation was then undertaken which takes into account the kinetic instability of **22a** (Figure 75). The reaction vessel was taken directly from

RT to reflux for 24 minutes, before rapid cooling to prevent thermal isomerisation and demetallation of the cyclometallated ligand in **22a** which was found to take place with extended reaction times. The solution, post-filtration, was notably less red in hue than in the first attempt at its synthesis, and after salt exchange appeared as a very intensely purple coloured powder. ^{1}H NMR spectroscopy confirmed that the heteroleptic complex salt **22a** was the dominant species, with only very minor daughter peaks corresponding to the homoleptic *bis*-terpyridyl salt **18a**. As such, the compound was analysed and used for subsequent doping as it was, without the need for lengthy and time consuming column chromatography which would jeopardise the modest yield of 77% which was obtained.

4.4 Electrochemical and spectroscopic probing of the complexes

4.4.1 Electrochemical studies

In the design of novel emissive ruthenium(II) *bis*-terpyridine derivatives, it is crucial to gain insight into the valence energy levels about both the ruthenium centre, and those localised primarily about the aromatic π system of the ligands, so as to understand the origin of an increase in fluorescence, or lack thereof, with respect to the parent *bis*-terpyridine complex **18a** which is non-emissive in fluid solution under ambient conditions. Electrochemical measurements, in particular cyclic voltammetry, provides a good measure of the valence levels, and those at higher energy through measurement of reduction potentials, and the degree of reversibility of the processes, and by extinction the stability of the solvated oxidised and reduced species. The ruthenium(II) complexes, which were isolated satisfactorily pure were subject to voltage sweeps. All complexes, with the exception of **15a** and **17b**, display fully electrochemically reversible ruthenium(III/II) processes. Without anomaly, all possess at least a single reduction process within the window of measurement, with the number of further observable reduction processes highly dependent upon the ligand backbone specific to the complex. The first reduction wave in ruthenium *bis*-terpyridyl derivatives has been accredited to a ligand based process, and in this inert series of complexes the difference between the first oxidation and reduction potentials can be considered to be a direct measure between the lowest energy MLCT process (Table 13).[7, 49]

Complex Salt	Σpk_a	M(III/II) / V	Reduction potentials / V	$E_{ox} - 1^{st} E_{red}$ / V
11a[a]	21.6	+1.14	-1.34[c], -1.64[d], -1.97[d]	2.48
14b[b]	14.8	+1.17	-1.25, -1.45, -1.8. -2.05[c]	2.42
15a[a]	3.32	+1.34[c]	-1.49[d]	2.83
17b[b]	10.8	+0.91[c]	-1.63[d]	2.54
18a[a]	31.2	+0.87	-1.66, -1.90	2.53
19a[a]	27.2	+0.69	-2.17[d]	2.86

Table 13 – Cyclic Voltammetric data for the successfully prepared non-cyclometallated ruthenium(II) complex salts. [a]Measurements performed in 0.1 M TBAT MeCN at a scan rate of 100 mV s^{-}. [b]Measurements performed in 0.1 M TBAH MeCN at a scan rate of 100 mV s^{-}. Couples are fully

electrochemically reversible, correspond to a one electron process and are quoted as their $E_{1/2}$ values unless otherwise stated against an Fc(III/II) internal reference. [c]Quasi-reversible process. [d]Chemically irreversible process, E_c quoted. ΣpK_a corresponds to the sum of the basicities of the respective heterocycles comprising the ligands.[50, 51]

As was predicted, all of the complexes exhibit oxidation waves more anodic than in the reference materials **18a** and **19a**, whose potentials match with those previously reported, in line with the stabilised valence t_{2g} orbital sets resulting from replacement of pyridine donors with less basic, electron deficient diazinyl and triazinyl heterocyclic donors.[18, 19, 52] The reduced reversibility of the oxidation in **15a** is probably attributable to a partial dechelation process, caused by the inability of the weakly coordinating bitrzpy to sustain coordination to the high energy ruthenium(III) state. The same explanation cannot be given in the case of **17b**, which may be due to a larger rearrangement of nuclear coordinates complicated by the acid-base equilibrium due to the highly acidic phenolic proton.[53] Additionally, replacement of a pyridyl donor cycle with that of a pyrazine about the proximal ring yields a comparable stabilisation of the t_{2g} level as that when both distal rings are changed from pyridyl to pyrimidyl rings, despite the much reduced combined basicity in the latter (Table 13), telling of the significantly stronger Ru-N_{prox} interaction.

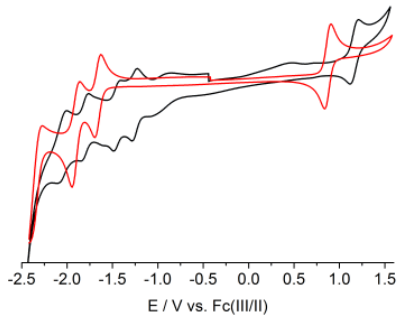

Figure 76 – Cyclic voltammograms of the ruthenium(II) complex salts 14b (black) and 18a (red). The voltammograms were measured in 0.1 M TBAH MeCN and 0.1 M TBAT MeCN for 14b and 18a respectively, at 100 mV s^{-1}. The spikes in current above 1.3 V and below -2.3 V arise due to oxidation and reduction respectively of the solvent.

As noted, the number of reduction processes varies appreciably between complex to complex, with both of the hydroxy substituted complexes **17b** and **19a** only exhibiting chemically irreversible processes. **11a** and **14b** show further reductions than the parent complex **18a**, which is a probable combination of their appearance within the solvent window because of their more anodic nature, but also a result of the lower energy π* molecular orbitals' increased stabilisation towards reduction without warranting destruction of the complex coordination sphere. Indeed **14b** exhibits two distinct pairs of reduction waves (Figure 76), each individual wave corresponding to a one electron process, which are

tentatively associated with sequential reduction of each ligand, followed by a second reduction of each ligand.[7]

The separation between first oxidation and reduction wave, E_{ox} – 1^{st} E_{red}, clearly displays that **11a** and **14b** possess a reduced energy gap between the t_{2g} set and the lowest π* level than the parent complex (Table 13), which is promising in view of achieving not only lower energy emission, but also of diminished accessibility of the excited non-emissive ^{3}MC state from the excited ligand π* levels with longer emission lifetimes. One cannot infer too much from the voltage separation between the potentials in the case of **15a** and **17b** however, as lack of chemical reversibility of both processes have meant that, as the E_{pa} and E_{pc} values are all that is deducible the separation between the two potentials is exaggerated.

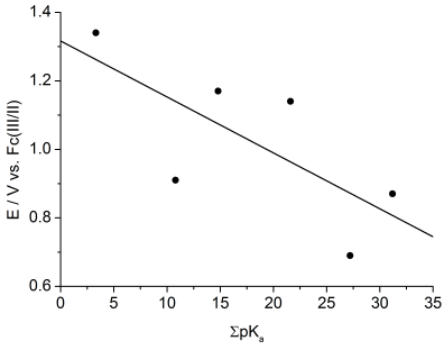

Figure 77 – Plot of the sum of the ligand basicities, ΣpK_a, against the M(III/II) formal oxidation potentials vs. the Fc(III/II) couple. For the irreversible processes the E_{pa} values have been used.

A plot of the first oxidation wave potentials of the series of ruthenium(II) complexes against the combined basicities of the heterocyclic donors about the ligand backbones reveals a rough trend which, as expected the oxidation potentials increase as the basicity of the chelating ligands is reduced (Figure 77). The trend is far from linear, as mentioned the oxidation potentials have increased sensitivity towards substitution and alteration of the proximal donor's basicity by virtue of a stronger and shorter Ru-N interaction. **17b** and **19a** deviate notably from the roughly linear trend, which can be explained by the fact that the reference basicity of the hydroxypyridine cycle which necessarily contributes to the calculated ΣpK_a value also accounts for the acid-base equilibrium of the phenolic group, resulting in a quoted value of smaller magnitude than is actually probably the case in reality in the coordinated moieties.

4.4.2 UV/Vis spectroscopy: investigation into the lowest energy MLCT band maxima

The UV/visible/near infra-red spectroscopic properties of the ruthenium complexes were investigated between 200 and 900 nm, both to infer further information on valence energy level separation within the terpyridine derivative series, and across the entire range

of complexes subject to discussion to deduce an appropriate excitation wavelength with which to screen for fluorescence. All complex salts within this series were readily soluble in MeCN in which the spectra were obtained and thus no discussion of solvent effects is included. The major absorption maxima, daughter peaks and any discernible shoulders have been tabulated and their extinction coefficients in acetonitrilic media quantified (Table 14).

Complex Salt	λ / nm (ε / dm^3 mol^{-1} cm^{-1})
11a	249 (34505), 274 (46969), 313 (53974), 344 (39605), 474 (15749), 512 (5701) *sh*
14b	267 (17875), 303 (35546), 322 (16276) *sh*, 457 (5647) *sh*, 494 (8518)
17b	251 (32820), 289 (14638), 378 (4496), 481 (5658)
18a	270 (37743), 308 (62063), 329 (23667) *sh*, 440 (8784) *sh*, 475 (14190)
19a	240 (44006), 267 (40047), 304 (49397), 349 (5882) *sh*, 486 (12945)
20a	236 (45258), 273 (34902), 280 (32759) *sh*, 345 (14109), 383 (18983)
21a	236 (39836), 273 (31790), 281 (30115) *sh*, 346 (11336), 384 (15745)
22a	203 (30867), 235 (31922), 274 (27039), 312 (33232), 360 (4763), 435 (3405) *sh*, 509 (8294)

Table 14 – UV/vis/NIR spectroscopic data for the set of ruthenium(II) complex salts in MeCN at 298 K. *Sh* denotes a shoulder.

The homoleptic ruthenium(II) *bis*-terpyridine derivatives, **11a**, **14b**, **17b**, **18a**, and **19a** possess broadly similar spectra, as one would expect, with the most notable differences arising in band shape and position of the low energy MLCT region, as well as variation in the number of peak maxima in the high energy domain (Figure 78). Transitions within the higher energy region, that is below 400 nm will not be scrutinised in detail as it is characterised mainly by intraligand excitations and higher energy MLCT absorptions which would be unlikely to yield emission within the visible spectrum.

The low energy MLCT region falls between 400 and 600 nm, and the band in the spectra of **11a**, **14b** and **18a** clearly consists of two if not more distinct transitions within the absorption envelope evident from the non-symmetrical band shapes. A distinct low energy shoulder is present in **11a**'s spectrum at 512 nm, whereas **14b** appears to possess a slightly less distinct shoulder that is present at higher energy at 457 nm. In contrast **17b** and **19a** both exhibit more symmetrical, highly broadened envelopes in this region because of hydrogen bonding both intermolecularly and to acetonitrile solvent molecules. Observing the lowest energy MLCT envelopes (Figure 78) more closely, the band maxima of the reference complexes, **18a** and **19a** whose spectra are consistent with the literature are clearly at higher energy than those complexes possessing distal diazinyl fragments, **14b** and **17b**.[7, 18, 52, 54] The situation is slightly different in **11a**, the only complex in the series to possess the weakly basic pyrazine donor in the proximal location, whose band maximum is, surprisingly, almost identical to that of **18a**, yet the band has a clear shoulder, characteristic of a new, lower energy transition.

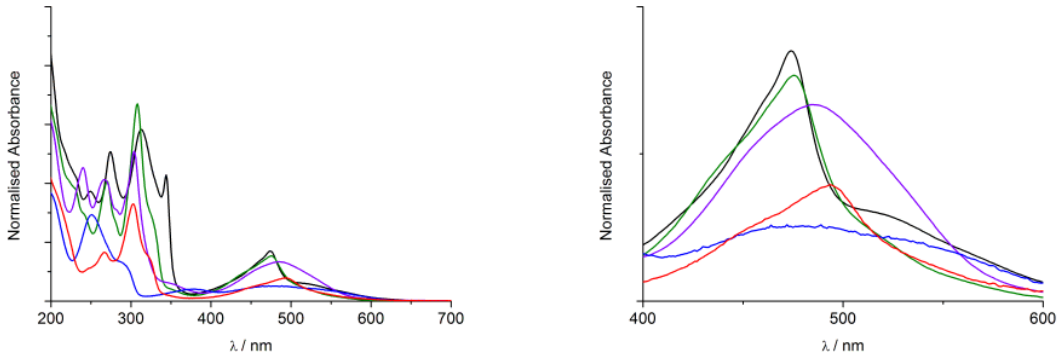

Figure 78 – Absorption spectra for the azinyl *bis*-terpyridyl derivative ruthenium(II) complex salts 11a (black), 14b (red), 17b (blue), 18a (green) and 19a (purple) run as 1 x 10^{-5} mol dm^{-3} MeCN solutions at 298 K. Left: Entire region of the spectra; Right: 400-600 nm region of the spectra encompassing the lowest energy MLCT envelope.

At this point it is necessary to mention two things. The first is that the bathochromic effect for those complexes which do possess red-shifted absorption maxima or shoulders with respect to **18a**, is less profound in the ruthenium(II) *bis*-terpyridyl derivatives than it is in their iron(II) analogues (Chapter 3). The second is that, both **11a** and **14b** exhibit an Ru(III/II) potential markedly higher than is seen in the electron poor [Ru(4-methylsulfonyl-terpyridine)$_2$]$^{2+}$ dication yet, surprisingly, **11a** has an absorption maxima which is practically unchanged from **18a**, significantly higher in energy than in the methylsulfonyl complex.[18, 19] The smaller absorption maxima shifts relative to the iron(II) series are attributable to the greater prominence of π-back-donation from the ruthenium because of its larger, more diffuse t_{2g} set as the ligands are made more electron deficient. This manifests in comparably similar variation in M(III/II) redox potentials across the two series, however the MLCT band positions appear at higher energies than expected due to the slight destabilisation of the π*-lobes involved in valence backdonation which makes a markedly higher contribution to the overall complex stability. This is reflected in the greater voltage separation between the M(III/II) oxidation and the first reduction potential in the ruthenium(II) complexes than in their iron(II) analogues (Table 13).

The increased backbonding contribution as the pyridyl donors are replaced with diazinyl heterocycles are is also partially responsible for the higher energy maxima in the absorption spectra than in homoleptic substituted complexes of comparable ruthenium(II) stabilisation. In contrast to terpyridines substituted at the central pyridine 4-position with appropriately electron withdrawing groups, the lowest energy π* levels about the diazinyl ligands are in closer proximity to the ruthenium(II) core. The net effect is that, with respect to the parent complex **18a**, replacing a pyridyl donor with a diazine stabilises the t_{2g} levels more than the π* levels about the ligands, opposite to the effects observed in electron deficient

substituted bis-terpyridine complexes of ruthenium(II). Hence the transitions occur at higher energies than predicted on the basis of ligand basicities and position of the Ru(III/II) redox couple.

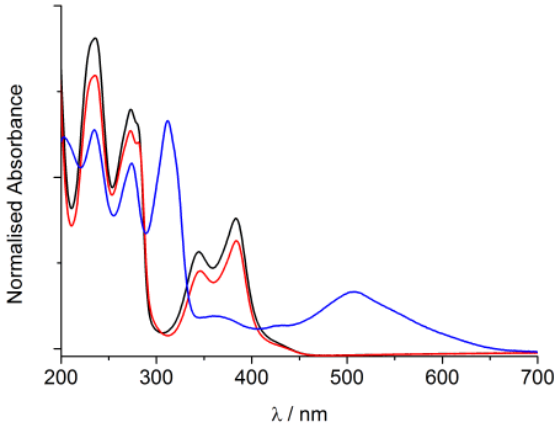

Figure 79 – Absorption spectra for the cyclometallated ruthenium(II) complex salts 20a (black), 21a (red), and 22a (blue) run as 1 x 10^{-5} mol dm^{-3} MeCN solutions at 298 K.

The spectra of the homoleptic alkylimidazolium complexes **20a** and **21a** are quite different from that of the heteroleptic species **22a**, with the latter characterised by a large, broad envelope above 400 nm, whereas the former two do not absorb appreciably above 450 nm (Figure 79). In **20a** and **21a**, the two lowest energy sharp absorptions between 300 and 400 nm are primarily of MLCT nature, appearing at relatively high energy due to the very strong σ interaction comprising the cyclometallated bonds.[55, 56] Cyclometallation in place of an Ru-N interaction causes significant increases in ligand field strength, causing the filled t_{2g} levels to reside at highly stabilised low energy levels.[14, 17, 23, 57] The 5-membered rings of the cyclometallated distal rings also contribute towards the magnitude of the MLCT absorptions, as the smaller, more constrained rings naturally have higher energy π* lobes which take part in the MLCT excited states. The spectra of **20a** and **21a** are predictably all but indiscernible, with **21a**'s slightly lower extinction values within the absorption manifolds probably arising due to minor inaccuracies of measurement during sample preparation.

The MLCT region encompasses a larger range of energies in **22a**, with the envelopes assigned as mainly MLCT in nature as their extinction values fall between 4,000 and 10,000. The lowest energy maxima at 509 nm which is at the centre of a broad envelope above 450 nm originates from at least one transition involving the t_{2g} levels and the non-cyclometallated tpy moiety. Two other less intense absorptions are visible at higher energy, with the maxima centred at 360 nm ascribed to an MLCT transition to the cyclometallated moiety Ctpy. The final transition within the manifold, located at 435 nm, probably involves

transferral of an electron from ruthenium to one of the bipyridyl fragments comprising both the cyclometallated and non-cyclometallated ligands.[58]

4.4.3 Emission studies

To assess suitability of the complexes for use as fluorescent dopants, the emission was screened at room temperature in fluid MeCN solution using an appropriate excitation wavelength (Table 15). The homoleptic terpyridyl complex series were excited at the absolute maxima of the low energy MLCT manifold even in the presence of more daughter absorptions and shoulders. **20a** and **21a** were screened for emission by exciting at the maxima of both distinct MLCT peaks and it was found that exciting at the lower energy of the two generated greater emission intensities, as has been reported for a number of salts of **20a**.[22, 45] **22a** emitted significantly more intensely when excited at 354 nm than at either of the two lower energy bands.

Complex Salt	Excitation wavelength / nm	Emission maxima / nm
11a	474	675, 625 *sh*
14b	493	652
17b	477	-
18a	475	614
19a	484	-
20a[a]	383	531
21a[a]	384	530
22a	354	783

Table 15 – Relevant excitation wavelengths and emission band maxima for the ruthenium(II) complex salts in MeCN at 298 K as 5 x 10^{-5} mol dm^{-3} solutions unless otherwise stated; *sh* denotes a shoulder. [a]At 1 x 10^{-5} mol dm^{-3}.

Neither of the complex salts with hydroxy appendages show emission at room temperature making them unsuited for use as dopants. The hexafluorophosphate salt of **19a** is weakly emissive at 77 K, and it is entirely possible that the same is true of **17b** but no low temperature measurements were performed.[19] The transient hydrogen bonding in fluid solution which both complexes are capable of is accredited to the quenching of any potentially emissive excited states. The complexes of ligands consisting entirely of parent azinyl heterocycles, **11a**, **14b** and **18a** all show emission in the 600 – 750 nm region, with **18a** possessing the very weak emission band at 614 nm as typified in previous studies.[7, 18, 19, 54] **11a** and **14b** show an increase in emission intensity with respect to **18a**, the largest of which belongs to **14b**. **11a**'s emission spectrum is clearly comprised of two distinct emissive levels, at 675 nm and a shoulder at 625 nm which are lower in intensity than in **14b**'s single sharper band. The emission maxima are all of lower energy than **18a**, indicative that the energy gap between the ^{3}MLCT and ^{3}MC states has been increased and non-radiative decay has been impeded (Figure 80). The larger ligand field of **11a** compared to **18a** is likely to be the origin of these effects as even though both complexes were excited at essentially

the same energy, the higher lying ^{3}MC states in **11a** result in a concomitant increase in the recorded emission.

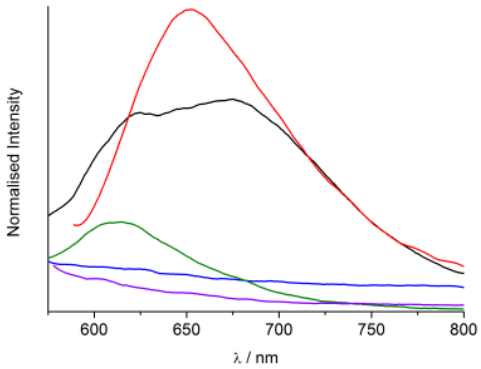

Figure 80 – Normalised emission data for the azinyl *bis*-terpyridyl derivative ruthenium(II) complex salts 11a (black), 14b (red), 17b (blue), 18a (green) and 19a (purple) as 5 x 10^{-5} M solutions in MeCN.

The emission of **20a** is caused by decay from a ^{3}MLCT state back into the complex ground state and is located at a much higher energy than in any of the *bis*-terpyridine derivatives in this study because of the poorly overlapping, electron dense π* lobes of the planar ligand backbone.[22] Replacement of the *N*-methyl groups with that of N-isopropyl appendages as in **21a** does not incur major changes upon the features of the spectrum, however the intensity of emission is slightly higher than in **20a** (Figure 81). This opposes the lower extinction coefficients of the excitation transitions as deduced from the UV/vis/NIR spectra of the two complexes and can be taken as proof of notably increased emission in **21a**. In the absence of detailed computational calculations as to the cause of this effect, increased rigidity imparted by the isopropyl substituents which make close steric contacts with the ruthenium(II) core in the xy plane are thought to be responsible. Indeed the larger isopropyl group probably does impose a small increase in conformational rigidity with respect to methyl groups, relinquishing spin orbit coupling in the excited state and, thus, resulting in a small increase in emission.

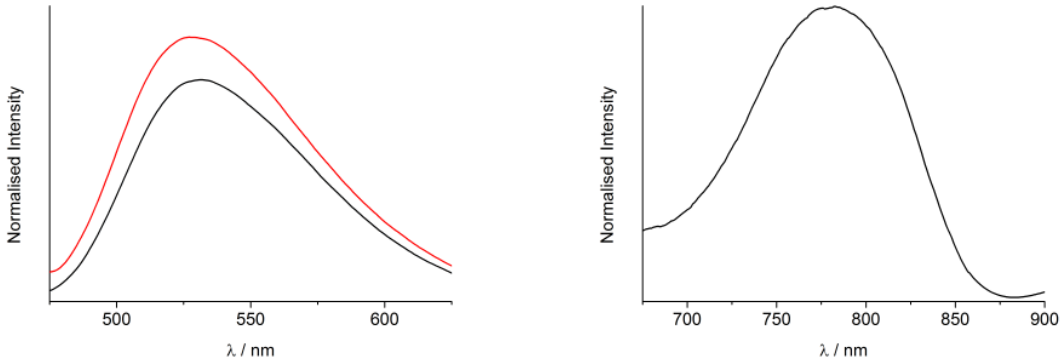

Figure 81 – Left: normalised emission data for the *bis*-dialkylimidazolium ruthenium(II) complex salts 20a (black) and 21 (red); right: normalised emission data for the heteroleptic ruthenium(II) complex salt 22a; all emission data performed upon 1 x 10^{-5} M solutions of the respective salts in MeCN.

22a emits the longest wavelength of light by some margin, caused by the decay of a low-lying triplet about the π* system of Ctpy back into the complex ground state. Emission intensity is not as high as in the homoleptic cyclometallated complexes **20a** and **21a** because of increased competition for radiationless decay directly from the ^{3}MLCT into the ground state as dictated by the energy gap law. The band shape and position match that as documented on the analogous hexafluorophosphate salt, and it is unlikely that emission would vary by any great extent between the two salts whose anions possess a similarly weak coordinating ability.[23]

4.5 Doping emissive ditetrafluoroborate complex salts into an inert spin crossover host lattice

The hybrid materials were prepared by crystallising $MeNO_2$ solutions of **20a** and **22a** together with the spin crossover iron(II) salt **25a** through slow diffusion of Et_2O, yielding solid solutions of the form $[Fe(1\text{-}bpp)_2]_x[Ru(MeImpy)_2]_{1-x}[BF_4]_2$ and $[Fe(1\text{-}bpp)_2]_x[Ru(tpy)(Ctpy)]_{1-x}[BF_4]_2$, where x = 0 – 1. The ruthenium(II) dopants of study were chosen from the set of screened complex salts on the basis of their ease of preparation, availability and purity as homogenous tetrafluoroborate salts, emissive ability and likelihood of incorporation into the host lattice. The latter factor was confirmed, where possible, by crystallographic measurements on the pure ruthenium(II) complex salts to assess crystal packing, shape and volume occupied by the complex dications. Furthermore, mixed solutions of the complexes in $MeNO_2$ were subject to NMR analysis over a period of days to check for ligand exchange or decomposition of the mixed solutions upon standing. Elemental analyses and magnetic measurements in tandem were used to quantify the precise value of x in the solid solutions, and powder patterns were collected, where appropriate, to assess phase purity.

4.5.1 Using highly emissive bis-(2,6-di(1'-methylimidazolium-3'-yl)pyridine) ruthenium (II) tetrafluoroborate

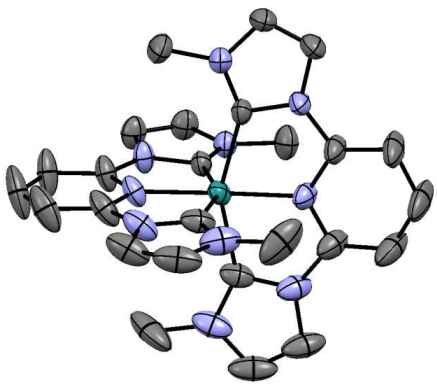

Figure 82 – View of one of the two unique complex dications in 20a.$MeNO_2$ at 150 K; thermal ellipsoids plotted at the 50% level; H atoms omitted for clarity. Atom colour code: carbon (grey), nitrogen (periwinkle) and ruthenium (turquoise).

20a forms bright yellow cuboidal blocks upon crystallisation by slow diffusion of Et_2O into $MeNO_2$ solutions of the complex which were determined to be nitromethane solvates in composition, **20a**.$MeNO_2$. The complex crystallises in the monoclinic space group C2/c, containing two unique dications, one of which is approximately D_{2d} symmetrical (Figure 82). There is a complete absence of the terpyridine embrace motif and there are no approximately planar π-π contacts between distal rings of neighbouring complex molecules (Figure 83). The average volume occupied per dication was calculated to be 724 $Å^3$, subtracting the volumes of the tetrafluoroborate counterions and $MeNO_2$ solvate molecules from the unit cell, taken as 38 and 71 $Å^3$ respectively.[59, 60] The calculated volume of 724 $Å^3$ is notably smaller than that taken from the structure of its tetraphenylborate salt, as solved by Chung *et al*, which gives an occupancy of 896 $Å^3$, taking the volume of the tetraphenylborate anion as 323 $Å^3$.[22, 59] The structure of the tetraphenylborate salt significantly contains far greater voids, by virtue of its completely different crystal packing, which will, at least in part, account for the much larger dicationic volume calculated for this salt. It is therefore more reliable to use the averaged dicationic volume of 724 from the structural data of **20a**.$MeNO_2$, which is closer to the true value as it corresponds to a lesser degree of void space in the crystal.

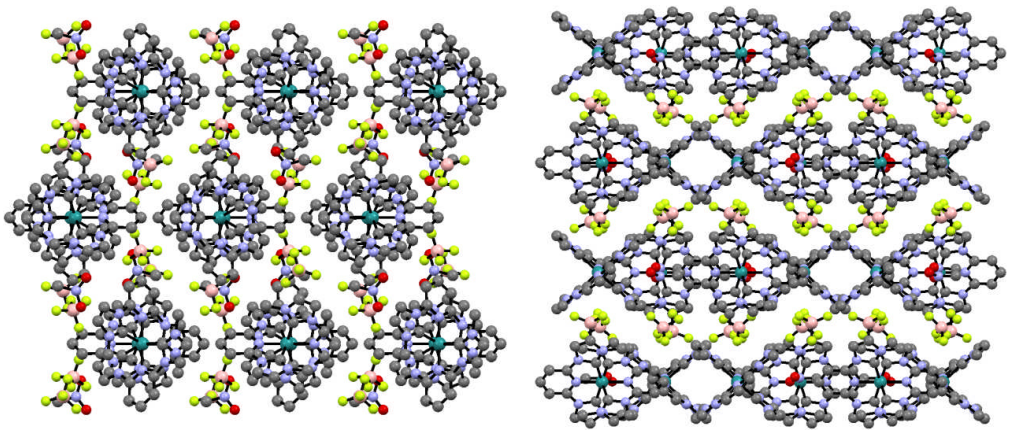

Figure 83 – Crystal packing of 20a.$MeNO_2$ 150 K, viewed along the crystallographic a axis (left) and the crystallographic c axis (right); ; H atoms omitted for clarity. Atom colour code: boron (pink), carbon (grey), fluorine (chartreuse yellow), nitrogen (periwinkle), oxygen (red) and ruthenium (turquoise).

The LS and HS volumes of the iron(II) complex dication in **25a** are 587 and 621 $Å^3$ respectively, making the $[Ru(MeImpy)_2]^{2+}$ dication in **20a** 17 – 23% larger.[61] The basis for the investigation, which is the successful doping of **18a** into **25a** with retained functionality, allowed the 677 $Å^3$ ruthenium(II) dications to be incorporated into the host lattice, despite being 9 – 15% larger in volume.[5, 6] A complex stability ^1H NMR study in $MeNO_2$-d_3 was conducted, to ensure that mixed solutions of the salts were inert towards one another and

didn't undergo any ligand redistribution or decomposition over time. Over a period of 17 days, the paramagnetic region remained visibly unchanged, containing the four broad contact shifted resonances at 34.3, 36.3, 56.6 and 61.3 originating from the 3 + 5, 5', 4' and 3' positions respectively about the ligand backbone of the $[Fe(1\text{-bpp})_2]^{2+}$ dication in **25a**. Over 3 days the aromatic region of the diamagnetic spectrum suggests no change in speciation, with all of the resonances corresponding to $[Ru(MeImpy)_2]^{2+}$ in **20a** remaining sharp and display the appropriate splitting (Figure 84). Further along in the study, however, the signals began to broaden and lose their signature features, up until the final spectrum was acquired after 17 days when no coupling could be detected in the 1D spectrum, and two new distinct resonances were observed at 6.57 and 8.71. The signal at 6.57 is characteristic of the 3' position about a pyrazolyl ring coordinated to a diamagnetic transition metal centre, suggestive of a new, diamagnetic 1-bpp containing complex centre, which could be either metal as the strong field MeImpy ligand would result in a purely LS iron(II) configuration if MeImpy were to coordinate.[62, 63] It is thought that, though the chelated ruthenium(II) complexes are inherently very stable, a slow dechelation process is occurring yielding free MeImpy, which then coordinates to the substitutionally labile HS iron(II) centres in **25a**, yielding the heteroleptic diamagnetic species $[Fe(1\text{-bpp})(MeImpy)]^{2+}$ which is in equilibrium with $[Fe(1\text{-bpp})_2]^{2+}$.[61] Novel ruthenium(II) species were disregarded, as octahedral imine complexes of ruthenium(II) typically have very high energy barriers towards formation. Though the complexes are undergoing ligand rearrangements, the process is evidently occurring slowly enough that the concentration of the new iron(II) species is negligible over a period of 3 days, which is typically the upper threshold of the solid solution crystallisation process employing Et_2O diffusing into $MeNO_2$ at ambient temperature.

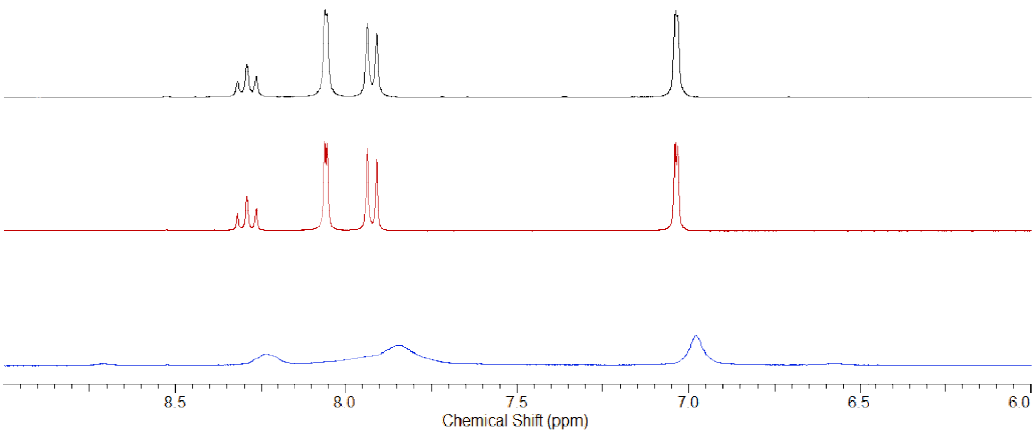

Figure 84 – The aromatic diamagnetic region of the spectrum of equimolar mixed solutions of 20a and 25a in $MeNO_2$-d_3 after 1 day (black), 3 days (red), and 17 days (blue). Spectra were recorded at 300 MHz on a Bruker DPX300 FT NMR spectrometer.

With the complexes deemed sufficiently stable to endure crystallisation over a 2 -3 day period, $MeNO_2$ solutions of the complexes in equimolar ratio were combined, and Et_2O diffused gradually into the crystallisation vessels. The doping process, which was repeated several times, was unsuccessful by visual inspection, which yielded crystals of two distinctly different materials. Semi-translucent brown crystals were observed to have formed preferentially on the inside walls of the crystallisation vials and the second form appeared as a bright yellow microcrystalline solid on the base. The two materials were separated manually and subject to ^{1}H NMR spectroscopic measurements. This concluded that no co-crystallisation had transpired, with the brown crystals exhibiting an NMR spectrum of pure **25a**, and the yellow microcrystalline exhibiting a total absence of any paramagnetically shifted signals. Mass spectrometry substantiated this, only displaying peaks originating from the parent dication in **20a** on upon the profile of the yellow microcrystalline material.

With pure **25a** crystallising preferentially before **20a**, it is apparent that the complex dications are structurally incompatible with one another as a co-crystallised ditetrafluoroborate salt. The significant increase in size of the ruthenium(II) diction as compared to the iron(II) complex molecules will be, at least in part, responsible for the inability of the two materials to crystallise homogenously alongside one another. It is unsure, however, if this is the deciding factor, as the methyl groups ortho to the coordination interaction of the distal rings in **20a** exert a repulsive effect preventing off-centre π-π stacking of distal rings in neighbouring complex molecules that might be responsible for the hindrance in adoption of the terpyridine embrace motif, necessary for co-crystallisation. It is of note that in octahedral complexes *bis*-chelated by the structurally related ligands 2-6,di(6'-methylpyridin-2'-yl)pyridine, 2,6-di(3'-methylpyrazol-1'-yl)pyridine and 2,6-di(1'-methylpyrazol-3'-yl)pyridine the formation of the terpyridine embrace in the lattice has not been reported.[64-66]

4.5.2 Successful doping of weakly emissive ((2,2':6,4''-terpyridine)(2,2':6',2''-terpyridine)) ruthenium (II) tetrafluoroborate

Direct structural information on the nature of the $[Ru(tpy)(Ctpy)]^{2+}$ dication in **22a** cannot be discussed as it does not readily form single crystals suitable for X-ray diffraction. A multitude of attempts to obtain singly crystalline material of the salt were made, using a host of different solvent combinations, however the material persisted in precipitating out as a fine, extremely dark purple powder or, in one instance, very thin pink/purple translucent crystalline films. The structure of the hexafluorophosphate salt has remained elusive and even our attempts to crystallise the tetraphenylborate salt, which have a tendency to do so readily because of the π-π stacking ability of the appended phenyl rings ended in failure. Though the size of the dication is likely to be of similar magnitude to that of the parent *bis*-

terpyridyl complex, it is entirely possible that its shape could differ somewhat as a result of induced distortions about the coordination sphere brought about by the pyridinium ring's potential to hydrogen bond. As this could not be confirmed, the decision was made to proceed is using the material as a luminescent dopant.

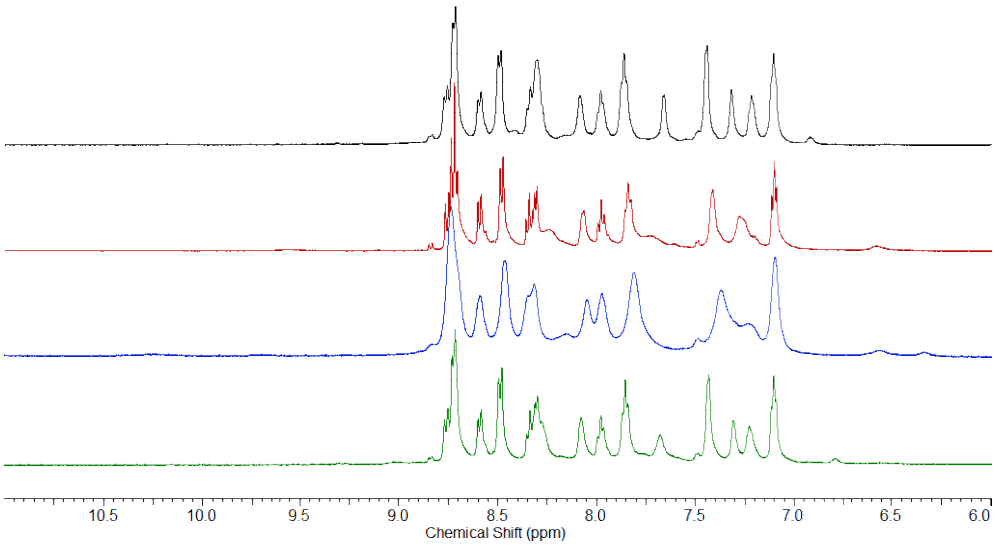

Figure 85 – The aromatic diamagnetic region of the spectrum of equimolar mixed solutions of 22a and 25a in $MeNO_2$-d_3 after 1 day (black), 5 days (red), 19 days (blue) and 22 days after vigorous shaking (green). Spectra were recorded at 300 MHz on a Bruker DPX300 FT NMR spectrometer.

Over a period of 2 – 3 days, the approximate timescale for solid solution formation, mixed solutions of the two salts **22a** and **25a** were sufficiently inert towards dechelation and ligand rearrangement, though initially it appeared otherwise. Left to stand together over a period of days in $MeNO_2$-d_3, the ^{1}H NMR spectrum was initially identical to the individual salts' spectra superimposed. During the course of the experiment, the paramagnetic region remained unchanged from that of pure **25a**. However the diamagnetic region underwent a number of changes which, at first, appeared quite complicated (Figure 85).

After five days, a number of signals had broadened noticeably and the signal corresponding to the 6' proton about the Ctpy ring had, inexplicably, disappeared. It is known that with prolonged heating, the ruthenium(II) *bis*-terpyridyl parent complex is the preferred species however the spectrum did not display evidence of any rearrangement into this species at room temperature (Table 16).[23] By day 19 the signals in the diamagnetic spectrum had broadened further, with two new signals appearing around 6.5 ppm suggestive of at least one diamagnetic centre coordinated to a pyrazolyl ring. **23a** and **24a**, containing both homo- and heteroleptically bound 1-bpp to a ruthenium(II) core, were prepared to compare with the unknown signals in the spectrum after 19 days. As the region is complicated and, by day 19, heavily broadened, it was impossible to deduce the exact nature of the newly formed complex species, but the signal near 6.5 ppm in all probability

corresponds to a diamagnetic heteroleptic complex coordinated by 1-bpp. It was noticed that significant precipitation of a dark solid had occurred in the NMR tube after 22 days, which was promptly shaken profusely until the material had fully redissolved. The spectrum returned to appear as it had done on the first day, and it was concluded that **22a** had, over time, precipitated out of solution which was responsible for most of the changes observed in the spectra before the tube was shaken. Nevertheless, there was spectral evidence for the formation of a heteroleptic complex, presumably of iron(II) due to its higher lability but the process was considered insignificant over a 2 – 3 day period.

Ligand	Position	**22a**	**18a**	**23a**	**24a**
Ctpy	3	8.75	-	-	-
	4	8.32	-	-	-
	5	8.70	-	-	-
	3’	8.58	-	-	-
	4’	7.97	-	-	-
	5’	7.21	-	-	-
	6’	7.65	-	-	-
	1’’	12.16	-	-	-
	2’’	7.31	-	-	-
	5’’	8.29	-	-	-
	6’’	8.07	-	-	-
Terpy	3	8.71	8.82	-	8.72
	4	8.28	8.48	-	8.43
	3’	8.48	8.55	-	8.52
	4’	7.85	7.94	-	7.97
	5’	7.10	7.19	-	7.23
	6’	7.44	7.48	-	7.53
1-bpp	3	-	-	8.26	8.33
	4	-	-	8.58	8.62
	3’	-	-	7.18	7.12
	4’	-	-	6.61	6.57
	5’	-	-	8.83	8.82

Table 16 – ^{1}H NMR chemical shifts for the possible heteroleptic and homoleptic ruthenium(II) species arising from ligand exchange of mixed solutions of 22a and 25a. Spectra recorded in $MeNO_2$-d_3 on a Bruker Avance 500 FT 500 MHz spectrometer.

Mixed $MeNO_2$ solutions of the complexes, of the form $[Fe(1\text{-}bpp)_2]_x[Ru(tpy)(Ctpy)]_{1-x}[BF_4]_2$ where x = 0.9, 0.75, 0.5, 0.25 and 0.1 were crystallised slowly by diffusion of Et_2O. The polycrystalline material which ranged from burgundy to deep purple in hue was manually extracted and left to dry in air. Microanalysis determined the actual composition of the solid solutions as X = 0.91, 0.82, 0.59, 0.25 and 0.17. Subject to susceptibility measurements between 10 and 300 K, the compositions were confirmed by comparison of the high temperature plateau $\chi_m T$ with respect to that of **25a** at 3.80 $cm^3\ mol^{-1}$ K. As the value of X is lowered, the $T_{1/2}$ moves to lower temperature (Figure 86) and the transitions

become less abrupt, with complete loss of hysteresis at X = 0.59. Oddly, at X = 0.17 the sharp feature of the transition is lost completely, showing a very gradual slope to higher $\chi_m T$ as the temperature is ramped, indicative of an almost entirely diamagnetic material in which the minority iron(II) centres remain predominately in the LS configuration. The loss of cooperativity as the concentration of iron(II) centres within the material is reduced is suggestive of successful doping as statistically the nearest neighbours of switching iron(II) centres are increasingly likely to be the ruthenium(II) dopant dication. The progressive decrease in $T_{1/2}$ tentatively supports this, with the predictably larger ruthenium(II) dication yielding lower cumulative lattice pressures causing a small stabilisation of the enlarged HS ions which is markedly more profound than in the analogous **18a** doped materials.[6]

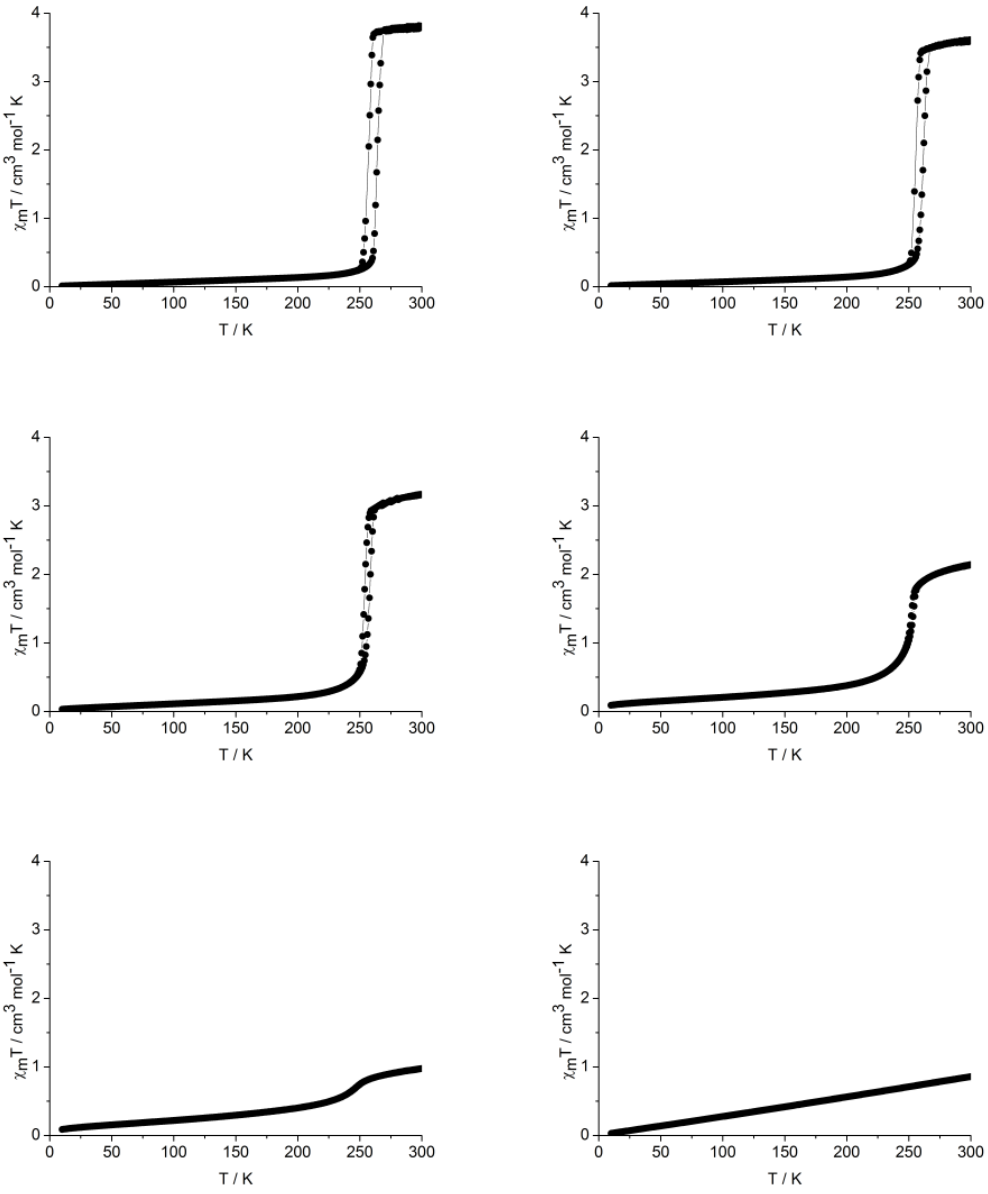

Figure 86 – Magnetic susceptibility curves for the solid solutions of form $[Fe(1\text{-}bpp)_2]_x[Ru(tpy)(Ctpy)]_{1-x}[BF_4]_2$ scanned in cooling and warming modes between 10 and 30 K, where x = 1 (top left), 0.91 (top right), 0.82 (middle left), 0.59 (middle right), 0.25 (bottom left) and 0.17 (bottom right).

Powder patterns were acquired on the five solid solutions in addition to the pure constituent components **22a** and **25a** (Figure 87). The patterns for the materials with x = 0.91 and 0.82 are almost identical to that of pure **25a** indicating the material has crystallised predominantly in the $P2_1$ space group, with peak intensity decreasing slightly as x is decreased with increasing ruthenium(II) dopant concentration. Furthermore, the peak shapes are not significantly broadened, and tend to slightly lower angle than in pure **25a** in agreement with the more voluminous unit cell that the larger ruthenium(II) dications would be expected to promote. As x is decreased further, the peaks broaden slightly which is often a sign of reduced crystallinity. The x = 0.25 and 0.17 materials contain a profile which matches almost identically to that of pure **22a** showing that these doped solid consist primarily of the same crystal phase as the ruthenium(II) dopant, however in x = 0.25 daughter peaks at higher angle coincide with those of **25a**, suggesting a lingering fraction of the $P2_1$ phase. Where x = 0.59 and the dopant-to-host ratio is closest to 1:1 there is not only a larger poorly crystalline component, as evidenced by poor signal-to-noise ratio and peak broadening but also clearly a mixture of crystalline phases. The $P2_1$ phase dominates as its peak intensities are larger which is expected on the basis of having a marginally higher concentration of host **25a**. The daughter set of peaks belong to **22a**'s phase, as the peak positions match with those of the pure dopant, which is best shown by observing the prevalence of the peak at 2Θ = 9.48 in the pattern of x = 0.59, which is the lowest angle peak of major intensity in pure **22a** and doesn't overlap with any peak observed in **25a**. Despite the existence of at least two phases in x = 0.59, both are thought to contain homogenously mixed solid solutions as compared to x = 0.82, the hysteresis has been completely lost and the transition curve has not only broadened, but $T_{1/2}$ resides at 252 K, lower than the $T_{1/2}$ of 256 K in x = 0.82 and suggestive of the reduced cooperativity and HS stabilisation caused by the statistical replacement of iron(II) nearest neighbours with the larger inert ruthenium(II) dications.

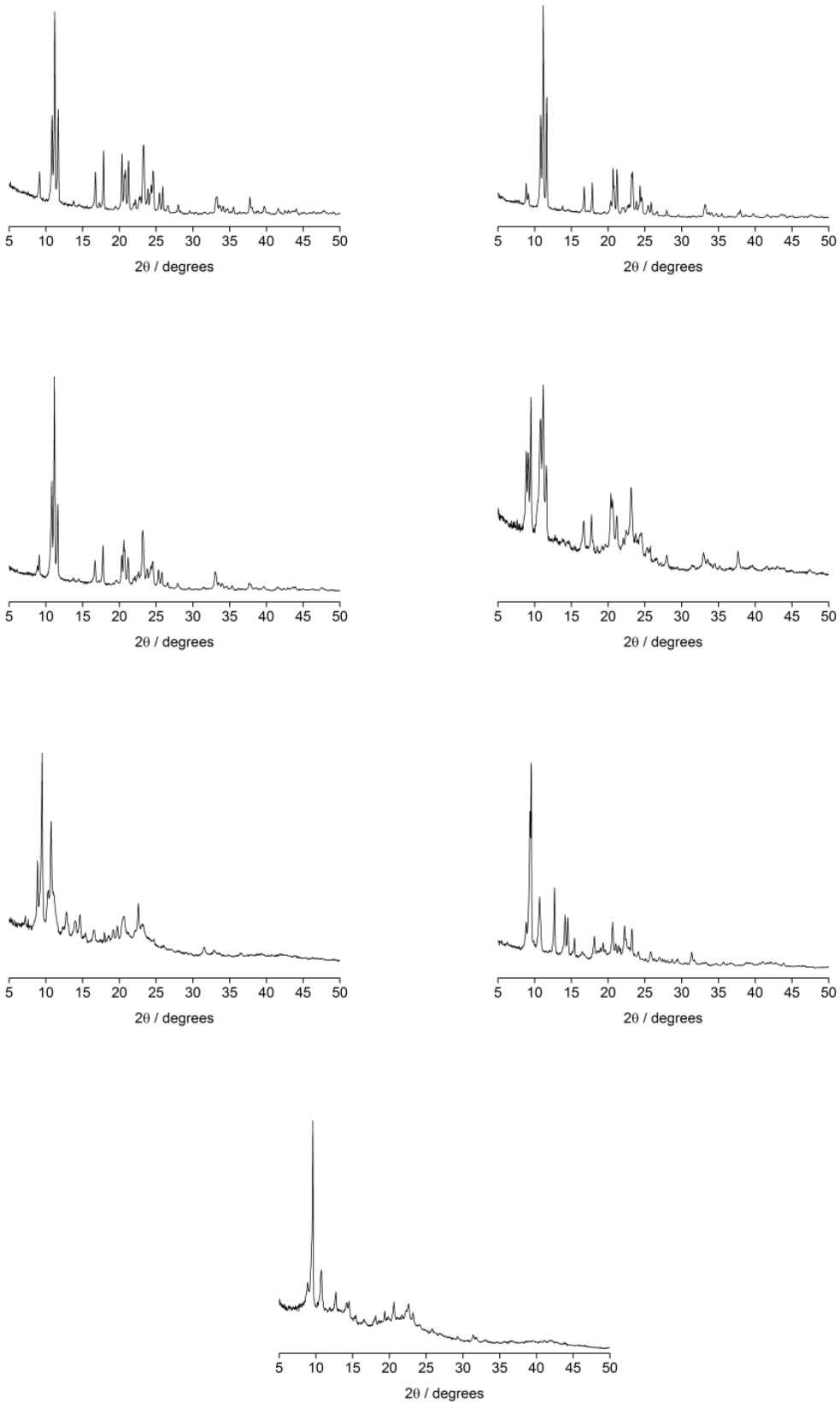

Figure 87 – Selected experimental powder patterns for the $[Fe(1\text{-}bpp)_2]_x[Ru(tpy)(Ctpy)]_{1-x}[BF_4]_2$ series of solid solutions, where x descends as the page is read, with X = 1, 0.91, 0.82, 0.59, 0.25, 0.17 and 0 respectively.

4.6 Conclusions

This work focuses on endeavours to prepare, isolate and successfully characterise derivative complexes of ruthenium(II) *bis*-terpyridine which, as a result of destabilisation of a non-emissive state through tuning of the orbital energies experience enhanced room temperature luminescence. This has involved careful selection of ligands related to terpy, whose ruthenium(II) complexes are stable towards oxidation and whose overall charge is compatible with the 2:1 electrolyte balance of the spin crossover host complex. Our choice of ligands and complexes was also limited by the roughly spherical shape that is required, which does not deviate markedly from that adopted by the host complex and whose size is not too large to be seamlessly incorporated into the spin crossover lattice during the crystallisation process.

As is discussed, a significant number of these complexes could not be studied electronically and screened for emission as synthetic difficulties severely problematised their isolation. Of the non-cyclometallated complexes, only three were subject to emission-based studies, and of the three one was unsuitable as a luminescent dopant because of non-radiative decay from the strongly hydrogen bonding nature of its ligand substituent effectively quenching the emissive states. Increased emission, of lower wavelength and, thus, less likely to be quenched by the iron(II) host's MLCT bands, was observed in solutions of the complexes. Of lesser intensity than perhaps was hoped for, this proved sufficient enough to warrant its use as a dopant. The use of these two materials as a dopant has yet to transpire however, as the synthetic routes toward the two constituent ligands are low yielding and require extensive purification meaning quantities insufficient for doping were acquired.

The three cyclometallated complexes, which all show significant emission in the visible spectrum were isolated in high enough abundance for the purposes of doping into the spin crossover host lattice. The first of these, through a combination of different steric effects was structurally incompatible with the host, and no studies upon the second emissive material were conducted as the structural incompatibilities between host and dopant were predicted to be exacerbated even further in this material. The third cyclometallated emissive complex which, in absence of structural evidence, was theorised to be closer in size to the host material than the previous two complexes, based upon the fact its ligand backbone was comprised solely of unsubstituted pyridyl rings. This was successfully doped into the iron(II) host **25a**, with structural and magnetic data supporting almost homogenous co-crystallised materials except when the host-to-dopant ratio is close to 1:1. At high iron(II) host concentrations the $P2_1$ phase of **25a** dominates, whereas at very low host concentrations the phase adopted by the ruthenium(II) dopant is prevalent. The broadening of the form of the spin transition and the reduction in $T_{1/2}$, as observed magnetically, suggests both doped

phases are homogenous, with the larger ruthenium(II) cores stabilising the HS configuration of the iron(II) complexes. The terpyridine embrace of **25a** has successfully accommodated another larger dication, even in the presence of a distal hydrogen bond donor, however the effect of the spin transition upon the emission of the ruthenium(II) cores within the doped materials has, as of yet, not been possible to study but is of high priority.

The limitations imposed, by virtue of having to electronically tune the dopant towards increased emission whilst at the same time effectively engineering the size and shape of the potential dopant to retain its structural compatibility have meant that, in using **25a** as a host, only a **22a**, which exhibits only modest emission, could be incorporated into the SCO host lattice. If progress is to be made in the field of discreet bifunctional materials, new iron(II) complexes, perhaps simply larger but retaining the same spherical shape are required, and must possess spin crossover behaviour interesting enough to warrant its incorporation into a doped material. Chapter 5 discusses a number of such switchable complex salts in great detail, some of which display exciting magnetic behaviour close to room temperature. The wealth of suitable dopants must also be expanded, allowing the optimisation of the emissive functionality without such tight constraints on size and shape. Osmium(II) in particular may be of use, as a vast array of its polypyridyl and cyclometallated polypyridyl complexes exhibit very promising emission, however again its larger size means that, again, the size of the spin crossover host needs to be increased so as to ensure its structural compatibility with a wider array of dopants.

4.7 References

1. C. Lashgari, M. Kritikos, R. Norrestam and T. Norrby, *Acta Cryst.*, 1999, 55, 64-67.
2. D. Craig, M. Scudder, W. McHale and H. Goodwin, *Aust. J. Chem.*, 1998, 51, 1131-1139.
3. M. Halcrow, *Chem. Commun.*, 2010, 46, 4761-4763.
4. R. Docherty, F. Tuna, C. Kilner, E. McInnes and M. Halcrow, *Chem. Commun.*, 2012, 48, 4055-4057.
5. G. Chastanet, C. Tovee, G. Hyett, M. Halcrow and J. Letard, *Dalton Trans.*, 2012, 41, 4896-4902.
6. C. Tovee, C. Kilner, J. Thomas and M. Halcrow, *CrystEngComm*, 2009, 11, 2069-2077.
7. R. Berger and D. McMillin, *Inorg. Chem.*, 1988, 27, 4245-4249.
8. E. Medlycott and G. Hanan, *Chem. Soc. Rev*, 2005, 34, 133-142.
9. A. Breivogel, M. Meister, C. Forster, F. Laquai and K. Heinze, *Chem. Eur. J.*, 2013, 19, 13745-13760.
10. P. Vallett and N. Damrauer, *J. Phys. Chem. A*, 2013, 117, 6489-6507.
11. Y. Sun, M. El Ojaimi, R. Hammitt, R. Thummel and C. Turro, *J. Phys. Chem. B*, 2010, 114, 14664-14670.
12. F. Schramm, R. Chandrasekar, T. Zevaco, M. Rudolph, H. Gorls, W. Poppitz and M. Ruben, *Eur. J. Inorg. Chem.*, 2009, 53-61.

13. K. Wu, C. Li, Y. Chi, J. Clifford, L. Cabau, E. Palomares, Y. Cheng, H. Pan and P. Chou, *J. Am. Chem. Soc.*, 2012, 134, 7488-7496.
14. Y. Z. W. Yang, S. Yoshikawa, J. Shao, S. Masaoka, K. Sakai, J. Yao, M. Haga, *Inorg. Chem.*, 2011, 51, 890-899.
15. M. Abrahamsson, M. Jager, R. Kumar, T. Osterman, P. Persson, H. Becker, O. Johansson and L. Hammarstrom, *J. Am. Chem. Soc.*, 2008, 130, 15533-15542.
16. M. Jager, R. Kumar, H. Gorls, J. Bergquist and O. Johansson, *Inorg. Chem.*, 2009, 48, 3228-3238.
17. J. Collin, M. Beley, J. Sauvage and F. Barigelletti, *Inorg. Chim. Acta.*, 1991, 186, 91-93.
18. E. Constable, A. Thompson, N. Armaroli, V. Balzani and M. Maestri, *Polyhedron*, 1992, 11, 2707-2709.
19. M. Maestri, N. Armaroli, V. Balzani, E. Constable and A. C. Thompson, *Inorg. Chem.*, 1995, 34, 2759-2767.
20. A. Stublla and P. Potvin, *Eur. J. Inorg. Chem.*, 2010, 3040-3050.
21. R. Leigghio, P. Potvin and A. Lever, *Inorg. Chem.*, 2001, 40, 5485-5486.
22. S. Son, K. Park, Y. Lee, B. Kim, C. Choi, M. Lah, Y. Jang, D. Jang and Y. Chung, *Inorg. Chem.*, 2004, 43, 6896-6898.
23. E. Constable, A. Thompson, J. Cherryman and T. Liddiment, *Inorg. Chim. Acta.*, 1995, 235, 165-171.
24. T. Matsumura-Inoue, M. Tanabe, T. Minami and T. Ohashi, *Chem. Lett.*, 1994, 23, 2443-2446.
25. E. Constable, J. Davies, D. Phillips and P. Raithby, *Polyhedron*, 1998, 17, 3989-3997.
26. D. Jameson, J. Blaho, K. Kruger and K. Goldsby, *Inorg. Chem.*, 1989, 28, 4312-4314.
27. J. Braddock and T. Meyer, *J. Am. Chem. Soc.*, 1973, 95, 3158-3162.
28. J. Delgado, Y. Zhang, B. Xu and I. Epstein, *J. Phys. Chem. A*, 2011, 115, 2208-2215.
29. F. Dwyer, H. Goodwin and E. Gyarfas, *Aust. J. Chem.*, 1963, 16, 42-50.
30. P. Evans, A. Spencer and G. Wilkinson, *Dalton Trans.*, 1973, 204-209.
31. C. Hecker, A. Gushurst and D. McMillin, *Inorg. Chem.*, 1991, 30, 538-541.
32. R. Crutchley and A. Lever, *Inorg. Chem.*, 1982, 21, 2276-2282.
33. R. Scanu, P. Manca, A. Zucca, G. Sanna, N. Spano, R. Seeber, C. Zanardi and M. Pilo, *Polyhedron*, 2013, 49, 24-28.
34. A. Philippopoulos, A. Terzis, C. Raptopoulou, V. Catalano and P. Falaras, *Eur. J. Inorg. Chem.*, 2007, 5633-5644.
35. E. Constable, N. Hostettler, C. Housecroft, P. Kopecky, M. Neuburger and J. Zampese, *Dalton Trans.*, 2012, 41, 2890-2897.
36. E. Constable and A. Thompson, *J. Chem. Soc. Dalton Trans.*, 1992, 3467-3475.
37. C. Bessel, R. See, D. Jameson, M. Rowen Churhill and K. Takeuchi, *J. Chem. Soc. Dalton Trans.*, 1993, 1563-1576.
38. J. Wang, E. Medlycott, G. Hanan, F. Loiseau and S. Campagna, *Inorg. Chim. Acta.*, 2007, 360, 876-884.
39. E. Constable, A. Thompson and D. Tocher, *New J. Chem.*, 1992, 16, 855-867.
40. E. Constable and M. Ward, *Dalton Trans.*, 1990, 1405-1409.
41. F. Barigelletti, L. Flamigni, V. Balzani, J. Collin, J. Sauvage, A. Sour, E. Constable and A. C. Thompson, *J. Chem. Soc. Chem. Commun.*, 1993, 942-944.

42. G. Baggi, M. Boiocchi, C. Ciarrocchi and L. Fabbrizzi, *Inorg. Chem.*, 2013, 52, 5273-5283.
43. K. Robson, B. Koivisto, A. Yella, B. Sporinova, M. Nazeeruddin, T. Baumgartner, M. Gratzel and C. Berlinguette, *Inorg. Chem.*, 2011, 50, 5494-5508.
44. F. Laurent, E. Plantalech, B. Donnadieu, A. Jimenez, F. Hernandez, M. Martinez-Ripoll, M. Biner and A. Llobet, *Polyhedron*, 1999, 18, 3321-3331.
45. H. Park, S. Yoo, I. Shin, Y. Chung and J. Kim, *Electroanalysis*, 2013, 25, 1111-1115.
46. H. Park and Y. Chung, *Dalton Trans.*, 2012, 41, 5678-5686.
47. L. Chung, K. Cho, J. England, S. Chan, K. Wieghardt and C. Wong, *Inorg. Chem.*, 2013, 52, 9885-9896.
48. H. Park, K. Kim, S. Choi, H. Kim, W. Lee, Y. Kang and Y. Chung, *Inorg. Chem.*, 2010, 49, 7340-7352.
49. J. Collin, S Guillerez, J. Sauvage, F. Barigelletti, L. De Cola, L. Flamigni and F. Balzani, *Inorg. Chem.*, 1991, 30, 4230-4238.
50. T. Brinck, J. Murray and P. Politzer, *J. Org. Chem.*, 1991, 56, 2934-2936.
51. R. Casasnovas, J. Frau, J. Ortega-Castro, A. Salva, J. Donoso and F. Munoz, *J. Mol. Struct. (THEOCHEM)*, 2009, 912, 5-12.
52. M. Beley, J. Collin, J. Sauvage, H. Sugihara, F. Heisel and A. Miehe, *Dalton Trans.*, 1991, 3157-3159.
53. S. Klein, W. Dougherty, W. Kassel, T. Dudley and J. Paul, *Inorg. Chem.*, 2011, 50, 2754-2763.
54. M. Stone and G. Crosby, *Chem. Phys. Lett*, 1981, 79, 169-173.
55. S. Wadman, M. Lutz, D. Tooke, A. Spek, F. Hartl, R. Havenith, G. van Klink and G. v. Koten, *Inorg. Chem.*, 2009, 48, 1887-1900.
56. B. Schulze, D. Brown, K. Robson, C. Friebe, M. Jager, E. Birckner, C. Berlinguette and U. Schubert, *Chem. Eur. J.*, 2013, 19, 14171-14180.
57. M. Beley, S. Chodorowski, J. Collin, J. Sauvage, L. Flamigni and F. Barigelletti, *Inorg. Chem.*, 1994, 33, 2543-2547.
58. A. Juris, V. Balzani, F. Barigelletti, S. Campagna, P. Belser and A. v. Zelewsky, *Coord. Chem. Rev.*, 1988, 84, 85-277.
59. D. Mingos and A. Rohl, *Dalton Trans.*, 1991, 3419-3425.
60. I. Bagryanskaya and Y. Gatilov, *J. Struct. Chem.*, 1983, 24, 150-151.
61. J. Holland, J. McAllister, Z. Lu, C. Kilner, M. Thornton-Pett and M. Halcrow, *Chem. Commun.*, 2001, 577-578.
62. D. McGuinness, V. Gibson and J. Steed, *Organometallics*, 2004, 23, 6288-6292.
63. Y. Liu, T. Harlang, S. Canton, P. Chabera, K. Suarez-Alcantara, A. Fleckhaus, D. Vithanage, E. Goransson, A. Corani, R. Lomoth, V. Sundstrom and K. Warnmark, *Chem. Commun.*, 2013, 49, 6412-6414.
64. J. Elhaik, C. Kilner and M. Halcrow, *Dalton Trans.*, 2006, 823-830.
65. T. Roberts, M. Little, L. Kershaw Cook, S. Barrett, F. Tuna and M. Halcrow, *Polyhedron*, 2013, 64, 4-12.
66. E. Constable, G. Baum, E. Bill, R. Dyson, R. van Eldik, D. Fenske, S. Kaderli, D. Morris, A. Neubrand, M. Neuburger, D. Smith, K. Wieghardt, M. Zehnder and A. Zuberbuhler, *Chem. Eur. J.*, 1999, 5, 498-508.

Chapter 5

Engineering new spin-crossover materials of iron(II) containing derivatisations of the 2,6-di(pyrazol-1’-yl)pyridine backbone

5 Engineering new spin-crossover materials of iron(II) containing derivatisations of the 2,6-di(pyrazol-1'-yl)pyridine backbone

5.1 Introduction

The focus of this chapter will centre on the study of novel octahedral iron(II) salts *bis*-coordinated by functionalised derivatives of the tridentate meridionally chelating 2,6-di(pyrazol-1'-yl)pyridine backbone. First reported in 1989, the 1-bpp backbone represents a structurally related analogue terpy, whose steric and electronic influence upon a coordinated metal ion can be readily varied by facile derivatisation at the pyrazolyl ring (Figure 88).[1] Though closely related, the coordination chemistry of 1-bpp and terpy differ, particularly in complex systems containing metal ions sensitive to subtle changes in σ-donor strength and ligand field. Replacement of the distal 6-membered 2-pyridyl rings with 5- membered pyrazol-1-yl rings inherently affects the stabilisation of the *tris*-heterocyclic system, but also imparts significant modulation of the combined σ-basicity of the respective N-donor atoms. Pyrazoles, 5-membered diazoles, exhibit lower σ-basicities as a consequence of their sp^2 lone pair being held more tightly than in the corresponding pyridines. In combination with this, they are less willing to accept back-donated π-density from coordinated metal atoms because of the higher energy more constrained 5-membered π-system, which is evident from energy differences in ligand based π* levels in respective octahedral metal complexes of terpy and 1-bpp which were determined spectroscopically to be of the order of 5200 – 5800 cm^{-1}.[1-3] The significantly smaller ligand field exerted by 2,6-di(pyrazol-1'-yl)pyridine derivatives, with retention of its chelate stability imparts it with coordination chemistry which often differs significantly from that of the well studied terpyridyl systems.

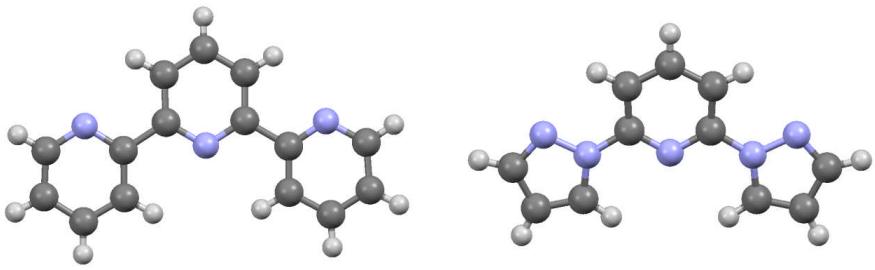

Figure 88 - Structures of a single molecule of the free organic ligands terpy (left) and 2,6-di(pyrazol-1'-yl)pyridine, 1-bpp (right) illustrating the slightly larger bite angles favoured by the latter due to its more constrained, 5-membered distal pyrazole rings.[4] Atom colour code: carbon (grey), hydrogen (white) and nitrogen (periwinkle).

Unlike terpy, the smaller ligand fields attributable to reduced σ-basicity and π-acidity associated with the 2,6-di(pyrazol-1'-yl)pyridine backbone are of the magnitude required to bring about a thermal spin transition in its iron(II) complexes, which is of special relevance

because it possesses the largest geometric, electronic and magnetic differences between the low and high spin configurations of any octahedral transition metal ion. Electronically, the parent dication $[Fe(1\text{-}bpp)_2]^{2+}$ switches with a $T_{1/2}$ of 250 K, yet its behaviour in the solid state is erratic, depending hugely upon the crystal packing and the ability of the centres to transmit their switching information, through the necessary changes in size, shape and charge distribution, cooperatively through the lattice.[3, 5-10] The most interesting behaviour from an industrial or commercial standpoint, is that which is observed through the adoption of the terpyridine embrace motif in the crystal, and is best characterised as having a large region of thermal bistability coupled with a small switching temperature regime. Typically, tetrafluoroborate and perchlorate counterions yield the most interesting materials, as their volume is not of the size which disrupts the discreet layers of dications interlocked in the terpyridine embrace, and they are sufficiently polar so as to occasionally impart communication between layers. However the existence of multiple solvates and polymorphs can regularly confound characterisation and understanding of the switching behaviour.

Complex derivatives functionalised at the ligand pyrazolyl 3-position with substituents larger than isopropyl groups remain high spin trapped as the substituents lie too close to the central iron(II) ion, ensuring that the bond lengths are unable to contract and adopt the low spin configuration.[9, 11-13] Smaller substituents result in complexes which generally adopt configurations based entirely upon electronics, exhibiting unremarkable behaviour characterised by gradual, if any, spin crossover features.[9, 12, 14] It is only the methyl derivatised complex which gives rise to interesting magnetic behaviour, specifically the tetrafluoroborate salt, as larger substituents inhibit adoption of the preferred terpyridine embrace motif which negates a cooperatively switching material.[8, 15] A similar situation is encountered in complexes of 4-pyrazolyl substituted 1-bpp, which possess equatorial steric bulk prohibiting crystal packing in the terpyridine embrace.[16-19]

The coordination chemistry of 4-pyridyl derivatised 1-bpp derivatives has, largely, been ignored because of the difficulty in accessing 4-substituted pyridine precursors. The majority whose spin crossover behaviour has been subject to investigation were anchored with large groups which not only cause significant deviations from the pseudo-spherical shape of the archetypal $[Fe(1\text{-}bpp)_2]^{2+}$ complexes, but also, by virtue of their effect upon the size which reduces the relative volume differences between the two spin states and all too often proved relatively uninteresting.[20-28] A number also contained larger groups which did not prevent packing in the terpyridine embrace, and which actively promoted cooperative switching through the introduction π-stacking of appendages between layers, or through strong inter layer hydrogen bonding with lattice water and counterions, yet at the expense of interlayer proximity.[26-36] Since such large substituents can be introduced without inhibition of

spin crossover cooperativity, the intention of this chapter is to expand the coordination chemistry of 1-bpp functionalised with discreet, small groups which exert purely an electronic influence, depending on their nature, upon an iron(II) centre. New iron(II) complexes containing hydrogen bonding groups are discussed, and their effect upon the crystal packing and intercomplex communication in the solid will be assessed. Multiple salts of each complex are studied crystallographically, magnetically and energetically so as to better grasp the interplay between the substituents' effect upon the isolated metal centre in each of the different salts. The differences in magnitude of the structural and energetic changes in isostructural materials upon undergoing a change in electronic configuration and how this impacts upon the degree of cooperativity within the lattice are also discussed.[37] The information imparted will hopefully further the understanding of the switching behaviour in discreet mononuclear materials and the effect of counterions, solvates and structural polymorphism on the stability of the spin states relative to each other in the study of this series of 4-functionalised derivatives of $[Fe(1\text{-bpp})_2]^{2+}$. The syntheses of the chelating ligands is described in detail in Chapter 2.

5.2 Aims and objectives

This chapter is a systematic study into the effects of sterically unencumbering substituents on the electronics of the iron(II) *bis*-2,6-di(pyrazol-1'-yl)pyridine core, thus its electronic ground state over a temperature range and the position of $T_{1/2}$ in both the solution and condensed phases. The first aim was to establish the existence of a trend in the isotropic solution phase spin state distribution of the complex salts and rationalise it if possible based on the nature of the appended groups. In the solid state, a combination of diffraction methods and magnetic measurements allows profiling of the spin crossover behaviour. Adoption of the terpyridine embrace motif will, where spin-crossover is thermally viable, result in consistently cooperative spin transitions whose degree of cooperativity can be understood by considering intermolecular interactions between neighbouring units in the crystal. Trends in behaviour are also to be investigated upon the nature of non-coordinating counterion, based upon their effects on lattice pressure and interactions with the complex units, a result of size/shape and polarity respectively. Implementing these findings, we are ultimately aiming to design a robust material which possesses a highly cooperative spin transition with wide hysteresis which ideally encompasses an operable temperature regime.

5.3 Solution behaviour

5.3.1 Complex stability and speciation of the oligomeric materials

The triflate, tetrafluoroborate and perchlorate iron(II) complex salts of the 4-substituted 2,6-di(pyrazol-1'-yl)pyridines were synthesised by addition of the appropriate ratio of

chelating ligand to the metal salt hydrates in either $MeNO_2$ or MeOH (Figure 89). The almost instantaneous colour change of the solutions indicated that complex formation occurs rapidly, and the salts were isolated purely either by addition of Et_2O or iPr_2O or by drying the reaction solution *in vacuo*. The exceptions were **34a**, **34b** and **34d**, whose solutions darkened severely when vacuumed to dryness at 50°C and were isolated as dark brown solids, but could be obtained as bright yellow pure powders when precipitated gradually (ca. 30 minutes) with either Et_2O or iPr_2O. Comparison of IR spectra of the respective salts showed that the darker solids exhibited a significantly weaker band at 2540 – 2555 cm^{-1}, indicating that upon heating partial disulfide formation had occurred. This is hardly surprising as 1-bppSH dimerises fully over the course of a few days in polar solvents, and the thermal energy provided during the drying process would only exacerbate this. The 1-bppSH containing complexes discussed in this chapter originate from the second method of salt isolation, which avoids the problem of dimerisation. Hexafluorophosphate salts were prepared by salt exchange and precipitation of the complexes with NH_4PF_6 from aqueous-methanolic solutions of their chloride salts (Figure 90). All were stable over a period of hours in water-methanol aside from those containing 1-bppNO$_2$, 1-bppSH and 1-bppDS which simply did not coordinate to iron in the presence of water. As a result, the hexafluorophosphate salts of their complexes could not be isolated. 1-bppNO$_2$'s very low basicity is perhaps accountable for its inability to chelate iron(II) in competition with water, however why 1-bppSH and 1-bppDS are ousted by water is less clear. Initially, it was attributed to 1-bppSH's extremely low solubility as to why the equilibrium strongly favours precipitation of the free ligand, but 1-bppDS is readily soluble in most moderately polar organic solvents so this cannot be the case.

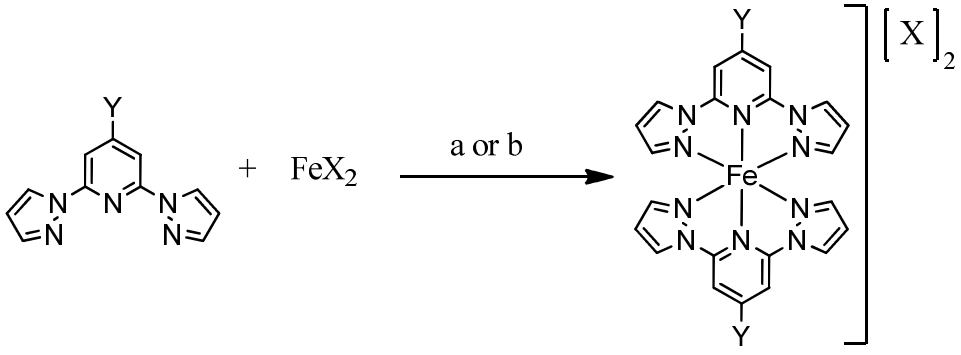

Figure 89 - Schematic representation of the one-pot synthesis of the 4-substituted 2,6-di(pyrazol-1'-yl)pyridine salts where X = BF_4, ClO_4, CF_3SO_3 and Y = H or appropriate substituent; a) Stirring the two components together in $MeNO_2$ before precipitation with either Et_2O or $^iPr_2O$ and collection by filtration; b) Dissolution of the two components in acetone and then standing at -20°C after addition of Et_2O to yield the salt which was collected by filtration.

As the disulfide 1-bppDS is ditopic, it was theorised that, in non-coordinating solvents such as MeCN and $MeNO_2$, its reaction with iron(II) would yield primarily

oligomeric/polymeric multinuclear materials. Reaction of the a suitable iron(II) source with 1-bppDS in a 1:1 ratio results in orange-yellow solutions, with the isolated complex salts appearing as brown microcrystalline solids. In an attempt to force the formation of lower-order structures over polynuclear species, the reaction was performed performed using 2.5 eq. of 1-bppDS, however after almost instantaneous colourisation of the solution a colourless solid remained undissolved even after prolonged reaction times and application of heat, which was filtered off and characterised as per prediction as free uncoordinated ligand. In addition, the brown material in the solution was of the same form as that from the 1:1 ratio complexation, and their ^{1}H NMR spectra were indistinguishable. This not only suggests that kinetically stable multinuclear bridged units form rapidly and preferentially discreet mononuclear units, but also in conjunction with their high solubility that they form oligomeric rather than polymeric structures.

The coordination chemistry of the closely related terpyridyl analogue bis-(2,6-di(2'-pyridyl)-pyridin-4-yl)disulfide with iron(II) yields the a tetranuclear ring, of form [Fe((2,6-di(2'-pyridyl)-pyridin-4-yl)disulfide)]$_4^{8+}$, as proven crystallographically, and its ^{1}H NMR spectrum consists of five sharp signals corresponding to a single ligand environment, with an approximated D_{2d} symmetry about each iron(II) centre.[38] All endeavours to grow single crystals of **36a** and **36b** proved futile, with the materials either decomposing or precipitating gradually as a very fine powder. Two substitutionally inert diamagnetic analogues using zinc(II) and ruthenium(II), **41c** and **42c** respectively, were also prepared to provide insight into the nuclearity of the isolated solids. However, the elusiveness of any singly crystalline material persisted which limited the study of these materials to purely the solution phase in order to elucidate the molecular structure.

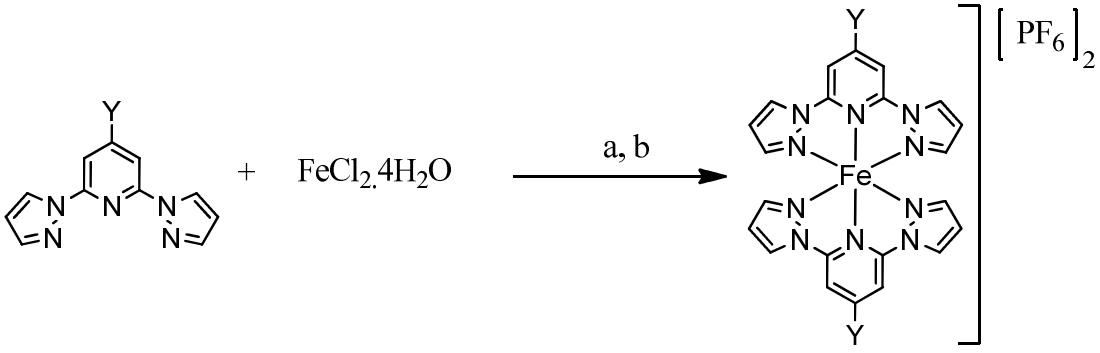

Figure 90 - Schematic representation of the synthesis of the 4-substituted 2,6-di(pyrazol-1'-yl)pyridine dihexafluorophosphate salts where Y = H or appropriate substituent; a) Stirring the two components together in MeOH-H_2O and filtering; b) Addition of a saturated aqueous solution of NH_4PF_6 standing and collection of the resulting precipitate.

The ^{1}H NMR spectra of **36a** and **36b** were identical, showing four primary resonances, highly contact shifted in accordance with the dominance of the high spin ground

state at ambient temperature, in agreement with averaged D_{2d} symmetry about each iron(II) centre as in the terpyridyl analogue. However, two peculiarities stand out, the first of which being that if one observes closely, the contact shifted resonances, though highly broadened, can clearly be seen to consist of two distinct maxima. Secondly, four sharper signals reside in the diamagnetic region between 6 and 8.5 ppm, suggesting proton environments about an uncoordinated 1-bpp core. The presence of residual free 1-bppDS could be excluded on the grounds that the four diamagnetic signals are sharper and significantly stronger than in $MeNO_2$ solutions of free 1-bppDS, which is only sparingly solubilised by $MeNO_2$, but also due to the non-superimposibility of the two sets of signals.

The disulfide bond, though flexible, shown to possess a C-S-S-C torsion angle of 61° in a sterically constrained dinuclear copper complex of 2,6-di(2'-pyridyl)-pyridin-4-yl)disulfide, would simply be unable to twist further into the conformations which would necessarily result in the dinuclear and trinuclear rings postulated, and therefore these can be excluded from further mention.[39] Tetranuclear systems would appear to be the most stable, in which the disulfide bond adopts a conformation close to 90°, almost identical to that which is found crystallographically in 1-bppDS and 2,6-di(2'-pyridyl)-pyridin-4-yl)disulfide.[38, 40] A pentanuclear ring would require a larger C-S-S-C angle than is normally observed, and though distortion about the high spin iron(II) coordination sphere could, potentially, accommodate such a torsion angle, this would impact severely on the material's ability to switch into the low spin configuration at lower temperature, effectively trapping at least one of the iron(II) centres about the ring in a highly distorted high spin configuration. As **36a** adopts a single Boltzmann distribution of spin states in the solution phase, the existence of a pentanuclear unit is also precluded. This second species is thought to be a discreet mononuclear complex, or a unit of the form $[Fe_n(1\text{-bppDS})_{n+1}]^{2n}$, where n = 1-3, which would be expected to possess a very similar, but distinct, set of contact shifted resonances for the protons about the coordinated 1-bpp domains which reflect slight electronic differences, causing a subtle change in the relative stabilisation of the two electronic configurations. The four signals in the diamagnetic region would hence originate from protons about the uncoordinated "chain ends". Interestingly, the zinc(II) analogue showed only a single set of signals, shifted with respect to free 1-bppDS, suggesting the existence of a single ligand environment, and hence a single species. This being said, the broadening of the signals may obscure resonances arising from non-coordinated domains or indeed those from minor species whose chemical shifts about the 1-bppDS backbones only differ by up to 0.3 ppm.

To further investigate the solution speciation of these oligomeric complexes of 1-bppDS, the conductance of solutions of **36a**, **36b**, **41c** and **42a** at 10^{-4}-10^{-3} M concentrations was quantified in order to assess the concentration dependence of the conductivity, and hence

the electrolyte ratio involved. Over the same concentration range, **34d** was also subject to conductance measurements as a 2:1 electrolyte reference with which to compare the other materials' conductivity plots to. Regrettably, as predicted from its ^{1}H NMR spectra which was particularly messy, consisting of a number of different inseparable complex species, the conductance of **41c** was the result of a number of highly impure electrolytes evident from its anomalous values, and it shall not be discussed further.

The information imparted from isolated conductance measurements, on a single substrate of known electrolyte type are only of significant use if the speciation of the material is known and if the counterions do not enter the coordination sphere. In the case of **36a**, **36b** and **42a**, a number of different species must be considered, and so the electrolyte type must be determined in order to infer information about the speciation of discreet, solvated units. This is achieved through use of the Onsager law, which relies on the fact that inequivalent electrolyte types of exhibit differing concentration dependences, which can be best illustrated through the use of the equation $\Lambda_0 = \Lambda_e + (A + B\omega\Lambda_0)c^{1/2}$. Λ_0 is the limiting conductivity at infinite dilution, Λ_e is the equivalent concentration, ω is a factor which represents the combined ionic mobilities of the charged species and A and B are constants which are dependent upon solvent viscosity and dialectric constant which illustrate that data cannot be directly compared in different solvent media.[41, 42] Large inaccuracies in conductance data arise at very low concentrations due to solvent's residual conductivity, 3.28 μS for our 99+% analytical grade $MeNO_2$, and therefore Λ_0 must be inferred by plotting Λ_e vs. $c^{1/2}$ to obtain Λ_0 as the intercept at the theoretical infinite dilution of each electrolyte. $\Lambda_0 - \Lambda_e$ is then plotted vs. $c^{1/2}$, resulting in a linear curve with positive gradient, the magnitude of which is larger for higher order electrolytes than it is for simple 1:1 electrolytes of comparable ionic mobility (Figure 91).[42]

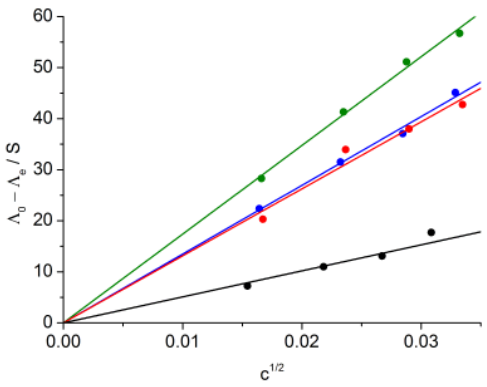

Figure 91 – Onsager conductance plots for dilute solutions of 34d (black), 36a (red), 36b (blue) and 42a (green) in nitromethane; the Onsager slopes, $A + \omega B\Lambda_0$, were calculated as being 509, 1313, 1347 and 1738 respectively.

The molar conductivity, Λ_m, Λ_0 and Onsager slope of **34d** were calculated as 105 S cm^2 mol^{-1}, 119 S cm^2 mol^{-1} and 509 respectively, in general agreement with the expected 2:1 electrolyte type, though the slightly lower Λ_m and Λ_0 values are probably attributable to the lower ionic mobility of the triflate with respect to the complex salts of smaller, more mobile anions which are usually reported.[42, 43] The Onsager slopes for **36a** and **36b** are almost identical, suggesting that as indicated by their ^{1}H NMR spectra the distribution of their speciation is uniform. One would also expect to see the same in **42a**, however the slope is notably steeper, suggestive of a greater proportion of higher electrolyte type present. With ^{1}H NMR of **42a** showing a lack of uncoordinated 1-bpp domains, it is proposed that as far as is discernible through ^{1}H NMR analysis, the entire material is macrocyclic in nature, with a zinc(II) nuclearity of four. The smaller Λ_0 values and Onsager slope exhibited by **36a** and **36b** indicate an "averaged" electrolyte type of 6:1, however a trinuclear macrocycle of this type is precluded by the restrictions imposed by the rigidity of the ditopic bridging ligand 1-bppDS. On this basis, it can be confidently concluded that **36a** and **36b** are made up of an almost identical ratio of tetranuclear macrocycles to acyclic $[Fe_n(1\text{-bppS})_{n+1}]^{2n}$ type units, of which the macrocycle is present in a large excess. The smaller Onsager slope is thus a result of the contributions of the acyclic species, which are expected to possess lower ionic mobilities per charge than the macrocyclic units, which manifest themselves in an overall lowering of the conductance of the bulk material and its concentration dependence.

5.3.2 Spin crossover behaviour in solution

$[Fe(L)_2]^{2+}$, L=	3 / ppm	3' / ppm	4' / ppm	5' / ppm	X_{CS}[a] / ppm	$T_{1/2}$ / K
1-bpp[5]	34.3	61.3	56.6	36.3	39.4	248
1-bppMe	40.8	70.2	61.5	40.8	45.6	221
1-tpp	42.1	71.4	61.8	41.5	46.5	227
1-bppCOOH	22.4	39.6	38.1	25.4	23.7	283
1-bppNH_2	52.7	78.9	60.8	47.7	52.3	<150
1-bppNO_2	19.6	34.2	34.2	22.9	20	305
1-bppOH	48.6	78.0	63.9	45.2	51.2	146
1-bppOMe	47.1	76.3	62.5	44.4	49.9	158
1-bppSH	36.9	64.8	55.4	38.1	41.1	246
1-bppSMe	43.2	72.5	60.6	42.5	47.0	194
1-bppDS	37.4	64.9	55.5	38.1	41.3	245
1-bppF	40.9	71.7	63.1	40.9	46.4	221
1-bppCl	37.2	66.6	59.7	38.6	42.8	229
1-bppBr	36.3	65.1	58.7	38.0	41.8	236
1-bppI	35.1	62.9	57.0	37.0	40.3	237

Table 17 – ^{1}H NMR paramagnetic contact shifts of the respective disubstituted iron (II) *bis*-tetrafluoroborate salts. [a]χ_{cs} is the averaged contact shift value, calculating by taking the average of the difference in chemical shift value at their respective positions about the 1-bpp backbone of the complex salts and that of $[Ru(1\text{-bpp})_2][BF_4]_2$, whereby $[Ru(1\text{-bpp})_2][BF_4]_2$ represents a completely diamagnetic isoelectronic reference.

The spin state population as a function of temperature, limited by the liquid range of the solvent of choice was investigated to quantify purely the electronic effect of the corresponding 4-substituted 1-bpp ligands upon the octahedral iron(II) centres (Table 17). This can be achieved through application of a technique known as the Evans method, which relies on the fact that the position of a signal of an inert reference is proportional to the bulk susceptibility of a medium. This paramagnetically shifted signal relative to its unaffected diamagnetic reference varies according to the paramagnetism of a substrate, and from this frequency shift the overall paramagnetism of the material of known concentration and composition at a given temperature can be calculated, which allows determination of $T_{1/2}$ through extrapolation of the susceptibility variation over a given temperature range (Figure 92). The relation through which the susceptibility of the solvated complex molecules can be calculated is defined as $\chi_g = ((3\Delta f)/(2\pi f m)) + \chi_0$, where χ_g is the gram susceptibility of the dissolved material, χ_0 is the susceptibility of the solvent medium as calculated from Pascal's constants, f is the frequency of the NMR spectrometer used, Δf is the frequency difference between the reference and paramagnetically shifted signals of the solvent, and m is the mass of dissolved substrate per cm^3 of solvent.[44, 45]

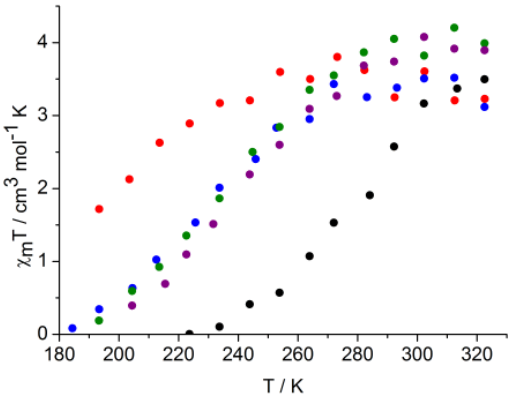

Figure 92 – Variable temperature magnetic susceptibility curves of selected solubilised complex ditetrafluoroborate salts measured in the warming mode in acedone-d_6 between 180 and 330 K; black (29a), red(35a), blue (38a), green (39a) and purple (40a).

To better interpret the variation in $T_{1/2}$ across the 4-pyridyl substituted 1-bpp iron(II) complexes, the data was compared with complexes substituted at the pyrazole 4-position (Figure 93). The $T_{1/2}$ values were plotted against the Hammett constants, σ, which are a linear measure of substituents' sigma withdrawing/releasing abilities upon an aromatic system to which they are directly attached. Unfortunately only a small number of iron(II) complexes functionalised about the distal pyrazole rings exist, most of which are at the 3 and 4 positions. All examples of 3-pyrazole substituted 1-bpp complexes will henceforth be ignored, as these groups often exert a profound steric influence which confounds

interpretation of their purely electronic effect upon the spin crossover behaviour. The 4-pyrazole substituted complex salts possess a trend in their solution spin crossover which was expected on the basis of their electron releasing/withdrawing properties upon the basicities of the pyrazole rings, and hence the strength of their σ-interaction with the iron centre. Indeed, a plot against their Hammett constants shows a reasonably linear relation correlation that as the pyrazole is made less basic, the $T_{1/2}$ decreases due to a reduction in Δ_{oct} by virtue of weaker Fe-N interactions. In the complexes containing atoms and groups appended to the central pyridine of the 1-bpp backbone, the trend is reversed, as evident in their $T_{1/2}$ vs. Hammett parameter plots (Figure 93), which conversely show an increase in $T_{1/2}$ as the electron withdrawing capacity of the substituent is increased.

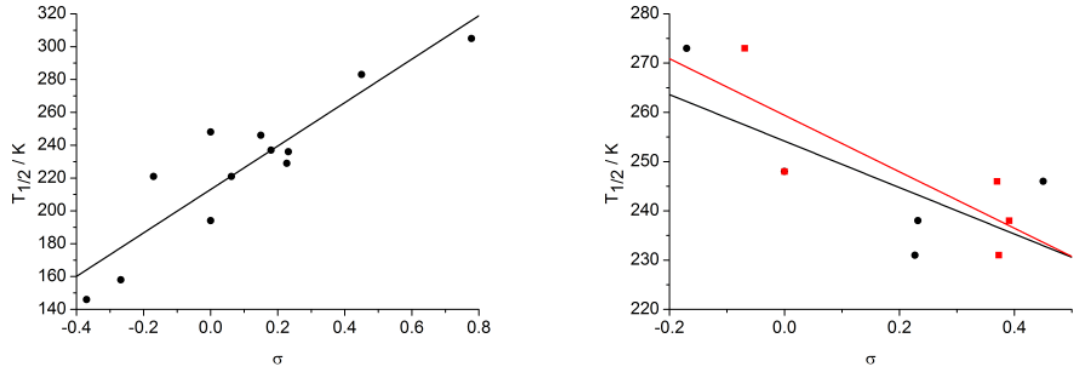

Figure 93 – Plots of the solution $T_{1/2}$ values vs. Hammett constants to illustrate the electronic effect of the relative stabilisation of the high and low spin configurations in iron(II) complexes of substituted 1-bpp derivatives.[46] Data was obtained from $MeNO_2$-d_3 or acetone-d_6 solutions of the respective salts; Left: Complex salts derivatised at the pyridine 4-position, data points are omitted for the iron(II) complexes of 1-bppNH$_2$, 1-bppDS and 1-tpp due to either the inability to obtain an accurate $T_{1/2}$, or the absence of a Hammett reference value for said substituent. Right: Complex salts derivatised at the pyrazole 4-positions, with data points extracted from the relevant references.[5, 17, 18] As no parameter exists to quantify the sigma donor/acceptor capability for substituents at the pyrazole 4-position, the $T_{1/2}$ values were plotted against the reference Hammet values for meta and para substituted benzene rings, σ_p (black) and σ_m respectively.

Until now, we had considered purely the Fe-N σ-interaction, and it is clear that the situation is not so simple when the aromatic π-system is of low enough energy that the π-backbonding interaction makes significant contribution to the bond strength. Since the trend is reversed based upon what was predicted from purely σ-effects, the changes imposed upon the iron's ability to backdonate electron density into the pyridine donor's π lobes are clearly the dominating factor in the spin equilibria of this series of complexes, as has been reported in some analogous terpyridinyl containing materials.[47] The complexes of interest which exhibit the largest shift in $T_{1/2}$ values, with respect to the 1-bpp chelated parent complex **25a**, are those functionalised with strongly π-acidic/basic groups which possess π-lobes of comparable size and energy to those about the 6-membered pyridine ring. The complexes of 1-bppOH, 1-bppOMe and 1-bppNH$_2$ switch at temperatures up to and beyond

100 K lower than in **25a**, telling of the dominance of the π-acidity over σ-induction, which serves to decrease the Δ_{oct} about the iron centre through a heavily reduced π-π* backbonding interaction. A strongly opposing effect is seen in the complexes of 1-bppNO$_2$ and 1-bppCOOH, which cause significant lowering of the ligand π* levels, concomitant with increased Fe-N backdonation. The heavier 4-halo-2,6-di(pyrazol-1'-yl)pyridines, 1-bppCl, 1-bppBr and 1-bppI, due to their much higher energy p orbitals, exhibit only neglible π effects, and hence their high spin configuration is stabilised slightly with respect to **23a**, with very similar $T_{1/2}$ values, in closer agreement with the Hammett σ-values. Fluorine in 1-bppF has better p-π overlap than the heavier halogens, and so the high spin state is stabilised to a higher degree in its solubilised complexes. As in the halogen containing ligands, sulfur also imparts only a small π-contribution because of its high energy p orbitals, however [Fe(1-bppSMe)$_2$]$^{2+}$ possesses a significantly lower $T_{1/2}$ than in [Fe(1-bppSH)$_2$]$^{2+}$ which probably reflects stronger π-basicity due to the sulfur's hyperconjugation with the C-H bonds about the methyl group.

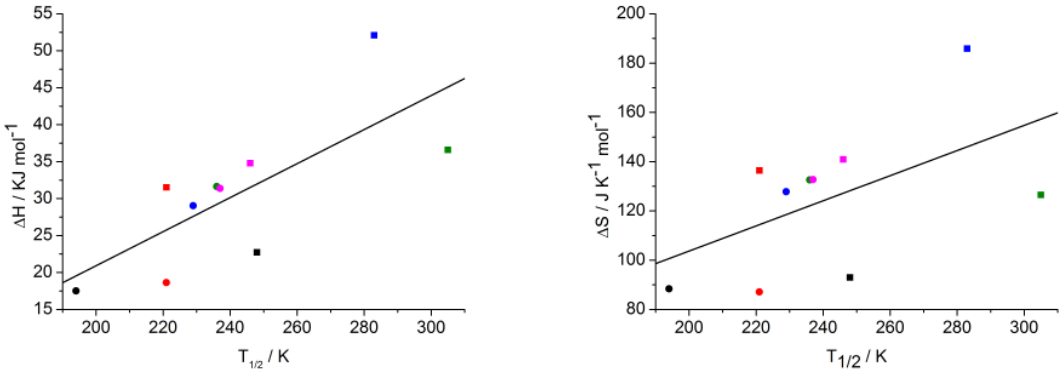

Figure 94 – ΔH (left) and ΔS (right) vs. $T_{1/2}$ of the complexes in solution which possessed an appreciable contribution to the spin state population of low spin centres. The complexes are of the form [Fe(L)$_2$]$^{2+}$, where L = 1-bpp (black square), 1-bppMe (red square), 1-bppCOOH (blue square), 1-bppNO$_2$ (green square), 1-bppSH (pink square), 1-bppSMe (black circle), 1-bppF (red circle), 1-bppCl (blue circle), 1-bppBr (green circle) and 1-bppI (pink circle.

The enthalpy and entropy changes of transition, ΔH and ΔS, of the materials in solution were obtained through the use of the Van't Hoff equation, lnK = (-ΔH/RT) + ΔS/R, where K is the equilibrium constant for the spin interconversion process, and R is the gas constant. The obtained values were then plotted against $T_{1/2}$ for the complexes which possessed an appreciable fraction of low spin centres above the solvent freezing point (Figure 94). It can be seen that, in accord with the larger ligand field changes upon undergoing a change in electronic configuration, ΔH and ΔS become greater in magnitude as the temperature of transition is increased. It should be pointed out that, for [Fe(1-bppCOOH)$_2$]$^{2+}$ the ΔH and ΔS values deviate strongly in a positive direction from the linear plot. This probably reflects more complicated behaviour arising from rearrangements in the

solvent sphere, and more subtle changes in the acid-base equilibrium of 1-bppCOOH as the spin state population shifts in addition to potential attack by the carboxylic groups on other iron(II) complex units.

All of the above in mind, it has still not been possible to obtain an accurate quantification of the difference in Δ_{oct} in the two spin states across the series of complexes. Δ_{oct} of the high spin state could rather trivially be calculated from analysis of UV/Vis spectra of the complexes, however as the majority of $T_{1/2}$ values lie extremely close to or below that of the solvent freezing point (dependent upon the use of $MeNO_2$ or acetone), d-d transitions within the low spin centres would be barely out of the noise of the spectrum and, expected to overlap with more intense MLCT bands, precluding a precise assignment of the d-d bands. Even so, electronically, by taking advantage of larger π-contributions in 4-pyridyl substituted 1-bpp to the overall ligand field strength, it has been possible to tune the spin state equilibrium over a range spanning room temperature, with $T_{1/2}$ values ranging from 146 – 305 K.[48] This furthers the understanding that iron(II)'s local electronic environment is more sensitive to changes in σ and π interactions than in cobalt(II), whose intrinsic smaller spin pairing energy difference between the HS and LS configurations result in more subtle, less predictable variation in the spin equilibrium.[3, 49]

5.4 Spin crossover in the solid and the effect of polymorphism upon iron(II) salts chelated by 2,6-di(pyrazol-1-yl)pyridine functionalised at the central pyridine 4-position

5.4.1 Iron(II) salts of 1-bppMe

Four complex salts were prepared *bis*-chelated by 1-bppMe, and the tetrafluoroborate, perchlorate and hexafluorophosphate salts, **27a**, **27b** and **27c** respectively, were all isolated as bright yellow power/microcrystalline solids. The triflate salt, **27d**, however took on a mustard brown appearance in its bulk form, isolated by precipitation with Et_2O from $MeNO_2$ solution, which is evocative of a mixture of iron(II) spin states in the solid. **27a** and **27b** are discussed separately to the other two salts, as their spin crossover behaviours are not only more interesting but also comparable in nature.

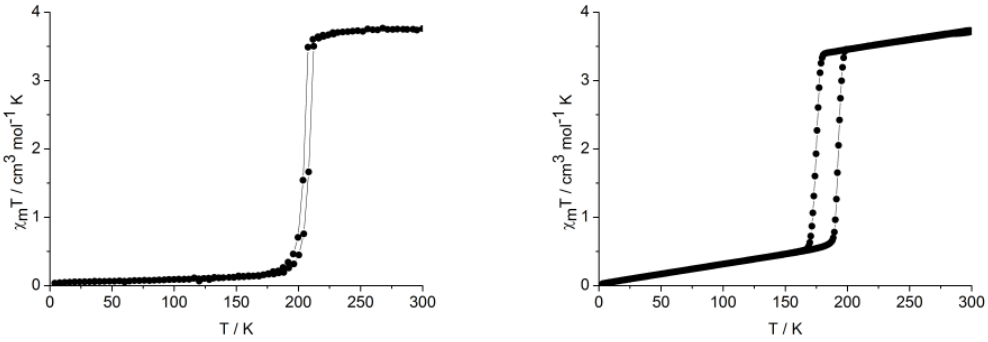

Figure 95 – Variable temperature magnetic susceptibility plots in cooling and warming modes between 3 and 300 K for solvent free powder 27a (left) and 27b (right).

Crushed into a fine powder post-desiccation, **27a** and **27b** both exhibited a single-phase hysteretic spin crossover as shown in their magnetic susceptibility curves (Figure 95), with the transitions centred at 207 and 184 K respectively. Thermodynamic measurements were omitted as the transitions occur predominantly outside of the window of measurement. The size of the hysteresis loops differed significantly, measured as 4 K in **27a** and 18 K in **27b** suggesting a much higher degree of cooperativity in the perchlorate which is discussed in greater detail below. Slow crystallisation by ethereal diffusion ($^{i}Pr_2O$, ^{t}BuOMe, Et_2O) into solutions of the salts in $MeNO_2$ yielded almost entirely very large cuboidal crystals whose very dark brown hues almost appeared black under certain lighting. This was indicative of a different crystalline phase to that of the as-prepared powders. These were shown crystallographically to be tetra-$MeNO_2$ solvates.

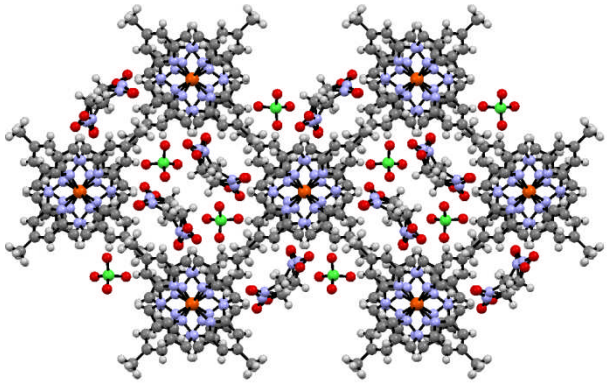

Figure 96 – Crystal packing diagram for 27b viewed along the crystallographic c axis, best illustrating the packing of $MeNO_2$ and ClO_4^{-4} in columns along the c axis. Atom colour code: carbon (grey), chlorine (lime green), iron (orange), hydrogen (white), nitrogen (periwinkle) and oxygen (red).

27a.4$MeNO_2$ and **27b**.4$MeNO_2$ both contain a single fully low spin iron(II) centre of d_{2d} symmetry, with a single molecule of $MeNO_2$ per quarter complex dication. The materials

are isostructural, both crystallising in the tetragonal space group I-4c2 and the $MeNO_2$ molecule is disordered over at least two sites. There are no interdication interactions, and the complexes form square arrays along the ab plane, with voids in the centre of the squares, in which the $MeNO_2$ and counterions pack down the c-axis essentially forming a channel (Figure 96). Upon exposure to air, unsurprisingly the nitromethane readily escapes the lattice over a period of a number of hours at ambient temperature, as evidenced by the change in colour of the dark brown blocks to bright yellow. It is proposed that as the nitromethane is lost, the close contacts of ca. 2.7 Å between the aromatic C-H and the O of the counterions is relieved, causing a drop in lattice pressure allowing the coordination sphere of the iron(II) centres to expand and adopt the HS configuration. The very regular coordination sphere in the crystal of **27a**.4$MeNO_2$ and **27b**.4$MeNO_2$ (Figure 97), a quarter of which lies in the asymmetric units, is probably also a result of two symmetry related $MeNO_2$ molecules which straddle the central pyridine rings both above and below, with an atom-to-plane distance of 3.06 Å.

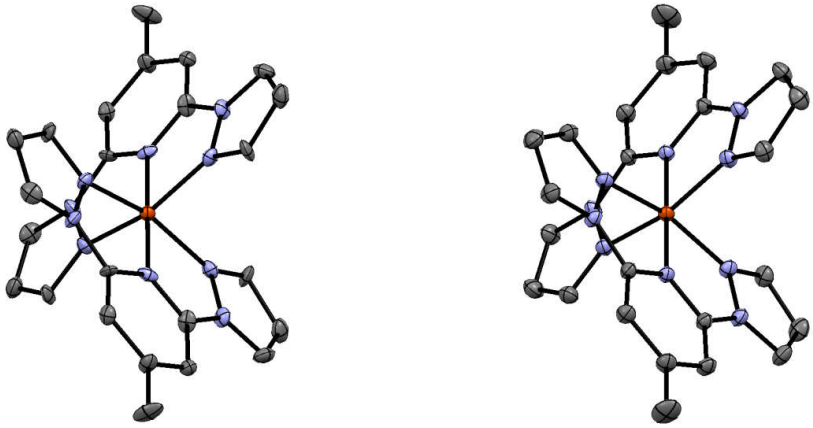

Figure 97 – Views of the discreet complex dications present in isostructural 27a.4$MeNO_2$ (left) and 27b.4$MeNO_2$ (right) along the crystallographic b axis collected at 100 and 150 K respectively; thermal ellipsoids plotted at the 50% level; H atoms omitted for clarity. Atom colour code: carbon (grey), iron (orange) and nitrogen (periwinkle).

Intriguingly, yellow material, both powder and crystalline, was observed during the slow crystallisation process in addition to the LS solvated phases of discussion above. In the case of **27a**, no HS material could be studied crystallographically as only one crystal of bright yellow colour was ever obtained which shattered when mounted under the cryostream at 100 K. Repeated attempts to grow any more of this singly crystalline yellow polymorph only ever resulted in the brown solvated blocks. It appears that the formation of the yellow crystalline material was very sensitive to the conditions of crystallisation, the exact nature of which were unclear since its growth could not be repeated. The formation of the yellow crystalline material of **25b** on the other hand was reproducible, and under the conditions of crystallisation the salt regularly forms large yellow needles/blocks in significant quantity. The

first crystal of study was mounted at 100 K and a data set collected at this temperature, before warming to 290 K where a second data set was collected. Both datasets were identical aside from the natural thermal expansion upon increasing the temperature to 290 K, containing a single HS trapped iron(II) centre typified by a large trans distortion (Figure 98). The solvent free polymorph of **27b** packs in P21/n, with discreet dication layers adopting a form of the terpyridine embrace along the ab plane, repeating every four layers.

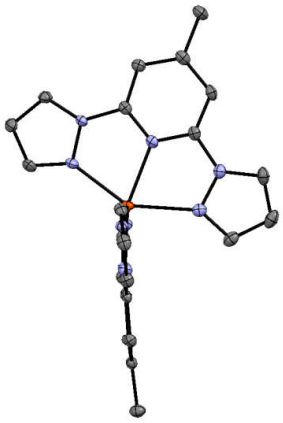

Figure 98 – View of the thermally HS trapped complex dication of solvent free 27b along the plane of one of the ligands at 100 K; thermal ellipsoids plotted at the 50% level; H atoms omitted for clarity. Atom colour code: carbon (grey), iron (orange) and nitrogen (periwinkle).

Between the distal rings of neighbouring dications within the layer, off-centre π-π distances between are 3.741 Å with C-H...π contacts of 3.119 Å make up the embrace motif at 100 K. A number of close interlayer contacts are also manifest along the c-axis perpendicular to the discreet layers, both between dications in neighbouring layers and as dication-perchlorate contacts (Figure 99). The highly distorted complex centres, with a trans angle fluctuating closely around 160° depending upon the temperature of measurement, were thought to be high spin trapped due to the lattice's inability to accommodate the large structural rearrangements required to overcome the trans distortion in the LS state. As such, powder **27b** which had shown a highly cooperative spin transition at 184 K was thought to be a solvate/hydrate as its behaviour did not appear to match with that of the HS trapped single crystals, however thermogravimetric analysis up to 120 K showed no mass loss up to 120 K, indicating that it too was almost certainly solvent free. Higher temperature mass loss could not be deduced due to the risk of explosion posed by perchlorate salts at elevated temperature.

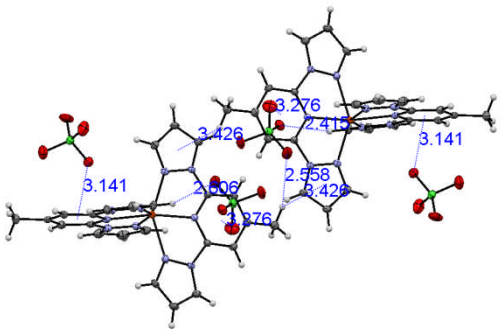

Figure 99 – Intercomplex and dication-anion contact distances in solvent free 27b thermally trapped at 100 K; thermal ellipsoids plotted at the 50% level. Atom colour code: carbon (grey), chlorine (lime green), iron (orange), hydrogen (white), nitrogen (periwinkle) and oxygen (red).

In the absence of powder data to better understand the differing behaviour of solvent free **27b**, another crystal grown from the same solvent media under identical conditions to the first was mounted at 200 K, just above the spin crossover temperature of the original powdered material. Crystallographically it was shown to be identical to the first crystal of study, with the highly distorted complex molecules possessing an N_{py}-Fe-N_{py} trans angle of 162.25° (Table 18). Upon cooling at a constant rate of 6 K min^{-1} to 100 K, between 150 and 160 the crystal was noted to become much darker in colour, and a network of cracks could be seen developing until any further cracking was indiscernible due to its intensely dark colour. Based on the p21/n space group, a dataset was acquired at 100 K however proved unsolvable due to severe twinning. The diffracted spots upon individual images were clearly broadened and split, and it was clear that, particularly along the c-direction, the crystal consisted of multiple closely overlapping domains resulting from cracking and splitting of the crystal into several much smaller crystallites. Though heavily twinned, the basic structure of the material could be seen upon attempting to solve in P21/n, however the incredibly noisy data and thus unsolvable structure did not permit the accurate quantification of metric parameters and distances. It could, however, be seen that the dications were of much higher symmetry and smaller in size, in support of the assumption that a thermal spin transition – in line with the $T_{1/2}$ of 184 K of the powdered material – had taken place. Though, it appears, the complex dication is not so highly distorted so as to prevent a thermal spin transition, the lattice on the macroscale cannot and numerous cracks propagate throughout the crystal.

Large structural and electronic redistributions are what is responsible for cooperative spin transitions in the solid state, and it clear that the complex overcoming its heavy trans distortion is responsible for the large hysteresis width, measured as 18 K in the powder. If one applies the relation for the inverse energy gap law for predicting T_{LIESST}, which correlates with the thermal trapping temperature above which the material relaxes rapidly back to the LS configuration, $T_{LIESST} = T_0 – 0.3T_{1/2}$, with a value of 150 K for a tridentate chelating ligand

as in **27b**, one obtains a value of 95 K. The material is clearly trapped above this temperature, so as to estimate its relaxation temperature the crystal was warmed up under the cryostream to 160 K at a rate of 6 K min^{-1}. Between 137 and 139 K, the crystal darkened and cracked indicating the destruction of the crystal concomitant with its spin crossover. It should be interesting to study the material in LIESST trapping experiments to more accurately quantify its relaxation temperature, in addition to the kinetics of the relaxation and better understand the exact origin of the crystal deformation. As noted above, the lone crystal of solvent free **27a** was destroyed upon undergoing a transition from HS → LS, yet its hysteresis width is significantly smaller than that in **27b**, however no direct comparisons between the two salts can be made so as to better understand this behaviour in the absence of structural data on spin crossover active solvent free **27a**.

No./polymorph	**27a**.4MeNO$_2$	**27b**			**27b**.4MeNO$_2$	**27c**
T / K	100	100[a]	290[a]	200[b]	150	100
Volume of Fe Polyhedron / Å^3	9.47(2)	12.163(7)	12.34(3)	12.185(13)	9.50525(18)	11.619(7)
Rhombic / °	94.44(37)	156.13(24)	150.5(10)	150.74(44)	86.44(31)	173.67(23)
Trigonal / °	308	478	471	474	283	518
Trans Angle / °	180.00	160.06(7)	163.6(3)	162.25(13)	180.00	157.93(9)
Least sq. planes difference / °	89.71(10)	89.625(18)	89.50(9)	89.80(4)	89.895(3)	67.69(3)
Av. bite angle / °	79.19(26)	73.30(14)	73.4(6)	73.46(25)	80.06(12)	72.71(12)
Av. Fe-N_{prox} / Å	1.893(8)	2.1300(27)	2.127(11)	2.124(4)	1.894(3)	2.1488(23)
Av. Fe-N_{dist} / Å	1.973(10)	2.1922(38)	2.197(16)	2.189(7)	1.971(4)	2.1823(34)

Table 18 - Geometric parameters for polymorphs of the homoleptic iron(II) salts of 1-bppMe.

Less interesting than their tetrafluoroborate and perchlorate cousins were the hexafluorophosphate and triflate salts, **27c** and **27d** respectively, possessing no cooperative spin crossover behaviour in any of their observed phases. Magnetically the salts obtained in powder form suggested the existence of at least two phases, one of which in each case was poorly crystalline and underwent gradual transitions spanning the thermal measurement regime (Figure 100). **27c** contains a major phase which is HS trapped, whereas at 330 K and upwards the susceptibility of **27d** is shown to increase sharply indicating high temperature spin crossover of one of its phases however measurement was limited to 350 K.

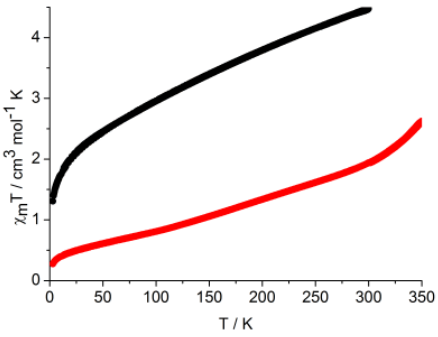

Figure 100 – Variable temperature magnetic susceptibility curves, collected in both cooling and warming modes, for powder 27c (black) and 27d (red), between 3 and 300 K and 3 and 350 K respectively.

27d, employing a counterion of non-spherical shape, did not form suitable single crystals during repeated recrystallisation endeavours. Instead, the salt precipitated out as fine powders of similar colour to that of the powdered material or as a polycrystalline film on the outside of crystallisation vials. **27c** formed bright yellow needles, the quality of which could be improved by slowing down the vapour diffusion as far as was feasible. Crystallising in I2/a, **27c** possesses a single unique iron(II) centre which is unambiguously HS at 100 K hence undergoes no change in spin state between 100 and 290 K. Unlike **27b**, the much larger hexafluorophosphate cannot fit between intercalating layers of dications and terpyridine embrace packing is not achieved. Nevertheless, complex molecules do pack in discreet layers along the ab plane as in their perchlorate counterpart, but intercomplex distances are much greater in magnitude in addition to severe angular distortions induced about the iron(II) centre induced by the hexafluorophosphate anions positioned between neighbouring molecules both inter- and intralayer (Figure 101).

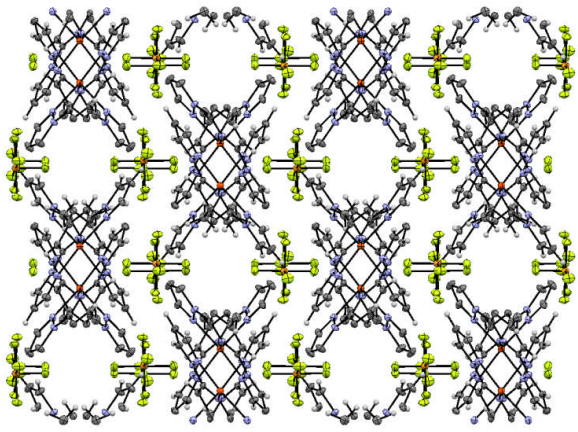

Figure 101 -Crystal packing of solvent free 27c at 100 K, viewed along the crystallographic c axis; thermal ellipsoids plotted at the 50% level. Atom colour code: carbon (grey), fluorine (chartreuse yellow), iron (orange), hydrogen (white), nitrogen (periwinkle) and phosphorus (peach).

The angular distortions in **27c** are almost certainly responsible for its indefinite adoption of a HS trapped configuration. **27c** possesses not only an extremely small N_{py}-Fe-N_{py} trans angle (Table 18) which in itself renders spin crossover impossible, but also a rarely observed Jahn-Teller distortion best described as twist about the least squared planes of the two meridionally chelating ligands.[5, 9, 14, 50] This meridional twist stabilises the HS slightly relative to the LS by virtue of a reduced antibonding interaction between one of the pyrazole σ-orbitals and the iron(II) $d_{x^2-y^2}$ lone pairs at the expense of the second distal pyrazole's antibonding interaction, reducing effective symmetry and causing a concomitant increase in the HS ligand field experienced by iron. The unusual twist is commonly induced by tris-chelating ligands which necessitate smaller bite angles because of electronic repulsion between groups/atoms with the iron e_g set, yet in this instance this is not the cause.[5] Instead, the distortion is forced because of the close contact of a methyl group about a coplanar ligand of a neighbouring dication with the π-lobes of one of the pyrazole rings (Figure 102), which are forced into close proximity by the sandwiching effect of the large hexafluorophosphate anions.

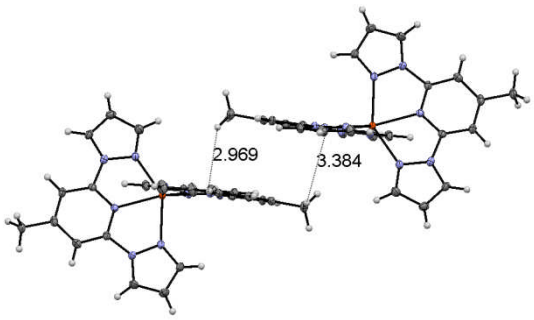

Figure 102 – Closest interlayer complex interactions between two of the highly distorted complex dications in solvent free 27c at 100 K; thermal ellipsoids plotted at the 50% level. Atom colour code: carbon (grey), iron (orange), hydrogen (white), and nitrogen (periwinkle).

5.4.2 Coordination chemistry of the electron withdrawing derivatives 1-bppCOOH, 1-bppNO$_2$

Only the tetrafluoroborate iron(II) salts of 1-bppCOOH and 1-bppNO$_2$, **29a** and **31a**, were studied in any detail in the solid state, primarily because of the very small quantities of the organic compounds at our disposal. **29a** was isolated as a brick-red powder, suggesting a mixed-spin system which analysed as a dihydrate. **31a**'s solvent free microcrystalline particulates took upon a deep purple hue whose spin-state could not be directly inferred visually due to contributions from strong intraligand bands in the high energy visible region. An extensive array of methods and solvent combinations was tried in order to acquire single

crystals of both complex salts, and all yielded either partially decomposed materials or powders precipitating out of the media.

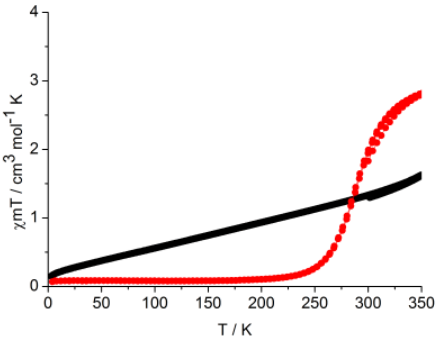

Figure 103 – Magnetic susceptibility curves for 29a (black) and 31a (red), scanned in cooling and warming modes between 3 and 350 K.

The bulk powders were subjected to magnetic measurements over the 3-350 K range and it was found that at RT **29a** is comprised of approximately 77% LS centres. The material undergoes a very gradual spin conversion, up to a maximum of 30% HS at 350 K. With an almost linear slope, the material switches almost linearly over the down to 24 K at a rate of 0.07% of centres switching per Kelvin, until the zero field splitting of the residual HS spin centres complicates the very low temperature region of the curve. The small discrepancy which is apparent between the heating and cooling modes above 300 K are outside of the error margin, however without structural clarification it is impossible to draw a solid conclusion. **31a** switches all but fully over quite a large temperature range of 120 K, centred at 287 K with no noticeable differences between data points in cooling and warming modes (Figure 103). Analysis of the form of the curve allows the estimation of the plateau at ca. 370 K, which could not be reached with the set up on the SQUID magnetometer employed. The plateau is oddly at χmT 2.9, which considering the absence of diamagnetic contaminants by ^{1}H NMR, mass spectrometry and microanalyses is probably the result of a minor secondary phase of entirely LS centres accounting for approximately 25% of the bulk powder.

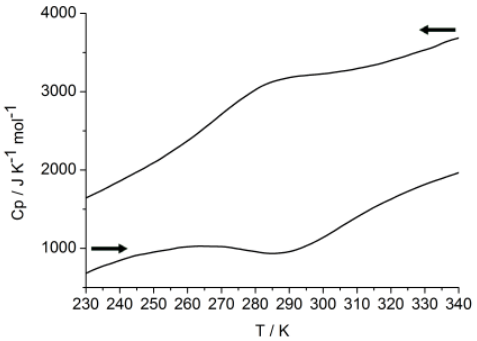

Figure 104 – Region of the differential scanning calorimetry curve of 31a, scanned in both cooling and warming modes between 218 and 368 K.

The enthalpy and entropy of the transitions were calculated as 18.54 kJ mol^{-1} and 65.26 J K^{-1} mol^{-1} during cooling, and 17.85 kJ mol^{-1} and 62.41 J K^{-1} mol^{-1} during warming by DSC. The $T_{1/2}$ values of 284 and 286 K in cooling and heating modes respectively matched very closely with that determined as 287 K magnetically, with the discrepancies probably arising because of the difficulty in pinpointing an absolute maxima and minima in the heat capacity fluctuations over the broad transition range (Figure 104). The energetic changes associated with this spin transition are, though certainly within range for typical thermal spin transitions of iron(II), in actual fact predicted to be in the region of 20 – 30 % greater than those which were calculated from the DSC curves. This being due to the minor diamagnetic phase which does not contribute to the head capacity fluctuations, as observed in the magnetic plot (Figure 103) but the inability of obtaining structural data upon either phase precludes further analyses. The $T_{1/2}$ of the major switching phase is, it should be noted, only 20 K below that of the solution phase value which means there is only very minor stabilisation of the HS state in the solid down to lattice effects and internal pressure.

5.4.3 Multiple polymorphism of the complex salts of 1-tpp

The spin crossover of three salts *bis*-chelated by 1-tpp was investigated as it had been previously shown that **28a** existed as multiple polymorphs, whose behaviours were known to contrast starkly depending upon the solvent content. An incomplete, unpublished study upon **28a** showed that magnetically in the bulk, **28a** consisted of either a biphasic mixture or two distinct iron(II) centres within a single phase, one of which switches gradually between 200 and 320 K, with the other remaining HS indefinitely.[51] Grown by slow vapour diffusion of Et_2O into a $MeNO_2$ solution, a single crystal was studied crystallographically at 150 K. The dataset solved as containing a single iron(II) environment in P-1, which had geometric parameters and bond lengths consistent with an almost completely LS configuration. Clearly, there exist discrepancies between the material phase studied crystallographically and those studied magnetically in the preliminary investigation.

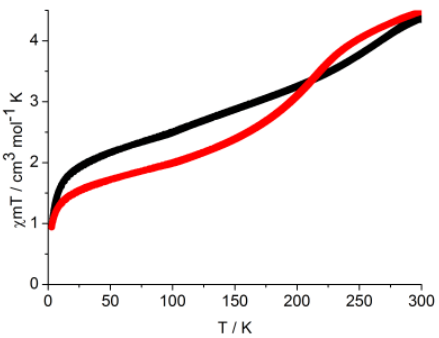

Figure 105 – Variable temperature magnetic susceptibility plots of powder 28a (black) and 28b (red), acquired in cooling and warming modes between 3 and 300 K.

28a and its perchlorate analogue **28b** were isolated both as fine powders, both having an almost identical yellow colour. Desiccating the powders for a period did not, as far as was visually noticeable, cause a change in their appearances. The magnetic susceptibility curves were similar, which appeared to indicate a gradual spin transition below 300 K in both salts, however a plateau below 140 K was more well defined in **28b** representing a significant quantity of HS centres remain trapped regardless (Figure 105). Interestingly this curve more closely matches that of the previously investigated sample of **28a**, than does the yellow **28a** prepared in this study whose behaviour is less well defined below 300 K.

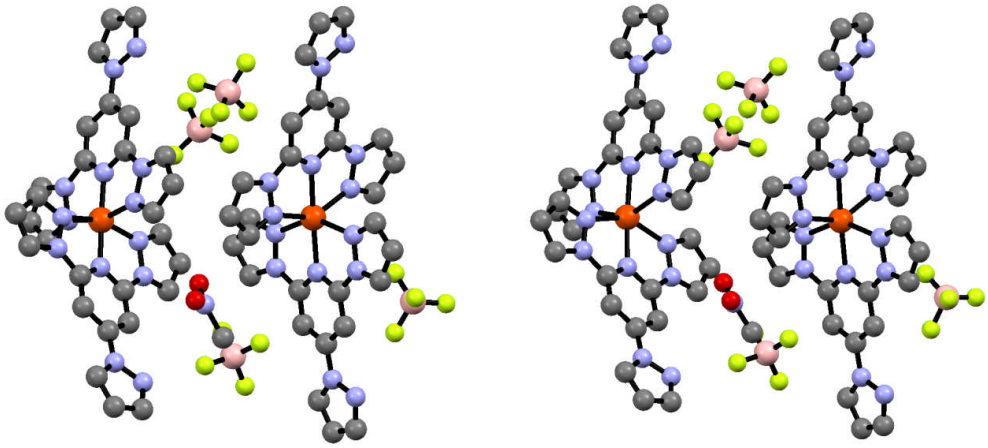

Figure 106 – Views down the crystallographic a axis of the asymmetric units containing the two unique iron(II) complex centres in 28a.$^1/_2$MeNO$_2$, at 100 K (left) and 350 K (right); the gradually switching Fe1 complex is shown on the left of each image, with the HS trapped Fe2 complex on the right; H atoms omitted for clarity. Atom colour code: boron (pink), carbon (grey), fluorine (chartreuse yellow), iron (orange), nitrogen (periwinkle) and oxygen (red).

Vapour diffusion of Et_2O into $MeNO_2$ solutions of **28a** and **28b**, under identical conditions to the original crystallisation of **28a**, yielded yellow needles for both complexes, which both underwent a change in colour to a darker orange-yellow upon lowering of the temperature to 100 K. The yellow needles were crystallographically isostructural to one another, comprising two unique iron(II) complexes, one of which was consistent with being entirely LS, dubbed Fe1 in both salts, and the other a distorted HS centre, labelled Fe2. A single $MeNO_2$ of crystallisation exists in the lattice, so that there resides half a molecule of $MeNO_2$ per complex dication. Upon warming to 290 K, between 200 and 290 K **28a**.$^1/_2$MeNO$_2$ and **28b.**$^1/_2$MeNO$_2$ both lightened in hue slightly, and a crystallographic dataset collected at this temperature on both crystals showed that the majority of Fe1 sites were now in the HS configuration as determined from its metric parameters (Table 20). At 350 K, **28a**.$^1/_2$MeNO$_2$ contains two crystallographically unique fully HS centres, with no loss of solvent from the lattice, and the situation is likely to be identical for **28b**.$^1/_2$MeNO$_2$ though no structure was collected on this solvate at this temperature.

In both salts of this solvate, the HS trapped Fe2 complexes are sandwiched above and below the central pyridine rings of both ligands by nearby counterions, which are not only responsible for its significant trans distortion but consequently the iron(II) centres' inability to overcome this distortion and contract, which is necessary to adopt a LS configuration. The spin transition in Fe1 appears to be promoted by a change in positional disorder in the lattice $MeNO_2$, with the concomitant reduction of lattice pressure about Fe1 allowing it to expand and adopt a relatively undistorted HS configuration. Upon warming from 100 K, somewhere between 200 and 290 K the molecule of $MeNO_2$ becomes highly disordered and undergoes not only a positional change, but also rotates primarily about the c-axis approximately 15° (Figure 106).

No./polymorph	**28a**.$^1/_2MeNO_2$					
T / K	100		290		350	
Fe centre	Fe1	Fe2	Fe1	Fe2	Fe1	Fe2
Volume of Fe polyhedron / Å^3	9.613(16)	12.160(19)	11.59(3)	12.20(3)	12.06(3)	12.25(3)
Rhombic / °	89.06(7)	153.44(67)	138.3(10)	151.6(10)	149.7(10)	155.1(10)
Trigonal / °	292	478	433	465	465	479
Trans angle / °	176.0(2)	167.4(2)	174.7(3)	169.5(3)	173.7(3)	169.1(3)
Least sq. planes difference / °	89.55(5)	88.11(5)	88.44(8)	88.66(8)	87.51(9)	88.19(9)
Av. bite angle / °	79.8(4)	73.2(4)	74.7(6)	73.4(5)	73.6(6)	73.1(6)
Av. Fe-N_{prox} / Å	1.901(7)	2.121(7)	2.067(9)	2.122(8)	2.103(10)	2.134(9)
Av. Fe-N_{dist} / Å	1.982(10)	2.181(10)	2.129(16)	2.178(15)	2.166(17)	2.179(16)

No./polymorph	**28b**.$^1/_2MeNO_2$			
T / K	100		290	
Fe centre	Fe1	Fe2	Fe1	Fe2
Volume of Fe polyhedron / Å^3	9.593(18)	12.02(2)	11.61(2)	12.16(2)
Rhombic / °	88.69(82)	149.53(69)	143.5(10)	152.9(8)
Trigonal / °	291	466	446	473
Trans angle / °	175.8(3)	168.1(2)	172.8(3)	169.1(2)
Least sq. planes difference / °	89.16(6)	89.77(6)	87.64(8)	88.97(8)
Av. bite angle / °	79.83(51)	73.55(40)	74.2(6)	73.3(4)
Av. Fe-N_{prox} / Å	1.900(8)	2.109(8)	2.081(8)	2.128(7)
Av. Fe-N_{dist} / Å	1.981(12)	2.167(13)	2.131(14)	2.173(14)

Table 19 – Geometric distortion parameters for the isostructural solvates 28a.$^1/_2MeNO_2$ and 28b.$^1/_2MeNO_2$.

A second solvate crystallises alongside **28a**.$^1/_2MeNO_2$ - not observed in **28b**'s case - which were distinctly different bright yellow blocks, as opposed to needles within the crystallisation vessels. Determination of its structure at 100 K, at which it took on a deep brown hue, revealed it is a trinitromethane solvate consisting of a single unique iron(II) complex unit. It was shown to be the same solvate as that which had been structurally characterised at 150 K previously within the group, crystallising in P-1 with the iron(II) centre fully in the LS configuration at both 100 and 150 K from inspection of geometric parameters (Table 20). The transition is reversible, proceeding in a reasonably gradual fashion between 200 and 265 K. After the initial data set was collected on the fully LS material at 100 K, ramping of the temperature to 265 allowed the attainment of a dataset of the material in its fully HS state. Returning to 200 K, the crystal returned to a brown colour and the metric parameters were in accord with an entirely LS configuration. The crystal cannot be held above 265 K long enough to acquire a full structural solution since loss of lattice $MeNO_2$ is facile close to room temperature as indicated by darkening of the material and loss and severe degradation of the crystal.

Curiously, changing the antisolvent from Et_2O to $^iPr_2O$ makes no difference in **28b**'s case and entirely needles of **28b**.$^1/_2MeNO_2$ are obtained, however the slower rate of crystallising **28a** yields a third polymorph, which is distinctly brown needles at room temperature. A crystallographic dataset collected at 100 K showed two entirely LS complex dications, which appear to be trapped given that there were no signs of thermochroism between 100 and 290 K. Out of the three solvate polymorphs of **28a**, **28a**.2$MeNO_2$ is the most tightly packed with distances of down to 2.5 Å between aromatic protons and both nitromethane methyl protons and counterion fluorides, which likely bear most responsibility for its inability to expand. Oddly, unlike in any of the other solvates, the non-coordinating pyrazole rings are bent significantly out of plane with the rest of the ligand backbone, with plane-plane twist angles of up to 20°. The most severe of these puckering is a result of two weak hydrogen bonding interactions, at 2.72 and 2.74 Å, between $MeNO_2$ solvate molecules. Though a relatively minor factor, it is to be mentioned that said deviation from planarity will contribute towards prevention of the iron(II) sites from switching into the HS state, through an increase in ligand field strength arising from weaker π-donor ability.

No./polymorph	**28a**.3$MeNO_2$			**28a**.2$MeNO_2$		**28c**.2$MeNO_2$
T / K	100	200	265	100		100
Fe centre	-	-	-	Fe1	Fe2	-
Volume of Fe polyhedron / Å^3	9.5122(2)	9.7683(4)	11.7050(8)	9.453(7)	9.401(7)	9.562(5)
Rhombic / °	87.71(35)	91.94(69)	152.8(10)	87.35(31)	83.70(32)	89.29(24)

Trigonal / °	287	299	471	282	273	289
Trans angle / °	173.8846 (3)	173.9412(7)	164.827(2)	178.11(8)	175.82(9)	178.11(7)
Least sq. planes diff. / °	89.431(3)	90.971(5)	89.751(9)	85.58(2)	86.90(2)	88.665(16)
Av. bite angle / °	79.93(20)	79.45(40)	73.5(6)	80.07(18)	80.39(19)	79.83(14)
Av. Fe-N_{prox} / Å	1.901(3)	1.911(7)	2.116(11)	1.893(3)	1.889(3)	1.8988(24)
Av. Fe-N_{dist} / Å	1.971(5)	1.978(10)	2.153(14)	1.966(4)	1.964(5)	1.9750(34)

Table 20 – Geometric parameters for non-magnetically characterised solvates of iron(II) salts bis-chelated by 1-tpp.

Returning to the susceptibility curves of **28a** and **28b**, the behaviour can now be better interpreted from the understanding of the switching ability of the different crystallographically characterised solvates. **28b** can almost unambiguously be said to correspond to **28b**.$^1/_2MeNO_2$, as the curve correlates to a single phase material containing two iron(II) centres, one of which remains indefinitely trapped whilst the other switches gradually above 200 K, which is what is seen crystallographically (Table 19). The less well defined behaviour of **28a** is suggestive both of multiple phases, but also of partial lattice solvent evaporation resulting in loss of crystallinity of at least one phase. **28a**.$2MeNO_2$ can be negated from discussion given that its appearance only manifests under the conditions of very slow conditions, and indeed may not form at all using Et_2O as antisolvent which was that used during preparation of the bulk material. The curve is instead represented by a majority **28a**.$^1/_2MeNO_2$ phase, contaminated by a small amount of **28a**.$2MeNO_2$.Et_2O which has partially, if not entirely, lost the ethereal solvent from the lattice. Crystals of **28a**.$2MeNO_2$.Et_2O lose Et_2O noticeably when left exposed to air over a period of hours and take on a much darker orange-brown. Powder **28a** was left standing for a number of weeks before subject to SQUID measurement, and as such it is unlikely any of the ethereal phase survived. The gradually switching component of the curve between 180 and 300 K, far more gradual than in **28b**, can be said to be the combined effect of Fe1 switching in **28a**.$^1/_2MeNO$ and that of a poorly crystalline phase post-loss of Et_2O.

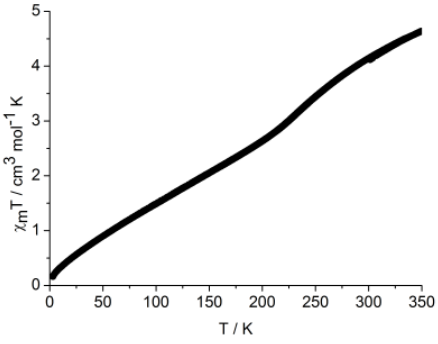

Figure 107 – Susceptibility vs. temperature plot for the bulk powder of 28c, scanned in cooling and warming modes between 3 and 350 K.

28c's magnetic profile is barely worth comment, switching only very gradually between 10 and 300 K, with a reduction in the slope towards the latter suggestive that by this temperature the entirety of the material is in the HS state (Figure 107). This material, it must be stressed, was isolated through a salt exchange precipitation in a medium consisting of MeOH-H_2O, and cannot be correlated with the singly crystalline **28c** solvates which were grown by vapour diffusion of Et_2O into $MeNO_2$.

Large, brown cuboidal blocks of **28c** were obtained over a course of 2 – 3 days, indicating a LS material at RT. At 100 K, the material was shown to contain a single iron(II) centre in the LS state as deduced from its geometry, with no evidence of thermally induced spin crossover between 100 and 290 K and containing two molecules of $MeNO_2$ per complex centre. This makes **28c** anomalous amongst the hexafluorophosphate salts of the series of complexes in this study, in that contrary to the usual HS trapping of the complex dications, the converse is observed. Unlike any of the crystallographically characterised solvates of **28a** and **28b**, the dications pack in a motif which is reminiscent of the terpyridine embrace. Like the terpyridine embrace, the dications are ordered into two unique alternating layers (Figure 108). There exist off-centre C-H...π interactions between pyrazole rings of neighbouring complexes, with distances of 2.936 and 3.394 Å. These interactions between closely associated neighbouring dications only run in a single direction however, along the c-axis. The close association is prevented from expanding in two directions due to the necessary occupation of the space between neighbouring dications along the b-axis by both protruding non-coordinating pyrazole rings from the layers directly above and below, but also by $MeNO_2$ solvent molecules. It is this extremely tight packing which is thought to be responsible for the inability of the complexes to expand and adopt the HS state, and hence remain entirely LS trapped due to the intrinsically high lattice pressure resulting from this packing motif.

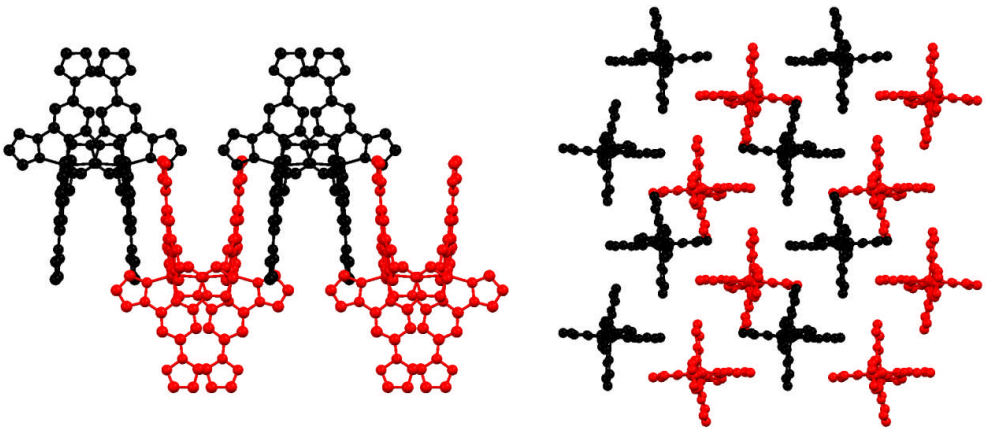

Figure 108 – Crystal packing diagrams of 28c at 100 K viewed parallel (left) and perpendicular (right) to the plane bisecting the iron(II) centres; discreet layers along which closely associating dication units pack are distinguished by their colour; H atoms are omitted for clarity.

A very small number of a secondary crystalline material also results from $MeNO_2/Et_2O$, however the quality of these crystals was markedly poor, appearing to be small bright yellow polycrystalline fractured blocks. At attempt was made to mount one of the crystalline fragments onto the diffractometer, however the crystal diffracted poorly, not beyond 1.3 Å, with large, smudged non-uniform spots. To increase the data quality, the temperature was cooled to 100 K, but it was noted that the crystal gradually became darker in colour until it was all but fully dark brown at 100 K. A dataset was collected, but could not be fully solved due to severe twinning. A preliminary structure determination showed that the complex crystallised in P-1, with two unique almost entirely LS complex centres. Splitting of the peaks about the ligand backbone were, as expected from the appearance of the diffraction images, indicative of the crystal containing multiple domains but also of a possible minor HS fraction alongside the dominant LS centres. The poor quality crystallographic data didn't permit a stoichiometric conclusion of the crystal, however the solvent content was definitely below that of **28c**.$2MeNO_2$ as judged from the residuals.

5.4.4 The hydroxy and methoxy complex salts

Upon crystallisation of **32a** and **32b** from $MeNO_2$ solutions by addition of Et_2O one obtains the salts as yellow solvent free materials, which were shown magnetically to consist of a single phase as from the complete, abrupt spin transition profiles centred at 221 and 207 K respectively (Figure 109). The spin transitions of both salts in addition to their abruptness possess 1 K hysteresis, suggestive of a high degree of crystallinity. When the solvent of crystallisation is changed to methanol, the profiles take on a different form in which it is clear the materials are biphasic. **32a** comprises primarily of high spin trapped centres, but **32b** switches gradually from LS → HS to about a third completeness between 3 and 300 K. Both materials contain abrupt discontinuities at 221 K in **32a** and 208 K in **32b**, which coincide with the $T_{1/2}$values for the solvent free polymorphs. Based on closer inspection of the curves, the solvent free contaminant phases of the solvated materials were estimated as consisting of 26% and 13% of the multiphase materials respectively.

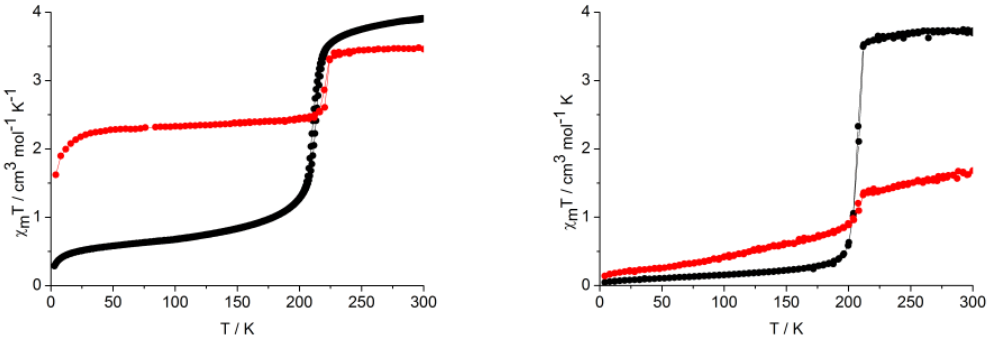

Figure 109 – Variable temperature magnetic curves for 32a (left) and 32b (right) between 3 and 300 K; bulks samples crystallised from $MeNO_2$ and MeOH are represented by black and red curves respectively.

Solvent free **32a** and **32b** do not readily form suitably sized single crystals, and therefore no structural information could be learned. The bulk solvent free materials were subject to thermodynamic measurements between 190 and 300 K, and both exhibited single maximum peaks in cooling and warming mode of the heat capacity curves, endothermic and exothermic respectively, as expected based upon their magnetic profiles (Figure 110). Though performed using the same scan rate, the hysteresis is clearer via DSC, with transition peak separation of 6 K for the tetrafluoroborate and 5 K in its perchlorate cousin (Figure 110). ΔH and ΔS of the transition process were calculated as 17.76 kJ mol^{-1} and 85.19 J K^{-1} mol^{-1} in cooling and 17.51 kJ mol^{-1} and 81.61 J K^{-1} mol^{-1} in warming for **32a**, and in **32b** the values were 22.16 kJ mol^{-1} and 108.38 J K^{-1} mol^{-1} in cooling and 21.22 kJ mol^{-1} and 101.29 J K^{-1} mol^{-1} during the warming cycle. The smaller ΔH and ΔS of **32a** can probably in part be ascribed a very minor paramagnetic impurity in the magnetic curve of its solvent free phase (Figure 109) which does not contribute to the transition energetics. If one assumes that the solvent free phases are isostructural in nature, due to the almost identical profiles of the curves, then this assertion is supported due to the slightly lower $T_{1/2}$ of **32b** than **32a**, which is an effect of the larger unit cells necessitated by the perchlorate cations with respect to the tetrafluoroborate. The larger cells effectively reduce the internal lattice pressure felt by the iron(II) dications, destabilising the low spin state to a degree which causes the observed reduction in $T_{1/2}$.

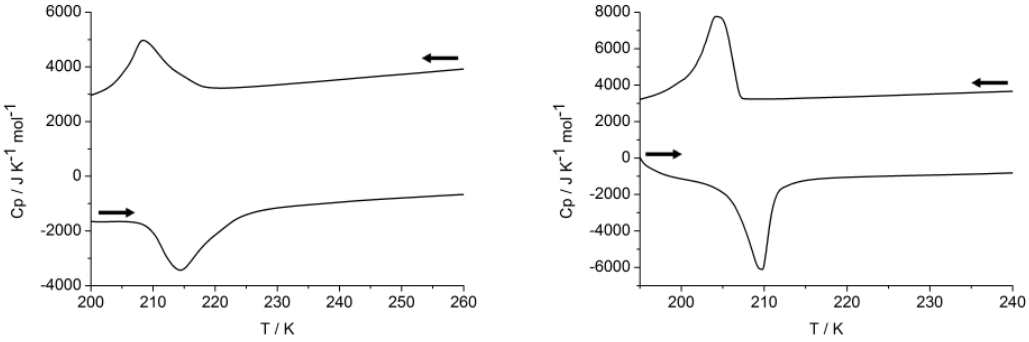

Figure 110 – Differential scanning calorimetry plots for 32a (left) and 32b(right), scanned in cooling and warming modes between 193 and 303 K.

In contrast with the solvent free phase, the methanol solvates crystallise as large yellow-brown wedges and blocks, in the case of **32a** and **32b** respectively. The brown sheen on the outer part of the crystals may result from partial desolvation at the surface. The materials are both disolvates, containing a molecule of methanol hydrogen bonded to the hydroxy functionalities about each 1-bpp backbone. Unusually, the perchlorate and tetrafluoroborate are not isostructural with one another, with the former possessing two unique iron(II) sites and crystallising in P21/c, and the latter packing in P-1 (Figure 111). The single iron centre in **32a** is entirely high spin, in strong agreement with its magnetic behaviour which remains fully high spin. Both iron(II) centres in **32b** have slightly shorter Fe-N distances, in addition to significantly smaller octahedral distortions (Table 21). Feasibly, the centres are switching gradually from HS→LS as the crystal was cooled to 150 K, which is also seen magnetically, however if one removes the contribution of the abruptly switching polymorph from the magnetic profiles one would expect parameters which represent a material in approximately 25% HS configuration. The crystallographic data implies a HS population of around 70%, and it is believed that partial desolvation and loss of crystallinity occurred in the ground, bulk sample of **32b**.2MeOH which accounts for its different magnetic spin-state population at 150 K to that of the crystallographically characterised sample.

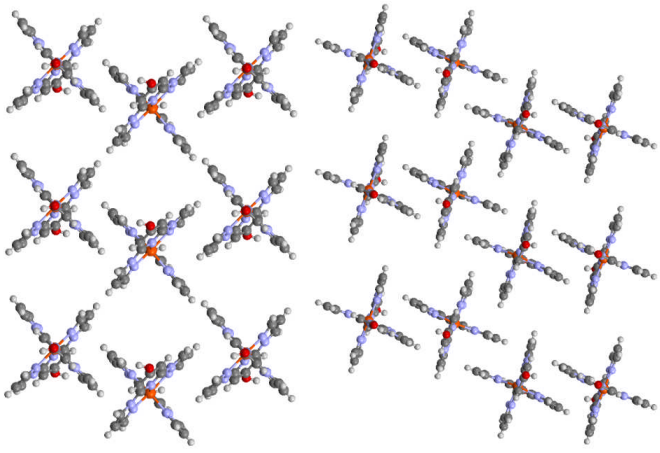

Figure 111 – Crystal packing diagrams of 32a.2MeOH (left) and 32b.2MeNO$_2$ (right) at 150 K viewed along one of the Fe-N$_{py}$ bonds of the complexes. Atom colour code: carbon (grey), iron (orange), hydrogen (white), nitrogen (periwinkle) and oxygen (red).

As the iron centres in the dimethanol solvates of **32a** and **32b** are not hugely distorted, in combination with the onset of a gradual low-temperature transition in **32b**.2MeOH as evidenced by its metric parameters, the hydrogen bonded methanol solvates (Figure 112) are almost certainly responsible for the stabilisation of the HS state with respect to the solvent free phase. Such behaviour is the diametric opposite of that which is usually observed, with strong localised hydrogen bonding interactions or networks effectively increasing the donor strength of coordinated pyrazoles, triazoles and simple amines resulting in a marked stabilisation of the low spin configuration.[52-55] This reversal in behaviour is in accord with findings in Section 5.3.2 that the lower energies of the central pyridine π* lobes mean their contribution to the Fe-N interaction is far more significant, and hence their sensitivity towards electronic changes is increased. Thus we see stabilisation of the high spin state as the Fe-N backbonding contribution is reduced, as in the heavily electron rich hydrogen bonded **32a** and **32b** dimethanol solvates.

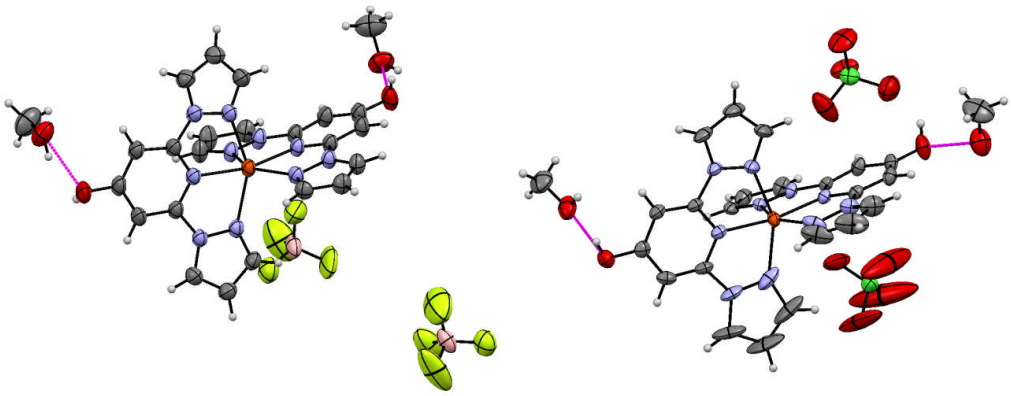

Figure 112 – Views of the iron(II) complex dication in 32a.2MeOH (left) and one of the two unique complex units in 32b (right) at 150 K; thermal ellipsoids plotted at the 50% level. Atom colour code: boron (pink), carbon (grey), chlorine (lime green), fluorine (chartreuse yellow), iron (orange), hydrogen (white), nitrogen (periwinkle) and oxygen (red).

The ground powders, obtained by diffusion of the ethers Et_2O, ^tBuOMe and $^iPr_2O$ into methanolic solutions of **32c**, analysing as a solvent free material, possessed a magnetic curve telling of an iron(II) material which remains almost entirely high spin down to 3 K (Figure 113). Single crystals of the material which, unlike the powder, were not left to stand for a period of days, showed it to exist as the dimethanol solvate (Figure 114), with MeOH molecules hydrogen bonded to the 4-hydroxy position as in the tetrafluoroborate and perchlorate salts.

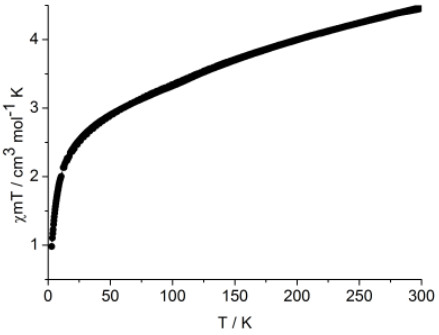

Figure 113 – Magnetic susceptibility curve for 32c measured both in cooling and warming modes between 3 and 300 K.

Both the solvent free and dimethanol solvate phases of **32c** are entirely HS at 100 K, as determined magnetically and crystallographically respectfully. The drop off in magnetism, which suggests approximately 30% of centres switch into the LS state between 300 and 100 K is not observed crystallographically in the solvated phase. Powder measurements revealed that the phases were not isostructural, with the solvent free phase retaining a high degree of crystallinity suggesting the different phases can be grown preferentially depending upon the speed of crystallisation. In absence of single crystals of the solvent free phase, the crystallographic discussion is limited to the dimethanol phase, with treatment of the two phases considered separately.

In the dimethanol solvate, the prevalence of the high spin state down to 100 K should come as no surprise given the observation that the lattice methanol results in a stabilisation of the high spin state. Crystallising in the orthorhombic space group Pccn, the complex dications associate closely with the closest offset π-π and C-H...π interactions 3.973 Å and 2.624 Å respectively. One of the methanol solvates forms a hydrogen bonded bridge between a 1-bppOH hydroxy group and fluorine of a counterion, whilst the other possesses a longer hydrogen bond length and is positioned too far from the second counterion to form a second interaction. One of the coordinated 1-bppOH moieties shows an odd perturbation from planarity of 10.36° between the coordinated distal pyrazoles. The cause of this puckering of the otherwise planar backbone is a probable result of the close steric contacts with a hexafluorophosphate counterion either side of the central pyridine ring, which are between 3.3 and 3.4 Å.

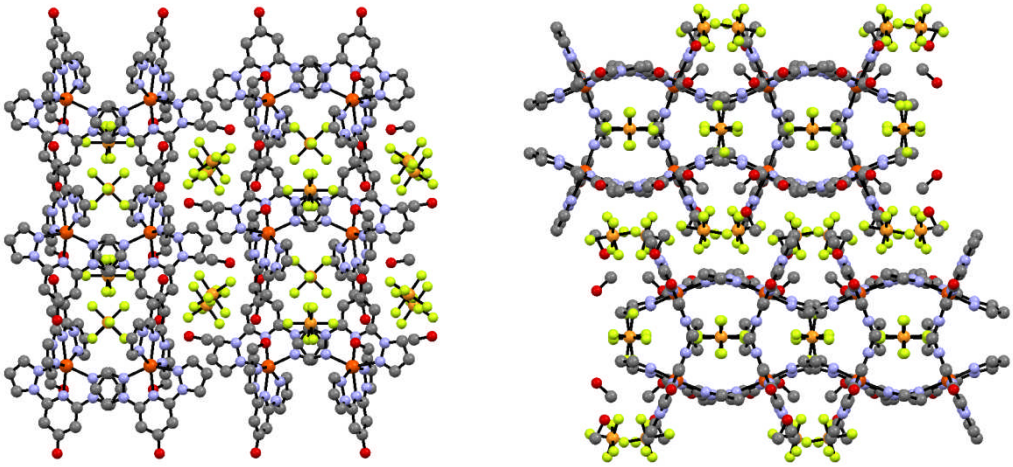

Figure 114 – Crystal packing of 32c.2MeOH along the crystallographic a axis (left) and c axis (right) at 100 K; H atoms omitted for clarity. Atom colour code: carbon (grey), fluorine (chartreuse yellow), iron (orange), nitrogen (periwinkle), oxygen (red) and phosphorus (peach).

No./polymorph	**32a**.2MeOH	**32b**.2MeOH		**32c**.2MeOH
T / K	150	150		100
Fe centre	-	Fe1	Fe2	-
Volume of Fe Polyhedron / Å^3	12.6291(9)	11.6186(17)	11.6153(17)	12.184(7)
Rhombic / °	154.06(31)	130.34(42)	126.66(42)	153.00(24)
Trigonal / °	481	414	414	475
Trans Angle / °	165.486(2)	169.203(3)	169.087(3)	166.70(7)
Least sq. planes difference / °	85.212(9)	86.651(13)	86.675(13)	87.354(18)
Av. bite angle / °	73.19(17)	75.54(23)	75.47(23)	73.34(14)
Av. Fe-N_{prox} / Å	2.151(3)	2.065(4)	2.069(4)	2.1214(25)
Av. Fe-N_{dist} / Å	2.213(5)	2.132(7)	2.130(7)	2.1810(38)

Table 21 - Geometric parameters for the crystallographically characterised dimethanol solvates of the 1-bppOH complex salts.

Upon methylation of the hydroxy group, 1-bppOMe forms complex salts which have far lower solubilities in protic solvents such as MeOH and EtOH, as the ability of the ligand backbones to hydrogen bond has been reduced appreciably. Instead, successful crystallisation was achieved by slow diffusion (ca. 3 – 5 days) of ^{t}BuOMe and ^{i}Pr$_2$O into $MeNO_2$ solutions of **33a** and **33c**. The intensely yellow blocks so obtained in each case were proven crystallographically to be a monohydrate and solvent free respectively. The crystals underwent no observable change in colour upon cooling to 100 K, and each comprise of a single fully high spin trapped iron(II) centre. Ground up crystalline **33a** showed an almost completely flat plateau until the sharp drop off at very low temperature due to zero field splitting, in accordance with the structural data on its monohydrate (Table 22). The values $\chi_m T$ maxima of 3.76 in **33a** and 4.00 in **33c** suggest that the entirety of the iron(II) centres are in the high spin configuration over the plateau at RT (Figure 115).

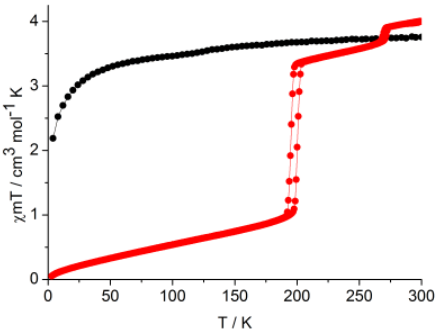

Figure 115 – Magnetic susceptibility plots of powder 33a (black) and 33c (red) during cooling and warming scans between 3 and 300 K.

Though **33a** is characterised by uninteresting magnetic behaviour in accord with a HS trapped material, the magnetic profile for **33c** below room temperature yielded a number of surprising features. The curve is comprised of at least three material phases, the first (minor) of which upon cooling accounts for the small discontinuity between 266 and 275 K, suggesting an abrupt SCO centred at 271 K. The second (major) switches abruptly and hysteretically at 198 K with a hysteresis width of 5 K. These two phases make up approximately 5 and 60% of the material, with the remainder (residual) 35% undergoing a very gradual transition spanning the entire temperature regime. None of these three phases match with the high spin trapped solvent free phase which was characterised crystallographically (Table 22). Thermogravimetric analysis on the powder showed only very gradual mass loss until, at above 500 K, the salt decomposes and 1-bppOMe begins to evaporate (Figure 116). Closer inspection of the curve however shows a small plateau during the lower temperature gradual mass loss at 438 K, accounting for evaporation of 1.79% of the mass. This value corresponds roughly to loss of a single molecule of H_2O per dication in the major phase. It is therefore proposed that this hydrate phase, which switches cooperatively at 198 K loses H_2O to the atmosphere upon prolonged exposure with a concomitant loss of crystallinity and, therefore, cooperativity in its spin crossover yielding the residual phase. No further speculation can be made as to the composition of the minor phase, as it accounts for too small a proportion of the sample to infer reliable information from the TGA profile.

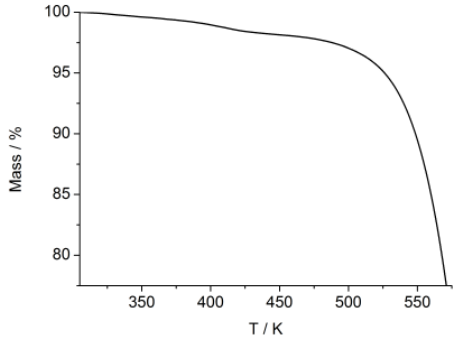

Figure 116 – Thermogravimetric analysis of multiphase 33c.

33a.H_2O and **33c** pack in Pbca and P21/c and possess extreme structural distortions about the iron octahedra, which are of such magnitude that the iron centre and indeed the entire crystal is simply unable to facilitate such a significant structural change. In particular, the N_{py}-Fe-N_{py} trans angles are very small, showing a large deviation from the ideal value of 180° (Figure 117), which in part is probably necessary in order to impart increased stabilisation of the HS ground state, by reduction of effective symmetry and amplification of the ligand field.[5, 9] The result is that the iron(II) complexes are both structurally and electronically forbidden from accessing the low spin configuration.

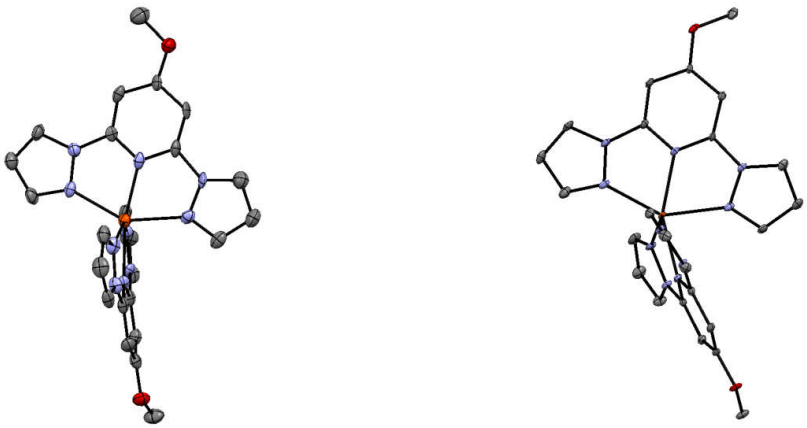

Figure 117 – The complex dications comprising 33a.H_2O (left) and 33c (right) viewed perpendicular to the plane of one of the 1-bppOMe ligands to illustrate the highly distorted iron(II) geometries; thermal ellipsoids plotted at the 50% level; H atoms omitted for clarity. Atom colour code: carbon (grey), iron (orange), nitrogen (periwinkle) and oxygen (red).

Though the trans distortion is notable in both complex salts, it is much more severe in **33c**. In **33a**, the tetrafluoroborate counterions sit above the planes of the central pyridine rings, whereas in **33c** the counterions sit centred in the same position above the two pyridines, but the much larger volume occupied by the hexafluorophosphate causes a more significant tilt of the meridional chelating system about the iron to which it is bound, which causes such a significant deviation of its trans angle. This distortion results in the 1-bpp backbone of two neighbouring dications coming into very close contact, with one of the

methoxy groups pointing away, out of the plane of the rest of the backbone at 13.169° to avoid clashing with a pyrazole ring directly below on the neighbouring molecule. It is worth mentioning that despite the fact that the crystallographic datasets for **33a**.H_2O and **33c** were collected at the same temperature, the ellipsoids (Figure 117) and ESDs (Table 22) are notably larger in the former's case in addition to bad crystallographic fitting parameters. This is a result of the lower quality crystals which were grown of **33a**.H_2O, and compounded by their degradation over time which could be caused by gradual loss of lattice water from the crystal surface yielding an overall loss of crystallinity.

No./polymorph	**33a**.H_2O	**33c**
T / K	100	100
Volume of Fe Polyhedron / Å^3	12.01(3)	11.581(6)
Rhombic / °	156.0(10)	186.70(21)
Trigonal / °	485	557
Trans Angle / °	166.0(3)	153.61(6)
Least sq. planes difference / °	82.43(8)	80.797(19)
Av. bite angle / °	73.2(6)	72.20(12)
Av. Fe-N_{prox} / Å	2.124(10)	2.1502(21)
Av. Fe-N_{dist} / Å	2.176(16)	2.1892(32)

Table 22 – Geometric distortion parameters for the iron(II) salts chelated by 1-bppOMe.

5.4.5 The mercaptan and thiomethyl complex salts

The lability of the 1-bppSH containing salts **34a**, **34b** and **34d** towards dimerisation, dechelation and hydrolysis meant that crystallisation could only be performed in a limited number of solvents, namely $MeNO_2$, MeCN and, where soluble, acetone. In every instance only powdered material aggregated from solution, and study of the different salts' spin crossover was limited to measurements on the bulk powder samples.

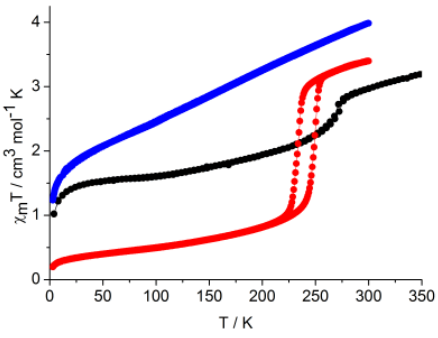

Figure 118 – Magnetic susceptibility plots in both cooling and warming modes for powdered 34a (black), 34b (red) and 34d (blue) measured between 3 – 300 K, with the exception of 34a which was subject to measurement between 3 and 350 K.

The triflate salt **34d**, as with all triflates subject to investigation in the series of complexes discussed in this chapter, possessed unremarkable behaviour in the solid state.

Its curve indicates the presence of poorly defined spin crossover, below 300 K, possibly extending above room temperature, with a residual high spin population of ca. 50% of the iron(II) centres just before the onset of zero field splitting below 25 K (Figure 118). This is telling of not only a lack of crystallinity, possibly due to partial loss of lattice solvent, but also of the existence of more than one phase. **34b** clearly consists of two phases, the lesser of the two is poorly crystalline and switches only gradually however the dominant phase possesses a striking 17 K hysteresis with a midpoint of 242 K. The situation for **34a** is juxtaposed somewhere between the perchlorate and triflate, in which the majority of the material is comprised of two phases, one poorly crystalline and switching gradually and the other remaining HS trapped, however there is a notable discontinuity between 260 and 277 K. The discontinuity is sharp and is attributable to abrupt thermal spin crossover at 270 K of a more highly crystalline phase buried deep within the solid.

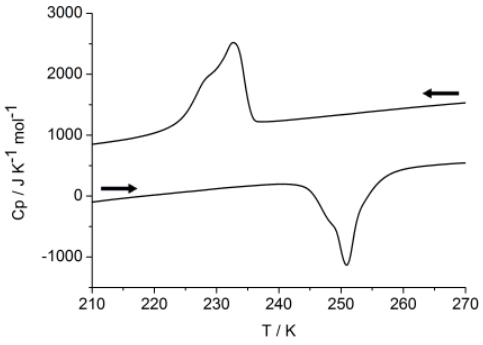

Figure 119 – Differential scanning calorimetry curve for 34b during the cooling and warming cycles between 193 and 303 K.

Thermodynamically, ΔH and ΔS of transition in **34b** were consistent with one another in cooling and warming mode, calculated as being 8.12 kJ mol^{-1} and 34.37 J K^{-1} mol^{-1} during cooling and 8.26 kJ mol^{-1} and 32.91 J K^{-1} mol^{-1} when rewarmed. Two things stand out, the first of which is that this is slightly outside of the usual region for thermally induced ΔH and ΔS, however this can be explained on the basis that **34b**, which was subject to DSC analysis, clearly comprises of a second contaminant phase as mentioned above. Thus, the actual ΔH and ΔS values are actually probably up to 40% larger, based on the relative proportions of the phases as deduced from the magnetic profile. The second is that the heat capacity fluctuations in the DSC profile of **34b** are clearly comprised of more than one maxima, as a shoulder is observed 3 – 5 K below that of the major maxima during both cooling and heating (Figure 119). The splitting of the spin transition into two distinct components is not observable in $\chi_m T$ vs. T magnetic plot, however the first derivative supports the thermodynamic data in that there are two maxima during the transitions, the separation of which is better defined in the cooling mode (Figure 120). The “smaller” of the

two peaks is broader, and on this basis the peaks appear to account for, as far as can be deduced, a switch in spin states of approximately a 1:1 ratio. Since the switching of two distinct phases at an almost identical temperature with hysteresis of almost 20 K is deemed unlikely, the situation must be that the abruptly switching phase contains two unique iron(II) environments which switch allosterically. That is, the switching of the second is mediated by a significant enough change in its immediate environment caused by the transition in the first centre, and vice versa. Further speculation about the exact nature of the allosteric switching cannot be drawn without suitable crystallographic data on the crystal.

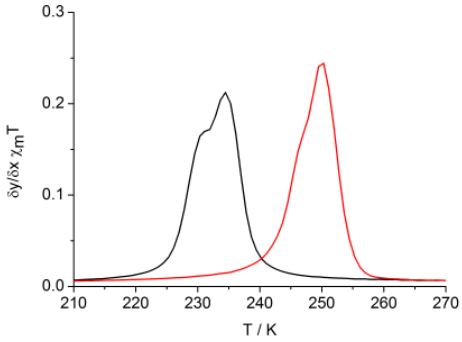

Figure 120 – First derivative of the magnetic susceptibility curve of 34b during cooling (black) and rewarming (red) showcasing the second order nature of its thermal spin transition in both directions.

In the absence of structural evidence on the solvent free tetrafluoroborate and perchlorate salts of 1-bppMe and 1-bppOH and, now 1-bppSH, it cannot unambiguously be stated however it is highly likely that the solvent free phases of the two different salts of the same complexes are isostructural. The logic being that the solvent free materials all exhibit highly cooperative thermal spin transitions, and in each case the mid-point of the transitions are centred at temperatures between 13 and 28 K lower in the perchlorates than in their corresponding tetrafluoroborates, correlating with the expected stabilisation of the HS states in the lattice because of the larger volume occupied by the perchlorate anions. It is therefore believed that the discontinuity in **34a** corresponds to an isostructural solvent free phase to that which makes up the majority of the bulk material in **34b**. During preparation, it is to be stated that **34b** was crystallised over a period of 1 h from its nitromethane solution, whereas **34a** precipitated rapidly before isolation, which may partially account for the much higher prominence of the highly crystalline, abruptly switching phase in **34b** compared to **34a**.

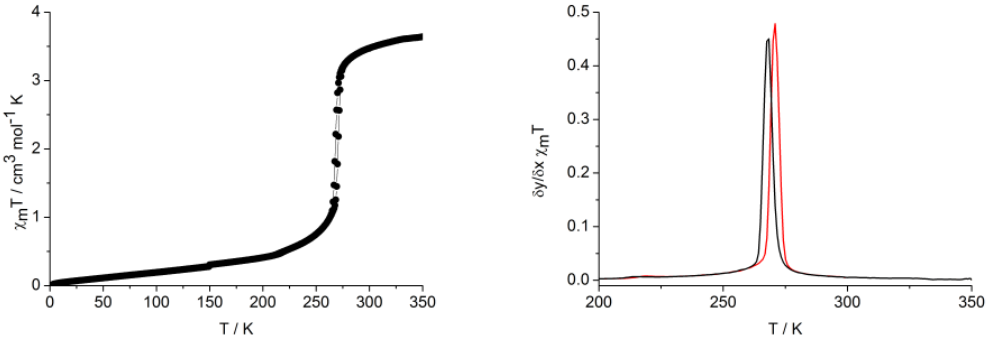

Figure 121 – Left: Magnetic susceptibility plot for powder 35a during cooling and warming between 3 and 300 K; right: First derivative of the magnetic susceptibility curve of 35a during cooling (black) and rewarming (red).

A single salt, the tetrafluoroborate **35a** was prepared to try and perform a comparative study between that and the oxygen containing analogue **33a**. **35a** in fact possesses rather interesting spin crossover behaviour, in stark contrast to **33a**. The yellow powder isolated from $MeNO_2/Et_2O$ begins to darken progressively at temperatures just below ambient. Susceptibility measurements between 300 and 3 K showed that the majority of the material undergoes an abrupt transition centred at 275 K with very narrow hysteresis just in excess of 1 K (Figure 121). DSC measurements at the same temperature scan rate revealed more accurately a $T_{1/2}$ of 269 K, with 3 K hysteresis (Figure 122). The values of ΔH and ΔS were a little lower than generally associated with a thermal spin transition, at 10.37 kJ mol^{-1} and 38.77 J K^{-1} mol^{-1} during the cooling and 9.80 kJ mol^{-1} and 36.19 J K^{-1} mol^{-1} during the warming cycle.

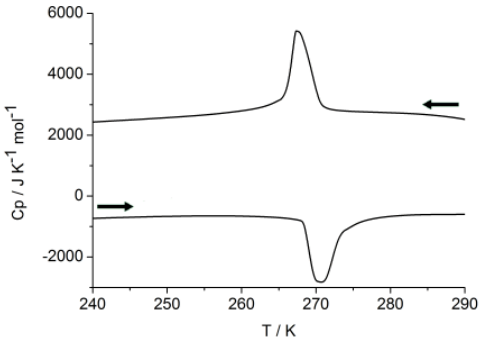

Figure 122 – Differential scanning calorimetry plot for powder 35a in the cooling and warming regime scanned between 193 and 303 K.

Crystallisation from $MeNO_2$ with various ethers yielded high quality single needles, which were amber in hue. At the first temperature of measurement 290 K, **35a** is entirely HS, containing two unique iron(II) centres, crystallising in Pbcn. The crystal was solvent free, and proposed to be the same phase as that which had been subject to both magnetic and thermodynamic study. Post-collection of the 290 K dataset, the crystal was cooled to 240 K

during which, between 270 and 250 K the crystal lost its translucency and took on a brown colour, essentially confirming that its behaviour matches with that of the bulk phase. At 240 K, the asymmetric unit comprises one and a half discreet dication with the full dication possessing metric parameters consistent with a fully LS configuration, however the half-dication still retains partial HS character (Figure 123).

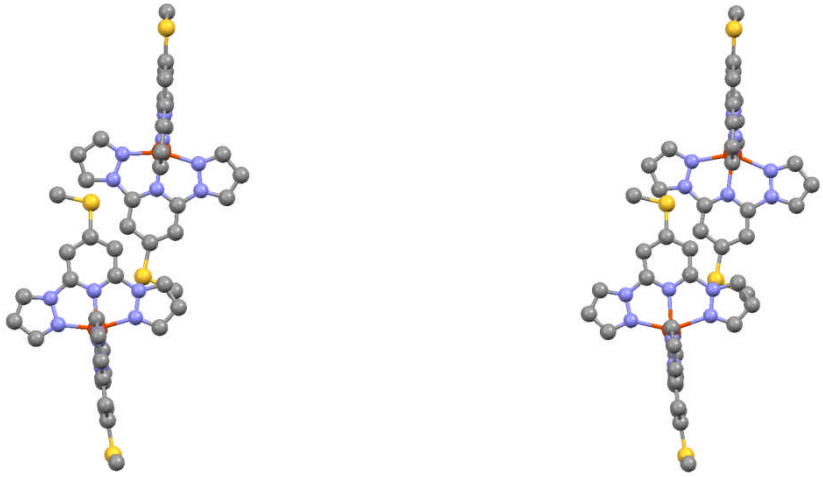

Figure 123 – The two unique complex dications in 35a while entirely LS at 240 K (left) and HS at 290 K (right), viewed perpendicular to the plane of one of the ligands with the H atoms omitted for clarity. Atom colour code: carbon (grey), iron (orange), hydrogen (white), nitrogen (periwinkle) and sulfur (yellow).

The crystal was then cooled even further to 100 K. At this temperature the asymmetric unit contained half a fully LS complex dication, and the particularly long c-axis associated with the 240 and 290 K structures had undergone a division by a factor of three. To clarify, the asymmetric unit at 100 K contained half a complex dication, as opposed to the one and a half as determined in the structures at 240 and 290 K, indicating that below 240 K the complexes had become degenerate crystallographically.

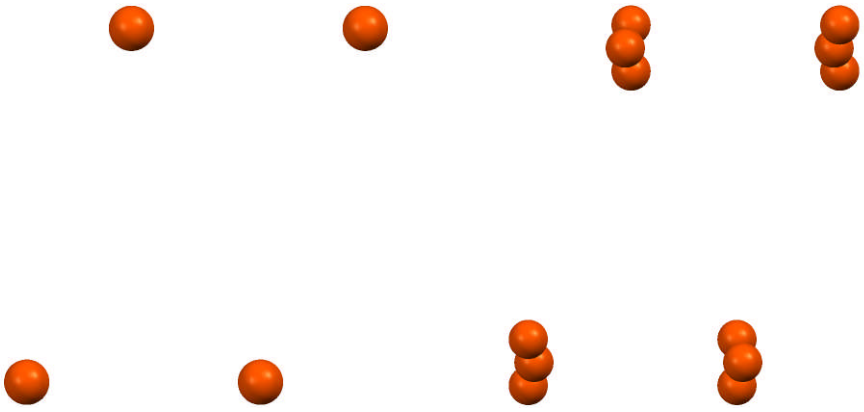

Figure 124 – Views of the displacement of the iron(II) centres about the bc plane in complex dications packing along the a axis at 100 K (left) and 240 K (right); the view is down the crystallographic a axis; all atoms aside from Fe have been omitted for clarity.

If one observes along the a axis the positions of the iron(II) complexes along the bc plane, it is clear that at 100 K all the iron(II) centres lie directly above one another (Figure 124). At 240 K, this is not the case with neighbouring complex molecules no longer lying directly above one another along the a axis, causing a concomitant tripling of the unit cell. The differences are emphasised further looking along the b axis (Figure 125), where as the complexes are followed along the a axis, there is a clear modulation regarding the position of neighbouring molecules in the c direction. The modulation repeats every six dication units along the a axis.

Figure 125 – Views of the displacement of the iron(II) centres along the c axis in complex dications packing along the a axis at 100 K (left) and 240 K (right); the view is down the crystallographic b axis; all atoms aside from Fe have been omitted for clarity.

To better understand the effect of the structural phase change upon the spin transition, and the regime over which it occurs, whether gradually or otherwise, a number of datasets were collected on different crystals. To our surprise, the structural phase change occurs at slightly different temperatures seemingly dependent upon the crystal of investigation. Some crystals exhibited diffraction images which were indicative of the tripled unit cell, however others had only very minor tripled reflections in the a direction which is, perhaps, suggestive of a mixture of phases. Two crystals were studied between 200 and 290 K, with datasets collected at 10 K and 5 K intervals using Mo and Cu radiation, starting at 290 K with the final collection acquired at 200 K. Both crystals contained no spots by 200 K indicative of the reduced symmetry tripled unit cell, establishing that the transition occurs above this temperature. The unit cell volumes show an expected significant drop in volume of 2 – 3 % between 250 and 270 K as the complexes switch configuration completely (Figure 126), in agreement with magnetic and thermodynamic data on the bulk power phase. Oddly, in both crystals, though the volume thermally contracts, the contraction is not uniform in all directions in the lattice. The crystals contract along the bc plane, however actually expand slightly between 250 and 210 K, occupying a greater magnitude along the c axis.

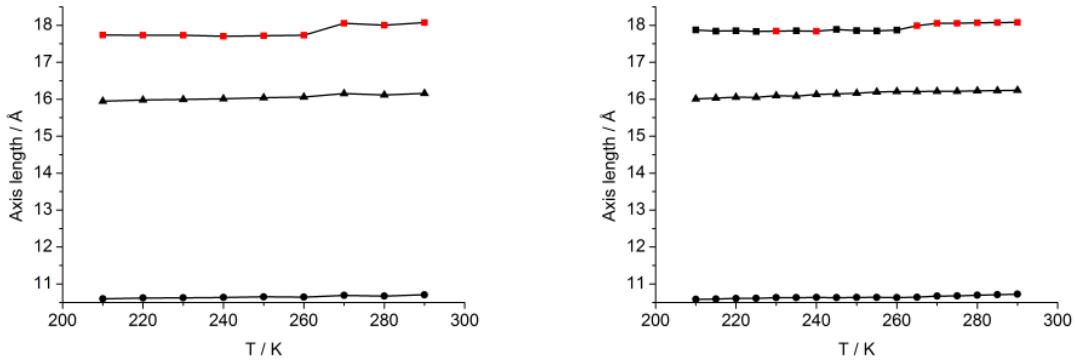

Figure 126 – Unit cell parameters derived from variable temperature studies of two crystals of 35a, measured from highest to lowest temperature using Mo (left) and Cu (right) radiation sources; the plots represent the crystallographic a, b and c axes as squares, circles and triangles respectively; the black symbols match the true cell length with the red symbols obtained by dividing the tripled unit cell length by 3.

In both crystals subject to variable temperature study, the tripled cell reflections, which disappear by 200 K, become more apparent as the temperature is increased, which is perhaps telling of a more gradual process whereby the iron(II) centres modulate their displacement along the bc plane. Plotting the intensity of the tripled reflections against those of the dominant single reflections along the a direction, one sees a sharp (Figure 127) increase between 200 and 210 K, which gradually drops off until 270 K which probably reflects the non-uniform nature of the spots over both the phase transition and the spin transition. The largest intensity ratio is seen at 280 K, just above the transition temperature, which sees a ratio of tripled-single spot intensities of 0.55. This is evidence that the crystals, even at room temperature, are not homogenous and actually still comprise of a mixture of both crystallographic phases, which is further evidenced by the low quality solutions obtained for these datasets which all contain significant electron density surrounding the dication ligand backbones.

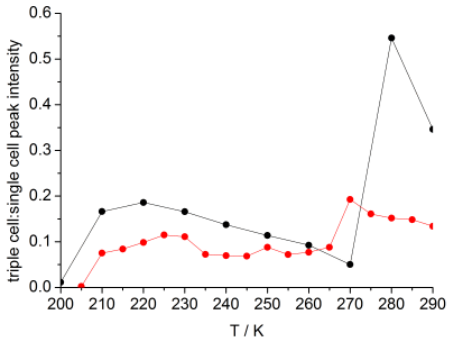

Figure 127 – Tripled daughter reflection to dominant single cell reflection ratios derived from variable temperature studies of two crystals of 35a, measured from highest to lowest temperature using Mo (black) and Cu (red) radiation sources.

Analysing the crystallographic data further, it becomes more apparent that the secondary phase transition occurs gradually above 200 K. Observing the spots in the unmerged image along 0, k, l in reciprocal space, one can clearly see the appearance of additional spots in the a direction, with spacing $^1/_3$ of that seen between the more intense spots which is a clear indication of the onset of tripling of the unit cell (Figure 128). The intensity of the spots originating from the tripled cell along the a direction, plotted against those of the expected single cell reflections, clearly illustrate the progression of the secondary phase change with respect to temperature (Figure 127). The crystals subject to variable temperature crystallographic measurements both illustrate that the phase change is all but complete by 220 K. Above 220 K, there is a slight reduction in the triple:single unit cell spot ratios, more than likely a combination of thermal broadening and inhomogeneity introduced at the onset of the spin transition. Above the spin transition, the values increase once again, as essentially the entirety of the crystal is all but homogenous once again and occupying the HS configuration. Though the precise values of the triple:single unit cell spot intensity ratios vary between the two crystals as given temperatures, this could be ascribed to differences in mosaicity and homogeneity in the crystals, as the form of the plots is very similar.

Figure 128 – Unmerged images of diffraction patterns along the 0,k,l zone in 35a using monochromated Cu-Kα radiation at 1.54184 mm^{-1} at 100 K (left) and 240 K (right).

Powder patterns were collected upon the same powder sample which had undergone magnetic measurements between 140 and 300 K, and bore very close resemblance to those as predicated using LazyPulverix upon the single crystal crystallographic data (Figure 129). Importantly, no peaks were observed in the experimental patterns that were not also present in those which were predicted, clarifying the phase purity of the powder sample and ruling

out a magnetic contaminant responsible for the inflexion seen in the magnetic susceptibility curve of **35a**.

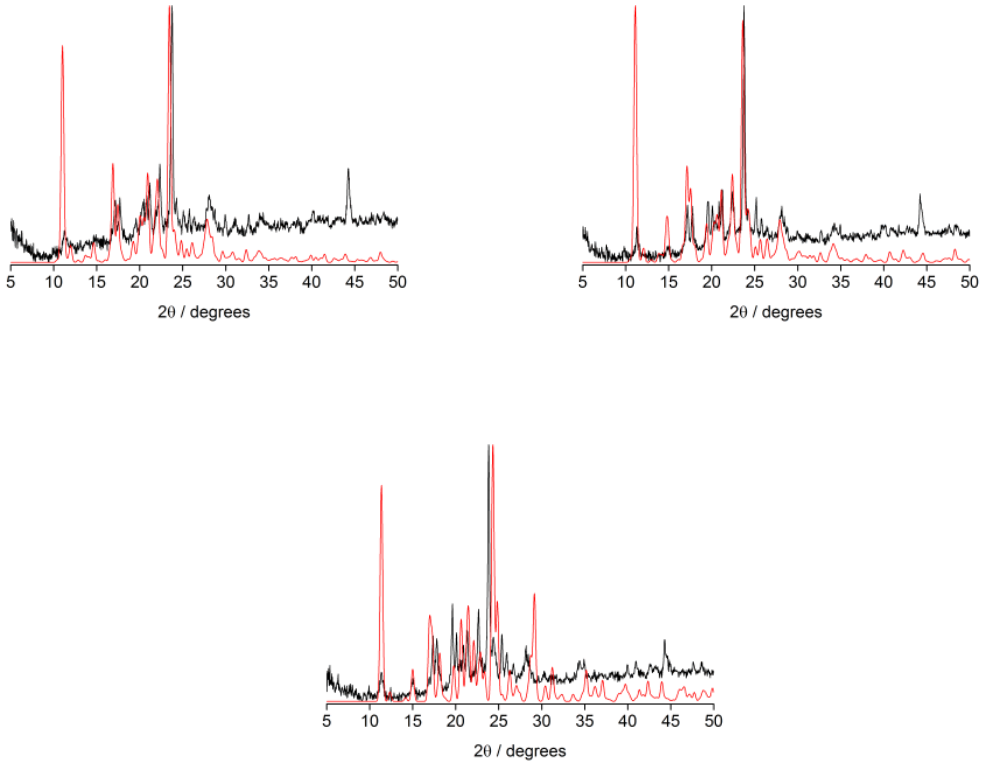

Figure 129 – Selected experimental (black) and simulated (red) powder patterns for 35a at 290 K (top left), 240 K (top right) and 100 K (bottom).

The magnetic and DSC curves, in conjunction with powder and single crystal X-ray crystallographic data allow us to draw the conclusion that **35a** undergoes two discreet transitions, one of which is possibly triggered by the first and thus allosteric in nature. With the possibility of a phase contaminant ruled out, the residual high spin fraction of iron(II) centres below the abrupt transition arise as a result of the half-dication in the asymmetric unit, which is more clearly seen in the first derivative of the magnetic susceptibility data and shows a prominent inflexion down to 200 K, characterised by the downward slope indicating a iron(II) centres are still switching over this period. The abruptly and gradually switching complex centres alternate along the c axis in a two-to-one manner to conserve their stoichiometry. The single molecule layer of gradually switching centres separates the abruptly switching dications preventing three dimensional cooperative switching. The switching information is transmitted in two dimensions along the two-fold layers of the abruptly switching domains, but reduced anion disorder in one of the dications which causes the removal of degeneracy above 200 K seemingly negates cooperative switching in the single-molecule layer which makes up the gradually switching component of the material.

The material is worthy of further study as two-thirds of the sample switch abruptly at a temperature which is just short of an ideal operating regime. Photomagnetic experiments are in process in order to absolutely confirm or rule out the allosteric switching, and to ascertain the T_{LIESST} of the two unique complex centres in the material.

5.4.6 Formation of self-assembled monolayers of iron(II) containing complexes of 1-bppSH

This work in this section was carried out primarily by Laurynas Pukenas, in collaboration with the department of physics, University of Leeds.

The successful isolation of 1-bppSH and three of its *bis*-chelated iron(II) salts, one of which undergoes an abrupt second-order spin transition prompted a study into surface chemistry and the spin crossover of monolayers of the materials on a gold surface.

Drop-cast films of 1-bppSH formed via the 1-bppI intermediate gave complicated S^{2p} and C^{1s} envelopes by XPS which were fitted according to their predicted binding energies and shown to contain both bound and unbound thiols in conjunction with partially oxidised thiols, namely disulfides and atomic sulfur.[56, 57] The relative intensities of the oxidised to non-oxidised materials bound to the surface were shown to depend strongly upon the solvent in which the drop casting of 1-bppSH onto Au was performed, with EtOH least favouring the formation of oxidised species (Figure 130).

In all instances, 1-bppSH formed poor quality SAMs, with XPS highly suggestive that there was competition for coordination to gold with an iodine/iodide containing moiety from the existence of two I^{3d} signals at 617-620 eV and 628-633 eV. The same bulk sample of 1-bppSH was confirmed as microanalytically pure, and the origin of the iodine/iodide signals was thought to be due to residual 1-bppI comprising less than 0.05% of the sample by weight and which could not be removed. The amount of bound iodine on the SAMs varied depending both upon choice of solvent and immersion time, however the S^{2p} to I^{3d} integrations were always significantly less than expected based upon its 0.05% abundance in the sample, often by several orders of magnitude.

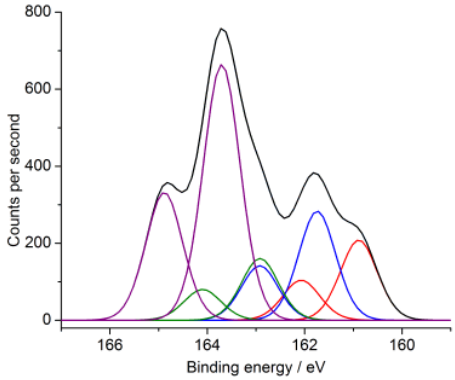

Figure 130 – X-ray photoelectron curves for the S 2*p* components for drop casted 1-bppSH from DCM solution; drop casted signal envelope (black), atomic sulfur (red), bound thiols (blue), unbound thiols (green) and oxidised thiols (purple).

To remove the issue of competitive binding, SAMs of a new sample of 1-bppSH prepared from 1-bppCl were studied by XPS and ellipsometry. Indeed, as expected the XPS data indicated the complete absence of bound iodine/iodide, however the C^{1s} and S^{2p} regions were still hugely complex (Figure 131). Microanalysis, ^{1}H NMR spectroscopy and mass spectrometric analyses precluded the existence of other sulfur containing species so the form of the envelopes of the C^{1s} and S^{2p} regions were ascribed to species formed either during SAM preparation or by post-coordination reactions occurring on the gold surface.

In addition to partially oxidised species present on the SAMs, which are likely to have arisen from *in situ* oxidation of 1-bppSH to 1-bppDS, a significant portion of the S^{2p} envelope is attributable to that of atomic sulfur, which goes some way towards explaining the anomalously large S^{2p} to C^{1s} integral ratios. The bound atomic sulfur is ascribable to a gold-catalysed desulfurisation process, which proceeds via disulfide formation at the surface between two closely neighbouring bound 1-bppSH moieties followed by sulfide formation resulting in atomic sulfur being retained at the surface. This has been previously observed in SAMs formed from 4-mercaptopyridine, and appears to be exclusive to directly bound aromatic thiols.[57, 58] The tendency of 1-bppSH to oxidise readily to its disulfide in solution only serves to worsen the issue. Ellipsometric measurements also resulted in unexpected finds, with absorbed layer thicknesses on the SAMs shown to be up to 34 Å in height. This substantiates further the non-uniform monolayer dispersion of bound 1-bppSH, with molecules of 1-bppSH and 1-bppDS possibly stacking upon one another through off-centre π-π interactions.

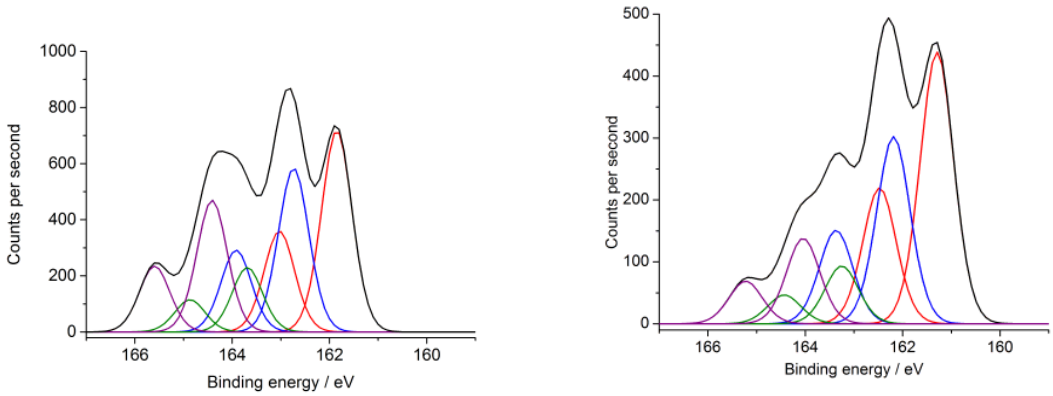

Figure 131 - X-ray photoelectron curves for the S 2*p* components of 1-bppSH SAMs formed from EtOH solution; SAMs formed from 1-bppSH via 1-bppI intermediate (left) and via 1-bppCl intermediate (right); SAM signal envelope (black), atomic sulfur (red), bound thiols (blue), unbound thiols (green) and oxidised thiols (purple).

All efforts to prepare SAMs of the pre-formed complex salt **34a** gave, again, S^{2p} to C^{1s} ratios, with the C^{1s} regions in particular being extremely noisy suggestive that essentially no S-bound [Fe(1-bppS)$_2$] moiety present on the surface. The surface chemistry of the Au-S-Ar bound molecules is not subject to any further investigation due to the facile desulfurisation processes which are predominant in the XPS spectra of SAMs of both 1-bppSH and its preformed complex. Attention will now be turned to iron(II) *bis*-1-bpp type complexes which possess an aliphatic spacer between the aromatic ligand backbone and the binding sulfur atom in order to prevent the gold catalysed desulfurisation which dominates in SAMs of 4-mercaptopyridines.

5.4.7 Structural and electronic effects upon varying the halide in 4-halo-2,6-di(pyrazol-1'-yl)pyridine iron(II) complexes

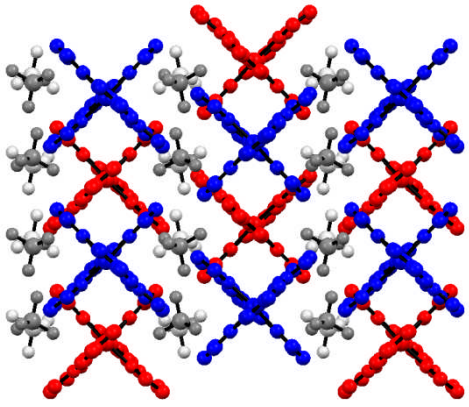

Figure 132 – Crystal packing of 38a at 100 K viewed along the crystallographic a axis, with dications and anions comprising the discreet layer closest to the viewer represented in blue and dark grey respectively and the second layer furthest away from the viewer represented in red and light grey respectively.

The tetrafluoroborate salts of 1-bppF, 1-bppCl, 1-bppBr and 1-bppI all crystallise as phase pure solvent free materials. The fluoro, bromo and iodo substituted complexes **37a,**

39a and **40a** show spin crossover in the solid which vary according to the magnitude of structural rearrangement required as a function of halide atom size rather than the relatively small electronic effects imposed along the series. X-ray structures were collected at low temperature (**37a** – 150 K, **38a**-**40a** – 100 K), showing a single, low spin iron(II) centre for each of the salts. **38a**-**40a** are all isostructural crystallising in *Pbcn*, whilst **37a** is defined by $P2_1$ and is therefore discussed separately later on in the section. The three isostructural salts pack in a variation of the terpyridine embrace, consisting of alternating intercalating layers of complex dications (Figure 132) with the tetrafluoroborate counterions located in small grooves between the intercalated layers. **38a** and **39a** possess very similar unit cell lengths at 100 K, varying by an amount in agreement with the volume differences between the respective chloride and bromide substituents.[36, 59] The unit cell volume is significantly larger in **40a** as would be expected due to the much larger iodine atom, yet the cell actually possesses much shorter a and c axes with the volumetric expansion a result of severe elongation of the b axis.

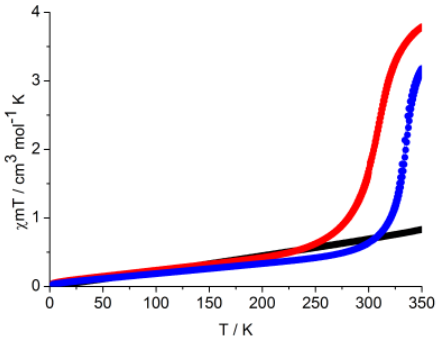

Figure 133 – Magnetic susceptibility curves for bulk powder 38a (black), 39a (red) and 40a (blue) during the cooling and warming cycles between 3 and 350 K.

Ground powder samples of **38a**-**40a** were subject to susceptibility measurements over the 350 – 3 K range and found to be in full agreement with the crystallographic findings (Figure 133). **39a** undergoes a characterisable spin transition, proceeding completely between 250 and 375 K, centred at 308 K as clarified from its heat capacity changes during differential calorimetry scan (Figure 134). **40a** begins to switch just below RT with a $T_{1/2}$ of 335 K and $\chi_m T$ reaching 3.16 cm^3 mol^{-1} K at 350 K which was the limit of our measuring capability. This is very similar to the spin crossover behaviour of the perchlorate analogue, $[Fe(1\text{-bppl})_2][ClO_4]_2$, which is isostructural and undergoes an abrupt spin transition centred at 333 K, the larger perchlorate anions causing only very minor stabilisation of the HS state.[31] **38a** remains all but entirely low spin up until 350 K, however a small fraction of centres become high spin as the temperature is increased, corresponding to 0.22 at 350 K.

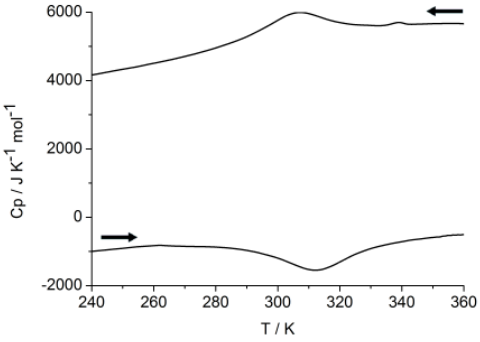

Figure 134 – Differential scanning calorimetric curve for 39a in cooling and warming modes between 193 – 373 K.

It is surprising that **38a** does not undergo a thermally accessible spin transition below 350 K given its structural similarities with **39a** and **40a** (Figure 135). There exist no striking structural differences in the metric parameters and intermolecular contacts for **38a**, **39a** and **40a** at 100 K which one could use to qualitatively predict the inaccessibility of the HS state in **38a** (Table 23 and Table 24). At 100 K, the geometric displacement along the a-axis between the two halogen atoms is 1.5 – 1.7 Å shorter in **40a** than it is in the corresponding chloride and bromide analogues **38a** and **39a** however this difference appears to have little bearing on its spin crossover as **40a** switches completely at a temperature of only 27 K higher than in **39a**.

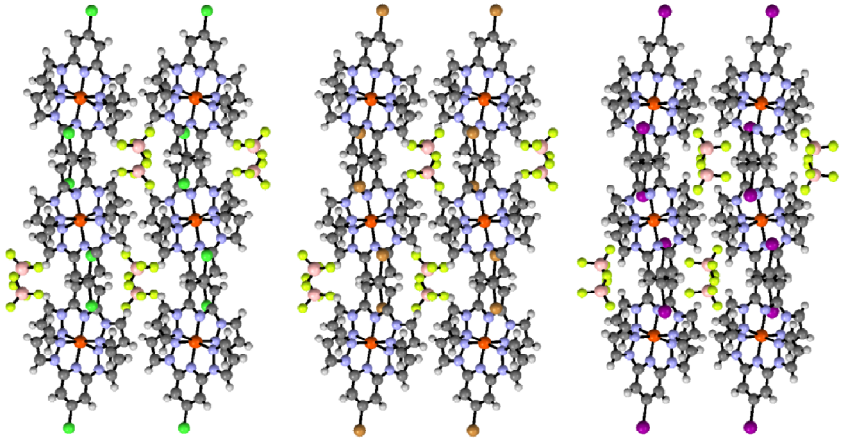

Figure 135 – Crystal packing along the b axis of the isostructural complex salts 38a (left), 39a (centre) and 40a (right) at 100 K. Atom colour code: boron (pink), bromine (brown), carbon (grey), chlorine (lime green), fluorine (chartreuse yellow), iodine (violet), iron (orange), hydrogen (white) and nitrogen (periwinkle).

Complex salt	a-axis / Å	b-axis / Å	c-axis / Å	Dicationic volume / Å^3	Intralayer π...π stacking distance / Å	Interlayer halogen-halogen separation / Å
38a	17.73	9.25	16.68	608	4.0797(17)	5.4456(10)
39a	17.86	9.37	16.57	617	4.021(2)	5.2822(6)
40a	16.84	11.15	15.54	653	3.749(11)	3.857(2)

Table 23 - Selected crystallographic parameters and contact distances for the homoleptic 4-halo-1-bpp iron(II) tetrafluoroborate salts 38a, 39a and 40a at 100 K; the dicationic volumes were estimated by subtracting the average volume for a tetrafluoroborate ion in the solid state.[60] Exact values for the unit cell parameters complete with ESDs can be found in the crystallographic data tables located in the appendix.

The reasoning behind the low spin state trapping of **38a** is instead ascribed to rather more subtle differences in the effect of temperature upon the structures. The only notable contact differences between the two salts, in the LS structures at 100 K is the reduction in contact distance between the halide and proton about the distal ring of a dication in the neighbouring layer at 2.955 Å (Figure 136), 0.02 Å shorter in **38a** than in its bromide analogue **39a**. Instead it is believed that increased anion disorder as temperature is increased plays a significant part in reduction of lattice pressure, and thus promotion of change to the HS across the series of isostructural halide derivatives, but as only a single structure was obtained at 100 K upon **38a** and **40a** a direct comparison at elevated regarding subtle changes in anion disorder temperature cannot be made.

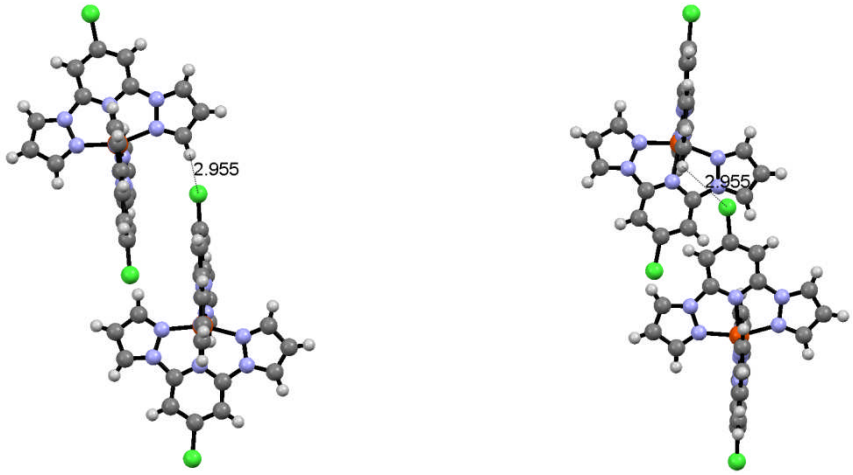

Figure 136 - View of two iron(II) complex dications from neighbouring layers in 38a at 100 K with the closest interlayer contact distance highlighted. Atom colour code: carbon (grey), chlorine (lime green), iron (orange), hydrogen (white) and nitrogen (periwinkle).

No./polymorph	**37a**		**38a**	**39a**			**40a**
T / K	150	290	100	100	250	350	100
Volume of Fe Polyhedron / Å^3	9.59(3)	12.28(3)	9.547(7)	9.535(8)	9.54(2)	11.86(3)	9.48(4)
Rhombic / °	87.4(14)	149.43(6	86.73(27	87.22(34	85.8(9)	152.1(8)	84.83(4

		0)	)	)			5)
Trigonal / °	283	462	279	286	281	467	290
Trans Angle / °	179.3(4)	175.4(2)	175.02(10)	175.62(13)	177.1(4)	175.9(3)	177.2(7)
Least sq. planes difference / °	89.11(9)	88.82(7)	87.30(3)	87.02(3)	89.47(10)	89.59(10)	86.98(13)
Av. bite angle / °	80.0(8)	73.59(36)	80.04(14)	79.99(18)	80.2(5)	73.3(4)	80.23(24)
Av. Fe-N_{prox} / Å	1.903(11)	2.122(7)	1.8982(27)	1.895(3)	1.897(8)	2.110(8)	1.898(4)
Av. Fe-N_{dist} / Å	1.975(18)	2.175(9)	1.9741(37)	1.975(4)	1.973(12)	2.144(12)	1.965(6)

Table 24 - Geometric parameters for the solvent free tetrafluoroborate complex salts of the 4-halosubstituted 1-bpp derivates.

Out of all of the 4-halo substituted 1-bpp derivative complex salts **37a** is the only salt to possess abrupt, hysteretic spin crossover. Magnetic data on the bulk, bright yellow powder tells of a highly crystalline, phase pure solid with a $T_{1/2}$ of 237 K, possessing a hysteresis width of 9 K (Figure 137). Thermodynamically this is confirmed, yet the separation of the endothermic and exothermic peaks via DSC suggests a slightly larger, however within experimental error, hysteresis width of 10 K of the first order spin transition. However, to complicate matters, ΔH and ΔS were significantly smaller in cooling mode than as calculated when the sample was rewarmed to room temperature. ΔH and ΔS were 11.86 kJ mol^{-1} and 50.81 J K^{-1} mol^{-1} during the cooling cycle, whereas upon rewarming the values had increased to 21.47 kJ mol^{-1} and 88.17 J K^{-1} mol^{-1} (Figure 138).

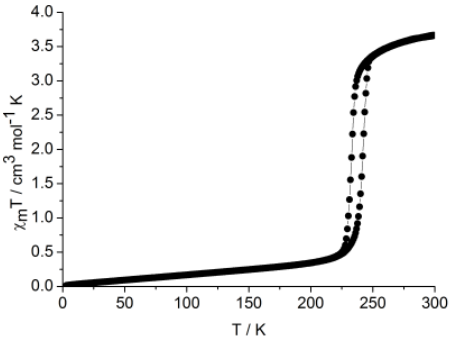

Figure 137 – Variable temperature magnetic susceptibility curve measured in both cooling and warming modes of 37a between 3 and 300 K.

The apparent discrepancy about the transition thermodynamics is perhaps indicative of a secondary phase change, perhaps irreversible in nature, meaning the exact nature of the transition differs in single cycles which were subject to investigation magnetically and thermodynamically. Multiple measurement cycles will, ultimately, be required to probe the

reversibility and indeed subtle changes between the spin transitions in the magnetic and thermodynamic profiles spanning the transition temperature regime.

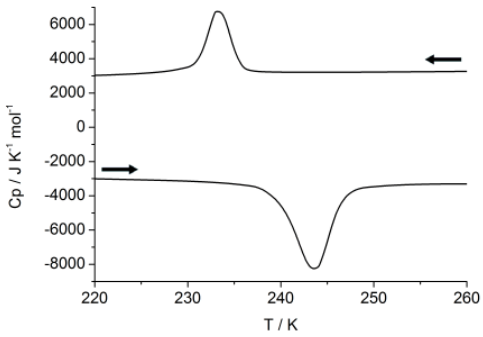

Figure 138 – Differential scanning calorimetric curve in both cooling and warming modes between 193 and 303 K.

The structural phase change accompanying the spin transition, suspected from the large differences in the transition energetics between the LS → HS transition and HS → LS transition was confirmed crystallographically. At 290 K, the crystal was shown to comprise of a single HS iron(II) centre, packing in discreet alternating layers down the c axis in Cc. Along the ab plane the solvent free material consists, unexpectedly, of layers of dications associating in the terpyridine embrace defined by distal ring off-centre π-π interactions between neighbouring dications within the same layer, and weak agnostic C-H...π interactions. Upon transcending the spin transition and cooling to 150 K, the fully LS crystal had undergone a small phase change, becoming $P2_1$ which is, it is of note, isostructural with the parent SCO complex **25a** (Figure 139). The phase change is, in actuality, very minor and is more than likely merely a result of the iron(II) coordination sphere becoming suitably regular to afford the lattice a centrosymmetric unit cell, and as a result is very likely to be reversible and not responsible for the thermodynamic discrepancies.

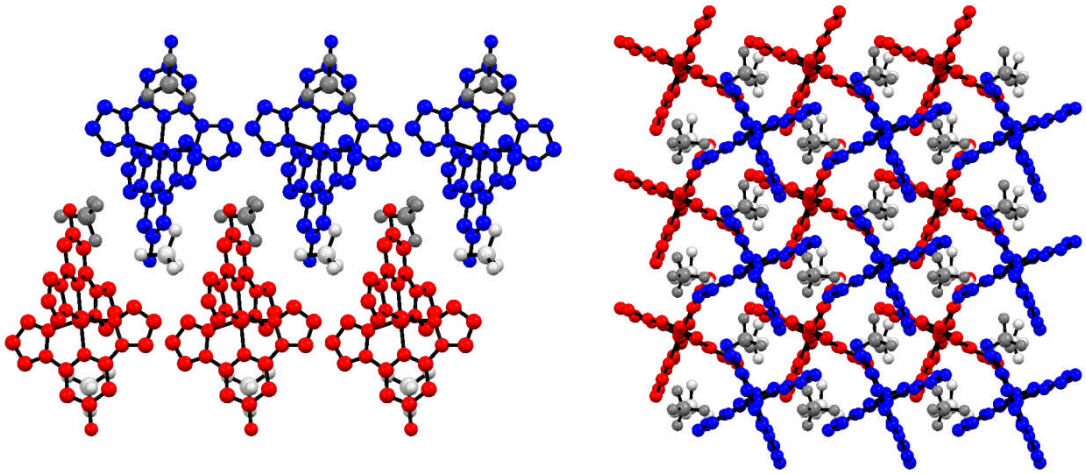

Figure 139 – Crystal packing of 37a at 150 K viewed along the crystallographic a axis (left) and c axis (right), with dications in alternating layers represented in blue and red, with the anions in said layers represented in dark grey and light grey respectively.

It is clear from analysis of distances between neighbouring dications at the two temperatures of measurement (Figure 140) that the lattice is able to accommodate the transition comfortably, which probably explains why $T_{1/2}$ only differs marginally from the value calculated in solution. This being said, the structural data was obtained on a crystal, of which the 290 K collection was performed before cooling to 100 K and collecting a second dataset at this temperature. Additional measurements on a crystal are required, to collect datasets on a crystal which has undergone at least one cooling and heating cycle at the two different temperatures, in conjunction with multiple cycle DSC and magnetic scans to clarify the nature of the thermodynamic differences and the true reversibility of the transitions.

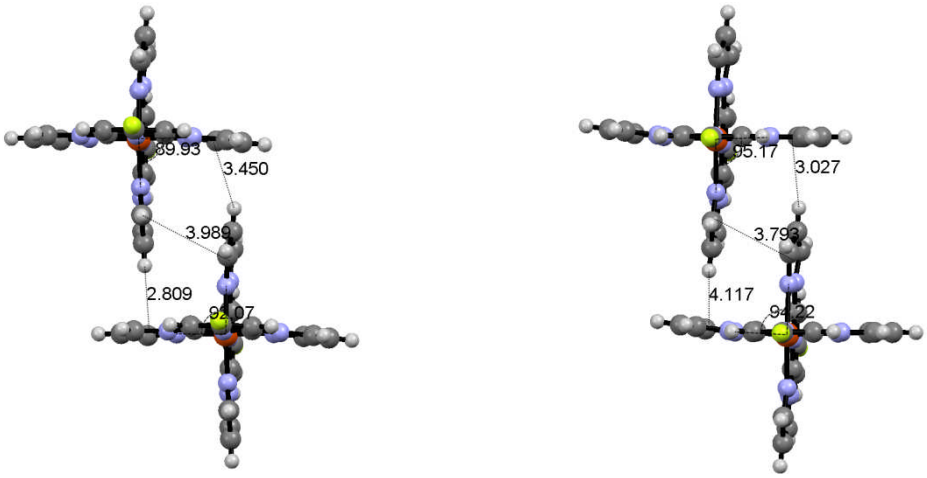

Figure 140 – Intralayer contact distances and angles comprising the rectangular space between embracing complex dications at 150 K (left) and 290 K (right) 37a; the view is along the crystallographic c axis. Atom colour code: carbon (grey), fluorine (chartreuse yellow), iron (orange), hydrogen (white) and nitrogen (periwinkle).

5.5 Conclusions

In this work we have presented a series of iron(II) complex salts derivatised about their *tris*-heterocyclic 2,6-di(pyrazol-1'-yl)pyridine framework in such a way, appended with relatively small moieties sufficiently far away, so as to exert no steric influence upon the iron(II) centre. Surprisingly, the terpyridine embrace motif, through which closely associated dications in discreet two-dimensional layers is retained in the solvent free materials even when relatively large atoms and groups are attached to the central pyridine 4-position, including iodo- and thiomethyl groups.

The electronic influence of the appended groups and atoms, deduced from measurements on the solvated materials, showed an opposite relationship with the $T_{1/2}$ values to that which was observed in previous studies on substituted iron(II) 2,6-di(pyrazol-1'-yl)pyridine complexes.[5, 12, 61, 62] The central pyridines' π systems contribute strongly to the

bonding interaction between the iron(II) and its donor ligands, as they are substantially lower in energy and more diffuse than the pyrazole π* lobes. The effect is that the π-effects dominate, resulting in π-electron donating substituents such as methyl and methoxy groups actually reducing $T_{1/2}$, as opposed to increasing it as is predicted purely on the grounds of σ-effects.[17, 18, 62-64]

In the solvent free salts which are shown crystallographically or, in the absence of suitable singly crystalline material are predicted to adopt one of the numerous forms of the terpyridine embrace motif the cooperative switching behaviour is, generally, retained. Small substituents show a dependence of $T_{1/2}$ in the solid materials similar to that predicted based on the solvated studies. Larger atoms, for example in the brominated and iodinated ligand salts, impede the lattice's ability to accommodate thermal spin crossover resulting in very high $T_{1/2}$ values which are beyond the scope of conventional application and measurement. The tetrafluoroborate and perchloroate salts show the most consistent and cooperative spin transitions, their small size meaning they are able to comfortably reside in voids between the intercalated embracing layers. In isostructural salts of the same complex, the perchlorates show a small stabilisation of the HS state relative to the tetrafluoroborates because of a reduction in lattice pressure due to the larger unit cell preferred by the perchlorates. With the exception of two examples, hexafluorophosphates inhibit the formation of the terpyridine embrace yielding highly distorted HS trapped complexes which are of no real value from a spin crossover standpoint. Triflates have been shown to promote spin crossover previously due to their higher polarity and hydrogen bonding affinity, however in this study all triflate salts proved to be poorly crystalline and often consisted of multiple unisolable phases.[65]

The primary problem in the characterisation and understanding of the spin crossover behaviour of the materials is the existence of multiple polymorphism and crystalline solvates, often making the bulk phase behaviour very complicated and difficult to deconvolute. It is almost impossible to predict which salts will readily form solvent free crystalline material, and often changing the solvents employed during crystallisation to try and inhibit solvate formation is not feasible due to limitations imposed by solubility and complex lability issues. One complex salt in this study was remarkably isolated and studied crystallographically as three different solvates, each possessing markedly different spin crossover behaviour. Contrary to the findings in other complex solvates in this study, the most solvent rich crystal actually exhibited the most interesting and abrupt spin crossover, however its rapid decomposition towards a poorly crystalline, LS trapped material serves to highlight the sensitivity and the synthetic and analytical issues encountered in this field of research.

To finish it must be said that this work has shown that, with so many unpredictable and sometimes conflicting factors at play, it is very difficult to predict the behaviour in the crystal, and whether or not stable solvent free crystalline material is formed is, as it stands, almost down to a matter of chance. The solvent free materials, appended with suitably small substituents do exhibit cooperative transitions, as in the parent 2,6-di(pyrazol-1'-yl)pyridine iron(II) tetrafluoroborate salt, often with hysteresis widths of up to 20 K. This is not the limit and larger hysteresis widths are possible in these materials when the lattice is not so rigid so as to accommodate such large geometric changes, but again these subtle differences in packing can be very difficult to predict and tune.[37]

Though to really understand the fundamentals, and allow better estimation to more efficiently tune the behaviour of these spin crossover materials, more emphasis must be placed on designing materials so as to omit the formation of solvates and promote the optimal packing for highly cooperative, hysteretic spin crossover and thus the systems must be kept simple. However, the author believes that, as there is a reasonably tight structure-function relationship in the solvent free spin crossover salts of substituted 2,6-di(pyrazol-1'-yl)pyridines, the systems must necessarily be made more complicated to really home in the type of material which is commercially and industrially viable to be incorporated as part of a device or sensor. In the absence of time restraints, further efforts would focus on the co-crystallisation of homoleptic substituted 2,6-di(pyrazol-1'-yl)pyridine iron(II) salts together, either by simple lattice doping or by encouraging hydrogen bonding between complex dications and assess the behaviour relative to the pure materials. Secondly, extending the π-aromatic system about the pyrazol-1'-yl rings, towards indazolyl containing systems and beyond is key, as one would effectively increase the contact area between neighbouring complex molecules and thus the extent of intercomplex interaction, theorised to be necessary in imparting even more highly cooperative and hysteretic materials.

5.6 References

1. D. Jameson, J. Blaho, K. Kruger and K. Goldsby, *Inorg. Chem.*, 1989, **28**, 4312-4314.
2. J. Holland, C. Kilner, M. Thornton-Pett and M. Halcrow, *Polyhedron*, 2001, **20**, 2829-2840.
3. T. Ayers, S. Scott, J. Goins, N. Caylor, D. Hathcock, S. Slattery and D. Jameson, *Inorg. Chim. Acta.*, 2000, **307**, 7-12.
4. C. Bessel, R. See, D. Jameson, M. Rowen Churhill and K. Takeuchi, *J. Chem. Soc. Dalton Trans.*, 1992, 3223-3228.
5. J. Holland, J. McAllister, C. Kilner, M. Thornton-Pett, A. Bridgeman and M. Halcrow, *Dalton Trans.*, 2002, 548-554.
6. M. Nihei, H. Tahira, N. Takahashi, Y. Otake, Y. Yamamura, K. Saito and H. Oshio, *J. Am. Chem. Soc.*, 2010, **132**, 3553-3560.

7. C. Carbonera, C. Kilner, J. Letard and M. Halcrow, *Dalton Trans*, 2007, 1284-1292.
8. J. Elhaik, C. Kilner and M. Halcrow, *Dalton Trans.*, 2006, 823-830.
9. J. Elhaik, D. Evans, C. Kilner and M. Halcrow, *Dalton Trans.*, 2005, 1693-1700.
10. J. Holland, J. McAllister, Z. Lu, C. Kilner, M. Thornton-Pett and M. Halcrow, *Chem. Commun.*, 2001, 577-578.
11. L. Han, M. Nihei and H. Oshio, *Polyhedron*, 2005, **24**, 2409-2412.
12. J. Holland, S. Barrett, C. Kilner and M. Halcrow, *Inorg. Chem. Commun.*, 2002, **5**, 328-332.
13. F. Pelascini, M. Wesolek, F. Peruch, A. De Cian, N. Kyritsakas, P. Lutz and J. Kress, *Polyhedron*, 2003, **24**, 3193-3199.
14. J. Elhaik, C. Kilner and M. Halcrow, *CrystEngComm*, 2005, **7**, 151-157.
15. V. Money, C. Carbonera, J. Elhaik, M. Halcrow, J. Howard and J. Letard, *Chem. Eur. J.*, 2007, **13**, 5503-5514.
16. C. Carbonera, J. Costa, V. Money, J. Elhaik, J. Howard, M. Halcrow and J. Letard, *Dalton Trans.*, 2006, 3058-3066.
17. R. Pritchard, C. Kilner, S. Barrett and M. Halcrow, *Inorg. Chim. Acta.*, 2009, **362**, 4365-4371.
18. R. Pritchard, H. Lazar, S. Barrett, C. Kilner, S. Asthana, C. Carbonera, J. Letard and M. Halcrow, *Dalton Trans.*, 2009, 6656-6666.
19. S. Basak, P. Hui and R. Chandrasekar, *Chem. Mater.*, 2013, **25**, 3408-3413.
20. M. Nihei, L. Han and H. Oshio, *J. Am. Chem. Soc.*, 2007, **129**, 5312-5313.
21. R. Chandrasekar, F. Schramm, O. Fuhr and M. Ruben, *Eur. J. Inorg. Chem.*, 2008, 2649-2653.
22. C. Rajadurai, O. Fuhr, R. Kruk, M. Ghafari, H. Hahn and M. Ruben, *Chem. Commun.*, 2007, 2636-2638.
23. C. Rajadurai, Z. Qu, O. Fuhr, B. Gopalan, R. Kruk, M. Ghafari and M. Ruben, *Dalton Trans*, 2007, 3531-3537.
24. M. Nihei, L. Han, H. Tahira and H. Oshio, *Inorg. Chim. Acta.*, 2008, **361**, 3926-3930.
25. M. Nihei, T. Maeshima, Y. Kose and H. Oshio, *Polyhedron*, 2007, **26**, 1993-1996.
26. R. Gonzalez-Prieto, B. Fleury, F. Schramm, G. Zoppellaro, R. Chandrasekar, O. Fuhr, S. Lebedkin, M. Kappes and M. Ruben, *Dalton Trans*, 2011, **40**, 7564-7570.
27. I. Salitros, J. Pavlik, R. Boca, O. Fuhr, C. Rajadurai and M. Ruben, *CrystEngComm*, 2010, **12**, 2361-2368.
28. K. Takahashi, Y. Hasegawa, R. Sakamoto, M. Nishikawa, S. Kume, E. Nishibori and H. Nishihara, *Inorg. Chem.*, 2012, **51**, 5188-5198.
29. F. H. M. Haryono, K. Petukhov, K. Gieb, P. Muller, A. Grohmann, *Eur. J. Inorg. Chem.*, 2009, 2136-2143.
30. F. S. C. Rajadurai, S. Brink, O. Fuhr, M. Ghafari, R. Kruk, M. Ruben, *Inorg. Chem.*, 2006, **45**, 10019-10021.
31. N. Madhu, I. Salitros, F. Schramm, S. Klyatskaya, O. Fuhr and M. Ruben, *C. R. Chim.*, 2008, **11**, 1166-1174.
32. J. Elhaik, C. Pask, C. Kilner and M. Halcrow, *Tetrahedron*, 2007, **63**, 291-298.
33. Y. Hasegawa, R. Sakamoto, K. Takahashi and H. Nishihara, *Inorg. Chem.*, 2013, **52**, 1658-1665.
34. I. Salitros, O. Fuhr, R. Kruk, J. Pavlik, L. Pogany, B. Schafer, M. Tatarko, R. Boca, W. Linert and M. Ruben, *Eur. J. Inorg. Chem.*, 2013, 1049-1057.
35. I. Salitros, O. Fuhr, A. Eichhofer, R. Kruk, J. Pavlik, L. Dlhan, R. Boca and M. Ruben, *Dalton Trans*, 2012, **41**, 5163-5171.

36. R. Pritchard, C. Kilner and M. Halcrow, *Chem. Commun.*, 2007, 577-579.
37. T. Roberts, M. Little, F. Tuna, C. Kilner and M. Halcrow, *Chem. Commun.*, 2013, **49**, 6280-6282.
38. E. Constable, B. Hermann, C. Housecroft, M. Neuburger, S. Schaffner and L. Scherer, *New J. Chem.*, 2005, **29**, 1475-1481.
39. E. Constable, C. Housecroft, M. Neuburger, J. Price and J. Zampese, *Aust. J. Chem.*, 2010, **63**, 1334-1341.
40. M. Silva, P. Bertoncello, N. Daskalakis, N. Spencer, B. Kariuki, P. Unwin and Z. Pikramenou, *Supramol. Chem.*, 2007, **19**, 115-127.
41. R. Hayter and F. Humiec, *Inorg. Chem.*, 1963, **2**, 306-312.
42. R. Feltham and R. Hayter, *J. Chem Soc.*, 1964, 4587-4591.
43. V. Marquez and J. Anacona, *Polyhedron*, 1997, **16**.
44. D. Evans, *J. Chem. Soc.*, 1959, 2003-2005.
45. G. Bain and J. Berry, *J. Chem. Educ.*, 2008, **85**, 532-536.
46. D. McDaniel and H. Brown, *J. Org. Chem.*, 1958, **23**, 420-427.
47. D. Hathcock, K. Stone, J. Madden and S. Slattery, *Inorg. Chim. Acta.*, 1998, **282**, 131-135.
48. S. Furukawa, Y. Hitomi, T. Shishido, K. Teramura and T. Tanaka, *J. Phys. Chem. A*, 2011, **115**, 13589-13595.
49. J. Chambers, B. Eaves, D. Parker, R. Claxton, P. Ray and S. Slattery, *Inorg. Chim. Acta.*, 2006, **359**, 2400-2406.
50. C. Kilner and M. Halcrow, *Polyhedron*, 2006, **25**, 235-240.
51. R. Mohammed, *"Iron Complexes of New Dipyrazolylpyridine Derivatives for Spin-Crossover Applications", University of Leeds, Leeds*, 2012.
52. S. Barrett, C. Kilner and M. Halcrow, *Dalton Trans.*, 2011, **40**, 12021-12024.
53. M. Scudder, D. Craig and H. Goodwin, *CrystEngComm*, 2005, **7**, 642-649.
54. A. Greenaway and E. Sinn, *J. Am. Chem. Soc.*, 1978, **100**, 8080-8084.
55. E. Coronado, M. Carmen Gimenez-Lopez, C. Gimenez-Saiz and F. Romero, *CrystEngComm*, 2009, **11**, 2198-2203.
56. T. Ishida, M. Hara, I. Kojima, S. Tsuneda, N. Nishida, H. Sasabe and W. Knoll, *Langmuir*, 1998, **14**, 2092-2096.
57. E. Ramirez, E. Cortes, A. Rubert, P. Carro, G. Benitez, M. Vela and R. Salvarezza, *Langmuir*, 2012, **28**, 6839-6847.
58. B. Lamp, D. Hobara, M. Porter, K. Niki and T. Cotton, *Langmuir*, 1997, **13**, 736-741.
59. M. Scudder, H. Goodwin and I. Dance, *New J. Chem.*, 1999, **23**, 695-705.
60. D. Mingos and A. Rohl, *Dalton Trans.*, 1991, 3419-3425.
61. J. Elhaik, V. Money, S. Barrett, C. Kilner, I. Evans and M. Halcrow, *Dalton Trans.*, 2003, 2053-2060.
62. J. E. V. Money, M. Halcrow and J. Howard, *Dalton Trans.*, 2004, 65-69.
63. S. Kang and D. Beveridge, *Theoret. chim. Acta*, 1971, **22**, 312-314.
64. S. Kang and M. Cho, *Int. J. Quantum Chem.*, 1973, **7**, 319-327.
65. G. Agusti, C. Bartual, V. Martinez, F. Munoz-Lara, A. Gaspar, M. Carmen Munoz and J. Real, *New J. Chem.*, 2009, **33**, 1262-1267.

Chapter 6

Experimental: materials and methods

6 Experimental: materials and methods

6.1 General methods

^{1}H NMR spectra were recorded at either 300 MHz on a Bruker DPX300 FT or at 500 MHz on a Bruker Avance 500 FT spectrometer at 298 ± 5 K unless otherwise stated. Chemical shifts are quoted in parts per million with respect to TMS or the respective residual solvent resonances. ^{13}C NMR spectra were run using broadband proton decoupling operating at 75 MHz on a Bruker Avance 500 FT spectrometer and quoted in parts per million with respect to the respective residual solvent resonances. ^{18}F NMR spectra were recorded at 282 MHZ on a Bruker DPX300 FT instrument, and quoted in parts per million relative to fluorobenzene at -113.1 ppm. Evans' method variable temperature solution based susceptibility measurements were collected on a Bruker DRX 500 MHz spectrometer by Mr Simon Barrett with exchange contact shifts quoted relative to either the respective inert reference solvent shifts or that of TMS at 0 ppm. Electrospray ionisation mass spectrometry (ES^{+}-MS) spectra were carried out by Mrs. Tanya Marinko-Covell, obtained on a Waters ZQ4000 spectrometer, from MeCN feed solutions. All mass peaks have the expected isotopic distributions for the proposed assignments. CHN microanalyses were carried out by the University of Leeds School of Chemistry microanalytical service by Mr Ian Blakely and Mrs Tanya-Marinko Covell. Infrared spectra were recorded on a Perkin-Elmer Spectrum One FT-IR infrared spectrophotometer and the samples analysed as solids.

Melting points were determined on an Electrothermal digital melting point apparatus. Electrochemical experiments were performed on an Autolab PGSTAT30 voltammetric analyser under an argon atmosphere using MeCN solutions of $[^{t}Bu_4N][BF_4]$ (0.1 M) as the supporting electrolyte. A Pt disk working electrode was employed in tandem with a Pt rod secondary electrode and an AgCl/Ag reference electrode. All quoted potentials are referenced to an internal ferrocenium/ferrocene standard and were obtained at a scan rate of 100 mV s^{-1}. The ferrocenium/ferrocene couple was at $+0.40 \leq E_{1/2} \leq 0.42$ V vs AgCl/Ag with a peak-to-peak separation (ΔEp) of 70 ± 9 mV. UV/vis/NIR absorption spectra were run on a Perkin Elmer Lambda 900 spectrometer using tungsten-halogen lamps and a R6872 photomultiplier/detector. Samples were run in a 1 cm quartz cuvette solvated in MeCN. A Perkin-Elmer LS-50B spectrometer was used for the fluorescence measurements, iwth the samples solvated in MeCN in a 1 cm quartz cuvette and emission measured at 90° to the excitation beam. X-band EPR spectra were obtained using a Bruker EMX spectrometer fitted with an ER4119HS resonator and ER4131VT cryostat. EPR spectra were simulated using Bruker SimFonia. Magnetic susceptibility measurements were performed on a Quantum Design SQUID magnetometer, in an applied field of 1000 Oe (Chaper 3) or a Quantum Design vibrating sample SQUID magnetometer in an applied field of 5000 Oe (Chapters 4

and 5) at a scan rate of 5 K min^{-1}. A diamagnetic correction for the sample was estimated from Pascal's constants; a diamagnetic correction for the sample holder was also applied to the data. Room temperature susceptibilities of the complexes were also carried out on a Sherwood Scientific susceptibility balance to validate the variable temperature data.

X-ray powder diffraction measurements were taken on a Bruker D8 diffractometer, using Cu-Kα radiation with samples measured from $5 \leq 2\theta \leq 50°$ in 0.0331° increments using fixed slits. Powder pattern simulations were performed through the Lazy Pulverix routine in X-SEED using the single crystal data. Single crystals were grown as described in the discussion of their respective structures. Single crystal X-Ray diffraction data was collected on a Bruker X8 Apex diffractometer using monochromated Mo-kα radiation (λ = 0.71 Å) or an Agilent Supernova dual source diffractometer employing Cu-kα radiation (λ = 1.54 Å) or Mo-kα radiation (λ = 0.71 Å). Structures were solved via direct and Patterson methods (SHELXS97) and refined via full matrix least squares on F^2 (SHELXL97).[1] Structural graphics were plotted using the Cambridge Crystallographic Database Centre's Mercury software (Mercury 2.4.5).

Differential scanning calorimetry was performed by Mr. Algy Kazlauciunas on a TA Instruments DSC Q20 model, heating at a rate of 5 K min^{-1} between 190 and 350 K using employing N_2 flow gas at a rate of 50 cm^3 min^{-1}. Thermogravimetric analyses were acquired by Mr. Algy Kazlauciunas using a TA Instruments TGA Q50 analyser heating at a rate of 5 K min^{-1} with N_2 balance flow rate of 40 cm^{-3} min^{-1} and sample purge flow rate of 60 cm^3 min^{-1}. Unless otherwise stated all commercially available reagents/solvents were used without further purification/drying.

6.2 Preparation of relevant ligands, synthetic intermediates and precursors

6.2.1 2,6-Di(2'-pyridyl)pyrazine (bipypz)

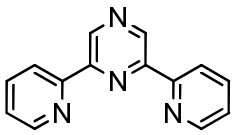

The preparation of this compound is according to that in the literature however omits the need to isolate the compound through column chromatography.[2] 2,6-Dichloropyrazine (1.360 g, 3.69 mmol) and 2-(tributylstannyl)pyridine (0.230 g, 1.54 mmol) were added to a Schlenk tube containing a 10 mol % catalyst loading of $Pd(PPh_3)_4$ (320 mg, 0.27 mmol) in dry toluene (25 cm^3) under N_2. The black solution was heated to reflux for 48 h, cooled to RT and DCM (150 cm^3) added before filtration. The black filtrate was separated with NH_4OH (100 cm^3)

and the organic extract washed with further NH_4OH (3x50 cm^3), dried with magnesium sulphate and filtered. The volatiles were removed *in vacuo* and isolated with silica gel chromatography (eluent: ethyl acetate, R_f value <0.5, 141 mg, 39% yield. ^1H NMR ($CDCl_3$) δ = 7.40 (dd, J = 7.1, 5.3 Hz, 2H, 5'), 7.90 (td, J = 7.7, 1.3 Hz, 2H, 4'), 8.55 (d, J = 8.1 Hz, 2H, 3'), 8.76 (d, J = 4.3 Hz, 2H, 6'), 9.68 (s, 2H, 3); ^{13}C NMR ($CDCl_3$) δ = 121.5 (3'), 124.4 (5'), 137.0 (4'), 142.8 (3), 149.5 (6'), 149.5 (2), 154.4 (2'); ES^+-MS *m/z* 235.1 $[(M + H)]^+$, 257.1 $[(M + Na)]^+$.

6.2.2 2,6-Di(2'-pyrazyl)pyridine (bipzpy)

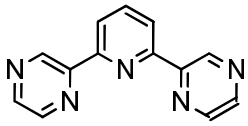

The preparation of this compound is according to that in the literature however omits the need to isolate the compound through column chromatography.[2] A Schlenk tube was charged with 2,6-dibromopyridine (351 mg, 1.48 mmol), 2-(tributylstannyl)pyrazine (1.090 g, 2.96 mmol), $Pd(PPh_3)_4$ (141 mg, 0.12 mmol) and dry toluene (25 cm^3) under N_2 and heated to reflux for 16 h. H_2O (25 cm^3) was added after cooling and the organic layer extracted with DCM (3 x 30 cm^3), dried with $MgSO_4$, filtered and the DCM removed *in vacuo*. The solid was suspended in pentane (50 cm^3) and filtered yielding the product as a colourless solid. 148 mg, 42% yield. ^1H NMR ($CDCl_3$) δ = 8.04 (t, J = 7.7 Hz, 1H, 4), 8.49 (d, J = 7.7 Hz, 2H, 3), 8.66 (m, 4H, 5'+6'), 9.85 (d, J = 0.9 Hz, 2H, 3'); ^{13}C NMR ($CDCl_3$) δ = 122.1 (3), 138.3 (4), 143.5 (3'/5'/6'), 143.6 (3'/5'/6'), 144.8 (3'/5'/6'), 150.8 (2'/2), 153.9 (2'/2); ES^+-MS *m/z* 236.1 $[(M + H)]^+$, 258.1 $[(M + Na)]^+$. Anal. Calcd for $C_{13}H_9N_5$: C, 66.37; H, 3.86; N, 29.77. Found: C, 65.90; H, 3.80; N, 29.15.

6.2.3 2,6-Di(2'-pyrazyl)pyrazine (terpz)

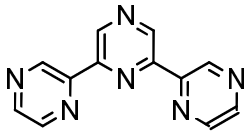

The preparation of this compound is according to that in the literature however omits the need to isolate the compound through column chromatography.[2] A solution of dichloropyrazine (179 mg, 1.20 mmol) in dry toluene (20 cm^3) was added to a schlenk containing 2-(tributylstannyl)pyrazine (955 mg, 2.59 mmol) and $Pd(PPh_3)_4$ (84 mg, 0.07 mmol) under N_2 and the contents left to reflux for 24h. After cooling, 20 cm^3 of H_2O was added to the now black solution and separation was achieved with DCM (3 x 25 cm^3) and was then dried with $MgSO_4$, filtered, washed with 2,2,2-trifluoroethanol (40 cm^3) and the solvent removed in vacuo. The yellow solid was dissolved in pentane, filtered and washed

with additional pentane and chloroform leaving a colourless solid.137 mg, 48% yield. ^{1}H NMR (CD_2Cl_2) δ = 8.70 (s, 4H, 5' + 6 '), 9.66 (s, 2H, 3'/3), 9.76 (s, 2H, 3'/3); ES^{+}-MS *m/z* 237.1 [(M + H)]$^{+}$, 259.1 [(M + Na)]$^{+}$. Anal. Calcd. for $C_{12}H_8N_6$: C, 56.7; H, 3.96; N, 33.1. Found: C, 56.5; H, 3.15; N, 32.9.

6.2.4 Methyl pyrazine carboxylate

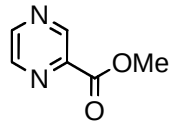

In methanolic (25 cm^3) concentrated H_2SO_4 (2 cm^3), pyrazine carboxylic acid (11.018 g, 88.78 mmol) was added and the solution heated at reflux for 18 h. After cooling the solvent was removed *in vacuo*, and extracted with $CHCl_3/H_2O$. Quenching the organic layer with $H_2O/NaCl/NaHCO_3$, followed by removal of the solvent gave the product as a pale yellow oil which solidified to form an off-white crystalline solid. 8.25 g, 67% yield. ^{1}H NMR ($CDCl_3$) δ = 4.05 (s, 3H, OMe), 8.72 (t, J = 1.9 Hz, 1H, 5'), 8.78 (d, J = 2.6 Hz, 1H, 6'), 9.32 (d, J = 1.1 Hz, 1H, 3'); ^{13}C NMR ($CDCl_3$) δ = 53.1 (OMe), 143.3 (2), 144.4 (5), 146.3 (3), 147.7 (6), 164.4 (CO).

6.2.5 1,5-Di(2'-pyrazinyl)pentane-1,3,5-trione

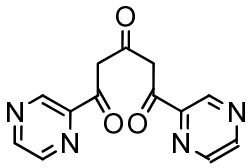

This preparation was based on an adapted literature preparation.[3, 4] To a NaH suspension (60% dispersion in mineral oil, 1.723 g) in 1,2-dimethoxyethane (50 cm^3) under N_2 was added methyl-2-pyrazine carboxylate (3.392 g, 24.56 mmol) and acetone (522 mg, 8.99 mmol) causing immediate effervescence. After stirring for 0.5 h, the now dark red solution was refluxed at 110°C for 6 h, cooled to RT and the volatiles removed *in vacuo*. H_2O (100 cm^3) was added dropwise yielding a red/orange suspension. Following filtration through celite, the solution was neutralised with dilute HCl causing precipitation of a light orange solid. The precipitate was collected via filtration and desiccated thoroughly. Yellow powder, 532 mg, 22% yield. M.p. 166-168°C (dec.). ^{1}H NMR ($CDCl_3$) δ = 6.79 (s, 4H, 2), 8.63 (d, J = 1.5 Hz, 2H, 5'), 8.71 (d, J = 2.5 Hz, 2H, 6'), 9.28 (d, J = 0.8 Hz, 2H, 3'); ES^{+}-MS *m/z* 271.1 [(M + H)]$^{+}$, 293.1 [(M + Na)]$^{+}$, 563.2 [(2M + Na)]$^{+}$. Anal. Calcd for $C_{13}H_{10}N_4O_3$: C, 57.78; H, 3.73; N, 20.73. Found: C, 57.00; H, 3.65; N, 19.45.

6.2.6 4-Hydroxy-2,6-di(2'-pyrazyl)pyridine (bipzpyOH)

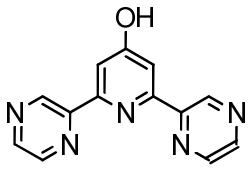

This compound was prepared according to a reported method.[4] 1,5-Bis(2'-pyrainzyl)pentane-1,3,5-trione (501 mg, 1.85 mmol) was added to ammonium acetate (1.141 g, 14.80 mmol) in ethanol (20 cm^3) and the mixture refluxed for 6 h under N_2. The dark orange solution was cooled to room temperature, concentrated to half volume and filtered. The solid collected was washed with diethyl ether (20 cm^3) and ethanol (5 cm^3). Pale brown solid, 408 mg, 82% yield. M.p. 283 - 285°C (dec.). ^{1}H NMR (DMSO-d_6) δ =7.85 (s, 2H, 3), 8.76 (m, 4H, 5' + 6'), 9.80 (d, J = 0.9 Hz, 2H, 3') 11.31 (br s, 1H, OH); ^{13}C NMR (DMSO-d_6) δ = 109.1 (3), 142.9 (3'), 143.9 (5'/6'), 145.2 (5'/6'), 149.8 (2'/2), 155.1 (2'/2), 166.2 (4); ES$^+$-MS *m/z* 252.1 $[(M + H)]^+$, 274.1 $[(M + Na)]^+$, 503.2 $[(2M + H)]^+$, 525.2 $[(2M+Na)]^+$. Anal. Calcd for $C_{13}H_9N_5O.1/2H_2O$: C, 59.99; H, 3.87; N, 26.91. Found: C, 60.75; H, 3.55; N, 26.45.

6.2.7 4-Methoxy-2,6-di(pyrazinyl)pyridine (bipzpyOMe)

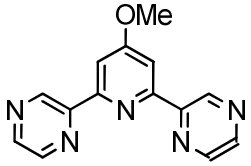

In a two-necked round bottom flask flushed with N_2, 4-hydroxy-2,6-di(pyrazinyl)pyridine (298 mg, 1.19 mmol), MeI (274 mg, 1.93 mmol) and K_2CO_3 (262 mg, 1.90 mmol) were refluxed together in acetone (25 cm^3) for 24 h. Once cool the volatiles were removed *in vacuo*, and the residue triturated in $CHCl_3$ (100 cm^3) and washed with aqueous NaOH (2 x 50 cm^3). The organic phase was decolourised with activated charcoal and filtered, before the $CHCl_3$ was removed. Pale yellow solid, 84.0 mg, 27% yield. M.p. 199-201°C (dec.). ^{1}H NMR ($CDCl_3$) δ = 4.05 (s, 3H, OMe), 8.02 (s, 2H, 3), 8.63 – 8.66 (m, 4H, 5' + 6'), 9.83 (d, J = 1.3 Hz, 2H, 3'); ^{13}C NMR ($CDCl_3$) δ = 55.7 (OMe), 108.0 (3), 143.5 (3'/5'/6'), 143.7 (3'/5'/6'), 144.8 (3'/5'/6'), 150.7 (2), 155.6 (2'), 167.9 (4); ES$^+$-MS *m/z* 266.1 $[(M + H)]^+$, 288.1 $[(M + Na)]^+$. No satisfactory microanalytical data was obtained for this novel compound.

6.2.8 Methyl pyrimidine-2-carboxylate

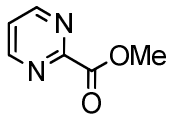

NaOH (12.213 g, 305.30 mmol) was added to a stirring solution of 2-cyano pyrimidine (9.978 g, 94.94 mmol) in H_2O (250 cm^3) and the mixture refluxed for 5 h. Once cool the solution

was acidified to pH 4 with dilute HCl and the H_2O removed *in vacuo*. The residue was then dissolved in MeOH (250 cm^3) acidified with concentrated H_2SO_4 (20 cm^3) and refluxed for a further 20 h. The MeOH was evaporated off, and the residue separated with $H_2O/CHCl_3$. The organic layer was washed with $NaHCO_3$, and a colourless solid was isolated following removal of the $CHCl_3$. 5.37 g, 41% yield. ^{1}H NMR ($CDCl_3$) δ = 4.07 (s, 3H, Me), 7.50 (t, J = 4.8 Hz, 1H, 5), 8.96 (d, J = 4.9 Hz, 2H, 4 + 6); ES^+-MS *m/z* 169 $[(M - H + 2Na)]^+$.

6.2.9 1,5-Di(2'-pyrimidyl)pentane-1,3,5-trione

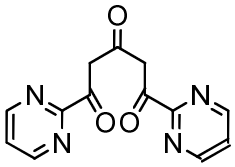

Parts of this synthetic scheme were adapted from literature methods.[4, 5] Under an atmosphere of N_2, a suspension of NaH (60% dispersion in mineral oil, 1.579 g) in glyme (40 cm^3) was stirred for 10 minutes before methyl pyrimidine-2-carboxylate (2.642 g, 19.13 mmol) and acetone (455 mg, 7.83 mmol) were dropped into the flask producing a cream coloured suspension. After an hour stirring at RT, the now yellow suspension was refluxed at 120°C for 4 h during which the evolution of H_2 was noted along with a gradual darkening to a red-brown. Once cool, the volatiles were removed in vacuo and H_2O (40 cm^3) added to carefully quench the resulting solid. The resulting precipitate was collected via vacuum filtration and the wet solid desiccated thoroughly. Orange solid, 936 mg, 44 % yield. M.p. 170-172°C (dec.). 1,5-Di(2'-pyrimidyl)pentane-1,3,5-trione was insufficiently soluble in all common organic solvents to produce well resolved ^{1}H/^{13}C NMR spectra. ES^+-MS *m/z* 293.1 $[(M + Na)]^+$, 563.1 $[(2M + Na)]^+$. No satisfactory microanalytical data was obtained for this novel compound.

6.2.10 2,6-Di(2'-pyrimidyl)-4-pyridone (2-bipympyOH)

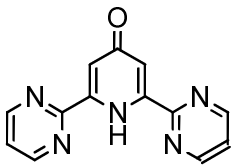

The preparation of this compound has been adapted and modified from literature reports.[4, 6] In dry EtOH (40 cm^3) 1,5-di(2'-pyrimidyl)pentane-1,3,5-trione (783 mg, 2.90 mmol) and ammonium acetate (2.25 g, 29.19 mmol) were refluxed under N_2 for 5 h. Once at RT, the solution was cooled and reduced in volume to ca. 50%, before filtering yielded a yellow solid. This was recrystallised from EtOH, filtered and the precipitate triturated in hot acetone and the resulting pale yellow powder collected on a glass frit. 193 mg, 27% yield. M.p. 303-305°C (dec.). ^{1}H NMR (DMSO-d_6): 7.37 (br s, 2H, 3), 7.69 (t, J = 3.3 Hz, 2H, 5'), 9.06 (d, J =

4.3 Hz, 4H, 4' + 6'), 11.41 (br s, 1H, NH); ES$^+$-MS *m/z* 252.1 [(M + H)]$^+$, 274.1 [(M + Na)]$^+$, 503.2 [(2M + H)]$^+$. Anal. Calcd for $C_{13}H_9N_5O.{}^1/_2H_2O$: C, 60.0; H, 3.87; N, 26.9%. Found: C, 60.7; H, 3.55; N, 26.5%.

6.2.11 4-Methoxy-2,6-di(2'-pyrimidyl)pyridine (2-bipympyOMe)

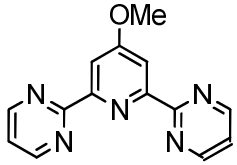

To a suspension of K_2CO_3 (117 mg, 0.84 mmol) and 2,6-di(2'-pyrimidyl)-4-pyridone (93 mg, 0.37 mmol) in acetone (8 cm^3) was added MeI (160 mg, 1.13 mmol). After flushing the flask thoroughly with N_2, the contents were heated to reflux for 24 h. Once cool, the volatiles were removed and the residue triturated in $CHCl_3$ and washed with aqueous NaOH (2 x 25 cm^3). Activated charcoal was added to the organic phase and the black suspension filtered, yielding a brown oily residue after removal of the volatiles. Trituration in Et_2O (5 cm^3) and filtration gave the pure compound as a grey solid. M.p. 171-173°C. 4.00 mg, 4% yield. ^{1}H NMR ($CDCl_3$) δ = 4.07 (s, 3H, OMe), 7.34 (t, J = 4.9 Hz, 2H, 5'), 8.18 (s, 2H, 3), 8.96 (d, J = 4.9 Hz, 4H, 4' + 6'); ^{13}C NMR ($CDCl_3$) δ = 55.7 (OMe), 110.9 (3), 120.5 (5'), 156.6 (2), 157.6 (4' + 6'), 163.6 (2'), 157.8 (4); ES$^+$-MS *m/z* 288.1 [(M + Na)]$^+$. No satisfactory microanalytical data was obtained for this novel compound.

6.2.12 2,6-Di(1',2',4'-triazin-3'-yl)pyridine (bitrzpy)

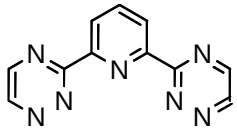

This compound was synthesised as previously reported.[7] Hydrazine monohydrate (5 cm^3) was added to a flask containing 2,6-dicyanopyridine (978 mg, 7.6 mmol) in EtOH (15 cm^3). The thick yellow suspension was heated to 55°C for 4 h, cooled and H_2O was added and the mixture separated with Et_2O. The resulting aqueous suspension was filtered, washed with Et_2O and desiccated overnight. The off-white dicarbamidrazone was then added to a stirring suspension of glyoxal trimer dihydrate (726 mg, 3.45 mmol) in MeOH (50 cm^3) under N_2. The mixture was stirred at RT for 3 h, before refluxing for 2 h. After cooling, the suspension was filtered and the bright yellow solid obtained desiccated. 903 mg, 50% yield. ^{1}H NMR (DMSO-d_6) δ = 8.33 (t, J = 7.7 Hz, 1H, 4), 8.66 (d, J = 7.7 Hz, 2H, 3), 9.08 (d, J = 2.6 Hz, 2H, 5'), 9.55 (d, J = 2.1 Hz, 2H, 6'); ^{13}C NMR (DMSO-d_6) δ = 125.6 (3), 138.9 (4), 149.7 (6'), 150.4 (5') 153.2 (2), 162.7 (3'); ES$^+$-MS *m/z* 238.1 [(M + H)]$^+$, 260.1 [(M + Na)]$^+$, 475.2 [(2M + H)]$^+$, 497 [(2M + Na)]$^+$.

6.2.13 2,6-Bis[(*N*,*N*-dimethylamino)-1-oxoprop-2-en-1-yl]pyridine

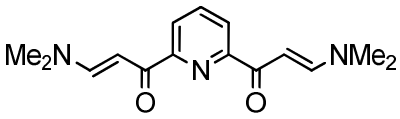

This compound was synthesised as in the literature.[8] *N*,*N*-dimethyl formamide dimethyl acetal (7 g, 58.74 mmol) was added to a flask containing 2,6-diacetylpyridine (2.385 g, 14.62 mmol) and heated to 120°C for 18 h. Concentration of the black mixture to half volume and crystallisation from THF/MeCN yielded the compound as a yellow microcrystalline solid. 2.40 g, 60% yield. ^{1}H NMR ($CDCl_3$) δ = 6.59 (s, 6H, NMe), 6.61 (s, 6H, NMe), 6.60 (d, J = 12.0 Hz, 2H, α-CO), 7.88 (t, J = 7.7 Hz, 1H, 4), 7.90 (d, J = 12.8 Hz, 2H, β-CO), 8.20 (d, J = 7.7 Hz, 2H, 3); ^{13}C NMR ($CDCl_3$) δ = 37.0 (NMe), 45.0 (NMe), 91.5 (α-CO), 123.5 (3), 137.3 (4), 154.4 (β-CO), 154.6 (2), 186.7 (CO); ES^+-MS *m/z* 296.1 $[(M + Na)]^+$.

6.2.14 2,6-Di(4'-pyrimidyl)pyridine (4-bipympy)

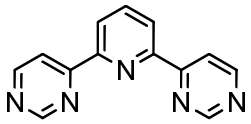

This compound was synthesised as in the literature.[8] Under an atmosphere of N_2 formamidine acetate (1.540 g, 14.45 mmol) was added to a flask charged with 2,6-bis[(*N*,*N*-dimethylamino)-1-oxoprop-2-en-1-yl]pyridine (791 mg, 2.89 mmol) in boiling EtOHl (50 cm^3) followed by the dropwise addition of sodium (697 mg, 30.32 mmol) in EtOH (20 cm^3) over a period of 0.5 h. Reflux was maintained for 16 h, after which the EtOH was removed from the dark purple. Dissolution in DCM and filtration, followed by column chromatography on neutral alumina (eluent: ethyl acetate-hexane, 4:1) allowed isolation of the pure product. Colourless solid, 268 mg, 39% yield. ^{1}H NMR ($CDCl_3$) δ = 8.09 (t, J = 7.7 Hz, 1H, 4), 8.55 (dd, J = 5.2, 1.6 Hz, 2H, 5'), 8.66 (d, J = 7.9 Hz, 2H, 3), 8.95 (d, J = 5.2 Hz, 2H, 6'), 9.35 (d, J = 1.2 Hz, 2H, 2'); ^{13}C NMR ($CDCl_3$) δ = 117.5 (5'), 123.4 (3), 138.6 (4), 153.6 (2), 158.1 (6'), 158.8 (2'), 162.3 (4'); ES^+-MS *m/z* 236.1 $[(M + H)]^+$, 258.1 $[(M + Na)^+$. Anal. Calcd for: $C_{13}H_9N_5.1/2H_2O$: C, 63.92; H, 4.13; N, 28.67. Found: C, 63.30; H, 3.65; N, 28.00.

6.2.15 2,6-Diacetylpyrazine

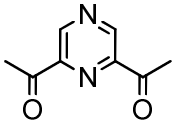

This preparation was adapted from the literature.[9, 10] Under an atmosphere of N_2, acetyl pyrazine (1.967 g, 16.11 mmol) was dissolved in H_2O (200 cm^3) and acidified with 18 M H_2SO_4 (1.8 cm^3). The flask was shielded from light, pyruvic acid dropped into the flask (4.405

g, 50.02 mmol) and heated to 50°C with stirring. Finally, aqueous solutions of $AgNO_3$ (0.225 g, 1.32 mmol) and $[NH_4]_2[S_2O_8]$ (11.237 g, 49.25 mmol) were added in tandem and the contents left at 50°C for 2 h. After cooling, the pH was increased to 12 using concentrated NaOH. Extraction with $CHCl_3$, drying with $MgSO_4$ and removal of the volatiles gave a crude brown solid. The pure compound was obtained via elution through a short silica column (eluent: ethyl acetate-pentane, 2:3). Yellow powder, 872 mg, 33% yield. ^{1}H NMR ($CDCl_3$) δ = 2.76 (s, 6H, Me), 9.26 (s, 2H, 3); ^{13}C NMR ($CDCl_3$) δ = 26.0 (Me), 142.3 (3), 149.1 (2), 198.8 (CO); ES$^+$-MS *m/z* 165.1 $[(M + H)]^+$, 187.0 $[(M + Na)]^+$, 351.1 $[(2M + Na)]^+$.

6.2.16 2,6-Bis[(*N*,*N*-dimethylamino)-1-oxoprop-2-en-1-yl]pyrazine

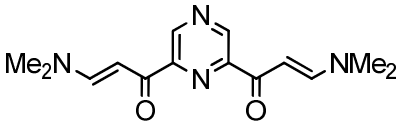

2,6-diacetyl pyrazine (857 mg, 5.22 mmol) is heated to 120°C in *N*,*N*-dimethyl formamide dimethyl acetal (25 cm^3, 186.72 mmol) for 18 h. The contents were cooled and the volatiles removed in vacuo, and the light brown solid recrystallised from MeCN-THF (4:1). The microcrystalline precipitate was filtered and collected on a glass sinter. Brick-red microcrystalline powder, 834 mg, 58 % yield. M.p. 272-274°C (dec.). ^{1}H NMR ($CDCl_3$) δ = 3.02 (s, 6H, NMe), 3.21 (s, 6H, NMe), 6.42 (d, J = 10.3 Hz, 2H, α-CO), 7.94 (d, J = 12.8 Hz, 2H, β-CO), 9.29 (s, 2H, 3); ^{13}C NMR ($CDCl_3$) δ = 37.6 (NMe), 45.3 (NMe), 91.5 (α-CO), 142.3 (3), 151.0 (2), 155.0 (β-CO), 185.1 (CO); ES$^+$-MS *m/z* 275 $[(M + H)]^+$.

6.2.17 2,6-Di(4'-pyrimidyl)pyrazine (4-bipympz)

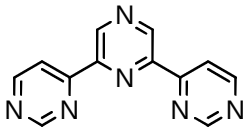

Formamidine acetate (1.605 g, 15.42 mmol) in EtOH (20 cm^3) was added to a boiling suspension of 2,6-Bis[(*N*,*N*-dimethylamino)-oxoprop-2-en-1-yl]pyrazine (775 mg, 2.83 mmol) in EtOH (20 cm^3). Over 0.5 h a solution of sodium (1.056 g, 45.93 mmol) in EtOH (15 cm^3) was dropped into the reaction vessel, which was held at reflux for 16 h. Once at RT, the EtOH was removed, followed by dissolution in DCM, filtration through a glass sinter and washing the solid with MeCN. After removal of the solvents, the crude solid was separated on a silica gel column (eluent: EtOAc) yielding a yellowish solid. Finally, dissolution in toluene and filtration followed by washing with portions of hexane and Et_2O gave the product as a sandy brown solid. 76.0 mg, 11% yield. ^{1}H NMR ($CDCl_3$) δ = 8.44 (dd, J = 5.1, 1.3 Hz, 2H, 5'), 8.97 (d, J = 5.1 Hz, 2H, 6'), 9.39 (d, J = 1.3 Hz, 2H, 2'), 9.80 (s, 2H, 3); ^{13}C NMR ($CDCl_3$) δ = 118.1 (5'), 142.7 (3), 150.0 (2), 158.5 (6'), 158.9 (2'), 160.6 (4'); ES$^+$-MS *m/z*

259.1 [(M + Na)]$^+$. No satisfactory microanalytical data was obtained for this novel compound.

6.2.18 3,3-Bis(methylsulfanyl)-1-(2-pyridyl)-2-propene-1-one

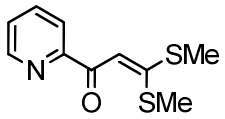

The preparation of this compound is adapted from the literature.[11] Under N_2, ^{t}BuOK (19.915 g, 177.48 mmol) was suspended in THF (200 cm^3), and 2-acetyl pyridine (10.175 g, 83.99 mmol) was dropped slowly into the flask over 10 minutes with stirring, turning the solution a light yellow. In succession, CS_2 (6.614 g, 86.87 mmol) and MeI (25.509 g, 179.72 mmol) were added carefully, resulting into a dark brown slurry which was stirred at RT for 24 h. The resulting slurry was poured onto ice water (500 cm^3) and stirred for an additional 4 h, before cooling to 0 °C and filtered. A crude brown solid was collected (11.9 g), which was subsequently recrystallised from EtOH to give the compound as a light brown crystalline solid. 7.43 g, 39% yield. ^{1}H NMR ($CDCl_3$) δ = 2.56 (s, 3H, SMe), 2.64 (s, 3H, SMe), 7.39 (ddd, J = 7.6, 4.7, 1.1 Hz, 1H, 5), 7.65 (s, 1H, α), 7.83 (td, 7.7, 1.7 Hz, 1H, 4), 8.17 (dt, J = 7.9, 0.9 Hz, 1H, 3), 8.64 (ddd, J = 4.7, 1.5, 0.8 Hz, 1H, 6); ^{13}C NMR ($CDCl_3$) δ = 14.9 (SMe), 17.3 (SMe), 108.7 (α-CO), 122.5 (3), 125.9 (5), 136.8 (4), 148.4 (6), 154.9 (2), 167.6 (β-CO), 184.2 (CO); ES$^+$-MS *m/z* 226.0 [(M + H)]$^+$, 248.0 [(M + Na)]$^+$, 473.0 [(2M + Na)]$^+$.

6.2.19 4-Thiomethyl-2-(2'-pyridyl)-6-(4''-pyridyl)pyridine

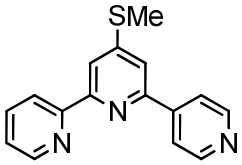

The preparation of this compound is adapted from the literature.[11] ^{t}BuOK (5.860 g, 52.32 mmol) was stirred suspended in dry THF (200 cm^3) for 10 minutes under N_2, before 4-acetylpyridine (3.094 g, 25.54 mmol) was dropped into the resulting suspension instantly forming a yellow paste. After a second 10 minutes had elapsed, 3,3-bis(methylsulfanyl)-1-(2-pyridinyl)-2-propen-1-one (5.717 g, 25.37 mmol) was inserted which over the course of 24 h stirring at RT caused the formation of a deep crimson solution. NH_4OAc (19.704 g, 255.63 mmol) followed by glacial acetic acid (75 cm^3) were then added, after which the THF was removed by slow distillation over 1 h. Once at RT, the resulting black solution was combined with H_2O (400 cm^3) and after stirring for a short period was filtered, washed profusely with water, and desiccated yielding 6.77 g of crude solid. This was then recrystallised from Et|OH. Grey solid, 2.58 g, 36% yield. ^{1}H NMR ($CDCl_3$) δ = 2.67 (s, 3H, SMe), 7.36 (ddd, J = 7.6, 4.9, 1.1 Hz, 1H, 5'), 7.63 (d, J = 1.7 Hz, 1H, 5), 7.87 (td, J = 7.7, 1.7 Hz, 1H, 4'), 8.01 (m,

2H, 3'' + 5''), 8.32 (d, J = 1.7 Hz, 1H, 3), 8.60 (dt, J = 7.9, 1.1 Hz, 1H, 3'), 8.70 (ddd, J = 4.7, 1.7, 1.0 Hz, 1H, 6'), 8.75 (m, 2H, 2'' + 6''); ^{13}C NMR ($CDCl_3$) δ = 14.0 (SMe), 116.4 (3), 117.1 (5), 121.1 (3'' + 5''), 121.5 (3'), 124.1 (5'), 136.9 (4'), 146.2 (4''c), 149.0 (6'), 150.4 (2'' + 6''), 152.6 (4), 153.3 (2), 155.5 (2'), 155.8 (6); ES^+-MS *m/z* 280.1 $[(M + H)]^+$.

6.2.20 2-(2'-Pyridyl)-6-(4''-pyridyl)pyridine (Ctpy)

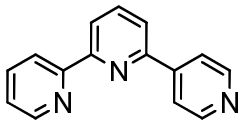

The preparation of this compound is adapted from the literature.[11] 4'-Methylsulfonyl-2,2':6',4''-terpyridine (2.483g, 8.89 mmol) and $NiCl_2.6H_2O$ (21.000 g, 88.34 mmol) were stirred in EtOH (150 cm^3) at 0°C under an atmosphere of N_2. Over a period of 4 h a solution of $NaBH_4$ (9.948 g, 262.97 mmol) in aqueous NaOH (40%) was added into the reaction mixture via a dropping funnel whilst the temperature was maintained at 0°C causing the gradual formation of a dark solid. After refluxing for 16 h and filtering hot through celite, the volatiles were removed leaving a yellow/orange paste which was added to ice-water (250 cm^3), extracted three times with DCM and dried with $MgSO_4$. Removal of the DCM and extraction with boiling hexane gave a yellow solution which was vacuumed to dryness. Cream/yellow solid. 811 mg, 39% yield. ^{1}H NMR ($CDCl_3$) δ = 7.36 (ddd, J = 7.4, 4.9, 1.3 Hz, 1H, 5'), 7.85 (dd, J = 7.7, 0.9 Hz, 1H, 5), 7.88 (td, J = 7.7, 1.9 Hz, 1H, 4'), 7.96 (t, J = 7.7 Hz, 1H, 4), 8.05 (m, 2H, 3''+5''), 8.50 (dd, J = 7.9 Hz, 0.9 Hz, 1H, 3), 8.63 (dt, J = 7.9, 0.9 Hz, 1H, 3'), 8.72 (ddd, J = 4.7, 1.7, 0.8 Hz, 1H, 6'), 8.77 (m, 2H, 2'' + 6''); ^{13}C NMR ($CDCl_3$) δ = 120.6 (5), 121.0 (3 + 3'' + 5''), 121.2 (3'), 124.0 (5'), 136.9 (4'), 138.0 (4), 146.3 (4''), 149.2 (6'), 150.4 (2'' + 6''), 153.6 (5), 155.8 (2'), 156.3 (3); ES^+-MS *m/z* 234.1 $[(M + H)]^+$.

6.2.21 2,6-Di(1'-methylimidazolium-3'-yl)pyridine dibromide (MeImpy)

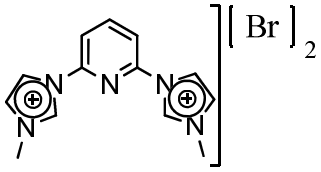

This preparation is adapted from the literature.[12, 13] Under an inert atmosphere of N_2, 1-methyl imidazole (2.574 g, 31.35 mmol) and 2,6-dibromopyridine (2.931 g, 12.37 mmol) were heated to 140°C for 18 h. After cooling, the grey solid produced was suspended in DCM, filtered and washed with ca. 25 cm^3 of DCM and Et_2O in succession and subsequently dried *in vacuo*. Off-white powder, 3.26 g, 66% yield. ^{1}H NMR (CD_3OD) δ = 4.15 (s, 6H, Me), 7.89 (d, J = 2.2 Hz, 2H, 5'), 8.17 (d, J = 8.1 Hz, 2H, 3), 8.50 (t, J = 8.1 Hz,1H, 4), 8.61 (d, J =

2.2 Hz, 2H, 4'), 10.30 (s, 2H, 2'); ^{13}C NMR (CD_3OD) δ = 37.5 (Me), 115.8 (3), 120.8 (4'), 126.4 (5'), 137.6 (2'), 146.3 (4), 147.3 (2); ES^+-MS *m/z* 238.0 $[(monosubstituted\ pyridine)]^+$.

6.2.22 1-Isopropyl imidazole

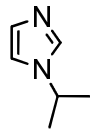

At 0°C MeCN (200 cm^3) was added to a mixture of imidazole (5.233 g, 76.67 mmol) and NaH as a 60% dispersion in mineral oil (5.375 g dispersion, 80.63 mmol sodium hydride) under N_2. The suspension was warmed to RT and stirred for 1 h until effervescence ceased. Re-cooling to 0°C, isopropyliodide (19.58 g, 115.21 mmol) was inserted into the reaction vessel. After stirring overnight at room temperature, the volatiles were removed *in vacuo* and the residue combined with DCM and an insoluble precipitate removed by vacuum filtration. Removal of the solvent gave an impure yellow oil (8.45 g) which was extracted by reduced pressure distillation. Colourless oil, 4.00 g, 47% yield. ^{1}H NMR ($CDCl_3$) δ = 1.45 (d, J = 6.8 Hz, 6H, Me), 4.31 (sp, J = 6.6 Hz, 1H, Methine), 6.93 (s, 1H, 5), 7.02 (s, 1H, 4), 7.50 (s, 1H, 2). ES^+-MS *m/z* 111.1 $[(M + H)]^+$, 133.0 $[(M + Na)]^+$.

6.2.23 2,6-Di(1'-isopropylimidazolium-3'-yl)pyridine dibromide (PrImpy)

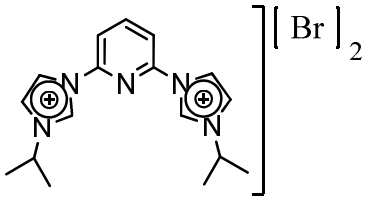

2,6-Dibromopyridine (3.324 g, 14.16 mmol) and 1-isopropyl imidazole (3.960 g, 35.95 mmol) were heated to 150°C under N_2 for 48 h. Once at room temperature the brown solid was broken up, suspended in THF, filtered and washed with further THF. The sandy powder obtained was desiccated to remove residual THF. 3.64 g, 56% yield. ^{1}H NMR (CD_3OD) δ = 1.74 (d, J = 6.8 Hz, 12H, Me), 4.96 (sp, J = 6.8 Hz, 2H, ^{i}Pr), 8.10 (d, J = 2.1 Hz, 2H, 5'), 8.23 (d, J = 8.1 Hz, 2H, 3), 8.51 (t, J = 8.0 Hz, 1H, 4), 8.67 (d, J = 2.1 Hz, 2H, 4'), 10.35 (m, 2H, 2'); ^{13}C NMR (CD_3OD) δ = 23.1 (Me), 55.9 (^{i}Pr), 116.0 (3), 121.3 (4'), 123.1 (5'), 135.7 (2'), 146.1 (4), 147.4 (2). Anal. Calcd for $Br_2C_{17}H_{23}N_5.H_2O$: C, 42.97; H, 5.30; N, 14.74. Found: C, 43.00; H, 5.35; N, 14.70.

6.2.24 2,6-Di(pyrazol-1'-yl)pyridine (1-bpp)

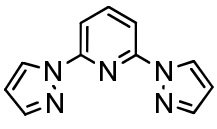

This compound's synthesis was adapted from the literature methods.[14, 15] At 70°C pyrazole (6.047 g, 88.82 mmol) and sodium hydride as a 60% dispersion in mineral oil (3.574 g dispersion, 89.35 mmol of sodium hydride) were stirred in diglyme (90 cm^3) until no more hydrogen gas was observed to bubble off. 2,6-dibromopyridine (6.874 g, 29.02 mmol) was added and the mixture heated to 110°C for 4 days. The diglyme was removed *in vacuo*, andsuspension in copious amounts of water, followed by collection by suction filtration and subsequent hexane washings allowed isolation of the pure ligand. 5.30 g, 87% yield. ^1H NMR ($CDCl_3$) δ = 6.49 (dd, J = 2.6, 1.7 Hz, 2H, 4'), 7.76 (d, J = 1.1 Hz, 2H, 3'), 7.83 - 7.95 (m, 3H, 3 + 4), 8.56 (dd, J = 2.6, 0.6 Hz, 2H, 5'); ^{13}C NMR ($CDCl_3$) δ = 107.9 (4'), 109.3 (3), 126.9 (5'), 141.3 (4), 142.3, (3') 150.5 (2); EI+-MS m/z 211.1 [(M)]+, 144.1 [(M – $C_3H_3N_2$)].

6.2.25 4-Hydroxy-2,6-dibromopyridine

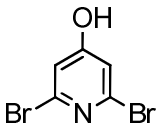

An aqueous 40% solution of $^tBu_4NOH$ (12 cm^3, 18.00 mmol) was added to 4-nitro-2,6-dibromopyridine (2.515 g, 8.92 mmol) in THF (15 cm^3) and the orange solution stirred for 48 h. The THF was removed and the dark oil resulting taken up in $CHCl_3$ and washed with H_2O, and the solvent removed *in vacuo*. The dark oily residue was triturated in H_2O and acidifed to pH2 yielding a yellow solid after filtration and desiccation. The compound was purified using silica gel chromatography (eluent DCM-EtOAc, 9:1). Colourless solid, 1.58 g, 70% yield. ^1H NMR (DMSO-d_6) δ = 7.05 (s, 2H, 3), 11.81 (s, 1H, OH); ^{13}C NMR (DMSO-d_6) δ = 114.9 (3), 140.2 (2), 167.1 (4);

6.2.26 4-Hydroxy-2,6-di(pyrazol-1'-yl)pyridine (1-bppOH)

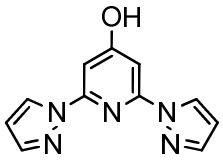

Under a dry atmosphere of dry N_2 at 70°C was added 1*H*-pyrazole (6.172 g, 90.66 mmol) to a stirring suspension of KH (1.590 g, 39.64 mmol) in dry diglyme (45 cm^3). When H_2 evolution had ceased, 4-hydroxy-2,6-dibromopyridine (2.608 g, 10.31 mmol) was inserted and the contents heated at 180°C for 3 days. After cooling to RT, the diglyme was removed *in vacuo* and the brown residue dissolved in H_2O, filtered, neutralised with HCl and the resulting crude light-brown solid collected on a glass sinter. Silica gel column chromatography (eluent: EtOAc-DCM, 1:1; Rf value: 0.29) produced the compound as a colourless solid. 258 mg, 11% yield. M.p. 214 - 216°C. ^1H NMR (DMSO-d_6) δ = 6.58 (dd, J = 2.0, 1.9 Hz, 2H, 4'), 7.21 (s, 2H, 3), 7.82 (d, J = 1.3 Hz, 2H, 3'), 8.86 (d, J = 2.6 Hz, 2H, 5')

11.50 (br s, 1H, OH); ^{13}C NMR (DMSO-d_6) δ = 96.4 (3), 108.0 (4'), 128.0 (5'), 142.3 (3'), 151.0 (2), 168.4 (4); ES$^+$-MS *m/z* 250.1 [(M + Na)]$^+$. Anal. Calcd for $C_{11}H_9N_5O$: C, 55.93; H, 4.26; N, 29.64. Found: C, 56.40; H, 3.90; N, 29.40.

6.2.27 2-Bromo-4-hydroxy-6-(pyrazol-1'-yl)pyridine

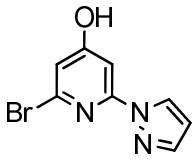

Isolated via silica gel column chromatography (eluent: EtOAc-DCM, 1:1; Rf value: 0.78) in the preparation of 4-hydroxy-2,6-di(pyrazol-1'-yl)pyridine. Off-white solid, 600 mg, 24% yield. M.p. 218 - 220°C. ^{1}H NMR (DMSO-d_6) δ = 6.56 (dd, J = 2.2, 2.1 Hz, 1H, 4'), 6.92 (d, J = 1.7 Hz, 1H, 3), 7.29 (d, J = 1.7 Hz, 1H, 5), 7.81 (d, J = 1.5 Hz, 1H, 3'), 8.46 (d, J = 2.6 Hz, 1H, 5'), 11.65 (br s, 1H, NH); ^{13}C NMR (DMSO-d_6) δ = 98.3 (5), 108.4 (4'), 113.1 (3), 127.4 (5'), 140.1 (2), 142.6 (3'), 151.9 (6), 167.7 (4); ES$^+$-MS *m/z* 262.0 [(M + Na)]$^+$. Anal. Calcd for $BrC_8H_6N_3O$.EtOAc: C, 43.92; H, 4.30; N, 12.80. Found: C, 43.70; H, 3.90; N, 13.90.

6.2.28 Di(2,6-di(bromo)pyridin-4-yl)ether

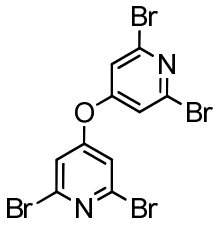

In an attempt to prepare 4-hydroxy-2,6-dibromo-pyridine, 4-nitro-2,6-dibromopyridine (10.038 g, 35.61 mmol) was added quickly to a stirring solution of 40% solution of tertiary butyl ammonium hydroxide (55 cm^3, 85.12 mmol) and THF (50 cm^3). The temperature immediately warmed to ca. 60°C and was subsequently left to stir continuously for 2 days. The volatiles were removed in vacuo and the residue triturated in H_2O, acidified to pH 2 and the fine yellow flocculate was collected through filtration. The material was eluted through a silica gel column (eluent: DCM-EtOAc 9:1; Rf value: 0.70) and isolated as a colourless solid which was confirmed as pure di(2,6-di(bromo)pyridin-4-yl)ether analytically. 8.47 g, 97% yield. M.p. 132 - 134°C. ^{1}H NMR (DMSO-d_6) δ = 7.33 (s, 4H, 3); ^{13}C NMR (DMSO-d_6) δ = 113.8 (3), 140.4 (2), 167.9 (4); ES$^+$-MS *m/z* 267.9 [(M + 2Na)]$^{2+}$. Anal. Calcd for $Br_4C_{10}H_4N_2O.^1/_2$EtOAc: C, 27.10; H, 1.51; N, 5.27. Found: C, 27.60; H, 1.85; N, 5.40.

6.2.29 2-Hydroxy-4,6-di(pyrazol-1'-yl)pyridine

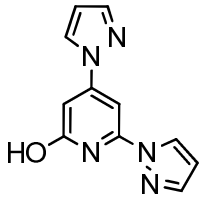

2-Hydroxy-4,6-di(pyrazol-1'-yl)pyridine was formed in an attempt to prepare di(2,6-di(pyrazol-1'-yl)pyridin-4-yl)ether from di(2,6-di(bromo)pyridin-4-yl)ether. After stirring a 60% mineral oil dispersion of NaH (6.862 g dispersion, 171.48 mmol of sodium hydride) in diglyme (130 cm^3) for 0.5 h under N_2, 1*H*-pyrazole was added slowly and carefully until no further evolution of H_2 could be observed. Di(2,6-dibromopyridin-4-yl)ether was then dropped into the flask which was then held at 130°C for 7 days. After cooling to RT, the volatiles were removed from the yellow suspension followed by careful quenching of the remaining NaH by addition of H_2O (300 cm^3). After shaking, a small insoluble solid remained which was removed by filtration and was unidentifiable by ^{1}H NMR. With dilute HCl, the basic filtrate solution was taken to pH 5 resulting forming large quantities of yellow precipitate which was collected, washed with further H_2O and dried over P_2O_5. The material was taken up in DCM, and the insolubles were removed by filtration before removal of the DCM from the filtrate. Cream-coloured solid 67.0 mg, 4% yield. M.p. 177 - 179°C (dec.). ^{1}H NMR (DMSO-d_6) δ = 6.58 (dd, J = 2.6, 1.7 Hz, 1H, 4'), 6.62 (dd, J = 2.6, 1.7 Hz, 1H, 4''), 7.05 (d, J = 1.3 Hz, 1H, 3), 7.83 (d, J = 0.9 Hz, 1H, 3'), 7.86 (d, J = 1.3 Hz, 1H, 3''), 7.87 (d, J = 1.3 Hz, 1H, 5), 8.49 (d, J = 2.6 Hz, 1H, 5'), 8.72 (d, J = 2.6 Jz, 1H, 5''), 11.42 (br s, 1H, OH); ^{13}C NMR (DMSO-d_6) δ = 92.5 (5), 94.7 (3), 108.1 (4'), 109.1 (4''), 127.1 (5'), 128.9 (5''), 142.2 (3'), 142.5 (3''), 150.2 (4), 150.5 (6), 164.3 (2); ES^+-MS *m/z* 228.1 $[(M + H)]^+$, 250.1 $[(M + Na)]^+$. Anal. Calcd for $C_{11}H_9N_5O.{}^1/_2.CH_2Cl_2$: C, 52.11; H, 3.74; N, 25.97. Found: C, 51.80; H, 3.00; N, 27.40.

6.2.30 2,6-Dibromo-4-(tetrahydropyran-2-yloxy)pyridine

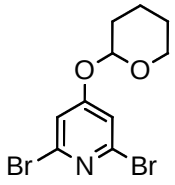

The synthesis of this compound is based on a modified literature method.[16] To a stirring solution of 4-hydroxy-2,6-dibromopyridne (4.613 g, 18.24 mmol) and 3,4-dihydropyran (4,611 g, 54.81 mmol) in DCM (650 cm^3) was added pyridinium *para*-toluene sulfonate (1.419 g, 56.50 mmol)), and the mixture stirred at RT for 36 h. The DCM was removed *in vacuo* leaving a golden oil, to which Et_2O was added (300 cm^3) and extracted with H_2O. The organic layer was dried with Na_2CO_3, filtered and the Et_2O removed. Silica gel column

chromatography (eluent: pentane-Et_2O 8:2; Rf value: 0.61) produced the compound as a colourless crystalline solid. 3.92 g, 64% yield. M.p. 214 - 216°C (dec.). ^{1}H NMR ($CDCl_3$) δ = 1.55 - 1.95 (m, 6H, 3' + 4' + 5'), 3.63 - 3.79 (m, 2H, 6'), 5.51 (t, J = 2.6 Hz, 1H, 2'), 7.15 (s, 2H, 3); ^{13}C NMR ($CDCl_3$) δ = 17.8 (Pn 4'), 24.7, (3'/5') 29.6 (3'/5'), 62.0 (6'), 96.8 (2'), 115.3 (3), 141.0 (2), 165.3 (4); ES$^+$-MS *m/z* 359.9 $[(M + Na)]^+$;

6.2.31 2,6-Di(pyrazol-1'-yl)-4-(tetrahydropyran-2-yloxy)pyridine

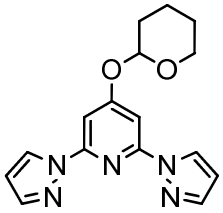

Attempts to prepare this compound via substitution of 2,6-dibromo-4-(tetrahydropyran-2-yloxy)pyridine at the 2,6- positions with the pyrazolate anion resulted in the trisubstituted species 2,4,6-tri(pyrazol-1'-yl)pyridine, the details of which are below.

6.2.32 2,4,6-Tri(pyrazol-1'-yl)pyridine (1-tpp)

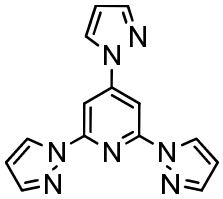

In an attempt to synthesise 2,6-di(pyrazol-1'-yl)-4-(tetrahydropyran-2-yloxy)pyridine, trisubstitution occurred resulting in 2,4,6-tri(pyrazol-1'-yl)pyridine. 1*H*-pyrazole (1.23 g, 18.07 mmol) in diglyme (90 cm^3) was added carefully with stirring to sodium hydride as a 60% dispersion in mineral oil (0.720 g dispersion, 18.00 mmol of sodium hydride) and kept at RT until no further hydrogen gas was evolved. 2,6-dibromo-4-(tetrahydropyran-2-yloxy)pyridine (2.028 g, 6.02 mmol) was dropped into the suspension and the contents were heated to 130°C for 5 days. The now pale brown solution was cooled to RT, reduced in volume and H_2O (250 cm^3) added. The resulting solid was collected, washed with additional H_2O and desiccated. Sand-coloured crystals, 820 mg, 49%. M.p. 185 - 187°C. ^{1}H NMR (CD_3Cl) δ = 6.53 (dd, J = 2.6, 1.7 Hz, 2H, 4'), 6.57 (dd, J = 2.6, 1.7 Hz, 1H, 4''), 7.80 (d, J = 0.9 Hz, 2H, 3'), 7.82 (d, J = 1.3 Hz, 1H, 3''), 8.21 (d, J = 2.6 Hz, 1H, 5''), 8.25 (s, 2H, 3), 8.60 (d, J = 2.6 Hz, 2H, 5'); ^{13}C NMR (CD_3Cl) δ = 98.4 (3), 108.2 (4'), 109.3 (4''), 127.2 (5''), 127.3 (5'), 142.6 (3'), 142.8 (3''), 150.4 (4), 151.5 (2); ES$^+$-MS *m/z* 300.1 $[(M + Na)]^+$.

6.2.33 4-Methoxy-2,6-di(pyrazol-1'-yl)pyridine (1-bppOMe)

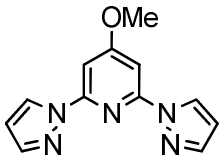

MeI (186 mg, 1.31 mmol) was added to a stirring acetone (10 cm^3) suspension of K_2CO_3 (178 mg, 1.29 mmol) and 4-hydroxy-2,6-di(pyrazol-1'-yl)pyridine (182 mg, 0.80 mmol) under N_2 and the contents refluxed for 24 h. The volume was reduced to ca. 25% and then made up to 50 cm^3 with $CHCl_3$. Aqueous NaOH (2 x 25 cm^3) was then used to wash the suspension, and the volatiles removed *in vacuo*. The resulting yellow solid was triturated in hexane (10 cm^3), collected on a glass frit and washed with a further few drops of hexane before drying in vacuo. 130 mg, 67% yield. M.p. 106 - 108°C. ^{1}H NMR (CD_3Cl) δ = 4.00 (s, 3H, OMe), 6.49 (dd, J = 2.4, 1.7 Hz, 2H, 4'), 7.41 (s, 2H, 3), 7.75 (dd, J = 1.2, 0.6 Hz, 2H, 3'), 8.56 (dd, J = 2.6, 0.8 Hz, 2H, 5'); ^{13}C NMR (CD_3Cl) δ = 56.1 (OMe), 95.7 (3), 107.8 (4'), 127.3 (5'), 142.2 (3'), 151.5 (2), 170.0 (4); ES^+-MS *m/z* 264.1 $[(M + Na)]^+$; Anal. Calcd for $C_{12}H_{11}N_5O$: C, 59.74; H, 4.60; N, 29.03. Found: C, 59.75; H, 4.65; N, 28.85.

6.2.34 4-Methoxy-2-bromo-6-(pyrazol-1'-yl)pyridine

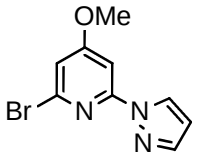

Under an intert atmosphere of N_2, MeI (621 mg, 4.38 mmol) was added to a two-necked flask containing an acetone (25 cm^3) suspension of K_2CO_3 (601 mg, 4.34 mmol) and 2-bromo-4-hydroxy-6-(pyrazol-1'-yl) (694 mg, 2.89 mmol) and this was then heated to reflux for 24 h. The volume was then reduced to 25%, the suspension triturated in $CHCl_3$ and washed with aqueous NaOH (2 x 50 cm^3). Removal of the volatiles *in vacuo* yielded a yellow oil which solidified upon standing. Cream-coloured solid, 663 mg , 90% yield. M.p. 64-66°C. ^{1}H NMR (CD_3Cl) δ = 3.94 (s, 3H, Me), 6.46 (dd, J = 2.6, 1.7 Hz, 1H, 4'), 6.91 (d, J = 2.2 Hz, 1H, 3), 7.47 (d, J = 2.2 Hz, 1H, 5), 7.72 (dd, J = 1.5, 0.5 Hz, 1H, 3'), 8.53 (dd, J = 2.9, 0.6 Hz, 1H, 5'); ^{13}C NMR (CD_3Cl) δ = 56.1 (OMe), 96.5 (5), 108.0 (4'), 112.3 (3), 127.8 (5'), 140.5 (2), 142.5 (3'), 152.5 (6), 168.8 (4); ES^+-MS *m/z* 254.0 $[(M + H)]^+$, 276.0 $[(M + Na)]^+$.

6.2.35 4-Amino-2,6-di(pyrazol-1'-yl)pyridine (1-bppNH$_2$)

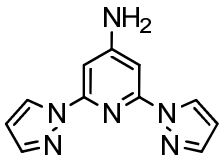

The method documented below has been modified from a literature report.[17] Under an atmosphere of N_2, a stirring suspension of sodium hydride (60% dispersion in mineral oil,12.134 g) in diglyme (150 cm^3) was cooled to -20°C and 1*H*-pyrazole (20.558 g, 301.97 mmol) was added carefully. The cream-coloured suspension was subsequently heated to 70°C and once all hydrogen expulsion was complete 4-amino-2,6-dichloropyridine (10.020 g, 61.47 mmol) was dropped into the mixture. Heating at 130°C yielded initially a yellow-orange suspension, which gradually darkened to a deep green and eventually brown after 7 days. Once at ambient temperature the contents were poured into a flask containing H_2O (600 cm^3) which caused immediate precipitation of a coarse brown solid. This precipitate was filtered, washed profusely with further H_2O and dried *in vacuo*. Once no further mass loss was observed, the solid was triturated in hexane, filtered and desiccated for 3 h. 13.0 g, 94% yield. ^{1}H NMR (DMSO-d_6) δ = 6.53 (t, J = 2.2 Hz, 2H, 4'), 6.72 (s, 2H, NH_2), 7.01 (s, 2H, 3), 7.76 (s, 2H, 3'), 8.76 (d, J = 2.2 Hz, 2H, 5'); ^{13}C NMR (DMSO-d_6) δ = 93.2 (3), 107.4 (4'), 127.5 (5'), 141.6 (3'), 150.4 (2), 158.8 (4); ES^+-MS *m/z* 228.3 $[(M + Na)]^+$.

6.2.36 4-Iodo-2,6-di(pyrazol-1'-yl)pyridine (1-bppI)

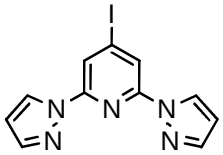

The method documented below has been modified from a literature report.[17] To a suspension of 4-amino-2,6-di(pyrazol-1'-yl)pyridine (3.819 g, 16.88 mmol) in 1:1 isopentyl nitrite-DCM (80 cm^3) under an atmosphere of dry N_2 was added KI (8.581 g, 451.69 mmol) and I_2 (8.653 g, 34.09 mmol) sequentially which caused mild effervescence and a change in the colour to dark orange-brown. Heating at reflux for 5 h resulted in a deep orange solution. The contents, once cool, were added to an aqueous saturated sodium thiosulfate solution (300 cm^3) and extracted with DCM (3 x 400 cm^3). The combined organic extracts were dried over $MgSO_4$ and thevolatiles removed *in vacuo*. 4-Iodo-2,6-di(pyrazol-1'-yl)pyridine was obtained pure via elution through a silica gel column (eluent: DCM-hexane, 3:2; Rf value: 0.30). Additional material was isolated via a short silica gel column of the retained red band (eluent: $CHCl_3$; Rf value: 0.71). Colourless solid, 2.969 g, 52% yield. M.p. 156 - 158°C. ^{1}H NMR ($CDCl_3$) δ = 6.51 (dd, J = 2.6, 1.7 Hz, 2H, 4'), 7.77 (dd, J = 1.5, 0.6 Hz, 2H, 3'), 8.28 (s, 2H, 3), 8.53 (dd, J = 2.6, 0.9 Hz, 2H, 5'); ^{13}C NMR ($CDCl_3$) δ = 108.1 (4'), 108.5 (4), 118.3 (3), 126.9 (5'), 142.6 (3'), 149.5 (2); ES^+-MS *m/z* 360.0 $[(M + Na)]^+$.

6.2.37 4-Nitro-2,6-di(pyrazol-1'-yl)pyridine (1-bppNO$_2$)

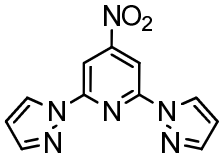

Isolated via silica gel column chromatography (eluent: $CHCl_3$; Rf value: 0.33.) in the preparation of 4-iodo-2,6-di(pyrazol-1'-yl)pyridine. Yellow solid, 71.0 mg, 1% yield. M.p. 197 - 199°C. ^{1}H NMR ($CDCl_3$) δ = 6.57 (dd, J = 2.8, 1.7 Hz, 2H, 4'), 7.83 (dd, J = 1.5, 0.6 Hz, 2H, 3'), 8.53 (s, 2H, 3), 8.56 (d, J = 2.6, 0.6 Hz, 2H, 5'); ^{13}C NMR ($CDCl_3$) δ = 103.8 (3), 109.2 (4'), 127.5 (5'), 143.6 (3'), 151.9 (2), 158.0 (4); ES$^+$-MS *m/z* 279.1 [(M + Na)]$^+$. Anal. Calcd for $C_{11}H_8N_6O_2$: C, 51.57; H, 3.15; N, 32.80. Found: C, 51.75; H, 3.10; N, 32.95.

6.2.38 4-Mercapto-2,6-di(pyrazol-1'-yl)pyridine (1-bppSH)

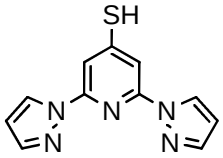

Addition of NaSH.H_2O (2.698 g, 36.42 mmol) to 4-iodo-2,6-di(pyrazol-1'-yl)pyridine (488 mg, 1.45 mmol) in DMF (100 cm^3) resulted in a darkening of the solution to translucent green, which was refluxed for 4 h. Once at RT, the DMF was removed *in vacuo* leaving a pale yellow residue which was taken up in H_2O (50 cm^3) and neutralized with HCl. The precipitate was collected on a glass frit and desiccated. Cream solid, 346 mg, 96% yield. M.p. 133 - 135°C. ^{1}H NMR (DMSO-d_6) δ = 6.60 (dd, J = 2.4, 1.7 Hz, 2H, 4'), 7.82 (s, 2H, 3), 7.84 (d, J = 1.1 Hz, 2H, 3'), 8.87 (d, J = 2.6 Hz, 2H, 5'); ^{13}C NMR (DMSO-d_6) δ = 106.6 (3), 108.5 (4'), 128.2 (5'), 142.7 (3'), 149.5 (2), 152.1 (4); ES$^+$-MS *m/z* 266.0 [(M + Na)]$^+$. Anal. Calcd for $C_{11}H_9N_5S$: C, 54.31; H, 3.73; N, 28.78. Found: C, 54.40; H, 3.55; N, 28.50.

6.2.39 4-Thiomethyl-2,6-di(pyrazol-1'-yl)pyridine (1-bppSMe)

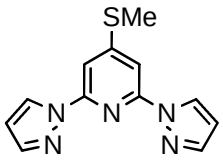

Under dry anhydrous conditions, 4-mercapto-2,6-di(pyrazol-1'-yl)mercapto pyridine (200 mg, 0.82 mmol) was added to a Schlenk tube containing K_2CO_3 (227 mg, 1.64 mmol) and MeI (328 mg, 2.31 mmol) and molecular sieves (ca. 10) in MeCN (25 cm^3) and the contents heated to 85°C for 18 h during which the suspension became pale yellow in colour. The contents, once cooled, were made up to 50 cm^3 with $CHCl_3$ (caution: strong odour), passed over a short silica pad and the silica washed with further 1:1 $CHCl_3$-MeCN (100 cm^3). The

volatiles were removed in vacuo and the yellow solid taken up in 1:2 hexane-EtOAc and filtered before the solvents were once again removed *in vacuo*. The compound was isolated by sublimation under reduced pressure at 130°C. Colourless solid, 78.0 mg, 37% yield. M.p. 140 - 142°C. ^{1}H NMR ($CDCl_3$) δ = 2.64 (s, 3H, SMe), 6.50 (br s, 2H, 4'), 7.71 (s, 2H, 3), 7.76 (br s, 2H, 3'), 8.56 (d, J = 2. 1 Hz, 2H, 5'); ^{13}C NMR ($CDCl_3$) δ = 14.2 (SMe), 105.1 (3), 108.0 (4'), 127.3 (5'), 142.3 (3'), 149.8 (2), 156.5 (4); ES^+-MS *m/z* 280.1 $[(M + Na)]^+$. Anal. Calcd for $C_{12}H_{11}N_5S$: C, 56.01; H, 4.31; N, 27.22. Found: C, 55.60; H, 4.35; N, 27.25.

6.2.40 *Bis*-(2,6-di(pyrazol-1'-yl)-pyridin-4-yl)disulfide (1-bppDS)

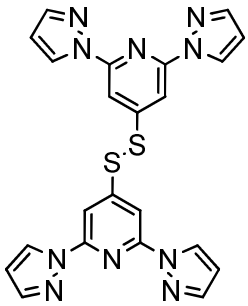

NaOH (29 mg, 0.73 mmol) and I_2 (84 mg, 0.33 mmol) were added to a stirring suspension of 4-mercapto-2,6-dipyrazol-1-yl)pyridine (152 mg, 0.62 mmol) in H_2O (15 cm^3), and stirring was continued for 20 h yielding a fluffy cream-coloured suspension. The solid was collected, washed with further H_2O, EtOH and Et_2O and dried over P_2O_5. Off-white solid, 137 mg, 91% yield. M.p. 240 - 242°C. ^{1}H NMR ($CDCl_3$) δ = 6.47 (t, J = 2.1 Hz, 4H, 4'), 7.74 (br s, 4H, 3'), 8.02 (s, 4H, 3), 8.51 (d, J = 2.6 Hz, 4H, 5'); ^{13}C NMR ($CDCl_3$) δ = 105.4 (3), 108.2 (4'), 127.3 (5'), 142.7 (3'), 150.4 (2), 152.4 (4); ES^+-MS *m/z* 507.1 $[(M + Na)]^+$. Anal. Calcd for $C_{22}H_{16}N_{10}S_2$: C, 54.53; H, 3.33; N, 28.91. Found: C, 54.30; H, 3.25; N, 29.05.

6.2.41 4-Bromo-2,6-di(pyrazol-1'-yl)pyridine (1-bppBr)

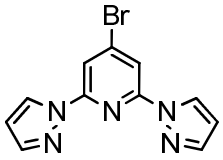

To a flask containing 4-amino-2,6-di(pyrazol-1'-yl)pyridine (392 mg, 1.73 mmol) and $NaNO_2$ (2.51 mg, 3.64 mmol) suspended in MeCN (25 cm^3) under an atmosphere of N_2 was added KBr (494 mg, 4.15 mmol) and 48% aqueous HBr (10 cm^3, 59.33 mmol) causing immediate darkening of the contents to brown. During stirring for 1 h the gentle evolution of N_2 was noted. The flask was then heated to 80°C for 1 h, and once cool the mixture was poured into saturated aqueous $Na_2S_2O_3$ (100 cm^3) and shaken zealously precipitating a pale solid. The solid was then collected on a glass frit and washed with H_2O. Purification through a silica gel column (eluent: DCM-hexane, 3:2; Rf value: 0.19) yielded the compound after

recrystallisation from n-hexane as a colourless crystalline solid. 159 mg, 32 % yield. M.p. 148 - 150°C. ^{1}H NMR ($CDCl_3$) δ = 6.52 (dd, J = 2.6, 1.7 Hz, 2H, 4'), 7.77 (dd, J = 1.7, 0.9 Hz, 2H, 3'), 8.06 (s, 2H, 3), 8.53 (dd, J = 2.6, 0.9 Hz, 2H, 5'); ^{13}C NMR ($CDCl_3$) δ = 108.4 (4'), 112.7 (3), 127.3 (5'), 136.7 (4), 142.9 (3'), 150.4 (2); ES^{+}-MS *m/z* 290.0 $[(M + H)]^{+}$, 312.0 $[(M + Na)]^{+}$. Anal. Cald for $BrC_{11}H_8N_5$: C, 45.54; H, 2.78; H, 24.14. Found: C, 45.50; H, 2.70; N, 23.90.

6.2.42 4-Bromo-2-(4'-bromopyrazol-1'-yl)-6-(pyrazol-1'-yl)pyridine

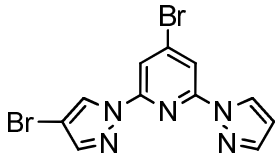

Isolated via silica gel column chromatography (eluent: DCM-hexane, 3:2; Rf value: 0.50) in the preparation of 4-bromo-2,6-di(pyrazol-1'-yl)pyridine. Colourless solid, 34.0 mg, 5% yield. M.p. 170 - 172°C. ^{1}H NMR ($CDCl_3$) δ = 6.52 (dd, J = 2.6, 1.7 Hz, 1H, 4''), 7.71 (s, 1H, 3'), 7.78 (d, J = 1.3 Hz, 1H, 3''), 8.01 (d, J = 1.3 Hz, 1H, 3/5), 8.09 (d, J = 1.1 Hz, 1H, 3/5), 8.51 (d, J = 2.6 Hz, 1H, 5''), 8.54 (s, 1H, 5'); ^{13}C NMR ($CDCl_3$) δ = 97.1 (4'), 108.6 (4''), 112.2 (3), 113.2 (5), 127.3 (5' + 5''), 136.9 (4), 143.0 (3''), 143.3 (3'), 149.7 (3), 150.5 (5); ES^{+}-MS *m/z* 370.0 $[(M + H)]^{+}$. Anal. Calcd for $Br_2C_{11}H_7N_5.{}^{1}/_{2}CH_2Cl_2$: C, 35.57; H, 1.96; N, 17.02. Found: C, 33.50; H, 1.95; N, 16.60.

6.2.43 4-Amino-3,5-dibromo-2,6-di(4'-bromopyrazol-1'-yl)pyridine

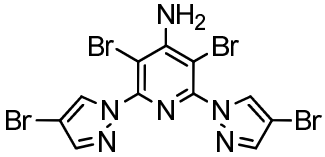

An original attempt to prepare 4-bromo-2,6-di(pyrazol-1'-yl)pyridine yielded 4-amino-3,5-dibromo-2,6-di(4'-bromopyrazol-1'-yl)pyridine in addition to 3,4-dibromo-2,6-di(4'-bromopyrazol-1'-yl)pyridine and 3,4,5-tribromo-2,6-di(4'-bromopyrazol-1'-yl)pyridine. Under N_2, 1:1 dry isopentyl nitrite-DCM (50 cm^3) were added via syringe to a flask containing 4-amino-2,6-di(pyrazol-1-yl)pyridine (977 mg, 4.32 mmol), Br_2 (2.916 g, 18.25 mmol) and KBr (1.775 g, 14.92 mmol). After H_2 evolution had ceased the contents were heated to 75°C for 5 h. Once at RT, a saturated aqueous solution of $Na_2O_3S_2$ was added (150 cm^3) and the biphasic system extracted with DCM (2 x 200 cm^3) and $CHCl_3$ (200 cm^3). All volatiles were removed and the solid was chromatographed over silica gel (eluent: DCM; Rf value: 0.33) yielding a pale yellow solid which was decolourised using activated charcoal. Cream solid, 326 mg, 14% yield. M.p. 182 - 184°C. ^{1}H NMR ($CDCl_3$) δ = 5.85 (br s, 2H, NH_2), 7.74 (s, 2H, 3'), 8.08 (s, 2H, 5'); ^{13}C NMR ($CDCl_3$) δ = 96.1 (4'), 96.5 (4), 130.5 (5'), 142.1 (3'), 146.2 (2),

153.5 (3); ES$^+$-MS *m/z* 542.7 [(M + H)]$^+$, 559.8 [(M + NH_4)]$^+$, 564.7 [(M +Na)]$^+$. Anal. Calcd for: $Br_4C_{11}H_6N_6.H_2O$: C, 23.60; H, 1.44; N, 15.01. Found: C, 23.40; H, 1.00; N, 14.10.

6.2.44 3,4-Dibromo-2,6-di(4'-bromopyrazol-1'-yl)pyridine

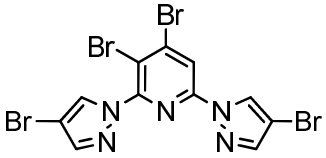

3,4-dibromo-2,6-di(4'-bromopyrazol-1'-yl)pyridine was obtained as a colourless solid from the crude multi-component material which was obtained through the initial column in the preparation above (eluent: DCM; Rf value: >0.75) by eluting through a second silica gel column (eluent: $CHCl_3$-hexane, 3:2; Rf value: 0.47). 776 mg, 34% yield. M.p. 230 - 232°C. ^{1}H NMR ($CDCl_3$) δ = 7.72 (s, 1H, 3''), 7.79 (s, 1H, 3'), 8.09 (s, 1H, 5'), 8.31 (s, 1H, 5), 8.48 (s, 1H, 5'); ^{13}C NMR ($CDCl_3$) δ = 96.3 (4'), 97.9 (4''), 113.5 (3), 116.5 (5), 127.7 (5''), 130.6 (5'), 141.6 (4), 142.4 (3'), 143.9 (3''), 148.0 (2/6), 148.3 (2/6);); ES$^+$-MS *m/z* 523.7 [(M + H)]$^+$, 549.7 [(M + Na)]$^+$. Anal. Calcd for $Br_4C_{11}H_5N_5$: C, 25.08; H, 0.96; H, 13.29. Found: C, 25.30; H, 0.95; N, 12.80.

6.2.45 3,4,5-Tribromo-2,6-di(4'-bromopyrazol-1'-yl)pyridine

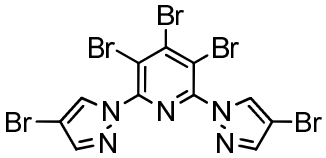

3,4,5-tribromo-2,6-di(4'-bromopyrazol-1'-yl)pyridine was obtained as a light cream-coloured solid from the crude multi-component material which was obtained through the initial column in the preparation above (eluent: DCM; Rf value: >0.75) by eluting through a second silica gel column (eluent: $CHCl_3$-hexane, 3:2; Rf value: 0.2). 252 mg, 10% yield. M.p. 229 - 231°C. ^{1}H NMR ($CDCl_3$) δ = 7.77 (s, 2H, 3'), 8.09 (s, 2H, 5'); ^{13}C NMR ($CDCl_3$) δ = 96.8 (4'), 116.6 (3), 130.7 (5'), 142.8 (3'), 146.4 (2/4), 146.8 (2/4); ES$^+$-MS *m/z* 605.6 [(M + H)]$^+$. Anal. Calcd for $Br_5C_{11}H_4N_5$: C, 21.81; H, 0.67; N, 11.56. Found: C, 22.20; H, 0.60; N, 11.40.

6.2.46 4-Chloro-2,6-di(pyrazol-1'-yl)pyridine (1-bppCl)

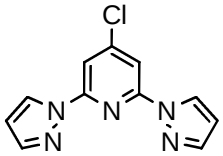

To a stirred acetonitrilic (30 cm^3) suspension of 4-amino-2,6-di(pyrazol-1'-yl)pyridine (405 mg, 1.79 mmol) and sodium nitrite (259 mg, 3.75 mmol) under N_2 was added KCl (337 mg, 4.52 mmol) and carefully 37% HCL (10 cm^3, 101.48 mmol) causing an instant change in

colour to a bright orange. The contents were heated to 80°C for 1 h during which nitrogen was expelled. Once cooled to RT, the now light orange-yellow solution was poured into a saturated aqueous sodium thiosulfate solution (100 cm^3) and shaken powerfully. A pale yellow solid was filtered off from the mixture and washed with further H_2O before thorough desiccation. The compound was isolated through silica gel chromatography (eluent: DCM; Rf value: 0.55). Colourless solid, 211 mg, 48% yield. M.p. 141 - 143°C. ^{1}H NMR ($CDCl_3$) δ = 6.52 (dd, J = 2.6, 1.7 Hz, 2H, 4'), 7.78 (d, J = 0.9 Hz, 2H, 3'), 7.90 (s, 2H, 3), 8.54 (d, J = 2.6 Hz, 2H, 5'); ^{13}C NMR ($CDCl_3$) δ = 108.4 (4'), 109.7 (3), 127.3 (5'), 142.9 (3'), 148.4 (4), 150.7 (2); ES^+-MS *m/z* 268.0 $[(M + Na)]^+$. Anal. Calcd for $C_{11}ClH_8N_5$: C, 53.78; H, 3.28; N, 28.51. Found: C, 53.70; H, 3.40; N, 28.50.

6.2.47 4-Chloro-2-(4'-chloropyrazol-1'-yl)-6-(pyrazol-1'-yl)pyridine

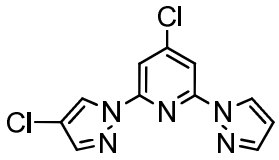

In the preparation of 4-chloro-2,6-di(pyrazol-1'-yl)pyridine, 2-(4'-chloropyrazol-1'-yl)pyridine was obtained by as a yellow solid by eluting the crude material through a silica gel column (eluent: DCM; Rf value: 0.85). 2.00 mg, <1 % yield. M.p. 175 - 177°C. ^{1}H NMR (CD_3Cl) δ = 6.53 (dd, J = 3.0, 1.7 Hz, 1H, 4''), 7.69 (s, 1H, 3'), 7.78 (d, J = 1.3 Hz,1H, 3''), 7.84 (d, J = 1.7 Hz, 1H, 3), 7.92 (d, J = 1.7 Hz, 1H, 5), 8.51 (s, 1H, 5'), 8.52 (s, 1H, 5''); ^{13}C NMR ($CDCl_3$) δ = 108.6 (4''), 109.2 (3), 110.3 (5), 113.7 (4'), 125.1 (5'), 127.3 (5''), 141.3 (3'), 143.0 (3''), 148.7 (4), 150.1 (2), 150.8 (6); ES^+-MS *m/z* 302.00 $[(M + Na)]^+$. An insufficient quantity for microanalysis was prepared.

6.2.48 4-Fluoro-2,6-di(pyrazol-1'-yl)pyridine (1-bppF)

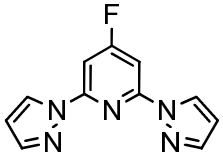

48% aqueous HBF_4 (10 cm^3, 54.66 mmol) was syringed into a Schlenk tube containing 4-amino-2,6-di(pyrazol-1'-yl)pyridine (289 mg, 1.28 mmol) under anaerobic conditions. The acidified contents were cooled to 0°C, and a degassed aqueous solution of $NaNO_2$ (195 mg, 2.83 mmol) was gradually added with stirring causing the precipitation of a bright yellow solid from the bulk solution. Heating slowly to 80°C resulted in no observable change, so MeCN (15 cm^3) was added to solubilise the diazonium salt. Immediate evolution of N_2 was noted, and heating at 80°C was maintained for 0.5 h after which time evolution had ceased. Once cool, the MeCN was removed *in vacuo* and the remaining yellow solution poured into H_2O

(30 cm^3) and neutralised with aqueous NaOH causing the formation of a pale yellow suspension. Extraction with $CHCl_3$ (3 x 50 cm^3), drying with $MgSO_4$, filtration and removal of the volatiles yielded a crude pale yellow solid which was purified through silica gel column chromatography (eluent: DCM; Rf value: 0.62). Colourless powder, 58.0 mg, 20% yield. M.p. 106 - 108°C. ^{1}H NMR ($CDCl_3$) δ = 6.52 (dd, J = 2.6, 1.7 Hz, 2H, 4'), 7.59 (d, J = 9.4 Hz, 2H, 3), 7.77 (d, J = 0.9 Hz, 2H, 3'), 8.55 (d, J = 2.6 Hz, 2H, 5'); ^{13}C NMR ($CDCl_3$) δ = 97.7 (d, J = 23.7 Hz, 3), 108.4 (4'), 127.3 (5'), 142.8 (3'), 152.1 (d, J = 13.4 Hz, 2), 171.8 (d, J = 257.7 Hz, 4); ^{19}F NMR ($CDCl_3$) δ = -95.6 (t, J = 9.2 Hz); ES^+-MS *m/z* 230.1 $[(M + H)]^+$. Anal. Calcd for $C_{11}FH_8N_5.{}^1/_4H_2O$: C, 56.53; H, 3.67; N, 29.96. Found: C, 56.60; N, 3.75; N, 29.00.

6.2.49 2,6-Di(pyrazol-1'-yl)pyridine-4-carboxylic acid (1-bppCOOH)

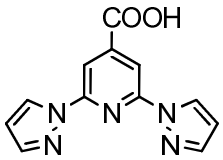

NaH (60% dispersion in mineral oil, 3.372 g, 84.31 mmol NaH) was stirred in diglyme (100 cm^3) for 0.5 h, after which 1*H*-pyrazole (5.276 g, 77.50 mmol) was carefully added to the suspension. Following complete H_2 evolution, 2,6-dibromo pyridine-4-carboxylic acid (7.229 g, 25.20 mmol) was dropped into the flask which was then heated to 130°C for 5 days. The cooled contents were poured onto H_2O (500 cm^3), and a crude oily solid obtained through acidification to pH 3 with 4M HCl. After thorough desiccation the solid was triturated in hexane and collected on a glass frit as a beige powder. Recrystallisation from acetone yielded the pure disubstituted acid, however a significant loss was incurred due to a spillage. Beige solid, 839 mg, 14% yield. ^{1}H NMR (DMSO-d_6) δ = 6.67 (dd, J = 2.6, 1.7 Hz, 2H, 4'), 7.91 (d, J = 1.3 Hz, 2H, 3'), 8.17 (s, 2H, 3), 8.99 (dd, J = 2.2, 0.8 Hz, 2H, 5'), 14.07 (br s, 2H, COOH); ^{13}C NMR (DMSO-d_6) δ = 108.1 (3), 108.8 (4'), 128.4 (5'), 143.2 (3'), 144.5 (2), 150.4 (4), 164.9 (COOH); ES^+-MS *m/z* 256.1 $[(M + H)]^+$, 278.0 $[(M + Na)]^+$.

6.2.50 2,2,6,6-*Tetrakis*-(pyrazol-1'-yl)-4,4-bipyridine (qpbpy)

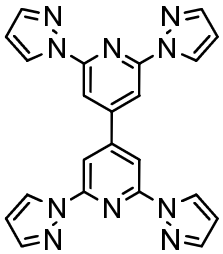

Over a steady stream of N_2, potassium carbonate (534 mg, 3.94 mmol), $Pd(PPh_3)_4$ (148 mg, 0.13 mmol) and *bis*(pinacolato)diboron (332 mg, 1.31 mmol) were added to a flask containing 4-iodo-2,6-di(pyrazol-1'-yl)pyridine (435 mg, 1.29 mmol) dissolved in DMSO (50

cm^3) and the contents were heated to 80°C for 18 h. The solution was filtered whilst hot with the black residue remaining further washed with $CHCl_3$ (250 cm^3). The filtrate solution was then washed with H_2O (3 x 100 cm^3), and the organic fraction dried with Na_2SO_3. Removal of the volatiles *in vacuo* gave a pale yellow/orange solid. The cream coloured compound was isolated by elution through a short silica gel column (eluent: EtOAc; Rf value: 1). 178 mg, 66% yield. ^{1}H NMR ($CDCl_3$) δ = 6.55 (dd, J = 2.6, 1.7 Hz, 4H, 4'), 7.82 (d, J = 1.7 Hz, 4H, 3'), 8.30 (s, 4H, 3), 8.63 (d, J = 2.3 Hz, 4H, 5'); ^{13}C NMR ($CDCl_3$) δ = 107.6 (3), 108.3 (4'), 127.3 (5'), 142.7 (3'), 150.9 (4), 151.0 (2); ES$^+$-MS *m/z* 443.1 $[(M + Na)]^+$.

6.3 Preparation of *bis*-azinyl iron(II) salts

6.3.1 *Bis*-(2,6-di(2'-pyridyl)pyrazine) Iron (II) tetrafluoroborate (1a)

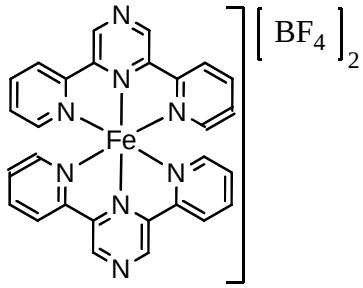

A round bottom flask was charged with $MeNO_2$ (20 cm^3) before the sequential addition of $Fe(BF_4)_2.6H_2O$ (44 mg, 0.13 mmol) and bipypz (58 mg, 0.25 mmol) which immediately turned the contents dark purple. After stirring for 0.5 h, the volume was reduced to ca. 3 – 5 cm^3 and crystallised by slow vapour diffusion of ^{i}Pr$_2$O into the solution before collection of the dark crystalline blocks. 75.0 mg, 83% yield. ^{1}H NMR ($MeNO_2$-d_3) δ =7.16 (t, J = 4.3 Hz, 4H, 5'), 7.21 (d, J = 3.8 Hz, 4H, 6'), 8.00 (t, J = 5.1 Hz, 4H, 4'), 8.72 (d, J = 6.9 Hz, 4H', 3'), 10.14 (s, 4H, 3); ^{13}C NMR ($MeNO_2$-d_3) δ =126.0 (3'), 129.4 (5'), 140.8 (4'), 144.3 (3), 154.5 (6'), 157.1 (2/2') 157.3 (2/2'); ES$^+$-MS *m/z* 262.1 $[(ML_2 – 2BF_4)]^{2+}$, 611.1 $[(ML_2 – BF_4)]^+$. Anal. Calcd for $B_2C_{28}F_8FeH_{20}N_8$: C, 48.18; H, 2.89; N, 16.05. Found: C, 48.20; H, 2.80; 15.80.

6.3.2 *Bis*-(2,6-di(2'-pyrazyl)pyridine) iron (II) tetrafluoroborate (2a)

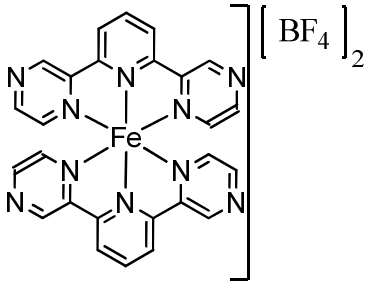

To a stirring $MeNO_2$ (20 cm^3) solution of $Fe(BF_4)_2.6H_2O$ (46 mg, 0.14 mmol) was added bipzpy (65 mg, 0.28 mmol). The deep purple solution was continuously stirred for a further

0.5 h before the volume was reduced to 5 cm^3. Crystallisation by vapour diffusion of $^{i}Pr_2O$ into the solution yielded the complex salt as a dark purple powder. 92.0 mg, 94% yield. ^{1}H NMR ($MeNO_2$-d_3) δ = 7.35 (dd, J = 3.0, 0.9 Hz, 4H, 6'), 8.26 (d, J = 3.4 Hz, 4H, 5'), 8.86 (t, J = 8.1 Hz, 2H, 4), 9.12 (d, J = 8.1 Hz, 4H, 3), 9.61 (d, J = 0.9 Hz, 4H, 3'); ^{13}C NMR ($MeNO_2$-d_3) δ =126.3 (3), 141.2 (4), 145.2 (3'), 149.1 (5'), 149.7 (6'), 154.7 (2), 160.1 (2'); ES^+-MS *m/z* 263.1 $[(ML_2 - 2BF_4)]^{2+}$. Anal. Calcd for $B_2C_{26}F_8FeH_{18}N_{10}$: C, 44.62; H, 2.59; N, 20.01. Found: C, 44.60; H, 2.55; N, 19.70.

6.3.3 *Bis*-(2,6-di(2'-pyrazyl)pyrazine) iron (II) tetrafluoroborate (3a)

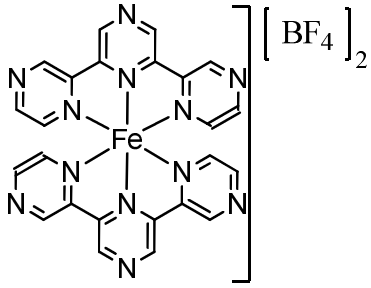

$Fe(BF_4)_2.6H_2O$ (22 mg, 0.07 mmol) was inserted into a stirred $MeNO_2$ (10 cm^3) suspension of terpz (32 mg, 0.14 mmol) and left at RT stirring for 18 h. Et_2O (40 cm^3) was added precipitating the complex salt, which was collected on a glass frit and washed with a few drops of Et_2O. Dark purple microcrystals, 36.0 mg, 73% yield. ^{1}H NMR ($MeNO_2$-d_3) δ = 7.36 (dd, J = 3.0, 1.3 Hz, 4H, 6'), 8.30 (d, J = 3.4 Hz, 4H, 5'), 9.78 (d, J = 0.9 Hz, 4H, 3'), 10.27 (s, 4H, 3); ^{13}C NMR ($MeNO_2$-d_3) δ = 145.6 (3), 146.1 (3'), 149.9 (5'/6'), 150.1 (5'/6'), 152.8 (2/2'), 155.6 (2/2'); ES^+-MS *m/z* 264.0 $[(ML_2 - 2BF_4)]^{2+}$. Anal. Calcd for $B_2C_{24}F_8FeH_{16}N_{12}.2H_2O$: C, 39.06; H, 2.73; N, 22.78. Found: C, 38.80; H, 2.55; N, 22.20.

6.3.4 *Bis*-(2,6-di(4'-pyrimidyl)pyridine) iron (II) tetrafluoroborate (4a)

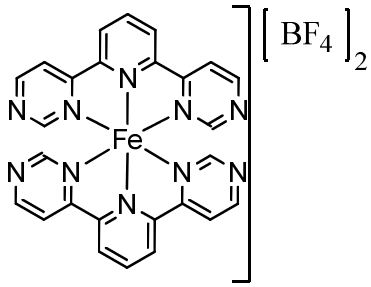

4-bipympy (61 mg, 0.26 mmol) and $Fe(BF_4)_2.6H_2O$ (43 mg, 0.13 mmol) were stirred together in $MeNO_2$ (20 cm^3) for 0.5 h. The volatiles were removed *in vacuo* and the purple solid so obtained was triturated in $CHCl_3$ (25 cm^3) and filtered before drying. Dark purple powder, 72.0 mg, 79% yield. ^{1}H NMR ($MeNO_2$-d_3) δ = 7.77 (d, J = 1.3 Hz, 4H, 2'), 8.52 (dd, J = 5.1, 1.3 Hz, 4H, 5'), 8.85 (d, J = 5.1 Hz, 4H, 6'), 8.94 (t, J = 8.1 Hz, 2H, 4), 9.29 (d, J = 8.1 Hz, 4H, 3); ^{13}C NMR ($MeNO_2$-d_3) δ = 120.5 (5'), 129.1 (3), 140.9 (4), 161.1 (2), 161.5 (6'), 162.8

(2'), 166.0 (4'); ES^+-MS *m/z* 263.1 $[(ML_2 - 2BF_4)]^{2+}$. Anal. Calcd. for $B_2C_{26}F_8FeH_{18}N_{10}.H_2O$: C, 43.50; H, 2.81; N, 19.51. Found: C, 43.35; H, 2.70; N, 18.70.

6.3.5 *Bis*-(2,6-di(1',2',4'-triazin-3'-yl)pyridine) iron (II)tetrafluoroborate (6a)

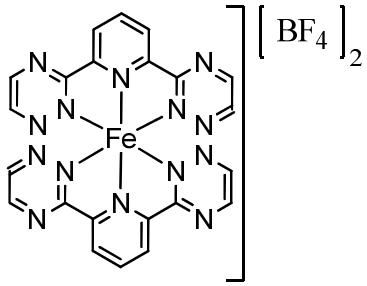

$Fe(BF_4)_2.6H_2O$ (71 mg, 0.21 mmol) was added to a stirred suspension of bitrzpy (104 mg, 0.44 mmol) in $MeNO_2$ (25 cm^3) turning the contents an intense burgundy colour. Once stirred for 3 h, the solution was filtered and the volatiles removed. Dark polycrystalline solid, 116 mg, 76% yield. ^1H NMR (CD_3CN) δ =8.87 (t, J = 8.4 Hz, 2H, 4), 8.89 (d, J = 2.0 Hz, 4H, 5'/6'), 8.93 (d, J = 2.4 Hz, 4H, 5'/6'), 9.13 (d, J = 8.0 Hz, 4H, 3); ^{13}C NMR (CD_3CN) δ = 128.4 (3), 141.6 (4), 151.9 (5'/6'), 152.8 (5'/6'), 156.8 (2), 167.2 (3'); ES^+-MS *m/z* 238.1 $[(L + H)]^+$, 260.1 $[(L + Na)]^+$, 265.0 $[(ML_2 - 2BF_4)]^{2+}$. Anal. Calc. For $B_2C_{22}F_8FeH_{14}N_{14}.2H_2O$: C, 35.71; H, 2.45; N, 26.50. Found: C, 35.95; H, 2.40; N, 25.80.

6.3.6 *Bis*-(4-hydroxy-2,6-di(2'-pyrazyl)pyridine) iron (II) tetrafluoroborate (7a)

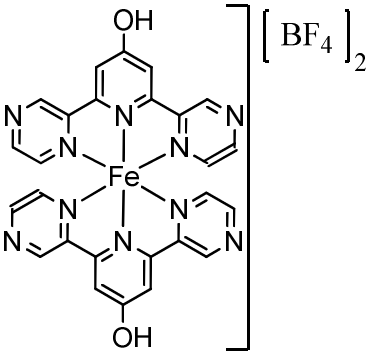

BipzpyOH (71 mg, 0.28 mmol) was added to a flask containing $Fe(BF_4)_2.6H_2O$ (49 mg, 0.14 mmol) in $MeNO_2$ (20 cm^3) causing immediate colouration to pink. During stirring for 0.5 h, the solution became progressively darker after which the volatiles were removed leaving a deep purple solid. 71.0 mg, 70% yield. ^1H NMR ($MeNO_2$-d_3) δ = 7.43 (d, J = 2.9 Hz, 4H, 6'), 8.26 (d, J = 3.3 Hz, 4H, 5'), 8.57 (s, 4H, 3), 9.48 (s, 4H, 3'); ES^+-MS *m/z* 279.0 $[(ML_2 - 2BF_4)]^{2+}$, 557.1 $[(ML_2 - 2BF_4 - H)]^+$. Anal. Calcd. for $B_2C_{26}F_8FeH_{18}N_{10}O_2.2H_2O$: C, 40.66; H, 2.89; N, 18.24. Found: C, 41.05; H, 2.50; N, 18.20.

6.3.7 *Bis*-(4-hydroxy-2,6-di(2'-pyrimidyl)pyridine) iron (II) tetrafluoroborate (8a)

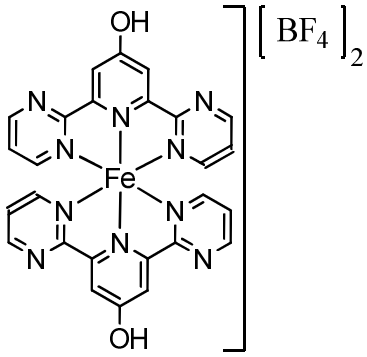

Upon addition of 2-bipympyOH (53 mg, 0.21 mmol) to $Fe(BF_4)_2.6H_2O$ (35 mg, 0.10 mmol) dissolved in $MeNO_2$ (15 cm^3) the solution became intense pink/purple in colour and was stirred for a further 0.5 h at RT. After filtration, Et_2O (100 cm^3) was added and the resulting precipitate collected on a glass frit and desiccated profusely. The material was subject to crystallisation by slow vapour diffusion of Et_2O into an acetone solution of the salt yielding a purple powder. 63.0 mg, 90% yield. ^{1}H NMR (CD_3CN) δ = 7.24 (t, J = 4.9 Hz, 4H, 6'), 8.00 (br s, 4H, 5'), 8.76 (s, 4H, 3) 8.83 (d, J = 4.2 Hz, 4H, 4'); ES$^+$-MS *m/z* 279.0 $[(ML_2 – 2BF_4)]^{2+}$, 557.1 $[(ML_2 – 2BF_4 – H)]^+$. Anal. Calcd. For $B_2C_{26}F_8FeH_{18}N_{10}O_2.1/2C_3H_6O$: C, 43.30; H, 2.78; N, 18.41. Found: C, 42.20; H, 2.90; N, 17.10.

6.3.8 *Bis*-(2,2':6',2''-terpyridine) iron (II) tetrafluroborate (9a)

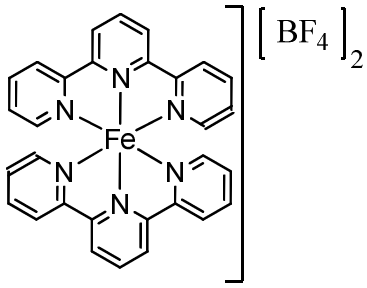

Terpy (206 mg, 0.88 mmol) was added to a round bottom flask containing $Fe(BF_4)_2.6H_2O$ (149 mg, 0.44 mmol) in $MeNO_2$ (50 cm^3) and stirred for 0.5 h. The volatiles were removed to give a dark purple powder. 245 mg, 80% yield. ^{1}H NMR ($MeNO_2$-d_3) δ = 7.10 (ddd, J = 7.7, 5.6 Hz, 1.3 Hz, 4H, 5'), 7.23 (ddd, J = 5.6 Hz, 1.7 Hz, 0.9 Hz, 4H, 6'), 7.91 (td, J = 7.7, 1.3 Hz, 4H, 4'), 8.53 (ddd, J = 8.1, 1.3, 0.9 Hz 4H, 3'), 8.75 (t, J = 7.7 Hz, 2H, 4), 8.98 (d, J = 8.1 Hz, 4H, 3); ^{13}C NMR ($MeNO_2$-d_3) δ = 124.7 (3/3'), 124.9 (3/3'), 128.6 (5'), 139.4 (4), 140.1 (4'), 154.3 (6'), 159.4 (2/2'), 161.9 (2/2'); ES$^+$-MS *m/z* 261.1 $[(ML_2 – 2BF_4)]^{2+}$.

6.3.9 *Bis*-(4-hydroxy-2,6-di(2'-pyridyl)pyridine) iron (II) tetrafluoroborate (10a)

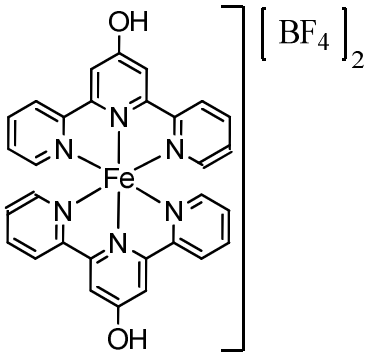

The complex salt was acquired as a purple solid by stirring terpyOH (121 mg, 0.49 mmol) and $Fe(BF_4)_2.6H_2O$ (81 mg, 0.24 mmol) together in $MeNO_2$ (30 cm^3) for 0.5 h before removal of the volatiles *in vacuo*. 131 mg, 75% yield. ^1H NMR (CD_3CN) δ = 7.10 (m, 8H, 5' + 6'), 7.81 (t, J = 7.9 Hz, 4H, 4'), 8.29 (s, 4H, 3), 8.33 (d, J = 7.9 Hz, 4H, 3'), 9.67 (s, 2H, OH); ES^+-MS *m/z* 277.1 $[(ML_2 – 2BF_4)]^{2+}$, 553.1 $[(ML_2 – 2BF_4 – H)]^+$.

6.3.10 *Bis*-(2,6-di(pyrazol-1'-yl)pyridine) iron (II) tetrafluoroborate (25a)

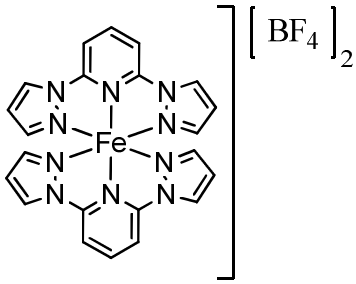

1-bpp (1.352 g, 6.40 mmol) and $Fe(BF_4)_2.6H_2O$ (1.064 g, 3.15 mmol) were stirred together in acetone (200 cm^3) for 0.5 h followed by filtration of the brown solution. The volume was reduced to ca. 70 cm^3 and made up to 150 cm^3 with Et_2O and chilled at -20°C for 24 h. The suspension was filtered, washed with a few drops of Et_2O and collected as a yellow powder after drying over P_2O_5. 1.83 g, 89% yield. ^1H NMR ($MeNO_2$-d_3) δ = 2.9 (4), 34.3 (3), 36.3 (5'), 56.6 (4'), 61.3 (3'); ES^+-MS *m/z* 234.1 $[(L + Na)]^+$.

6.3.11 *Bis*-(2,2,6,6-tetra(pyrazol-1'-yl)-4,4-bypridine) iron (II) tetrafluoroborate (26a)

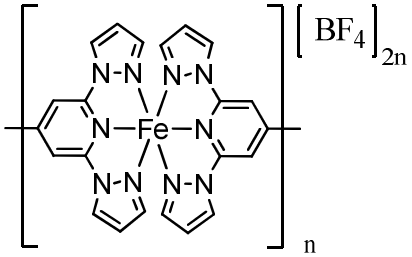

Upon addition of a stoichiometric amount of qpbpy (76 mg, 0.18 mmol) to a $MeNO_2$ (20 cm^3) solution of $Fe(BF_4)_2.6H_2O$ (61 mg, 0.18 mmol), the solution immediately turned deep

red/purple, and during stirring for 1 h became orange in colour. The solution was filtered, vacuumed to dryness, triturated in $CHCl_3$ and the resulting brick-red microcrystalline solid collected on a glass frit. 43.0 mg, 37% yield. ES^+-MS *m/z* 443.1 $[(L + Na)]^+$, 863.3 $[(2L + Na)]^+$. No satisfactory microanalytical data was obtained for this novel compound.

6.3.12 *Bis*-(4-methyl-2,6-di(pyrazol-1'-yl)pyridine) iron (II) salts of the form $[Fe(1\text{-}bppMe)_2][X]_2$, where X = tetrafluoroborate (27a), perchlorate (27b), hexafluorophosphate (27c) and trifluoromethansulfonate (27d)

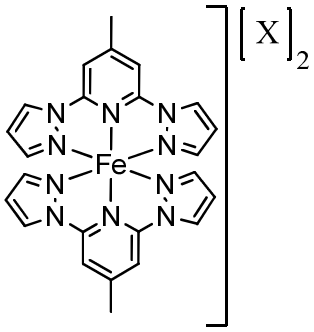

27a: $Fe(BF_4)_2.6H_2O$ (74 mg, 0.22 mmol) was dropped into a suspension of 1-bppMe (99 mg, 0.44 mmol) in $MeNO_2$ (30 cm^3) and after stirring for 1 h the solution was filtered. Et_2O (100 cm^3) was then added and the salt collected on a glass frit and washed with further Et_2O and dried by heating to 50°C. Bright yellow solid, 136 mg, 90% yield. ^1H NMR ($MeNO_2$-d_3) δ = 7.8 (Me), 40.8 (3 + 5'), 61.5 (4'), 70.2 (3'). Anal. Calcd for $B_2C_{24}F_8FeH_{22}N_{10}.H_2O$: C, 41.30; H, 3.47; N, 20.07. Found: C, 41.65; H, 3.15; N, 20.25.

27b: To a stirring suspension of 1-bppMe (99 mg, 0.44 mmol) in $MeNO_2$ (25 cm^3) was added $Fe(ClO_4)_2.3H_2O$ (66 mg, 0.21 mmol) and stirred for 1 h. The salt was isolated by precipitating with Et_2O desiccated. Bright yellow solid, 115 mg, 78% yield. ^1H NMR ($MeNO_2$-d_3) δ = 7.8 (Me), 40.9 (3 + 5'), 61.5 (4'), 70.3 (3'). Anal. Calcd for $C_{24}Cl_2FeH_{22}N_{10}O_8$: C, 40.87; H, 3.14; N, 19.86. Found: C, 40.80; H, 3.10; N, 19.90.

27c: $FeCl_2.4H_2O$ (36 mg, 0.15 mmol) and 1-bppMe (70 mg, 0.31 mmol) were stirred in 2:1 MeOH-H_2O (20 cm^3) for 1 h. Insolubles were removed and NH_4PF_6 saturated 2:1 MeOH-H_2O (15 cm^3) was added. After stirring the hexafluorophosphate salt was collected and washed with H_2O, MeOH and Et_2O. Yellow powder, 67.0 mg, 56% yield. ^1H NMR ($MeNO_2$-d_3) δ = 7.8 (Me), 40.8 (3 + 5'), 61.5 (4'), 70.2 (3'). Anal. Calcd for $C_{24}F_{12}FeH_{22}N_{10}P_2$: C, 36.2; H, 2.78; N, 17.59. Found: C, 36.40; H, 2.70; N, 17.30.

27c: $Fe(CF_3SO_3)_2$ (72 mg, 0.20 mmol) was added to a $MeNO_2$ (25 cm^3) suspension of 1-bppMe (92 mg, 0.41 mmol) which resulted in an immediate coloration to yellow-orange. After stirring for 1 h until no further dissolution was observed, the solution was filtered and Et_2O (80 cm^3) added with stirring and the resulting precipitate collected and washed with

additional Et_2O. Mustard coloured solid, 114 mg, 71% yield. ^{1}H NMR ($MeNO_2$-d_3) δ = 7.8 (Me), 40.8 (3 + 5'), 61.5 (4'), 70.2 (3'). Anal. Calcd for $C_{26}F_6FeH_{22}N_{10}O_6S_2.H_2O$: C, 37.97; H, 2.94; N, 17.03. Found: C, 38.10; H, 2.65; N, 16.95.

6.3.13 *Bis*-(2,4,6-tri(pyrazol-1'-yl)pyridine) iron (II) salts of the form $[Fe(1\text{-tpp})_2][X]_2$, where X = tetrafluoroborate (28a), perchlorate (28b) and hexafluorophosphate (28c)

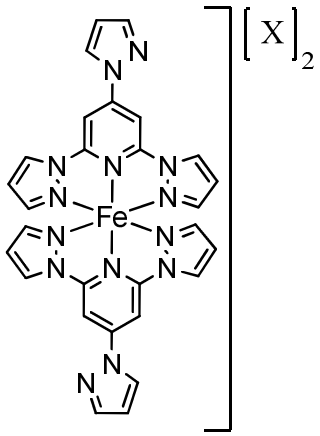

28a: 1-tpp (124 mg, 0.45 mmol) was added to a solution of $Fe(BF_4)_2.6H_2O$ (72 mg, 0.21 mmol) in $MeNO_2$ (35 cm^3). After stirring for 1 h all insolubles were filtered off. Addition of Et_2O (250 cm^3) precipitated the complex salt, which was subsequently collected on a glass sinter funnel and washed with Et_2O. Bright yellow powder, 105 mg, 64% yield. ^{1}H NMR ($MeNO_2$-d_3) δ = 5.5 (4''), 6.5 (3'') 8.1 (5''), 41.5 (5'), 42.1 (3), 61.8 (4'), 71.4 (3'); ES^+-MS *m/z* 300.1 $[(L + Na)]^+$, 577.2 $[(2L + Na^+)]^+$. Anal. Calcd for $B_2C_{28}F_8FeH_{22}N_{14}.{}^1/_2MeNO_2$: C, 42.03; H, 2.91; N, 24.93. Found: C, 42.00; H, 2.80; N, 24.70.

28b: 1-tpp (126 mg, 0.45 mmol) was added to a $MeNO_2$ (30 cm^3) solution of $Fe(ClO_4)_2.3H_2O$ (66 mg, 0.21 mmol) and stirred for 1 h. Filtration of the solution and addition of Et_2O (200 cm^3) gave a cloudy suspension. The precipitate was collected, washed with further Et_2O and desiccated. Bright yellow solid, 107 mg, 63% yield. ^{1}H NMR ($MeNO_2$-d_3) δ = 5.5 (4''), 6.5 (3''), 8.2 (5'), 41.5 (5'), 42.1 (3), 61.8 (4'), 71.3 (3'); ES^+-MS *m/z* 300.1 $[(L + Na)]^+$, 577.2 $[(2L + Na^+)]^+$. Anal. Calcd for $C_{28}Cl_2FeH_{22}N_{14}O_8.{}^1/_2MeNO.H_2O$: C, 39.90; H, 3.00; N, 23.68. Found: C, 39.90; H, 2.80; N, 23.40.

28c: To a stirring suspension of 1-tpp (105 mg, 0.38 mmol) in 5:1 MeOH-H_2O (50 cm^3) was added $FeCl_2.4H_2O$ (36 mg, 0.16 mmol) and allowed to stir at RT for 2 h. The insoluble solids were removed through filtration, and a saturated aqueous solution of NH_4PF_6 was dropped slowly into the solution precipitating the complex as its hexafluorophosphate salt. Orange-yellow powder, 105 mg, 67% yield. ^{1}H NMR ($MeNO_2$-d_3) δ =5.5 (4'') 6.5 (3''), 8.1 (5'), 41.5 (5'), 42.2 (3) 61.8 (4'), 71.5 (3'); ES+-MS m/z 278.1 [(L + H)]+, 300.1 [(L + Na)]+, 577.2 [(2L

+ Na)]+. Anal. Calcd for $C_{28}F_{12}FeH_{22}N_{14}P_2.2H_2O$: C, 35.92; H, 2.80; N, 20.94. Found: C, 35.70; H, 2.60; N, 21.10.

6.3.14 *Bis*-(2,6-di(pyrazol-1'-yl)pyridine-4-carboxylic acid) iron (II) tetrafluoroborate (29a)

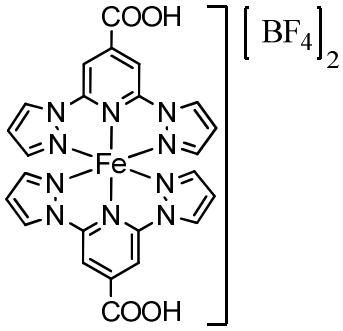

1-bppCOOH (210 mg, 0.82 mmol) was added to a solution of $Fe(BF_4).6H_2O$ (138 mg, 0.41 mmol) in $MeNO_2$ (40 cm^3) and during stirring for 1 h the solution became orange-red. The mixture was filtered, precipitated by addition of Et_2O (150 cm^3), collected on a glass frit and washed with further Et_2O. Orange-brown powder, 216 mg, 71% yield. ^{1}H NMR ($MeNO_2$-d_3) δ = 22.4 (3), 25.4 (5'), 38.1 (4'), 39.6 (3'). Anal. Calcd for $B_2C_{24}F_8FeH_{18}N_{10}O_4.2H_2O$: C, 37.15; H, 2.85; N, 18.05. Found: C, 37.65; H, 2.35; N, 17.90.

6.3.15 *Bis*-(4-amino-2,6-di(pyrazol-1'-yl)pyridine) iron (II) tetrafluoroborate (30a)

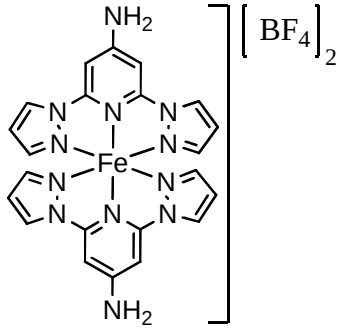

$Fe(BF_4)_2.6H_2O$ (40 mg, 0.12 mmol) was added to a suspension of 1-bppNH$_2$ (56 mg, 0.25 mmol) in $MeNO_2$ (20 cm^3) and stirred for 0.5 during which the colour became yellow-green. The solution was filtered and the volatiles removed *in vacuo*. The solid thus obtained was triturated in $CHCl_3$, filtered and dried over P_2O_5. Yellow-brown powder, 53.0 mg, 65% yield. ^{1}H NMR ($MeNO_2$-d_3) δ = 47.7 (5'), 52.7 (3), 60.8 (4'), 78.9 (3'); ES$^+$-MS *m/z* 249.1[(L + Na)]$^+$, 475.2 [(2L + Na)]$^+$.

6.3.16 *Bis*-(4-nitro-2,6-di(pyrazol-1'-yl)pyridine iron (II) tetrafluoroborate (31a)

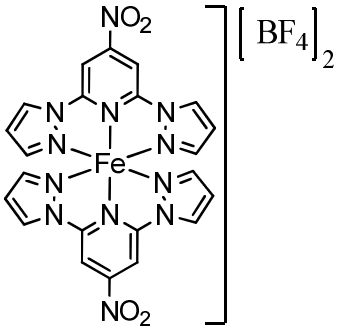

In $MeNO_2$ (30 cm^3), 1-bppNO$_2$ (49 mg, 0.19 mmol) and $Fe(BF_4)_2.6H_2O$ (31 mg, 0.09 mmol) were stirred for 1 h. The burgundy solution was filtered, and the volatiles were removed. Dark Purple powder, 61.0 mg, 91% yield. ^{1}H NMR ($MeNO_2$-d_3) δ = 19.6 (3), 22.9 (5'), 34.2 (3' + 4'); ES$^+$-MS *m/z* 279.1 [(L + Na)]$^+$. Anal. Calcd for $B_2C_{22}F_8FeH_{16}N_{12}O_2.{}^1/_2H_2O$: C, 35.19; H, 2.28; N, 22.38. Found: C, 35.20; H, 2.10; N, 22.10.

6.3.17 *Bis*-(4-hydroxy-2,6-di(pyrazol-1'-yl)pyridine) iron (II) salts of the form [Fe(1-bppOH)$_2$[X]$_2$, where X = tetrafluoroborate (32a), perchlorate (32b) and hexafluorophosphate (32c)

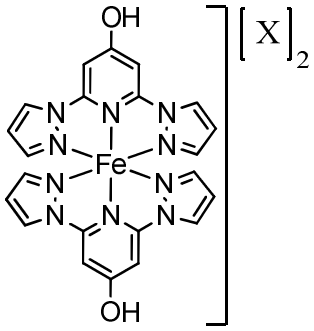

32a: To a stirred suspension of 1-bppOH (105 mg, 0.46 mmol) in $MeNO_2$ (25 cm^3) was added $Fe(BF_4)_2.6H_2O$ (76 mg, 0.23 mmol). After the orange solution was stirred for 1 h, filtration, addition of Et_2O (50 cm^3) and collection yielded an impure sample (128 mg) of the *bis*-chelated metal salt. The complex was subsequently crystallised by vapour diffusion of $^iPr_2O$ into a methanolic solution of the crude powder, and the large cuboidal brown crystals extracted manually and confirmed as the desired dicationic species by ^{1}H NMR and X-ray diffraction. 54.0 mg, 34% yield. ^{1}H NMR ($MeNO_2$-d_3) δ = 45.2 (5'), 48.6 (3), 63.9 (4'), 78.0 (3'); ES$^+$-MS *m/z* 250.1 [(L + Na)]$^+$. Anal. Calcd for $B_2C_{22}F_8FeH_{18}N_{10}O_2$: C, 38.64; H, 2.65; N, 20.48. Found: C, 38.60; H, 2.60; N, 20.50.

32b: 1-bppOH (101 mg, 0.44 mmol) and $Fe(ClO_4)_2.3H_2O$ (64 mg, 0.21 mmol) were stirred together in $MeNO_2$ (25 cm^3) for 1 h followed by filtraton. Addition, whilst stirring, of Et_2O (50 cm^3) to the solution precipitated a solid which was collected on a glass frit. Yellow-brown powder, 111 mg, 75% yield. ^{1}H NMR ($MeNO_2$-d_3) δ = 44.5 (5'), 47.8 (3), 63.0 (4'), 76.7 (3');

ES^+-MS *m/z* 250.1 $[(L + Na)]^+$. Anal. Calcd for $C_{22}Cl_2FeH_{18}N_{10}O_{10}$: C, 37.26; H, 2.56; N, 19.75. Found: C, 36.90; H, 2.40; N, 19.60.

32c: A suspension of 1-bppOH (32 mg, 0.14 mmol) in 5:1 MeOH-H_2O (25 cm^3) was added to a flask containing $FeCl_2.4H_2O$ (13 mg, 0.07 mmol) causing immediate colouration to bright yellow. Following stirring for 0.5 h, the contents of the flask were filtered and the volume of the filtrate reduced. Saturated aqueous NH_4PF_6 was dropped into the solution, and stirring for 1 h precipitated the hexafluorophosphate salt which was collected via filtration as a bright yellow powder. 31.0 mg, 57% yield. ^{1}H NMR ($MeNO_2$-d_3) δ = 45.2 (5'), 48.6 (3), 63.7 (4'), 77.9 (3'); ES^+-MS *m/z* 250.1 $[(L + Na)]^+$. Anal. Calcd for $C_{22}F_{12}FeH_{18}N_{10}O_2P_2$: C, 33.02; H, 2.27; N, 17.50. Found: C, 32.90; H, 2.30; N, 17.20.

6.3.18 *Bis*-(4-methoxy-2,6-di(pyrazol-1'-yl)pyridine) iron (II) salts of the form $[Fe(1\text{-}bppOMe)_2][X]_2$, where X = tetrafluoroborate (33a) and hexafluorophosphate (33c)

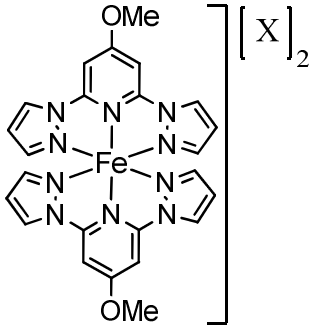

33a: 1-bppOMe (63 mg, 0.26 mmol) was dropped into a solution of $Fe(BF_4)_2.6H_2O$ (43 mg, 0.13 mmol) in $MeNO_2$ (10 cm^3). After 1 h the solution was filtered to remove any insolubles and Et_2O (70 cm^3) added to the filtrate resulting in precipitation of the salt which was collected and washed with additional Et_2O. Intense yellow powder, 74.0 mg, 80% yield. ^{1}H NMR ($MeNO_2$-d_3) δ = 6.6 (OMe), 44.4 (5'), 47.1 (3), 62.5 (4'), 76.3 (3'). No satisfactory microanalytical data was obtained for this novel compound.

33c: In 2:1 MeOH-H_2O (20 cm^3) was stirred 1-bppOMe (60 mg, 0.25 mmol) and $FeCl_2.4H_2O$ (24 mg, 0.12 mmol) for 1 h after which a small quantity of insoluble material was removed by filtration. The MeOH was removed carefully *in vacuo* and to the remaining aqueous solution was added saturated aqueous NH_4PF_6 which precipitated a yellow material upon stirring. The precipitate was filtered, washed with a few drops of H_2O and desiccated. Bright yellow powder, 98.0 mg, 99% yield. ^{1}H NMR ($MeNO_2$-d_3) δ = 6.5 (OMe), 44.4 (5'), 47.0 (3), 62.5 (4'), 76.3 (3'); Anal. Calcd for $C_{24}F_{12}FeH_{22}N_{10}O_2P_2.H_2O$: C, 34.06; H, 2.86; N, 16.55. Found: C, 34.30; H, 2.60; N, 16.60.

6.3.19 *Bis*-(4-mercapto-2,6-di(pyrazol-1'-yl)pyridine) iron (II) salts of the form form $[Fe(1\text{-}bppSH)_2][X]_2$, where X = tetrafluoroborate (34a), perchlorate (34b) and trifluoromethansulfonate (34d)

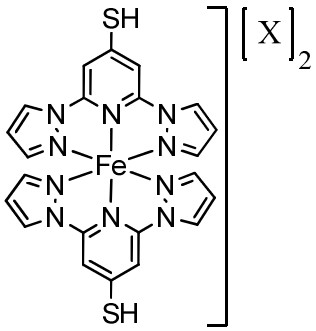

34a: Addition of $Fe(BF_4)_2.6H_2O$ (107 mg, 0.32 mmol) to a $MeNO_2$ (40 cm^3) suspension of 1-bppSH resulted in an opaque yellow-orange solution after stirring for 2 h. Post-filtration Et_2O (100 cm^3) was added to the filtrate, precipitating the salt which was collected on a glass frit and desiccated. Yellow solid, 175 mg, 76% yield. ^1H NMR ($MeNO_2$-d_3) δ = 36.9 (3), 38.1 (5'), 55.4 (4'), 64.8 (3'); ES^+-MS *m/z* 266.0 $[(L + Na)]^+$.

34b: Under an atmosphere of N_2, $Fe(ClO_4)_2.3H_2O$ (38 mg, 0.12 mmol) was dropped into a flask containing a suspension of 1-bppSH (61 mg, 0.25 mmol) in $MeNO_2$ (10 cm^3) and the mixture left to stir until complete dissolution of all solids. Using an N_2 purged syringe, $^iPr_2O$ (25 cm^3) was dropped slowly into the stirring solution causing formation of a yellow solid. This was collected by filtration, washed with a further few drops of $^iPr_2O$ and desiccated over P_2O_5. Yellow powder, 65.0 mg, 73% yield. ^1H NMR ($MeNO_2$-d_3) δ = 36.9 (3), 38.1 (5'), 55.4 (4'), 64.8 (3'); ES^+-MS *m/z* 266.0 $[(L + Na)]^+$. Anal. Calcd for $C_{22}Cl_2FeH_{18}N_{10}O_8S_2.H_2O$: C, 34.80; H, 2.65; N, 18.45. Found: C, 35.10; H, 2.40; N, 18.20.

34d: $Fe(CF_3SO_3)_2$ (63 mg, 0.18 mmol) and 1-bppSH (88mg, 0.36 mmol) were dropped into a flask containing $MeNO_2$ (30 cm^3) and stirred at RT for 0.5 h. Additional $MeNO_2$ (25 cm^3) was added due to the low solubility of the complex salt, and Et_2O (100 cm^3) added slowly to the stirring solution. The precipitate was collected, washed with a few drops of Et_2O and dried *in vacuo*. Yellow solid, 88.0 mg, 58% yield. ^1H NMR ($MeNO_2$-d_3) δ = 37 (3), 38 (5'), 56 (4'), 65 (3'); ES^+-MS *m/z* 266.0 $[(L + Na)]^+$.

6.3.20 *Bis*-(4-thiomethyl-2,6-di(pyrazol-1'-yl) pyridine) iron (II) tetrafluoroborate (35a)

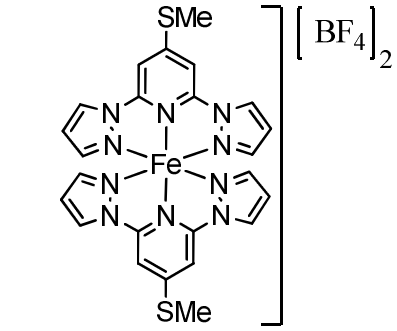

1-bppSMe (70 mg, 0.27 mmol) was dropped into a stirred solution of $Fe(BF_4)_2.6H_2O$ (45 mg, 0.13 mmol) in $MeNO_2$ (20 cm^3) and stirring was continued for an additional 1 h. The orange-yellow solution was filtered, and precipitated over 1 h by slow addition of Et_2O (75 cm^3). The resultant solid was collected, washed with additional E_2O and dried in vacuo. Yellow powder, 96.0 mg, 99% yield. ^1H NMR ($MeNO_2$-d_3) δ = 6.2 (SMe), 42.5 (5'), 43.2 (3), 60.6 (4'), 72.5 (3'); ES^+-MS *m/z* 280.1 $[(L + Na)]^+$.Anal. Calcd for $B_2C_{24}F_8FeH_{22}N_{10}S_2$: C, 38.74; H, 2.98; N, 18.82. Found: C, 38.40; H, 2.95; N, 18.45.

6.3.21 *Bis*-(*bis*-(2,6-di(pyrazol-1'-yl)pyridin-4-yl)disulfide) iron (II) salts of the form $[Fe(1\text{-}bppDS)]_n[X]_{2n}$, where X = tetrafluoroborate (36a) and perchlorate (36b)

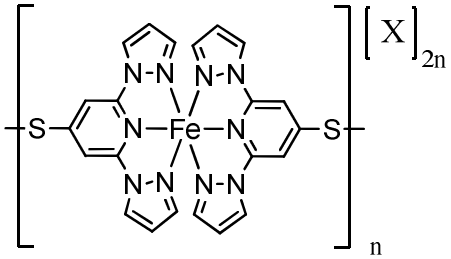

36a: $Fe(BF_4)_2.6H_2O$ (49 mg, 0.15 mmol) was added to 1-bppDS (70 mg, 0.14 mmol) suspended in $MeNO_2$ (30 cm^3) causing colouration to a bright orange, and was stirred for 0.5 h. The solution was then filtered and the $MeNO_2$ removed *in vacuo*. Brick-red microcrystalline solid, 77.0 mg, 77% yield. ^1H NMR ($MeNO_2$-d_3) δ = 37.4 (3), 38.1 (5'), 55.5 (4'), 64.9 (3'); ES^+-MS *m/z* 485.1 $[(L + H)]^+$, 507.1 $[(L + Na)]^+$.

36b: 1-bppDS (77 mg, 0.16 mmol) and $Fe(ClO_4)_2.3H_2O$ (50 mg, 0.16 mmol) were stirred at RT in $MeNO_2$ (30 cm^3) for 0.5 h, followed by filtration and the volatiles subsequently removed from the filtrate. Orange-brown solid, 52 mg, 44% yield. ^1H NMR ($MeNO_2$-d_3) δ = 37.4 (3), 38.1 (5'), 55.5 (4'), 64.9 (3'); ES^+-MS *m/z* 507.1 $[(L + Na)]^+$.

6.3.22 *Bis*-(4-fluoro-2,6-di(pyrazol-1'-yl)pyridine) iron (II) tetrafluoroborate (37a)

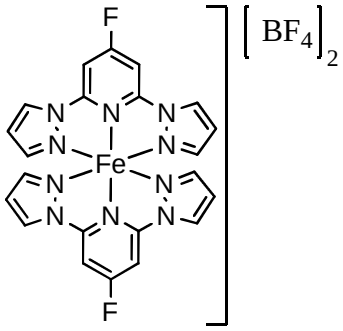

1-bppF (40 mg, 0.17 mmol) and $Fe(BF_4)_2.6H_2O$ (28 mg, 0.08 mmol) were added to a flask containing $MeNO_2$ (10 cm^3) and stirred together for 1 h. The yellow solution was filtered, and Et_2O (50 cm^3) added to the filtrate. The precipitate was filtered, and the solid washed sparingly with Et_2O. Desiccation caused darkening to a yellow-orange, but after further desiccation overnight a bright yellow solid was obtained. 43.0 mg, 78% yield. ^1H NMR ($MeNO_2$-d_3) δ = 40.9 (3 + 5'), 63.1 (4'), 71.7 (3'). Anal. Calcd for $B_2C_{22}F_{10}FeH_{16}N_{10}$: C, 38.38; H, 2.34; N, 20.36. Found: C, 38.60; H, 2.35; N, 20.10.

6.3.23 *Bis*-(4-chloro-2,6-di(pyrazol-1'-yl)pyridine) iron (II) tetrafluoroborate (38a)

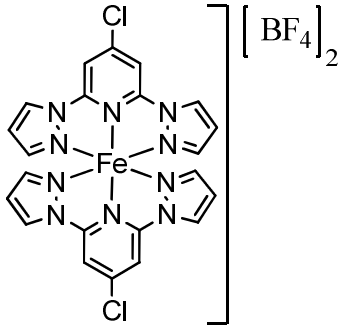

1-bppCl (64 mg, 0.26 mmol) was stirred in $MeNO_2$ (10 cm^3) in the presence of $Fe(BF_4)_2.6H_2O$ (43 mg, 0.13 mmol) with the solution darkening to a light orange over the course of 1 h followed by filtration Et_2O (60 cm^3) precipitated the salt, which was collected on a glass frit and, washed with additional Et_2O and dried. Orange-brown powder, 78.0 mg, 83% yield. ^1H NMR ($MeNO_2$-d_3) δ = 37.2 (3), 38.6 (5'), 59.7 (4'), 66.6 (3'). Anal. Calcd for $B_2C_{22}Cl_2F_{18}FeH_{16}N_{10}$: C, 36.66; H, 2.23; N, 19.43. Found: C, 36.75; H, 2.25; N, 19.50.

6.3.24 *Bis*-(4-bromo-2,6-di(pyrazol-1'-yl)pyridine) iron (II) tetrafluoroborate (39a)

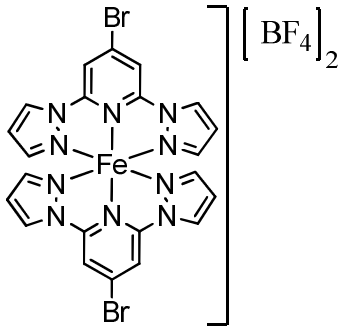

1-bppBr (72 mg, 0.25 mmol) and $Fe(BF_4)_2.6H_2O$ (41 mg, 0.12 mmol) were stirred in $MeNO_2$ (10 cm^3) for 1 h, filtered and reduction of the volume to 50%. The salt was precipitating by addition of Et_2O (100 cm^3), collected on a glass frit, washed with Et_2O and desiccated. Orange-yellow powder, 85.0 mg, 87% yield. ^1H NMR ($MeNO_2$-d_3) δ = 36.3 (3), 38.0 (5'), 58.7 (4'), 65.1 (3'); ES^+-MS *m/z* 312.0 $[(L + Na)]^+$. Anal. Calcd for $B_2Br_2C_{22}F_8FeH_{16}N_{10}$: C, 32.63; H, 1.99; N, 17.30. Found: C, 32.50; H, 1.90; N, 16.90.

6.3.25 *Bis*-(4-iodo-2,6-di(pyrazol-1'-yl)pyridine) iron (II) tetrafluoroborate (40a)

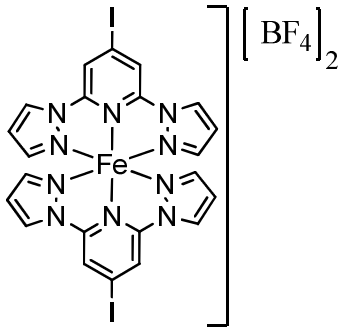

In $MeNO_2$ (25 cm^3), 1-bppI (72 mg, 0.21 mmol) and $Fe(BF_4)_2.6H_2O$ (35 mg, 0.10 mmol) were stirred for 1 h and the orange solution was filtered, reduced in volume to ca. 50% and the salt precipitated with Et_2O (100 cm^3). The suspension was filtered, the solid washed with additional Et_2O and dried *in vacuo*. Orange solid, 86.0 mg, 95% yield. ^1H NMR ($MeNO_2$-d_3) δ = 35.1 (3), 37.0 (5'), 57.0 (4'), 62.9 (3'); ES^+-MS *m/z* 360.0 $[(L + Na)]^+$. Anal. Calcd for $B_2C_{22}F_8FeH_{16}I_2N_{10}$: C, 29.24; H, 1.78; N, 15.50. Found: C, 29.30; H, 1.70; N, 15.50.

6.4 Preparation of *bis*-azinyl cobalt(II) salts

6.4.1 *Bis*-(2,6-di(2'-pyridyl)pyrazine) cobalt (II) tetrafluoroborate (1b)

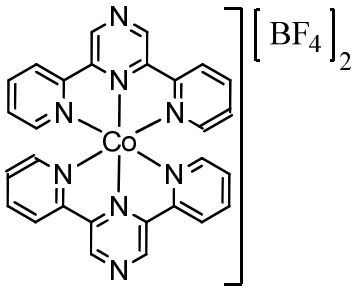

A round bottom flask containing bipypz (55 mg, 0.23 mmol) and $Co(BF_4)_2.6H_2O$ (41 mg, 0.12 mmol) dissolved in $MeNO_2$ (20 cm^3) was left on stir for 0.5 h before the volatiles were removed from the red solution and the resulting material was dried over P_2O_5. Red-brown powder, 75.0 mg, 89% yield. ^1H NMR ($MeNO_2$-d_3) δ =10.2 (4'), 33.2 (5'), 34.8 (3 + 5'), 50.4 (3'), 91.3 (6'); ES^+-MS *m/z* 263.6 $[(ML_2 - 2BF_4)]^{2+}$, 614.2 $[(ML_2 - BF_4)]^+$. Anal. Calcd for $B_2C_{28}CoF_8H_{20}N_8$.: C, 47.43; H, 2.84; N, 15.80. Found: C, 47.20; H, 2.80; N, 15.75.

6.4.2 *Bis*-(2,6-di(2'-pyrazinyl)pyridine) cobalt (II) tetrafluoroborate (2b)

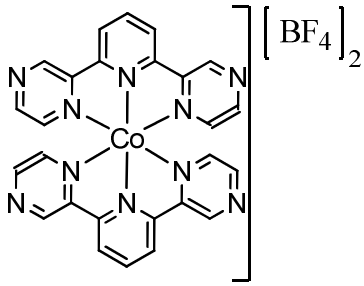

To $Co(BF_4)_2.6H_2O$ (51 mg, 0.15 mmol) suspended in $MeNO_2$ (20 cm^3) was added bipzpy (70 mg, 0.30 mmol) causing coloration to orange. During stirring for 0.5 h, the solution progressively darkened and the volatiles removed yielding the salt. Orange-brown powder, 99.0 mg, 94% yield. ^1H NMR ($MeNO_2$-d_3) δ = 22.4 (4), 32.8 (3' + 5'), 45.7 (3), 82.6 (6'); ES^+-MS *m/z* 236.1 $[(L + H)]^+$, 258.1 $[(L + Na)]^+$, 264.6 $[(ML_2 - 2BF_4)]^{2+}$. Anal. Calcd for $B_2C_{26}CoF_8H_{18}N_{10}$: C, 44.42; H, 2.58; N, 19.92. Found: C, 44.30; H, 2.40; N, 19.55.

6.4.3 *Bis*-(2,6-di(2'-pyrazinyl)pyrazine) cobalt (II) tetrafluoroborate (3b)

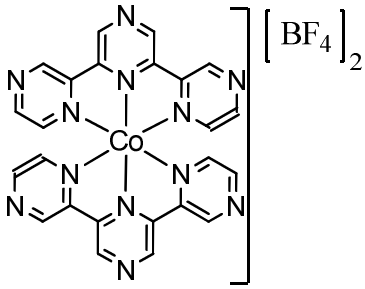

$Co(BF)_4.6H_2O$ (68 mg, 0.20 mmol) was added to a stirred suspension of terpz (96 mg, 0.41 mmol) in $MeNO_2$ (30 cm^3) causing the formation of an orange coloured solution. After further stirring for 24 h, Et_2O (120 cm^3) was added and the complex so precipitated was collected on a glass frit and washed with further Et_2O. Orange brown solid, 115 mg, 80% yield. ^1H NMR ($MeNO_2$-d_3) δ = 24.2 (5'), 33.1 (3), 43.7 (3'), 81.5 (6'); ES^+-MS *m/z* 237.1 $[(L + H)]^+$, 259.1 $[(L + Na)]^+$. Anal. Calcd for $B_2CoC_{24}F_8H_{16}N_{12}.2H_2O$: C, 38.9; H, 2.72; N, 22.7. Found: C, 38.8; H, 2.55; N, 22.4.

6.4.4 *Bis*-(2,6-di(4'-pyrimidyl)pyridine) cobalt (II) tetrafluoroborate (4b)

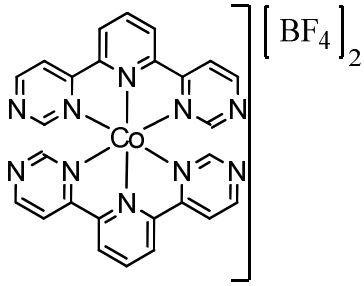

After addition of $Co(BF_4)_2.6H_2O$ (77 mg, 0.23 mmol) to 4-bipympy (110 mg, 0.47 mmol) in $MeNO_2$ (25 cm^3) the solution became orange, was filtered after stirring for 1 h and the volatiles removed. The resulting orange/brown solid was washed with Et_2O (20 cm^3) and dried *in vacuo*. 101 mg, 62% yield. ^1H NMR ($MeNO_2$-d_3) δ = 11.2 (6'), 23.6 (4), 65.1 (3), 70.0 (2'), 75.1 (5'); ES^+-MS *m/z* 236.1 $[(L + H)]^+$, 258.1 $[(L + Na)]^+$, 264.1 $[(ML_2 – 2BF_4)]^{2+}$. Anal. Calcd for $B_2C_{26}CoF_8H_{18}N_{10}$: C, 44.42; H, 2.58; N, 19.92. Found: C, 44.35; H, 2.60; N, 19.60.

6.4.5 *Bis*-(2,6-di(1',2',4'-triazin-3'-yl)pyridine) cobalt (II) tetrafluoroborate (6b)

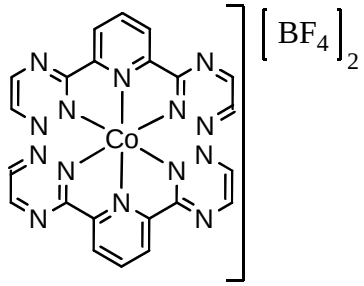

A flask charged with a $MeNO_2$ (40 cm^3) solution of $Co(BF_4)_2.6H_2O$ (107 mg, 0.31 mmol) and bitrzpy (151 mg, 0.64 mmol) was stirred for 3 h after which the resulting dark orange solution was filtered and the volatiles removed. Black crystals, 138 mg. 63% yield. Nothing is resolvable in the contact shifted paramagnetic region of the ^1H NMR spectrum, though a set of overlapping, highly broadened signals are present between 8 and 10 ppm. ES^+-MS *m/z* 238.1 $[(L + H)]^+$, 260.1 $[(L + Na)]^+$, 497.1 $[(2L + Na)]^+$. Anal. Calcd for $B_2C_{22}CoF_8H_{14}N_{14}.2H_2O$: C, 35.56; H. 2.44; N, 26.39. Found: C, 35.45; H, 2.25; N, 25.85.

6.4.6 *Bis*-(4-hydroxy-2,6-di(2'-pyrazinyl)pyridine) cobalt (II) tetrafluoroborate (7b)

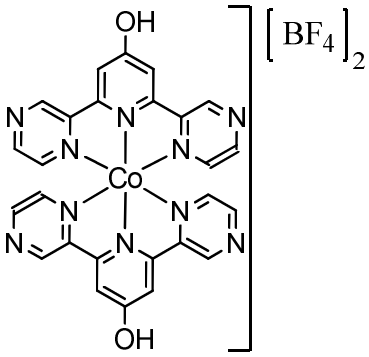

A methanolic solution (25 cm^3) of $Co(BF_4)_2.6H_2O$ (37 mg, 0.11 mmol) was added to a flask containing bipzpyOH (55 mg, 0.22 mmol) and were stirred together at RT for 0.5 h. After complete dissolution of the ligand, Et_2O (20 cm^3) was added and the precipitate so formed collected and washed with small volumes of Et_2O. Brick-red solid, 71.0 mg, 88% yield. ^1H NMR ($MeNO_2$-d_3) δ = 33.7 (5'), 59.7 (4H, 3), 64.8 (3'), 97.3 (6'); ES^+-MS *m/z* 560.1 $[(ML_2 – 2BF_4 – H)]^+$, 582.1 $[(ML_2 – 2BF_4 – 2H + Na)]^+$. Anal. Calcd. for $B_2C_{26}CoF_8H_{18}N_{10}O_{10}.2H_2O$: C, 40.50; H, 2.88; N, 18.17. Found: C, 40.75; H, 2.55; N, 18.15.

6.4.7 *Bis*-(4-hydroxy-2,6-di(2'-pyrimidyl)pyridine) cobalt (II) tetrafluoroborate (8b)

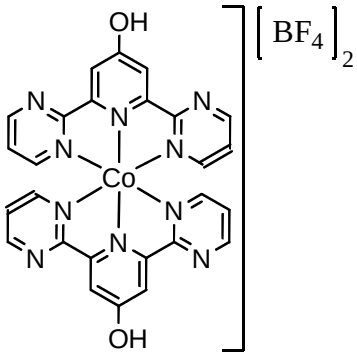

$Co(BF_4)_2.6H_2O$ (75 mg, 0.22 mmol) was dissolved in $MeNO_2$ (25 cm^3) and 2-bipympyOH (111 mg, 0.44 mmol) added. After stirring for 1 h the dark orange solution was filtered and the salt precipitated by addition of Et_2O (150 cm^3). The salt was recrystallised by diffusion of $^iPr_2O$ into acetone solution. Beige solid, 120 mg, 74% yield. ^1H NMR ($MeNO_2$-d_3) δ = 9.6 (4'), 25.7 (5'), 93.2 (6'), protons at the 3 position not observable; ES^+-MS *m/z* 280.5 $[(M – 2BF_4)]^{2+}$, 560.1 $[(M – 2BF_4 – H)]^+$. Anal. Calcd. For $B_2C_{26}CoF_8H_{18}N_{10}O_2.C_3H_6O.1/2C_3H_6O$: C, 43.23; H, 2.77; N, 18.33. Found: C, 43.15; H, 3.00; N, 17.90.

6.4.8 *Bis*-(2,2':6',2''-terpyridine) cobalt (II) tetrafluoroborate (9b)

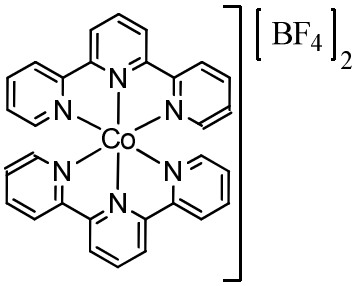

Terpy (211 mg, 0.91 mmol) was dropped into a stirred $MeNO_2$ (50 cm^3) solution of $Co(BF_4)_2.6H_2O$ (151 mg, 0.44 mmol). Stirring for 0.5 h gave a dark orange/brown solution which was vacuumed to dryness and the solid collected. Brick-red powder, 281 mg, 91% yield. ^{1}H NMR ($MeNO_2$-d_3) δ = 9.0 (4'), 21.6 (4), 34.4 (5'), 47.3 (3), 56.6 (3'), 98.5 (6'); ES^+-MS *m/z* 262.6 $[(ML_2 – 2BF_4)]^{2+}$, 612.1 $[(ML_2 – BF_4)]^+$.

6.4.9 *Bis*-(4-hydroxy-2,6-di(2'-pyridyl)pyridine) cobalt (II) tetrafluoroborate (10b)

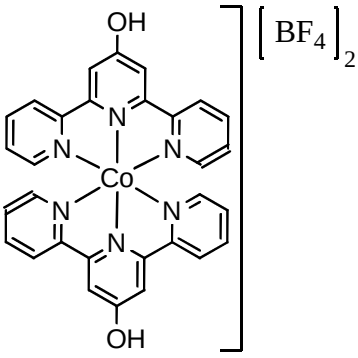

A $MeNO_2$ (50 cm^3) solution of $Co(BF_4)_2.6H_2O$ (118 mg, 0.35 mmol) and terpyOH (172 mg, 0.69 mmol) were stirred together for 0.5 h and after full dissolution of all solids the volatiles were removed to give the complex salt. Brown/orange solid, 183 mg, 72% yield. ^{1}H NMR ($MeNO_2$-d_3) δ =6.2 (4'), 34.5 (5'), 71.1 (3), 77.5 (3'), 112.1 (6'); ES^+-MS *m/z* 278.6 $[(ML_2 – 2BF_4)]^{2+}$, 556.1 $[(ML_2 – 2BF_4 – H)]^+$.

6.5 Preparation of *bis*-azinyl zinc(II) salts

6.5.1 *Bis*-(*bis*-(2,6-di(pyrazol-1'-yl)pyridin-4-yl)disulfide) zinc (II) tetrafluoroborate (42a)

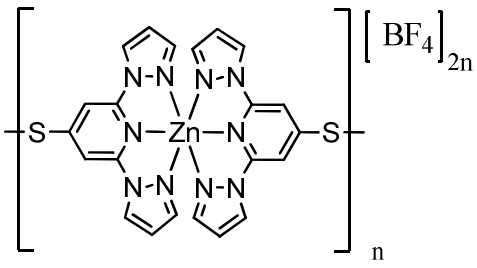

$Zn(BF_4)_2.6H_2O$ (51 mg, 0.15 mmol) and 1-bppDS (70 mg, 0.14 mmol) were stirred together in 1:2 $MeNO_2$-MeCN (20 cm^3) for 1 h. The solvents were removed, the pale yellow residue triturated in Et_2O (80 cm^3) and the salt collected on a glass frit. Colourless polycrystalline solid, 65.0 mg, 64% yield. ^{1}H NMR ($MeNO_2$-d_3) δ = 6.67 (br s, 4H, 4'), 7.65 (br s, 4H, 3'), 8.18 (br s, 4H, 3), 8.68 (br s, 4H, 5'); ^{13}C NMR ($MeNO_2$-d_3) δ = 106.9 (3), 113.1 (4'), 131.5 (5'), 144.5 (3'), 147.0 (2), 155.6 (4). Anal. Calcd for $(B_2C_{22}F_8H_{16}N_{10}S_2Zn)_n.0.5nEt_2O$: C, 37.84; H, 3.09; N, 18.03. Found: C, 38.10; H, 2.90; N, 18.50.

6.6 Preparation of heteroleptic and homoleptic *bis*-azinyl ruthenium(II) salts and ruthenium(II) and (III) precursors

6.6.1 Dichlorotetrakis(dimethylsulfoxide)ruthenium (II)

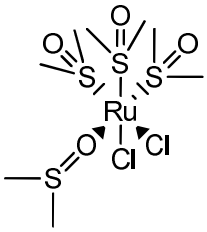

The *cis*-isomer was synthesised according to a literature method.[18] A flask containing $RuCl_3.3H_2O$ (603 mg, 2.30 mmol) in DMSO (5 cm^3) was refluxed at 185°C for 5 minutes. Evaporation of *ca.* 25% of the solution followed by addition of acetone (50 cm^3) gave bright yellow crystals. The crystals were filtered and washed with Et_2O. Overnight further crystallisation occurred in the mother liquor and were isolated as above. 747 mg, 67% yield. The ^{1}H NMR spectrum was complicated between 3.3 and 3.6 ppm due to several S-bonded methyl proton environments but is in general agreement with previously reported spectra.[19] IR (solid) υ (cm^{-1}): 920 (S-O), 1094 (S-O), 1121 (S-O), 2918 (C-H), 2999 (C-H), 3011 (C-H), 3027 (C-H); ES^+-MS *m/z* 430.9 $[(M - DMSO + Na)]^+$, 471.9 $[(M - DMSO + Na + MeCN)]^+$. Anal. Calcd for $C_8Cl_2H_{24}O_4RuS_4$: C, 19.83; H, 4.99. Found: C, 20.45; H, 4.95.

6.6.2 Trichloro(2,2':6',2''-terpyridine)ruthenium (III)

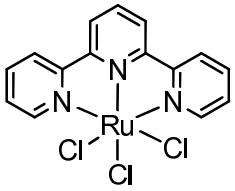

This compound was prepared according to the literature.[20] To a flask containing black ethanolic (250 cm^3) solution of $RuCl_3.3H_2O$ (545 g, 2.08 mmol) was added terpy (487 mg, 2.09 mmol) and the contents were heated to reflux for 3 h, before cooling and room temperature and the insoluble monosubstituted complex filtered off and dried *in vacuo*. 831

mg, 91% yield. ES^+-MS *m/z* . Anal. Calcd for $C_{15}Cl_3H_{11}N_3Ru.H_2O$: C, 39.27; H, 2.86; N, 9.16. Found: C, 39.80; H, 2.50; N, 9.10.

6.6.3 *Bis*-(2,6-di(2'-pyridyl)pyrazine) ruthenium (II) tetrafluoroborate (11a)

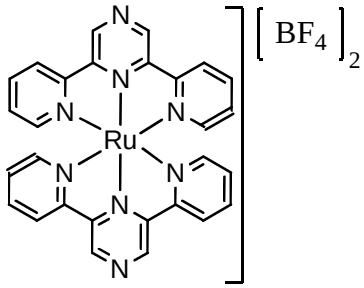

To a stirring suspension of bipypz (144 mg, 0.61 mmol) in ethylene glycol (30 cm^3) was added $RuCl_3.3H_2O$ (76 mg, 0.29 mmol) and the mixture heated at 110°C for 4 h. The deep red solution was filtered and a saturated aqueous $NaBF_4$ solution was added. Upon standing at *ca.* 5°C for five days, a dark red solid precipitated which was collected and dried. Dark red powder, 92.0 mg, 43% yield. ^{1}H NMR ($MeNO_2$-d_3) δ = 7.25 (t, J = 6.4 Hz, 4H, 5'), 7.48 (d, J = 5.1 Hz, 4H, 6'), 8.03 (t, J = 7.7 Hz, 4H, 4'), 8.71 (d, J = 8.1 Hz, 4H, 3'), 9.92 (s, 4H, 3); ^{13}C NMR ($MeNO_2$-d_3) δ = 126.2 (3'), 129.4 (5'), 140.1 (4'), 144.6 (3), 151.3 (2/2'), 154.1 (6'), 157.2 (2/2'); ES^+-MS *m/z* 285.0 $[(ML_2 - 2BF_4)]^{2+}$. Anal. Calcd for $B_2C_{28}F_8H_{20}N_8Ru.H_2O$: C, 44.18; H, 2.91; N, 14.72. Found: C, 41.50; H, 2.80; N, 14.25.

6.6.4 *Bis*-(2,6-di(2'-pyrazyl)pyridine) ruthenium (II) tetrafluoroborate (12b)

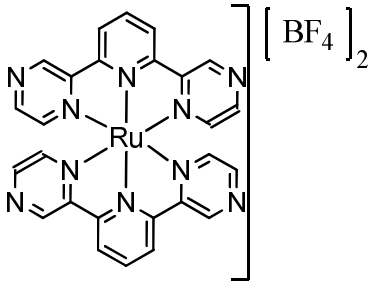

A round bottom flask was charged with $RuCl_3.3H_2O$ (21 mg, 0.08 mmol) and bipzpy (40 mg, 0.17 mmol) suspended in ethylene glycol (5 cm^3). The contents were heated to 160°C for 4 days, during which the colour changed from a black/brown, through green until eventually forming a deep red solution. The volume was reduced to ca. 1 cm^3 by subjecting the contents to vacuum at 110°C and to the cooled residue was added a saturated aqueous NH_4PF_6 solution (3 cm^3) and shaken vigorously. The dark precipitate formed was collected on a glass frit and washed with a few drops of H_2O, EtOH and Et_2O and dried over P_2O_5. The hexafluorophosphate salt could not be purified any further with all attempts resulting in loss of material with no observable increase in purity. Dark red solid, 20.0 mg, 29 % yield. ^{1}H

NMR (CD_3CN) δ = 7.41 (dd, J = 3.2, 1.0 Hz, 4H, 6'), 8.35 (d, J = 3.0 Hz, 4H, 5'), 8.55 (t, J = 8.3 Hz, 2H, 4), 8.90 (d, J = 8.1 Hz, 4H, 3), 9.61 (s, 4H, 3').

6.6.5 *Bis*-(2,6-di(2'-pyrazyl)pyrazine) ruthenium (II) tetrafluoroborate (13b)

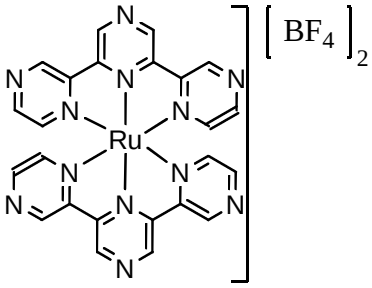

terpz (39 mg, 0.17 mmol) was added to a viscous solution of $RuCl_3.3H_2O$ (21 mg, 0.08 mmol) in ethylene glycol (10 cm^3) before heating firstly to 130°C for 3 days followed by 3 days at 150°C . The resulting orange/red solution was filtered and the ethylene glycol removed at high temperature from the filtrate. The minimum amount of H_2O (5 cm^3) was added to completely dissolve the black residue and aqueous NH_4PF_6 was added (5 cm^3) resulting in a brown/purple precipitate. The solid material was collected on a glass frit, washed with a few drops of H_2O, EtOH and Et_2O sequentially and desiccated. The hexafluorophosphate salt could not be purified any further with all attempts resulting in loss of material with no observable increase in purity. Brown solid, 44.0 mg, 64% yield. ^{1}H NMR (CD_3CN) δ = 7.48 (br s, 4H, 6'), 8.42 (br s, 4H, 5'), 9.76 (s, 4H, 3'), 10.03 (s, 4H, 3).

6.6.6 *Bis*-(2,6-di(4'-pyrimidyl)pyridine) ruthenium (II)hexafluorophosphate (14b)

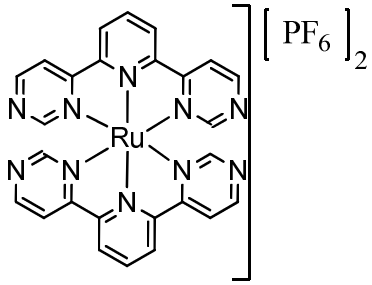

To an ethylene glycol (10 cm^3) solution of $RuCl_3.3H_2O$ (59 mg, 0.23 mmol) was added 4-bipympy (108 mg, 0.46 mmol) and the resulting dark suspension stirred at 150°C for 48 h. The contents were cooled to RT and filtered to remove the insoluble black solid that remained. Saturated aqueous NH_4PF_6 (5 cm^3) was added and the flask was left to stand at 5°C for 48 h. The dark precipitate so formed was collected on a glass sinter. Dark burgundy solid, 32.0 mg, 27% yield. ^{1}H NMR (CD_3CN) δ = 7.98 (d, J = 0.9 Hz, 4H, 2'), 8.44 (dd, J = 5.3, 1.1 Hz, 4H, 5'), 8.54 (t, J = 8.1 Hz, 2H, 4), 8.86 (d, J = 5.3 Hz, 4H, 6'), 8.97 (d, J = 8.1 Hz, 4H, 3); ^{13}C NMR (CD_3CN) δ = 121.0 (5'), 129.0 (3), 138.3 (4), 155.8 (2), 160.3 (6'), 162.5

(2'), 166.0 (4'); ES$^+$-MS *m/z* 286.0 $[(M - 2PF_6)]^{2+}$, 717.0 $[(M - PF_6)]^+$. Anal. Calcd for $C_{26}F_{12}H_{18}N_{10}P_2Ru.4H_2O$: C, 33.54; H, 2.81; N, 15.00. Found: C, 33.20; H, 2.50; N, 15.10.

6.6.7 *Bis*-(2,6-di(1',2',4'-triazin-3'-yl)pyridine) ruthenium (II) tetrafluoroborate (15a)

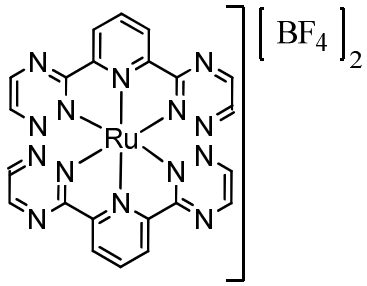

An acetontrilic solution (50 cm^3) of bitrzpy (112 mg, 0.47 mmol), $RuCl_2(DMSO)_4$ (110 mg, 0.23 mmol) and silver tetrafluoroborate (2 eq.) was heated at reflux for 3 h during which the colour turned from a bright yellow to a dark brown. After cooling the solution was filtered to remove silver chloride and the acetonitrile removed in vacuo leaving a dark oil. Dissolution in fresh acetonitrile followed by precipitation with chloroform and filtration gave a dark impure solid after desiccation. The tetrafluoroborate salt could not be purified any further with all attempts resulting in loss of material with no observable increase in purity. 133 mg, 77% yield. ^{1}H NMR (CD_3CN) δ = 8.63 (t, J = 8.0 Hz, 2H, 4), 8.86 (d, J = 2.9 Hz, 4H, 5'/6'), 8.90 (d, J = 2.4 Hz, 4H, 5'/6'), 9.01 (d, J = 8.0 Hz, 4H, 3); ES$^+$-MS *m/z* 238.1 $[(L + H)]^+$, 260.1 $[(L + Na)]^+$, 288.0 $[(ML_2 - 2BF_4)]^{2+}$, 633.0 $[(ML_2 - BF_4)]^+$.

6.6.8 *Bis*-(4-hydroxy-2,6-di(2'-pyrazinyl)pyridine) ruthenium (II) tetrafluoroborate (16a)

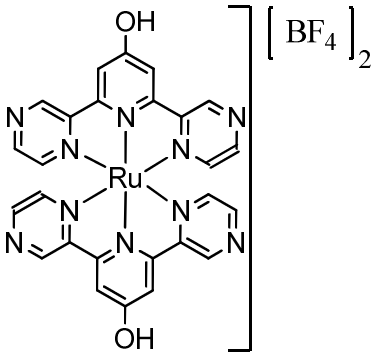

$RuCl_3.3H_2O$ (27 mg, 0.10 mmol) and bipzpyOH (54 mg, 0.21 mmol) suspended in ethylene glycol (10 cm^3) were heated to 150°C for 8 days during which the colour of the solution gradually progressed from black to dark green, and through an orange brown eventually took on a deep red hue. Once cooled, H_2O (10 cm^3) was added and the solution filtered. The filtrate was saturated with $NaBF_4$ and HBF_4 (5 drops) were added to ensure no dissociation of the phenolic groups. No precipitation of the salt occurred, even standing for 4 days at 5°C. The H_2O/glycol mixture was evaporated to dryness at high temperature and the residue

taken up in $MeNO_2$ (25 cm^3). Et_2O (120 cm^3) was added and the dark burgundy precipitate collected via filtration. The solid was redissolved in $MeNO_2$ (20 cm^3) and the fine insoluble particulates allowed to settle for 6 h, after which the $MeNO_2$ was decanted off from the insolubles. The volume of the $MeNO_2$ solution was reduced to 10 cm^3 and Et_2O (50 cm^3) was added with the precipitate once again isolated by filtration. The tetrafluoroborate salt could not be purified any further with all attempts resulting in loss of material with no observable increase in purity. Near-black solid, 29.0 mg, 37% yield. NMR ($MeNO_2$-d_3) δ = 7.62 (d, J = 2.7 Hz, 4H, 6'), 8.33 (m, 4H, 5'), 8.55 (s, 4H, 3), 9.53 (d, J = 3.6 Hz, 4H, 3'); ES^+-MS *m/z* 277.1 $[(L+MeCN+H)]^+$, 603.1 $[(ML_2 - 2BF_4 - H)]^+$.

6.6.9 *Bis*-(4-hydroxy-2,6-di(2'-pyrimidyl)pyridine ruthenium (II) hexafluorophosphate (17b)

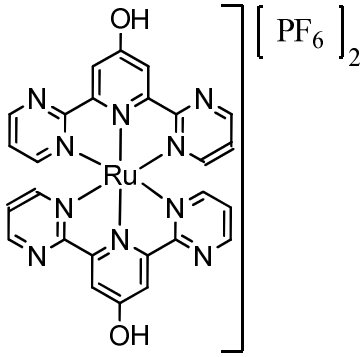

In ethylene glycol (15 cm^3) 2-bipympyOH (84 mg, 0.33 mmol) was stirred at 120°C with $RuCl_3.3H_2O$ (42 mg, 0.16 mmol) for 48 h. Once at RT, the intensely coloured red solution was filtered and aqueous NH_4PF_6 (10 cm^3) was added with the precipitated material collected on a glass frit, washed with a few drops of H_2O and desiccated. Tangerine solid, 59.0 mg, 41% yield. ^1H NMR (CD_3CN) δ = 7.19 (t, J = 5.6 Hz, 4H, 5'), 7.76 (dd, J = 6.0, 2.2 Hz, 4H, 6'), 8.39 (s, 4H, 3), 8.82 (dd, J = 4.7, 2.2 Hz, 4H, 4'); ^{13}C NMR (CD_3CN) δ = 116.6 (3), 124.1 (5'), 156.9 (4), 158.8 (4'), 162.6 (6'), 167.0 (2/2'), 167.4 (2/2'); ES^+-MS *m/z* 302.0 $[(M - 2PF_6)]^{2+}$, 603.1 $[(M - 2PF_6 - H)]^+$, 749.0 $[(M - PF_6)]^+$.

6.6.10 *Bis*-(2,2':6',2''-terpyridine) ruthenium (II) tetrafluoroborate (18a)

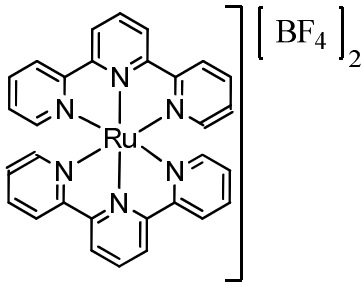

This compound was prepared identically to a literature report.[14] $RuCl_3.3H_2O$ (272 mg, 1.04 mmol) was added to a stirring solution of terpy (482 mg, 2.07 mmol) in ethylene glycol (100

cm^3) and heated to 110°C for 4 h. The dark red solution was allowed to cool, filtered and a saturated solution of sodium tetrafluoroborate was added to which precipitated a bright red solid which was then filtered and washed with ice-cold diethyl ether. 664 mg, 86% yield. ^{1}H NMR (CD_3CN) δ = 7.16 (ddd, J = 7.3, 5.6, 1.3 Hz, 4H, 5'), 7.34 (d, J = 5.6 Hz, 4H, 6'), 7.91 (td, J = 8.1, 1.7 Hz, 4H, 4'), 8.41 (t, J = 8.2 Hz, 2H, 4), 8.50 (d, J = 8.1 Hz, 4H, 3'), 8.76 (d, J = 8.2 Hz, 4H, 3); ^{13}C NMR (CD_3CN) δ = 125.1 (3), 125.8 (3'), 128.8 (5'), 137.2 (4), 139.4 (4'), 153.8 (6'), 156.7 (2), 159.4 (2'); ES$^+$-MS *m/z* 284.1 $[(M - 2BF_4)]^{2+}$.

6.6.11 *Bis*-(4-hydroxy-2,6-di(2'-pyridyl)pyridine) ruthenium (II) tetrafluoroborate (19a)

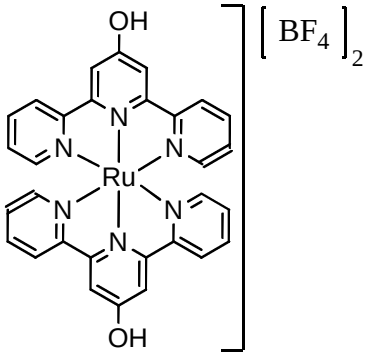

To an aqueous solution (10 cm^3) of $RuCl_2(DMSO)_4$ (188 mg, 0.19 mmol) was added terpyOH (197 mg, 0.97 mmol) in EtOH (10 cm^3) and the mixture held at reflux for 3 h. After cooling a saturated aqueous solution (10 cm^3) of $NaBF_4$ was added and the subsequent precipitation of a bright red solid led to filtration, collection and desiccation. 160 mg, 53% yield. ^{1}H NMR (CD_3CN) δ = 7.13 (d, J = 6.4 Hz, 4H, 5'), 7.39 (d, J = 5.6 Hz, 4H, 6'), 7.87 (td, J = 7.7, 1.3 Hz, 4H, 4'), 8.20 (s, 4H, 3), 8.39 (d, J = 8.1 Hz, 4H, 3'); ^{13}C NMR (CD_3CN) δ = 113.0 (3), 125.4 (3'), 128.6 (5'), 138.9 (4'), 153.8 (6'), 157.7 (4), 159.5 (2/2'), 165.8 (2/2'); ES$^+$-MS *m/z* 300.0 $[(ML_2 - 2BF_4)]^{2+}$, 599.1 $[(ML_2 - H - 2BF_4)]^+$.

6.6.12 *Bis*-(2,6-di(1'-methylimidazolium-3'-yl)pyridine) ruthenium (II) tetrafluoroborate (20a)

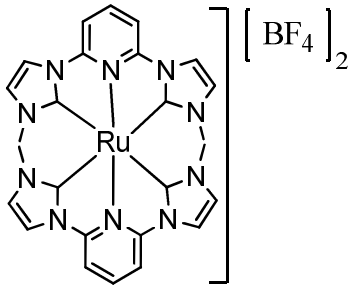

In ethylene glycol (7 cm^3), $RuCl_3.3H_2O$ (101 mg, 0.39 mmol) and MeImpy (311 mg. 0.78 mmol) were held at 190°C for 4 h, and after cooling H_2O added (10 cm^3) and the solution saturated with $NaBF_4$. Stirring for ca. 30 minutes yielded a bright yellow precipitate which was filtered off, washed in succession with a few drops of H_2O, MeOH and Et_2O and

desiccated overnight. Yellow solid, 117 mg, 41% yield. ^{1}H NMR ($MeNO_2$-d_3) δ = 2.74 (s, 12 H, Me), 7.02 (d, J = 2.3 Hz, 4H, 5'), 7.91 (d, J = 8.3 Hz, 4H, 3), 8.04 (d, J = 2.3 Hz, 4H, 4'), 8.28 (t, J = 8.1 Hz, 2H, 4); ^{13}C NMR ($MeNO_2$-d_3) δ = 36.4 (Me), 107.0 (5'), 117.5 (3), 125.4 (4'), 138.9 (2), 153.0 (4), 192.0 (2'); ES$^+$-MS *m/z* 290.1 $[(ML_2 - 2BF_4)]^{2+}$. Anal. Calcd For $B_2C_{13}F_8H_{13}N_{10}Ru.0.5MeNO_2$: C, 40.61; H, 3.53; N, 18.76. Found: C, 40.80; H, 3.40; N, 18.30.

6.6.13 *Bis*-(2,6-di(1'-isopropylimidazolium-3'-yl)pyridine) ruthenium (II) tetrafluoroborate (21a)

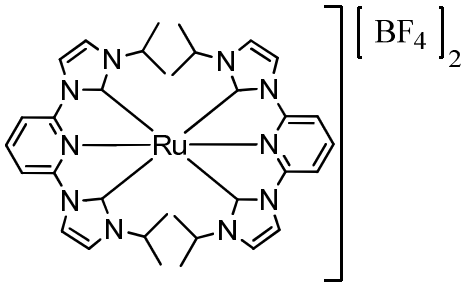

In a 25 cm^3 round bottom flask, ethylene glycol (10 cm^3), $RuCl_3.3H_2O$ (167 mg, 0.64 mmol) and PrImpy (587 mg, 1.28 mmol) were heated to 190°C for 4 h. Post-cooling, the dark solution was combined with H_2O (50 cm^3) and MeOH (20 cm^3) yielding the appearance of a small amount of yellow/orange solid which was removed. The solution was saturated with $NaBF_4$, and stirring overnight gave the desired salt. Filtration and desiccation allowed isolation of the bright yellow solid. 150 mg, 27% yield. ^{1}H NMR ($MeNO_2$-d_3) δ = 0.84 (d, J = 6.8 Hz, 24H, Me), 2.81 (sp, J = 6.8 Hz, 4H, ^{i}Pr), 7.25 (d, J = 2.3 Hz, 4H, 5'), 7.95 (d, J = 8.3 Hz, 4H, 3), 8.14 (d, J = 2.3 Hz, 4H, 4'), 8.33 (t, J = 8.3 Hz, 2H, 4); ^{13}C NMR ($MeNO_2$- d_3) δ = 22.4 (Me), 53.4 (^{i}Pr), 107.2 (5'), 118.4 (3), 120.4 (4'), 139.6 (2), 153.0 (4), 189.9 (2'). Anal. Calcd For $B_2C_{34}F_8H_{42}N_{10}Ru$: C, 47.19; H, 4.89; N, 16.18. Found: C, 47.00; H, 4.85; N, 16.05.

6.6.14 ((2,2':6',4''-Terpyridine)(2,2':6',2''-terpyridine)) ruthenium (II) tetrafluoroborate (22a)

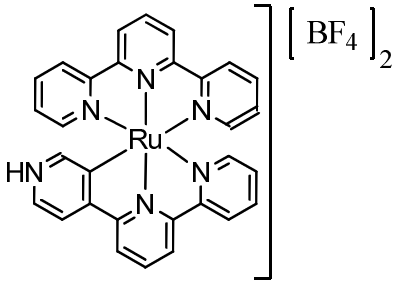

Cterpy (182 mg, 0.78 mmol) was dropped into a dark ethylene glycol suspension of trichloro(2,2':6',2''-terpyridine)ruthenium (III) (337 mg, 0.78 mmol) and the contents held at reflux for 0.4 h. After prompt cooling to RT, the solution was filtered and saturated aqueous

$NaBF_4$ (150 cm^3) was dropped into the solution which resulted in precipitation of the tetrafluoroborate complex salt which was collected on a glass frit. The complex was recrystallised by slow diffusion of Et_2O into $MeNO_2$ solutions of the salt. Dark purple powder, 446 mg, 77% yield. ^{1}H NMR (CD_3CN) δ = 7.05 (s, 1H, 2''c), 7.06 (ddd, J = 7.3, 5.6, 1.3 Hz, 2H, 5't), 7.17 (ddd, J = 7.3, 5.2, 1.3 Hz, 1H, 5'c), 7.29 (ddd, J = 5.6, 1.7, 0.9 Hz, 2H, 6't), 7.52 (ddd, J = 5.1, 1.7, 0.9 Hz, 1H, 6'c), 7.82 (td, J = 7.3, 1.7 Hz, 2H, 4't), 7.93 (td, J = 7.7, 1.7 Hz, 1H, 4'c), 7.95 (dd, J = 6.0, 1.3 Hz, 1H, 6''c), 8.17 (d, J = 6.0 Hz, 1H, 5''c), 8.22 (t, J = 8.1 Hz, 1H, 4t), 8.25 (t, J = 8.1 Hz, 1H, 4c) 8.43 (ddd, J = 8.2, 1.6, 0.8 Hz, 2H, 3't), 8.51 (ddd, J = 8.3, 1.2, 0.9 Hz, 1H, 3'c), 8.61 (dd, J = 8.2, 0.9 Hz, 1H, 5c), 8.65 (d, J = 8.2 Hz, 2H, 3t), 8.67 (dd, J = 8.1, 0.9 Hz, 1H, 3c), 13.11 (s, 1H, 1''c) ; ^{13}C NMR (CD_3CN) δ = 120.5 (5''c), 124.1 (3t), 124.5 (5c), 124.8 (3'c), 124.9 (3't), 125.2 (3c), 128.0 (5't), 128.2 (5'c), 133.3 (4t), 134.7 (6''c), 136.3 (4c), 137.6 (4't), 139.4 (4'c), 146.3 (2''c), 152.1 (6'c), 152.6 (6't), 155.2 (2t), 156.9 (2c), 157.4 (2'c), 158.4 (2't), 160.9 (6c), 167.0 (4''c), 182.4 (3''c); ES^+-MS *m/z* 284.0 $[(M - 2BF_4)]^{2+}$, 567.1 $[(M - 2BF_4 - H)]^+$. Anal. Calcd for $B_2C_{30}F_8H_{22}N_6Ru.MeNO_2.H_2O$: C, 45.39; H, 3.32; N, 11.95. Found: C, 45.20; H, 3.00; N, 11.20.

6.6.15 *Bis*-(2,6-di(pyrazol-1'-yl)pyridine) ruthenium (II) tetrafluoroborate (23a)

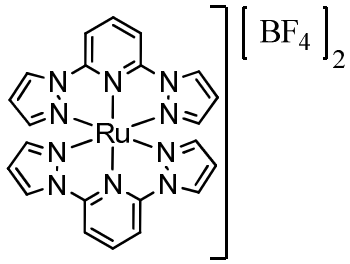

An ethylene glycol solution (20 cm^3) of $RuCl_3.3H_2O$ (104 mg, 0.40 mmol) and 1-bpp (175 mg, 0.83 mmol) was heated to 110°C for 4h. Once at RT, an insoluble black solid was removed from the orange-yellow solution by filtration and a saturated aqueous solution of $NaBF_4$ (20 cm^3) added to precipitate the tetrafluoroborate salt which was collected on a glass frit and washed with a few drops of H_2O, EtOH and Et_2O sequentially. Yellow powder, 170 mg, 61% yield. ^{1}H NMR ($MeNO_2$-d_3) δ = 6.61 (dd, J = 3.4, 2.1 Hz, 4H, 4'), 7.18 (d, J = 2.1 Hz, 4H, 3'), 8.26 (d, J = 8.2 Hz, 4H, 3), 8.58 (t, J = 8.6 Hz, 2H, 4), 8.83 (d, J = 3.5 Hz, 4H, 5'); ^{13}C NMR ($MeNO_2$-d_3) δ = 109.4 (3), 111.9 (4'), 133.9 (5'), 142.0 (4), 147.8 (3'), 151.5 (2).

6.6.16 ((2,6-Di(pyrazol-1'-yl)pyridine)(2,2':6',2''-terpyridine)) ruthenium (II) tetrafluoroborate

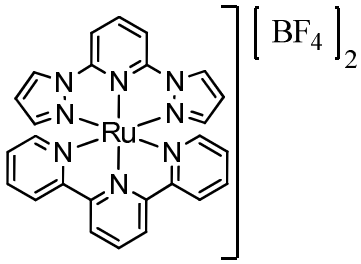

A MeOH suspension (15 cm^3) suspension of trichloro(2,2':6',2''-terpyridine)ruthenium (III) (88 mg, 0.20 mmol)and 1-bpp was heated to reflux in the presence of *N*-ethylmorpholine (5 drops). Once cool, the dark orange solution was filtered and saturated aqueous $NaBF_4$ (20 cm^3) was added. The precipitate was collected and washed with small volumes of H_2O, EtOH and Et_2O. Red powder, 70 mg, 49% yield. ^{1}H NMR ($MeNO_2$-d_3) δ = 6.57 (dd, J = 3.5, 2.2 Hz, 2H, 4'b), 7.12 (d, J = 2.2 Hz, 2H, 3'b), 7.23 (ddd, J = 7.7, 5.6, 1.3 Hz, 2H, 5't), 7.53 (ddd, J = 5.6, 1.3, 0.9 Hz, 2H, 6't), 7.97 (td, J = 7.7, 1.7 Hz, 2H, 4't), 8.33 (d, J = 8.5 Hz, 2H, 3b), 8.43 (t, J = 8.1 Hz, 1H, 4t), 8.52 (dd, J = 8.1, 0.9 Hz, 2H, 3't), 8.62 (t, J = 8.6 Hz, 1H, 4b), 8.72 (d, J = 8.1 Hz, 2H, 3t), 8.82 (d, J = 3.0 Hz, 2H, 5'b); ^{13}C NMR ($MeNO_2$-d_3) δ = 109.9 (3b), 111.9 (4'b), 124.2 (3t), 125.3 (3't), 128.6 (5't), 133.7 (5'b), 137.6 (4t), 139.6 (4't), 141.7 (4b), 147.3 (3'b), 150.4 (2b), 154.0 (6't), 158.4 (2t), 160.2 (2't).

6.7 Preparation of the solid solutions using *Bis*-(2,6-di(pyrazol-1'-yl)pyridine) iron(II) tetrafluoroborate, 25a, as the host material

6.7.1 Solid solutions of the form $[Fe(1\text{-}bpp)_2]_x[Ru(MeImpy)_2]_{1-x}[BF_4]_2$ where X = 0 – 1

X = 0.5: Solutions of **25a** (262 mg, 0.40 mmol) and **20a** (304 mg, 0.40 mmol) in $MeNO_2$ (50 cm^3) were combined, filtered and over a period of 3 days Et_2O was allowed to diffuse into the solutions to mediate full crystallisation. Visual and spectroscopic analyses concluded that the materials had crystallised separately and homogenously and no further characterisation of their solid state properties or composition is warranted.

6.7.2 Solid solutions of the form $[Fe(1\text{-}bpp)_2]_x[Ru(terpy)(Ctpy)]_{1-x}[BF_4]_2$ where X = 0 – 1

The chosen molar ratios of **25a** and **22a** were dissolved in $MeNO_2$ (5 cm^3), homogenously mixed and left and crystallised by vapour diffusion of Et_2O into the solutions over 3 days.

X = 0.91: **25a** (98 mg, 0.15 mmol) and **20a** (12 mg, 0.02 mmol) yielded a purple red-powder. 86.0 mg, 77% yield. Anal. Calcd for $(B_2C_{22}F_8FeH_{18}N_{10})_{0.91}(B_2C_{30}F_8H_{22}N_6Ru)_{0.09}$: Found: C, 41.25; H, 2.75; N, 20.59. Found: C, 40.75; H, 2.80; N, 21.05.

X = 0.82: **25a** (78 mg, 0.12 mmol) and **20a** (30 mg, 0.04 mmol) yielded a dark powder. 70.0 mg, 65% yield. Anal. Calcd for $(B_2C_{22}F_8FeH_{18}N_{10})_{0.82}(B_2C_{30}F_8H_{22}N_6Ru)_{0.18}$: C, 41.98; H, 2.81; N, 19.65. Found: C, 41.55; H, 2.90; N, 19.45.

X = 0.59: **25a** (52 mg, 0.08 mmol) and **20a** (59 mg, 0.08 mmol) gave a dark microcrystalline solid. 61.0 mg, 55% yield. Anal. Calcd for $(B_2C_{22}F_8FeH_{18}N_{10})_{0.59}(B_2C_{30}F_8H_{22}N_6Ru)_{0.41}$: C, 43.84; H, 2.84; N, 17.33. Found: C, 42.85; H, 2.95; N, 16.40.

X = 0.25: **25a** (26 mg, 0.04 mmol) and **20a** (88 mg, 0.12 mmol) yielded a dark polycrystalline material. 78.0 mg, 68% yield. Anal. Calcd for $(B_2C_{22}F_8FeH_{18}N_{10})_{0.25}(B_2C_{30}F_8H_{22}N_6Ru)_{0.75}$: C, 46.78; H, 2.94; N, 13.64. Found: C, 45.15; H, 3.10; N, 13.25.

X = 0.17: **25a** (8 mg, 0.01 mmol) and **20a** (84 mg, 0.11 mmol) yielded large dark purple crystals. 67.0 mg, 77% yield. Anal. Calcd for $(B_2C_{22}F_8FeH_{18}N_{10})_{0.17}(B_2C_{30}F_8H_{22}N_6Ru)_{0.83}$: C, 47.25; H, 2.99; N, 13.08. Found: C, 45.65; H, 3.15; N, 12.15.

6.8 References

1. G. Sheldrick, *Acta Crystallogr., Sect. A: Found. Crystallogr.*, 2008, 112-122.
2. M. Darabantu, L. Boully, A. Turck and N. Ple, *Tetrahedron*, 2004, **61**, 2897-2905.
3. D. Chizhov, K. Pashkevich and G. Roschenthaler, *J. Flourine Chem.*, 2003, **123**, 267-272.
4. E. Constable and M. Ward, *Dalton Trans.*, 1990, 1405-1409.
5. D. von Schriltz, M. Miles and C. Hauser, *J. Org. Chem.*, 1967, **32**, 1774-1778.
6. S. Work and C. Hauser, *J. Org. Chem.*, 1963, **28**, 725-730.
7. C. Boucher, M. Drew, P. Giddings, L. Harwood, M. Hudson, P. Iveson and C. Madic, *Inorg. Chem. Commun.*, 2002, **5**, 596-599.
8. E. Bejan, A. Ait Haddou, J. Daran and G. Balavoine, *Synthesis*, 1996, 1012-1018.
9. L. Beaufort, F. Benvenuti and A. Noels, *J. Mol. Catal. A: Chem.*, 2006, **260**, 210-214.
10. F. Fontana, F. Minisci, M. Barbosa and E. Vismara, *J. Org. Chem.*, 1991, **56**, 2866-2869.
11. E. Constable, A. Thompson, J. Cherryman and T. Liddiment, *Inorg. Chim. Acta.*, 1995, **235**, 165-171.
12. S. Son, K. Park, Y. Lee, B. Kim, C. Choi, M. Lah, Y. Jang, D. Jang and Y. Chung, *Inorg. Chem.*, 2004, **43**, 6896-6898.
13. H. Park, K. Kim, S. Choi, H. Kim, W. Lee, Y. Kang and Y. Chung, *Inorg. Chem.*, 2010, **49**, 7340-7352.
14. D. Jameson, J. Blaho, K. Kruger and K. Goldsby, *Inorg. Chem.*, 1989, **28**, 4312-4314.
15. D. Jameson and K. Goldsby, *J. Org. Chem.*, 1990, **55**, 4992-4994.
16. J. Elhaik, C. Pask, C. Kilner and M. Halcrow, *Tetrahedron*, 2007, **63**, 291-298.
17. S. Basak, P. Hui and R. Chandrasekar, *Synthesis*, 2009, 4042-4048.
18. G. Canard and C. Piguet, *Inorg. Chem.*, 2007, **46**, 3511-3522.
19. P. Evans, A. Spencer and G. Wilkinson, *Dalton Trans.*, 1973, 204-209.
20. M. Maestri, N. Armaroli, V. Balzani, E. Constable and A. C. Thompson, *Inorg. Chem.*, 1995, **34**, 2759-2767.

7 Appendix

Crystal	1-bppNO$_2$	1-bppDS	**1a**.MeNO$_2$	**2b**	**4a**.3MeNO$_2$
Molecular Formula	$C_{11}H_8N_6O_2$	$C_{22}H_{16}N_{10}S_2$	$B_2C_{29}F_8FeH_{23}N_9O_2$	$B_2C_{26}CoF_8H_{18}N_{10}$	$B_2C_{29}F_8FeH_{27}N_{13}O_6$
M_r	256.22	484.57	759.02	703.04	883.07
Class	Monoclinic	Triclinic	Monoclinic	Tetragonal	Monoclinic
Space group	C2/*c*	P-1	P2$_1$/*c*	P-42$_1$/*c*	P2$_1$/*c*
a / Å	13.042(2)	8.9223(13)	8.8102	8.7106	11.506
B / Å	9.6584(16)	10.2903(14)	8.8297	-	14.577
C / Å	9.7663(17)	13.341(2)	39.8492	19.178	23.439
α / °	90.00	90.512(6)	90.00	90.00	90.00
β / °	114.067(6)	107.862(7)	90.181	90.00	96.533
γ / °	90.00	100.271(6)	90.00	90.00	90.00
V / Å^3	1123.2(3)	1144.5(3)	3099.9	1455.1	3890.7
Z	4	2	4	2	4
T / K	150	150	150	150	150
Rad. Source	Mo-Kα	Mo-Kα	Mo-Kα	Mo-Kα	Mo-Kα
μ / mm^{-1}	0.71073	0.71073	0.581	0.679	0.485
Measured reflections	4359	38438	64980	29757	116433
Independent Reflections	2124	9310	5507	2176	11369
Independent Reflections > 2σ	1395	7103	5030	2102	7058
R_{int}	0.1076	0.0650	0.050	0.063	0.086
R_1, I > 2σ(*I*)[a]	0.0751	0.0480	0.072	0.061	0.073
wR_2, all data[b]	0.2588	0.1813	0.171	0.133	0.234
Goodness of fit	1.703	1.2734	1.113	1.132	1.043

Crystal	**4b**	**6b**.2$MeNO_2$	**20a**.$MeNO_2$	**27a**.4$MeNO_2$	**27b**
Molecular Formula	$B_2C_{26}CoF_8H_{18}N_{10}$	$B_2C_{24}CoF_8H_{20}N_{16}O_4$	$B_2C_{27}F_8H_{29}N_{11}O_2Ru$	$B_2C_{28}F_8FeH_{34}N_{14}O_8$	$C_{24}Cl_2FeH_{22}N_{10}O_8$
M_r	703.04	829.07	814.28	924.12	695.17
Class	Monoclinic	Monoclinic	Monoclinic	Tetragonal	Monoclinic
Space group	$P2_1/c$	$C2/c$	$C2/c$	$I\text{-}4c2$	$P2_1/n$
a / Å	18.672	16.3196	17.337(2)	16.2226(3)	8.4719(3)
B / Å	10.146	15.2244	21.751(2)	16.2226(3)	8.5349(3)
C / Å	15.074	29.303	18.712(3)	14.8493(5)	39.1597(12)
α / °	90.00	90.00	90.00	90.00	90.00
β / °	98.816	100.352	99.186(8)	90.00	91.010(3)
γ / °	90.00	90.00	90.00	90.00	90.00
V / $Å^3$	2821.9	7162	6965.7(15)	3907.93(17)	2831.06(15)
Z	4	8	8	4	4
T / K	150	150	150	100	100
Rad. source	Mo-Kα	Mo-Kα	Mo-Kα	Mo-Kα	Cu-Kα
μ / mm^{-1}	0.700	0.587	0.71073	0.71073	1.54184
Measured reflections	86656	45108	93662	10584	8717
Independent Reflections	17974	3332	11922	2478	4951
Independent Reflections > 2σ	9943	3038	6999	2234	4490
R_{int}	0.1105	0.070	0.1294	0.1026	0.0378
R_1, I > 2σ(*I*)[a]	0.0589	0.100	0.0715	0.0952	0.0333
wR_2, all data[b]	0.194	0.342	0.2148	0.2860	0.0859
Goodness of fit	1.011	1.877	1.046	2.140	1.049

Crystal	**27b**	**27b**	**27b**.4$MeNO_2$	**27c**	**28a**.$^1/_2$$MeNO_2$
Molecular Formula	$C_{24}Cl_2FeH_{22}N_{10}O_8$	$C_{24}Cl_2FeH_{22}N_{10}O_8$	$C_{28}Cl_2FeH_{34}N_{14}O_{16}$	$C_{24}F_{12}FeH_{22}N_{10}O_8P_2$	$B_2C_{28.5}F_8FeH_{23.5}N_{14.5}O$
M_r	695.17	695.17	939.33	924.27	814.55
Class	Monoclinic	Monoclinic	Tetragonal	Monoclinic	Triclinic
Space group	$P2_1/n$	$P2_1/n$	I-4*c*2	I2/*a*	P-1
a / Å	8.5622(8)	8.5607(8)	16.3995(3)	15.2542(6)	10.8739(7)
B / Å	8.5622(8)	8.6545(6)	16.3995(3)	10.9900(4)	15.8851(10)
C / Å	39.271(12)	39.632(3)	14.9340(7)	18.7822(8)	19.5405(14)
α / °	90.00	90.00	90.00	90.00	92.046(6)
β / °	90.00	90.812(8)	90.00	99.561(4)	103.220(6)
γ / °	90.00	90.00	90.00	90.00	91.971(5)
V / $Å^3$	2879.0(10)	2936.0(4)	4016.4(2)	3105.0(2)	3280.6(4)
Z	4	4	4	4	4
T / K	200	290	150	100	100
Rad. Source	Mo-Kα	Cu-Kα	Mo-Kα	Mo-Kα	Mo-Kα
μ / mm^{-1}	0.71073	1.54184	0.71073	0.71073	0.71073
Measured reflections	9217	9232	28490	11544	40026
Independent Reflections	5810	5407	4864	3812	15749
Independent Reflections > 2σ	4564	3431	4717	3191	6762
R_{int}	0.0972	0.1541	0.0617	0.0492	0.2149
R_1, I > 2σ(*I*)[a]	0.0752	0.1114	0.0602	0.0380	0.0909
wR_2, all data[b]	0.1581	0.3345	0.1608	0.1363	0.2670
Goodness of fit	1.137	1.089	1.213	0.935	0.946

Crystal	**28a**.$^1/_2$MeNO$_2$	**28a**.$^1/_2$MeNO$_2$	**28a**.2MeNO$_2$.Et$_2$O	**28a**.2MeNO$_2$.Et$_2$O	**28a**.2MeNO$_2$.Et$_2$O
Molecular Formula	$B_2C_{28.5}F_8FeH_{23.5}N_{14.5}O$	$B_2C_{28.5}F_8FeH_{23.5}N_{14.5}O$	$B_2C_{34}F_8FeH_{38}N_{16}O_5$	$B_2C_{34}F_8FeH_{38}N_{16}O_5$	$B_2C_{34}F_8FeH_{38}N_{16}O_5$
M_r	814.55	814.55	980.23	980.23	980.23
Class	Triclinic	Triclinic	Triclinic	Triclinic	Triclinic
Space group	P-1	P-1	P-1	P-1	P-1
a / Å	11.0949(12)	11.1653(13)	11.8280(4)	11.8949(8)	11.8642(16)
b / Å	16.1941(16)	16.3197(19)	12.7687(4)	12.8666(9)	12.9995(10)
c / Å	19.6976(19)	19.714(2)	13.7564(4)	13.9705(10)	14.3634(14)
α / °	93.018(8)	93.241(10)	101.993(3)	102.163(6)	101.882(7)
β / °	102.632(9)	102.605(10)	98.975(3)	99.544(6)	101.152(10)
γ / °	92.866(9)	93.165(9)	96.207(3)	96.079(6)	95.112(9)
V / Å^3	3441.8(6)	3491.6(7)	1986.03(11)	2039.1(2)	2107.6(4)
Z	4	4	2	2	2
T / K	290	350	100	200	265
Rad. Source	Mo-Kα	Mo-Kα	Mo-Kα	Mo-Kα	Mo-Kα
μ / mm^{-1}	0.71073	0.71073	0.71073	0.71073	0.71073
Measured reflections	50919	50238	25910	25038	23006
Independent Reflections	16743	17264	9734	9865	9144
Independent Reflections > 2σ	4591	4290	7085	5234	3964
R_{int}	0.3591	0.3930	0.0950	0.1884	0.2455
R_1, I > 2σ(I)[a]	0.1083	0.1098	0.0640	0.1079	0.1318
wR_2, all data[b]	0.3141	0.3539	0.1629	0.2554	0.3227
Goodness of fit	0.998	0.956	1.035	1.228	1.280

Crystal	**28a**.2MeNO$_2$	**28b**.$^1/_2$MeNO$_2$	**28b**.$^1/_2$MeNO$_2$	**28c**.2MeNO$_2$	**32a**.2MeOH
Molecular Formula	$B_2C_{30}F_8FeH_{28}N_{16}O_4$	$C_{28.5}Cl_2FeH_{23.5}N_{14.5}O_9$	$C_{28.5}Cl_2FeH_{23.5}N_{14.5}O_9$	$C_{30}F_{12}FeH_{28}N_{16}O_4P_2$	$B_2C_{24}F_8FeH_{26}N_{10}O_4$
M_r	906.11	839.84	839.84	1022.43	747.99
Class	Triclinic	Triclinic	Triclinic	Monoclinic	Triclinic
Space group	P-1	P-1	P-1	$P2_1/c$	P-1
a / Å	12.7159(4)	10.9972(6)	11.190(2)	18.2548(6)	11.8299(12)
b / Å	15.7893(5)	15.9276(11)	16.263(3)	15.3399(4)	13.2017(18)
c / Å	19.3269(6)	19.6673(14)	19.662(3)	15.7211(6)	13.2459(13)
α / °	95.574(3)	92.794(6)	93.203(14)	90.00	73.272(7)
β / °	103.300(3)	101.907(6)	102.056(14)	113.086(4)	63.487(5)
γ / °	100.220(3)	92.702(5)	93.449(15)	90.00	63.525(5)
V / Å^3	3677.6(2)	3361.0(4)	3484.3(11)	4049.8(2)	1646.8(3
Z	4	4	4	4	2
T / K	100	100	290	100	150
Rad. source	Mo-Kα	Mo-Kα	Mo-Kα	Mo-Kα	Mo-Kα
μ / mm^{-1}	0.71073	0.71073	0.71073	0.71073	0.71073
Measured reflections	28439	46440	25830	29549	42666
Independent Reflections	16858	16381	15386	9959	11605
Independent Reflections > 2σ	14081	7060	5019	7910	8163
R_{int}	0.0709	0.2624	0.2905	0.0601	0.1023
R_1, I > 2σ(I)[a]	0.0589	0.1171	0.0942	0.0436	0.0775
wR_2, all data[b]	0.1925	0.2246	0.2428	0.0958	0.2538
Goodness of fit	1.335	1.064	0.986	1.027	1.034

Crystal	**32b**.2MeOH	**32c**.2MeOH	**33a**.H_2O	**33c**	**35a**
Molecular Formula	$C_{24}Cl_2FeH_{26}N_{10}O_{12}$	$C_{24}F_{12}FeH_{26}N_{10}O_4P_2$	$B_2C_{24}F_8FeH_{24}N_{10}O_3$	$C_{24}F_{12}FeH_{22}N_{10}O_2P_2$	$B_2C_{24}F_8FeH_{22}N_{10}S_2$
M_r	773.28	864.31	719.16	828.28	721.91
Class	Monoclinic	Orthorhombic	Orthorhombic	Monoclinic	Orthorhombic
Space group	$P2_1/c$	P*ccn*	P*bca*	$P2_1/c$	P*bcn*
a / Å	12.478(3)	12.46201(17)	34.612(2)	19.0570(3)	18.1992(3)
b / Å	28.434(7)	28.4031(4)	10.7827(10)	9.72803(13)	10.2991(2)
c / Å	18.806(5)	18.7480(3)	15.9463(16)	16.9819(2)	15.5914(3)
α / °	90.00	90.00	90.00	90.00	90.00
β / °	90.202(13)	90.00	90.00	106.2656(16)	90.00
γ / °	90.00	90.00	90.00	90.00	90.00
V / $Å^3$	6672(3)	6636.03(16)	5951.4(9)	3022.21(8)	2922.38(10)
Z	8	8	8	4	4
T / K	150	100	100	100	100
Rad. source	Mo-Kα	Cu-Kα	Mo-Kα	Cu-Kα	Cu-Kα
μ / mm^{-1}	0.71073	1.54184	0.71073	1.54184	1.54184
Measured reflections	223932	17673	17387	11462	7466
Independent Reflections	23288	6582	5158	5937	2878
Independent Reflections > 2σ	15189	5707	3295	5536	2642
R_{int}	0.1222	0.0409	0.1827	0.0361	0.0531
R_1, I > 2σ(*I*)[a]	0.0840	0.0330	0.1261	0.0334	0.0493
wR_2, all data[b]	0.2882	0.1060	0.2917	0.0879	0.1371
Goodness of fit	1.822	0.5334	1.103	0.5983	1.062

Crystal	**35a**	**35a**	**37a**	**37a**	**38a**
Molecular Formula	$B_2C_{24}F_8FeH_{22}N_{10}S_2$	$B_2C_{24}F_8FeH_{22}N_{10}S_2$	$B_2C_{22}F_{10}FeH_{16}N_{10}$	$B_2C_{22}F_{10}FeH_{16}N_{10}$	$B_2Cl_2F_8FeH_{16}N_{10}$
M_r	721.91	721.91	711.91	711.91	744.82
Class	Orthorhombic	Orthorhombic	Monoclinic	Monoclinic	Orthorhombic
Space group	P*bcn*	P*bcn*	$P2_1$	C*c*	P*bcn*
a / Å	53.2503(12)	54.2154(15)	8.4314(14)	12.2891(3)	17.7251(3)
b / Å	10.6457(4)	10.7072(6)	8.5715(11)	11.8379(3)	9.25231(17)
c / Å	16.0369(4)	16.1589(6)	18.352(3)	19.0184(4)	16.6822(3)
α / °	90.00	90.00	90.00	90.00	90.00
β / °	90.00	90.00	97.240(19)	99.2038(19)	90.00
γ / °	90.00	90.00	90.00	90.00	90.00
V / $Å^3$	9091.1(5)	9380.2(7)	1315.7(3)	2731.13(10)	2735.84(9)
Z	12	12	2	4	4
T / K	240	290	150	290	100
Rad. source	Cu-Kα	Cu-Kα	Cu-Kα	Cu-Kα	Cu-Kα
μ / mm^{-1}	1.54184	1.54184	1.54184	1.54184	1.54184
Measured reflections	22476	23206	4982	5176	11479
Independent Reflections	8098	8367	3416	3195	2746
Independent Reflections > 2σ	5602	5363	3171	3075	2552
R_{int}	0.1210	0.1292	0.1081	0.0539	0.0415
R_1, I > 2σ(*I*)[a]	0.0899	0.0911	0.1024	0.0505	0.0387
wR_2, all data[b]	0.2669	0.2944	0.2936	0.1571	0.1066
Goodness of fit	1.024	1.035	1.2914	1.098	1.037

Crystal	**39a**	**39a**	**39a**	**40a**
Molecular Formula	$B_2Br_2C_{22}F_8FeH_{16}N_{10}$	$B_2Br_2C_{22}F_8FeH_{16}N_{10}$	$B_2Br_2C_{22}F_8FeH_{16}N_{10}$	$B_2C_{22}F_8FeH_{16}I_2N_{10}$
M_r	833.72	833.72	833.72	927.71
Class	Orthorhombic	Orthorhombic	Orthorhombic	Orthorhombic
Space group	P*bcn*	P*bcn*	P*bcn*	P*bcn*
a / Å	17.8625(3)	17.5486(9)	17.2631(5)	16.8364(4)
b / Å	9.36656(16)	9.9817(9)	10.4120(5)	11.1465(5)
c / Å	16.5749(3)	16.4985(11)	16.6989(8)	15.5406(5)
α / °	90.00	90.00	90.00	90.00
β / °	90.00	90.00	90.00	90.00
γ / °	90.00	90.00	90.00	90.00
V / $Å^3$	2773.15(8)	2890.0(4)	3001.5(2)	2916.46(17)
Z	4	4	4	4
T / K	100	250	350	100
Rad. source	Cu-Kα	Cu-Kα	Cu-Kα	Mo-Kα
μ / mm^{-1}	1.54184	1.54184	1.54184	0.71073
Measured reflections	10444	5624	5966	15286
Independent Reflections	2768	2735	2854	2976
Independent Reflections > 2σ	2541	2006	1820	2445
R_{int}	0.0386	0.1112	0.1228	0.0434
R_1, I > 2σ(*I*)[a]	0.0350	0.0918	0.0906	0.0323
wR_2, all data[b]	0.0897	0.2807	0.2745	0.0719
Goodness of fit	1.0497	1.057	1.560	1.053

Table 25 – Experimental details and crystallographic parameters for the single crystal structure determinations discussed. [a] $\Sigma[|F_o| - |F_c|]/\Sigma|F_o|$. [b] $wR = [\Sigma w(F_o^2 - F_c^2)/\Sigma wF_o^4]^{1/2}$..